ILLINOIS CENTER FOR TRANSPORTATION

Report No. FHWA-ICT-26-004

Optimizing the Use of Local Aggregate in Stone-Mastic Asphalt

Imad L. Al-Qadi
Javier J. García Mainieri
Hong Lang
Lara Diab
Greg Renshaw

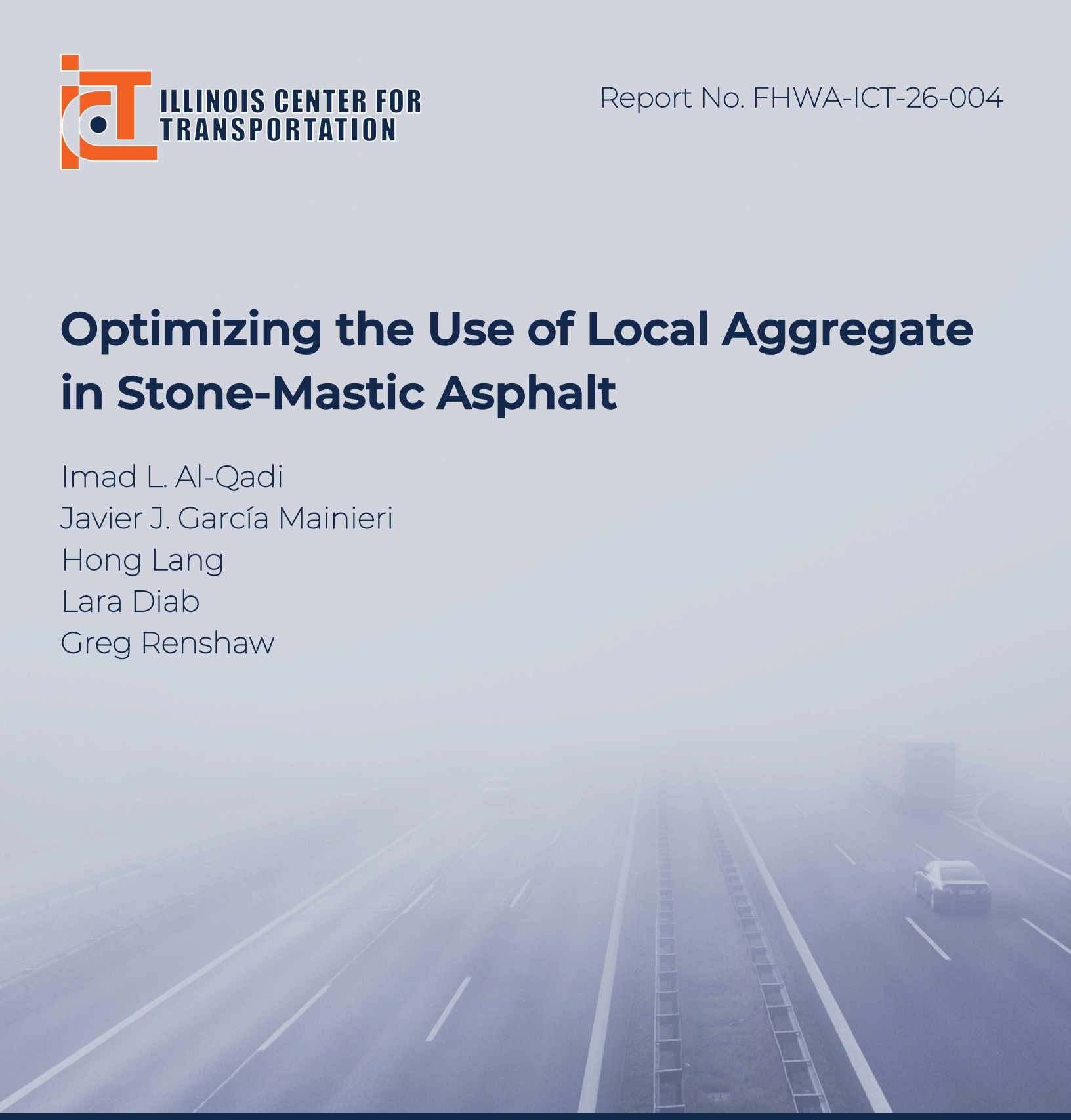

ICT Project R27-216

April 2026

ISSN: 0197-9191
ICT Series Report No. 26-004
https://doi.org/10.36501/0197-9191/26-004

TECHNICAL REPORT DOCUMENTATION PAGE

1. Report No.	2. Government Accession No.	3. Recipient's Catalog No.
FHWA-ICT-26-004	N/A	N/A

4. Title and Subtitle	5. Report Date
Optimizing the Use of Local Aggregate in Stone-Mastic Asphalt	April 2026
	6. Performing Organization Code N/A

7. Authors	8. Performing Organization Report No.
Imad L. Al-Qadi (https://orcid.org/0000-0002-5824-103X), Javier J. García Mainieri, (https://orcid.org/0000-0002-8302-474X), Hong Lang (https://orcid.org/0000-0003-1015-5797), Lara Diab (https://orcid.org/0000-0001-8489-2015), Greg Renshaw	ICT-26-004 UILU-2026-2004

9. Performing Organization Name and Address	10. Work Unit No.
Illinois Center for Transportation Department of Civil and Environmental Engineering University of Illinois Urbana-Champaign 205 North Mathews Avenue, MC-250 Urbana, IL 61801	N/A **11. Contract or Grant No.** R27-216

12. Sponsoring Agency Name and Address	13. Type of Report and Period Covered
Illinois Department of Transportation (SPR) Bureau of Research 126 East Ash Street Springfield, IL 62704	Final Report 8/16/20–4/30/26 **14. Sponsoring Agency Code**

15. Supplementary Notes

Conducted in cooperation with the U.S. Department of Transportation, Federal Highway Administration.

https://doi.org/10.36501/0197-9191/26-004

16. Abstract

This study investigated the potential pavement performance, resiliency, cost-effectiveness, and environmental efficiency of incorporating locally sourced Illinois aggregates into stone-mastic asphalt (SMA) through an integrated laboratory and full-scale assessment. SMAs were designed using local aggregates with different lithology and durability levels. The potential performance of SMAs with local aggregates was benchmarked against those using imported aggregates. Optimized SMA designs with local aggregates were developed, and aggregate degradation was quantified at successive stages of mixture production, construction, and loading. Full-scale pavement sections were built; six SMAs were placed on top of a 2 in hot-mix asphalt binder layer overlaying continuously reinforced concrete pavement. The sections were instrumented and tested using the Illinois Accelerated Pavement Tester. Varying loading configurations and temperatures were applied to measure the response of each section. Then, the pavement was loaded under constant tandem loads at approximately 80°F. Pavement performance was interpreted using SMA strains and surface rut depth. Peak transverse tensile strain proved effective for characterizing viscoelastic recovery and distinguishing mixture behavior under repeated loading. The strain-based recovery measurements were incorporated into a viscoelastic-based rutting progression framework and used to compare SMA performance. Aggregate breakage was measured and was primarily associated with compaction and laboratory loading processes, whereas accelerated traffic loading produced negligible additional degradation, indicating that aggregate stability was governed by mixture design and construction rather than in-service loading. Life cycle assessment and life cycle cost analysis suggested that using local aggregates is not only cost effective, but also reduces negative environmental impacts while maintaining SMA's expected performance and resiliency. Through integrated laboratory mixture design and performance testing, full-scale pavement construction, accelerated pavement testing, instrument responses, and life cycle cost analysis and environmental assessment, this study demonstrated that SMA incorporating locally sourced Illinois aggregates could achieve performance comparable to conventional SMA while reducing costs and environmental impact. Hence, this study recommends designing and adopting 50 gyration SMA with local aggregates.

17. Key Words	18. Distribution Statement
Stone-Mastic Asphalt, Local Aggregates, Aggregate Gradation, Mix Design, Life Cycle Assessment, Life Cycle Cost Analysis	No restrictions. This document is available through the National Technical Information Service, Springfield, VA 22161.

19. Security Classif. (of this report)	20. Security Classif. (of this page)	21. No. of Pages	22. Price
Unclassified	Unclassified	202+ appendices	N/A

Form DOT F 1700.7 (8-72) **Reproduction of completed page authorized**

ACKNOWLEDGMENT, DISCLAIMER, MANUFACTURERS' NAMES

This publication is based on the results of **ICT-R27-216: Optimizing the Use of Local Aggregates in Stone-Mastic Asphalt**. ICT-R27-216 was conducted in cooperation with the Illinois Center for Transportation; the Illinois Department of Transportation; and the U.S. Department of Transportation, Federal Highway Administration.

Members of the Technical Review Panel (TRP) were the following:

- Brian Hill, TRP Chair, Illinois Department of Transportation
- David Adedokun, Federal Highway Administration
- Dennis Bachman, Federal Highway Administration (Retired)
- Dan Barnstable, Vulcan Materials Company
- Sheila Beshears, RiverStone Group
- Kevin Burke, Illinois Asphalt Pavement Association
- Dan Eichholz, Illinois Association of Aggregate Producers
- Greg Heckel, Illinois Department of Transportation
- Stephen Jones, Illinois Department of Transportation
- Ally Kelley, Illinois Department of Transportation
- Jeff Kern, Open Road Paving
- Tim Murphy, Murphy Pavement Technology
- Bill Pine, Heritage Construction and Materials
- John Senger, Illinois Department of Transportation
- Andrew Stolba, Illinois Department of Transportation
- Jim Trepanier, Former TRP Chair, Illinois Department of Transportation (Retired)
- Ron Wagoner, Illinois Department of Transportation

The authors acknowledge ICT doctoral students William Villamil for his work on performing the finite element analysis to determine the thickness and temperature corrections of pavement responses and Aditya Singh for his work on the development of the rutting prediction models. They also recognize

those who assisted with instrumentation and lab testing, including ICT research engineers Mohsen Motlagh and Uthman Mohamed Ali, as well as all ICT graduate students.

EXECUTIVE SUMMARY

Stone-mastic asphalt (SMA) provides superior durability and rutting resistance compared with dense-graded hot-mix asphalt (HMA). However, its use in Illinois has been limited due to the relatively higher initial costs, largely driven by the need to import high-quality aggregates from out of state. SMAs incorporating locally available Illinois aggregates were designed in a lab, produced in a plant, and constructed at a full-scale testing facility. The research focused on optimizing SMA design. The laboratory design compaction effort was reduced, while the aggregate skeleton was preserved. Volumetric analysis and performance tests were conducted on the developed SMA designs. The laboratory findings were validated using full-scale accelerated pavement testing. In addition, life cycle cost analysis and life cycle assessment were performed to quantify the economic and environmental benefits, respectively. All testing and analysis of designed SMA with local aggregates were benchmarked against that of SMA with known imported durable aggregates.

In addition to volumetrics, laboratory testing addressed cracking and rutting potential, complex modulus, moisture susceptibility, and aggregate breakage potential. The SMAs were designed using both imported control aggregates and Illinois local aggregates with varying lithologies and qualities. Reduced design compaction was considered and applied to limit aggregate degradation while maintaining stone-on-stone contact, attempting to ensure stability and rutting resistance.

Aggregate breakage was evaluated systematically at multiple stages of the SMA life cycle, including after laboratory design compaction, Hamburg wheel-tracking testing, field compaction during construction, and full-scale accelerated pavement testing. Aggregate breakage was observed during laboratory compaction, laboratory loading, and field compaction, with the magnitude governed by aggregate quality and compaction effort. In contrast, little to no additional aggregate breakage was measured following accelerated pavement testing, indicating that once the SMA aggregate skeleton was established during construction, it remained stable under severe repeated traffic loading. The findings highlighted the critical role of mixture design and construction processes—rather than in-service traffic loading—in controlling SMA aggregate breakage. SMA possible aggregate friction loss is an important component that requires consideration.

To validate laboratory findings, six SMAs were produced at an asphalt plant and constructed as part of full-scale pavement section overlays of a continuously reinforced concrete pavement (CRCP). Dense-graded HMA was used above the CRCP and below the SMA to provide support for the SMA. The sections were instrumented and tested under controlled loading configurations and a range of temperatures to measure the pavement behavior under various loading and environmental conditions using the Illinois Accelerated Pavement Tester, which applied both single- and tandem-axle loading configurations. Pavement responses, recovery behavior, surface deformation, and post-testing aggregate degradation were measured.

Pavement recovery and SMA response under accelerated loading were characterized. Peak transverse tensile strain at the bottom of the SMA effectively captured the viscoelastic recovery between successive wheel loads. The difference in transverse tensile strain response and recovery rate was used to distinguish SMAs and calculate rutting progression.

All SMA sections exhibited excellent resiliency under accelerated loading, with minimal observed SMA surface rutting. Because rutting was limited and pavement responses were strongly influenced by temperature, a viscoelastic-shear-based rutting progression model was employed to characterize performance. This approach isolated the viscoelastic behavior, allowing meaningful differentiation among SMA aggregates when conventional rut-depth measurements alone were insufficient.

The combined life cycle assessment (LCA) and life cycle cost analysis (LCCA) results demonstrated that aggregate source location strongly influenced the long-term environmental and economic performance of SMA pavements. Although locally sourced aggregates resulted in higher acidification impacts during material production and, in some cases, shorter rutting-based service life, these effects were offset by substantially lower transportation-related impacts. Long-haul transport of non-local aggregates consistently increased life cycle environmental burdens. From a cost perspective, earlier or additional rehabilitation required for local-aggregate SMA increased discounted rehabilitation costs, but these increases were generally smaller than the savings from reduced hauling. Overall, the results indicate that the use of local aggregates can provide net environmental and economic benefits when evaluated over the full pavement life cycle.

Through integrated laboratory mixture design and performance testing, full-scale pavement construction, accelerated pavement testing, instrument responses, and life cycle cost analysis and environmental assessment, this study demonstrated that SMA incorporating locally sourced Illinois aggregates could achieve performance comparable to conventional SMA while reducing costs and environmental impact. Hence, this study recommends designing and adopting 50 gyration SMA with local aggregates assuming adequate friction characteristics are maintained.

TABLE OF CONTENTS

CHAPTER 1: INTRODUCTION 1

BACKGROUND 1

OBJECTIVES AND SCOPE 3

METHODOLOGY 4

Task 1: Laboratory Design and Experimental Program 4

Task 2: Full-scale Pavement Construction and Instrumentation 5

Task 3: Accelerated Pavement Testing 5

Task 4: Life Cycle Assessment and Life Cycle Cost Analysis 5

IMPACT 5

CHAPTER 2: SMA DESIGN AND POTENTIAL PERFORMANCE 7

SMA DESIGN PARAMETERS AND LIMITATIONS 7

COARSE AGGREGATE SELECTION AND CHARACTERIZATION 8

Aggregate Qualities 9

Aggregate Shape and Texture 10

OTHER SMA COMPONENTS 11

VOLUMETRIC DESIGN 11

SMAs Modified with Hydrated Lime 13

SMA POTENTIAL PERFORMANCE 14

AGGREGATE BREAKAGE IN THE LABORATORY 17

EFFECT OF AGGREGATE QUALITY AND SKELETON ON SMA STABILITY 18

SUMMARY 22

CHAPTER 3: FULL-SCALE PAVEMENT TEST SECTIONS 23

PAVEMENT SECTION LAYOUTS 23

PAVEMENT LAYER CONSTRUCTION 25

HMA Binder Preparation 27

SMA Paving 27

SMA PRODUCTION PROPERTIES 31

Binder Contents (P_b) 32

Aggregate Gradation 32
Volumetrics 34
Asphalt Binder Quality 35
SMA FIELD DENSITY AND THICKNESS 36
CRACKING AND RUTTING POTENTIAL 39
DYNAMIC MODULI OF SMA WITH LOCAL AGGREGATES 40
SMA AGGREGATE SKELETON AFTER CONSTRUCTION 42
SUMMARY 48
CHAPTER 4: INSTRUMENTATION RESPONSE ANALYSIS 49
INSTRUMENTATION 49
Earth Pressure Cells 50
Strain Gauges 52
Temperature Sensors 55
Instrument Connection and Data Acquisition System 58
ILLINOIS ACCELERATED PAVEMENT TESTER 59
Remote Monitoring and Data Transfer 59
Temperature Control 60
Single and Tandem Half-Axle Loading 61
Tires 62
Axle Spacing 63
SENSOR DATA ACQUISITION AND PROCESSING 63
TEST SCENARIOS WITH VARYING LOADING CONFIGURATIONS 67
PAVEMENT RESPONSES 69
Effects of Temperature and Layer Thickness on SMA Measurements 70
Effect of a Tandem Axle on Pavement Responses 91
Relative Comparison of Peaks across Tandem-Axle Loading Conditions 95
Effect of SMA on Pavement Recovery 117
Differential Tire Inflation Pressure Impact on Pavement Response 120
SUMMARY 126
CHAPTER 5: ACCELERATED LOADING OF FULL-SCALE SMA PAVEMENT SECTIONS 128

PAVEMENT RESPONSES DURING CONTINOUS LOADING 129
RUTTING PROGRESSION 136
Permanent Deformation Measurements 136
Verification of Measurement Goodness 142
Permanent Deformation Results 146
AGGREGATE BREAKAGE AFTER I-APT LOADING 147
PAVEMENT RECOVERY DURING LOADING 148
RELATIONSHIP BETWEEN I-APT AND HWTT RUTTING MEASUREMENTS 152
RELATIONSHIP BETWEEN I-APT AND HWTT BASED ON SMA AGGREGATE SKELETON AND PROPERTIES 153
RUTTING PREDICTION MODEL FOR SMA OVERLAYS 155
Surrogate for Mechanistic Input 157
Rutting Model Calibration and Validation 158
Estimating Parameter C from Mixture Characteristics 160
SUMMARY 162

CHAPTER 6: BENEFIT QUANTIFICATION 164
BACKGROUND 164
LIFE CYCLE ASSESSMENT METHODOLOGY 165
Goal and Scope Definition 165
Life Cycle Inventory 168
LIFE CYCLE IMPACT ASSESSMENT 176
Results 176
LIFE CYCLE COST ANALYSIS 180
Goal and Scope 180
Net Present Worth Formulation 181
Results 181
SUMMARY 183

CHAPTER 7: SUMMARY, FINDINGS, CONCLUSIONS, AND RECOMMENDATIONS 185
SUMMARY 185
FINDINGS 186

CONCLUSIONS **188**
RECOMMENDATIONS **188**

REFERENCES **190**

APPENDIX A: CURRENT STATE OF KNOWLEDGE OF STONE-MASTIC ASPHALT **203**
CONSTITUENT MATERIALS OF SMA **203**
Aggregates 203
Asphalt Binder 203
Mineral Fillers 204
Fibers 205
ADVANTAGES AND CHALLENGES OF USING SMA **206**
STONE-MASTIC ASPHALT DESIGN **206**
Gyration Number 206
Nominal Maximum Aggregate Size 208
Aggregate Proportioning 208
CURRENT USE AND SPECIFICATIONS IN ILLINOIS **210**
Aggregate Sources Available in Illinois 211
Current Stone-Mastic Asphalt Specifications in Illinois 211
Current Performance Tests in Illinois for SMA Design Approval 214
Stone-Mastic Asphalt Construction Particularities Specified in Illinois 214
USE AND SPECIFICATION OF SMA IN OTHER STATES **214**
Use and Specification of SMA in Other Countries 218
ADDITIONAL PERFORMANCE TESTS FOR STONE-MASTIC ASPHALT DESIGN APPROVAL **219**
Aggregate Breakdown 219

APPENDIX B: ACCELERATED PAVEMENT TESTING INSTRUMENTATION **221**
ILLINOIS ACCELERATED PAVEMENT TESTING **221**

APPENDIX C: QUARRY SURVEY AND RESPONSES **224**
SURVEY SAMPLE **224**
RESPONSES **228**

APPENDIX D: DISTRICT QUESTIONNAIRE AND RESPONSES **233**

QUESTIONNAIRE 233
RESPONSES 235
APPENDIX E: I-APT SMA DESIGNS 240
APPENDIX F: I-APT HMA LAYER MIX DESIGN 262
APPENDIX G: FIELD CORE AGGREGATE GRADATIONS 263
APPENDIX H: CRITICAL RESPONSES FOR VARIOUS LOADING SCENARIOS 266
APPENDIX I: PAVEMENT SECTION RESPONSES 287
APPENDIX J: LISTS OF QUARRIES 353

LIST OF FIGURES

Figure 1. Photo. Field core from an interstate project with broken carbonate crushed stone. 2
Figure 2. Schematic. Aggregate breakage measurement..... 3
Figure 3. Equation. Aggregate breakage index..... 3
Figure 4. Graph. Visual description of an aggregate breakage gradation curve. 4
Figure 5. Graph. LA abrasion histogram for CA from Illinois. 8
Figure 6. Graph. FI of laboratory SMAs. 14
Figure 7. Graph. HWTT rut progression of laboratory SMAs. 15
Figure 8. Graph. Conditioned and unconditioned ITS and TSR of laboratory SMAs. 16
Figure 9. Graph. Individual specimen indirect tensile strength and sensitivity to air voids. 16
Figure 10. Graph. Breakage plots for laboratory-produced, laboratory-compacted SMA. 17
Figure 11. Graph. ABI for laboratory-produced, laboratory-compacted SMA. 18
Figure 12. Graph. Relationship between rutting potential and CA quality. 20
Figure 13. Graph. Relationship between HWTT rut depth and ABI after compaction to 7.5 ± 0.5% air void content and 62 mm height. 20
Figure 14. Graph. Shape of smaller coarse aggregate stockpile versus ABI after design compaction. . 21
Figure 15. Graph. Relationship between ABI and aggregate qualities. 22
Figure 16. Photo. Southmost lane of the ICT full-scale testing yard. 23
Figure 17. Illustration. Pavement section. 24
Figure 18. Schematic. Test strip layout with as-built lengths of SMA. 24
Figure 19. Schematic. Side view of test section locations with I-APT for reference. 24
Figure 20. Graph. Transverse cross-section of the pavement with shear strain distribution. 25
Figure 21. Photo. Bare CRCP supports the HMA and SMA layers. 26
Figure 22. Photo. CRCP tack coat application. 26
Figure 23. Photo. N90E mix paving. 27
Figure 24. Photo. Coating between layers. 28
Figure 25. Photo. Material transfer device and paver used to pave SMA sections. 29
Figure 26. Graph. VMA increase to compensate for loss through plant. 31
Figure 27. Graph. Difference in aggregate gradations between design and after plant production. ... 34

Figure 28. Graph. Laboratory- and plant-produced binder absorption. 35
Figure 29. Photo. Steps for obtaining SMA cores. 37
Figure 30. Graph. (a) Comparison of densities measured with nuclear gauge and from field cores, and (b) comparison of G_{mm} of laboratory- and plant-produced samples. 38
Figure 31. Graph. Flexibility index comparison of SMA after STA and LTA. 39
Figure 32. Graph. HWTT results: (a) STA comparison, and (b) rut progression for L2-50-12.5-0. 40
Figure 33. Graph. SMA master curves at 68°F reference temperature. 41
Figure 34. Graph. Moduli and phase angle of SMAs at 5 Hz and 82°F. 42
Figure 35. Bar plot. Aggregate breakage in plant-produced SMA 42
Figure 36. Photo. Sawed aggregate removal procedure. 43
Figure 37. Graph. Field core breakage 44
Figure 38. Box Plot. Field core ABIs. 45
Figure 39. Bar plot. Flat, elongated, and flat and elongated particle counts for respective predominant stockpiles on samples passing the #8 and retained on the #4 sieve 45
Figure 40. Bar plot. ABI for laboratory versus field compaction on ABI 46
Figure 41. Graph. Density versus compactor passes. 46
Figure 42. Graph. Field core ABI versus compactor passes. 47
Figure 43. Graph. Relationship between ABI after field compaction and change in texture during Micro-Deval testing, measured with AIMS 47
Figure 44. Illustration. Sensor location. 49
Figure 45. Photo. String and flag instrument location. 50
Figure 46. Photo. Stem bend drawing provided to the manufacturer 51
Figure 47. Photo. Earth pressure cell, illustrating bent tube and transducer wire protection. 51
Figure 48. Photo. Placement of a pressure cell on HMA mat before compaction 52
Figure 49. Photo. Strain gauge calibration verification setup. 53
Figure 50. Photo. (a) Placement of a strain gauge placeholder plate on SMA mat prior to compaction, (b–d) placeholder plates and pressure cells during compaction. 53
Figure 51. Photo. (a) Saw cutting for wire host slot, (b) cleaning of saw-cut reservoir, and (c) slot filling with PG 64-22 binder over the strain gauge wire 54
Figure 52. Photo. Strain gauge “floating” over Ottawa sand slurry. 55
Figure 53. Photo. SMA compaction over a strain gauge prior to paving. 55

Figure 54. Photo. Finished thermocouple tip. 56
Figure 55. Photo. Thermocouple placement before paver. 56
Figure 56. Photo. Thermocouple placement after paver and before compaction. 57
Figure 57. Photo. Verification thermocouple at section D4-50-12.5-0. 57
Figure 58. Photo. (a) Researchers trenching to protect cables, (b) placement of cables over sand, and (c) tamper compaction of sand over cables. 58
Figure 59. Photo. I-APT (a) with temperature-insulating skirt open and (b) during winter operation.. 59
Figure 60. Photo. (a) Wi-Fi router under I-APT, (b) motion-sensitive cameras, and (c) nighttime monitoring of the data acquisition system—control system and camera footage. 60
Figure 61. Photo. (a) Cooling units, (b) heaters, and (c) control unit of the air heating/cooling system.. 61
Figure 62. Photo. I-APT carriage configured for 3.5 ft center-to-center spacing applying different loads on each tire. 62
Figure 63. Photo. I-APT carriage configured for 4.5 ft center-to-center spacing. 63
Figure 64. Flowchart. Capture and processing critical pavement responses from embedded sensors. 64
Figure 65. Photo. LabView program user interface. 65
Figure 66. Graph. Comparison of stresses before and after low-pass filtering. 65
Figure 67. Graph. Comparison of strains before and after low-pass filtering. 66
Figure 68. Photo. I-APT carriage loading tires at different inflation pressures with 10 kip. 67
Figure 69. Graph. Stability of sensor readings. 69
Figure 70. Graph. Microstrain values at different passes of the same loading scenario. 69
Figure 71. Graph. Haversine curve fit examples used to determine t_c. 70
Figure 72. Equation. Strain correction for reference temperature. 71
Figure 73. Graph. Change in moduli over the testing temperature range in D4-50-12.5-0. 71
Figure 74. Equation. Temperature correction factor referenced to 80°F. 71
Figure 75. Equation. General thickness correction formula. 73
Figure 76. Equation. Thickness correction function. 73
Figure 77. Equation. Thickness correction independent of load. 73
Figure 78. Equation. Thickness correction for vertical stress. 73
Figure 79. Equation. Example of thickness correction for vertical stress. 74
Figure 80. Equation. Thickness correction for vertical stress in D2-50-12.5-0. 74

Figure 81. Equation. Thickness correction formula for longitudinal strain. 75

Figure 82. Equation. Thickness correction formula for transverse strain. 75

Figure 83. Equation. Thickness correction formula for vertical/transverse shear strains. 76

Figure 84. Graph. Effect of speed, load magnitude, and tire inflation pressure on pavement responses in T1-80-12.5-0. 78

Figure 85. Graph. Effect of speed, load magnitude, and tire inflation pressure on pavement responses in T1-50-12.5-0. 80

Figure 86. Graph. Effect of speed, load magnitude, and tire inflation pressure on pavement responses in D2-50-12.5-0. 82

Figure 87. Graph. Effect of speed, load magnitude, and tire inflation pressure on pavement responses in L2-50-12.5-0. 84

Figure 88. Graph. Effect of speed, load magnitude, and tire inflation pressure on pavement responses in D3-50-9.5-0. 86

Figure 89. Graph. Effect of speed, load magnitude, and tire inflation pressure on pavement responses in D4-50-12.5-0. 88

Figure 90. Graph. Effect of temperature and axle spacing on pavement responses in T1-80-12.5-0. .. 89

Figure 91. Graph. Effect of temperature and axle spacing on pavement responses in T1-50-12.5-0. .. 90

Figure 92. Graph. Comparison of pavement responses across sections under single-axle loading (120 psi tire inflation pressure, 10 kip axle load, and 5 mph). 92

Figure 93. Graph. Comparison of pavement responses across sections under tandem-axle loading (120 psi–120 psi tire inflation pressure, 10 kip–10 kip axle loads, 5 mph, and 3.5 ft axle spacing). 94

Figure 94. Equation. Pavement response peak difference calculation. 95

Figure 95. Graph. Longitudinal strain peak variations at different temperatures. 96

Figure 96. Graph. Transverse strain peak difference at various temperatures. 97

Figure 97. Graph. Vertical stress peak difference at various temperatures. 98

Figure 98. Graph. Longitudinal strain peak difference at various axle-load spacings: (a) 3.5 ft, (b) 4.0 ft, and (c) 4.5 ft. 100

Figure 99. Graph. Transverse strain peak difference at various axle-load spacings: (a) 3.5 ft, (b) 4.0 ft, and (c) 4.5 ft. 101

Figure 100. Graph. Vertical stress peak difference at various axle-load spacings: (a) 3.5 ft, (b) 4.0 ft, and (c) 4.5 ft. 102

Figure 101. Graph. Longitudinal strain peak difference at (a) 1 mph, (b) 3 mph, and (c) 5 mph. 103

Figure 102. Graph. Transverse strain peak difference at (a) 1 mph, (b) 3 mph, and (c) 5 mph. 104

Figure 103. Graph. Vertical stress peak difference at (a) 1 mph, (b) 3 mph, and (c) 5 mph. 105

Figure 104. Graph. Longitudinal strain peak difference for various loads: (a) 8 kip, (b) 9 kip, (c) 10 kip, (d) 12 kip, and (e) 14 kip. 107

Figure 105. Graph. Transverse strain peak difference for various loads: (a) 8 kip, (b) 9 kip, (c) 10 kip, (d) 12 kip, and (e) 14 kip. 109

Figure 106. Graph. Vertical stress peak difference for various loads: (a) 8 kip, (b) 9 kip, (c) 10 kip, (d) 12 kip, and (e) 14 kip. 111

Figure 107. Graph. Longitudinal strain peak difference at various tire pressures: (a) 80 psi, (b) 100 psi, and (c) 120 psi. 114

Figure 108. Graph. Transverse strain peak difference at various tire pressures: (a) 80 psi, (b) 100 psi, and (c) 120 psi. 115

Figure 109. Graph. Vertical stress peak difference at various tire pressures: (a) 80 psi, (b) 100 psi, and (c) 120 psi. 116

Figure 110. Graph. Longitudinal strain response at 10 kip, 120 psi, 5 mph, and 80°F: (a) single axle on D4-50-12.5-0, (b) tandem axle on D4-50-12.5-0, and (c) tandem axle on L2-50-12.5-0. 117

Figure 111. Box plot. Material and loading characteristic effects on transverse strain peak difference. 118

Figure 112. Graph. Effect size (η^2) comparison across all parameters. 119

Figure 113. Graph. Variance explained (%) for all parameters affecting transverse strain peak difference. 120

Figure 114. Graph. D4-50-12.5-0 pavement section responses under tandem-axle load with an underinflated tire. 121

Figure 115. Graph. Comparison of pavement responses across sections under tandem-axle loading (80 psi–120 psi tire inflation pressure, 10 kip–10 kip axle loads, 5 mph, and 3.5 ft axle spacing). 122

Figure 116. Graph. Comparison of pavement section responses under tandem-axle loading (120 psi–80 psi tire inflation pressure, 10 kip–10 kip axle loads, 5 mph, and 3.5 ft axle spacing). 123

Figure 117. Graph. Effect of deflated tire pressure of a tandem axle on longitudinal strain peak difference: (a) 80/120 psi and (b) 120/80 psi. 124

Figure 118. Graph. Effect of a deflated tire pressure of a tandem axle on transverse strain peak difference: (a) 80/120 psi and (b) 120/80 psi. 125

Figure 119. Graph. Effect of a deflated tire pressure of a tandem axle on vertical stress peak difference: (a) 80/120 psi and (b) 120/80 psi. 126

Figure 120. Graph. Pavement temperature recorded for T1-80-12.5-0. 130

Figure 121.Graph. Pavement responses recorded and corrected for Section T1-80-12.5-0: (a) measured vertical stress and thickness-corrected vertical stress; (b) measured data, temperature- and thickness-corrected data, and response curves at every 2,500 passes. 130

Figure 122. Graph. Pavement temperature recorded for T1-50-12.5-0. 131

Figure 123.Graph. Pavement responses recorded and corrected for T1-50-12.5-0: (a) measured vertical stress and thickness-corrected vertical stress; (b) measured data, temperature- and thickness-corrected data, and response curves at every 2,500 passes..... 131

Figure 124. Graph. Pavement temperature recorded for D2-50-12.5-0..... 132

Figure 125. Graph. Pavement responses recorded and corrected for D2-50-12.5-0: (a) measured vertical stress and thickness-corrected vertical stress; (b) measured data, temperature- and thickness-corrected data, and response curves at every 2,500 passes..... 132

Figure 126. Graph. Pavement temperature recorded for L2-50-12.5-0..... 133

Figure 127. Graph. Pavement responses recorded and corrected for L2-50-12.5-0: (a) measured vertical stress and thickness-corrected vertical stress; (b) measured data, temperature- and thickness-corrected data, and response curves at every 2,500 passes..... 133

Figure 128. Graph. Pavement temperature recorded for D3-50-9.5-0..... 134

Figure 129. Graph. Pavement responses recorded and corrected for D3-50-9.5-0: (a) measured vertical stress and thickness-corrected vertical stress; (b) measured data, temperature- and thickness-corrected data, and response curves at every 2,500 passes..... 134

Figure 130. Graph. Pavement temperature recorded for D4-50-12.5-0..... 135

Figure 131.Graph. Pavement responses recorded and corrected for D4-50-12.5-0: (a) measured vertical stress and thickness-corrected vertical stress; (b) measured data, temperature- and thickness-corrected data, and response curves at every 2,500 passes..... 135

Figure 132. Photo. Manual and laser rutting profile measurements on D4-50-12.5-0. 136

Figure 133. Photos. I-APT rutting measurement system: (a) automated laser profiler, (b) encoder, and (c) Keyence data collection software. 138

Figure 134. Photos. Workflow of the laser-scanner and rutting profile analysis..... 139

Figure 135. Photo. Shoving and rutting parameter computation..... 140

Figure 136. Graph. Laser transverse profiles progression for T1-80-12.5-0. 140

Figure 137. Graph. Accumulation of shoving and depression in the wheel path during continuous loading for two sections. 141

Figure 138. Graph. Rutting progression for SMA section T1-80-12.5-0 with piecewise trend fitting. 143

Figure 139. Graph. Rutting progression for SMA section T1-50-12.5-0 with piecewise trend fitting. 143

Figure 140. Graph. Rutting progression for SMA section D2-50-12.5-0 with piecewise trend fitting. 144
Figure 141. Graph. Rutting progression for SMA section L2-50-12.5-0 with piecewise trend fitting.. 144
Figure 142. Graph. Rutting progression for SMA section D3-50-9.5-0 with piecewise trend fitting... 145
Figure 143. Graph. Rutting progression for SMA section D4-50-12.5-0 with piecewise trend fitting. 145
Figure 144. Graph. Damage accumulation during I-APT loading. 146
Figure 145. Graph. ABI for field cores taken before and after I-APT loading..... 148
Figure 146. Graph. Pavement recovery progression during APT. 150
Figure 147. Graph. Recovery slope at $t = t_o + 0.2$ s as a function of pass number and temperature for all SMA sections. 151
Figure 148. Graph. I-APT (a) rut depth and (b) rutting slope versus aggregate surface texture loss (ΔTexture) measured using AIMS after Micro-Deval testing. 153
Figure 149. Graph. Relationships between aggregate combined soundness and APT rutting performance for the evaluated SMA sections: (a) total rut depth and (b) rutting slope. 153
Figure 150. Graph. ABI for all SMAs measured at laboratory, field-compacted, and post I-APT stages, illustrating the evolution of aggregate degradation through production, compaction, and trafficking. 154
Figure 151. Graph. Partial Pearson correlation between ABI measured on plant-produced, field-compacted cores and I-APT rutting after 10,000 passes. 155
Figure 152. Graph. Calculated strains of section T1-50-12.5-0 at the bottom of the SMA layer. 156
Figure 153 Equation. Incremental rutting transfer function. 157
Figure 154. Equation. Normalized transverse-vertical shear strain. 157
Figure 155 Equation. Time hardening rutting progression model. 157
Figure 156. Equation. Normalized ME term. 158
Figure 157. Equation. General rutting transfer function using normalized ME term. 158
Figure 158. Equation. Proposed ME rutting transfer function. 158
Figure 159. Graph. Measured and predicted rut depth progression for section D3-50-9.5-0..... 159
Figure 160. Equation. Proposed definition of *C* as a function of combined soundness. 160
Figure 161. Graph. Relationship between *C* and aggregate soundness (percentage loss). 161
Figure 162. Graph. Predicted rut progression for SMA sections under 12 kip/tire loading. 161
Figure 163. Graph. Rut depth response for SMA section L2-50-12.5-0: experimental piecewise fit and shear-model predictions (10/12/14 kip/tire). 162

Figure 164. Illustration. Project locations used for the LCA scenarios. 166
Figure 165. Illustration. Life cycle assessment system boundary. 167
Figure 166. Equation. Total emission of asphalt binder. 168
Figure 167. Equation. Total hauling emission. 169
Figure 168. Equation. Cover per pass calculation. 170
Figure 169. Equation. Number of hours operated by a roller. 171
Figure 170. Illustration. Field pavement section. 171
Figure 171. Graph. Rutting progression of the three field sections. 172
Figure 172. Equation. Rutting damage rate calculation. 172
Figure 173. Equation. Field rut depth calculation. 173
Figure 174. Equation. Total emission of asphalt binder. 173
Figure 175. Equation. I-APT number of passes to reach rutting threshold. 173
Figure 176. Equation. Time to rehabilitate due to rutting. 174
Figure 177. Graph. IRI progression for each field section. 175
Figure 178. Graph. LCA results for material production processes 177
Figure 179. Graph. LCA results for material transportation. 178
Figure 180. Graph. Construction equipment global warming potential. 178
Figure 181. Graph. Global warming potential results for rehabilitation stage. 179
Figure 182. Graph. Excess fuel consumption for each field pavement section. 180
Figure 183. Equation. Calculation of net present worth. 181
Figure 184. Graph. Material hauling cost results. 182
Figure 185. Graph. Initial construction and rehabilitation cost results. 183
Figure 186. Illustration. The chosen unit weight of SMA coarse aggregate (Vavrik et al. 2002) 209
Figure 187. Photo. I-APT facility and major components of the test machine. 222
Figure 188. Graph. Comparison of measured and corrected vertical stress under single-axle loading (P_1 = 100 psi; L_1 = 10 kip; speed = 5 mph) 287
Figure 189. Graph. Comparison of measured and corrected vertical stress under tandem-axle loading (P_1 = 100 psi, P_2 = 100 psi; L_1 = 10 kip, L_2 = 10 kip; speed = 5 mph; axle spacing = 3.5 ft) 288
Figure 190. Graph. Comparison of measured and corrected vertical stress under single-axle loading (P_1 = 120 psi; L_1 = 10 kip; speed = 1 mph) 289

Figure 191. Graph. Comparison of measured and corrected vertical stress under single-axle loading (P_1 = 120 psi; L_1 = 10 kip; speed = 3 mph) 290

Figure 192. Graph. Comparison of measured and corrected vertical stress under single-axle loading (P_1 = 120 psi; L_1 = 10 kip; speed = 5 mph) 291

Figure 193. Graph. Comparison of measured and corrected vertical stress under single-axle loading (P_1 = 120 psi; L_1 = 12 kip; speed = 5 mph) 292

Figure 194. Graph. Comparison of measured and corrected vertical stress under single-axle loading (P_1 = 120 psi; L_1 = 14 kip; speed = 5 mph) 293

Figure 195. Graph. Comparison of measured and corrected vertical stress under single-axle loading (P_1 = 120 psi; L_1 = 8 kip; speed = 5 mph) 294

Figure 196. Comparison of measured and corrected vertical stress under single-axle loading (P_1 = 120 psi; L_1 = 9 kip; speed = 5 mph) 295

Figure 197. Graph. Comparison of measured and corrected vertical stress under tandem-axle loading (P_1 = 120 psi, P_2 = 120 psi; L_1 = 10 kip, L_2 = 10 kip; speed = 1 mph; axle spacing = 3.5 ft) 296

Figure 198. Graph. Comparison of measured and corrected vertical stress under tandem-axle loading (P_1 = 120 psi, P_2 = 120 psi; L_1 = 10 kip, L_2 = 10 kip; speed = 3 mph; axle spacing = 3.5 ft) 297

Figure 199. Graph. Comparison of measured and corrected vertical stress under tandem-axle loading (P_1 = 120 psi, P_2 = 120 psi; L_1 = 10 kip, L_2 = 10 kip; speed = 5 mph; axle spacing = 3.5 ft) 298

Figure 200. Graph. Comparison of measured and corrected vertical stress under tandem-axle loading (P_1 = 120 psi, P_2 = 120 psi; L_1 = 12 kip, L_2 = 12 kip; speed = 5 mph; axle spacing = 3.5 ft) 299

Figure 201. Graph. Comparison of measured and corrected vertical stress under tandem-axle loading (P_1 = 120 psi, P_2 = 120 psi; L_1 = 14 kip, L_2 = 14 kip; speed = 5 mph; axle spacing = 3.5 ft) 300

Figure 202. Graph. Comparison of measured and corrected vertical stress under tandem-axle loading (P_1 = 120 psi, P_2 = 120 psi; L_1 = 8 kip, L_2 = 8 kip; speed = 5 mph; axle spacing = 3.5 ft) 301

Figure 203. Graph. Comparison of measured and corrected vertical stress under tandem-axle loading at high temperature (P_1 = 120 psi, P_2 = 120 psi; L_1 = 8 kip, L_2 = 8 kip; speed = 5 mph; axle spacing = 3.5 ft)..... 302

Figure 204. Graph. Comparison of measured and corrected vertical stress under tandem-axle loading at low temperature (P_1 = 120 psi, P_2 = 120 psi; L_1 = 8 kip, L_2 = 8 kip; speed = 5 mph; axle spacing = 3.5 ft)..... 303

Figure 205. Graph. Comparison of measured and corrected vertical stress under tandem-axle loading (P_1 = 120 psi, P_2 = 120 psi; L_1 = 9 kip, L_2 = 9 kip; speed = 5 mph; axle spacing = 3.5 ft) 304

Figure 206. Graph. Comparison of measured and corrected vertical stress under tandem-axle loading with asymmetric tire pressures (P_1 = 120 psi, P_2 = 80 psi; L_1 = 10 kip, L_2 = 10 kip; speed = 5 mph; axle spacing = 3.5 ft)..... 305

Figure 207. Graph. Comparison of measured and corrected vertical stress under single-axle loading (P_1 = 80 psi; L_1 = 10 kip; speed = 5 mph) 306

Figure 208. Graph. Comparison of measured and corrected vertical stress under tandem-axle loading with asymmetric tire pressures (P_1 = 80 psi, P_2 = 120 psi; L_1 = 10 kip, L_2 = 10 kip; speed = 5 mph; axle spacing = 3.5 ft)..... 307

Figure 209. Graph. Comparison of measured and corrected vertical stress under tandem-axle loading (P_1 = 80 psi, P_2 = 80 psi; L_1 = 10 kip, L_2 = 10 kip; speed = 5 mph; axle spacing = 3.5 ft) 308

Figure 210. Graph. Comparison of measured and corrected longitudinal microstrain under single-axle loading (P_1 = 100 psi; L_1 = 10 kip; speed = 5 mph)..... 309

Figure 211. Graph. Comparison of measured and corrected longitudinal microstrain under tandem-axle loading (P_1 = 100 psi, P_2 = 100 psi; L_1 = 10 kip, L_2 = 10 kip; speed = 5 mph; axle spacing = 3.5 ft) 310

Figure 212. Graph. Comparison of measured and corrected longitudinal microstrain under single-axle loading (P_1 = 120 psi; L_1 = 10 kip; speed = 1 mph)..... 311

Figure 213. Graph. Comparison of measured and corrected longitudinal microstrain under single-axle loading (P_1 = 120 psi; L_1 = 10 kip; speed = 3 mph)..... 312

Figure 214. Graph. Comparison of measured and corrected longitudinal microstrain under single-axle loading (P_1 = 120 psi; L_1 = 10 kip; speed = 5 mph)..... 313

Figure 215. Graph. Comparison of measured and corrected longitudinal microstrain under single-axle loading (P_1 = 120 psi; L_1 = 12 kip; speed = 5 mph)..... 314

Figure 216. Graph. Comparison of measured and corrected longitudinal microstrain under single-axle loading (P_1 = 120 psi; L_1 = 14 kip; speed = 5 mph)..... 315

Figure 217. Graph. Comparison of measured and corrected longitudinal microstrain under single-axle loading (P_1 = 120 psi; L_1 = 8 kip; speed = 5 mph)..... 316

Figure 218. Graph. Comparison of measured and corrected longitudinal microstrain under single-axle loading (P_1 = 120 psi; L_1 = 9 kip; speed = 5 mph)..... 317

Figure 219. Graph. Comparison of measured and corrected longitudinal microstrain under tandem-axle loading (P_1 = 120 psi, P_2 = 120 psi; L_1 = 10 kip, L_2 = 10 kip; speed = 1 mph; axle spacing = 3.5 ft) 318

Figure 220. Graph. Comparison of measured and corrected longitudinal microstrain under tandem-axle loading (P_1 = 120 psi, P_2 = 120 psi; L_1 = 10 kip, L_2 = 10 kip; speed = 3 mph; axle spacing = 3.5 ft) 319

Figure 221. Graph. Comparison of measured and corrected longitudinal microstrain under tandem-axle loading (P_1 = 120 psi, P_2 = 120 psi; L_1 = 10 kip, L_2 = 10 kip; speed = 5 mph; axle spacing = 3.5 ft) 320

Figure 222. Graph. Comparison of measured and corrected longitudinal microstrain under tandem-axle loading (P_1 = 120 psi, P_2 = 120 psi; L_1 = 12 kip, L_2 = 12 kip; speed = 5 mph; axle spacing = 3.5 ft) 321

Figure 223. Graph. Comparison of measured and corrected longitudinal microstrain under tandem-axle loading (P_1 = 120 psi, P_2 = 120 psi; L_1 = 14 kip, L_2 = 14 kip; speed = 5 mph; axle spacing = 3.5 ft) 322

Figure 224. Graph. Comparison of measured and corrected longitudinal microstrain under tandem-axle loading (P_1 = 120 psi, P_2 = 120 psi; L_1 = 8 kip, L_2 = 8 kip; speed = 5 mph; axle spacing = 3.5 ft).... 323

Figure 225. Graph. Comparison of measured and corrected longitudinal microstrain under tandem-axle loading at high temperature (P_1 = 120 psi, P_2 = 120 psi; L_1 = 8 kip, L_2 = 8 kip; speed = 5 mph; axle spacing = 3.5 ft)..... 324

Figure 226. Graph. Comparison of measured and corrected longitudinal microstrain under tandem-axle loading at low temperature (P_1 = 120 psi, P_2 = 120 psi; L_1 = 8 kip, L_2 = 8 kip; speed = 5 mph; axle spacing = 3.5 ft)..... 325

Figure 227. Graph. Comparison of measured and corrected longitudinal microstrain under tandem-axle loading (P_1 = 120 psi, P_2 = 120 psi; L_1 = 9 kip, L_2 = 9 kip; speed = 5 mph; axle spacing = 3.5 ft).... 326

Figure 228. Graph. Comparison of measured and corrected longitudinal microstrain under tandem-axle loading with asymmetric tire pressures (P_1 = 120 psi, P_2 = 80 psi; L_1 = 10 kip, L_2 = 10 kip; speed = 5 mph; axle spacing = 3.5 ft)..... 327

Figure 229. Graph. Comparison of measured and corrected longitudinal microstrain under single-axle loading (P_1 = 80 psi; L_1 = 10 kip; speed = 5 mph)..... 328

Figure 230. Graph. Comparison of measured and corrected longitudinal microstrain under tandem-axle loading with asymmetric tire pressures (P_1 = 80 psi, P_2 = 120 psi; L_1 = 10 kip, L_2 = 10 kip; speed = 5 mph; axle spacing = 3.5 ft)..... 329

Figure 231. Graph. Comparison of measured and corrected longitudinal microstrain under tandem-axle loading (P_1 = 80 psi, P_2 = 80 psi; L_1 = 10 kip, L_2 = 10 kip; speed = 5 mph; axle spacing = 3.5 ft).... 330

Figure 232. Graph. Comparison of measured and corrected transverse microstrain under single-axle loading (P_1 = 100 psi; L_1 = 10 kip; speed = 5 mph)..... 331

Figure 233. Graph. Comparison of measured and corrected transverse microstrain under tandem-axle loading (P_1 = 100 psi, P_2 = 100 psi; L_1 = 10 kip, L_2 = 10 kip; speed = 5 mph; axle spacing = 3.5 ft) 332

Figure 234. Graph. Comparison of measured and corrected transverse microstrain under single-axle loading (P_1 = 120 psi; L_1 = 10 kip; speed = 1 mph)..... 333

Figure 235. Graph. Comparison of measured and corrected transverse microstrain under single-axle loading (P_1 = 120 psi; L_1 = 10 kip; speed = 3 mph)..... 334

Figure 236. Graph. Comparison of measured and corrected transverse microstrain under single-axle loading (P_1 = 120 psi; L_1 = 10 kip; speed = 5 mph)..... 335

Figure 237. Graph. Comparison of measured and corrected transverse microstrain under single-axle loading (P_1 = 120 psi; L_1 = 12 kip; speed = 5 mph)..... 336

Figure 238. Graph. Comparison of measured and corrected transverse microstrain under single-axle loading (P_1 = 120 psi; L_1 = 14 kip; speed = 5 mph)..... 337

Figure 239. Graph. Comparison of measured and corrected transverse microstrain under single-axle loading (P_1 = 120 psi; L_1 = 8 kip; speed = 5 mph)..... 338

Figure 240. Graph. Comparison of measured and corrected transverse microstrain under single-axle loading (P_1 = 120 psi; L_1 = 9 kip; speed = 5 mph)..... 339

Figure 241. Graph. Comparison of measured and corrected transverse microstrain under tandem-axle loading (P_1 = 120 psi, P_2 = 120 psi; L_1 = 10 kip, L_2 = 10 kip; speed = 1 mph; axle spacing = 3.5 ft) 340

Figure 242. Graph. Comparison of measured and corrected transverse microstrain under tandem-axle loading (P_1 = 120 psi, P_2 = 120 psi; L_1 = 10 kip, L_2 = 10 kip; speed = 3 mph; axle spacing = 3.5 ft) 341

Figure 243. Graph. Comparison of measured and corrected transverse microstrain under tandem-axle loading (P_1 = 120 psi, P_2 = 120 psi; L_1 = 10 kip, L_2 = 10 kip; speed = 5 mph; axle spacing = 3.5 ft) 342

Figure 244. Graph. Comparison of measured and corrected transverse microstrain under tandem-axle loading (P_1 = 120 psi, P_2 = 120 psi; L_1 = 12 kip, L_2 = 12 kip; speed = 5 mph; axle spacing = 3.5 ft) 343

Figure 245. Graph. Comparison of measured and corrected transverse microstrain under tandem-axle loading (P_1 = 120 psi, P_2 = 120 psi; L_1 = 14 kip, L_2 = 14 kip; speed = 5 mph; axle spacing = 3.5 ft) 344

Figure 246. Graph. Comparison of measured and corrected transverse microstrain under tandem-axle loading (P_1 = 120 psi, P_2 = 120 psi; L_1 = 8 kip, L_2 = 8 kip; speed = 5 mph; axle spacing = 3.5 ft) 345

Figure 247. Graph. Comparison of measured and corrected transverse microstrain under tandem-axle loading at high temperature (P_1 = 120 psi, P_2 = 120 psi; L_1 = 8 kip, L_2 = 8 kip; speed = 5 mph; axle spacing = 3.5 ft)..... 346

Figure 248. Graph. Comparison of measured and corrected transverse microstrain under tandem-axle loading at low temperature (P_1 = 120 psi, P_2 = 120 psi; L_1 = 8 kip, L_2 = 8 kip; speed = 5 mph; axle spacing = 3.5 ft)..... 347

Figure 249. Graph. Comparison of measured and corrected transverse microstrain under tandem-axle loading (P_1 = 120 psi, P_2 = 120 psi; L_1 = 9 kip, L_2 = 9 kip; speed = 5 mph; axle spacing = 3.5 ft) 348

Figure 250. Graph. Comparison of measured and corrected transverse microstrain under tandem-axle loading with asymmetric tire pressures (P_1 = 120 psi, P_2 = 80 psi; L_1 = 10 kip, L_2 = 10 kip; speed = 5 mph; axle spacing = 3.5 ft)..... 349

Figure 251. Graph. Comparison of measured and corrected transverse microstrain under single-axle loading (P_1 = 80 psi; L_1 = 10 kip; speed = 5 mph)..... 350

Figure 252. Graph. Comparison of measured and corrected transverse microstrain under tandem-axle loading with asymmetric tire pressures (P_1 = 80 psi, P_2 = 120 psi; L_1 = 10 kip, L_2 = 10 kip; speed = 5 mph; axle spacing = 3.5 ft)..... 351

Figure 253. Graph. Comparison of measured and corrected transverse microstrain under tandem-axle loading (P_1 = 80 psi, P_2 = 80 psi; L_1 = 10 kip, L_2 = 10 kip; speed = 5 mph; axle spacing = 3.5 ft) 352

LIST OF TABLES

Table 1. High-Quality Coarse Aggregate Required for SMA (AASHTO M 325) 1
Table 2. LA Abrasion Ranking, Categories, and Reference Value 9
Table 3. Qualities of CA Stockpiles 10
Table 4. AIMS Results for the CA of the SMA 11
Table 5. Design Mix Formulas and VCA of SMAs 12
Table 6. SMA Design Aggregate Gradations 12
Table 7. Volumetric Characteristics of SMAs 13
Table 8. Original and Modified Aggregate Gradations Incorporating HL 14
Table 9. Parameters for FE Model 25
Table 10. Base Layer Achieved Densities (Average) 27
Table 11. Thermal Camera Images 29
Table 12. Job Mix Formula Adjustments 31
Table 13. Target and Measured P_b (%) of Plant-Produced SMA Using Different Methods 32
Table 14. Aggregate Gradations after Plant Production 32
Table 15. Aggregate Gradations after Plant Production with District Measurements for T1-50-12.5-0 33
Table 16. Aggregate Gradations after Plant Production with District Measurements for L2-50-12.5-0 33
Table 17. Aggregate Gradations after Plant Production with District Measurements for D4-50-12.5-0 33
Table 18. Plant-Produced SMA G_{mm} and G_{mb} 34
Table 19. Plant-Produced SMA Volumetrics 35
Table 20. SMA Layer Achieved Densities (Average of 5) 36
Table 21. SMA Lift Thickness and Density from Field Cores 38
Table 22. I-FIT and HWTT Results 39
Table 23. Tire Specifications 62
Table 24. Testing Scenarios with Varying Loading Configurations 68
Table 25. Temperature Correction Equations 72

Table 26. Prediction Errors between Modulus Ratios from Complex Modulus Master Curves and Measured Strain Ratios on Full-scale APT Sections at 82°F and 96°F 72
Table 27. Thickness Correction Factor for Vertical Stress 74
Table 28. Thickness Correction Equations for Longitudinal Strains in SMA Sections 74
Table 29. Thickness Correction Factor for Longitudinal Strains in SMA Sections 75
Table 30.Thickness Correction Equation for Transverse Strains in SMA Sections 75
Table 31. Thickness Correction Factor for Transverse Strain in SMA Sections 75
Table 32. Thickness Correction Equations for Vertical/Transverse Shear Strains in SMA Sections..... 76
Table 33. Thickness Correction Factor for Vertical/Transverse Strains in SMA Sections..... 76
Table 34. Pavement Responses to Trailing Axle with 10 kip and 120 psi Tire Pressure for Two Speeds at 80°F 91
Table 35. Tire-Pavement Contact Length Change with Various Loading (De Beer et al. 2012) 112
Table 36. Total Damage Recorded..... 147
Table 37. SMA Lift Thickness and Density from Wheel-path Field Cores after I-APT Loading..... 147
Table 38. Section Average Peak Transverse Strain Difference..... 151
Table 39. HWTT Rut Depths and Damage Rates 152
Table 40. Pearson Correlation between HWTT Metrics and I-APT Performance Indicators 152
Table 41 Rutting Model Performance 160
Table 42. Construction Equipment Properties 170
Table 43. Number of Roller Compactor Passes Obtained from GPR Measurements 170
Table 44. Estimated Number of Passes Per Year of I-APT Sections Using Field Sections 174
Table 45. Projected Rehabilitation Trigger Period 174
Table 46. Field Section Traffic Details..... 176
Table 47. Percentage Changes in Cost Across the Scenarios 183
Table 48. Control Sieves for SMA 209
Table 49. Recommended Ranges for Aggregate Ratios in SMA 209
Table 50. Frictional Requirements for Surface Mixtures from Chapter 53 of IDOT's Bureau of Design and Environment Manual 212
Table 51. Illinois Specifications for Components of SMA and Mix Design Requirements 213
Table 52. Current SMA Design Approval Performance Tests 214

Table 53. SMA Component and Mix Design Requirements for Selected States 215
Table 54. SMA Design Approval Performance Tests in the Six States 217
Table 55. Countries for Which Research Related to the Development and Use of SMA Was Identified 218
Table 56. I-APT Specifications after the 2024 Renovation 223
Table 57. Pressure and Strain Measurements for Section T1-80-12.5-0 266
Table 58. Temperature Measurements for Section T1-80-12.5-0 267
Table 59. CoV of Measurements for Section T1-80-12.5-0 268
Table 60. CoV of Measurements for Section T1-80-12.5-0 (Continued) 269
Table 61. Pressure and Strain Measurements for Section T1-50-12.5-0 270
Table 62. Temperature Measurements for Section T1-50-12.5-0 271
Table 63. CoV of Measurements for Section T1-50-12.5-0 272
Table 64. CoV of Measurements for Section T1-50-12.5-0 (Continued) 273
Table 65. Pressure and Strain Measurements for Section D2-50-12.5-0 274
Table 66. Temperature Measurements for Section D2-50-12.5-0 275
Table 67. CoV of Measurements for Section D2-50-12.5-0 276
Table 68. CoV of Measurements for Section D2-50-12.5-0 (Continued) 277
Table 69. Pressure and Strain Measurements for Section L2-50-12.5-0 278
Table 70. Temperature Measurements for Section L2-50-12.5-0 279
Table 71. CoV of Measurements for Section L2-50-12.5-0 280
Table 72. CoV of Measurements for Section L2-50-12.5-0 (Continued) 281
Table 73. Pressure and Strain Measurements for Section D3-50-9.5-0 282
Table 74. Temperature Measurements for Section D3-50-9.5-0 283
Table 75. CoV of Measurements for Section D3-50-9.5-0 284
Table 76. Pressure, Temperature, and Strain Measurements for Section D4-50-12.5-0 285
Table 77. CoV of Measurements for Section D4-50-13.5-0 286
Table 78. List of Local Quarries 353
Table 79. List of Non-Local Quarries 356

CHAPTER 1: INTRODUCTION

Stone-mastic asphalt (SMA), also known as stone-matrix asphalt, is a special form of hot-mix asphalt (HMA) that provides relatively greater durability. It uses strong low-abrasion aggregate packed in a gap-graded skeleton. In addition, it has a relatively thick film of polymer-modified binder, improved with fibers. Hence, it usually provides longer service life than HMA, and its price per ton is higher. In Illinois, a significant portion of the cost is attributed to the relatively long-distance transport of high-quality aggregates, which are not readily available locally. This project aimed to reduce SMA costs utilizing locally sourced aggregates through an optimized SMA design. Beyond cost savings, utilizing local materials could reduce emissions associated with long-haul transport. In certain parts of Illinois, where ideal SMA aggregates are approximately 120 mi away from a plant, a 40% reduction in coarse aggregate hauling costs could be expected.

BACKGROUND

Stone-mastic asphalt was developed in Germany to withstand studded tires during the winter. It relies on stone-on-stone contact to provide a sturdy skeleton to HMA. The SMA aggregate blends are gap-graded; coarse aggregates are tightly packed, and fines fill the remaining voids, creating a highly rut-resistant material with desired structural capacity for pavement layers. Hence, high-quality aggregates must be available to construct SMA pavement surfaces. Polymer-modified asphalt binder, another component of SMA, provides elastic recovery to the material through a thick film. Fibers are introduced to avoid binder drain down through the large and interconnected voids.

When SMA was introduced to the US, high-quality aggregates were used (Table 1) as well as high design compaction effort. Design compaction effort in HMA is the number of Superpave gyratory compactor (SGC) gyrations—or N_{des}—used to achieve target volumetrics in the laboratory, which are also sought in the field. At the time, 100 gyrations were used for aggregates with Los Angeles (LA) abrasion lower than 30 (Hughes, 2002). AASHTO M 325 (2008) still specifies requirements referring to specimens compacted at 100 gyrations. However, 100 gyrations were found to be excessive for weak aggregates and increased aggregate breakdown by 0.62% (Xie et al., 2005). As a result, Xie et al. studied 65 gyrations for SMA compaction based on optimum asphalt content, voids in mineral aggregate (VMA), and rut depth. The study found that mixes designed using 65 gyrations meet VMA requirements without increasing rutting potential.

Table 1. High-Quality Coarse Aggregate Required for SMA (AASHTO M 325)

Test	Threshold
LA abrasion, % loss	< 30
Flat and elongated, % (3 to 1)*	< 20
Flat and elongated, % (5 to 1)*	< 5
Absorption, %	< 2.0
Soundness (5 cycles), %, sodium sulfate	< 15
Soundness (5 cycles), %, magnesium	< 20
Crushed content, %, one face	> 100
Crushed content, %, two face	> 90

*Apply to the design aggregate blend

Illinois has no economically minable igneous rocks (Lasemi & Butler, 2015). Therefore, higher-quality coarse aggregates are unavailable within 50 miles of any asphalt plants, which may make trucking quite expensive. The use of crushed gravel and calcium carbonate–based aggregates, which are predominant in Illinois, is restricted in SMA due to concerns for meeting potential friction, durability, and performance requirements. These Illinois aggregates typically lack the hardness and angularity required to meet the specifications of high-performance SMA. In addition, aggregate breakage has been experienced in Illinois (as presented in Figure 1), so surface SMA layers typically used in Illinois utilize the following coarse aggregates: steel slag from Gary, Indiana; quartzite from Wisconsin; trap rock from Iron Mountain, Missouri and Canada; and chert gravel from Missouri (James Trepanier, former IDOT HMA Operations Engineer, pers. comm., Dec. 28, 2020).

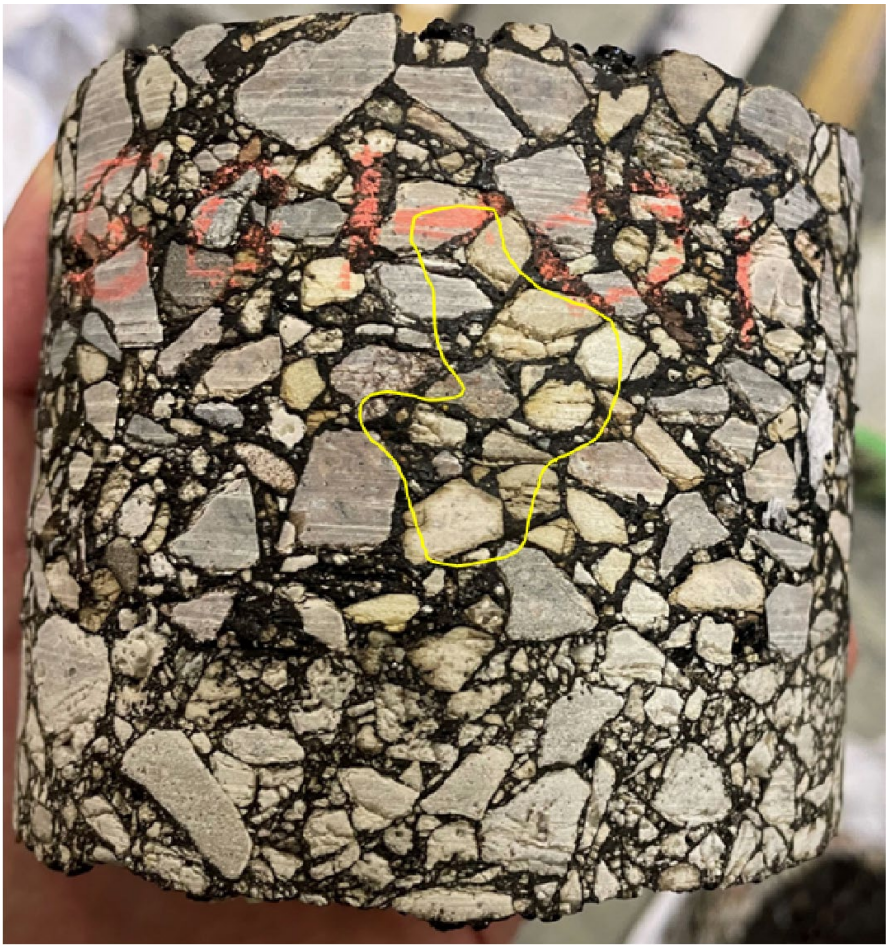

Figure 1. Photo. Field core from an interstate project with broken carbonate crushed stone.

Source: Brian Hill, IDOT Bureau of Materials

Aggregate breakage can be measured through changes in aggregate gradation before and after loading. Extractions are performed to recover the aggregates. Aggregate breakage is measured (as presented in Figure 2) on recovered aggregates from HMA specimens after compaction using the design number of gyrations. Breakage is also measured on recovered aggregate from specimens after the Hamburg wheel-tracking test (HWTT).

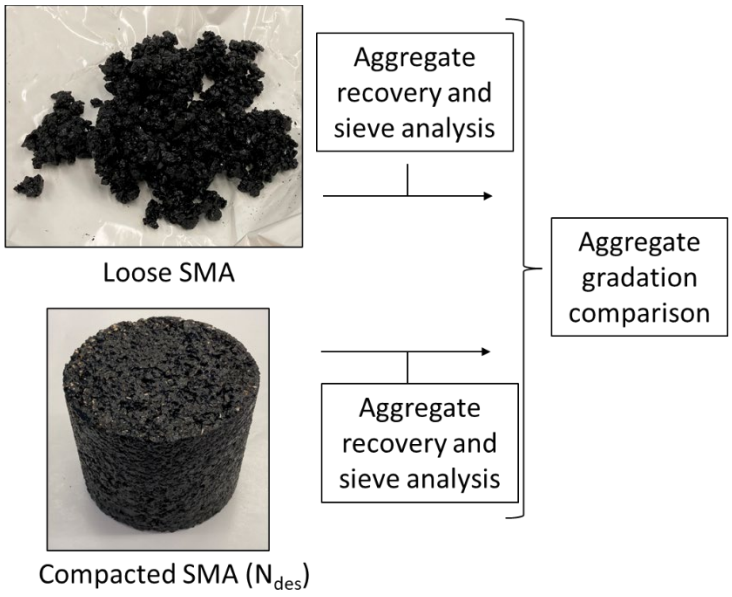

Figure 2. Schematic. Aggregate breakage measurement.

Weight proportions retained on sieves describe the spatial arrangement of the coarse aggregates in SMA. According to García Mainieri and Al-Qadi (2024), the aggregate breakage index (ABI), presented in Figure 3, could capture the changes in gradation caused by aggregate breakage:

$$ABI = 3.3 \times \frac{|\%Before_{\#4} - \%After_{\#4}|}{\%Before_{\#4}} + 48.4 \times \frac{|\%Before_{\#8} - \%After_{\#8}|}{\%Before_{\#8}} + 48.3 \times \frac{|\%Before_{\#16} - \%After_{\#16}|}{\%Before_{\#16}}$$

Figure 3. Equation. Aggregate breakage index.

In this equation, “Before” refers to the aggregate blend gradation in a loose mix state before compaction, and “After” refers to the aggregate gradation after compaction and/or loading. Figure 4 illustrates an example of ABI and aggregate breakage.

OBJECTIVES AND SCOPE

The objective of the project was to design, test, and disseminate SMAs using local Illinois aggregates that meet performance requirements. Hence, through reducing design compaction effort, the study focused on understanding the extent of aggregate breakage that preserves SMA’s aggregate skeleton while not compromising performance. To achieve the goal, the following steps were conducted.

1. SMAs were designed with local and higher-quality (control) aggregates using different compaction efforts to meet volumetric targets.

2. Potential performance was predicted in the laboratory using standard tests.

3. Aggregate breakage was measured and quantified during SMA compaction and loading tests in the laboratory.

4. Full-scale tests were performed to validate the laboratory findings.

5. Impacts of SMA with local Illinois aggregates on potential performance, economy, and environment were quantified.

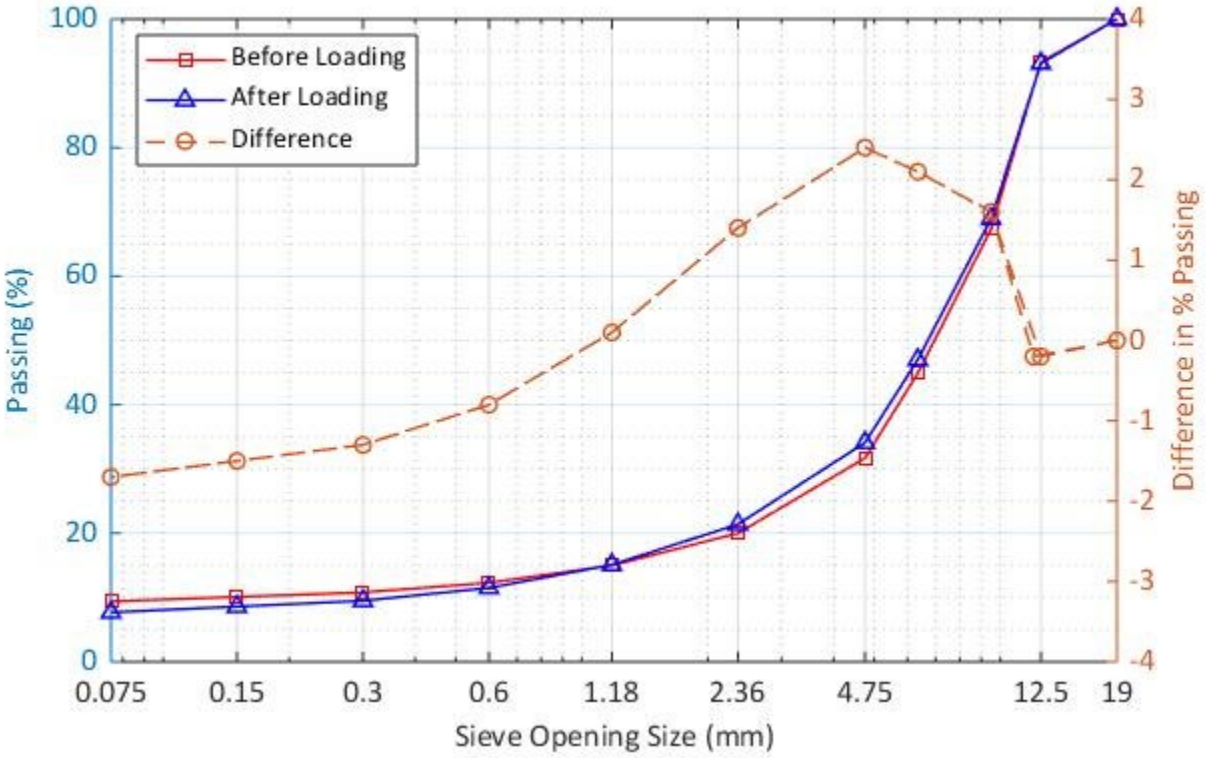

Figure 4. Graph. Visual description of an aggregate breakage gradation curve.

METHODOLOGY

The following tasks were conducted to achieve the project's goals:

Task 1: Laboratory Design and Experimental Program

1. Illinois coarse aggregate products and sources were selected and sampled, and their properties were measured.

2. SMAs were designed to achieve volumetric, drain down, and aggregate gradation and interlock requirements. The SMA design parameters were selected to represent common practice in Illinois.

3. The potential performance of SMA designs was evaluated in accordance with Illinois-modified AASHTO specifications T 393, T 324, and T 166 (IDOT, 2021b) to complete the

following tests: the Illinois Flexibility Index Test (I-FIT, at short- and long-term aging), Hamburg wheel-tracking test (HWTT), and indirect tensile strength (ITS) test—on both wet and dry specimens to obtain the tensile strength ratio (TSR). The tests identify potential for cracking, rutting, and stripping, respectively. The SMA designs with local aggregates were evaluated against SMA with imported aggregates, which is currently used in Illinois.

4. The aggregate skeleton change of SMA with local aggregates was assessed by measuring aggregate breakage.

Task 2: Full-scale Pavement Construction and Instrumentation

To validate the findings from the laboratory experimental program, a full-scale experimental program was executed using the Illinois Accelerated Pavement Tester (I-APT), which can apply tandem loading. I-APT was used for the first time in Illinois, and Appendix B provides background about accelerated pavement testing systems and I-APT. Six optimum laboratory-designed SMAs, produced by a local asphalt plant, were constructed. The SMAs were constructed on a binder mix placed on CRCP. A 500 ft instrumented pavement section was constructed as an overlay and was tested using I-APT. The instruments were installed to monitor the response of SMA sections to various loading under controlled temperature.

Task 3: Accelerated Pavement Testing

The pavement sections were tested to evaluate their response to varying loading conditions, including speed, tire pressure, axle loading, and tandem distance. Then, the sections underwent three sets of loading cycles. Transverse pavement profiles were collected at regular intervals to monitor surface deformation. After testing, aggregate breakage was assessed to determine the extent of damage.

Task 4: Life Cycle Assessment and Life Cycle Cost Analysis

Life cycle assessment (LCA) and life cycle cost analysis (LCCA) were conducted to quantify the impact of utilizing local aggregates in SMA on cost efficiency and emission reduction.

IMPACT

The current average service life of an HMA overlay is between 10 and 15 years (Hajek et al., 1987; Thompson et al., 2012). This lifespan falls short of expectations and carries economic and environmental consequences for the paving industry, roadway networks, and drivers. In contrast, SMA pavements have demonstrated durability in excess of 20 years (Dahhan & Miller, 2018). Extending pavement life by even a single year could result in substantial savings.

Despite its performance advantages, SMA still represents a small portion of total asphalt paving in the US, with national annual usage estimated between 68,000 and 1.87 million tons (Yin & West, 2018). The primary barrier is its higher initial cost—typically 20% to 25% more than dense-graded HMA (NAPA 2002)—due in part to the need for specialized aggregates, polymers, and stricter specifications. Over the past five years in Illinois, the average cost difference between a ton of SMA and non-polymer HMA was 28%. In 2024, surface SMA was, on average, 5% (or $8/ton) more

expensive than polymer-modified HMA and 16% (or $25/ton) more expensive than non-surface mixes (based on data from Brian Hill, IDOT Bureau of Materials, pers. comm., May 16, 2025).

With an estimated 5 million US tons of HMA/SMA paved annually in Illinois—within IDOT's typical 4–8 million US tons/year range (Hajj et al., 2021)—this corresponds to approximately 3,580 lane-mi, based on a bulk specific gravity of 2.323, a 3 in layer thickness, a 12 ft lane width, and an assumed ~25% excess. Using a national average cost of $2.33 million per lane-mi (Manzo, 2014) and assuming an average pavement layer service life of 15 years, this level of activity corresponds to resurfacing approximately 1/15 of the network each year under a steady-state rehabilitation cycle. Extending the average pavement service life from 15 to 16 years reduces annual resurfacing demand to 1/16 of the network, corresponding to a 6.25% reduction in annual resurfacing needs and yielding savings of approximately $33 million per year.

Reducing aggregate hauling distances can lower production costs and reduce contractor risk by buffering against fuel price volatility and aggregate supply disruptions. Moreover, decreased compaction effort in the field may further reduce contractor cost during SMA paving projects. Together, these factors may lead to lower SMA bid prices. In fact, the savings from reduced aggregate hauling alone may exceed 5%, potentially making SMA cost-competitive with polymer-modified HMA.

This report serves as a resource for increasing local industry knowledge about SMA mix design, production, and construction practices. Broader contractor familiarity could foster more competitive bidding, enhance market efficiency, and reduce costs. As a result, road owners may be more inclined to adopt SMA for a wider range of applications.

The primary outcome of this research supports the use of locally sourced aggregates in SMA. It reduces material and transportation costs, improves contractor accessibility, and enhances the overall feasibility of SMA implementation. In addition, it promotes the broader adoption of durable SMA pavements, extending roadway service life, and provides long-term economic and environmental benefits.

CHAPTER 2: SMA DESIGN AND POTENTIAL PERFORMANCE

This chapter details the laboratory experimental program, material selection, and mix design parameters. Prior to studying the use of local Illinois aggregates in SMA, the following were analyzed:

- National and international construction specifications and available literature.
- SMA designs in IDOT's database for the past 10 years.
- Illinois quarries that would eventually produce aggregate for SMA were surveyed for their input. Forty responses were received.
- Input from IDOT's district materials engineers was collected through a questionnaire. All districts responded.

Appendix A synthesizes the document review. Appendix C presents the quarry survey outcome, while Appendix D presents the responses to the questionnaire by IDOT's district materials engineers.

SMA DESIGN PARAMETERS AND LIMITATIONS

New SMAs were designed because local lithology is not used in a blend of coarse aggregate (CA) for SMA in Illinois. Nominal maximum aggregate sizes (NMAS) of 12.5 and 9.5 mm were selected based on survey results, reflecting input from IDOT districts. All Illinois districts expressed an expected increase in SMA usage if local aggregates were available. Two SMAs were designed at 80 gyrations (N_{des}) using an SGC, which is commonly used in Illinois. SMA aggregate structures (or design aggregate gradations) were modified to accommodate the reduced N_{des} of 50 gyrations. A reduced N_{des} may be more commonly used in SMA once the CA structure is achieved, as additional compaction may not provide further mix stability. All selected aggregate gradations were within the Illinois-modified AASHTO M 325 bands (IDOT, 2021b).

Other design requirements were established for this study:

- No recycled asphalt pavement (RAP) or recycled asphalt shingles (RAS) content was used to avoid their stabilizing effects and to minimize mix variability.
- Only two CA stockpiles were used per design to limit the number of sampled stockpiles.
- Less than 8.1% mineral filler content was used to avoid any modifications to existing plants. Mix designs in Illinois generally contained less than 8.1% of mineral filler.
- One-hour short-term aging at 306°F (compaction temperature) was used for the mixing temperature of 325°F. When the combined aggregate blend absorption was high (> 2.5%), 2-hour short-term aging was used, with stirring midway through.
- Hydrated lime was added dry, resulting in adjusting the mineral filler content by 1.0%.

Two verifications were used for SMA designs that are not typically used for dense-graded HMA:

- Measured voids in CA in dry rodded conditions (VCA_{DRC}) were greater than those computed for the aggregate blend in the SMA (VCA_{MIX}), ensuring stone-to-stone contact. Aggregates in the mix are more tightly packed than in the dry rodded state ($VCA_{MIX} < VCA_{DRC}$). The VCA measurements in this study were performed on materials retained on the #8 sieve.

- The drain down of loose SMA subject to high temperatures (at mixing temperature and at 27°F greater than typical, non-polymer HMA) was lower than 0.3% by weight of SMA.

COARSE AGGREGATE SELECTION AND CHARACTERIZATION

Baseline SMA designs were developed with trap rock CA, typically sourced from Missouri. When designing local-aggregate SMA, the CA was the only component changed. The available types of CA lithologies (dolomite, limestone, and crushed gravel) were identified using geological maps and the responses received from the 40 quarries. Products CM 13, CM 14, and CM 16 were used (in accordance with Illinois specifications). The selection of the aggregate products corresponded to a preliminary analysis of the aggregate gradations required to produce SMA with the selected NMAS and the availability of the products determined by the survey.

An anonymized dataset from IDOT was used to identify CA stockpiles representative of the LA abrasion loss values, as presented in Figure 5. Consequently, SMAs with CA of different LA abrasion levels were designed and ranked in Table 2. Each SMA has CA from one quarry, with selected quarries evenly distributed throughout the state. Note that CA quality requirements, present in Illinois-modified AASHTO M 325 (IDOT, 2021b), were not enforced for tested local aggregates.

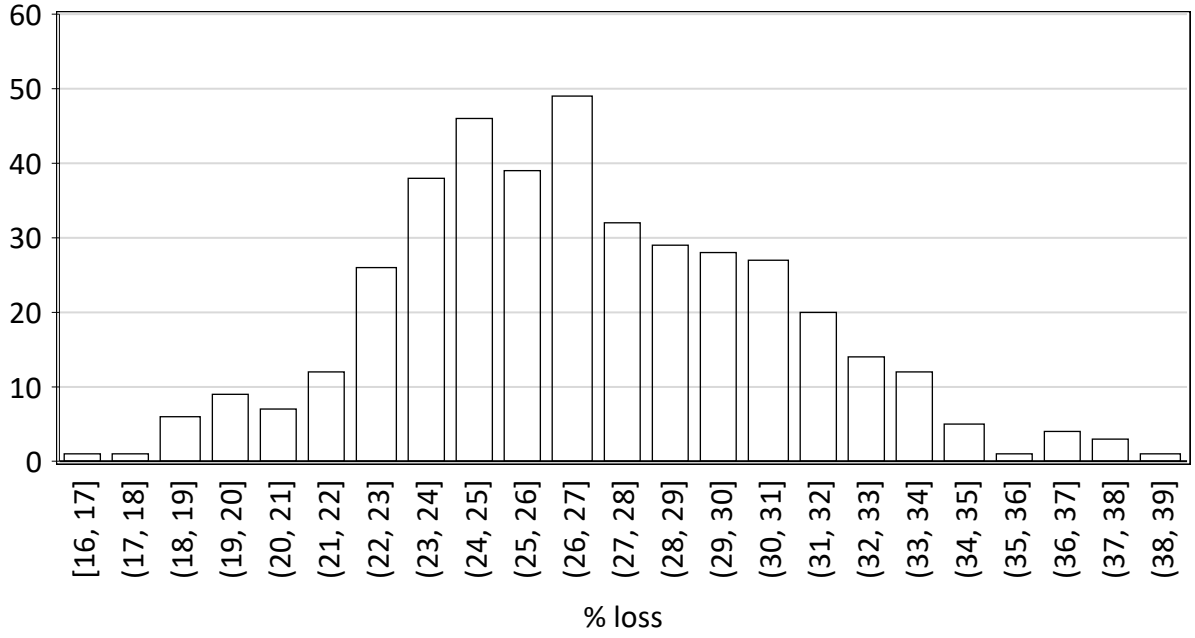

Figure 5. Graph. LA abrasion histogram for CA from Illinois.

Table 2. LA Abrasion Ranking, Categories, and Reference Value

LA Abrasion Ranking	LA Abrasion Category	LA Abrasion (% loss) Reference/Target Value
1	Unavailable in Illinois	–
2	75th percentile in Illinois	22.7
3	50th percentile in Illinois	25.0
4	25th percentile in Illinois	27.6

Aggregate Qualities

The quality designations of all CA used in the SMA designs were characterized to understand their role in SMA design, performance, and CA breakage (Table 3). The values were obtained per standard practice by IDOT's Central Bureau of Materials, using material sampled simultaneously with the material used in the mix design process.

- The lithology of the carbonate CAs was verified with the magnesium oxide (MgO) proportion.

- The insoluble residue proportion and the deleterious material proportion were obtained to quantify the amount of unsuitable material that may be present in carbonate aggregates. For a CA to be Class A—suitable for SMA—in Illinois, the deleterious shall be less than 5.0%.

- The soundness (sodium sulfate % loss), LA abrasion % loss, and Micro-Deval % loss were obtained as indicators of the CA's resistance to weathering and freeze-thaw cycles, abrasion, and impact in dry and soaked conditions, respectively. Per Illinois-modified AASHTO M 325 (IDOT, 2021b), soundness shall be less than 15% and LA abrasion less than 30% for SMA CA, respectively. There is no standard recommendation or requirement for SMA CA for Micro-Deval % loss results. In Indiana, the Micro-Deval % loss value for an acceptable CA or blend of CA should be 18.0% or less (Indiana Department of Transportation, 2015).

- Per Illinois-modified AASHTO M 325 (IDOT, 2021b), recommended flat or elongated (F/E) ratios for SMA aggregate blends are lower than 20 and 5, respectively. A few stockpiles had relatively high ratios, which would affect packing and could be susceptible to breakage.

- Aggregate absorption was obtained from IDOT's published values for each aggregate source for the years of sampling (IDOT, 2021). Illinois-modified AASHTO M 325 (IDOT, 2021b), recommends it is lower than 2.0%. Most aggregates sourced from Illinois had relatively high absorption, which is an indication of porosity that results in increased asphalt binder absorption.

The higher quality associated with the trap rock CA is manifested in lower % loss in weathering, abrasion, and polishing tests as well as lower absorption.

Table 3. Qualities of CA Stockpiles

LA abrasion Rank	Lithology	Product No.	MgO (%)	Insoluble Residue (%)	Deleterious (%)	Soundness	LA Abrasion	Micro-Deval	F/E 3:1 (%)	F/E 5:1 (%)	Absorption
4	Dolomite	CM 14	17.4	7.1	0.3	4.6	22.4	20.3	18.8	1.0	**2.1**
4	Dolomite	CM 16	17.9	7.9	0.2	7.1	28.3	12.3	**30.4**	**5.8**	**2.6**
3	Dolomite	CM 13	18.0	3.4	0.7	7.6	25.8	12.7	15.5	0.8	**2.2**
3	Dolomite	CM 16	18.9	3.9	0.5	8.2	27.2	13.4	12.9	1.6	**2.3**
2	Dolomite	CM 14	18.1	5.4	1.8	3.0	17.7	9.9	7.4	0	**2.8**
2	Dolomite	CM 16	18.4	5.9	0.8	4.3	20.4	8.8	11.6	0.6	**2.4**
4	Limestone	CM 14	1.2	3.1	0	7.8	26.6	17.5	11.8	0.1	1.7
4	Limestone	CM 16	1.4	2.7	0	10.1	29.5	16	10.1	0.5	**2.0**
3	Limestone	CM 14	2.3	2.4	**5.4**	6.1	24.6	13.6	13.3	0.8	1.7
3	Limestone	CM 16	2.1	2.6	0	9.1	26.2	14.4	**26.3**	3.1	1.8
2	Limestone	CM 14	1.0	6.2	0	5.2	21.0	12.5	7.1	0	**2.4**
2	Limestone	CM 16	1.0	3.7	0	5.8	24.6	13.3	7.6	0.5	1.7
1	Trap Rock	CM 14	2.2	85.1	0	0.3	15.7	1.4	**28.0**	3.2	0.3
1	Trap Rock	CM 16	2.6	82.1	0	0.6	15.9	2.3	16.8	1.0	0.8

Aggregate Shape and Texture

The Aggregate Imaging System (AIMS) is designed to analyze the shape, angularity, and texture of CA. These attributes affect SMA volumetrics and aggregate structure and, hence, SMA performance (Vavrik et al. 2002). For analysis, images of 250 particles passing the 3/8 in sieve and retained on the #4 sieve from a CA source were taken per an outlined approach (Eluri, 2018).

Table 4 presents the median and interquartile range (IR) of angularity, sphericity, and texture indices obtained from AIMS for measurements before Micro-Deval abrasion. The change after 10,500 revolutions of Micro-Deval degradation at 100 rpm is included in the table as "Δ." According to the AIMS cluster classifications, all CA were sub-rounded (angularity classification) and had low sphericity. In terms of texture, they were polished or smooth, except trap rock which had the most texture and the least loss.

Among the tested CA sources, trap rock CA had the highest angularity and texture, which are properties sought for achieving interlock in an SMA CA structure. The changes after abrading were relatively low, indicating minor breakage or degradation potential, while angularity and texture magnitudes remain almost the same. On the other hand, changes were greater for limestone sources than for dolomite sources.

Table 4. AIMS Results for the CA of the SMA

LA Abrasion Rank	Lithology	Angularity			Texture			Sphericity		
		Median	IR	Δ	Median	IR	Δ	Median	IR	Δ
4	Dolomite	2902	778	−14%	56	37	−23%	0.628	0.135	3%
3	Dolomite	2649	921	−13%	102	77	−14%	0.677	0.129	−2%
2	Dolomite	2755	879	−16%	152	64	−21%	0.689	0.128	0%
4	Limestone	2560	878	−28%	134	80	−30%	0.698	0.091	0%
3	Limestone	2899	834	−24%	175	88	−37%	0.631	0.118	0%
2	Limestone	2628	894	−24%	88	47	−10%	0.687	0.103	−2%
1	Trap Rock	2903	867	−5%	373	85	−6%	0.674	0.124	0%

OTHER SMA COMPONENTS

The following materials were used in all SMA designs.

- SBS PG 76-28: Asphalt binder modified with styrene-butadiene-styrene (SBS) polymer is required by IDOT for full-depth pavements (Illinois Department of Transportation, 2020) with standing traffic in the six northern IDOT districts.
- SMA cellulose fiber: The fiber was added to control asphalt binder drain down (0.3% by weight of SMA). Cellulose fibers are practically superior to mineral fibers when both technical aspects and costs are considered (Wonson, 1996).
- Mineral filler: Obtained from the byproduct fines of a dolomite quarry in Thornton, Illinois.
- Manufactured fine aggregate: The same stockpile of manufactured limestone sand was used for all SMA designs.

VOLUMETRIC DESIGN

Each SMA was labeled using the CA lithology—trap rock (T), dolomite (D), or limestone (L)—followed by the LA abrasion ranking, the NMAS, and an indicator (0 or 2) for the use of hydrated lime as an antistripping additive. For example, L3-50-12.5-0 is an SMA with limestone CA ranked third based on LA abrasion in Illinois, N_{des} of 50, 12.5 mm NMAS, and no antistripping agent.

Following the procedure described by García Mainieri and Al-Qadi (2024), using IDOT's short-term aging protocol, SMAs were designed targeting 4.0% air void content. Two to seven trials were required to finalize the aggregate blend for each design. Each trial consisted of preparing a set of an aggregate blend batch, two loose samples of mix (aggregates, binder, and fiber), and compacted SMA specimens. A washed sieve analysis was performed on the batch to verify the as-produced aggregate blend. The maximum theoretical specific gravity (G_{mm}) and the bulk specific gravity (G_{mb}) of the mix,

per Illinois-modified AASHTO T 209 and T 166 (IDOT, 2021b), were measured on the loose samples and compacted specimens, respectively.

As-produced aggregate blend gradations were verified to be a good representation of design aggregate gradations. For every batch of aggregate blends, prepared for volumetric trials or when specimens were prepared for performance measurements, a companion aggregate blend batch was washed and sieved. The aggregate proportion passing each sieve was within 1% of the design value for all aggregate blends.

A VMA of 17.5±0.3% and 16.5±0.3% were targeted for SMA with 9.5 mm and 12.5 mm NMAS, respectively, by proportioning the respective coarse aggregate (82.3%–69.3% by weight of aggregate blend) from two stockpiles with fine aggregate (22.6%–10.7%) and mineral filler (6.0%–8.1%). The predominant CA stockpile was CM 14 or CM 13 in all designs. Table 5 lists the composition of these SMAs.

Table 5. Design Mix Formulas and VCA of SMAs

SMA	CM 14/13 (%)	CM 16 (%)	FM 20 (%)	MF (%)	VCA	
					DRC	MIX
T1-80-12.5-0	59.5	11.2	21.3	8.0	40.8	35.7
T1-50-12.5-0	58.3	11.0	22.6	8.1	40.1	37.0
D2-50-12.5-0	63.6	11.4	17.6	7.4	41.0	33.5
L2-50-12.5-0	66.2	11.7	15.0	7.1	39.4	32.4
D3-50-12.5-0	65.7	16.6	10.7	7.0	39.7	35.0
D4-50-12.5-0	67.6	10.8	13.6	8.0	40.9	32.3

Table 6 presents the combined aggregate blend gradations of the designed SMAs along with gradation bands from Art. 1030.05 of IDOT's (2022) *Standard Specifications for Road and Bridge Construction* (*SSRBC*). Due to the iterative nature of the current design practice, aggregate breakage is indirectly accounted for when volumetric targets are sought. Two N_{des} were used to evaluate the effect on SMA potential performance and aggregate breakage.

Table 6. SMA Design Aggregate Gradations

Sieve	T1-80-12.5-0	T1-50-12.5-0	D2-50-12.5-0	L2-50-12.5-0	D3-50-9.5-0	D4-50-12.5-0	IDOT Gradation Bands	
							12.5 mm NMAS	9.5 mm NMAS
3/4"	100	100	100	100	100	100	100	100
1/2"	93.6	93.7	94.3	92.9	98.4	89.9	99-90	95-100
3/8"	67.9	68.6	71.7	66.6	87.6	63.2	85-50	95-70
#4	33.4	34.7	29.8	30.9	42.8	29.7	40-20	50-30
#8	23.3	24.3	20.9	19.5	21.6	19.3	24-16	30-20
#16	16.6	17.2	15.6	14.8	14.4	14.5	–	>21
#30	12.9	13.3	12.6	12.2	12.2	12.0	–	>18
#50	10.9	11.2	11.1	10.8	11.0	10.8	–	>15
#100	10.1	10.3	10.4	10.2	10.4	10.2	–	–
#200	9.4	9.6	9.7	9.5	9.1	9.7	11-8	11-8

The VMAs in Table 7 were achieved for the SMAs in this study. Binder content (P_b) was optimized to achieve 4% air void content by preparing sets of two loose samples and compacted specimens with three different binder contents and interpolating the measured G_{mm} and the bulk specific gravity of the mix (G_{mb}). Binder content (P_b) was verified by measuring G_{mm} and G_{mb} on a set of two loose samples and two compacted specimens (García Mainieri & Al-Qadi, 2024).

SMA performance is known to be affected by VMA and effective binder content (P_{be}). G_{mm} and G_{mb} measurements and the computed bulk specific gravity of the aggregate blend (G_{sb}) were used to compute P_{be}. The G_{sb} of each aggregate stockpile was obtained from IDOT's published values. Approximately equal VMA and P_{be} were achieved for SMAs of the same NMAS. SMA having different NMAS resulted in dissimilar SMA P_{be} because the target VMA was different.

Because Illinois aggregates have higher absorptions than imported trap rock, the combined water absorption of the aggregate blends was expected to be higher and the proportion of asphalt binder that was absorbed by the aggregate (P_{ba}) was higher for local aggregates.

Table 7. Volumetric Characteristics of SMAs

SMA	G_{mm}	G_{mb}	G_{sb}	VMA	VFA	P_b (%)	Combined Water Absorption	P_{ba} (%)	P_{be} (%)
T1-80-12.5-0	2.460	2.362	2.658	16.5	75.8	6.0	1.07	0.76	5.5
T1-50-12.5-0	2.456	2.358	2.657	16.8	76.2	6.3	1.11	0.94	5.6
D2-50-12.5-0	2.444	2.346	2.613	16.5	75.8	7.0	2.73	1.80	5.5
L2-50-12.5-0	2.439	2.341	2.630	16.7	76.0	6.4	1.71	0.99	5.6
D3-50-9.5-0	2.456	2.358	2.650	17.3	76.9	7.0	2.26	1.41	5.8
D3-50-9.5-2	2.447	2.348	2.653	17.5	77.2	6.8	2.21	1.07	6.0
D4-50-12.5-0	2.451	2.353	2.629	16.6	75.9	6.8	2.24	1.54	5.5
D4-50-12.5-2	2.444	2.349	2.629	16.4	75.6	6.4	2.23	1.00	5.8

SMAs Modified with Hydrated Lime

SMAs with low strength and high rutting potential (HWTT rut > 12.5 mm) were modified with hydrated lime (HL) to enhance their performance. Using 1% by weight of aggregates, HL was added dry to the aggregates before adding cellulose fibers, inert mineral filler, and asphalt binder. Appendix B.17 of IDOT's (2021b) *Manual of Test Procedures for Materials* was followed. A change in aggregate gradation, which would densify the aggregate blend, was needed to accommodate the incorporation of HL. Table 8 presents the original and modified aggregate blends. The addition of HL reduced P_b and P_{ba} and increased P_{be} (as presented in Table 7).

Table 8. Original and Modified Aggregate Gradations Incorporating HL

Sieve	D3-50-9.5-0	D3-50-9.5-2	D4-50-12.5-0	D4-50-12.5-2
3/4"	100	100	100	100
1/2"	98.4	98.4	89.9	89.8
3/8"	87.6	87.3	63.2	62.7
#4	42.8	41.4	29.7	28.7
#8	21.6	20.6	19.3	18.4
#16	14.4	14.2	14.5	14
#30	12.2	12.5	12.0	11.6
#50	11.0	11.7	10.8	10.5
#100	10.4	11.2	10.2	10
#200	9.1	9.9	9.7	9.4

SMA POTENTIAL PERFORMANCE

As presented in Figure 6, all SMAs passed the short-term aging (STA) and long-term aging (LTA) I-FIT flexibility index (FI) thresholds of 16.0 and 10.0, respectively, as defined by IDOT's (2022) standard specifications. Modification with HL increased cracking potential.

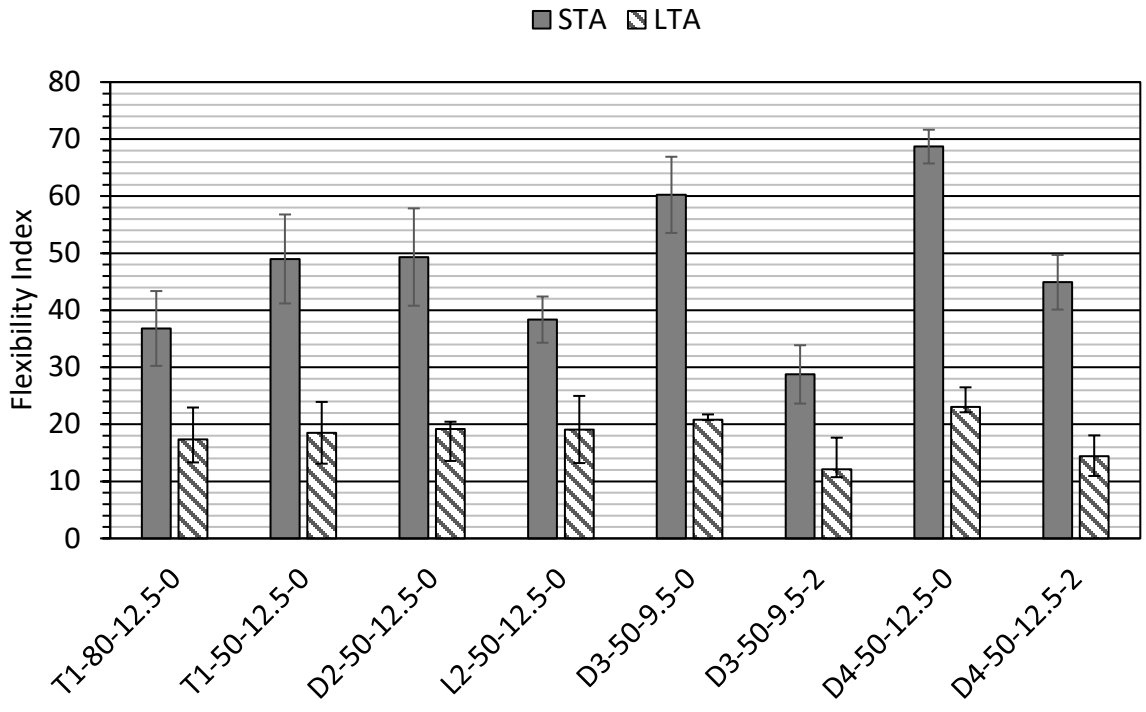

Figure 6. Graph. FI of laboratory SMAs.

All SMAs had rutting less than 12.5 mm after 20,000 HWTT passes, except D3-50-9.5-0 and D4-50-12.5-0, as presented in Figure 7. Rutting for both SMAs was affected by LA abrasion ranking and lithology. This finding supports that rutting potential is dependent on volumetric design and CA properties, and it appears to be independent of N_{des}. Moisture susceptibility during HWTT loading was not observed. Modification with HL stabilized both D3-50-9.5-0 and D4-50-12.5-0. After 20,000 passes, the HWTT rut depth decreased by 52.8% and 51.2% for those SMAs, respectively, and passed the 20,000 cycles threshold.

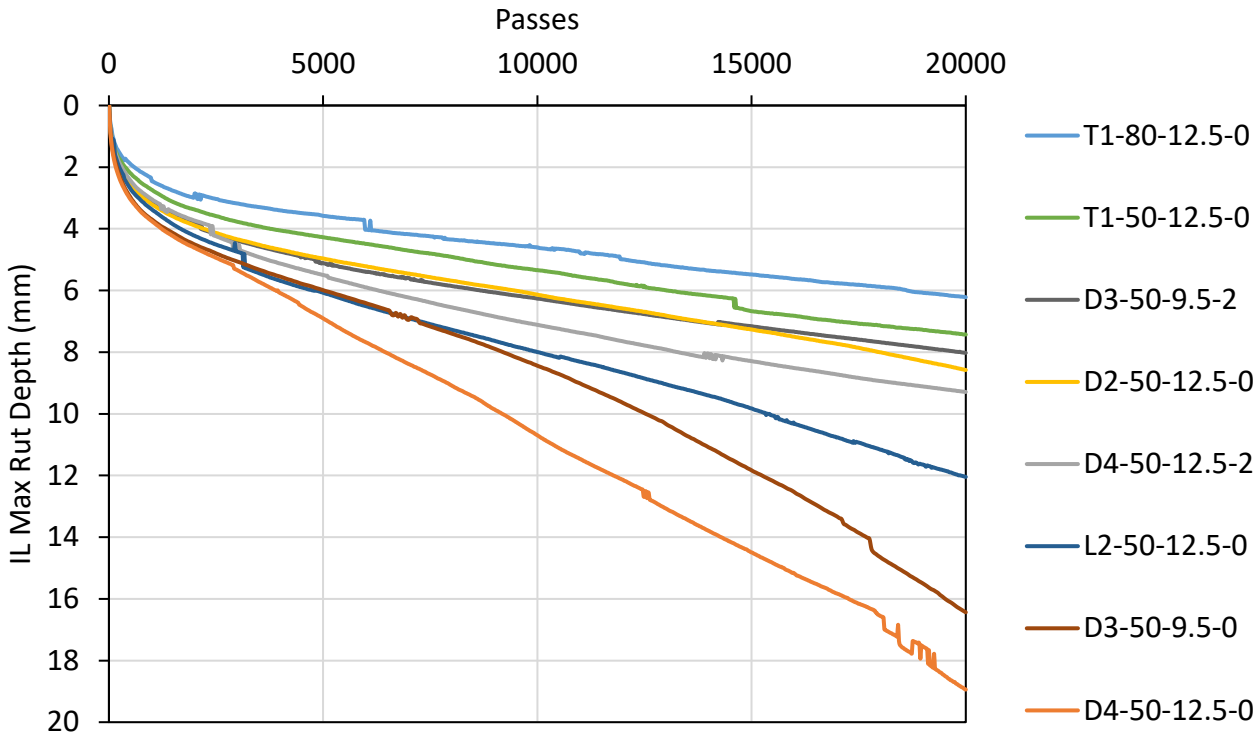

Figure 7. Graph. HWTT rut progression of laboratory SMAs.

As presented in Figure 8, not all SMAs had tensile strength over 80 psi and a TSR over 0.85. Dry modification with HL increased strength, but IDOT's threshold for conditioned specimens' average was not met for D4-50-12.5-2. IDOT's requirements for this test changed during this study in 2024, based on test results for this task. Air void requirements were reduced from 7±1% to 6±1%. With this change, all SMAs in this study would meet the requirements. Based on regression analysis, ITS increases with decreasing air voids, with typical sensitivities on the order of approximately 10–15 psi/%AV for unconditioned specimens and 5–10 psi/%AV for conditioned specimens. Applying these relationships to normalize results to 6.0% AV indicates that all mixtures meet or exceed the 80 psi threshold, as shown in Figure 9, where individual specimen results are shown.

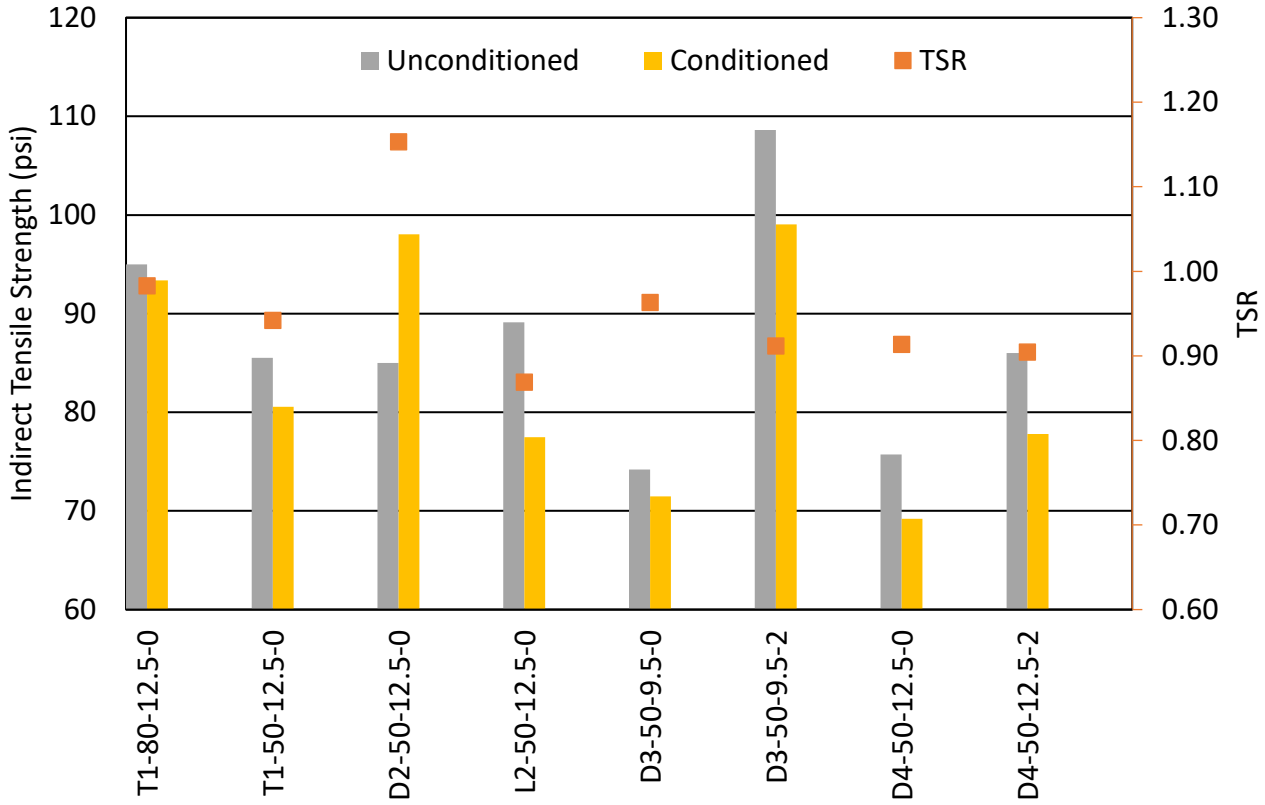

Figure 8. Graph. Conditioned and unconditioned ITS and TSR of laboratory SMAs.

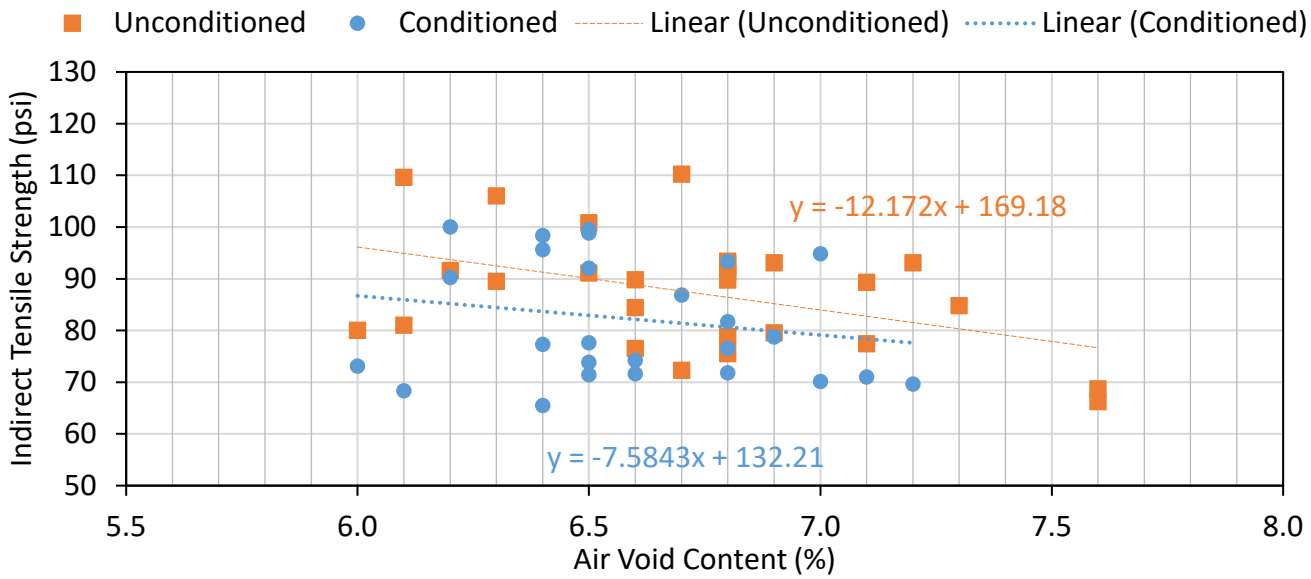

Figure 9. Graph. Individual specimen indirect tensile strength and sensitivity to air voids.

AGGREGATE BREAKAGE IN THE LABORATORY

García Mainieri and Al-Qadi (2024) suggested that lowering design compaction could reduce potential aggregate breakage. Aggregate breakage, due to design and HWTT, and ABI are presented in Figure 10 and Figure 11, respectively. The breakage in T1-80-12.5-0 and T1-50-12.5-0 is minimal. The ABI values indicate that aggregate breakage in SMA after compaction could be related to aggregate lithology and LA abrasion. In addition, breakage could decrease when SMAs were modified with HL.

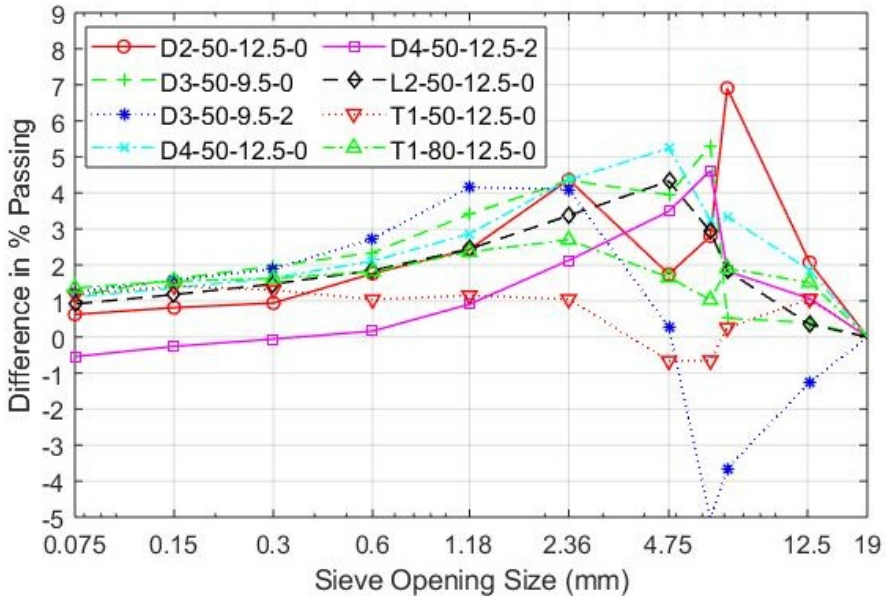

(a) Design Compaction

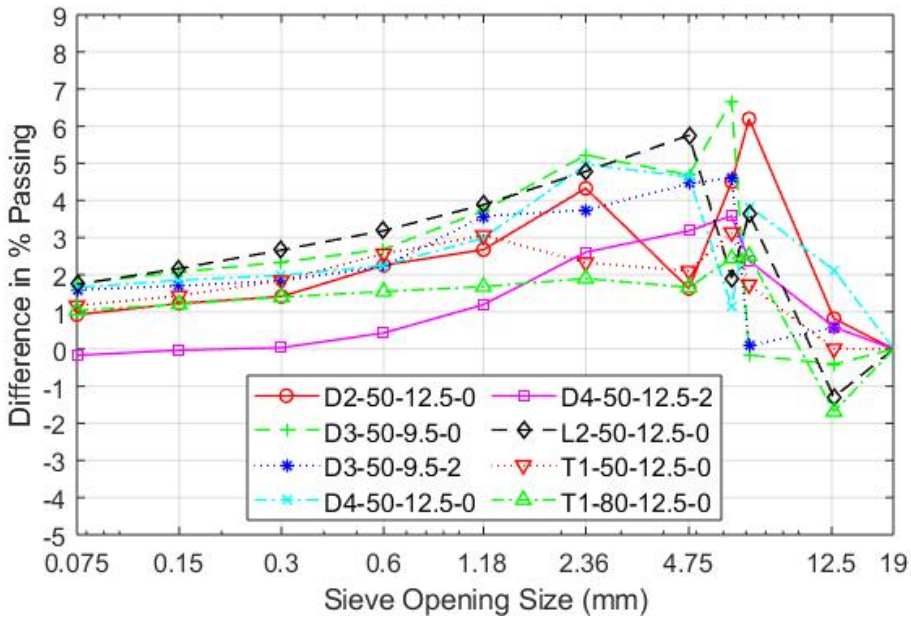

(b) 7.0% Air Void Content Compaction + HWTT

Figure 10. Graph. Breakage plots for laboratory-produced, laboratory-compacted SMA.

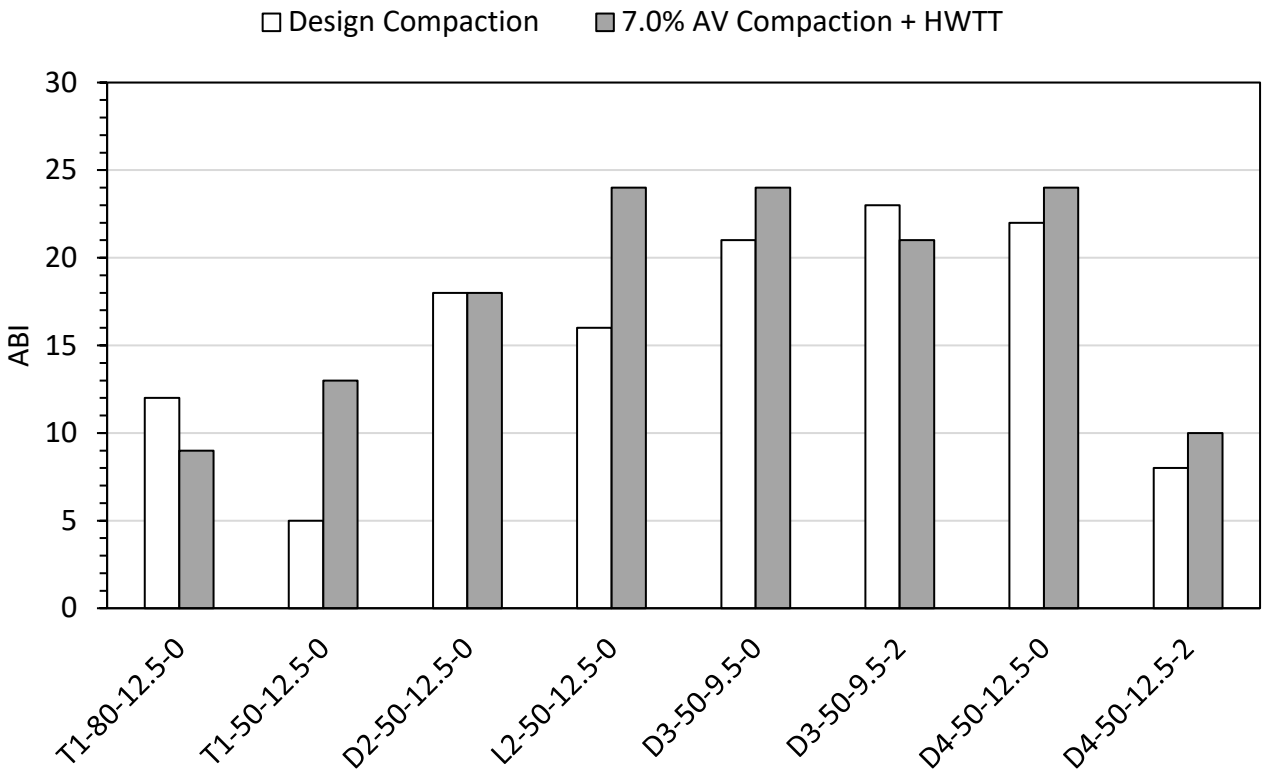

Figure 11. Graph. ABI for laboratory-produced, laboratory-compacted SMA.

EFFECT OF AGGREGATE QUALITY AND SKELETON ON SMA STABILITY

Potential rutting of SMA, as measured with the HWTT, could be related to CA characteristics, as presented in Figure 12. Soundness appeared to have the strongest agreement with HWTT rut depth. Internal pressures applied to the aggregates during the rutting test could potentially be a more realistic representation of rutting in SMA compared to the impact with steel balls in LA abrasion and Micro-Deval durability tests. The results indicate that increased rut depth and higher rutting progression rates in SMA are associated with changes in aggregate texture, as measured by AIMS after the Micro-Deval test.

To illustrate the "combined" quality, each CA stockpile was multiplied by its corresponding quality. For example, the combined soundness of T1-80-12.5-0 is $0.595 \times 0.3 + 0.112 \times 0.6 = 0.246$. This computation is an indicator of SMA's CA quality and does not represent the whole aggregate blend. Furthermore, SMA rutting potential may be related to ABI after compaction to 7.5 ± 0.5% air void content and 62 mm height, as presented in Figure 13. The ABI describes the state of the SMA aggregate skeleton change. The lower the ABI, the higher the probability that the aggregate skeleton has maintained intact.

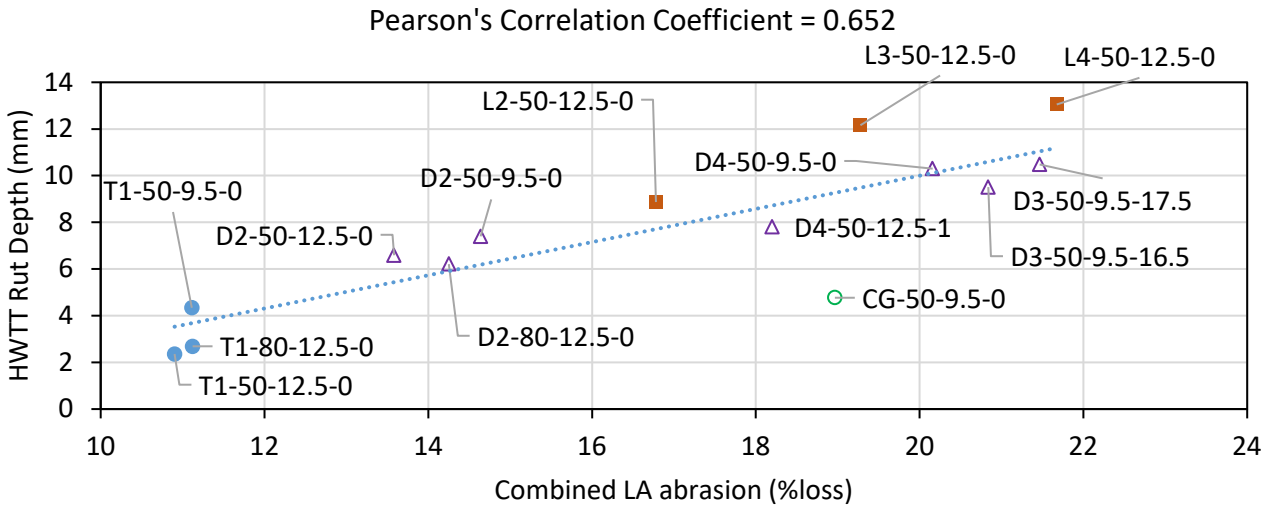
Pearson's Correlation Coefficient = 0.652
HWTT Rut Depth (mm)
Combined LA abrasion (%loss)
L3-50-12.5-0
L4-50-12.5-0
L2-50-12.5-0
D4-50-9.5-0
D2-50-9.5-0
T1-50-9.5-0
D3-50-9.5-17.5
D2-50-12.5-0
D4-50-12.5-1
D3-50-9.5-16.5
CG-50-9.5-0
D2-80-12.5-0
T1-80-12.5-0
T1-50-12.5-0

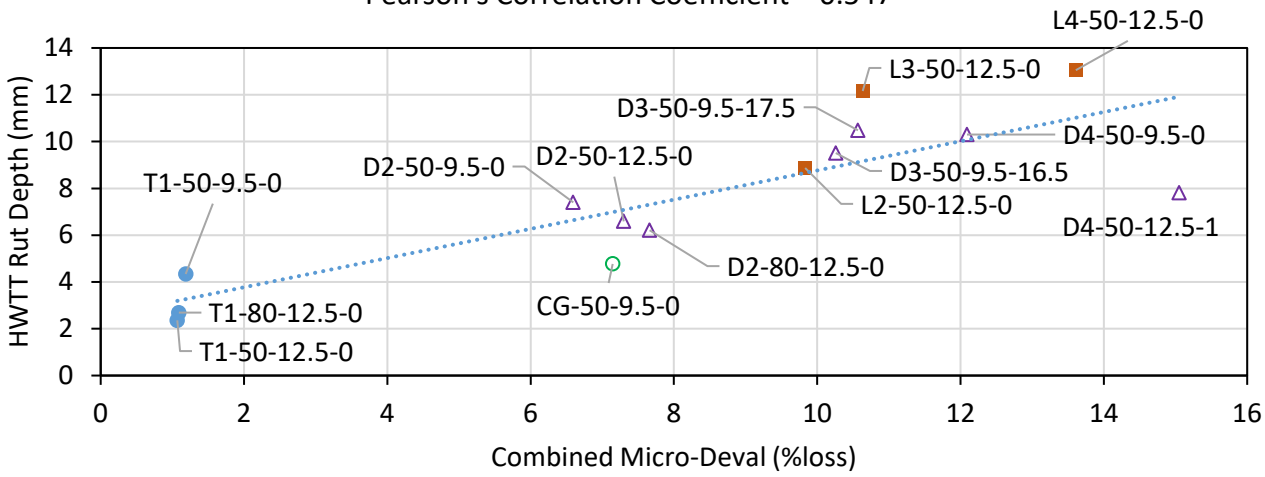
Pearson's Correlation Coefficient = 0.547
HWTT Rut Depth (mm)
Combined Micro-Deval (%loss)
L4-50-12.5-0
L3-50-12.5-0
D3-50-9.5-17.5
D4-50-9.5-0
D2-50-9.5-0
D2-50-12.5-0
T1-50-9.5-0
D3-50-9.5-16.5
L2-50-12.5-0
D4-50-12.5-1
D2-80-12.5-0
CG-50-9.5-0
T1-80-12.5-0
T1-50-12.5-0

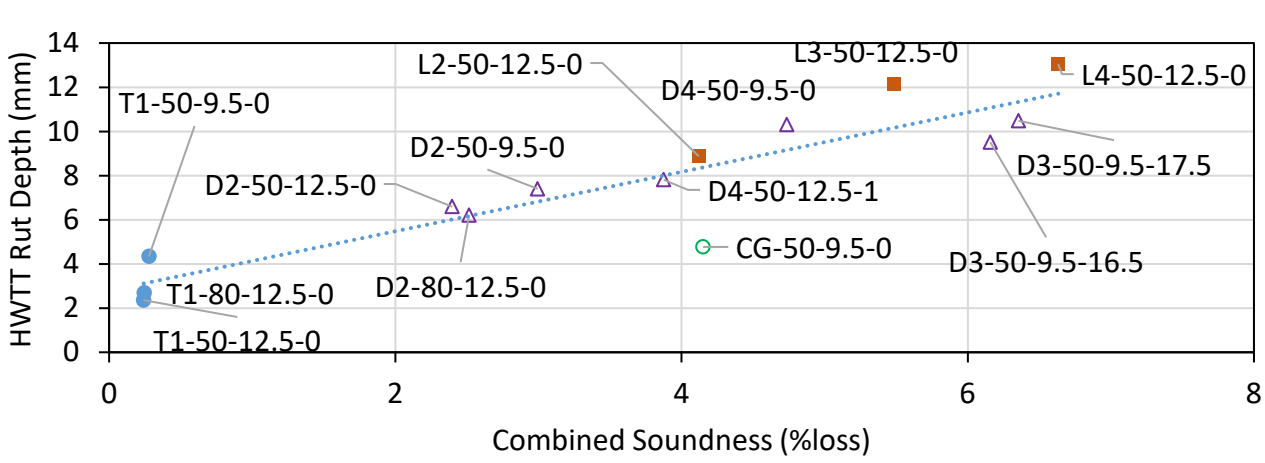
Pearson's Correlation Coefficient = 0.819
HWTT Rut Depth (mm)
Combined Soundness (%loss)
L2-50-12.5-0
L3-50-12.5-0
L4-50-12.5-0
T1-50-9.5-0
D4-50-9.5-0
D2-50-9.5-0
D3-50-9.5-17.5
D2-50-12.5-0
D4-50-12.5-1
CG-50-9.5-0
D3-50-9.5-16.5
T1-80-12.5-0
D2-80-12.5-0
T1-50-12.5-0

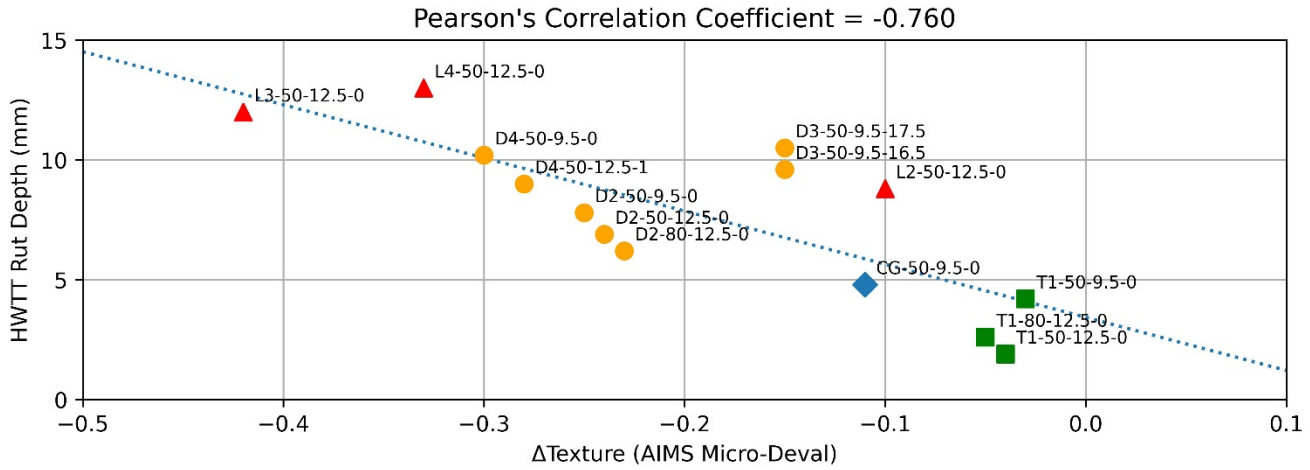

Figure 12. Graph. Relationship between rutting potential and CA quality.

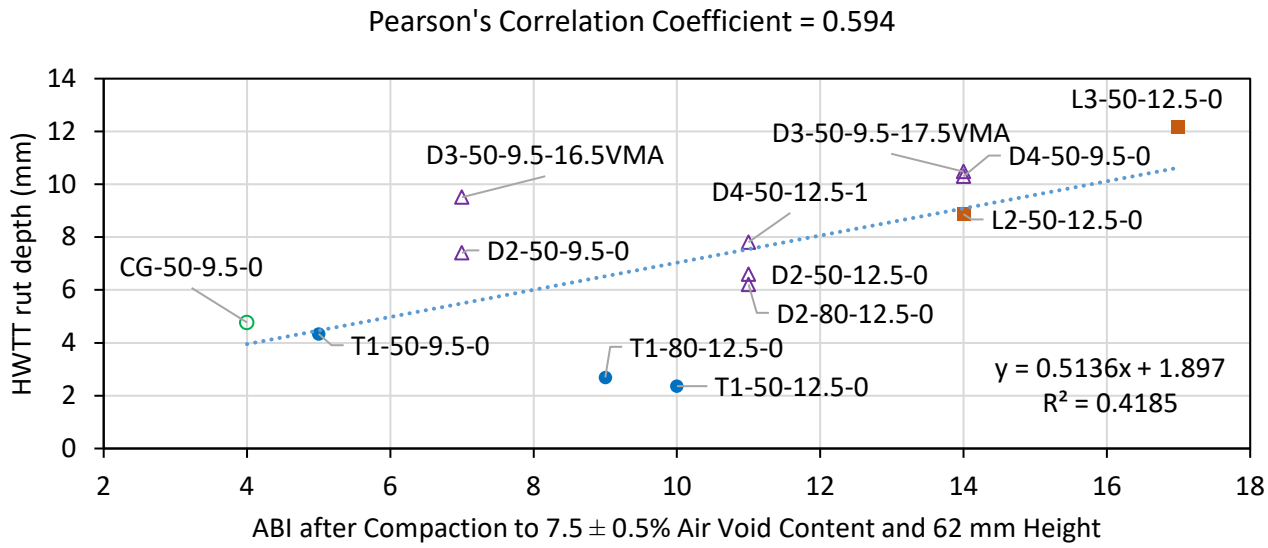

Figure 13. Graph. Relationship between HWTT rut depth and ABI after compaction to 7.5 ± 0.5% air void content and 62 mm height.

Additionally, aggregate properties could be related to aggregate breakage, elucidating a practical link to expected performance during the design process. The shape of particles with a size of 4.75–1.18 mm describes aggregate breakage (as presented in Figure 14). Figure 15 presents an empirical relationship to simplify aggregate breakage susceptibility.

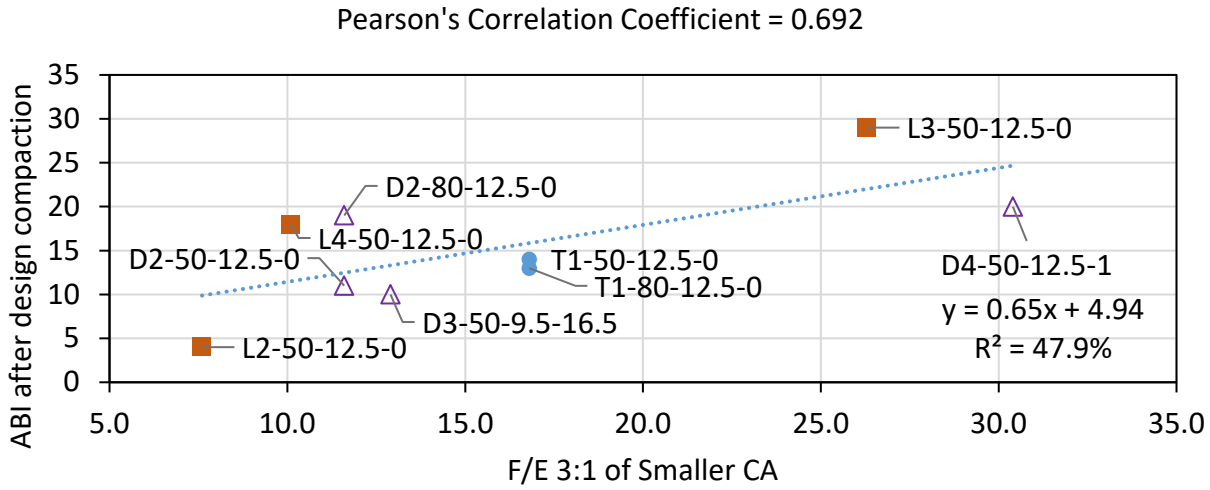

Figure 14. Graph. Shape of smaller coarse aggregate stockpile versus ABI after design compaction.

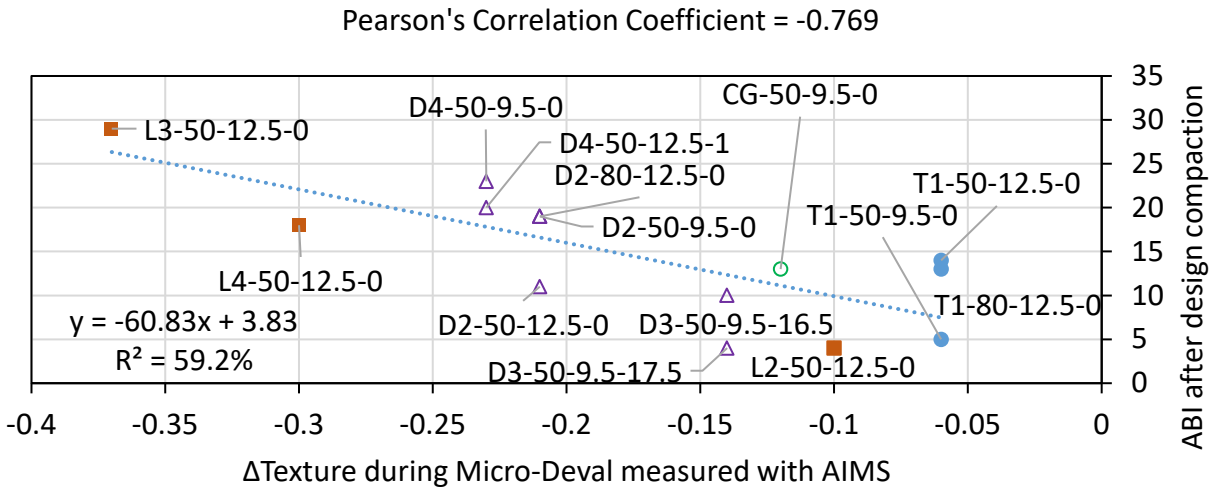

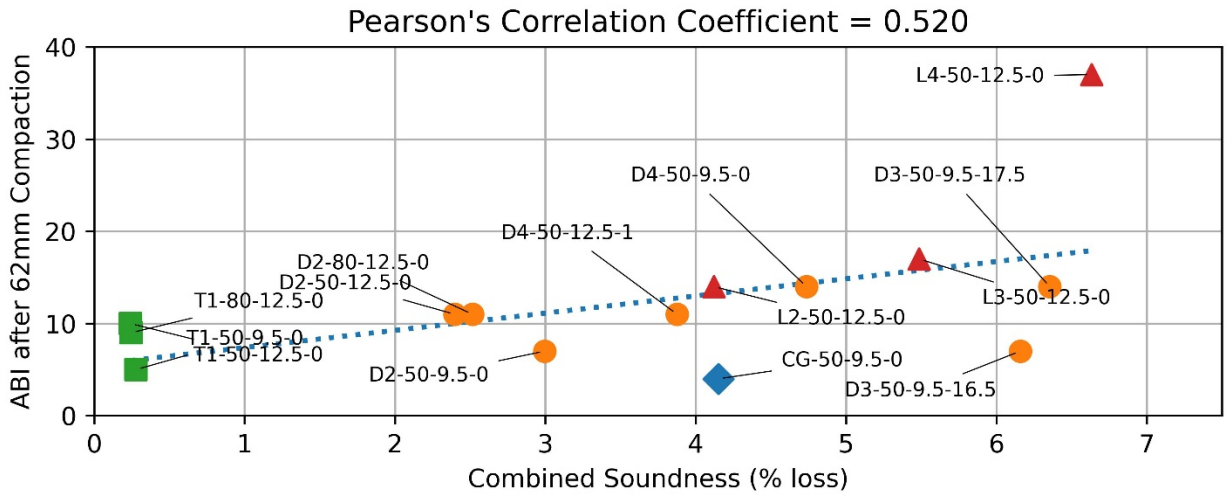

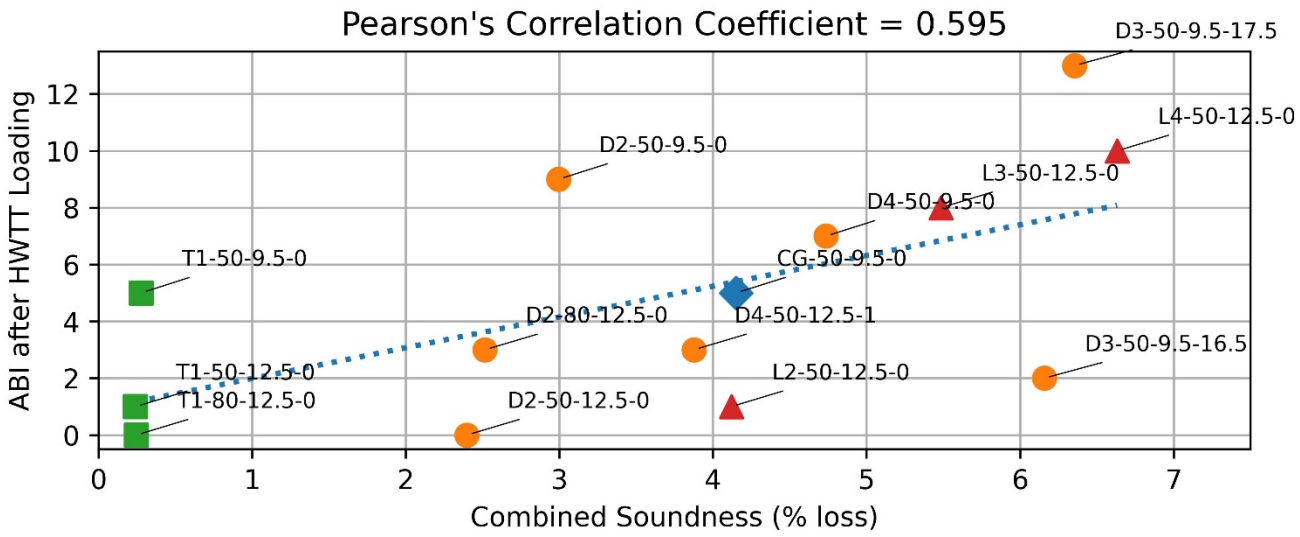

Figure 15. Graph. Relationship between ABI and aggregate qualities.

SUMMARY

SMAs were designed to meet volumetric requirements and were found to be adequate as per standard laboratory potential performance thresholds, despite aggregate breakage due to compaction. The design compaction (N_{des}) was reduced to 50 gyrations to accommodate local aggregate. Hence, SMAs with local aggregate and reduced N_{des} may have the potential to perform similarly with SMAs containing imported aggregate with respect to durability. Two SMAs showed potential for rutting and low strength, so they were modified with dry HL. Dry HL modification reduced P_{ba}, and consequently P_b, and stabilized those SMAs. This reduced HWTT rut depth by half, increased strength, and reduced aggregate breakage. The aggregate breakage in the laboratory-produced, laboratory-compacted specimens and HWTT—determined by ABI—may be related to SMA coarse aggregate quality.

CHAPTER 3: FULL-SCALE PAVEMENT TEST SECTIONS

Six SMAs, without hydrated lime, were selected for full-scale accelerated testing using the Illinois Accelerated Pavement Tester (I-APT). This chapter documents the construction of the test lane, SMA quality, and SMA aggregate skeleton change after construction. The lane was built on the southmost existing lane at Illinois Center for Transportation's full-scale testing yard (Figure 16).

Figure 16. Photo. Southmost lane of the ICT full-scale testing yard.

PAVEMENT SECTION LAYOUTS

The full-scale pavement test lane was initially paved with a dense-graded HMA binder course over existing continuously reinforced concrete pavement (CRCP), to provide an even and smooth surface for the SMA layer, followed by six SMA sections, as presented in Figure 17. Figure 18 displays the paved lengths of the SMA sections. I-APT, represented in Figure 19, is 120 ft long. The test area includes loading gear at a stable speed. Each test section is 23 ft long. Transition sections (30 ft long) of SMA that were not part of the test sections were paved next to and between them (displayed in gray). This allowed the contractor to adjust the paver and transition between SMAs during construction.

The pavement structure is as follows:

- The CRCP layer has a thickness of 10 in, except the last 200 ft (west to east), where the thickness is 14 in (Kohler & Roesler, 2006). The thick CRCP allowed for all-season testing without concerns related to subgrade saturation or freezing and provided a strong base to localize rutting damage in the flexible layers and mitigate the potential for cracking.

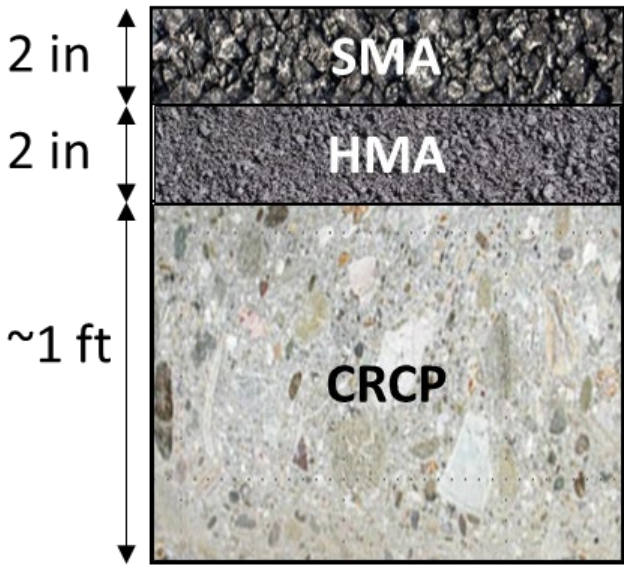

Figure 17. Illustration. Pavement section.

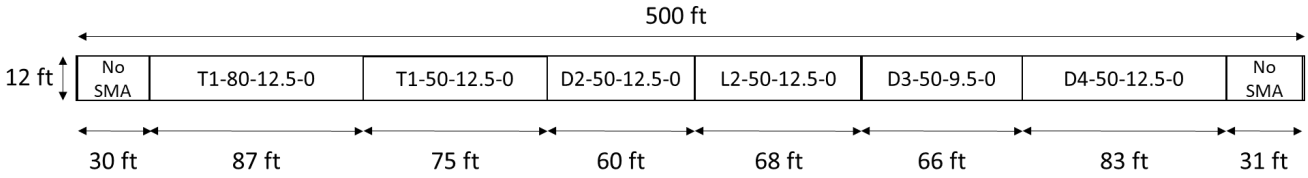

Figure 18. Schematic. Test strip layout with as-built lengths of SMA.

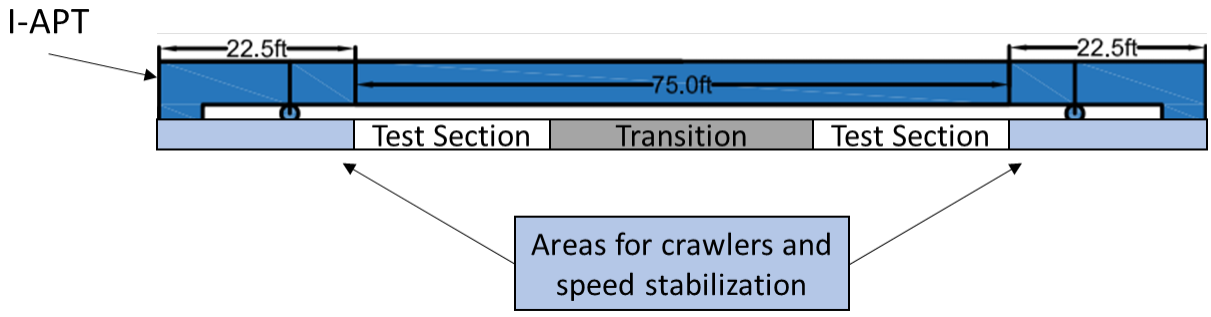

Figure 19. Schematic. Side view of test section locations with I-APT for reference.

- The SMA sections comprise one control SMA and five experimental sections; each design is presented in Appendix E. The SMA was placed over an HMA layer.
- The HMA binder layer is a dense-graded surface course. This mix contains crushed gravel, crushed limestone, natural sand, mineral filler, RAP, and PG 70-22 modified binder. The design VMA was 15.5% at a N_{des} of 90 gyrations. More details of the mix design are presented in Appendix F.

To verify that maximum shear would occur in the SMA layer, an advanced 3D finite element (FE) pavement model was developed and run using the parameters in Table 9. The FE model incorporates actual tire loading, SMA and HMA linear viscoelasticity characteristics, and advanced layer interactions between layers that are usually ignored in conventional analyses. More details on the FE analysis approach may be found elsewhere (Wang & Al-Qadi, 2013; Hernandez et al., 2016; Gamez et al., 2018, Ramakrishnan & Al-Qadi, 2023).

Table 9. Parameters for FE Model

Parameter	Value
Tire Pressure	110 psi
Tire Type	Dual Tire Assembly
Axle Loading	10 kip

After postprocessing, the maximum shear location was 0.92 in from the surface. Figure 20 presents the transverse plane shear strain distribution. Two layers could be observed distinctly, and the maximum shear strain was located approximately in the SMA layer at mid-depth.

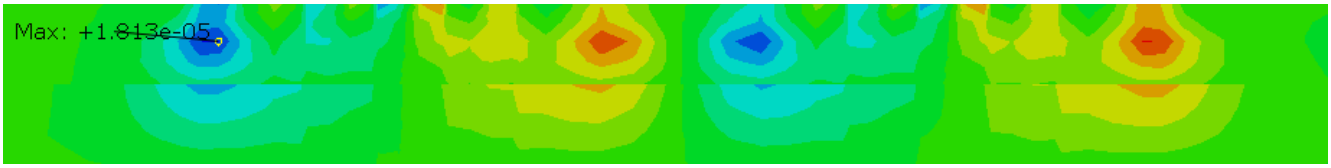

Figure 20. Graph. Transverse cross-section of the pavement with shear strain distribution.

PAVEMENT LAYER CONSTRUCTION

The construction was awarded to a local contractor based on experience in paving SMA and the bid cost. The preexisting HMA surface was completely milled on May 10, 2023. The remaining surface was bare CRCP with minimal visible distresses, as presented in Figure 21. Tack coat was applied to the CRCP surface on May 12, 2023. NTEA (non-tracking emulsified asphalt) asphalt emulsion at 62% residual asphalt was applied at a rate of 0.1 gal/yd^2, as presented in Figure 22.

To ensure a leveled surface adequate for SMA compaction, the N90 HMA binder layer was placed over the CRCP on May 15, 2023 (Figure 23). The achieved volumetrics, reported by the contractor, were as follows: G_{mm} = 2.432, G_{mb} = 2.365, air void content = 2.8%, VMA = 15.1%, and measured $P_{b\,(\%)}$ = 6.5%. The P_b and VMA were within IDOT's control limits per Art. 1030.09 (c) of the *SSRBC*. The thickness of the layer (2 in) was verified by obtaining 24 cores after construction. The mix was delivered to the hopper by haul trucks (Figure 24). An AP1055F Caterpillar track paver was used to place the mat. The HMA binder layer delivery temperature was approximately 321°F. Two compactors were used: a Caterpillar (Cat) CB13 and a Hamm HD+110i VO. The Cat CB13 was set to high/high (average mat temperature was 252°F). Five passes were applied, averaging 2–3 per compaction lane. The Hamm HD+110i VO, oscillating and vibrating on the highest setting (average mat temperature was 220°F), applied 10–11 passes. The right side of the lane, where pavement would be loaded by I-APT, experienced 2 passes by the Cat and 11 passes by the Hamm. However, the last test section (eastmost) received 8 passes by the Hamm.

Figure 21. Photo. Bare CRCP supports the HMA and SMA layers.

Figure 22. Photo. CRCP tack coat application.

Figure 23. Photo. N90E mix paving.

Five uncorrelated nuclear gauge measurements were taken across the lane in the middle of each test section. Table 10 presents the results. Sections are numbered from east to west.

Table 10. Base Layer Achieved Densities (Average)

Location	Section 1	Section 2	Section 3	Section 4	Section 5	Section 6
4 ft left from middle	96.6	93.9	96	97.4	94.2	95.5
Left wheel path	95.7	93.6	94.5	94.9	94.1	96.0
Middle	91.0	92.4	93.9	93.7	92.1	92.1
I-APT wheel path	95.3	93.1	95.5	96.3	95.2	95.9
4 ft right from middle	96.1	96.8	95.6	96.9	93.1	95.3
Average	95.0	94.0	95.1	95.9	93.8	95.0

HMA Binder Preparation

The HMA binder course was coated with NTEA asphalt emulsion at an application rate of 0.2 gal/y^2 on May 17, 2023. The residual asphalt was 0.62%. Figure 24 illustrates the tack coat spraying.

SMA Paving

The six SMA designs were provided to the contractor. Three SMA sections were paved on May 18, 2023, and the other three were paved on May 19, 2023. For the SMA, 200 tons of each aggregate stockpile were hauled to the contractor's plant in Urbana, Illinois. The first 50–60 tons of each SMA were discarded before loading to the site as well as 40–50 tons after loading each SMA. Only 14 tons of each SMA were needed and were hauled to the site.

Figure 24. Photo. Coating between layers.

A Cat AP1000 paver and a material transfer device (MTD), a 2015 Weiler remixing transfer machine, was used to reduce segregation and to retain heat (Figure 25). The heater was off during the first day of SMA paving. The three SMA sections were paved continuously. A construction joint was sawed at the beginning of the second day of SMA paving where the fourth SMA was placed. Each day, exact amounts of SMA were transferred from the MTD to the paver to achieve the desired section length. When the paver was almost out of SMA, the next SMA was loaded. A Hamm HD+110i VO compactor compacted the SMA. No vibration was used at the beginning of compaction. The vibrator was turned on to the correct low densities measured on the first few passes. On the second day of paving, the vibrator was turned on during the initial passes. Even though vibration is not allowed for SMA in Illinois, only one compactor was used to achieve compaction effort before the mat was cold so vibration was required to reach acceptable density.

IDOT Central Bureau of Materials personnel recorded placement and compaction temperatures with a FLIR1618 thermal camera. Some of the images are presented in Table 11.

Figure 25. Photo. Material transfer device and paver used to pave SMA sections.

Table 11. Thermal Camera Images

SMA	Image during placement	Image during compaction	Image during nuclear gauge readings
T1-80-12.5-0	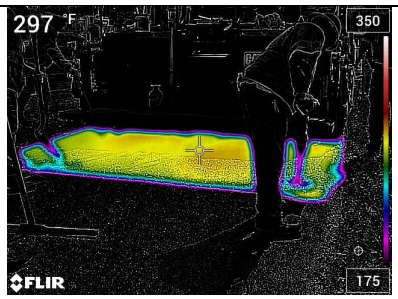	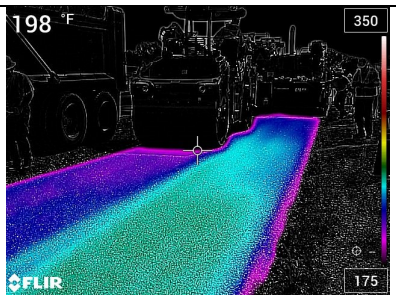	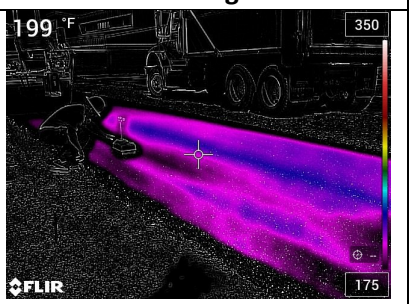

SMA	Image during placement	Image during compaction	Image during nuclear gauge readings
T1-50-12.5-0	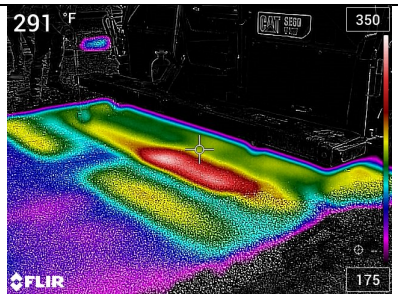	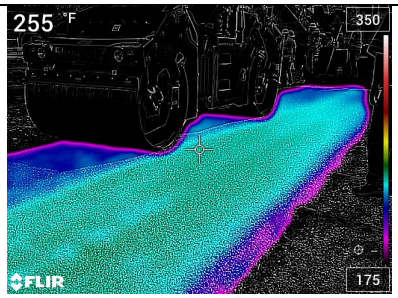	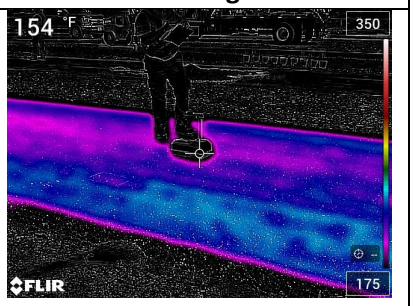
D2-50-12.5-0	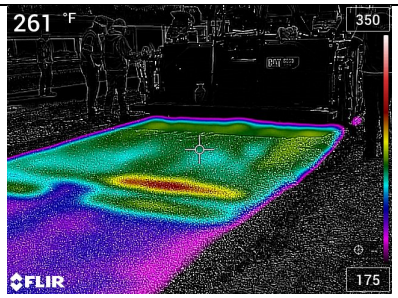	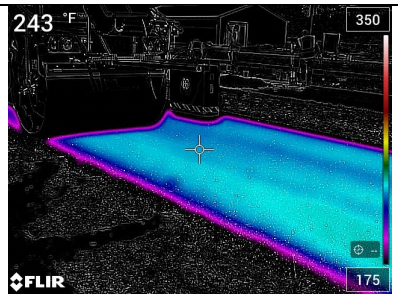	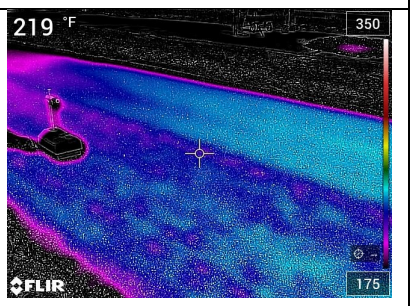
L2-50-12.5-0	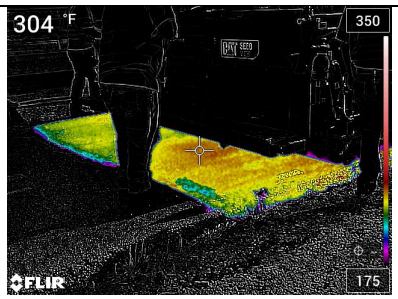	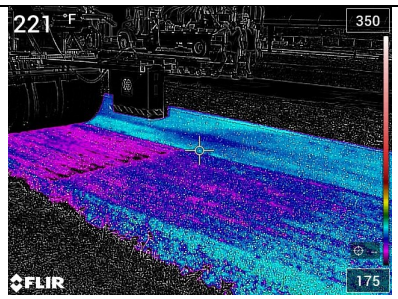	Unavailable
D3-50-9.5-0	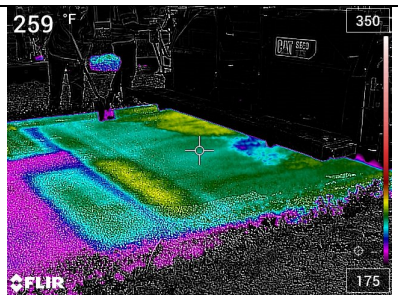	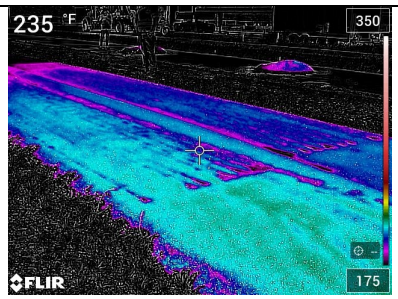	Unavailable
D4-50-12.5-0	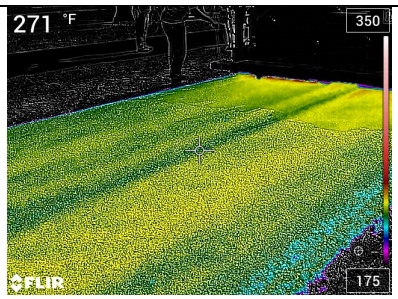	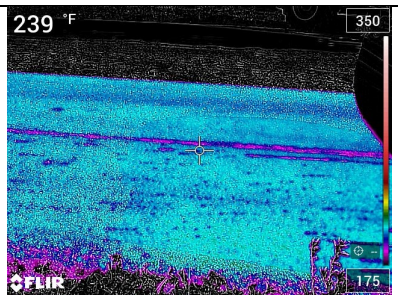	Unavailable

SMA PRODUCTION PROPERTIES

SMAs were produced at an Urbana HMA plant. The plant was dedicated exclusively to producing the SMAs for three days to mitigate material variability. The adjustments in Table 12 were applied to stockpile proportions on the design mix formula based on the Bailey Method and field experience for the following reasons:

- Stockpile gradations may differ at the plant compared to those used in the laboratory because of material variability over time, handling, and storage variations. The aggregate gradations used in the laboratory were obtained from quarry samples. However, plant aggregate gradations reflect stockpiles at the plant site.

- VMA changes due to dust content increases from plant breakdown. Aggregates break down as they move through a drum during the production process, releasing dust. Limestone and dolomite aggregates were expected to release more dust and degrade more than trap rock.

- VMA changes due to particle shape and texture loss. Rounded and smoother particles were expected to reduce VMA. The VMA compensation sought is presented in Figure 26, based on the contractor's experience with the respective lithologies of the coarse aggregates in the SMAs and aggregate LA abrasion.

Table 12. Job Mix Formula Adjustments

Aggregate Stockpile Type	T1-80-12.5-0	T1-50-12.5-0	D2-50-12.5-0	L2-50-12.5-0	D3-50-9.5-0	D4-50-12.5-0
Coarse	0	0	0	−6	−1.7	−7.6
Coarse	2.5	2.5	3.1	9.8	−0.1	11.2
Fine	−2.5	−2.5	−2.8	−3.2	2.3	−2.6
Mineral Filler	0	0	−0.3	−0.6	−0.5	−1.0

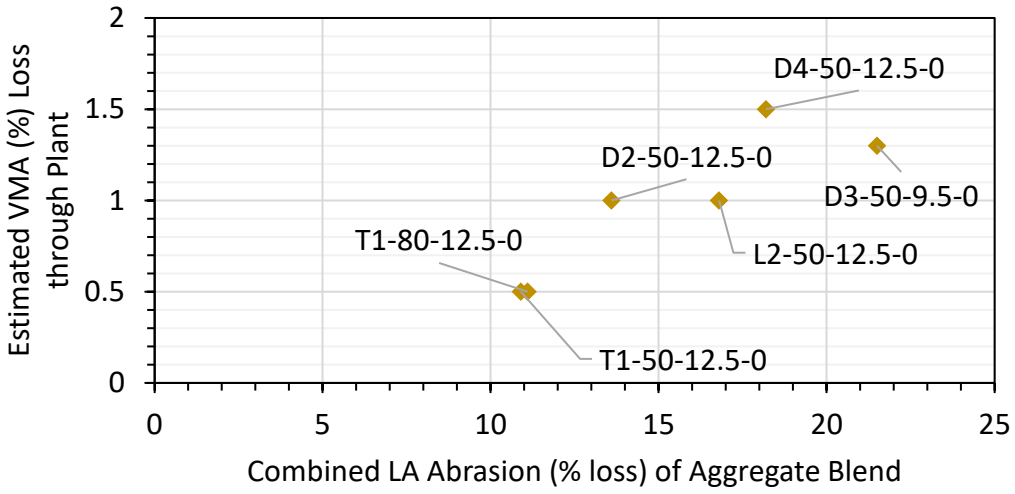

Figure 26. Graph. VMA increase to compensate for loss through plant.

Representative samples of plant-produced loose SMA were collected at the plant site after 1 hour of surge-bin storage time. Such storage is limited by IDOT to 8 hours and a maximum temperature of 350°F (Section 1102, *SSRBC*). Two samples were processed by the contractor and two samples by ICT. The differences in results reported by both entities were within expected tolerances based on studies by Rivera-Perez et al. (2022) and Sholar et al. (2002).

Binder Contents (P_b)

Table 13 lists the target P_b and the measured P_b. Three selected SMAs were further investigated using two asphalt analyzers at IDOT's District 1 Schaumburg Laboratory. D2-50-12.5-0 and D4-50-12.5-0 appear to have had less binder than the original target. T1-80-12.5-0 and T1-50-12.5-0 appear to have had more. All except one of the measurements are within ±0.4% of the design value. One value is over by 0.7%. Art. 1030.09 (c) of the *SSRBC* indicates a ±0.2% control limit, but, considering the small size of the batches produced, the binder contents were acceptable.

Table 13. Target and Measured P_b (%) of Plant-Produced SMA Using Different Methods

SMA Section	Target	Method and Laboratory							
		Reflux—Contractor		Automated—ICT		Automated—District 1		Automated*—District 1	
T1-80-12.5-0	6.0	6.1	6.3	6.4	6.4	–		–	
T1-50-12.5-0	6.3	6.5	6.3	7.0	6.5	6.4	6.5	6.5	6.6
D2-50-12.5-0	7.0	6.9	6.6	6.7	6.9	–		–	
L2-50-12.5-0	6.4	7.0	6.7	6.7	6.5	6.5	6.4	6.6	6.5
D3-50-9.5-0	7.0	7.0	7.0	6.8	6.8	–		–	
D4-50-12.5-0	6.8	6.7	6.7	6.5	6.5	6.6	6.6	6.6	6.6

*An automated extractor of a different brand was used to remove binder.

Aggregate Gradation

The aggregate gradations achieved during production are presented in Tables 14 through 17.

Table 14. Aggregate Gradations after Plant Production

Sieve		T1-80-12.5-0			D2-50-12.5-0			D3-50-9.5-0		
		Contractor		ICT	Contractor		ICT	Contractor		ICT
19.0 mm	3/4"	100	100	100	100	100	100	100	100	100
12.5 mm	1/2"	95	94	95.3	93	95	94.6	100	98	98.2
9.5 mm	3/8"	69	73	73.3	75	75	75.9	90	90	90.2
4.75 mm	#4	34	36	36.3	31	30	29.2	48	49	46.5
2.36 mm	#8	22	23	24.6	19	19	18.2	22	22	22.1
1.18 mm	#16	16	16	18.0	14	14	13.6	14	14	14.3
0.600 mm	#30	13	13	12.7	12	12	11.4	11	12	11.7
0.300 mm	#50	11	12	11.4	11	11	10.6	11	11	10.8
0.150 mm	#100	11	11	11.0	11	10	10.2	10	10	10.5
0.075 mm	#200	9.5	9.8	10.3	9.4	9.1	9.5	9.2	9.3	9.9

Table 15. Aggregate Gradations after Plant Production with District Measurements for T1-50-12.5-0

Sieve		T1-50-12.5-0						
		Contractor		ICT	District 1*		District 1	
19.0 mm	3/4"	100	100	100	100	100	100	100
12.5 mm	1/2"	95	94	93.4	94	96	97	94
9.5 mm	3/8"	74	74	71.5	72	75	76	74
4.75 mm	#4	35	35	38.6	34	36	36	35
2.36 mm	#8	23	24	28.9	23	24	23	23
1.18 mm	#16	16	17	21.0	16	17	17	16
0.600 mm	#30	13	13	16.5	13	14	13	13
0.300 mm	#50	11	12	14.3	12	12	12	12
0.150 mm	#100	11	11	13.3	11	11	11	11
0.075 mm	#200	9.6	9.7	12.3	10.6	10.9	10.3	10.1

Table 16. Aggregate Gradations after Plant Production with District Measurements for L2-50-12.5-0

Sieve		L2-50-12.5-0						
		Contractor		ICT	District 1*		District 1	
19.0 mm	3/4"	100	100	100	100	100	100	100
12.5 mm	1/2"	91	89	89.5	92	93	90	93
9.5 mm	3/8"	66	67	63.5	62	63	62	66
4.75 mm	#4	31	32	28.9	30	29	29	31
2.36 mm	#8	18	18	16.8	17	17	17	17
1.18 mm	#16	13	13	12.4	13	12	12	13
0.600 mm	#30	11	11	10.6	11	11	11	11
0.300 mm	#50	11	11	10.2	11	10	10	10
0.150 mm	#100	10	11	9.9	10	10	10	10
0.075 mm	#200	9.5	9.6	9.4	10.0	9.8	9.4	9.6

Table 17. Aggregate Gradations after Plant Production with District Measurements for D4-50-12.5-0

Sieve		D4-50-12.5-0						
		Contractor		ICT	District 1*		District 1	
19.0 mm	3/4"	100	100	100	100	100	100	100
12.5 mm	1/2"	88	89	90.7	89	91	90	88
9.5 mm	3/8"	64	63	63.3	65	64	62	63
4.75 mm	#4	30	29	27.9	28	29	28	29
2.36 mm	#8	19	18	17.3	17	17	17	17
1.18 mm	#16	14	13	12.8	13	13	13	13
0.600 mm	#30	12	11	11.0	11	11	11	11
0.300 mm	#50	11	11	10.5	11	11	11	11
0.150 mm	#100	10	10	10.3	11	11	10	10
0.075 mm	#200	9.6	9.6	9.8	10.3	10.5	9.8	9.9

*An automated extractor of a different brand was used to remove binder.

Aggregate gradation of produced SMA (averaged contractor and ICT results) is presented in Figure 27. It is compared to design aggregate gradations in Table 6. A correction is deemed necessary if trends show misalignment with control limits per Art. 1030.09 (c) of the *SSRBC*. Limits for an individual test are presented here for reference.

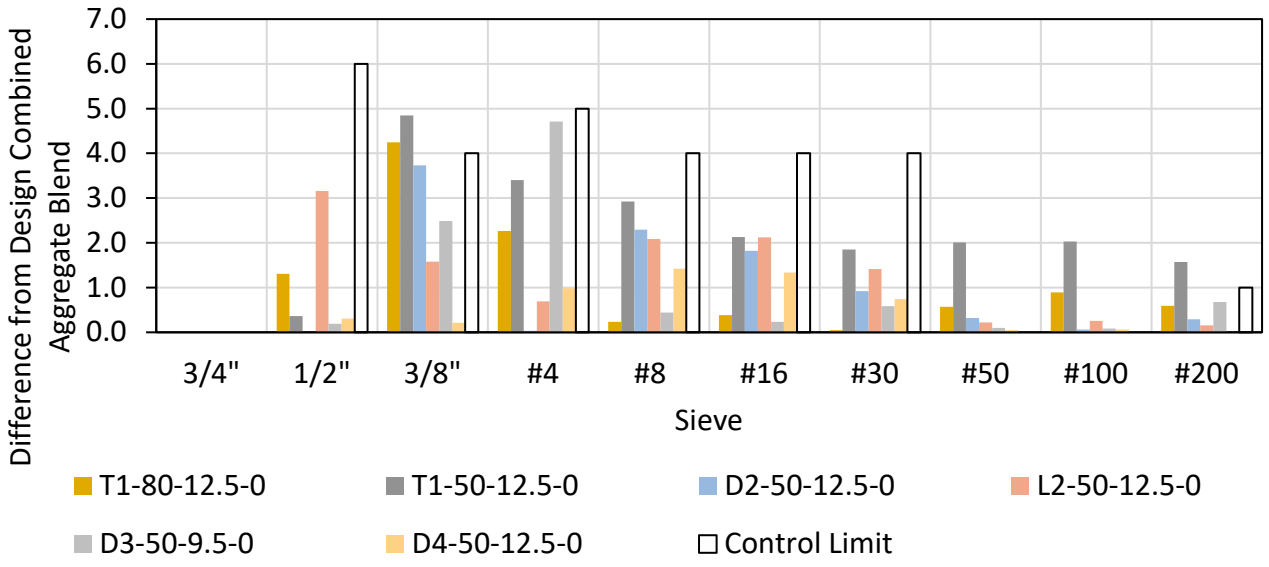

Figure 27. Graph. Difference in aggregate gradations between design and after plant production.

Volumetrics

Maximum theoretical specific gravity (G_{mm}) and G_{mb} values (Table 18) were measured to obtain air void content and VMA (Table 19). Air void contents were between 2.7%–5.1%. VMA measurements were over the target values for all but D3-50-9.5-0 and D4-50-12.5, for which VMA was on target. These two SMAs were produced last; by then the contractor had experience with the production of two other SMAs with aggregates meeting relatively lower quality. Air void contents and VMAs were within IDOT's control limits for an individual test (Art. 1030.09 (c), *SSRBC*). The design G_{sb} from Table 7 was used.

Table 18. Plant-Produced SMA G_{mm} and G_{mb}

SMA Section	G_{mm}		G_{mb}	
	ICT	Contractor	ICT	Contractor
T1-80-12.5-0	2.436	2.437	2.325	2.319
T1-50-12.5-0	2.433	2.424	2.308	2.319
D2-50-12.5-0	2.444	2.426	2.322	2.311
L2-50-12.5-0	2.431	2.413	2.338	2.338
D3-50-9.5-0	2.464	2.446	2.341	2.337
D4-50-12.5-0	2.445	2.417	2.347	2.351

Table 19. Plant-Produced SMA Volumetrics

SMA Section	AV (%)			VMA (%)		
	Target	ICT	Contractor	Target	ICT	Contractor
T1-80-12.5-0	4.0	4.6	4.8	16.5	18.1	18.2
T1-50-12.5-0	4.0	5.1	4.3	16.5	19.0	18.3
D2-50-12.5-0	4.0	5.0	4.7	16.5	17.2	17.5
L2-50-12.5-0	4.0	3.8	3.1	16.5	17.0	17.2
D3-50-9.5-0	4.0	5.0	4.5	17.5	17.7	18.0
D4-50-12.5-0	4.0	4.0	2.7	16.5	16.5	16.6

Binder absorption was computed and compared to lab-produced values (Figure 28).

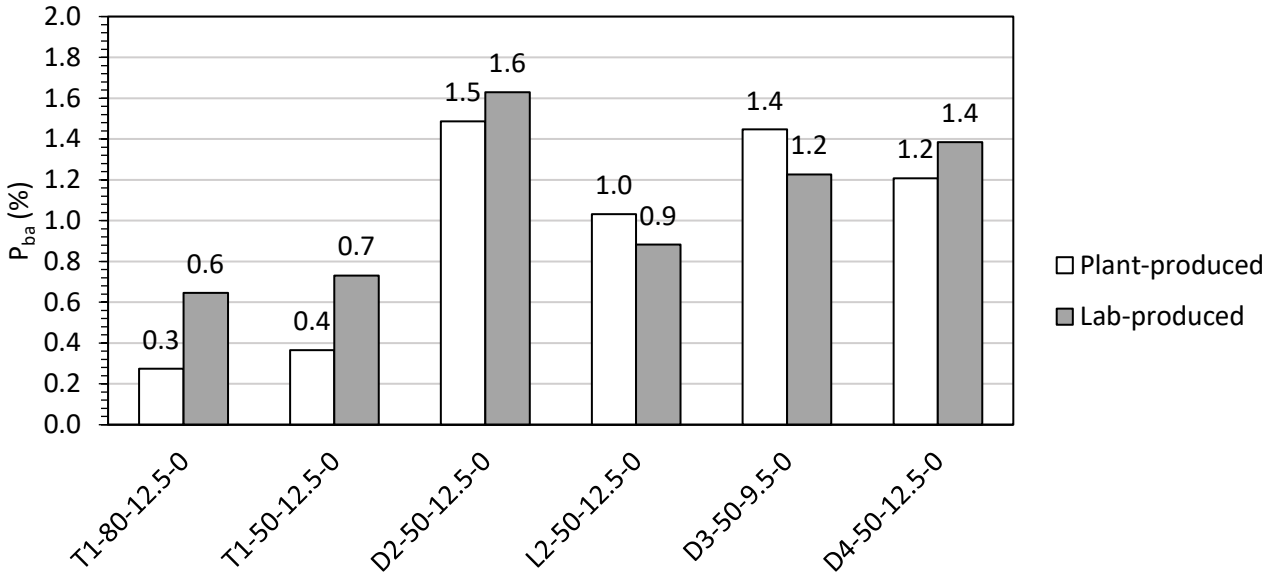

Figure 28. Graph. Laboratory- and plant-produced binder absorption.

Asphalt Binder Quality

IDOT's Central Bureau of Materials tested binder from four cans—taking random, representative samples—during the first day of paving. ΔT_c after 40 hr pressure aging vessel (PAV) was measured as −5.8 on average with a coefficient of variation of 10%. The SBS PG 76-28 binder was tested for SMA and met IDOT's requirements. The following tests were conducted: bending beam rheometer (BBR) after 20 hr PAV, flash point Cleveland open cup, separation of polymer, SBS polymer in asphalt binder, original dynamic shear rheometer (DSR), DSR after PAV, rotational viscosity, elastic recovery, DSR after rolling thin-film oven (RTFO), and change in mass after RTFO. Appendix E presents the results.

SMA FIELD DENSITY AND THICKNESS

Two inch SMA lifts were paved on the experimental lane. Uncorrelated nuclear gauge measurements were taken during compaction. After compaction, the contractor took five final nuclear gauge measurements across the lane in the middle of each test section. Table 20 presents the results. Sections are numbered from east to west. Density in section 1 (T1-80-12.5-0) was lower than the control limits (93.5%–97.4%), but within acceptable limits (92.0%–98.0%), according to Art. 1030.09 of the *SSRBC*. The design G_{mm} value was input for the computation of the nuclear gauge's reading.

Table 20. SMA Layer Achieved Densities (Average of 5)

Location (ft from edge—far from I-APT wheel path)	Section 1	Section 2	Section 3	Section 4	Section 5	Section 6
SMA	T1-80-12.5-0	T1-50-12.5-0	D2-50-12.5-0	L2-50-12.5-0	D3-50-9.5-0	D4-50-12.5-0
2	93.0	95.4	95.5	95.9	94.4	96.4
4	89.7	94.3	94.5	94.5	95.3	95.8
6	91.0	93.5	94.2	96.8	95.3	96.1
8	90.8	94.4	95.5	96.5	95.0	96.2
9.5	93.6	95.3	95.3	98.3	95.3	96.5
Average	91.6	94.6	95.0	96.4	95.1	96.2
No. of passes with oscillation drum on	19	10	6	16	14	16
No. of passes with vibration drum on	4	10	4	6	4	6

Four field cores were obtained from each SMA section, in the middle of the lane, 4 ft and 6 ft away from the orthogonal center. The core holes were filled immediately with a fine mix and sealed, as illustrated in Figure 29. After lift thickness measurement, the SMA cores were separated using a chisel and a hammer from the HMA layer. The field cores were cooled to 14°F prior to separation.

The measured G_{mb} from SMA field cores and the G_{mm} from plant-produced samples were used to compute the SMA densities (Table 21). The densities are slightly higher than those measured with a nuclear gauge and reported by the contractor (see Figure 30). The nuclear gauge values may be lower because the input G_{mm}—from the design—was higher than the G_{mm} obtained for plant-produced SMA (see Figure 30-b). Field core densities are all within the control limits (93.5%–97.4%), except T1-80-12.5-0. All were within acceptable limits (92.0%–98.0%). The thicknesses were within reasonable range—the highest deviation (+20%) from the plan was 0.4 in for D2-50-12.5-0. Typically, mill and fill overlays are paid by weight with no thickness requirements. Article 407.10 of the *SSRBC* provides guidance for thickness tolerance, 10% deviation from plan, for full-depth paving.

(1)

(2)

(3)

(4)

(5)

(6)

(7)

Figure 29. Photo. Steps for obtaining SMA cores.

Table 21. SMA Lift Thickness and Density from Field Cores

SMA	Core	Average thickness of 6 measurements (in)	**Average Thickness (in)**	Standard Deviation of Thickness	G_{mb}	Density (%)	**Average Density (%)**	Standard Deviation of Density
T1-80-12.5-0	1	1.9	2.0	0.1	2.254	92.6	93.4	0.6
	2	2.0			2.270	93.2		
	3	2.0			2.288	93.9		
	4	2.0			2.286	93.8		
T1-50-12.5-0	1	1.8	1.9	0.1	2.332	95.9	96.0	0.5
	2	1.8			2.332	95.9		
	3	1.8			2.329	95.7		
	4	2.0			2.353	96.7		
D2-50-12.5-0	1	2.6	2.4	0.1	2.339	95.7	96.2	0.5
	2	2.4			2.356	96.4		
	3	2.4			2.343	95.9		
	4	2.3			2.363	96.7		
L2-50-12.5-0	1	2.0	2.0	0.0	2.348	96.6	96.6	0.3
	2	2.0			2.335	96.1		
	3	2.0			2.354	96.8		
	4	2.0			2.351	96.7		
D3-50-9.5-0	1	2.2	2.2	0.1	2.358	95.7	95.1	1.4
	2	2.3			2.300	93.4		
	3	2.1			2.383	96.7		
	4	2.2			2.332	94.7		
D4-50-12.5-0	1	2.1	2.1	0.2	2.385	97.5	97.3	0.3
	2	2.4			2.371	97.0		
	3	2.0			2.376	97.2		
	4	2.1			2.383	97.5		

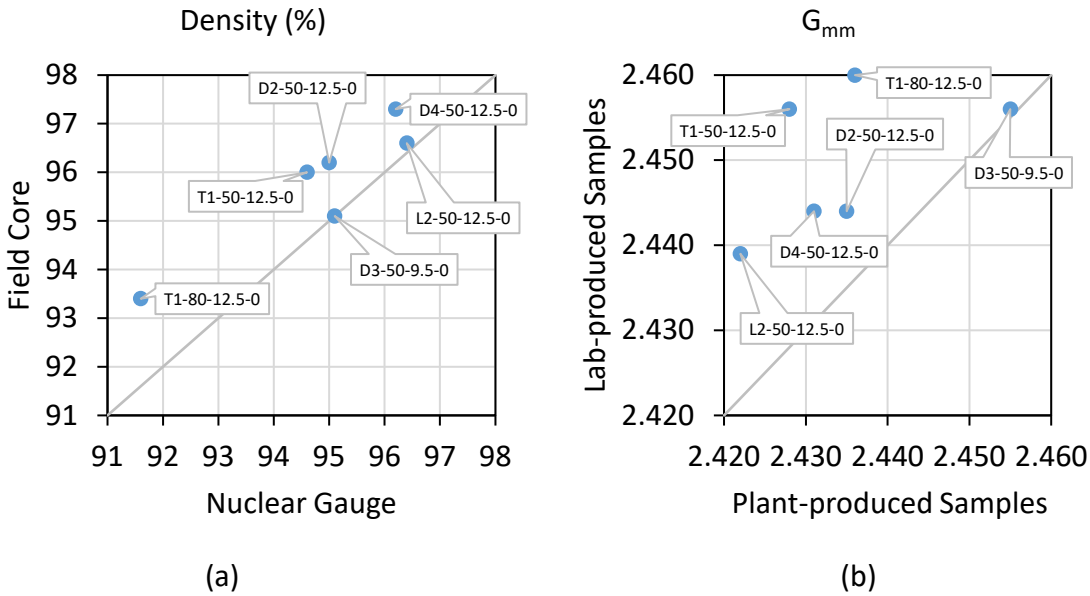

Figure 30. Graph. (a) Comparison of densities measured with nuclear gauge and from field cores, and (b) comparison of G_{mm} of laboratory- and plant-produced samples.

CRACKING AND RUTTING POTENTIAL

Flexibility index and HWTT rut depth were measured on plant-produced SMA. Table 22 presents the results. IDOT's thresholds were met, indicating the adequacy of the paved SMA. Plant-produced SMA with local aggregates are more flexible but less stable compared to imported aggregate counterparts.

Table 22. I-FIT and HWTT Results

SMA	STA FI	LTA FI	Rut Depth after 20,000 Passes (mm)
T1-80-12.5-0	16.14	11.12	3.51
T1-50-12.5-0	19.59	17.07	4.18
D2-50-12.5-0	29.73	19.06	4.83
L2-50-12.5-0	41.20	14.59	6.52
D3-50-9.5-0	33.65	18.40	7.44
D4-50-12.5-0	29.24	18.69	8.33
IDOT Threshold	≥ 16	≥ 10	< 12.5

ANOVA and pairwise t-tests with α of 0.10 indicated that FI (STA) values and HWTT rut depth values were significantly different for plant-produced SMA (Figure 31). The FI of laboratory-produced SMA after STA conditioning was higher than that for the plant-produced counterparts. However, both types were similar after LTA conditioning in the oven. The effect of aging diminishes with exposure time. In general, the rut depth for laboratory-produced SMA was 95% greater than that for plant-produced SMA (Figure 32). No inflection point was observed in rut progression, as illustrated for L2-50-12.5-0.

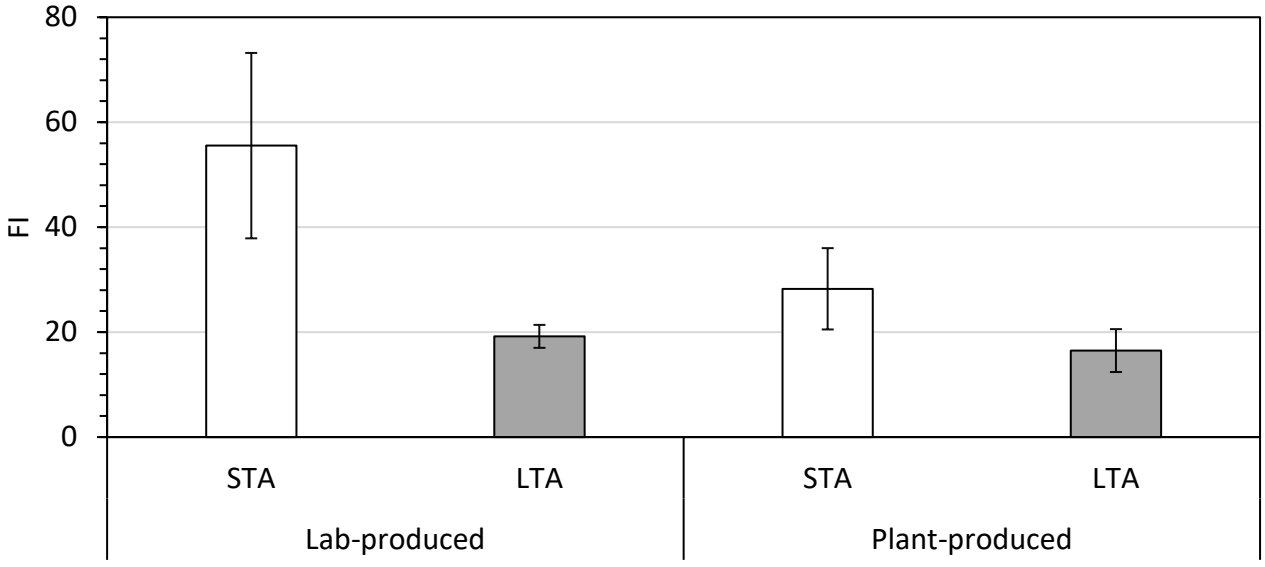

Note: Error bars indicate one standard deviation.

Figure 31. Graph. Flexibility index comparison of SMA after STA and LTA.

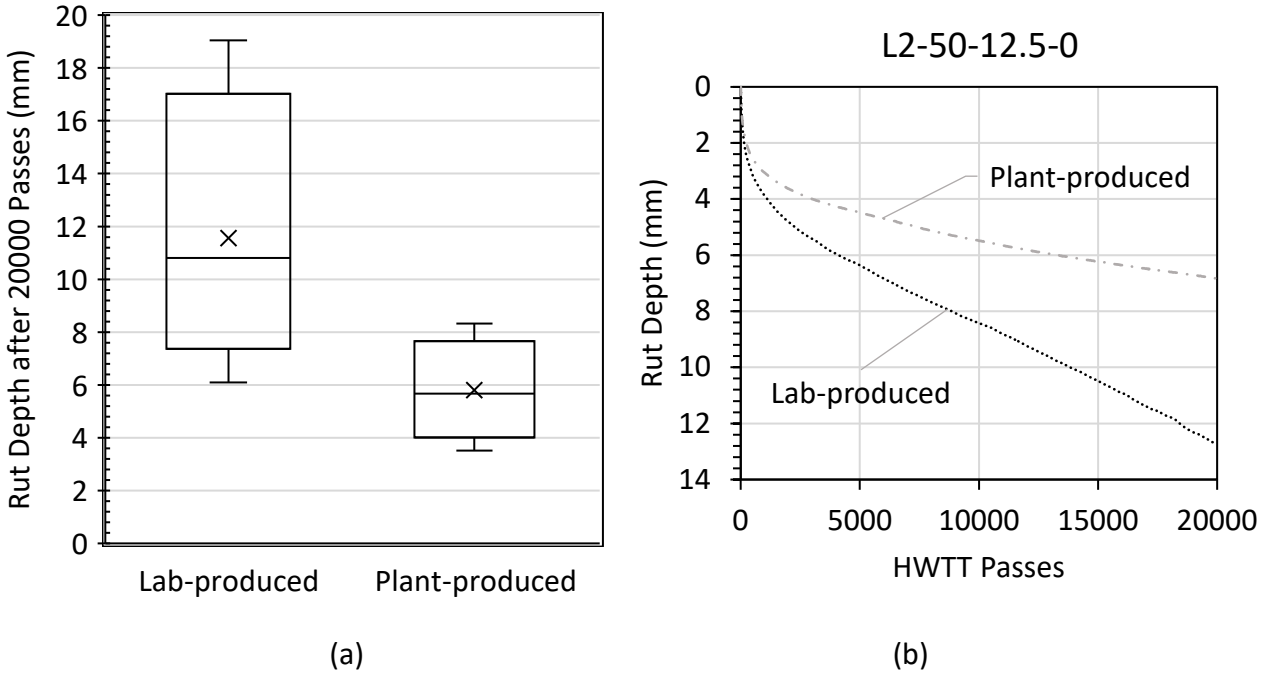

Figure 32. Graph. HWTT results: (a) STA comparison, and (b) rut progression for L2-50-12.5-0.

Aging in plant-produced SMA is expected to be more intense than that in a lab. Additionally, a reheating cycle was required to prepare plant-produced SMA specimens. When a higher intensity STA was applied to lab-produced SMA, results became similar to those obtained for plant-produced SMA using ANOVA and pairwise t-tests with α of 0.10. Consequently, a higher intensity STA appears to better simulate the effect of plant production for the mixtures included in this study.

DYNAMIC MODULI OF SMA WITH LOCAL AGGREGATES

To evaluate the mechanical behavior of SMA, complex moduli of plant-produced, lab-compacted specimens were determined in accordance with AASHTO T378 (2017). The test was conducted using an AMPT (Asphalt Mixture Performance Tester) machine, which measures phase angle and complex modulus. The tests were performed at 39.2°F, 68°F, and 113°F. Time-temperature superposition was used to develop complex moduli master curves, as presented in Figure 33. The moduli for SMA with local aggregates are higher than those for SMA with imported aggregates. The N_{des} for SMA specimens with imported aggregates was 80 gyrations, while it was 50 gyrations for SMA specimens with local aggregates. Complex moduli specimens are compacted to a fixed height (160 mm before sawing top and bottom) and AV (7.0 ± 0.5%), which requires a lower compaction energy than during design. At a lower compaction state, the lower the N_{des} SMA could have achieved a more structured aggregate skeleton.

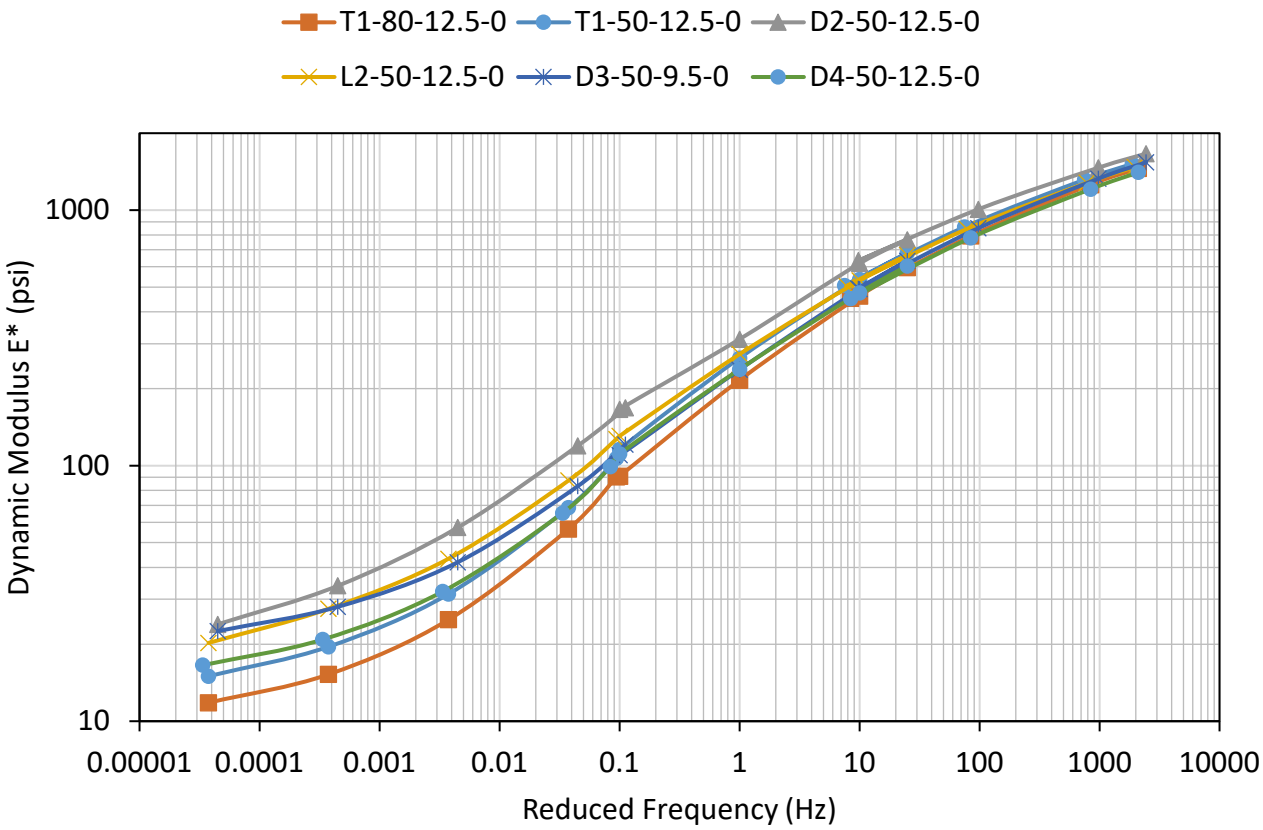

Figure 33. Graph. SMA master curves at 68°F reference temperature.

Reduced frequencies higher than 10 Hz are expected for loads during service (truck speeds 45–75 mph). At 5 mph, which was the speed selected for I-APT (based on Steyn, 2012), a load pulse of 0.15 sec was observed, indicating a loading frequency at 5 Hz. The temperature was controlled at 82°F during testing. The SMA moduli and phase angles, under those conditions, are presented in Figure 34. D2-50-12.5-0 had the highest modulus and smallest phase angle. This finding suggests relatively more elastic behavior, which could result in a relatively slower rate of permanent deformation accumulation in the field, assuming that the aggregate skeleton was preserved during construction.

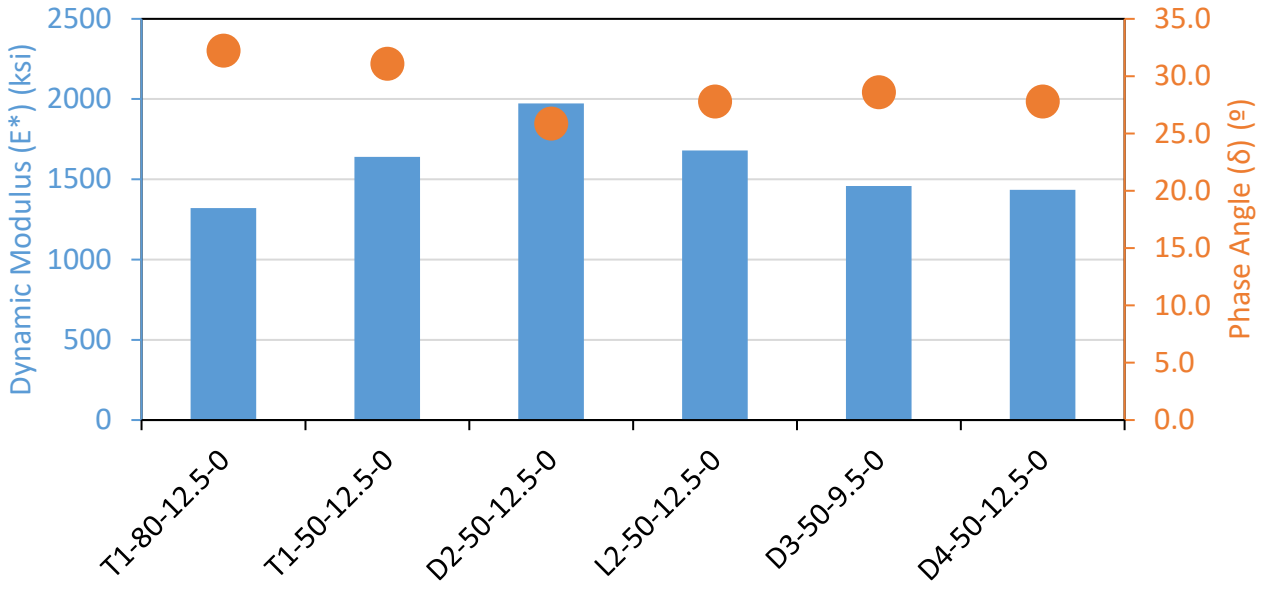

Figure 34. Graph. Moduli and phase angle of SMAs at 5 Hz and 82°F.

SMA AGGREGATE SKELETON AFTER CONSTRUCTION

The aggregate breakage index and breakage plots were obtained for SMA produced at the plant to evaluate the preservation of the aggregate structure during production and construction. The SMA samples, used to determine the volumetrics from Table 19, were tested to obtain ABI after laboratory compaction to N_{des}. Figure 35 presents the effect of STA intensity on aggregate breakage. T1-80-12.5-0 may have experienced breakage in the laboratory because of its high design compaction effort (N_{des}). ABI could be greater (in general) for plant-produced SMA because of the heating and drying approach. The properties of aggregates may have changed when heated and dried using a burner and high temperatures in the drum, which does not occur in a lab forced-draft oven.

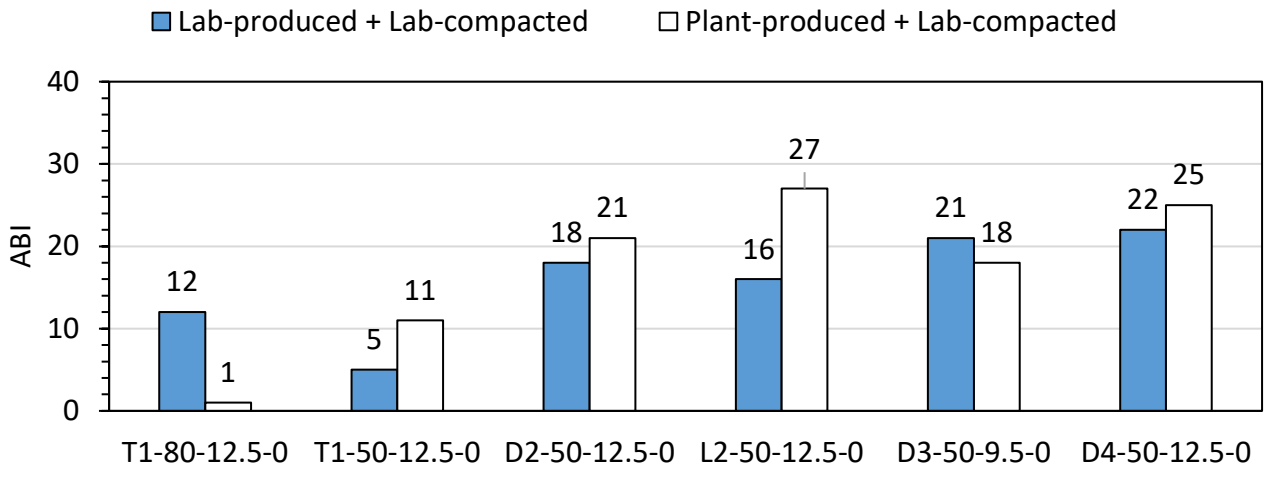

Figure 35. Bar plot. Aggregate breakage in plant-produced SMA.

Aggregate breakage occurring during plant production and construction was measured from field cores (Table 21). The aggregates on the sawed surface of the cores were removed before the aggregates were recovered, as illustrated in Figure 36. The sawed surface was coated with two layers of fast-curing epoxy mastic. The coated cores were heated at 275°F for 1 hour, and the sawed aggregates were discarded along with the adhered coating.

(1)

(2)

(3)

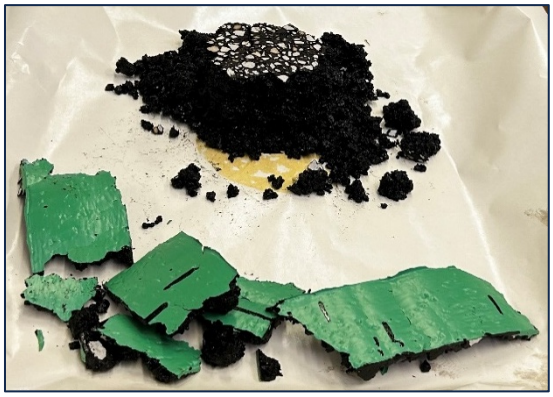

(4)

Figure 36. Photo. Sawed aggregate removal procedure.

The uncut aggregates from the center of the cores were recovered using an automated extraction process. The recovered aggregates were sieved to obtain the SMA gradation after plant production and field compaction. The average changes for four cores per SMA are presented in Figure 37. Appendix G presents detailed results of each core. A tolerance of 1% difference in percent passing of any sieve was considered for the replicates.

Aggregate breakage plots obtained from cores with imported aggregates had negative values for sizes #16 to #4, while the values were positive for SMA with local aggregates.

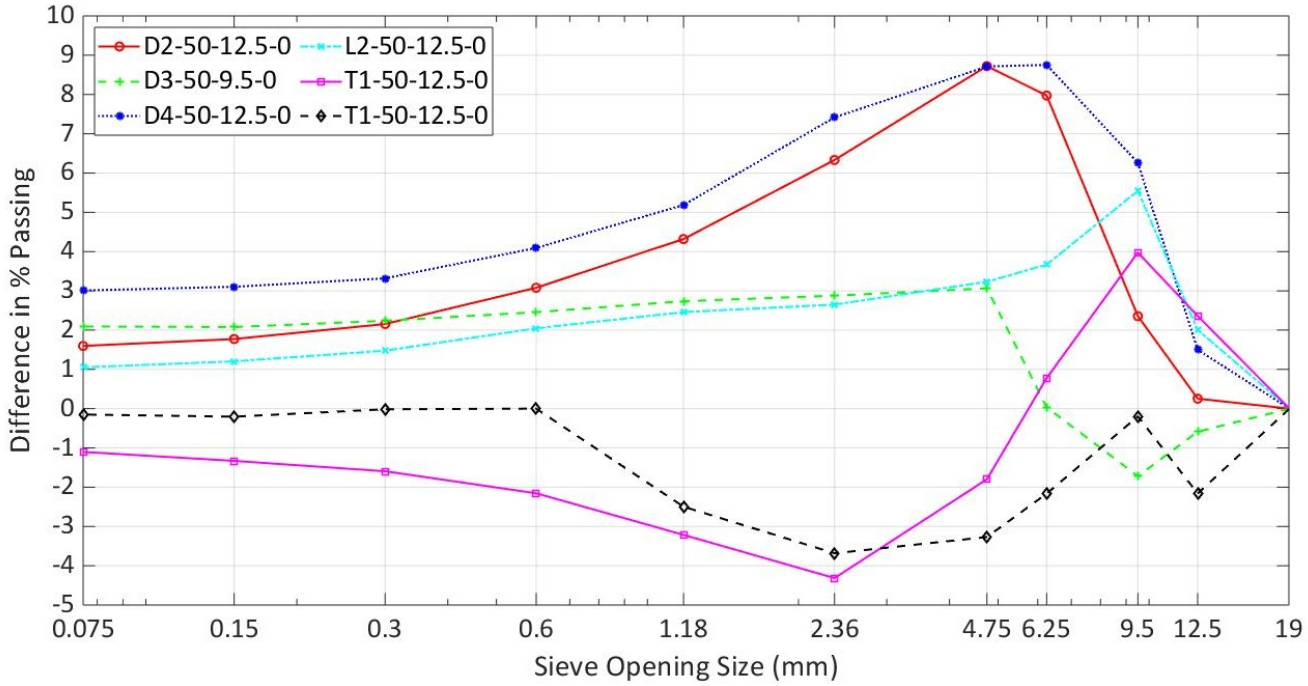

Figure 37. Graph. Field core breakage.

The ABIs for field cores are presented in Figure 38. As expected, the trap rock SMAs have relatively low ABI. D3-50-9.5-0 may have lower than expected aggregate breakage because it has a 3:8 NMAS/lift thickness ratio, which is larger than for the rest (1:4). This could reduce stress transmitted to aggregates during field compaction. In addition, due to its predominant stockpile (CM 14 or CM 13) and having a lower flat and elongated particle count (F/E 3:1 per Table 3), L2-50-12.5-0 demonstrated lower than expected aggregate breakage. Such observations were noted for both laboratory- and plant-produced samples (Figure 14).

To explain the relatively low ABI of L2-50-12.5-0, a detailed analysis of flat, elongated, and flat and elongated (F&E) particles was conducted, focusing on the predominant stockpiles contributing to the 2.36–4.75 mm size range. Though typically excluded from standard F&E ratio tests, these smaller coarse particles account for 12%–24% of the aggregate blend and play a key role in the SMA skeleton's structure. When such particles are flat or elongated, they are more prone to breakage due to bending stress. As presented in Figure 39, L2-50-12.5-0 has fewer of these particles, potentially contributing to its relatively higher stability.

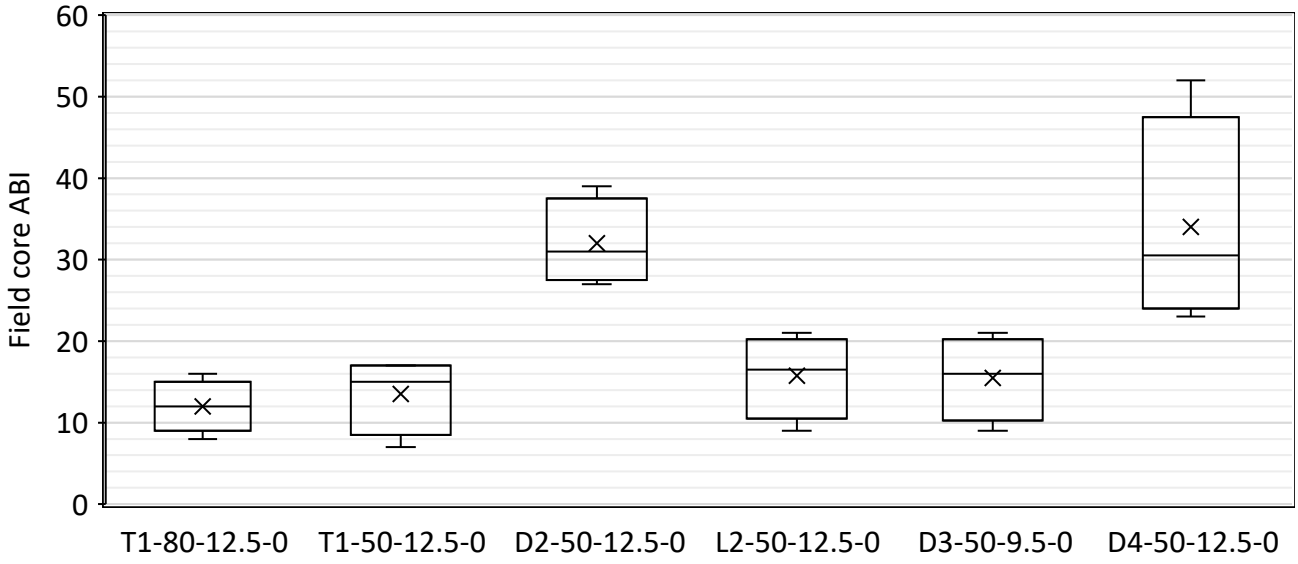

Figure 38. Box Plot. Field core ABIs.

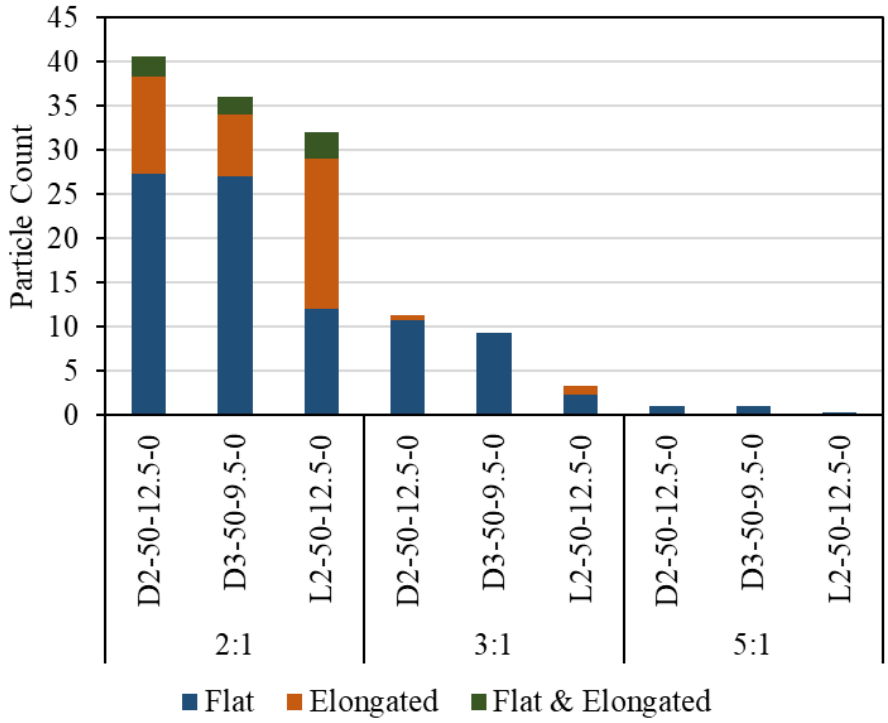

Figure 39. Bar plot. Flat, elongated, and flat and elongated particle counts for respective predominant stockpiles on samples passing the #8 and retained on the #4 sieve.

Figure 40 presents a comparison of ABIs for SMA produced in a plant and compacted using two methods: (1) in the lab, to a thick specimen, using an SGC, and (2) in the field, at a test section, using construction equipment. ABI after field compaction was greater for all SMA, except D3-50-9.5-0 and L2-50-12.5-0. The NMAS/lift thickness ratio and F&E ratio may contribute to the difference of both mixes, respectively.

Figure 40. Bar plot. ABI for laboratory versus field compaction on ABI.

A positive relationship between the number of passes during compaction and mat density may be expected. This relationship is not evident for T1-80-12.5-0 and D2-50-12.5-0 in Figure 41. For T1-80-12.5-0, lower densities were achieved, as the vibration drum was not on for the first passes. The mat may have been cool by the time it was turned on, so higher viscosity mastic may have protected the aggregates, lowering the ABI. The relationship between field core ABI and number of compaction passes is unclear in Figure 42, because ABI may have a greater dependence on aggregate qualities and because of other impactful variables.

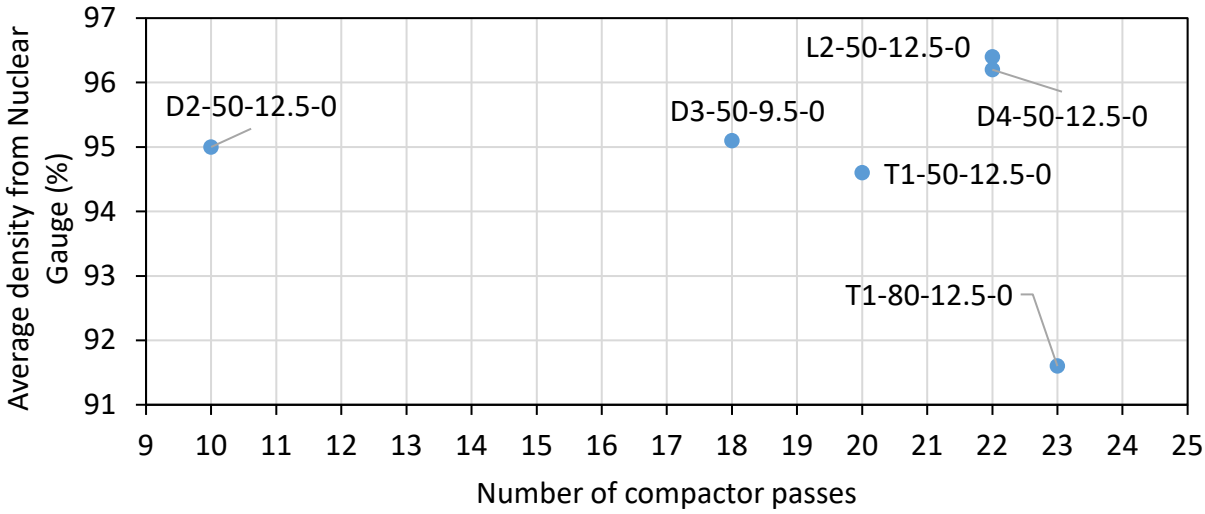

Figure 41. Graph. Density versus compactor passes.

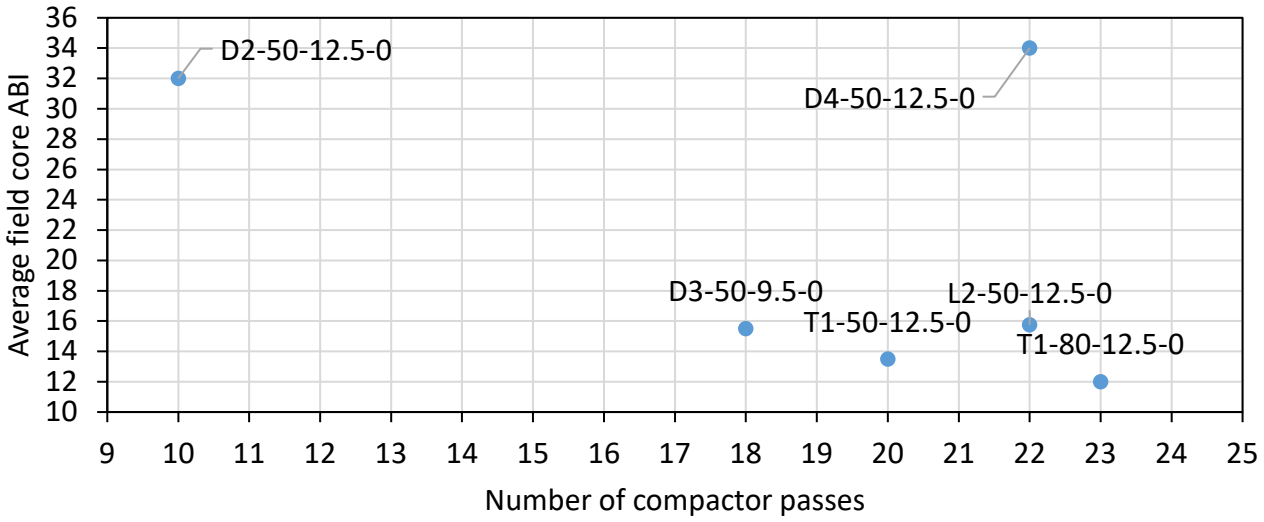

Figure 42. Graph. Field core ABI versus compactor passes.

Preserving SMA's aggregate skeleton through production and construction processes should be considered during its design. Excessive aggregate breakage may cause tenderness. However, ABI depends on several factors, including aggregate strength and shape, SMA production process, compaction method and magnitude, and relative lift thickness (NMAS/lift thickness). As presented in Figure 43, for the SMAs paved in this project, a negative relationship may exist between ABI and the change in texture after Micro-Deval testing, similar to the one in Figure 15. In this case—after field compaction—the correlation is stronger, and its effect is greater (slope of the curve). This could be an approach to select and produce local aggregates for durable SMA with local aggregates.

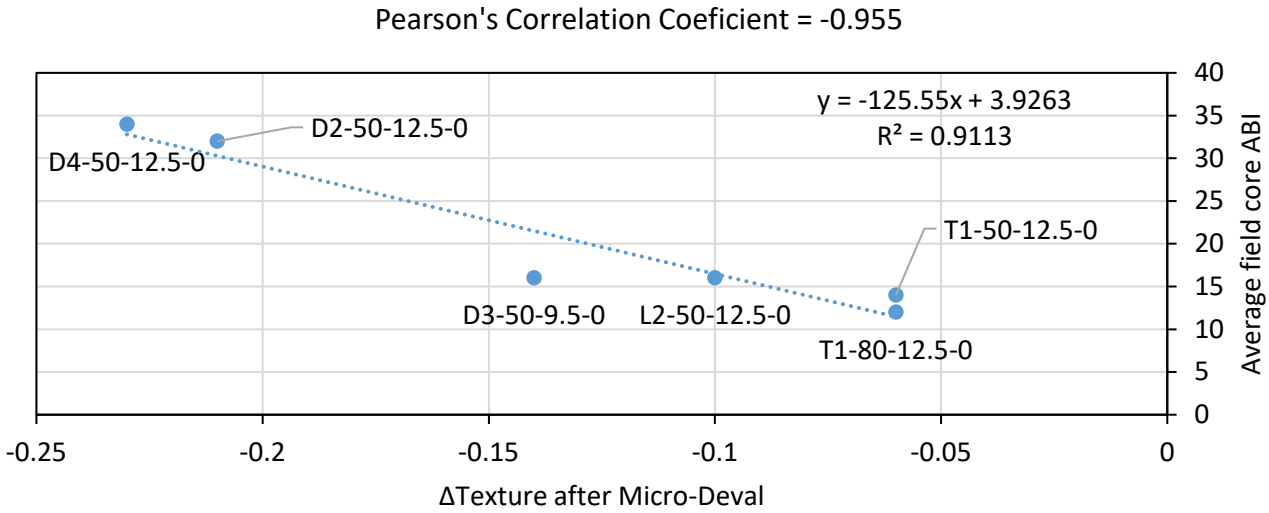

Figure 43. Graph. Relationship between ABI after field compaction and change in texture during Micro-Deval testing, measured with AIMS.

SUMMARY

A 450 ft long lane was paved to perform full-scale accelerated loading testing of SMA with local aggregates. A 2 in thick levelling layer was paved over existing 10–14 in CRCP. Two in thick SMAs with local and imported aggregates designed with 80 and 50 gyrations were paved on the surface. The cracking and rutting resistance properties of the SMA produced are excellent, with high FI and lower-than-design HWTT rut depths. Expected variations in P_b, air void content, and VMA were found. The construction of the SMA layer was acceptable. The only deviations from the plan were the average density of field cores of T1-80-12.5-0 being 0.1% lower than the lower control limit and the thickness of field cores of D2-50-12.5-0 being 0.4 in thicker.

Aggregate breakage occurring during plant production and field compaction was measured. The effect of production and compaction processes were assessed by evaluating the field core and laboratory ABIs and aggregate qualities. The resistance of aggregates to polish has potential to estimate ABI in the field. Although this relationship is not independent, its validation may be useful for the industry when SMA with local aggregates are used in Illinois.

CHAPTER 4: INSTRUMENTATION RESPONSE ANALYSIS

Extracting pavement data is essential for planning maintenance triggers. The primary objective of this chapter was to distinguish SMA sections based on their mechanical behavior. For this, pavement responses were measured using earth pressure cells, strain gauges, and thermocouples under varied loads, tire inflation pressures, speeds, temperatures, and load spacings applied by I-APT. Furthermore, pavement responses were related to SMA characteristics, including aggregate lithology.

INSTRUMENTATION

A total of 47 sensors were embedded in the pavement test sections during construction. The sensors, along with the calibration and installation procedures, are described in this section. Each SMA test section was monitored with thermal, pressure, and strain sensors. The sensors were distributed as presented in Figure 44, which illustrates the layout for two sections. The instrumentation for each pair of sections was connected to a single data acquisition system.

The lane included areas before each test section to allow the loading system to reach stable speed and clearly define changes between each SMA. These 30 ft long SMA transition zones, which were not part of the test area (Figure 45), separated the test sections. In addition, the transition zone allows the I-APT carriage to reposition, move, and rest during testing. Each test section was 23 ft long.

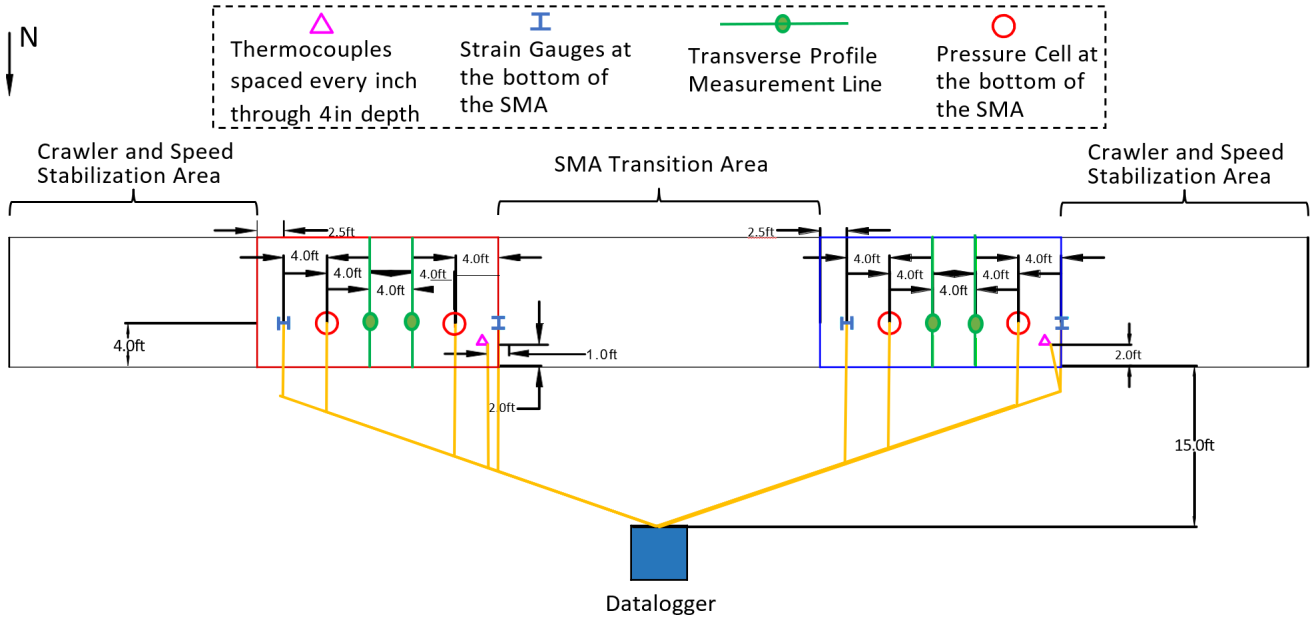

Figure 44. Illustration. Sensor location.

Sensor locations were marked before construction using flagged strings stretched between stakes along the lane. The strings were re-tensioned as needed during sensor placement, as presented in Figure 45. Sensor selection, preparation, and placement followed best practices (Tabatabaee et al.,

1992; Baker et al., 1994; Brandon et al., 1996; Loulizi et al., 2001; Al-Qadi et al., 2008; Al-Qadi et al., 2004; Al-Qadi et al., 2010; Neves et al., 2023).

Figure 45. Photo. String and flag instrument location.

Earth Pressure Cells

Circular 9 in diameter RST strain-based pressure cells were installed (Figure 46). The pressure cell, measuring vertical pressure under the SMA layer, has a capacity of 145 psi. A steel stem tube connects the two welded plates to a transducer. To host the transducer in the bottom layer without affecting the SMA layer, the drawings in Figure 46 were provided to the manufacturer. Two bends were placed in the stem tube (toward the sensitive side, downward) so the transducer sits 1 in below the sensed surface. The bends were placed 6 in away from the transducer (Figure 46). The manufacturer calibrated the pressure cells after the tube was bent. The provided calibration curves allow the conversion of measured voltage to pressure and were input to the datalogger. The calibration was verified using a universal testing machine through applying cyclic loading on the cells. Heat-resistant wires were used, which were covered with an asphalt-rich geosynthetic during construction to protect them along with the transducer. They were placed after the paver and before compaction using a bubble level (Figure 48), allowing complete and accurate flushing with the paved base layer.

Figure 46. Photo. Stem bend drawing provided to the manufacturer.

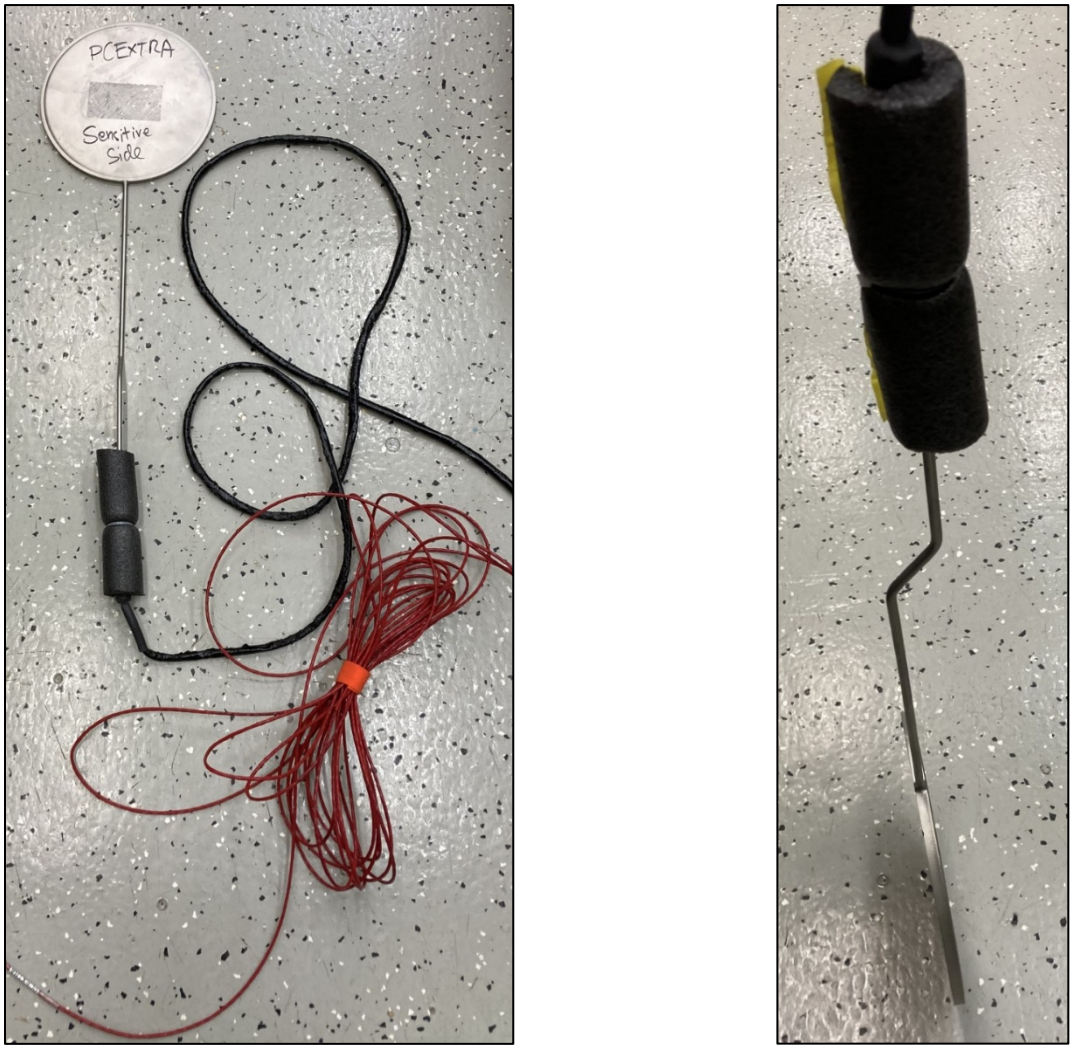

Note: The styrofoam cover over the transducer was removed before placement.

Figure 47. Photo. Earth pressure cell, illustrating bent tube and transducer wire protection.

Figure 48. Photo. Placement of a pressure cell on HMA mat before compaction.

Strain Gauges

Dynatest PAST-II “H” strain gauges were selected to measure longitudinal (with respect to traffic and compaction) and transverse strains at the bottom of the SMA. The resistance, lead resistance, and gauge factor were input to the data collection system. A source power of 3.3 V was selected. A quarter-bridge wiring configuration was used. All strain gauges have an initial offset that may be filtered during post-processing of the measurements. Their correct functionality was verified by applying a known difference of −300 με and a difference of 1,000 με using the setup presented in Figure 49.

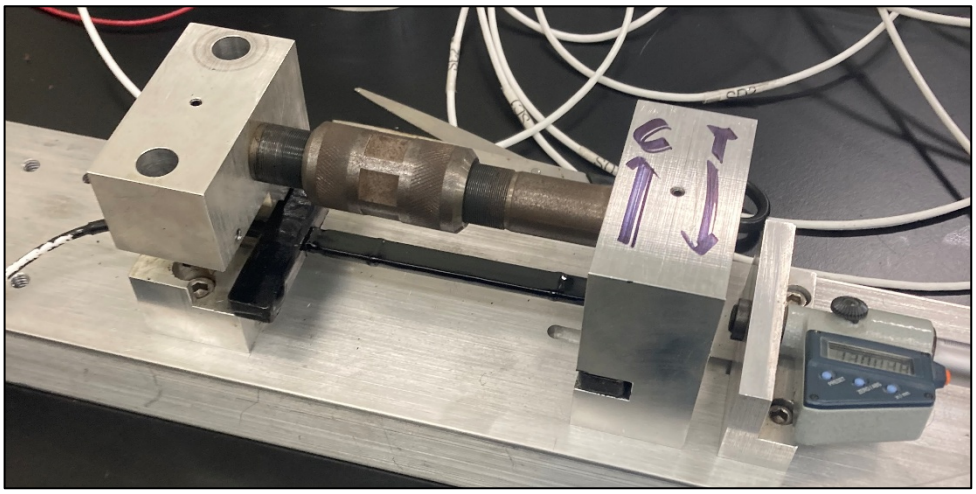

Figure 49. Photo. Strain gauge calibration verification setup.

Aluminum plates (with half the thickness of the gauges) were placed after the paver and before the compactor passes to generate a surface depression that would later host the strain gauge, as presented in Figure 50.

Figure 50. Photo. (a) Placement of a strain gauge placeholder plate on SMA mat prior to compaction, (b–d) placeholder plates and pressure cells during compaction.

After the host layer (HMA lift) was cooled, a 0.5 in deep saw-cut reservoir (the thickness of the wires) was made in the host layer to direct the wires to the edge of the pavement. After cleaning the saw-cut reservoir, the wires were placed and covered with PG 64-22 binder to fill the saw-cut reservoir and protect the thermal-resistant wires, as presented in Figure 51.

(a) (b)

(c)

Figure 51. Photo. (a) Saw cutting for wire host slot, (b) cleaning of saw-cut reservoir, and (c) slot filling with PG 64-22 binder over the strain gauge wire.

A slurry of Ottawa sand and PG 64-22 asphalt were mixed on-site and used to fill the depression to host the strain gauge. Each gauge was placed to “float” on the slurry, as presented in Figure 52. This allows the strain gauge to be controlled by the SMA layer above it, which is stiffer than the slurry.

Figure 52. Photo. Strain gauge "floating" over Ottawa sand slurry.

Moments before the SMA layer was paved, the strain gauges were covered with the respective SMA material and hand compacted using a metal plate and a hand roller in the direction opposite of strain measurement (Figure 53).

Figure 53. Photo. SMA compaction over a strain gauge prior to paving.

Temperature Sensors

A T-Type wire (20 gauge with fluorinated ethylene propylene insulation and jacket) was used to make temperature sensors. After the wire pair was twisted and soldered, the exposed end was surrounded by copper tubing. The tubing was then attached to the cable insulation by heat-shrinkable tubing to

insulate the tubing from the exposed wire pair and to provide a reservoir for epoxy. Epoxy was used to surround the thermocouple and to serve as a barrier to environmental effects (Figure 54).

Figure 54. Photo. Finished thermocouple tip.

After fabrication and before placement, the response from the thermocouples was calibrated at two reference temperatures: room temperature water and hot water. The response from each thermocouple was recorded and compared to a reading from a reference calibrated thermometer. From this procedure, the thermocouples yielded results that were within operational ranges. (The largest difference between the measured and actual temperature was 2.7°F.)

During paving of each layer, a thermocouple was placed on the surface of the existing surface (HMA binder layer) and was fixed in place using the respective HMA binder layer. Another thermocouple was placed on top of the HMA binder and 1 in into the SMA with respect to the pre-existing surface. Alternatively, in some cases, the thermocouples were embedded after the paver and before the compactor using a measuring rod and a spatula, as presented in Figure 55 and Figure 56.

Figure 55. Photo. Thermocouple placement before paver.

Figure 56. Photo. Thermocouple placement after paver and before compaction.

An additional verification temperature sensor was installed in each section after construction by drilling a 1 in deep hole into the pavement (Figure 57).

Figure 57. Photo. Verification thermocouple at section D4-50-12.5-0.

Instrument Connection and Data Acquisition System

To ensure good signal quality from all sensors, instrument cable lengths were minimized by planning for three datalogger locations. Each instrument had a designated location and cable length. As displayed in Figure 58, to protect all wires outside the pavement and the datalogger, trenches were dug to guide the loose wires. Sand was used to cover the wires. Any particle larger than 0.2 in was removed. A tamper was used to compact the sand gently.

(a)

(b)

(c)

Figure 58. Photo. (a) Researchers trenching to protect cables, (b) placement of cables over sand, and (c) tamper compaction of sand over cables.

ILLINOIS ACCELERATED PAVEMENT TESTER

The Illinois Accelerated Pavement Tester (I-APT) (Figure 59) was recently renovated after nearly two decades of service. The upgrades included load control, data quality, and test-monitoring improvements. The original winch system was replaced with a more stable and electrically isolated hydraulic system. This reduces noise interference with embedded sensor signals (Renshaw et al., 2024). This study was the first to utilize the refurbished I-APT, which supports tandem-axle loading with variable axle spacing, temperature-controlled testing, and remote data access.

(a) (b)

Figure 59. Photo. I-APT (a) with temperature-insulating skirt open and (b) during winter operation.

Remote Monitoring and Data Transfer

The I-APT control system continuously recorded data on wheel loading, carriage position, speed, and acceleration. All data were automatically uploaded to the Illinois Campus Cluster via Research Storage as a Service (RSaaS) through the Illinois Campus Cluster Program. Remote monitoring was enabled through a Wi-Fi router and motion-sensitive security cameras (Figure 60). Both the data acquisition system and I-APT control interface were accessed via remote desktop software to ensure real-time monitoring and data backup.

(a)

(b)

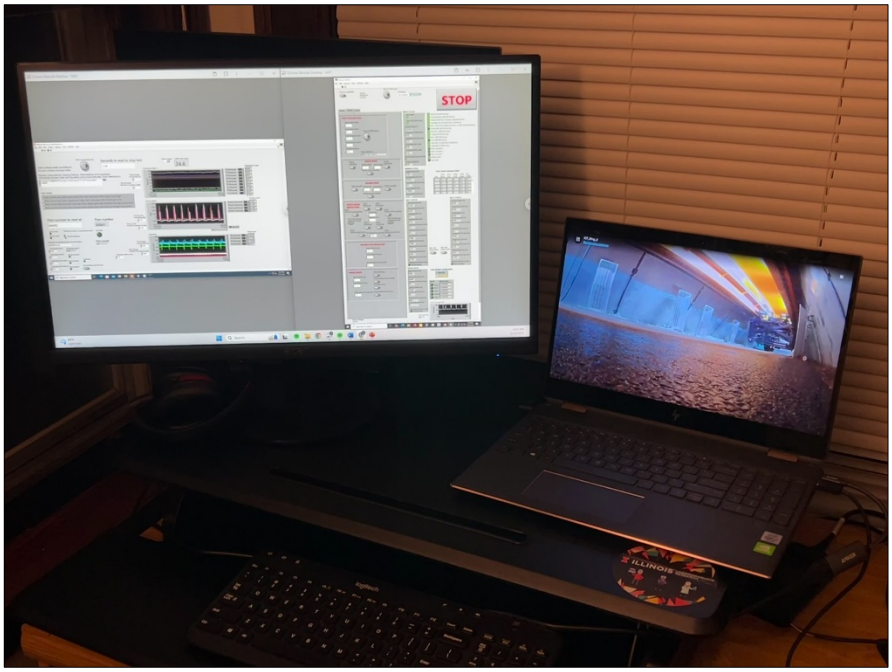

(c)

Figure 60. Photo. (a) Wi-Fi router under I-APT, (b) motion-sensitive cameras, and (c) nighttime monitoring of the data acquisition system—control system and camera footage.

Temperature Control

Maintaining target pavement temperatures was essential during testing. Pavement temperature was regulated using embedded thermocouples and an alert system developed in LabVIEW. Heating was achieved using 16 industrial heaters distributed across three independently controlled thermal zones. Each zone was instrumented with three thermocouples, which provided real-time feedback to a control unit regulating heater output (Figure 61-b and Figure 61-c). To enable testing during hot weather, cooling with portable air conditioning units and a relatively large in-place unit was used

(Figure 61-a). Insulation materials—including foam panels, spray foam, fiberglass insulation, sand, and heavy-duty tape—were applied around the perimeter and beneath the I-APT skirts to reduce heat transfer, helping to stabilize internal temperatures and allowing year-round operation. The heating and insulation system was designed to maintain a 50°F differential (outside vs. inside).

(a)

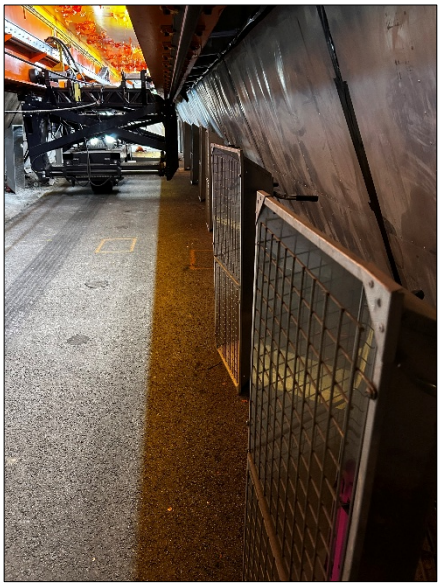

(b)

(c)

Figure 61. Photo. (a) Cooling units, (b) heaters, and (c) control unit of the air heating/cooling system.

Single and Tandem Half-Axle Loading

The I-APT carriage supports testing under either single- or tandem-axle configurations. For simplicity the word “axle” is used instead of “half axle” in this report. In this study, tandem axles were used to simulate realistic loading and increase test severity during loading cycles. Each axle could be loaded independently and positioned variably, providing precise control of loading patterns (Figure 62).

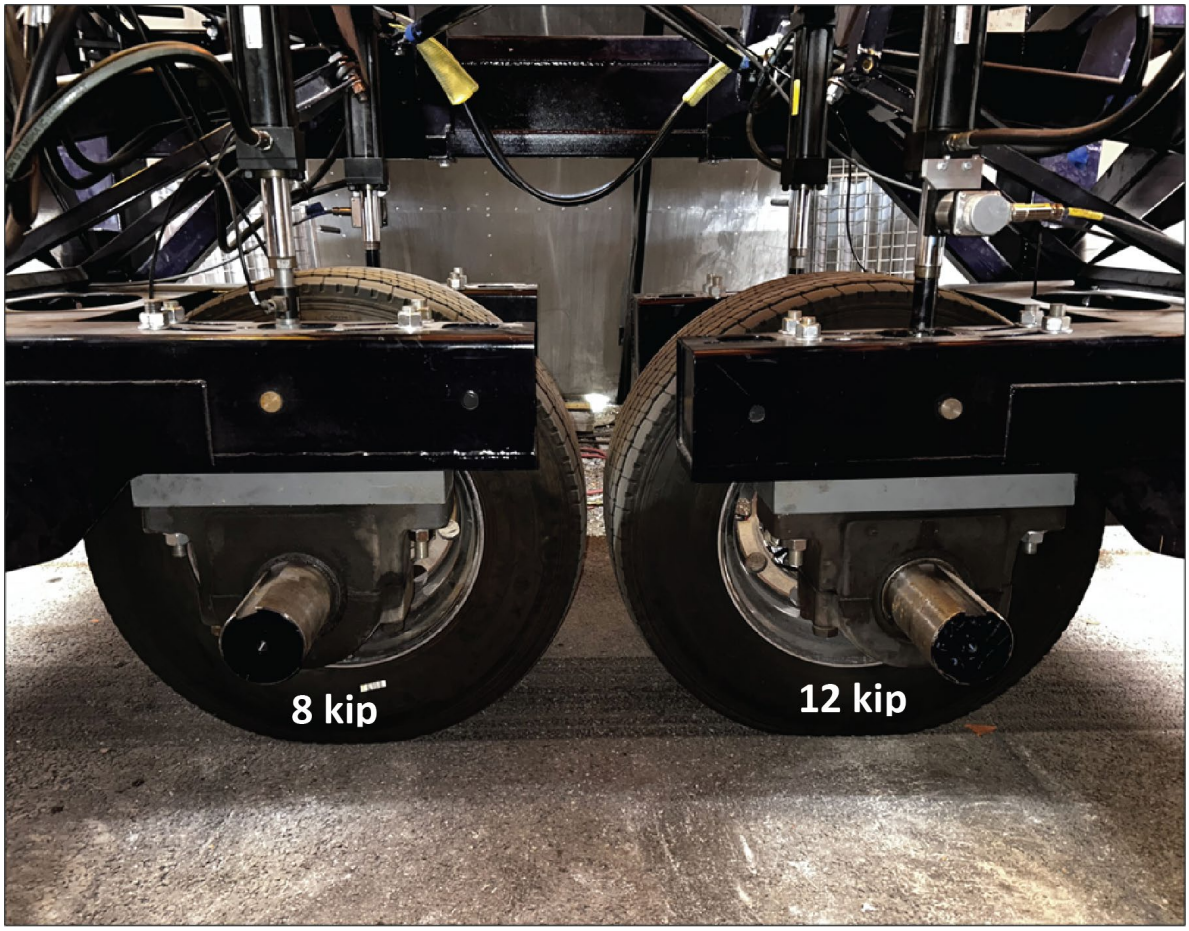

Figure 62. Photo. I-APT carriage configured for 3.5 ft center-to-center spacing applying different loads on each tire.

Tires

Wide-base single tires were selected due to their higher induced pavement responses compared to conventional dual tires (Al-Qadi et al., 2018). The ones used in this study (Table 23) were provided at no cost by the manufacturer. This tire has radial reinforcement that permits the sidewalls and the crown to work independently.

Table 23. Tire Specifications

Tire Characteristics	Parameter
Size	445/50R22.5
Ply Rating	20PR
Brand	Michelin
Model	X1 Line Grip D
Inflation Pressure (psi)	120
Overall Diameter (in)	40.4
Overall Width (in)	17.1

Source: www.otrusa.com

Axle Spacing

In commercial trucks, tire size determines the minimum and maximum spacing between the leading and trailing tires. For typical truck tires with an outside diameter of approximately 37 in, the tread-to-tread spacing can range from 0 to 37.5 in. The space between tires in the I-APT depends on tire size and the mechanical limits of the carriage. In this study, the tire spacing for I-APT was set to 3.5, 4.0, and 4.5 ft (Figure 63) center to center, resulting in calculated tread-to-tread distances of 5, 11, and 17 in, respectively.

Figure 63. Photo. I-APT carriage configured for 4.5 ft center-to-center spacing.

SENSOR DATA ACQUISITION AND PROCESSING

Figure 64 illustrates the flowchart used to capture and process critical pavement responses from embedded sensors.

A PXIe-1095 main chassis by National Instruments was used to log data. PXIe-4330 bridge analog input cards were used to collect strain gauge signals, PXIe-4353 thermocouple input cards for temperature readings, and PXIe-6363 multifunction modules to connect the pressure cells.

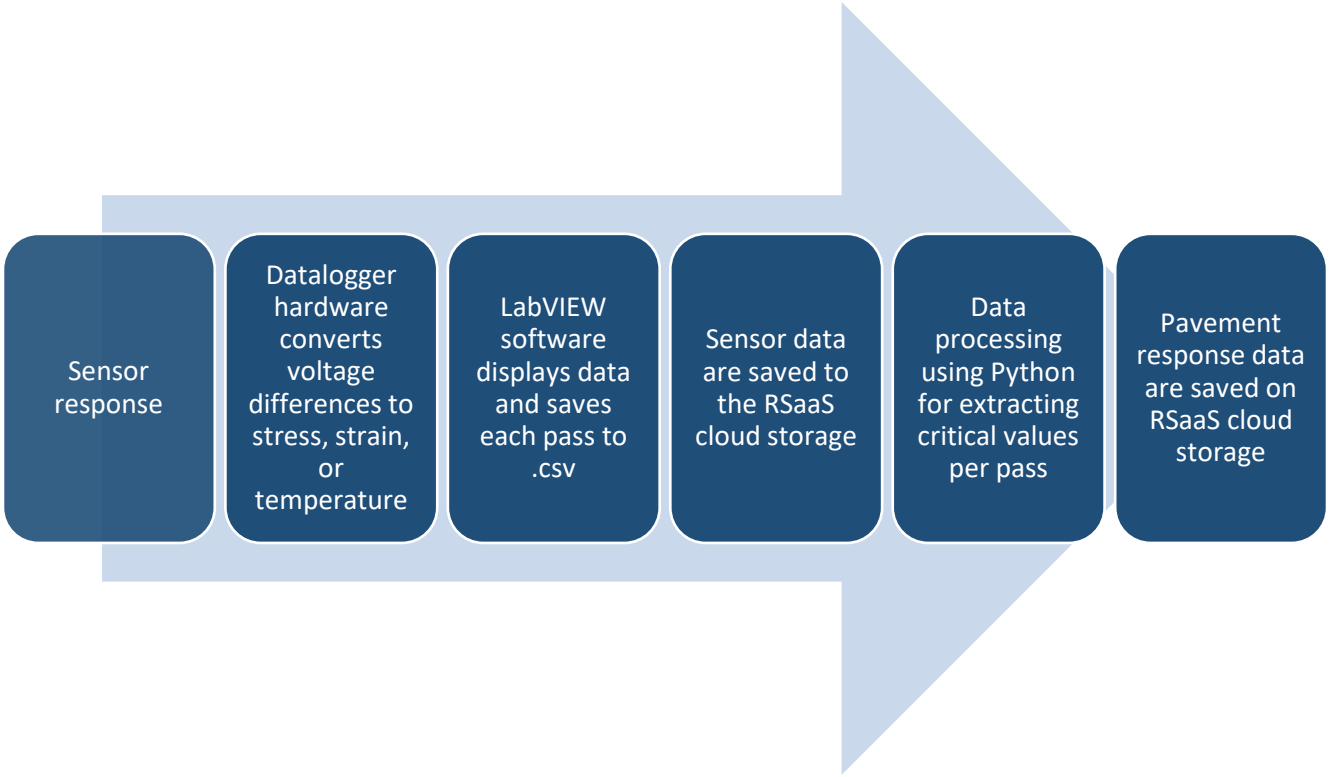

Figure 64. Flowchart. Capture and processing critical pavement responses from embedded sensors.

To monitor the tests, a LabVIEW-based visual interface was developed to display temperature control values (Figure 65, area 1); sensor outputs for pressure, temperature, and strain (area 2); and real-time system status. The LabVIEW program was configured to record data during each I-APT pass. One CSV file per instrument per pass was saved to local hardware (area 3) and uploaded to the RSaaS cloud server. Operators could select datalogging formats (area 4), and the software was also programmed to issue email alerts if the pavement temperature exceeded expected bounds or changed rapidly (area 5). For each pavement section:

- Earth pressure cells recorded instantaneous voltage changes at a 1,000 Hz sampling rate. Vertical stress was calculated using a linear calibration curve.
- Strain gauges were recorded at 1,000 Hz and measured either longitudinal or transverse strains. Initial voltage offsets were corrected using stored values.
- Four to six thermocouples recorded temperature at 1 Hz.

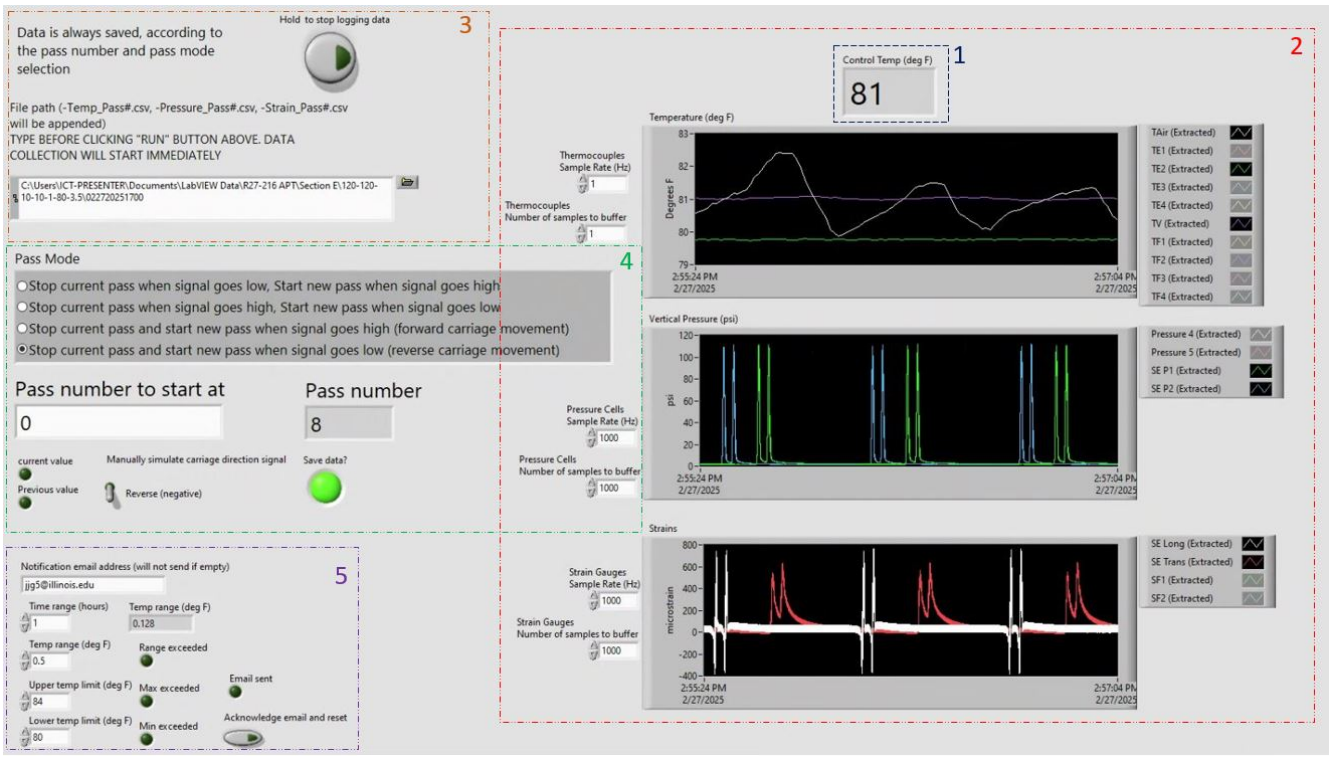

Figure 65. Photo. LabView program user interface.

Raw sensor data were retrieved from RSaaS for post-processing. Due to fluctuations in excitation voltage and electrical noise, high-frequency signals were occasionally superimposed on the raw measurements. To preserve low-frequency signals related to pavement responses, a low-pass filter was applied to the pressure and strain data. Figure 66-a and Figure 66-b illustrate the improvement of the signal, without distorting the actual stress behavior.

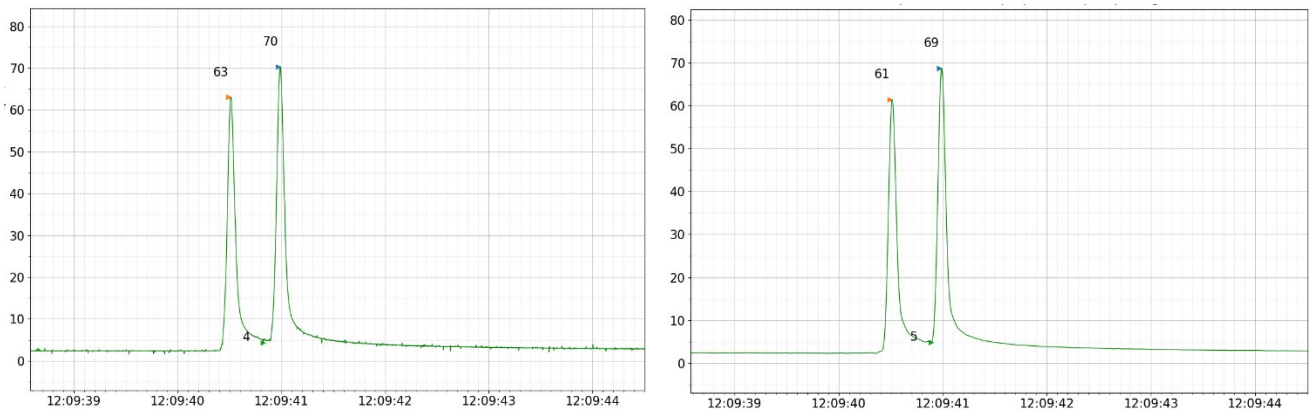

(a) Raw vertical stress (psi)

(b) Filtered vertical stress (psi)

Figure 66. Graph. Comparison of stresses before and after low-pass filtering.

For strain, the unfiltered signals demonstrated small, jagged variations near peak and valley points (Figure 67a-c). After filtering, smoother waveforms were obtained, revealing more interpretable pavement strain responses. A typical I-APT pass (e.g., at 5 mph) lasted 11 sec.

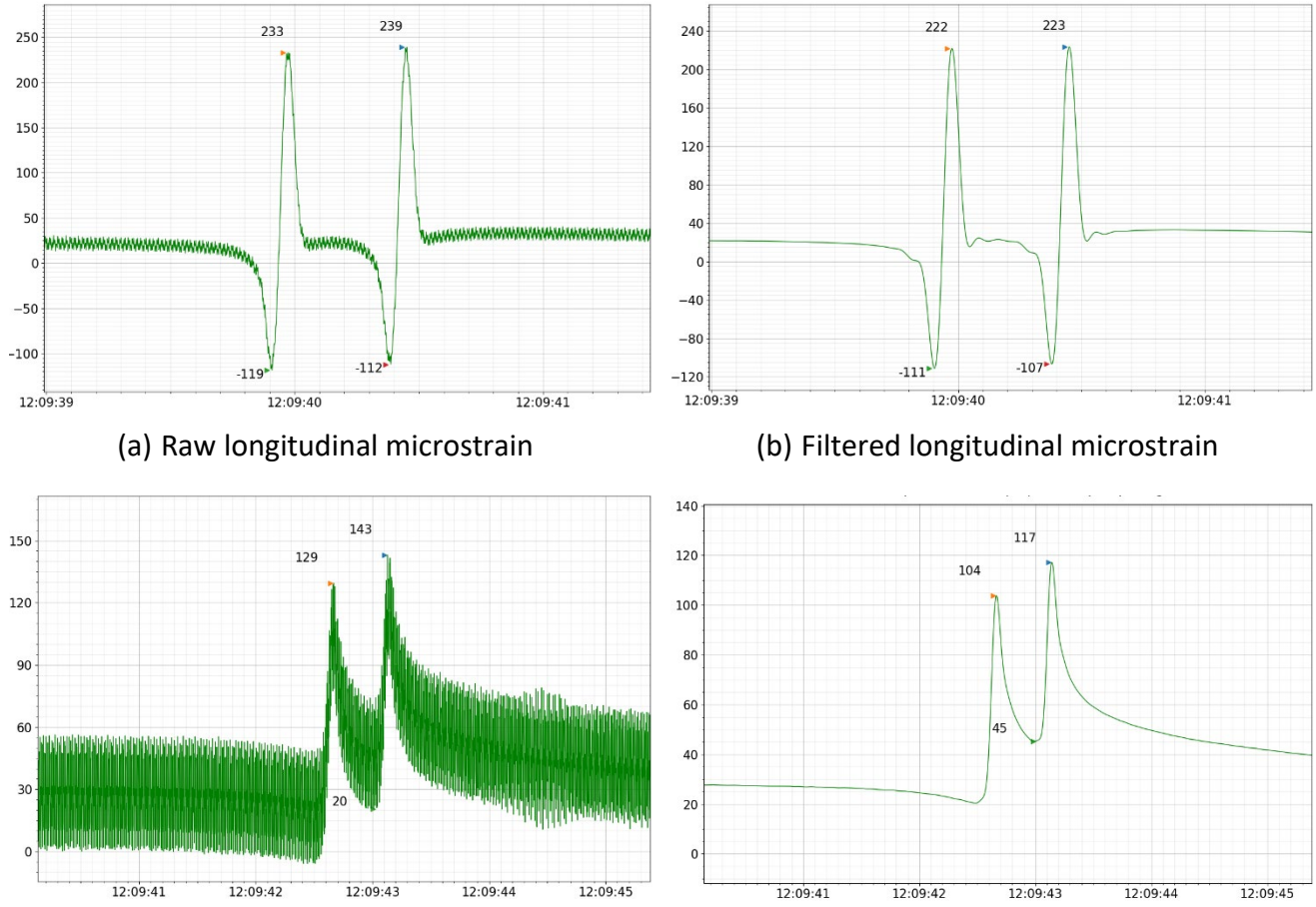

(a) Raw longitudinal microstrain

(b) Filtered longitudinal microstrain

(c) Raw transverse microstrain

(d) Filtered transverse microstrain

Figure 67. Graph. Comparison of strains before and after low-pass filtering.

Sensor voltages at the start of each pass were rarely zero due to temperature changes between installation and testing. To capture true stress and strain values for each pass, baseline corrections were applied using the mode of the initial voltage points: (i) strain data used the mode of the first 200–300 points, and (ii) stress data used the mode of the first 500–1,000 points. Peak and valley values were adjusted accordingly to obtain relative responses.

Critical response metrics were extracted for each pass. For each loading scenario, mean values and coefficient of variation (COV) were computed using the last 10 stabilized passes, and the processed data were put in CSV format and uploaded to the RSaaS cloud storage for subsequent analysis.

TEST SCENARIOS WITH VARYING LOADING CONFIGURATIONS

To assess the response of each pavement section, the loading parameters were varied to examine the effects of different loading conditions. The scenarios included single- and tandem-axle loads ranging from 8 to 14 kip to assess potential overloading; tire inflation pressures of 80, 100, and 120 psi to investigate the impact of tire pressure deflation, including asymmetric inflation conditions where one tire is deflated and the other remains inflated (Figure 68); and speeds of 1, 3, and 5 mph to evaluate the influence of speed on pavement responses. Axle spacings of 3.5, 4.0, and 4.5 ft center to center were used to study spacing effects. The target pavement temperature was varied, with target levels of approximately 65°F, 80°F, and 95°F.

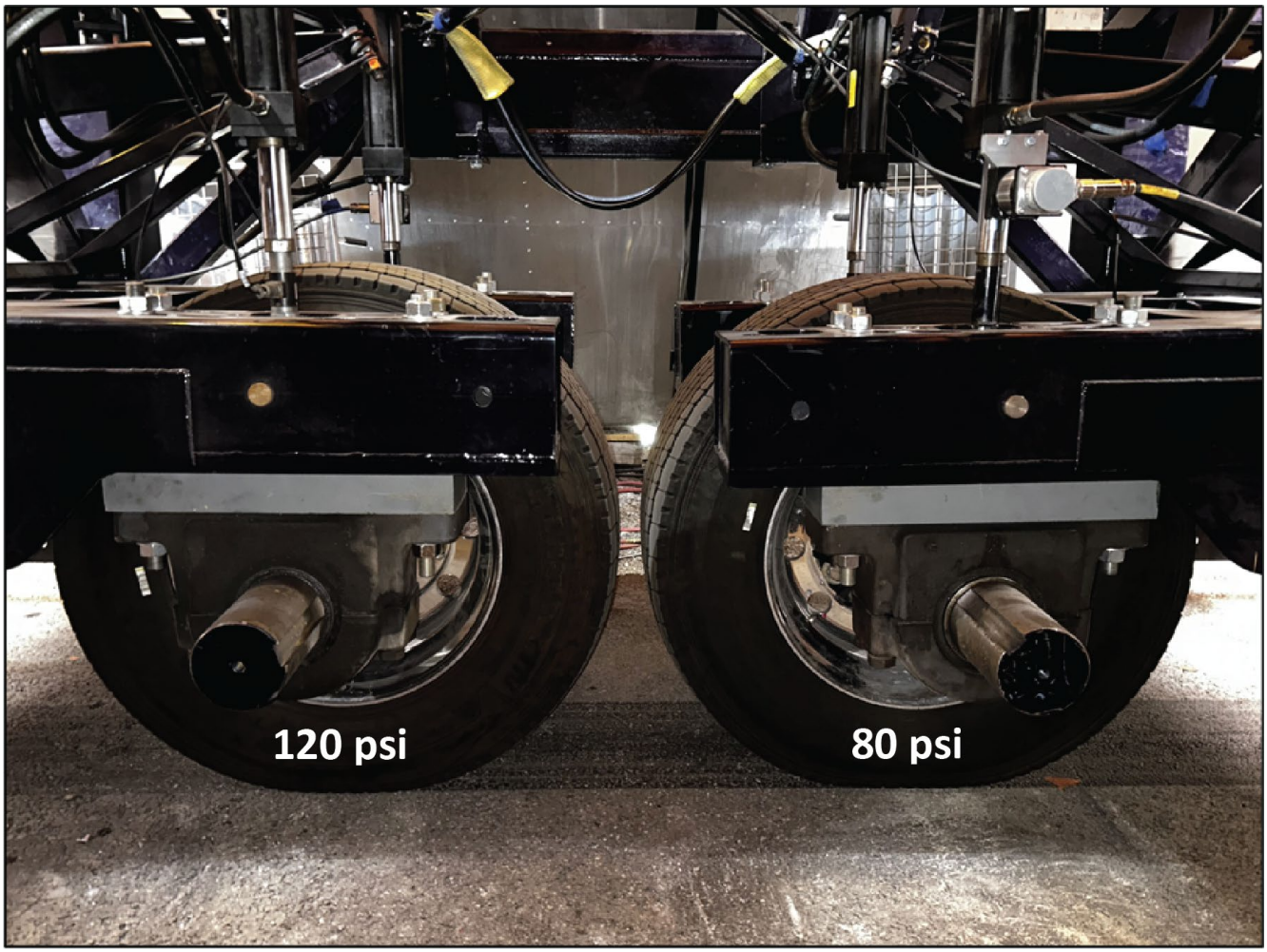

Figure 68. Photo. I-APT carriage loading tires at different inflation pressures with 10 kip.

For clarity, the cases are color-coded as follows: Single-tire deflation is purple, tire deflation is blue, load magnitude is green, axle spacing is yellow, speed is orange, and temperature is brown. The case matrix is presented in Table 24.

Table 24. Testing Scenarios with Varying Loading Configurations

Scenario	Tire 1 Inflation Pressure (psi)	Tire 2 Inflation Pressure (psi)	Tire 1 Load (kip)	Tire 2 Load (kip)	Speed (mph)	Axle Spacing (ft)	Target Temperature (°F)
A	120	0	8 ▲	0	5		80
B*	120	0	10 ▲	0	5		80
C*	120	0	12 ▲	0	5		80
D*	120	0	14 ▲	0	5		80
E	120	0	10	0	1 ★		80
F	120	0	10	0	3 ★		80
G	100 ●	0	10	0	5		80
H	80 ●	0	10	0	5		80
Baseline	120	120	10	10	5	3.5	80
A-T*	120	120	8 ▲	8 ▲	5	3.5	80
B-T*	120	120	12 ▲	12 ▲	5	3.5	80
C-T*	120	120	14 ▲	14 ▲	5	3.5	80
D-T	120	120	10	10	1 ★	3.5	80
E-T	120	120	10	10	3 ★	3.5	80
F-T	100 ●	100 ●	10	10	5	3.5	80
G-T	80 ●	80 ●	10	10	5	3.5	80
H-T	120 ◆	80 ◆	10	10	5	3.5	80
I-T	80 ◆	120 ◆	10	10	5	3.5	80
J-T	120	120	10	10	5	4.5 ■	80
K-T**	120	120	10	10	5	5.5 ■	80
L-T**	120	120	10	10	5	3.5	~65 ✚
M-T**	120	120	10	10	5	3.5	~95 ✚

* The loads applied on section D4-50-12.5-0 were 8, 9, and 10 kip/tire.

**Only applied to two sections: T1-80-12.5-0 and T1-50-12.5-0.

Symbol Key for Table 24: ◆ single-tire deflation, ● tire deflation, ▲ load magnitude, ■ axle spacing, ★ speed, and ✚ temperature

For each scenario, the pavement was loaded with 60 passes in the same configuration to ensure stabilized responses (Figure 69). Data collected during each pass were visualized (Figure 70), and for each scenario, critical values were extracted and averaged over the last 10 passes. The COV for all results remained below 3%, indicating strong measurement repeatability.

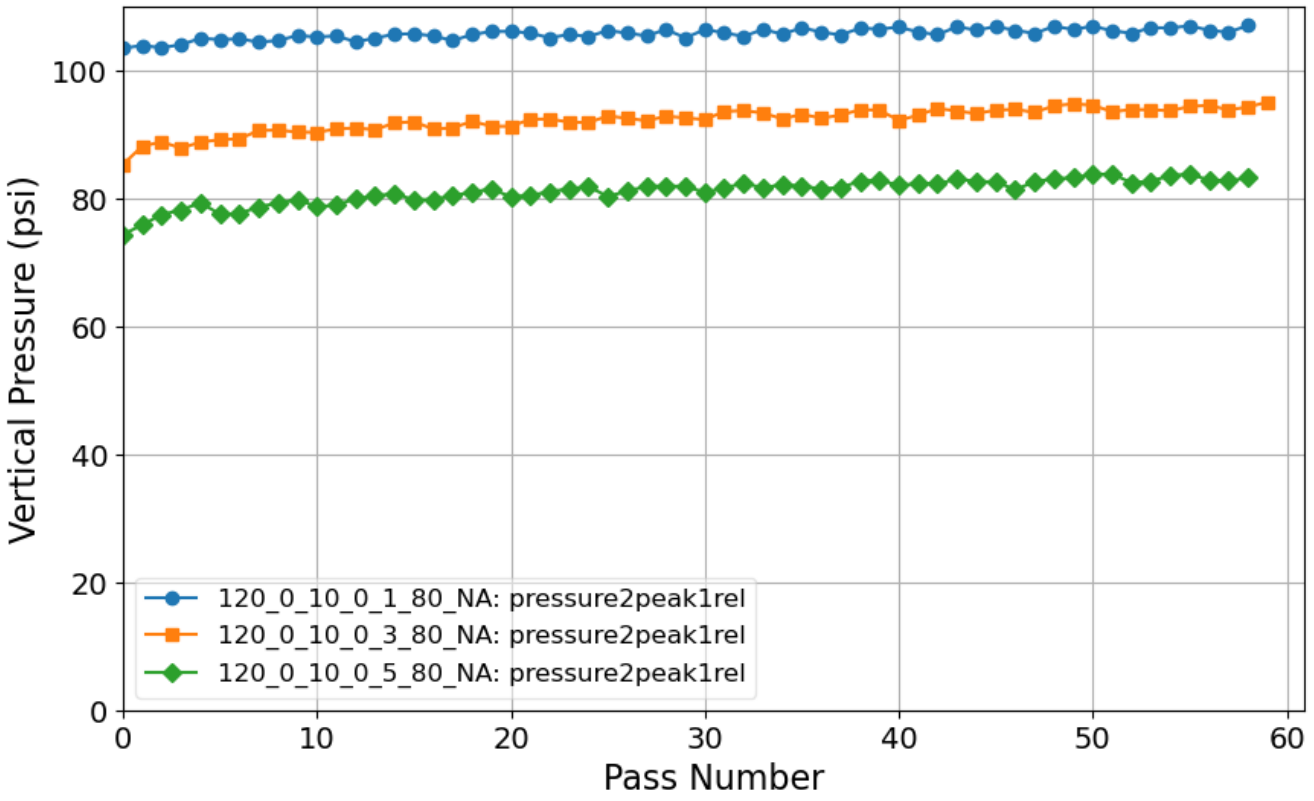

Figure 69. Graph. Stability of sensor readings.

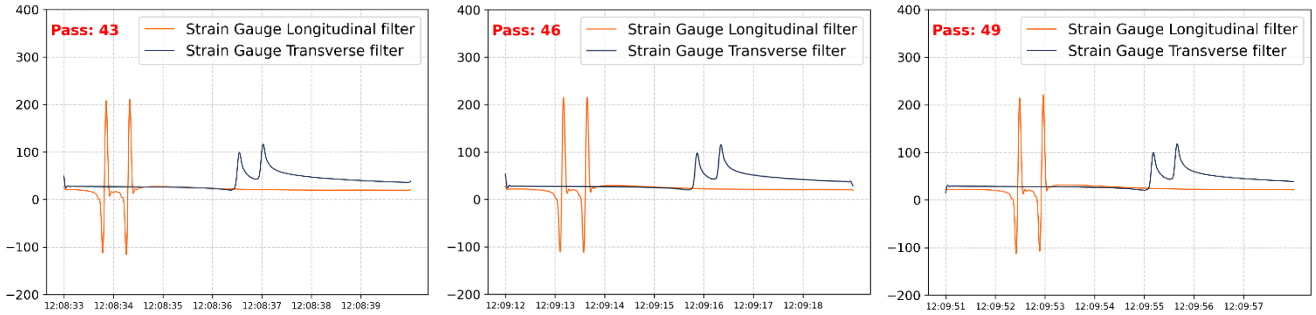

(a) Pass 43 (b) Pass 46 (c) Pass 49

Figure 70. Graph. Microstrain values at different passes of the same loading scenario.

PAVEMENT RESPONSES

This section presents an analysis of the SMA critical responses under various loading scenarios. The average values and COV for all features extracted from each waveform are presented in Appendix H without correction. Increasing the loading speed reduced the magnitude of pavement responses, while increasing the load magnitude resulted in higher stresses and strains, as expected. In some cases, the expected trends were partially masked by pavement temperature. Across all sections, SMA temperature ranged from 80 to 83°F (26.7 to 28.3°C), and SMA thickness varied from 1.9 to 2.4 in. (48

to 61 mm). The response waveforms from a single pass are presented along with respective temperatures and SMA layer thicknesses in Appendix I. Deviations from the target thickness would contribute to variability.

Effects of Temperature and Layer Thickness on SMA Measurements

Temperature Correction of Pavement Response Data

During accelerated pavement testing, temperature fluctuated between 75°F and 85°F, which affected the measured pavement responses. To isolate the effect of temperature on structural behavior, all subsequent measurements were corrected to a reference temperature of 80°F. The correction was based on the master curves presented in Figure 33, using time–temperature superposition principles to adjust the effective loading frequency for temperature variations.

The contact time (t_c) of the wheel load at the bottom of the SMA layer was determined from the vertical stress pulse measured by the embedded pressure cells, which was observed to be 0.15 s. Figure 71 illustrates an example of stress pulse analysis, where a Haversine curve was fitted to obtain t_c. Considering that the pressure cells have a diameter of 9 in, 0.01 s was subtracted (travel time over the plate at 5 mph) to determine the effective contact duration of 0.14 s for any infinitesimal point along the wheel path. Following Van Der Poel (1954), the same modulus may be obtained using either creep or dynamic testing when $f = 1/(2\pi t_c)$. Therefore, the equivalent loading frequency in a laboratory complex modulus test was 1.137 Hz.

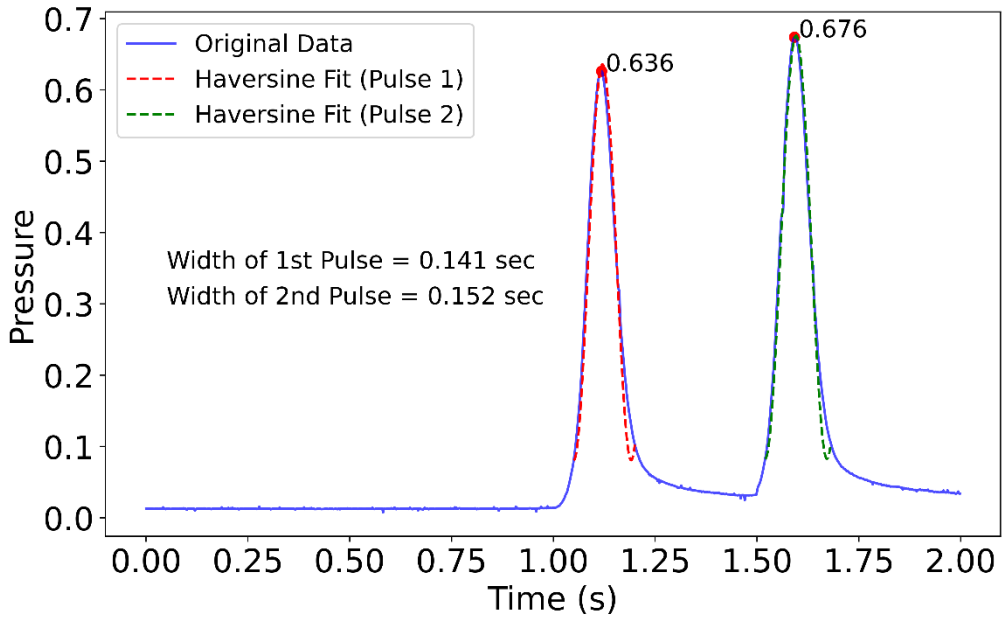

Figure 71. Graph. Haversine curve fit examples used to determine t_c.

Under linear viscoelastic assumptions, a change in modulus produces an inversely proportional change in strain. Accordingly, the temperature-corrected strains ($\varepsilon_{T=80°F}$) can be computed as follows in Figure 72:

$$\varepsilon_{T=80°\mathrm{F}} = \varepsilon_T \times \frac{E_T}{E_{T=80°\mathrm{F}}}$$

Figure 72. Equation. Strain correction for reference temperature.

where E_T and $E_{T=80°\mathrm{F}}$ are mixture moduli at the test temperature and reference temperature, respectively. This ratio depends on SMA temperature during measurement. For example, in D4-50-12.5-0, the modulus differed by approximately +26% or −20% relative to the 80°F reference (Figure 73), illustrating the magnitude of temperature-induced effect. Within this narrow temperature range, the assumption of linearity is valid.

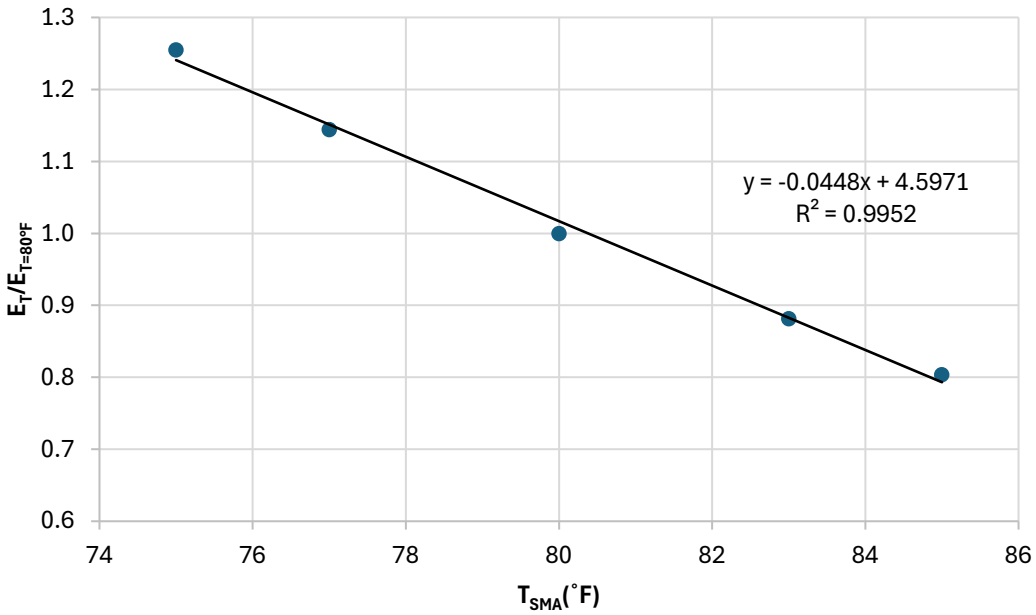

Figure 73. Graph. Change in moduli over the testing temperature range in D4-50-12.5-0.

Because this correction is intended to be pure scaling (dimensionless coefficient) rather than a regression equation for prediction, the modulus ratio was expressed in a form that forces unity at the reference temperature (i.e., $\frac{E_T}{E_{80°\mathrm{F}}}|_{T=80}$=1). As presented in Figure 73, the modulus ratio was approximated as linear:

$$\frac{E_T}{E_{80°\,F}} = 1 + k(T_{SMA} - 80)$$

Figure 74. Equation. Temperature correction factor referenced to 80°F.

The following correction equations (Table 25) were obtained for each section based on its measured response data and fitted modulus–temperature relationship:

Table 25. Temperature Correction Equations

SMA Section	k (per °F)	$\frac{E_T}{E_{80^\circ F}} = 1 + k(T_{SMA} - 80)$	Equivalent from $aT_{SMA} + b$ (anchored at 80°F)
T1-80-12.5-0	−0.0485	$1 - 0.0485(T_{SMA} - 80)$	$-0.0485 \times T_{SMA} + 4.88$
T1-50-12.5-0	−0.0483	$1 - 0.0483(T_{SMA} - 80)$	$-0.0483 \times T_{SMA} + 4.864$
D2-50-12.5-0	−0.0345	$1 - 0.0345(T_{SMA} - 80)$	$-0.0345 \times T_{SMA} + 3.760$
L2-50-12.5-0	−0.0408	$1 - 0.0408(T_{SMA} - 80)$	$-0.0408 \times T_{SMA} + 4.264$
D3-50-12.5-0	−0.0397	$1 - 0.0397(T_{SMA} - 80)$	$-0.0397 \times T_{SMA} + 4.176$
D4-50-12.5-0	−0.0448	$1 - 0.0448(T_{SMA} - 80)$	$-0.0448 \times T_{SMA} + 4.584$
Average	−0.0428	$1 - 0.0428(T_{SMA} - 80)$	–

To further validate the temperature-correction approach, an independent comparison was conducted using two additional temperature levels (82°F and 96°F). Although the correction is primarily applied within the test temperature range (75–85°F), this comparison provides a consistency check between modulus ratios obtained from the complex modulus master curves and strain ratios measured on the full-scale I-APT sections. Table 26 reports the prediction errors relative to the strain ratios measured on the full-scale APT sections.

Table 26. Prediction Errors between Modulus Ratios from Complex Modulus Master Curves and Measured Strain Ratios on Full-scale APT Sections at 82°F and 96°F

Case (120 psi air inflation pressure and 10 kip load)	Section T1-80-12.5-0			Section T1-50-12.5-0		
	$E_{96ºF}/E_{82ºF}$	$\varepsilon_{82ºF}/\varepsilon_{96ºF}$ (Measured)		$E_{96ºF}/E_{82ºF}$	$\varepsilon_{82ºF}/\varepsilon_{96ºF}$ (Measured)	
		Transverse	Longitudinal		Transverse	Longitudinal
Leading Tire of a Single Axle	0.512	0.599	0.443	0.542	0.463	0.598
Trailing Tire of a Tandem Axle		0.542	0.440		0.498	0.582
Average		0.506			0.535	
Error	1.2%			1.2%		

Thickness Correction of Pavement Response Data

First, for each response of interest, the depth-dependent profiles were extracted at the in-plane locations corresponding to the maximum response and subsequently fitted using analytical functions. Across all I-APT sections, the functional forms that best captured the depth variation were found to be cubic for the vertical stress (S22) and quadratic for both the longitudinal strain (E11) and the transverse strain (E33).

Second, given that SMA layers were modeled as linear viscoelastic materials, and that within each I-APT section all other parameters were held constant, the relationship between the applied wheel load and the resulting responses could be approximated as linear for the limited variation in

thickness. Accordingly, a proportional load-scaling term was incorporated into the depth fitted functions.

A 2 in thickness was taken as the reference thickness to build thickness correction factors that could be applied to the measured responses. The general correction to any measured response has the following form (Figure 75):

$$R_{Corrected} = R_{Measured} * F_{Thick}$$

Figure 75. Equation. General thickness correction formula.

where $R_{measured}$ is measured response, $R_{Corrected}$ is corrected response, and F_{Thick} is thickness correction factor. F_{Thick} is thickness correction parameter evaluated at the reference SMA thickness ($T_0 = 2.0$ in) and evaluated at the corresponding section SMA thickness (T):

$$F_{Thick}(T_0, T, L) = \frac{f(T_0, L)}{f(T, L)}$$

Figure 76. Equation. Thickness correction function.

The proportional load-scaling term (L) is cancelled out. Therefore, the F_{Thick} is independent of the load (Figure 77):

$$F_{Thick}(T_0, T) = \frac{f(T_0, L)}{f(T, L)}$$

Figure 77. Equation. Thickness correction independent of load.

The correction factor is presented for each measured response of each I-APT section:

The thickness correction for the vertical stress (SS2) is presented in the steps in: (i) the general equation; (ii) the thickness correction function, including load; and (iii) the thickness function independent of load:

$$S22(T, L) = L(1.195T^3 - 5.998T^2 + 8.881T + 8.975)$$

$$F_{Thick}(T_0, T, L) = \frac{L(1.195T_0^3 - 5.998T_0^2 + 8.881T_0 + 8.975)}{L(1.195T^3 - 5.998T^2 + 8.881T + 8.975)}$$

$$F_{Thick}(T_0, T) = \frac{1.195T_0^3 - 5.998T_0^2 + 8.881T_0 + 8.975}{1.195T^3 - 5.998T^2 + 8.881T + 8.975}$$

Figure 78. Equation. Thickness correction for vertical stress.

For instance, D3-50-9.5-0 has an average SMA thickness of 2.2 in, so F_{Thick} is as follows (Figure 79):

$$F_{Thick}\,(2\text{ in}, 2.2\text{ in}) = \frac{1.195(2)^3 - 5.998(2)^2 + 8.881(2) + 8.975}{1.195(2.2)^3 - 5.998(2.2)^2 + 8.881(2.2) + 8.975}$$

$$F_{Thick_{D3-50-9.5-0}} = \frac{12.31}{12.21}$$

$$F_{Thick_{D3-50-9.5-0}} = 1.01$$

Figure 79. Equation. Example of thickness correction for vertical stress.

For this case, the thickness correction form is as follows (Figure 80):

$$S22_{Corrected} = S22_{Measured} * F_{Thick_{D3-50-9.5-0}}$$

$$S22_{Corrected} = S22_{Measured} * 1.01$$

Figure 80. Equation. Thickness correction for vertical stress in D2-50-12.5-0.

Table 27 presents the thickness correction factors for the vertical stress (S22) in SMA sections:

Table 27. Thickness Correction Factor for Vertical Stress

S22	Section T1-80-12.5-0	Section T1-50-12.5-0	Section D2-50-12.5-0	Section L2-50-12.5-0	Section D3-50-9.5-0	Section D4-50-12.5-0
T	2.0	1.9	2.4	2.0	2.2	2.1
F_{Thick}	1.00	0.997	1.032	1.00	1.01	1.006

Following the same approach, and using the developed thickness correction equations, the equations for the longitudinal strains are presented in Table 28.

Table 28. Thickness Correction Equations for Longitudinal Strains in SMA Sections

Section	Equation	R^2
T1-80-12.5-0	$E11(T, L) = L(-4.26T^2 + 10.56T + 6.481)$	0.9957
T1-50-12.5-0	$E11(T, L) = L(-3.11T^2 + 8.223T + 4.427)$	0.999
D2-50-12.5-0	$E11(T, L) = L(-3.81T^2 + 13.529T - 1.689)$	0.9948
L2-50-12.5-0	$E11(T, L) = L(-3.708T + 10.385T + 5.464)$	0.9991
D3-50-9.5-0	$E11(T, L) = L(-3.8y^2 + 10.693T + 5.162)$	0.9986
D4-50-12.5-0	$E11(T, L) = L(-3.676T^2 + 9.721T + 5.094)$	0.9984

The thickness correction factor formula for longitudinal strain (E11) is presented in Figure 81, and the calculated factors for all SMA sections are presented in Table 29.

$$E11_{Corrected} = E11_{Measured} * F_{Thick}$$

Figure 81. Equation. Thickness correction formula for longitudinal strain.

Table 29. Thickness Correction Factor for Longitudinal Strains in SMA Sections

E11	Section T1-80-12.5-0	Section T1-50-12.5-0	Section D2-50-12.5-0	Section L2-50-12.5-0	Section D3-50-9.5-0	Section D4-50-12.5-0
T	2.0	1.9	2.4	2.0	2.2	2.1
F_{Thick}	1.00	0.956	1.146	1.00	1.102	1.058

Following the same approach, and using the developed thickness correction equations, the transverse strain equation for each section is presented in Table 30:

Table 30.Thickness Correction Equation for Transverse Strains in SMA Sections

Section	Equation	R^2
T1-80-12.5-0	$E33(T,L) = L(1.072T^2 - 6.228T + 14.942)$	0.996
T1-50-12.5-0	$E33(T,L) = L(0.943T^2 - 4.737T + 11.142)$	0.998
D2-50-12.5-0	$E33(T,L) = L(0.577T^2 - 2.627T + 8.657)$	0.970
L2-50-12.5-0	$E33(T,L) = L(1.071T^2 - 5.191T + 13.227)$	0.996
D3-50-9.5-0	$E33(T,L) = L(0.853T^2 - 4.701T + 12.767)$	0.993
D4-50-12.5-0	$E33(T,L) = L(0.894T^2 - 4.927T + 12.366)$	0.996

The thickness correction formula for the transverse strain (E33) is presented in Figure 82, and the calculated correction factors are presented in Table 31.

$$E33_{Corrected} = E33_{Measured} * F_{Thick}$$

Figure 82. Equation. Thickness correction formula for transverse strain.

Table 31. Thickness Correction Factor for Transverse Strain in SMA Sections

E33	Section T1-80-12.5-0	Section T1-50-12.5-0	Section D2-50-12.5-0	Section L2-50-12.5-0	Section D3-50-9.5-0	Section D4-50-12.5-0
T	2.0	1.9	2.4	2.0	2.2	2.1
F_{Thick}	1.00	0.981	1.006	1.00	1.034	1.021

Following the same approach, and using the developed thickness correction equations, the equations for the vertical/transverse shear strains (E23) for each section are presented in Table 32:

Table 32. Thickness Correction Equations for Vertical/Transverse Shear Strains in SMA Sections

Section	Equation	R^2
T1-80-12.5-0	$E23(T,L) = L(12.522T^3 - 49.881T^2 + 66.919T + 11.724)$	0.971
T1-50-12.5-0	$E23(T,L) = L(10.754T^3 - 41.801T^2 + 55.192T + 6.829)$	0.980
D2-50-12.5-0	$E23(T,L) = L(6.288T^3 - 29.737T^2 + 42.260T + 8.644)$	0.935
L2-50-12.5-0	$E23(T,L) = L(10.158T^3 - 41.690T^2 + 55.896T + 8.602)$	0.968
D3-50-9.5-0	$E23(T,L) = L(10.334T^3 - 44.632T^2 + 60.930T + 10.834)$	0.949
D4-50-12.5-0	$E23(T,L) = L(12.019T^3 - 49.388T^2 + 65.936T + 9.789)$	0.966

The thickness correction factor formula for vertical/transverse shear strains is presented in Figure 83, and the calculated factors for all SMA sections are presented in Table 33.

$$E23_{Corrected} = E23_{Measured} * F_{Thick}$$

Figure 83. Equation. Thickness correction formula for vertical/transverse shear strains.

Table 33. Thickness Correction Factor for Vertical/Transverse Strains in SMA Sections

E33	Section T1-80-12.5-0	Section T1-50-12.5-0	Section D2-50-12.5-0	Section L2-50-12.5-0	Section D3-50-9.5-0	Section D4-50-12.5-0
T	2.0	1.9	2.4	2.0	2.2	2.1
F_{Thick}	1.00	1.043	0.954	1.00	0.947	0.964

As presented in Figure 84, Figure 85, Figure 86, Figure 87, Figure 88, and Figure 89, the measured SMA responses in the six sections exhibited predominantly viscoelastic behavior regardless of aggregate lithology. For sections with imported aggregates, additional scenarios were applied to measure responses at different temperatures and axle spacings.

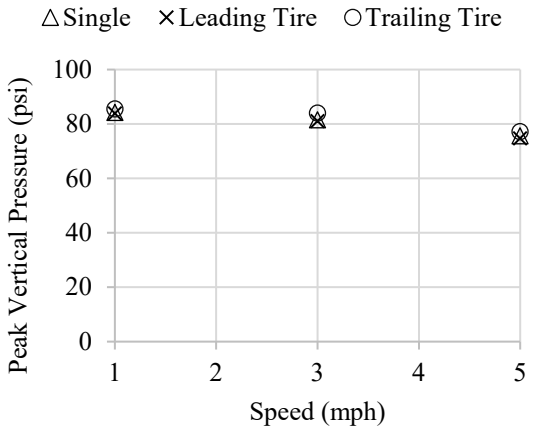
△Single ×Leading Tire ○Trailing Tire
Peak Vertical Pressure (psi)
100
80
60
40
20
0
1
2
3
4
5
Speed (mph)

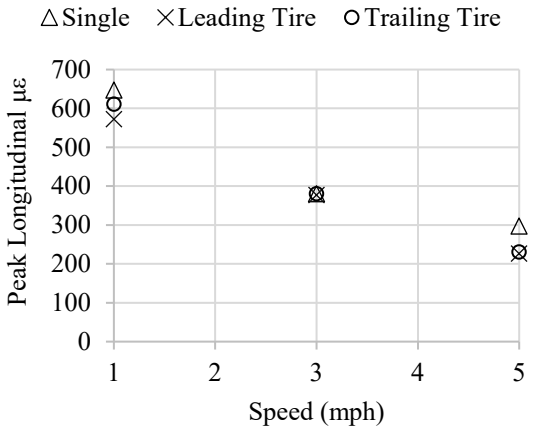
△Single ×Leading Tire ○Trailing Tire
Peak Longitudinal με
700
600
500
400
300
200
100
0
1
2
3
4
5
Speed (mph)

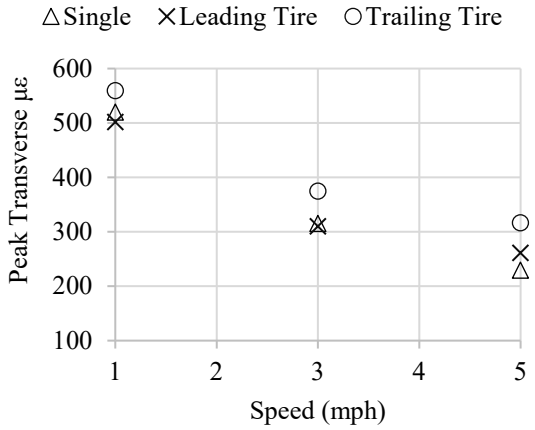
△Single ×Leading Tire ○Trailing Tire
Peak Transverse με
600
500
400
300
200
100
1
2
3
4
5
Speed (mph)

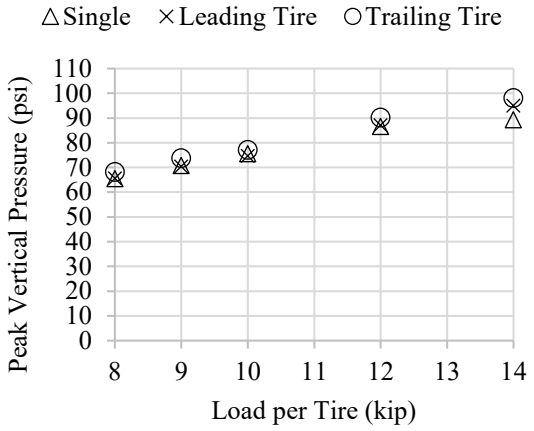
△Single ×Leading Tire ○Trailing Tire
Peak Vertical Pressure (psi)
110
100
90
80
70
60
50
40
30
20
10
0
8
9
10
11
12
13
14
Load per Tire (kip)

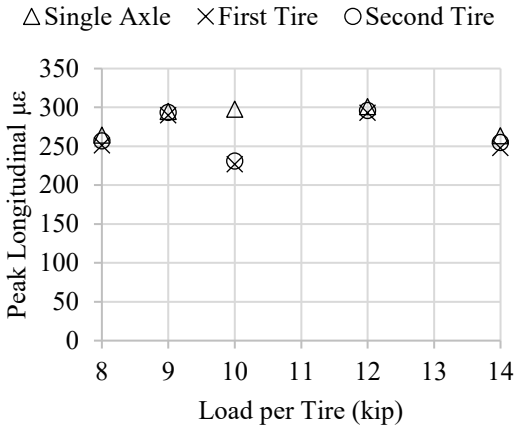
△Single Axle ×First Tire ○Second Tire
Peak Longitudinal με
350
300
250
200
150
100
50
0
8
9
10
11
12
13
14
Load per Tire (kip)

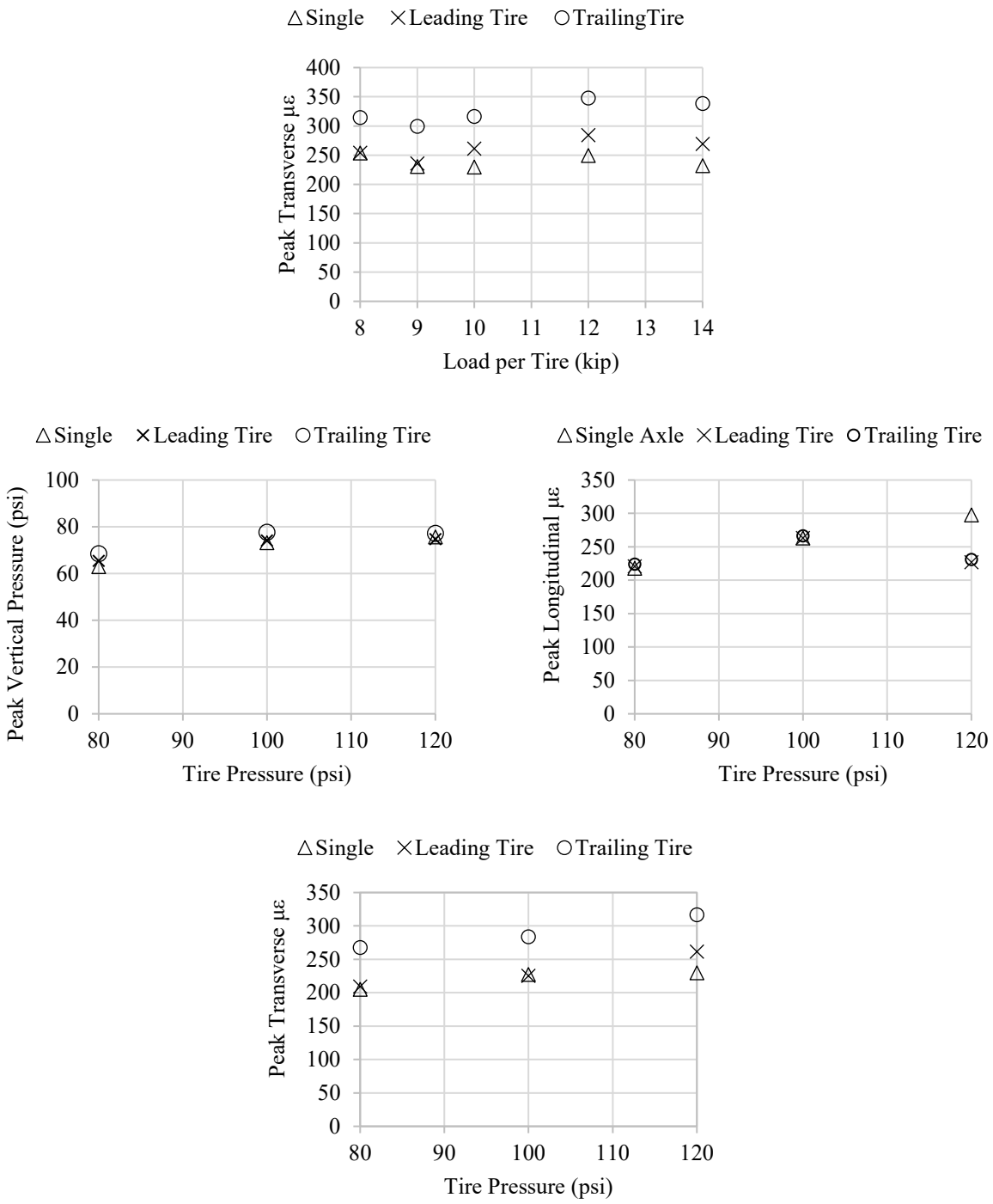

Figure 84. Graph. Effect of speed, load magnitude, and tire inflation pressure on pavement responses in T1-80-12.5-0.

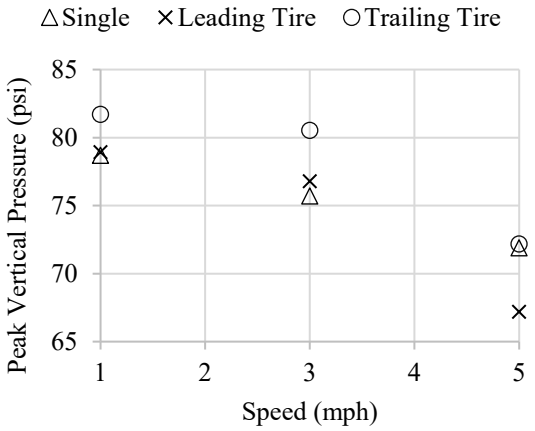
△Single ×Leading Tire ○Trailing Tire
Peak Vertical Pressure (psi)
85
80
75
70
65
1
2
3
4
5
Speed (mph)

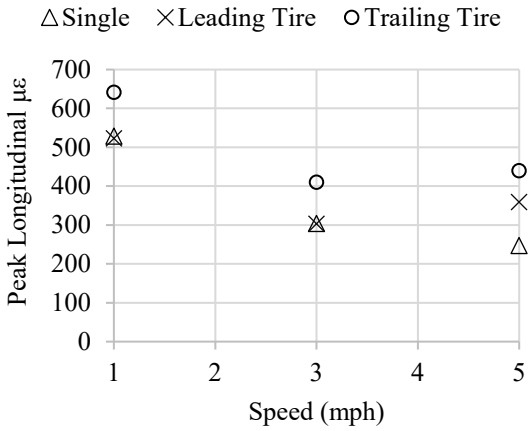
△Single ×Leading Tire ○Trailing Tire
Peak Longitudinal με
700
600
500
400
300
200
100
0
1
2
3
4
5
Speed (mph)

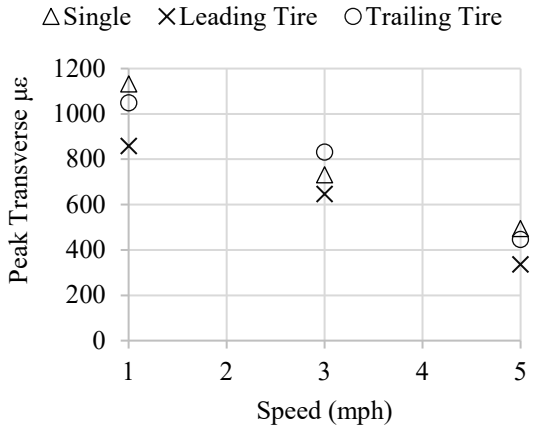
△Single ×Leading Tire ○Trailing Tire
Peak Transverse με
1200
1000
800
600
400
200
0
1
2
3
4
5
Speed (mph)

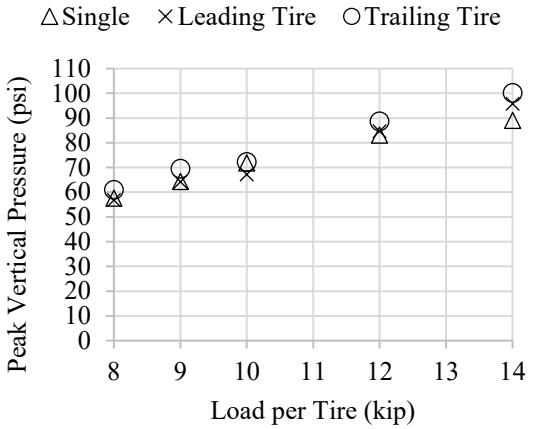
△Single ×Leading Tire ○Trailing Tire
Peak Vertical Pressure (psi)
110
100
90
80
70
60
50
40
30
20
10
0
8
9
10
11
12
13
14
Load per Tire (kip)

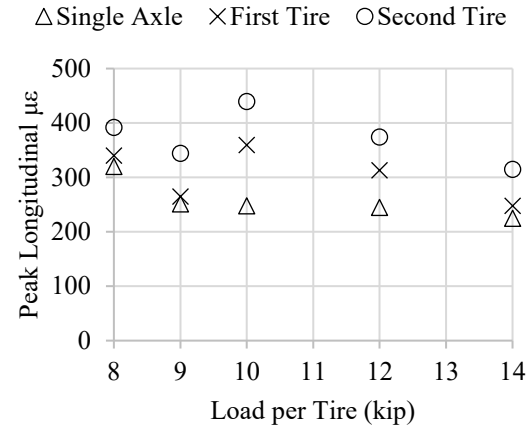
△Single Axle ×First Tire ○Second Tire
Peak Longitudinal με
500
400
300
200
100
0
8
9
10
11
12
13
14
Load per Tire (kip)

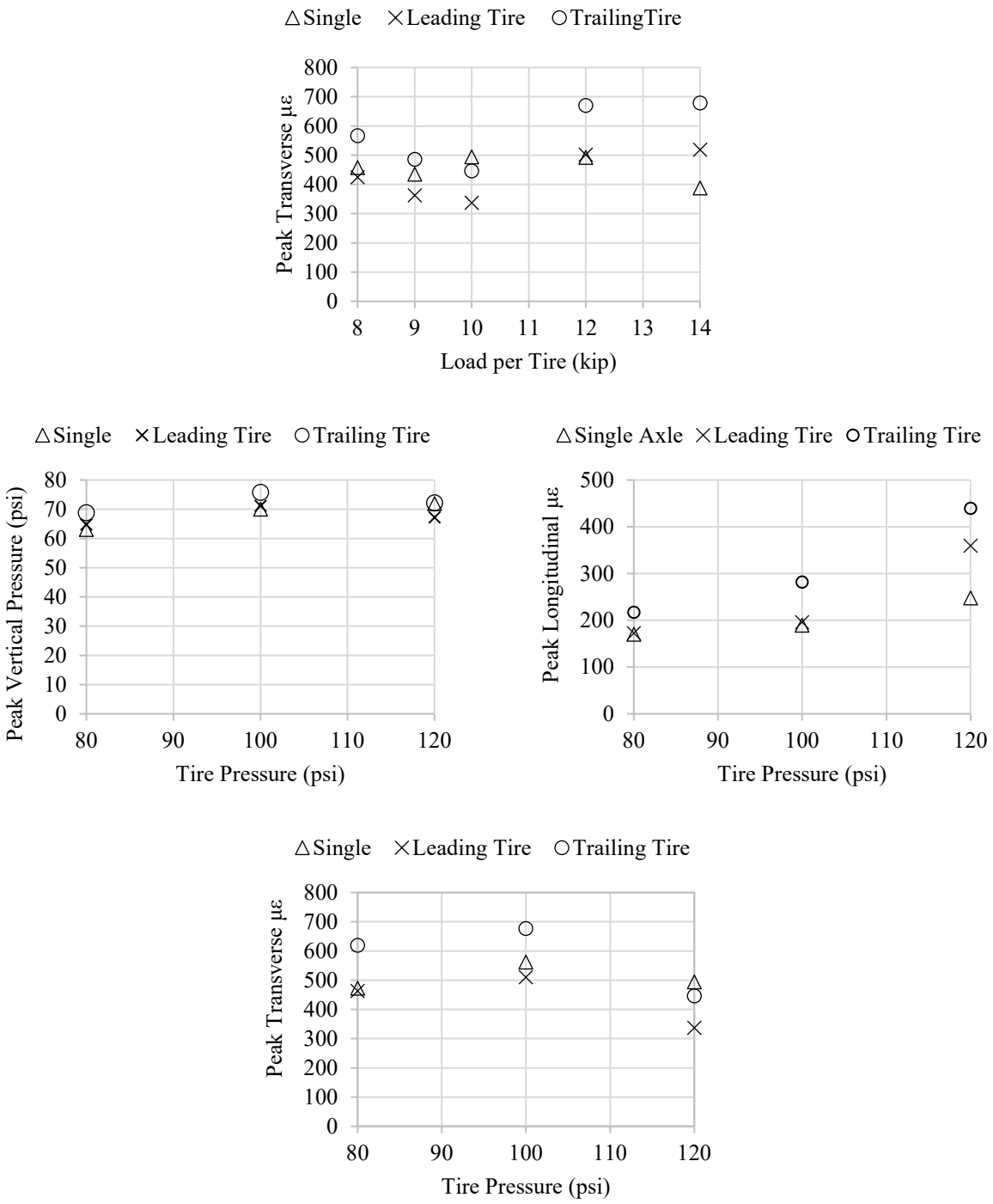

Figure 85. Graph. Effect of speed, load magnitude, and tire inflation pressure on pavement responses in T1-50-12.5-0.

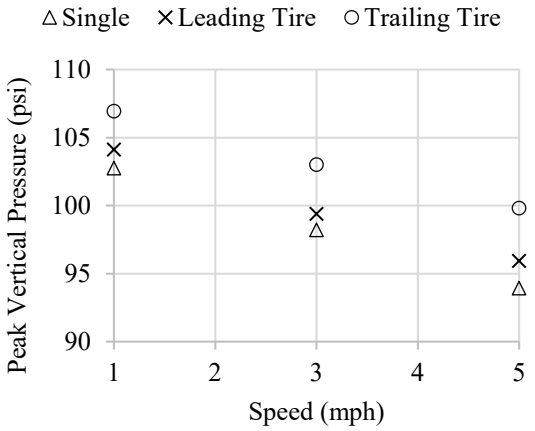
△Single ×Leading Tire ○Trailing Tire
Peak Vertical Pressure (psi)
110
105
100
95
90
1
2
3
4
5
Speed (mph)

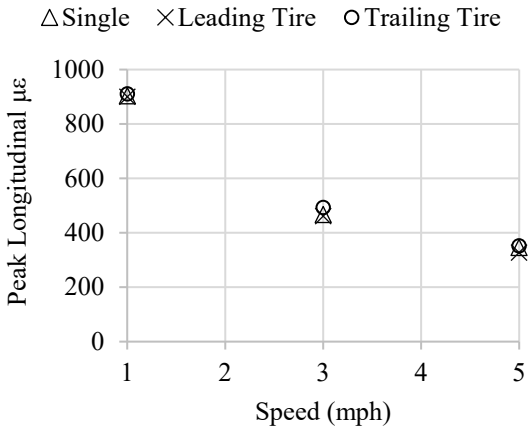
△Single ×Leading Tire ○Trailing Tire
Peak Longitudinal με
1000
800
600
400
200
0
1
2
3
4
5
Speed (mph)

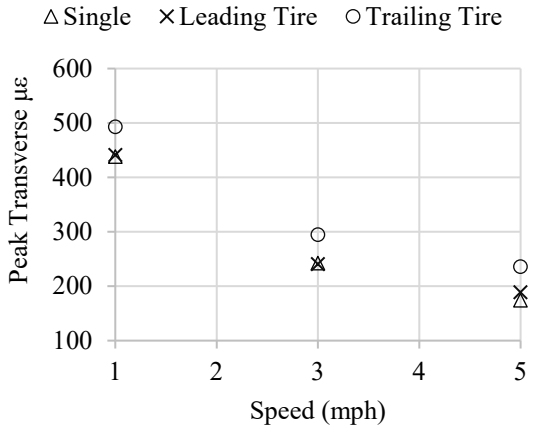
△Single ×Leading Tire ○Trailing Tire
Peak Transverse με
600
500
400
300
200
100
1
2
3
4
5
Speed (mph)

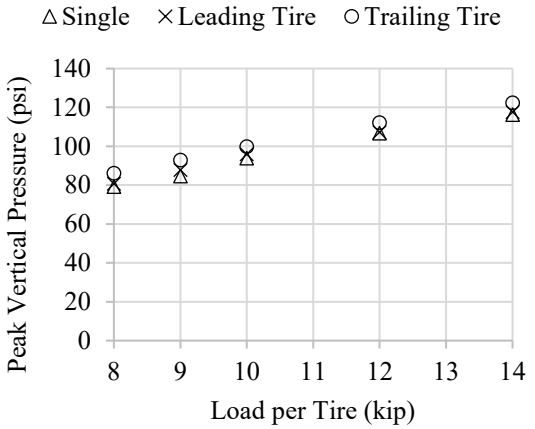
△Single ×Leading Tire ○Trailing Tire
Peak Vertical Pressure (psi)
140
120
100
80
60
40
20
0
8
9
10
11
12
13
14
Load per Tire (kip)

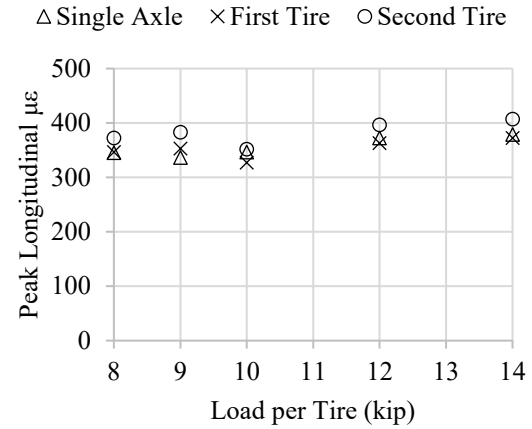
△Single Axle ×First Tire ○Second Tire
Peak Longitudinal με
500
400
300
200
100
0
8
9
10
11
12
13
14
Load per Tire (kip)

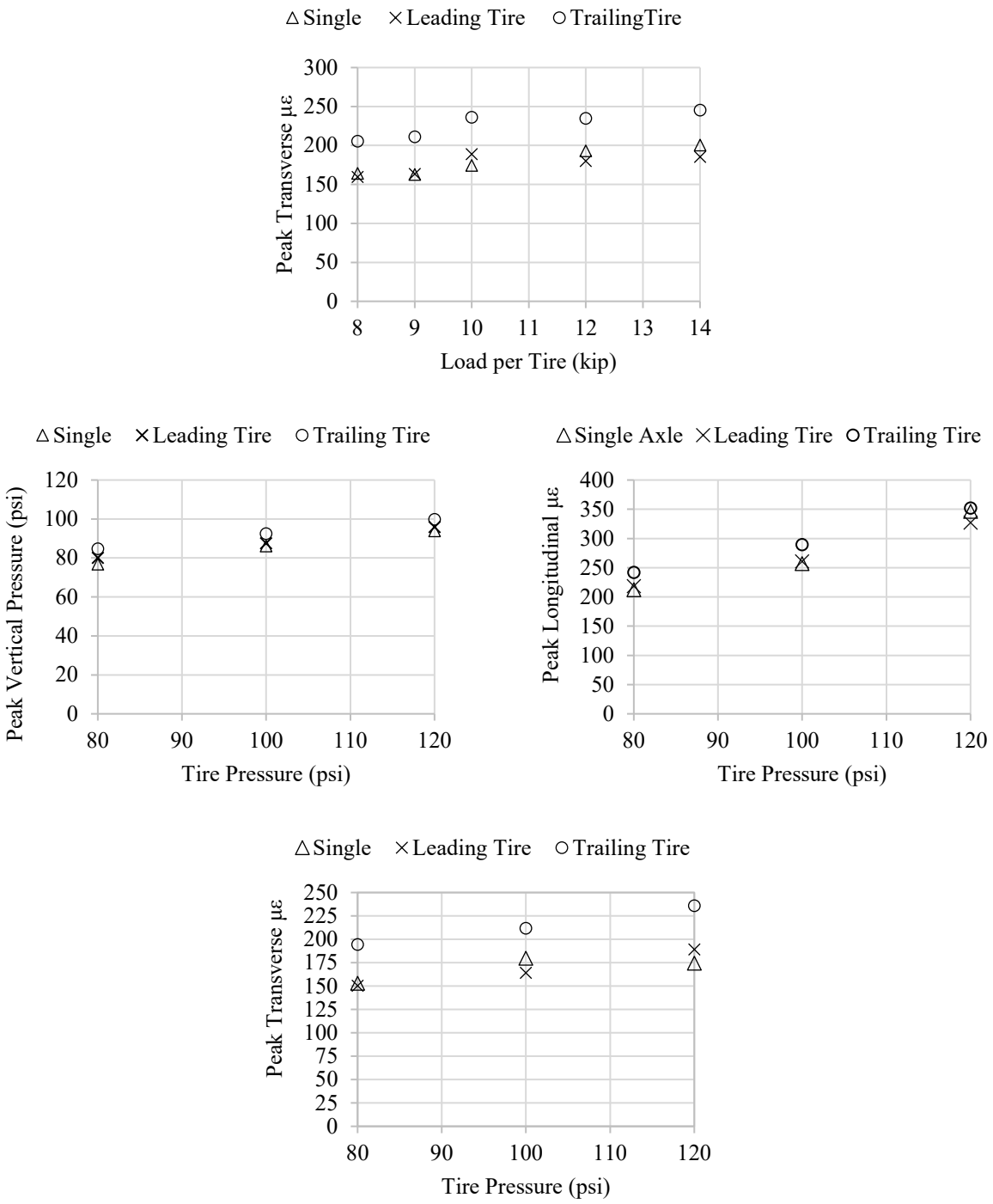

Figure 86. Graph. Effect of speed, load magnitude, and tire inflation pressure on pavement responses in D2-50-12.5-0.

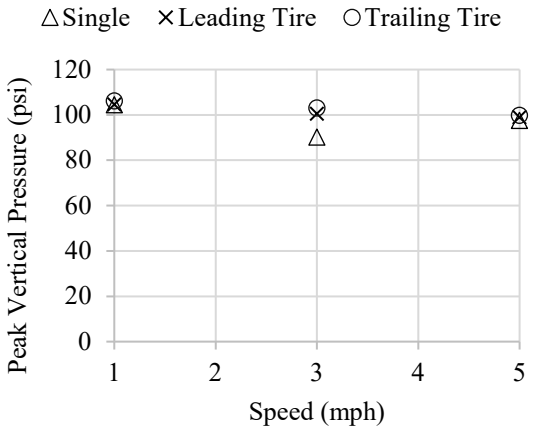
△Single ×Leading Tire ○Trailing Tire
Peak Vertical Pressure (psi)
120
100
80
60
40
20
0
1
2
3
4
5
Speed (mph)

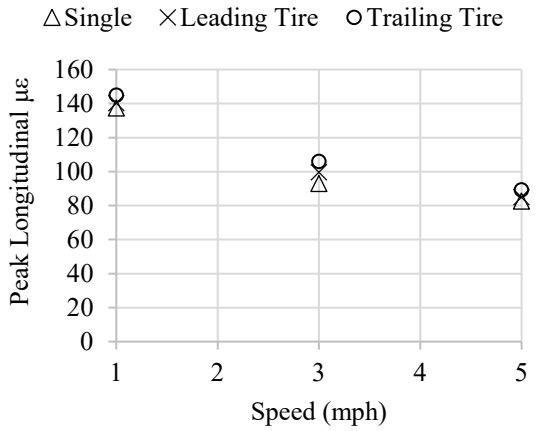
△Single ×Leading Tire ○Trailing Tire
Peak Longitudinal με
160
140
120
100
80
60
40
20
0
1
2
3
4
5
Speed (mph)

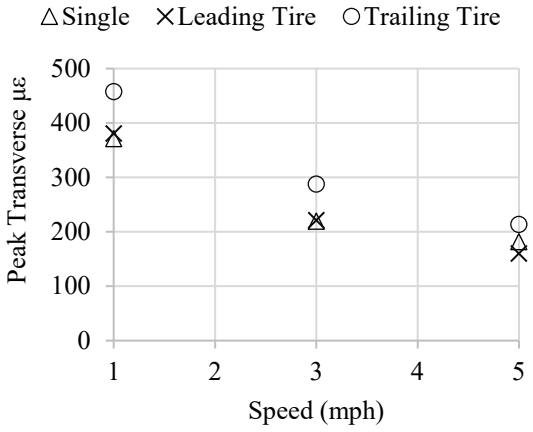
△Single ×Leading Tire ○Trailing Tire
Peak Transverse με
500
400
300
200
100
0
1
2
3
4
5
Speed (mph)

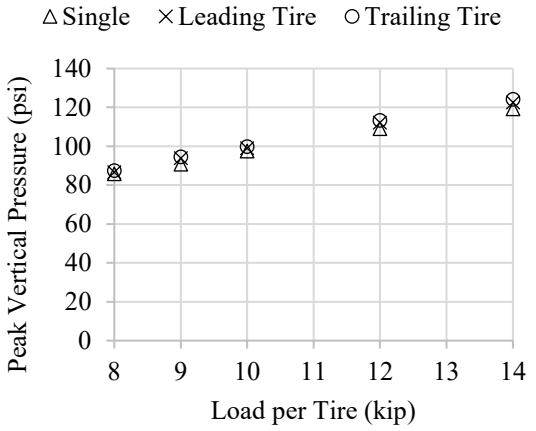
△Single ×Leading Tire ○Trailing Tire
Peak Vertical Pressure (psi)
140
120
100
80
60
40
20
0
8
9
10
11
12
13
14
Load per Tire (kip)

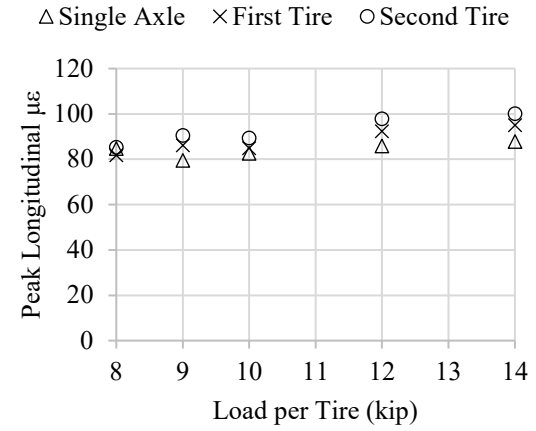
△Single Axle ×First Tire ○Second Tire
Peak Longitudinal με
120
100
80
60
40
20
0
8
9
10
11
12
13
14
Load per Tire (kip)

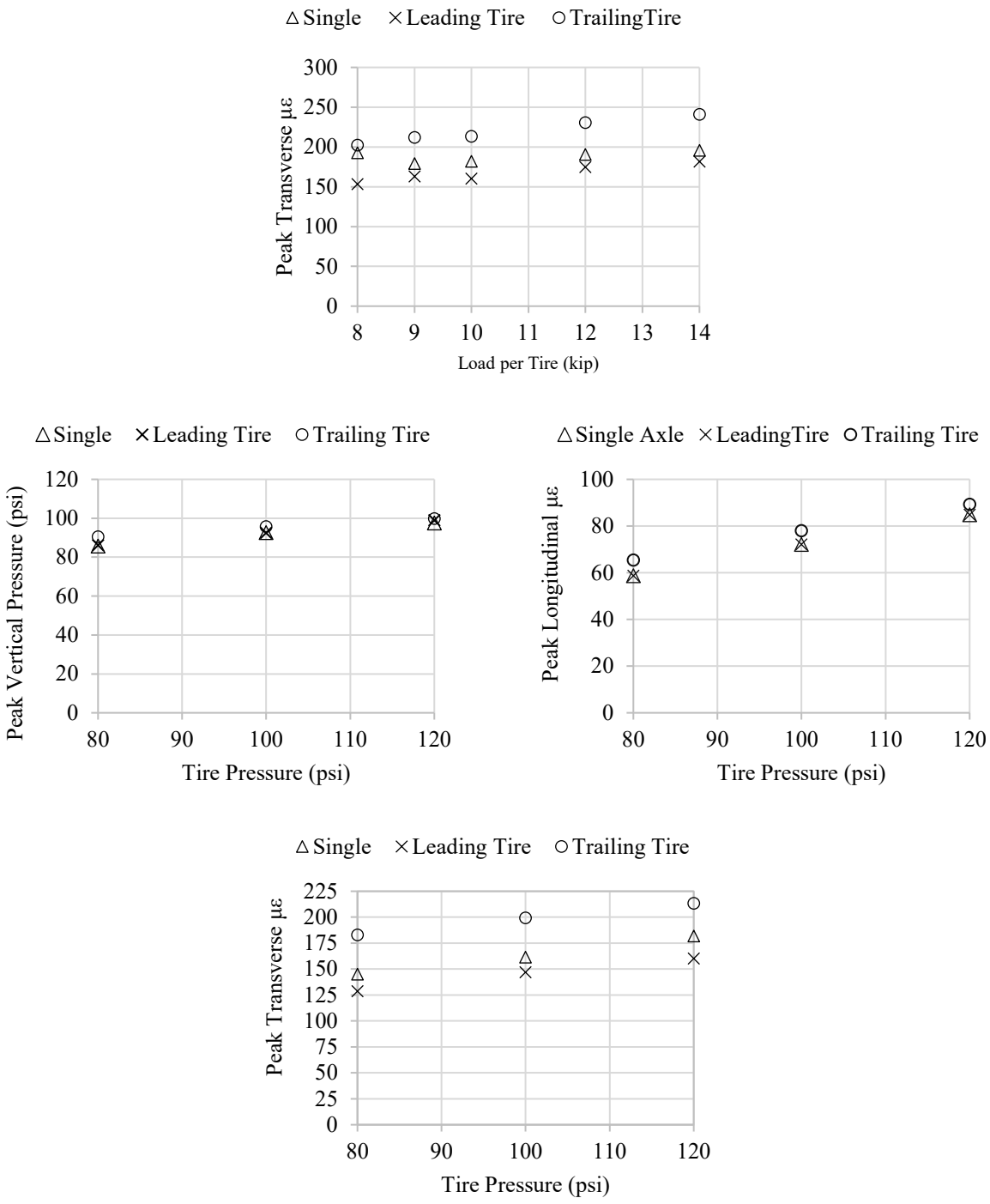

Figure 87. Graph. Effect of speed, load magnitude, and tire inflation pressure on pavement responses in L2-50-12.5-0.

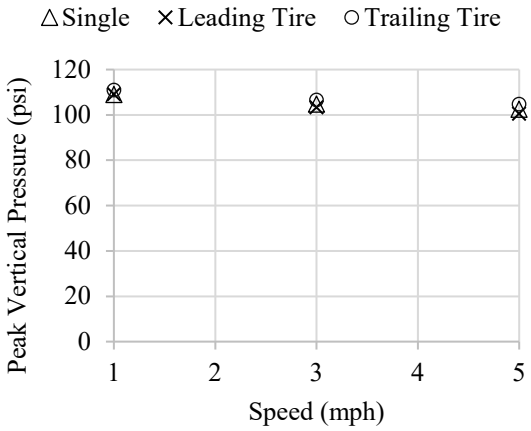
△Single ×Leading Tire ○Trailing Tire
Peak Vertical Pressure (psi)
120
100
80
60
40
20
0
1
2
3
4
5
Speed (mph)

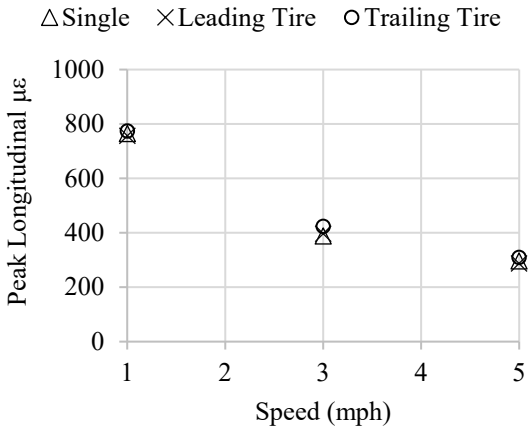
△Single ×Leading Tire ○Trailing Tire
Peak Longitudinal με
1000
800
600
400
200
0
1
2
3
4
5
Speed (mph)

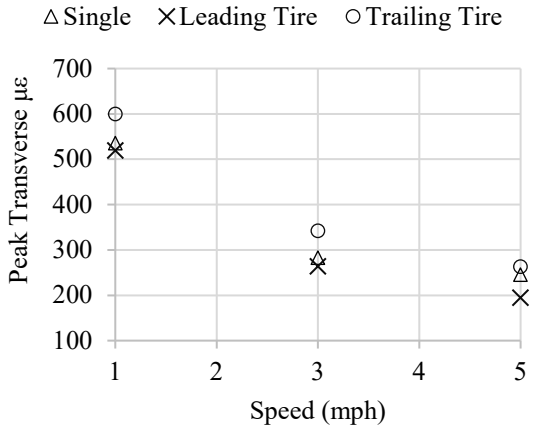
△Single ×Leading Tire ○Trailing Tire
Peak Transverse με
700
600
500
400
300
200
100
1
2
3
4
5
Speed (mph)

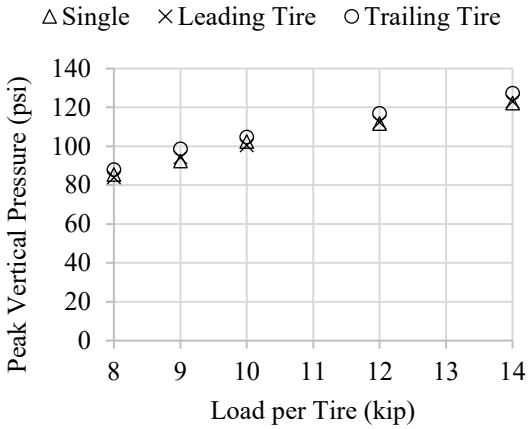
△Single ×Leading Tire ○Trailing Tire
Peak Vertical Pressure (psi)
140
120
100
80
60
40
20
0
8
9
10
11
12
13
14
Load per Tire (kip)

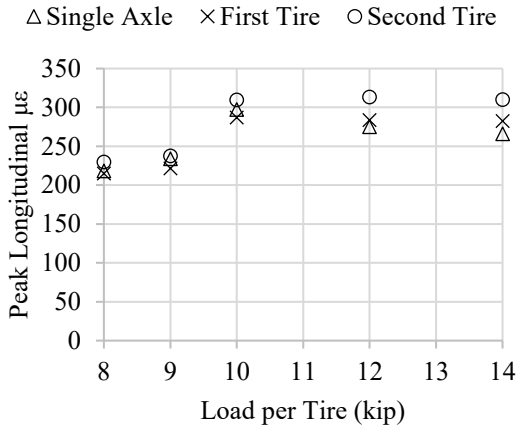
△Single Axle ×First Tire ○Second Tire
Peak Longitudinal με
350
300
250
200
150
100
50
0
8
9
10
11
12
13
14
Load per Tire (kip)

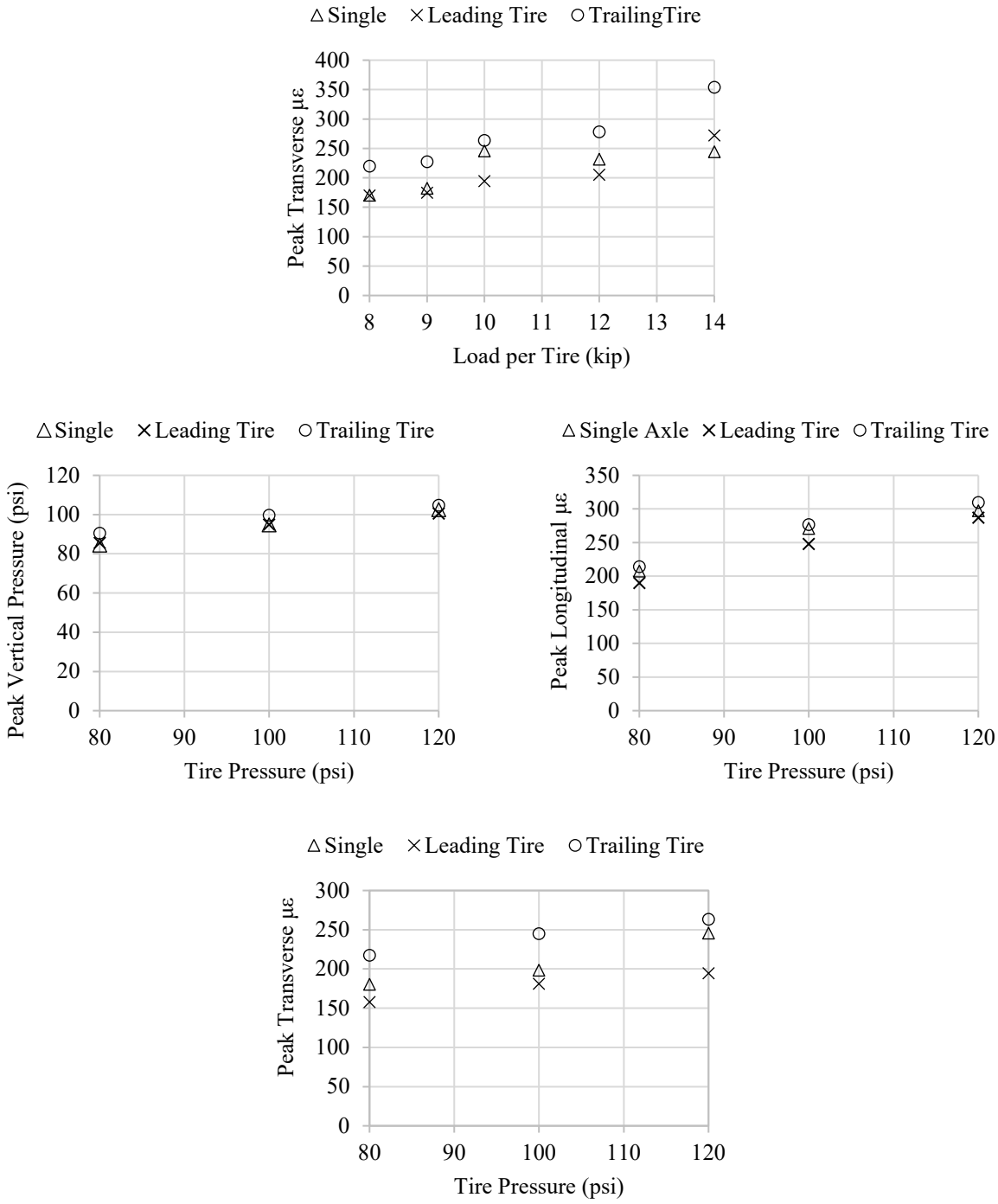

Figure 88. Graph. Effect of speed, load magnitude, and tire inflation pressure on pavement responses in D3-50-9.5-0.

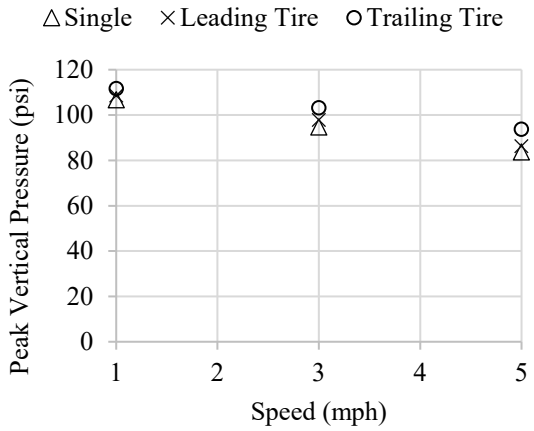
△Single ×Leading Tire ○Trailing Tire
Peak Vertical Pressure (psi)
120
100
80
60
40
20
0
1
2
3
4
5
Speed (mph)

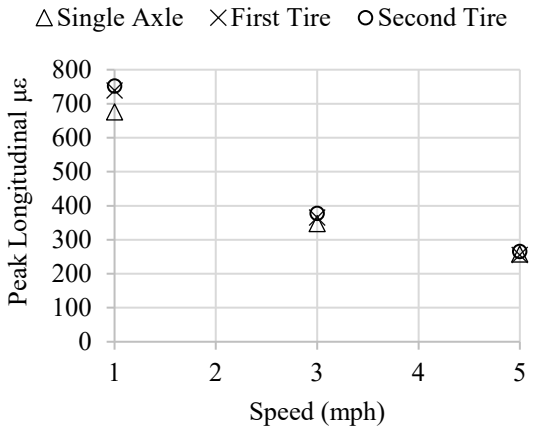
△Single Axle ×First Tire ○Second Tire
Peak Longitudinal με
800
700
600
500
400
300
200
100
0
1
2
3
4
5
Speed (mph)

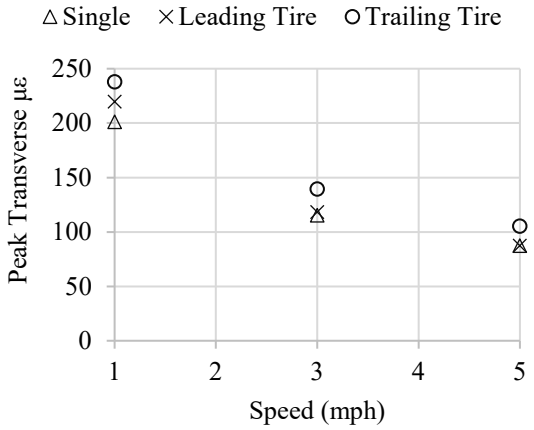
△Single ×Leading Tire ○Trailing Tire
Peak Transverse με
250
200
150
100
50
0
1
2
3
4
5
Speed (mph)

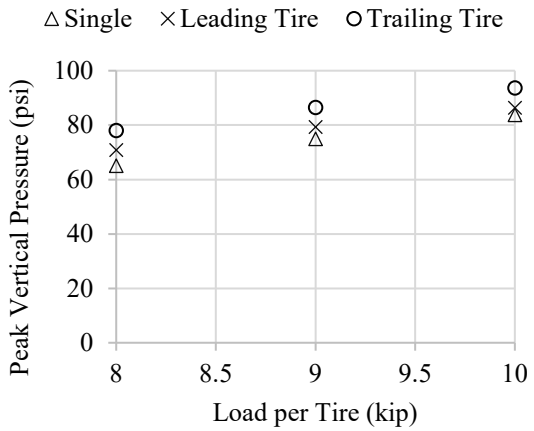
△Single ×Leading Tire ○Trailing Tire
Peak Vertical Pressure (psi)
100
80
60
40
20
0
8
8.5
9
9.5
10
Load per Tire (kip)

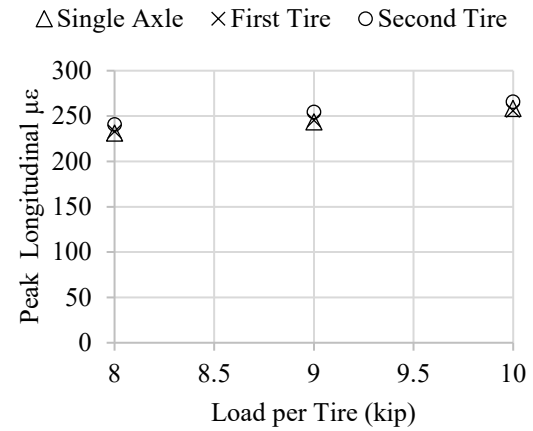
△Single Axle ×First Tire ○Second Tire
Peak Longitudinal με
300
250
200
150
100
50
0
8
8.5
9
9.5
10
Load per Tire (kip)

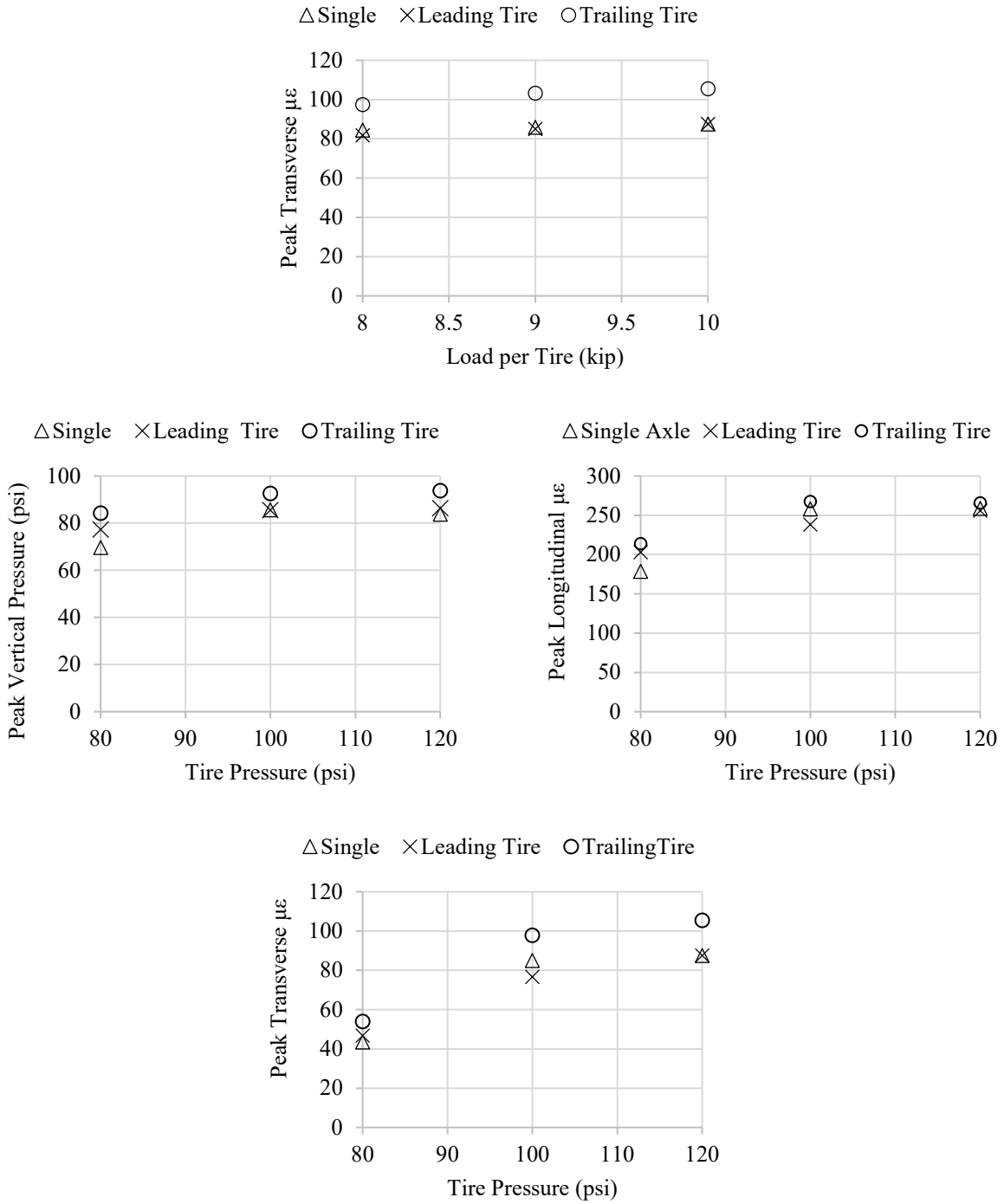

Figure 89. Graph. Effect of speed, load magnitude, and tire inflation pressure on pavement responses in D4-50-12.5-0.

For sections with imported aggregates, additional scenarios were applied to measure responses at different temperatures and axle spacings. The results are presented in Figure 90 and Figure 91 and demonstrate the significance of pavement temperature impact on the responses, which may be greater than other parameters explored in this study.

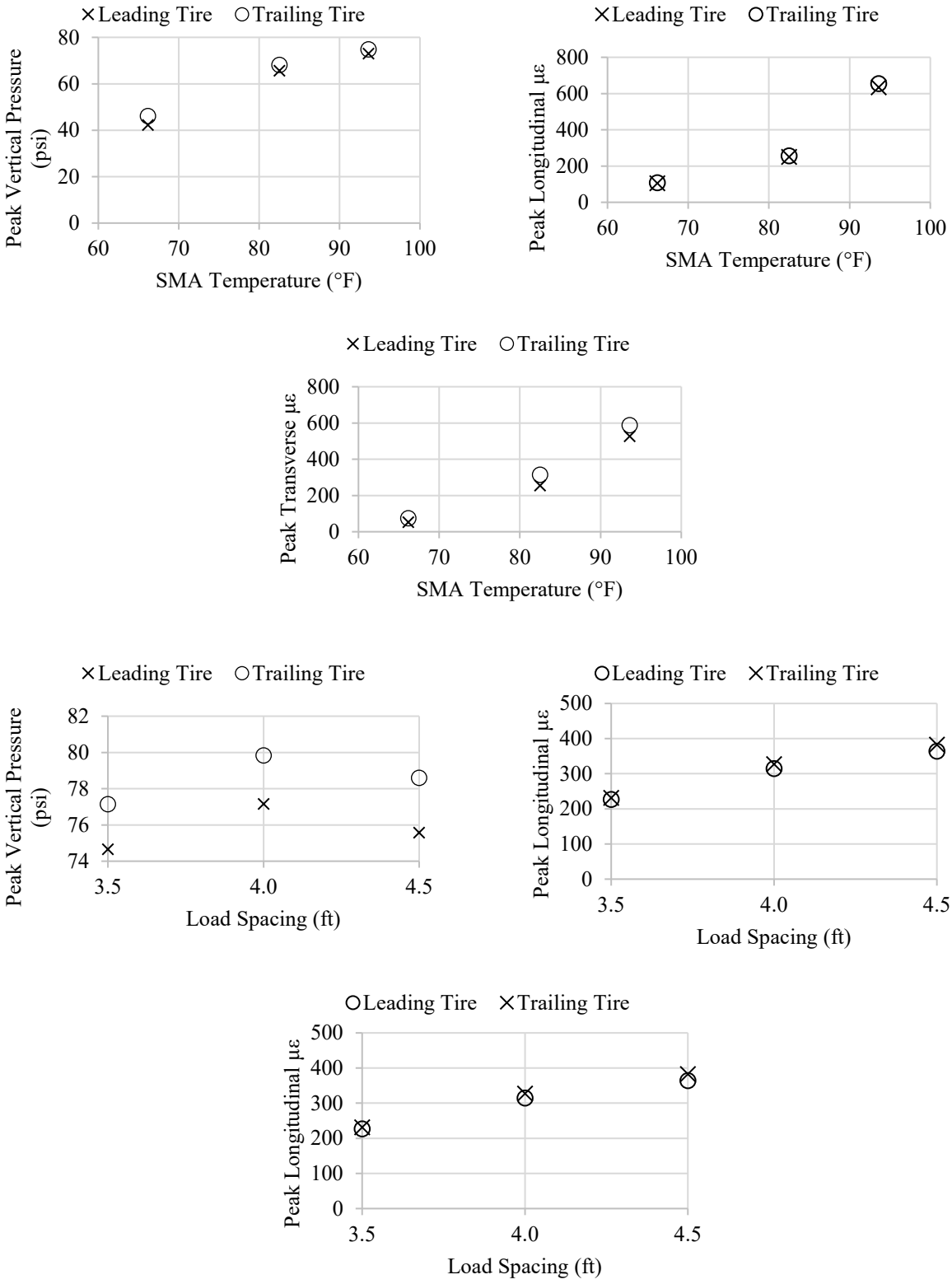

Figure 90. Graph. Effect of temperature and axle spacing on pavement responses in T1-80-12.5-0.

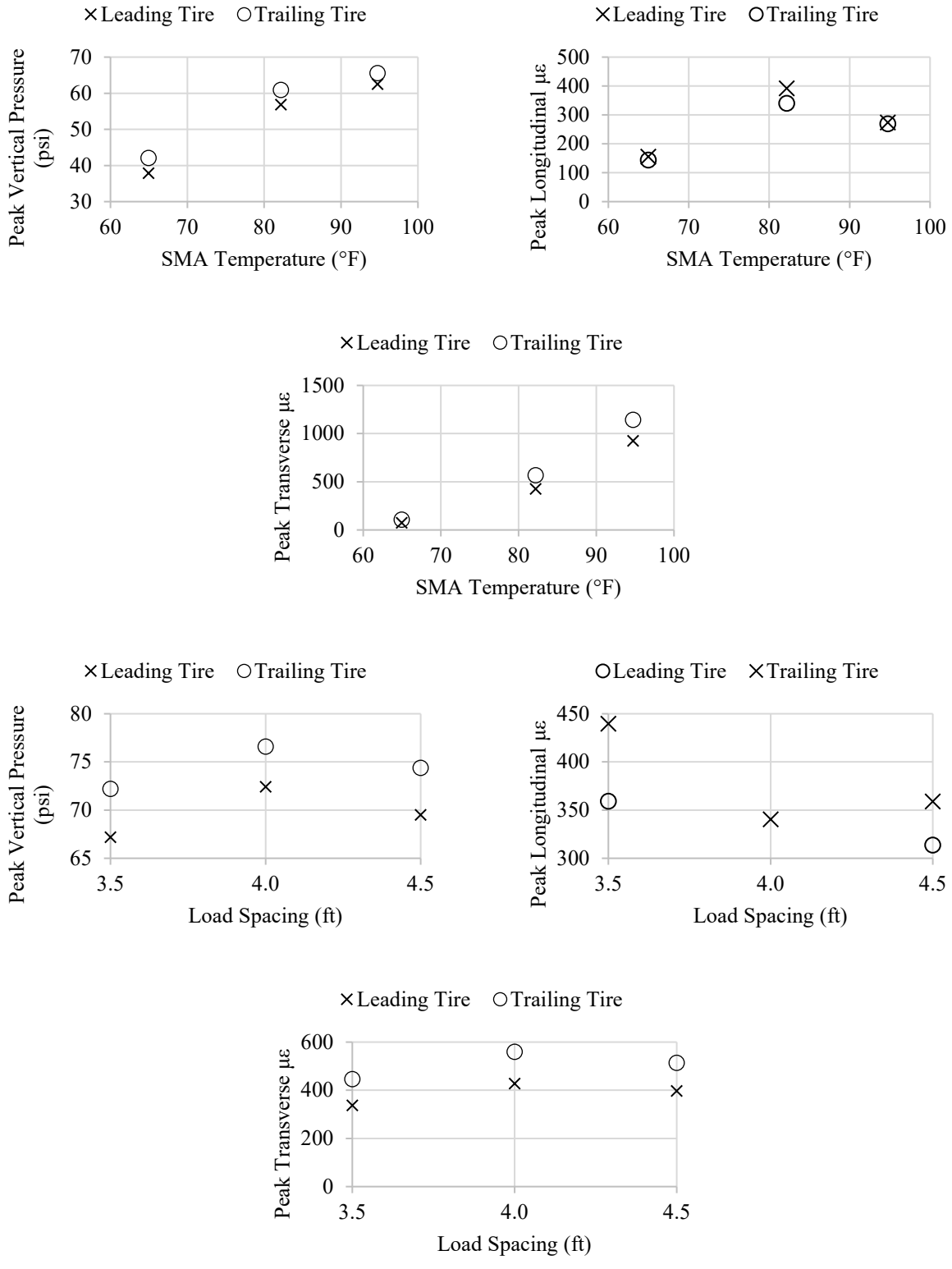

Figure 91. Graph. Effect of temperature and axle spacing on pavement responses in T1-50-12.5-0.

Differences in strain magnitudes across the pavement sections may be attributed to variations in material, lift thickness, and construction. To emphasize the directional dependency of the mechanical behavior and the differing sensitivity to loading, Table 34 presents a subset of measured responses in three sections. While the vertical stresses were consistent, longitudinal and transverse strain magnitudes were not proportional across the pavement sections, nor were their responses to speed change. This suggests that while pressure distribution into the pavement structure is governed by mainly load (and tire inflation pressure, not displayed in the table), strain responses are influenced by other properties specific to SMA characteristics.

Table 34. Pavement Responses to Trailing Axle with 10 kip and 120 psi Tire Pressure for Two Speeds at 80°F

SMA Section	Speed = 5 mph			Speed = 3 mph		
	Peak Vertical Stress (psi)	Longitudinal Strain Amplitude (με)	Peak Transverse Strain (με)	Peak Vertical Stress (psi)	Longitudinal Strain Amplitude (με)	Peak Transverse Strain (με)
L2-50-12.5-0	100	85	213	103	100	288
D3-50-9.5-0	104	310	263	107	424	342
D4-50-12.5-0	94	256	105	98	366	140

Effect of a Tandem Axle on Pavement Responses

Two selected scenarios were studied to understand the effect of tandem-axle loading with respect to single-axle loading. Responses from pass 58 were used to illustrate pavement behavior across all six SMA sections. The selected single-axle loading consisted of a 120 psi tire inflation pressure, a 10 kip axle load, and a vehicle speed of 5 mph (scenario B). The respective tandem-axle loading used 120 psi–120 psi tire inflation pressures, 10 kip–10 kip axle loads, 5 mph speed, and 3.5 ft axle spacing (baseline loading scenario in Table 24). Figure 92 and Figure 93 present longitudinal strain, transverse strain, and vertical stress for all sections. Each waveform represents approximately 3 sec (~3,000 samples) of the most active response window.

In Figure 92, waveform shapes remain consistent across sections, while magnitudes differ due to variations in layer characteristics (thickness and density) and SMA properties detailed in Chapter 3. For longitudinal strain, the thinner lifts (T1-80-12.5-0 and T1-50-12.5-0) demonstrated greater tensile peaks, while the thickest section (D2-50-12.5-0, 2.4 in) exhibited smaller amplitudes. Transverse strain demonstrated greater variation across sections: D3-50-9.5-0 resulted in the highest lateral strain (~275 με), while D4-50-12.5-0 exhibited the lowest (~90 με). Vertical stress peaks ranged from ~72 psi to 102 psi; D3-50-9.5-0 had the highest, while T1 sections had the lowest.

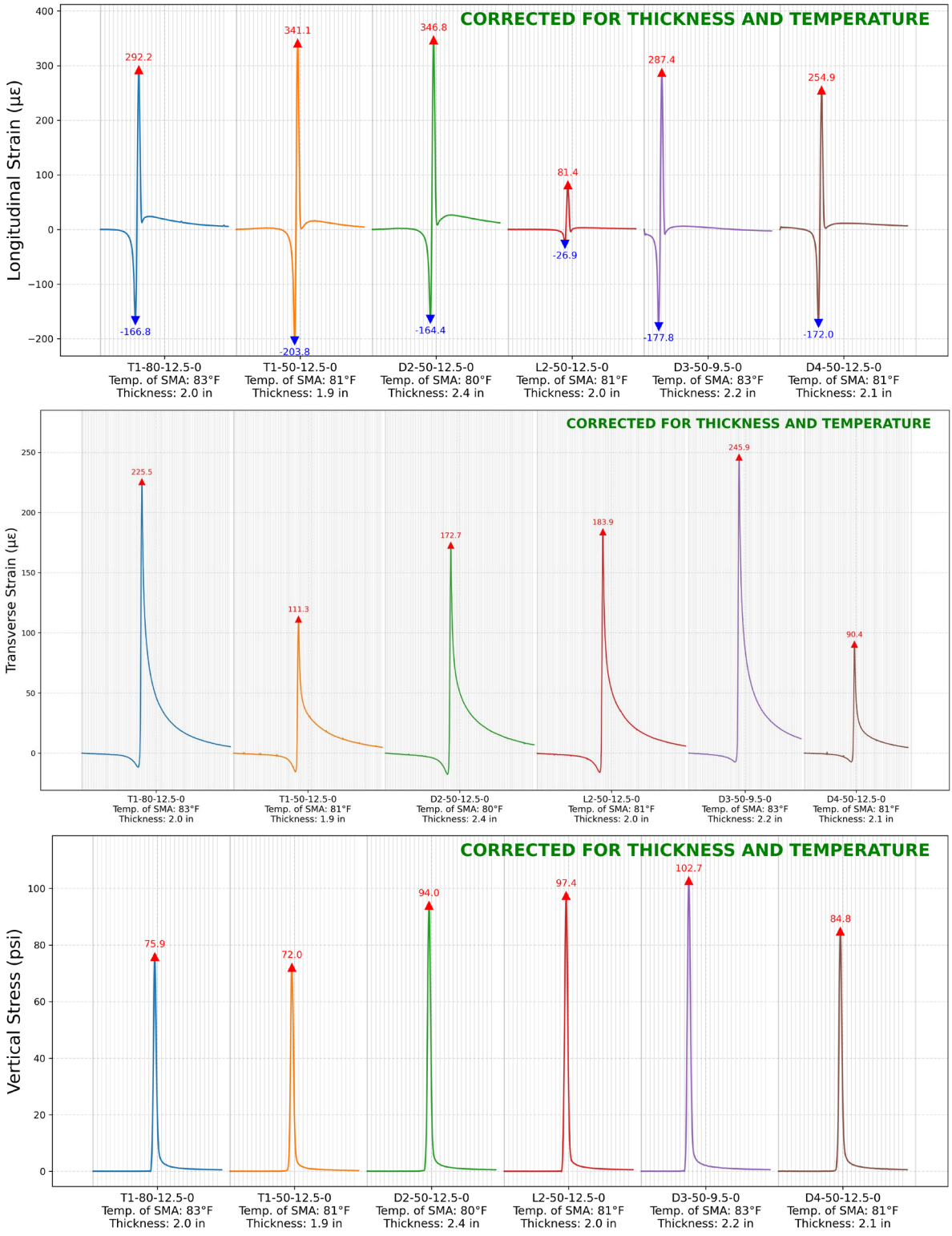

Note: Examination of all L2-50-12.5-0 longitudinal strain data indicated consistently low readings.

Figure 92. Graph. Comparison of pavement responses across sections under single-axle loading (120 psi tire inflation pressure, 10 kip axle load, and 5 mph).

Under tandem-axle loading (Figure 93), two closely spaced pulses were observed, demonstrating consistent waveform patterns across sections. For longitudinal strain, T1-50-12.5-0 exhibited the highest tensile peaks under tandem-axle loading, with first-axle peaks on the order of 440 με. The remaining sections, including T1-80-12.5-0, D2-50-12.5-0, and D4-50-12.5-0, demonstrated lower tensile amplitudes that generally fell within a narrower range of approximately 260–300 με. Transverse strain exhibited clear dual-peak behavior under tandem loading. The highest transverse strain was observed in T1-80-12.5-0 and D3-50-9.5-0, with peak values on the order of 300 με. The lowest transverse strain was noted in D4-50-12.5-0, with peak values near 110 με. The remaining sections fell between the two ranges. Vertical stress peaks across all sections ranged from approximately 67 psi to 104 psi, with the highest values observed in D3-50-9.5-0.

Both T1 sections exhibited the lowest vertical stress levels; however, their strain responses differed. T1-50-12.5-0 demonstrated the lowest vertical stress (approximately 67–73 psi) along with the highest longitudinal tensile strain (on the order of 440–450 με), whereas T1-80-12.5-0 also exhibited low vertical stress (approximately 75–77 psi) but much higher transverse strain (approximately 310–370 με). These different stress–strain responses are consistent with differences in SMA design and mixture volumetrics (e.g., design gyration level). While the aggregate packing is stable, T1 has greater binder content than the target, likely resulting in relatively higher strain. The other sections exhibited intermediate stress magnitudes within this range. Overall, the relative differences among sections observed under single-axle loading may also be observed under tandem-axle loading, with trailing axle response always greater than the leading axle.

Overall, loading results demonstrated that variations in SMA temperature, SMA properties, and layer properties could result in measurable differences in instantaneous pavement response under identical loading conditions, though they do not significantly alter the shape of the waveforms.

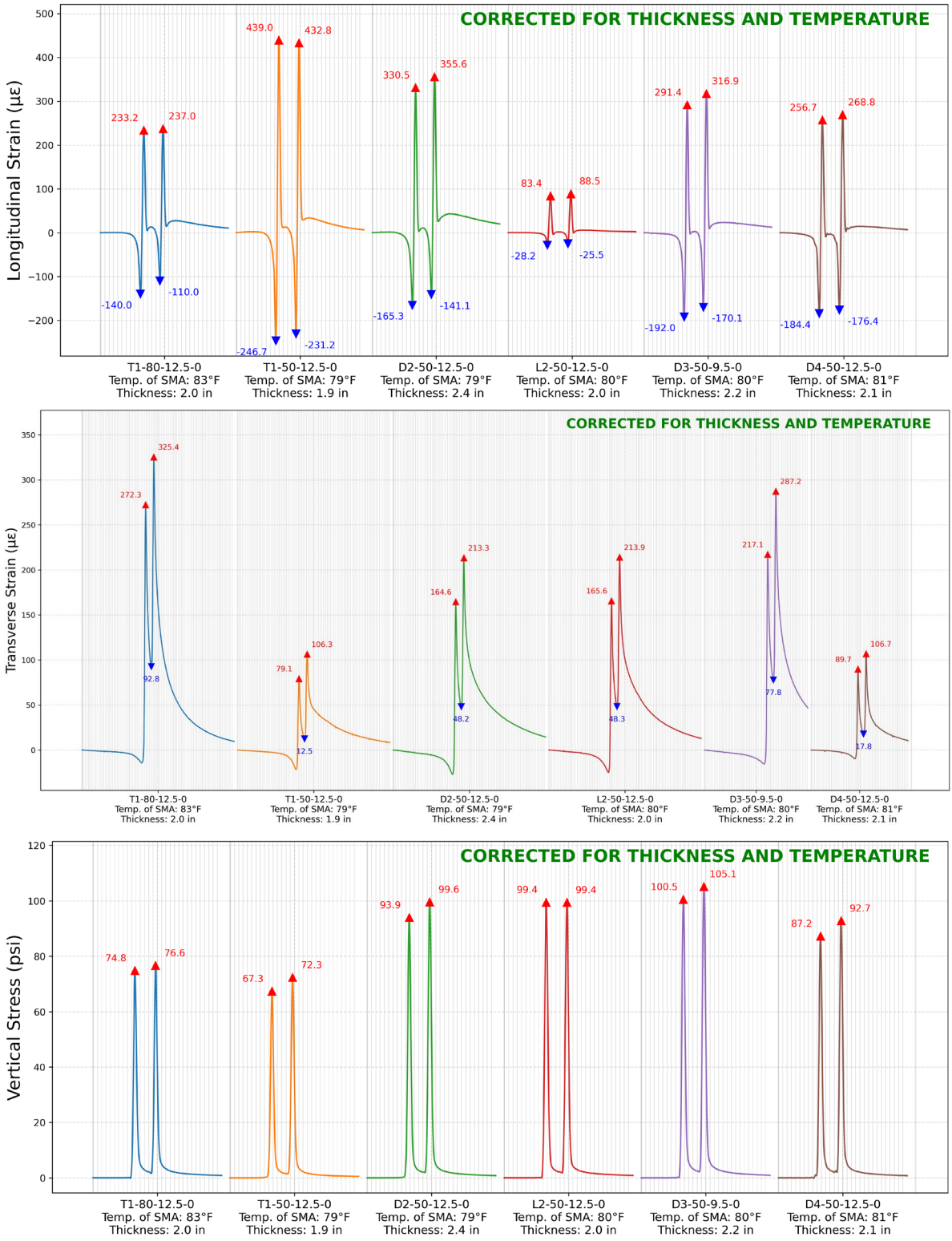

Note: Examination of all L2-50-12.5-0 longitudinal strain data indicate consistently low readings, likely due to gauge misalignment.

Figure 93. Graph. Comparison of pavement responses across sections under tandem-axle loading (120 psi–120 psi tire inflation pressure, 10 kip–10 kip axle loads, 5 mph, and 3.5 ft axle spacing).

Relative Comparison of Peaks across Tandem-Axle Loading Conditions

To compare pavement behavior across sections, the difference between the leading- and trailing-tire peak strain responses was analyzed as a measure of pavement recovery. The larger peak difference suggests the pavement recovered less (or more delayed) from the load applied by the leading tire before the trailing tire passed, indicating reduced recovery rate and/or capacity.

The peak differences (%) of vertical stress, longitudinal strain, and transverse strain were compared. Each peak difference was calculated as follows in Figure 94:

$$Peak\ Difference\ (\%) = \frac{Peak_{trailing} - Peak_{leading}}{Peak_{leading}} \times 100\%$$

Figure 94. Equation. Pavement response peak difference calculation.

A positive value indicates a larger response under the trailing tire; a negative value indicates a larger response under the leading tire.

Effect of Temperature on Pavement Recovery

Across the temperature-controlled tests, longitudinal strain peak differences remained small, ranging from approximately 2.3% to 5.2%. Values were lowest near 80°F, where both sections demonstrated nearly identical responses (2.3%–2.5%). Slightly larger peak differences were observed at the lower (65–67°F) and higher (95–96°F) temperature conditions (Figure 95). This is expected, as longitudinal strain recovery is usually complete and rapid because it is the direction of the traffic. However, the transverse strain is expected to be different.

Transverse strain peak differences were greater than those of the longitudinal strain peak differences and consistently decreased with increased temperature, from 42%–43% at 65°F to 12% at 95°F, especially in T1-80-12.5-0, implying binder becomes more dominant at warmer SMA temperature, resulting in reduced lateral strain contrast (Figure 96). In addition, SMA recovers more rapidly at higher temperatures, as asphalt binder is relatively softer, allowing faster stress relaxation which enables SMA to return toward its original condition between tire loads.

Vertical stress differences followed a similar temperature-driven reduction, indicating improved load dissipation and faster stress relaxation in warmer material. The differences were slightly greater in the thinner T1-50-12.5-0 because of its increased sensitivity to surface-level stress gradients, tire contact stresses, and/or reduced layer stiffness (Figure 97). On the other hand, the SMA sections behaved similarly at approximately 65°F–67°F, suggesting SMA responded comparably and the effect of the coarse aggregate's lithological characteristics were not manifested.

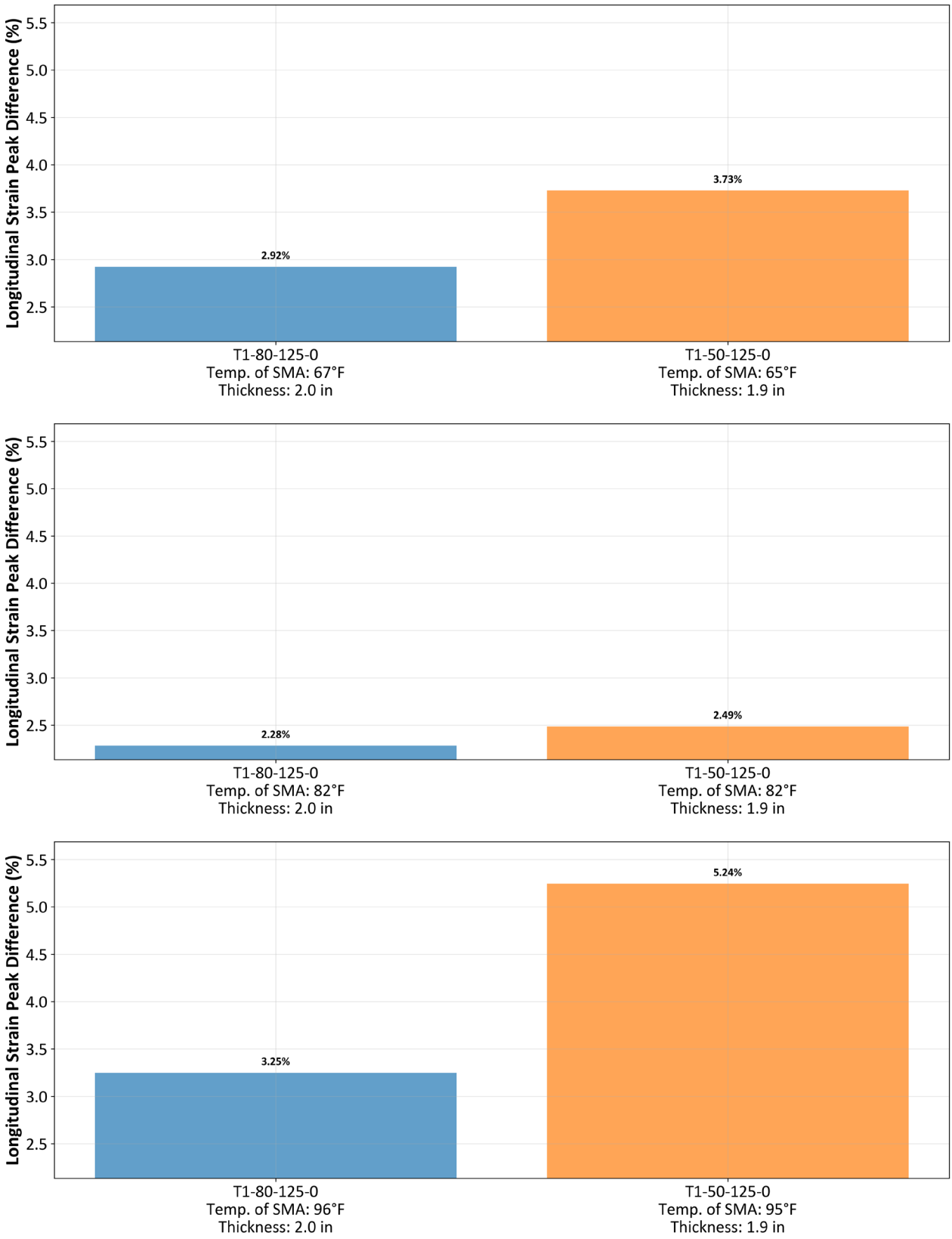

Figure 95. Graph. Longitudinal strain peak variations at different temperatures.

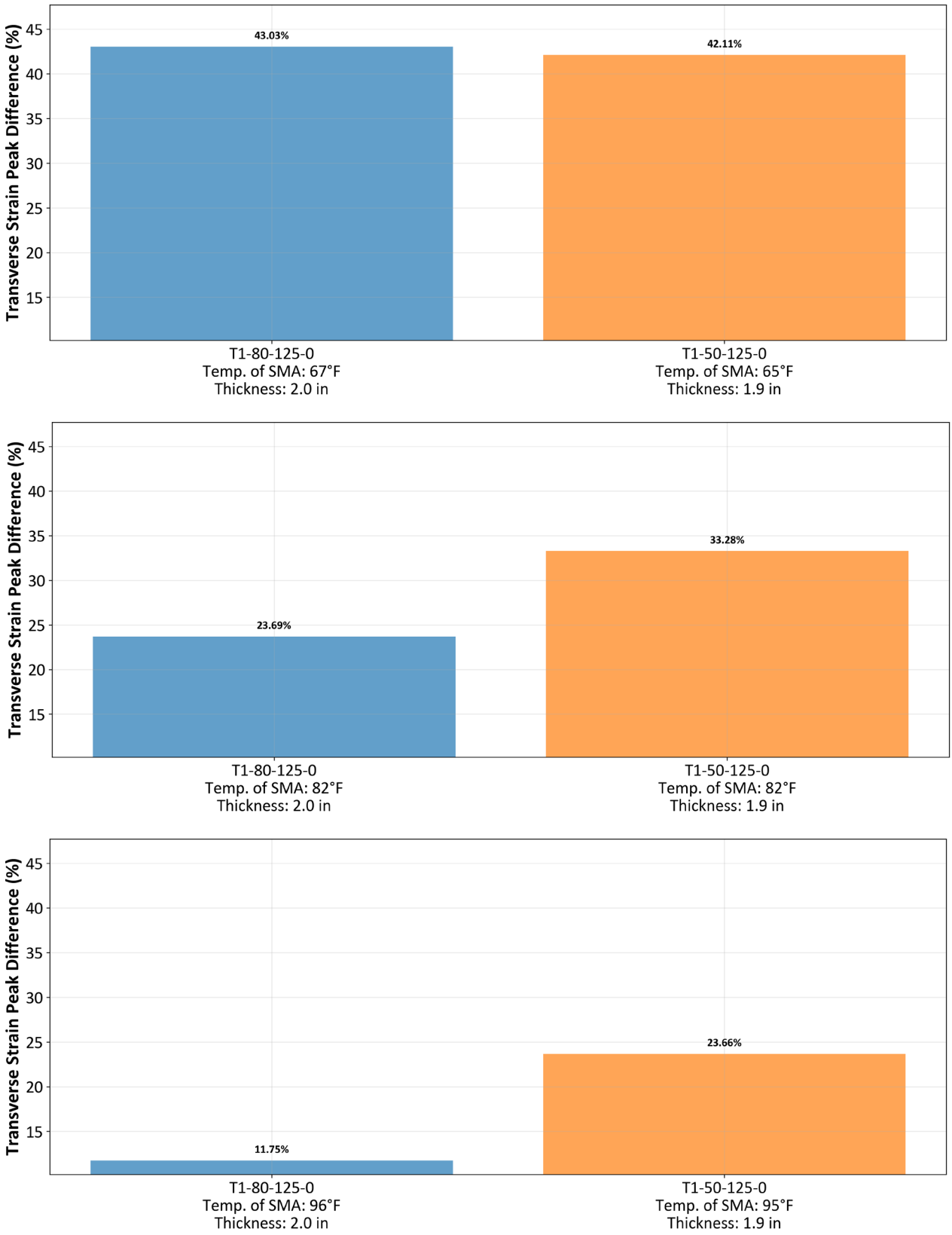

Figure 96. Graph. Transverse strain peak difference at various temperatures.

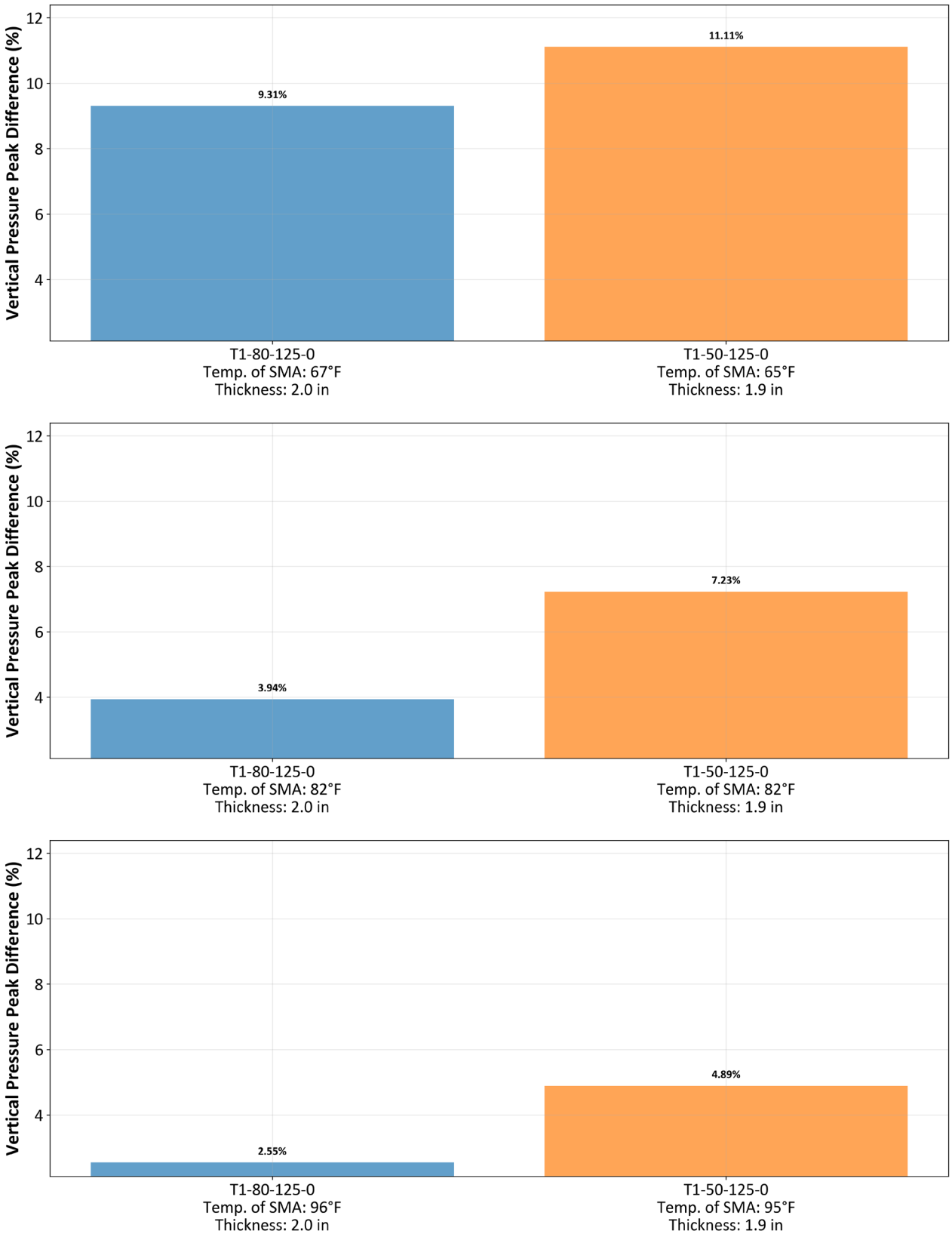

Figure 97. Graph. Vertical stress peak difference at various temperatures.

Effect of Axle Spacing on Pavement Recovery

As axle spacing varied from 3.5 ft to 4.5 ft, longitudinal strain peak differences rose from about 2% to 5% in T1-80, while they remained near 2% in T1-50 (Figure 98). Transverse strain peak differences remained within a moderate range (approximately 21%–33%) across spacing conditions (Figure 99). The thinner T1-50 layer exhibited greater case-to-case variation than T1-80, implying stronger shear sensitivity when axles were closely spaced. Overall, axle spacing had a more pronounced effect on longitudinal strains than on transverse strains.

Vertical stress differences changed slightly with spacing, shifting from roughly 3.3%–7.5% at 3.5 ft to about 4.0%–7.1% at 4.5 ft (Figure 100). Thinner sections (T1-50) demonstrated larger variability in vertical stress, while thicker layers (T1-80) remained comparatively stable, reflecting better stress continuity and reduced interaction between axles. The larger axle spacing allowed more independent loading impact, whereas thinner sections are more surface-sensitive. When considering the effect of temperature, the influence of axle spacing on load peak differences was systematic and modest. In general, increased axle spacing allowed more time for partial strain relaxation between axles, particularly in relatively thicker SMA layers.

Pavement Recovery Across Sections

To characterize each SMA based on its ability to recover, relative comparisons of peak responses were analyzed under tandem-axle loading conditions across multiple loading scenarios. To assess SMA pavement sections' recovery, loading speeds were increased from 1 to 5 mph. For SMA with local aggregates, longitudinal strain peak differences became larger with reduced rest time (Figure 101). At 1 mph, variation was below 4%, while at 5 mph, stiffer sections (D2, D3) reached 7%–8% at faster tire passage.

Transverse strain peak differences also increased with speed, rising from approximately 10%–22% at 1 mph to 20%–35% at 5 mph (Figure 102). Thinner SMA layers (T1, T1-50) exhibited the highest variability, while thicker or stiffer sections (D2, D4) were relatively more stable and maintained comparatively lower contrast. Sections T1-80 and D4-50 demonstrated the lowest transverse strain peak differences at high speed, indicating faster lateral recovery and reduced strain accumulation in those mixtures. T1-80 asphalt content was slightly above target, while D4-50 was lower than the target.

Vertical stress differences increased from ~2%–3% at 1 mph to above 8% at 5 mph (Figure 103). Thinner or softer sections (T1-50, D4) demonstrated greater sensitivity to short contact duration, whereas stiffer or thicker layers (D2, L2) displayed lower variation. The greater speed, the stiffer the response and the variation, indicating better stress continuity under rapid loading conditions.

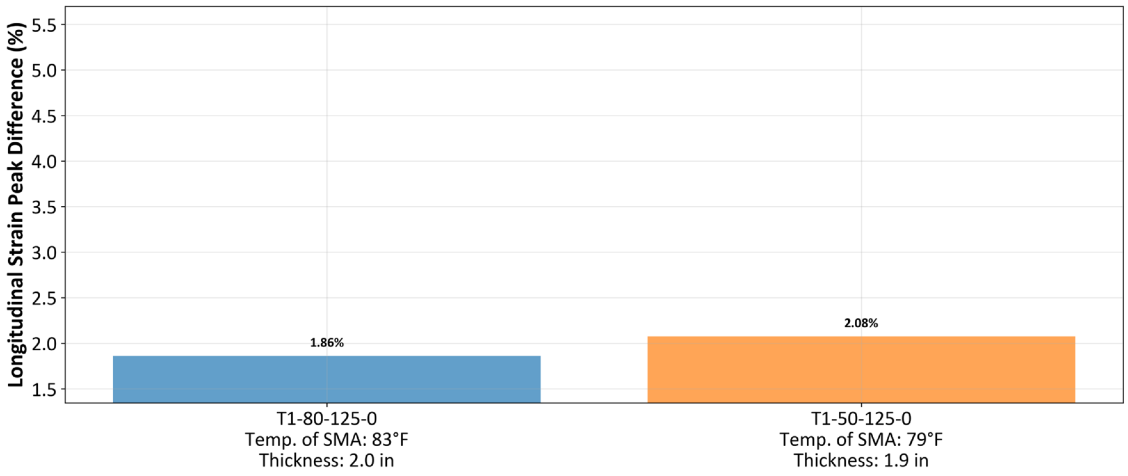

(a) 3.5 ft

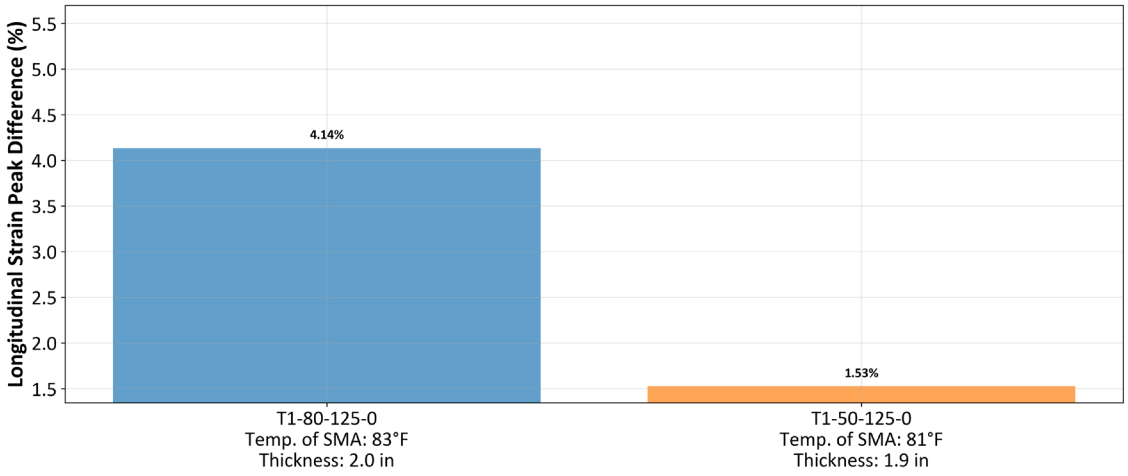

(b) 4.0 ft

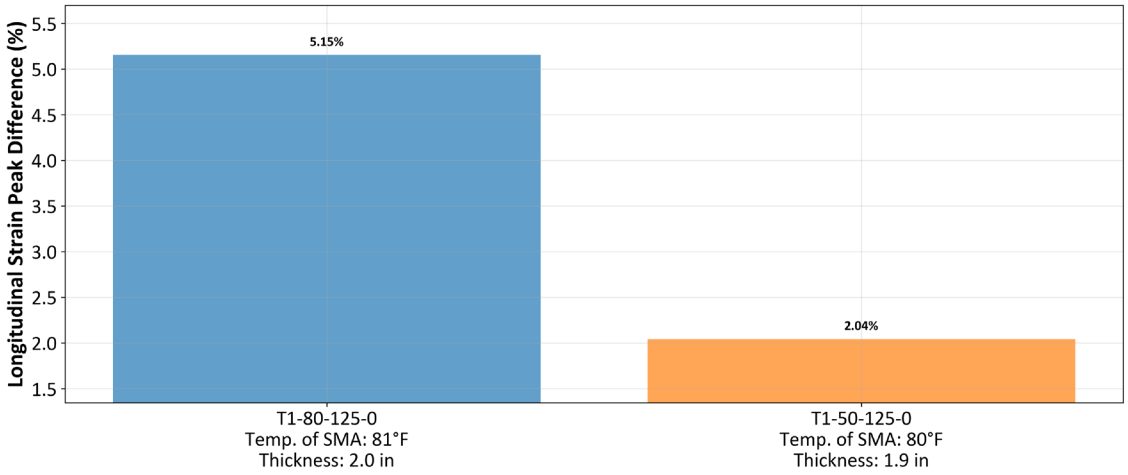

(c) 4.5 ft

Figure 98. Graph. Longitudinal strain peak difference at various axle-load spacings: (a) 3.5 ft, (b) 4.0 ft, and (c) 4.5 ft.

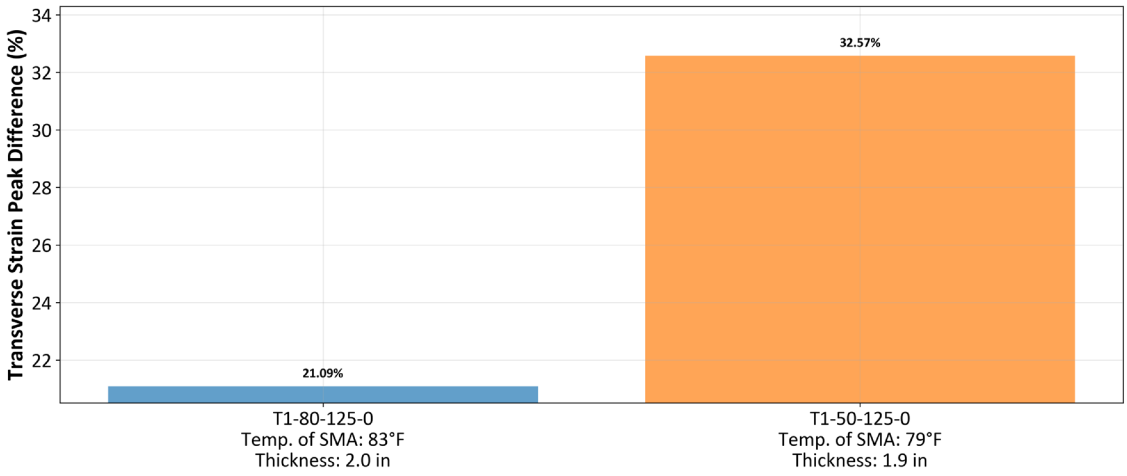

(a) 3.5 ft

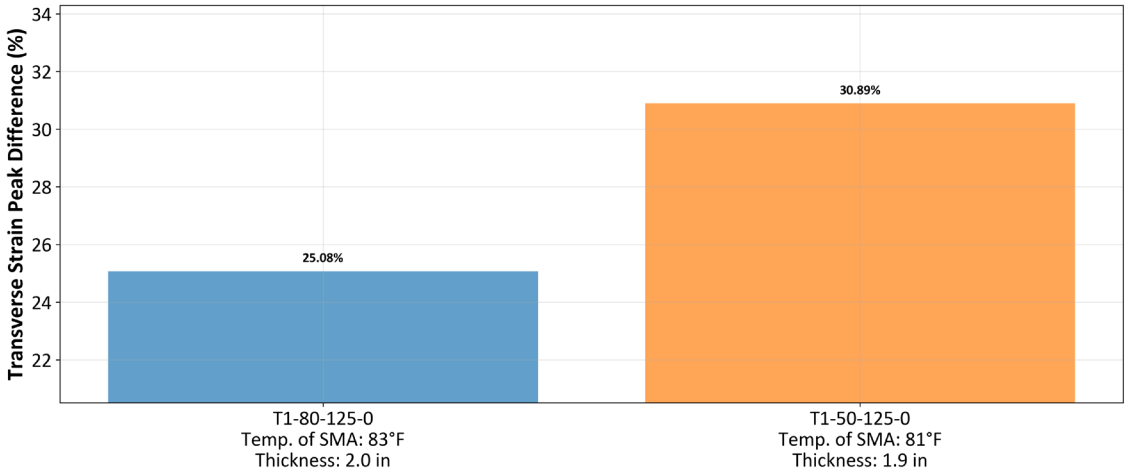

(b) 4.0 ft

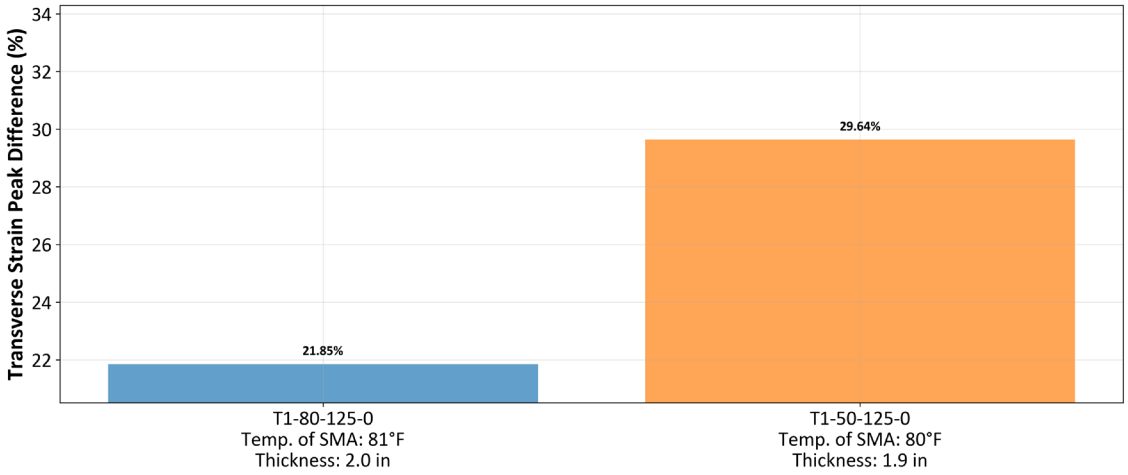

(c) 4.5 ft

Figure 99. Graph. Transverse strain peak difference at various axle-load spacings: (a) 3.5 ft, (b) 4.0 ft, and (c) 4.5 ft.

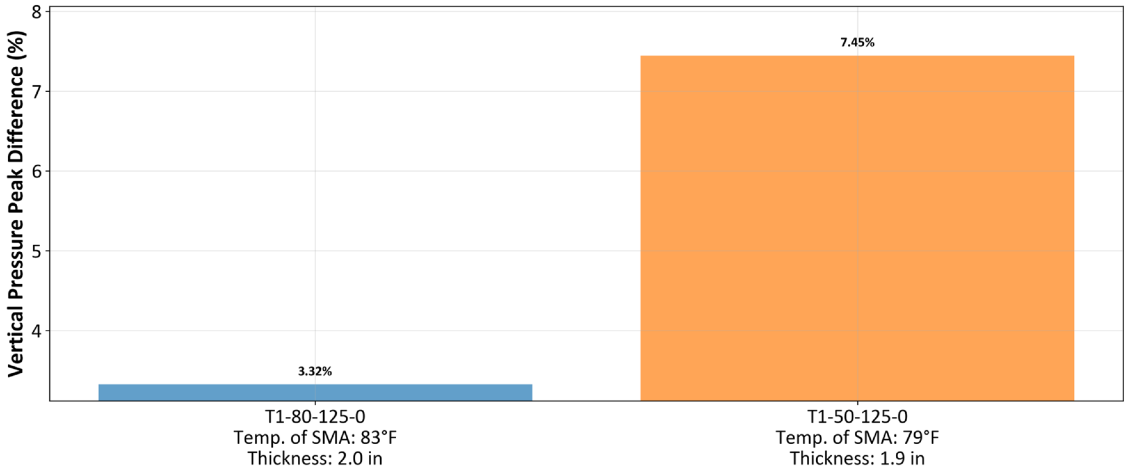

(a) 3.5 ft

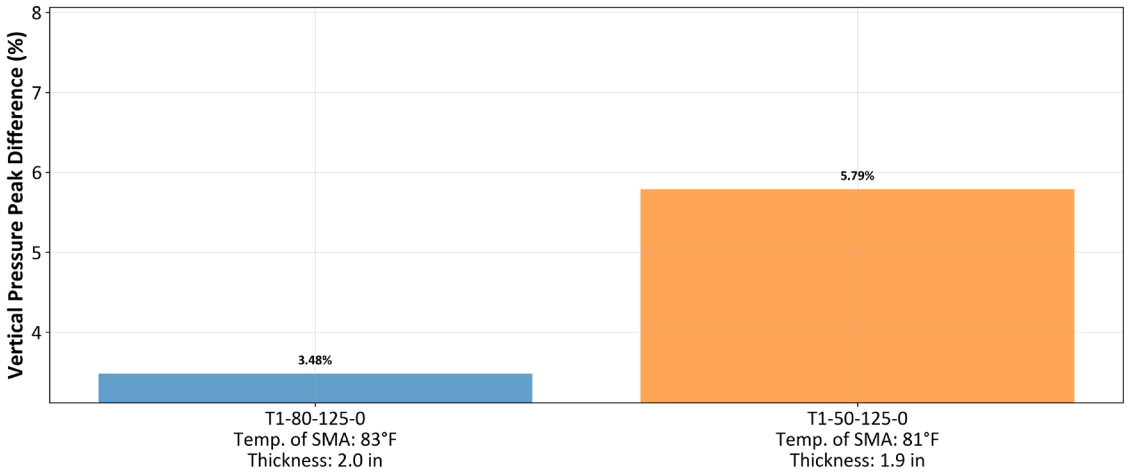

(b) 4.0 ft

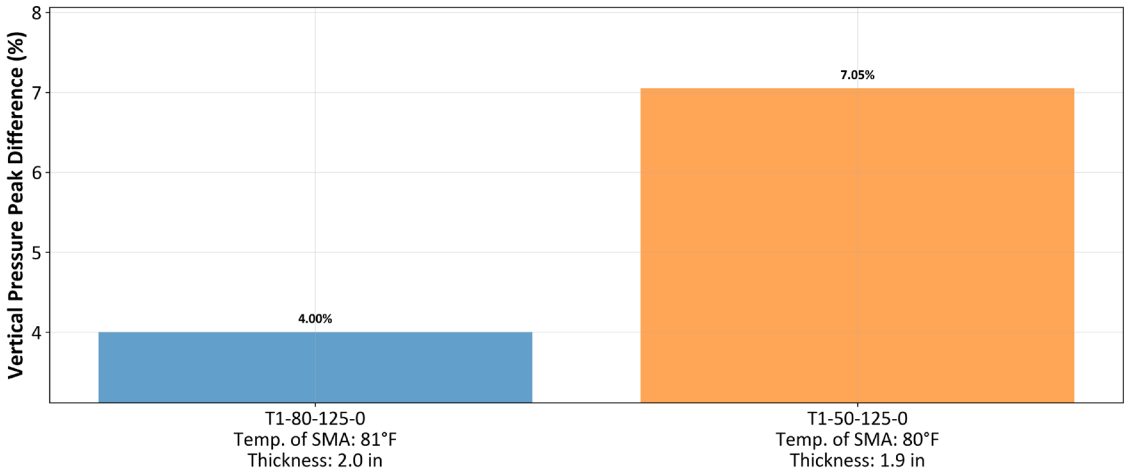

(c) 4.5 ft

Figure 100. Graph. Vertical stress peak difference at various axle-load spacings: (a) 3.5 ft, (b) 4.0 ft, and (c) 4.5 ft.

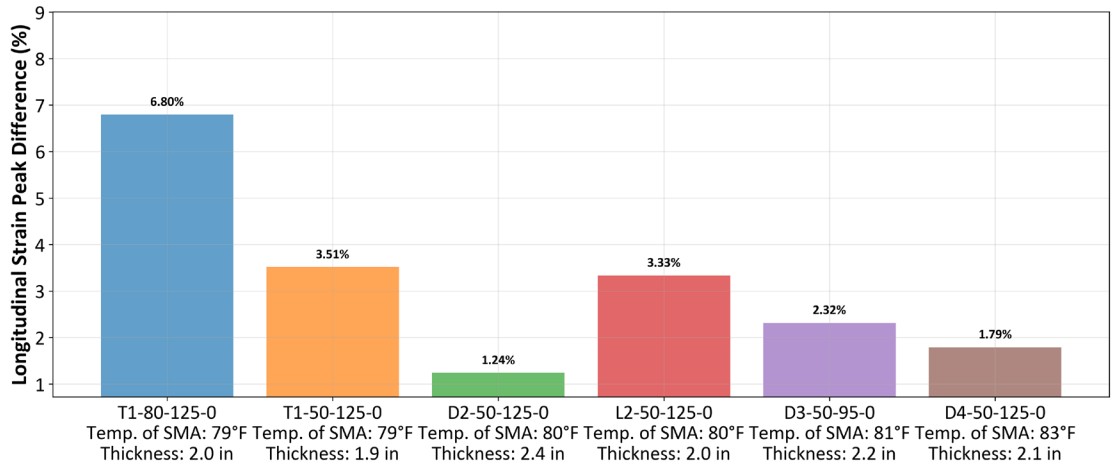

(a) 1 mph

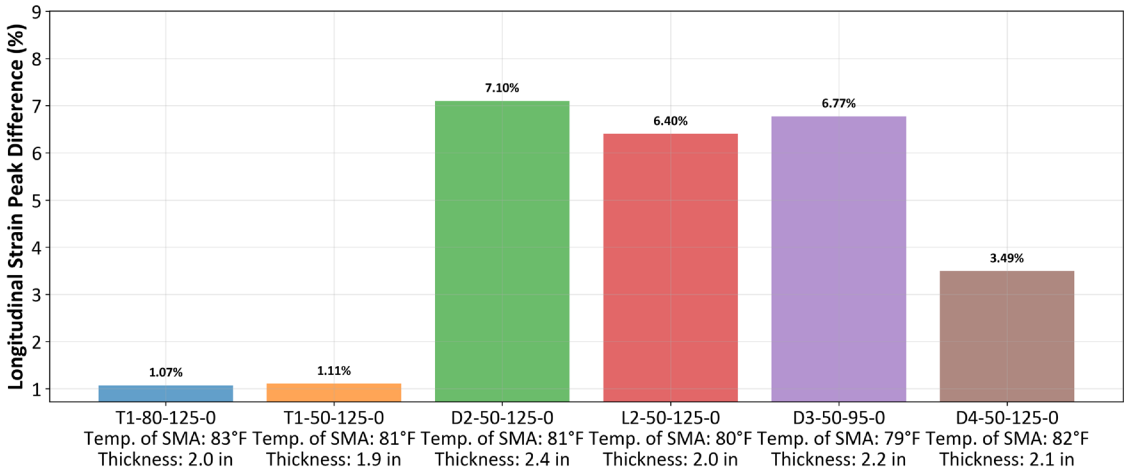

(b) 3 mph

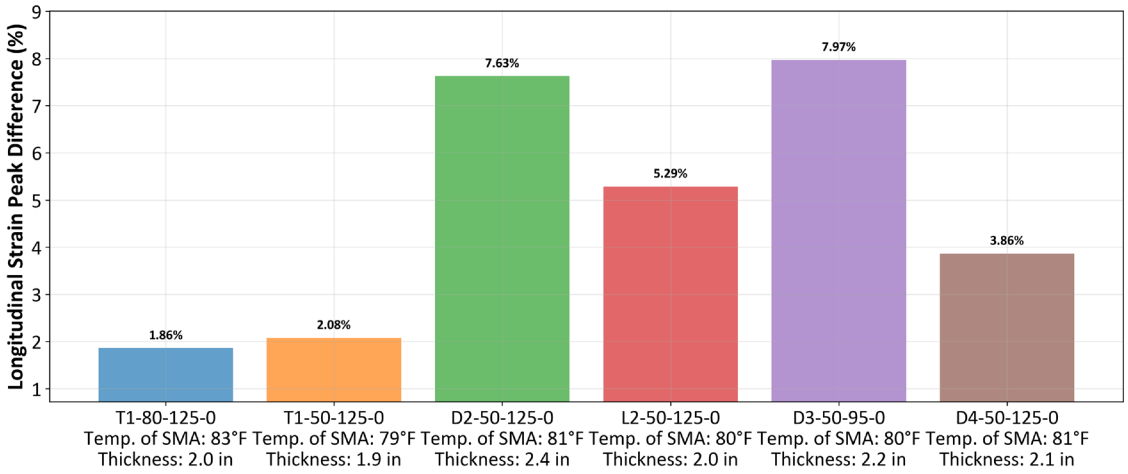

(d) 5 mph

Figure 101. Graph. Longitudinal strain peak difference at (a) 1 mph, (b) 3 mph, and (c) 5 mph.

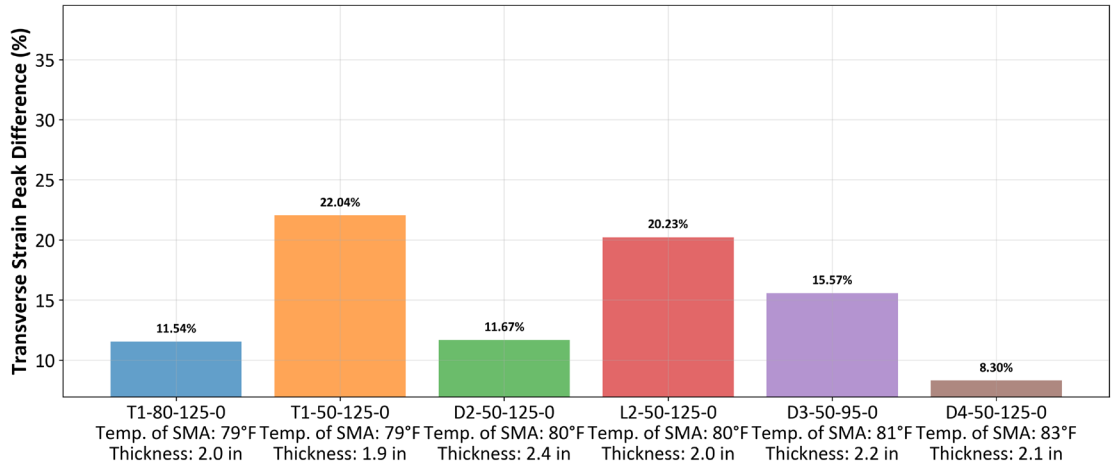

(a) 1 mph

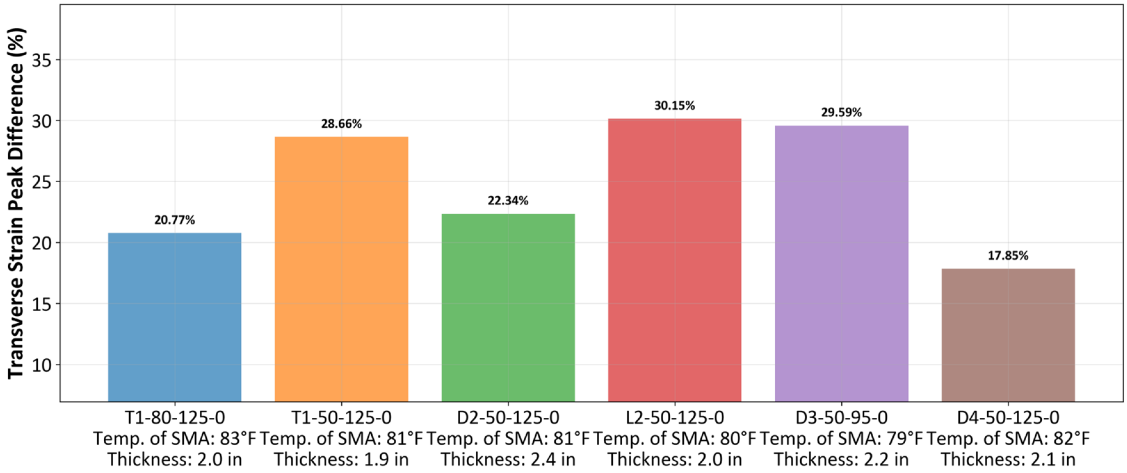

(b) 3 mph

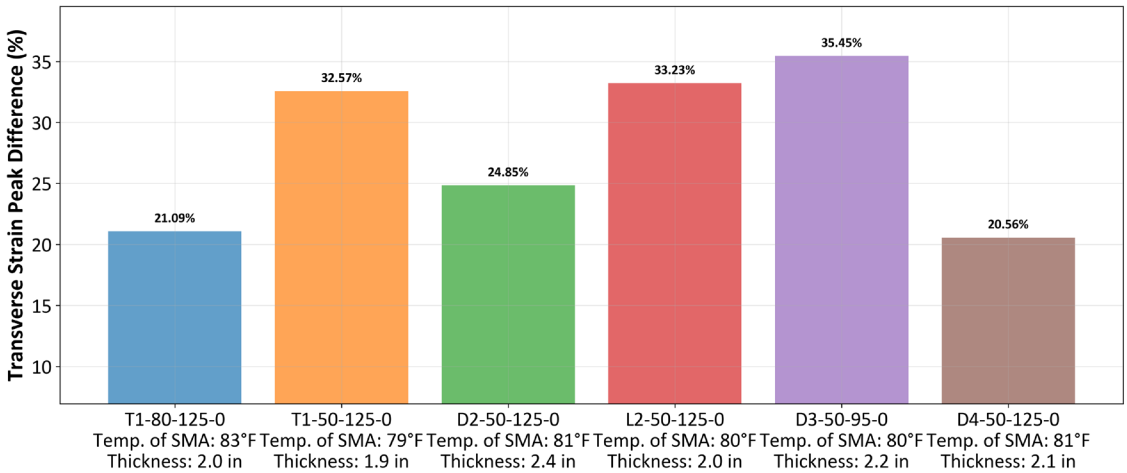

(c) 5 mph

Figure 102. Graph. Transverse strain peak difference at (a) 1 mph, (b) 3 mph, and (c) 5 mph.

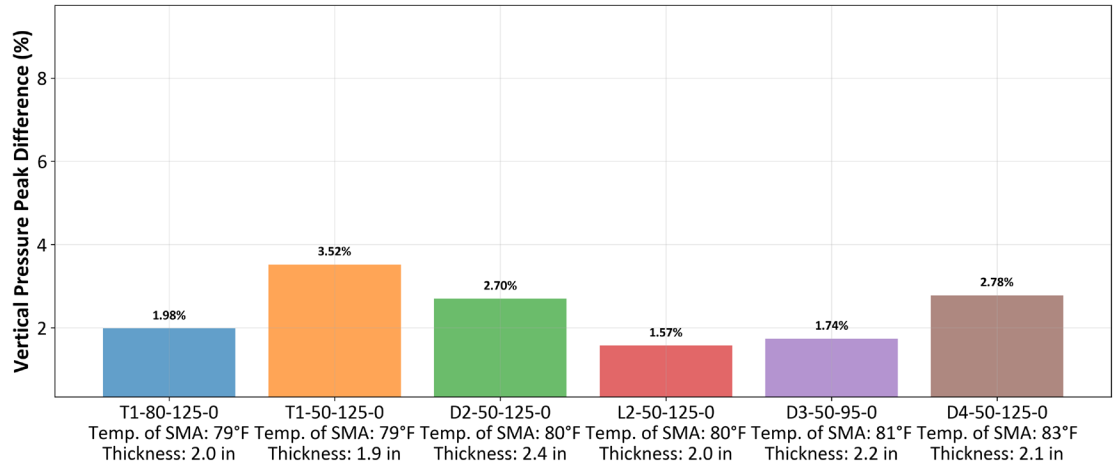

(a) 1 mph

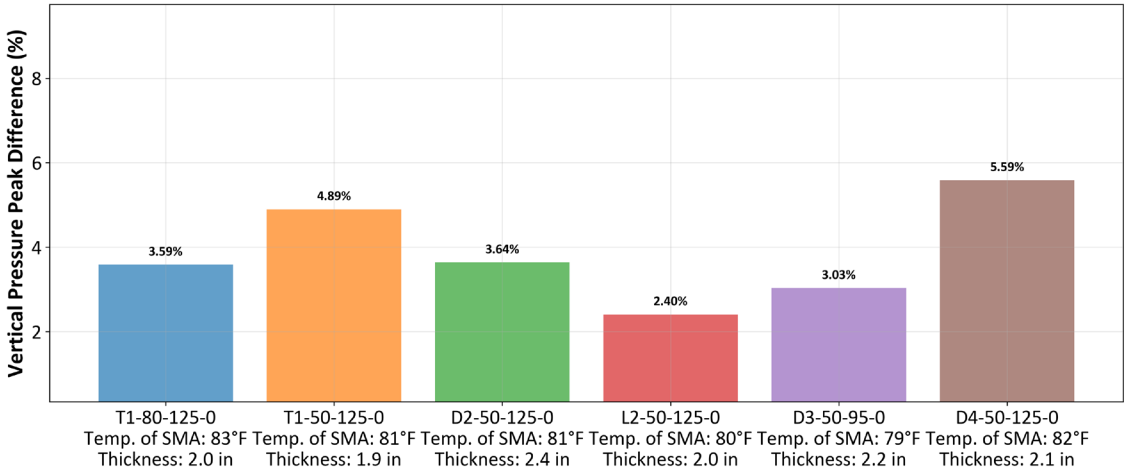

(b) 3 mph

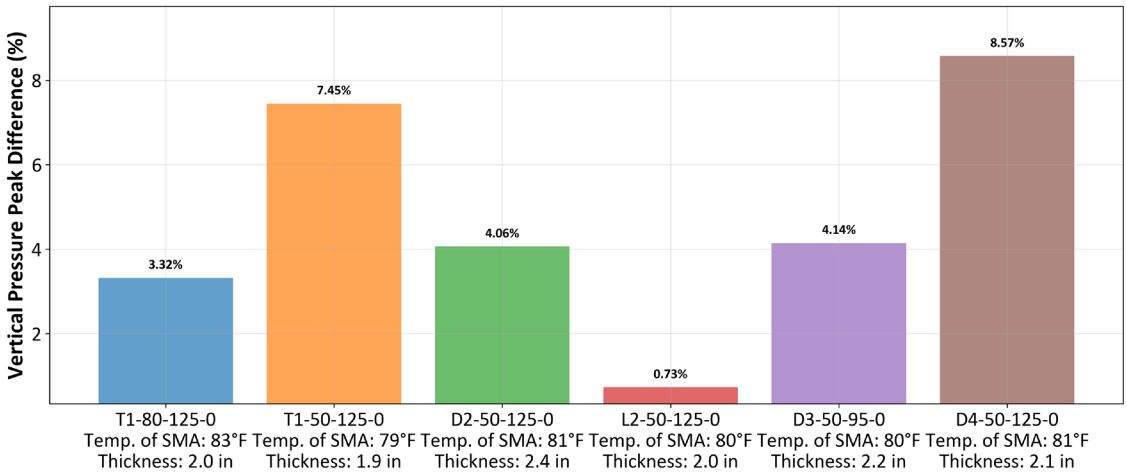

(c) 5 mph

Figure 103. Graph. Vertical stress peak difference at (a) 1 mph, (b) 3 mph, and (c) 5 mph.

Effect of Load on Pavement Recovery

As load increased from 8 to 14 kip, the longitudinal strain peak differences increased across most sections (Figure 104). However, thicker sections (D2, D3) demonstrated slightly higher variation (up to ~10%), while thinner sections (e.g., T1-50-12.5-0) remained near ~1%–3%. This confirms that load level only modestly amplifies longitudinal strain disparity. In contrast, transverse strain peak differences ranged from approximately 20%–35% across all sections (Figure 105). Thinner layers (e.g., T1-50-12.5-0) exhibited higher variability (up to ~33%), whereas thicker or stiffer mixes (D2, D4) maintained lower values (~25%–32%), indicating greater stability under higher loading conditions. Notably, T1-80 and D4-50 exhibited the lowest transverse strain differences, suggesting faster recovery in the lateral direction for those sections.

Vertical stress differences decreased slightly with increasing load (Figure 106). At low loads (8–9 kip), thinner layers (T1-50, D4) demonstrated higher variation (~9%–10%), while at 12–14 kip, all sections stabilized at ~3%–5%, reflecting more uniform vertical stress transfer between the leading and trailing tires. At heavier loads, effective tire-pavement contact length increased, expanding the overlap of influence zones and enhanced homogeneous stress distribution. Table 35 illustrates the increase in contact length with load.

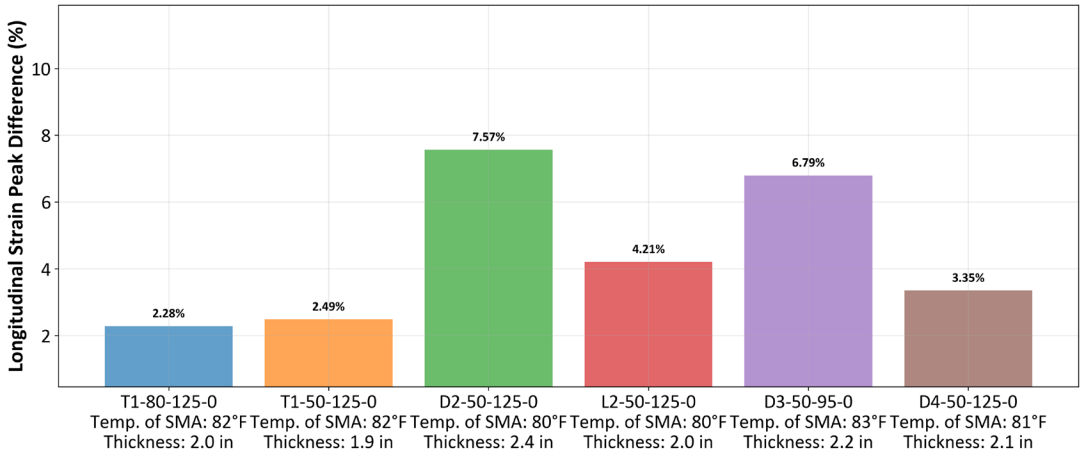

(a) 8 kip

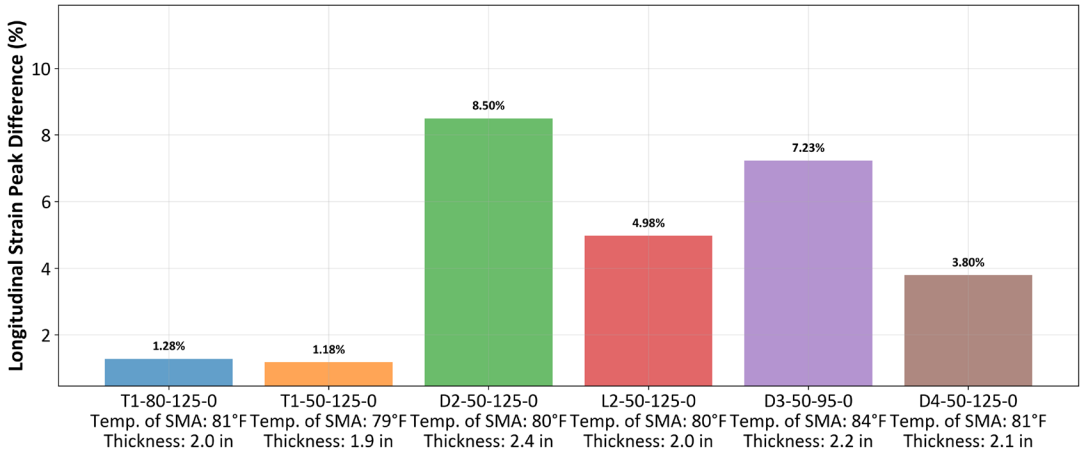

(b) 9 kip

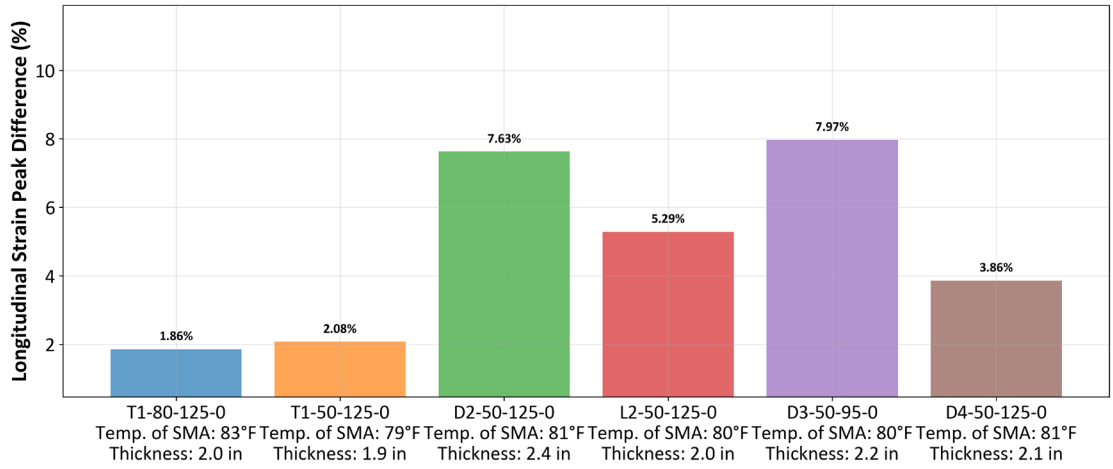

(c) 10 kip

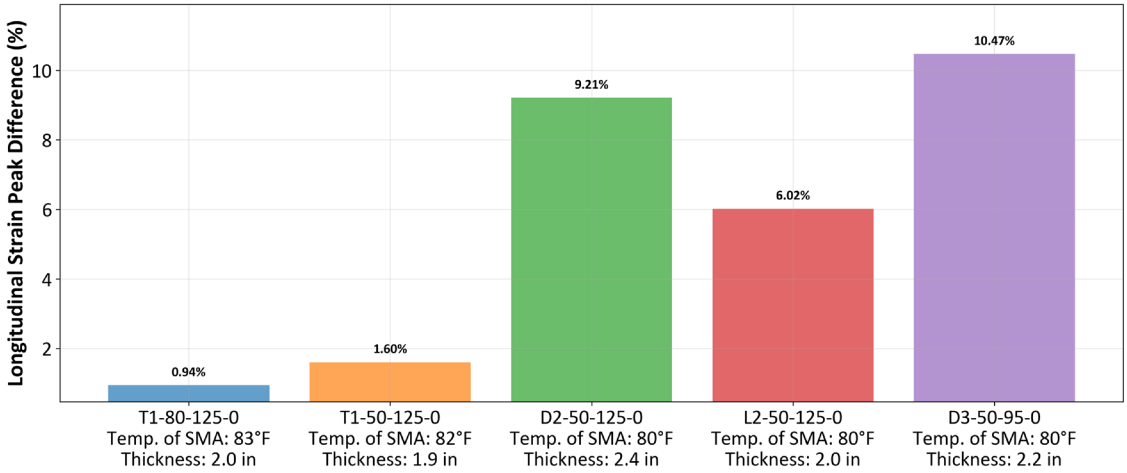

(d) 12 kip

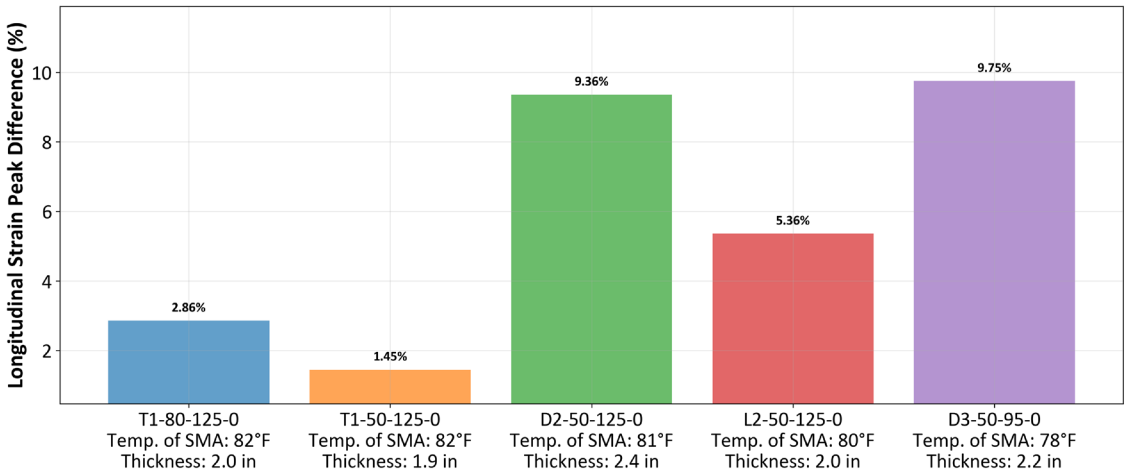

(e) 14 kip

Figure 104. Graph. Longitudinal strain peak difference for various loads: (a) 8 kip, (b) 9 kip, (c) 10 kip, (d) 12 kip, and (e) 14 kip.

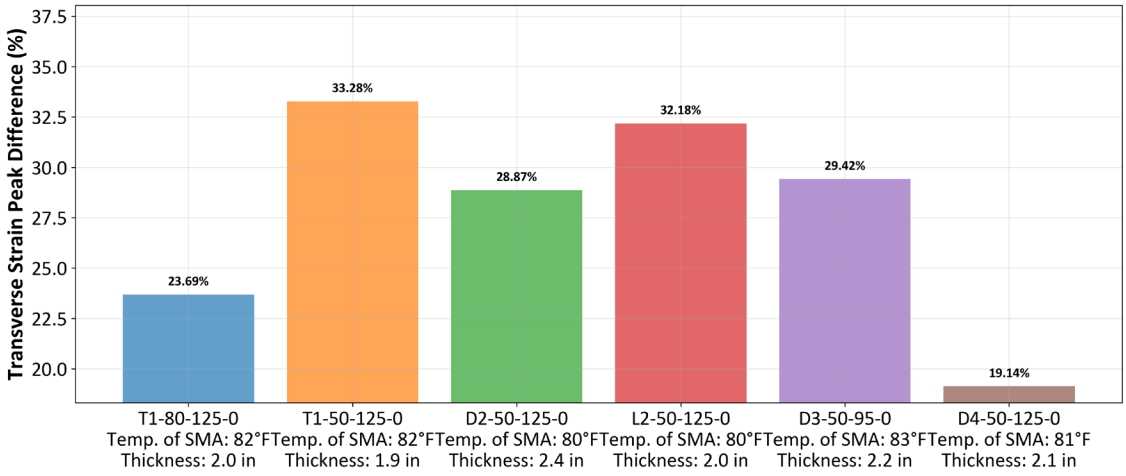

(a) 8 kip

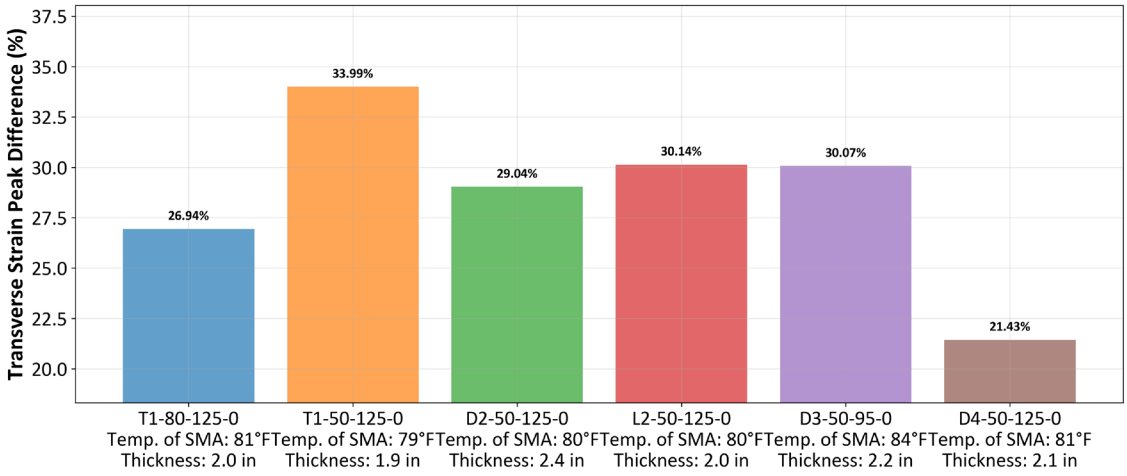

(b) 9 kip

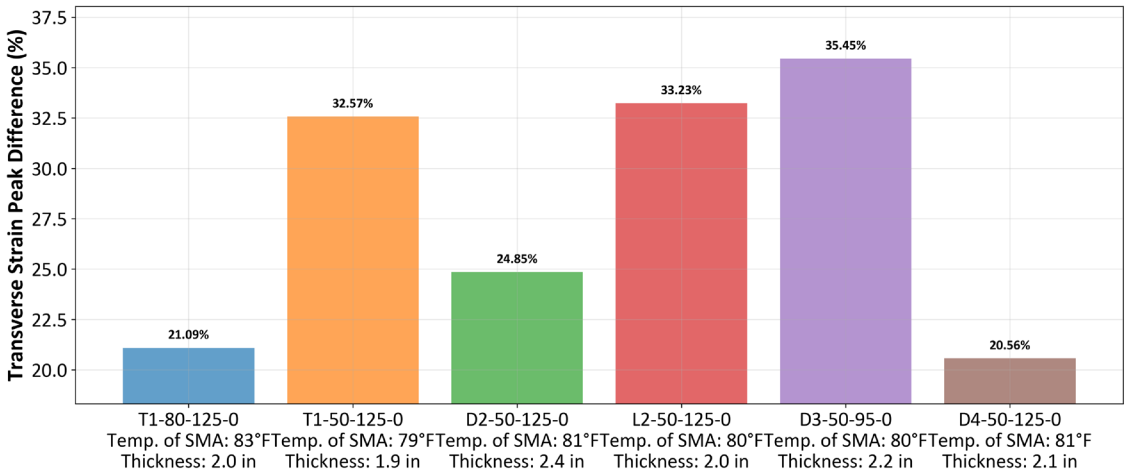

(c) 10 kip

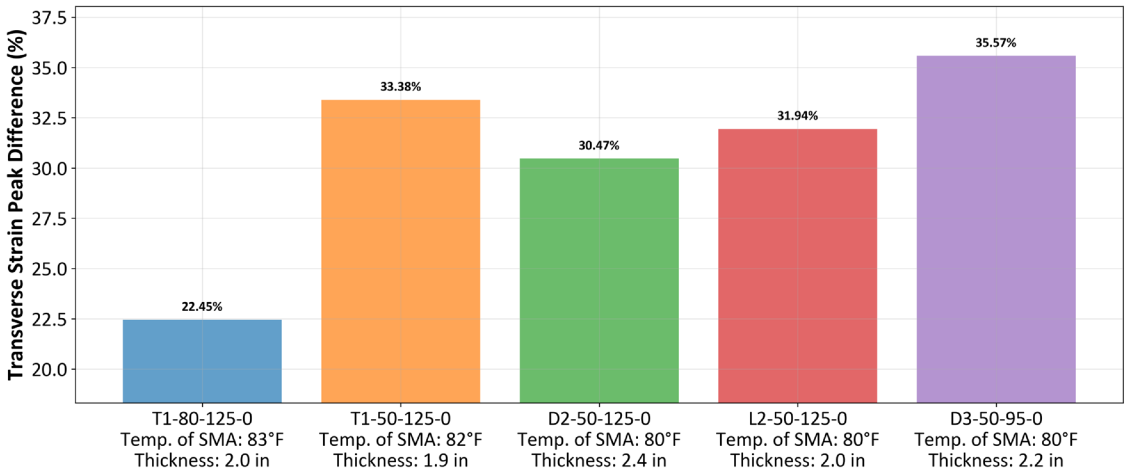

(d) 12 kip

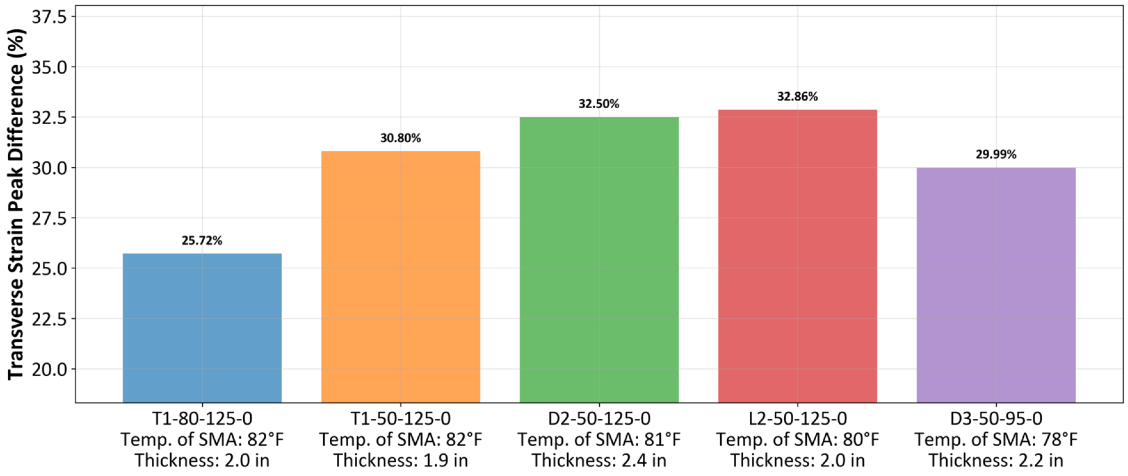

(e) 14 kip

Figure 105. Graph. Transverse strain peak difference for various loads: (a) 8 kip, (b) 9 kip, (c) 10 kip, (d) 12 kip, and (e) 14 kip.

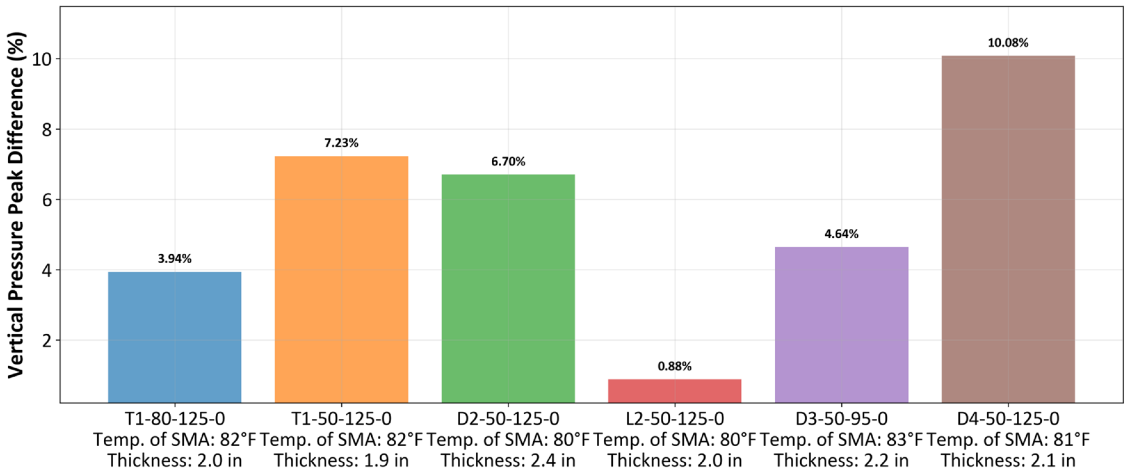

(a) 8 kip

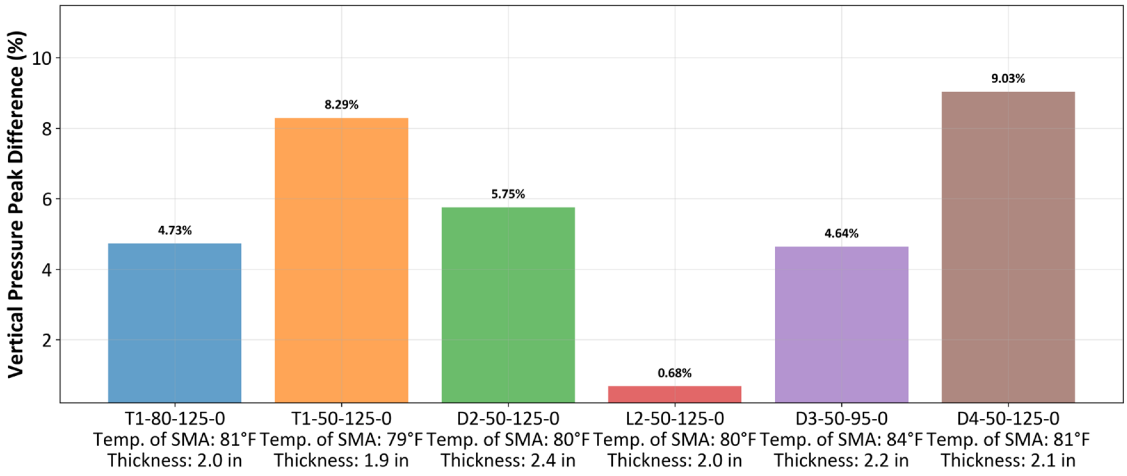

(b) 9 kip

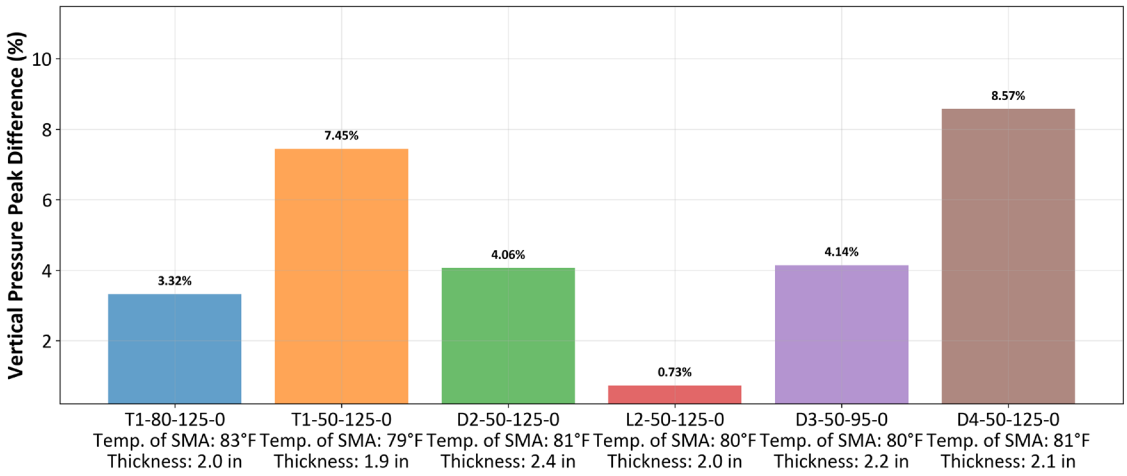

(c) 10 kip

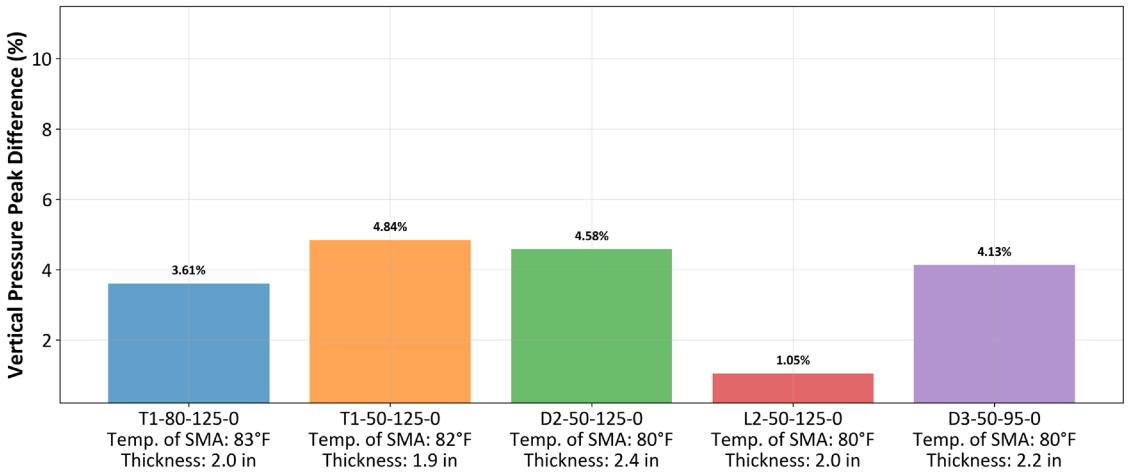

(d) 12 kip

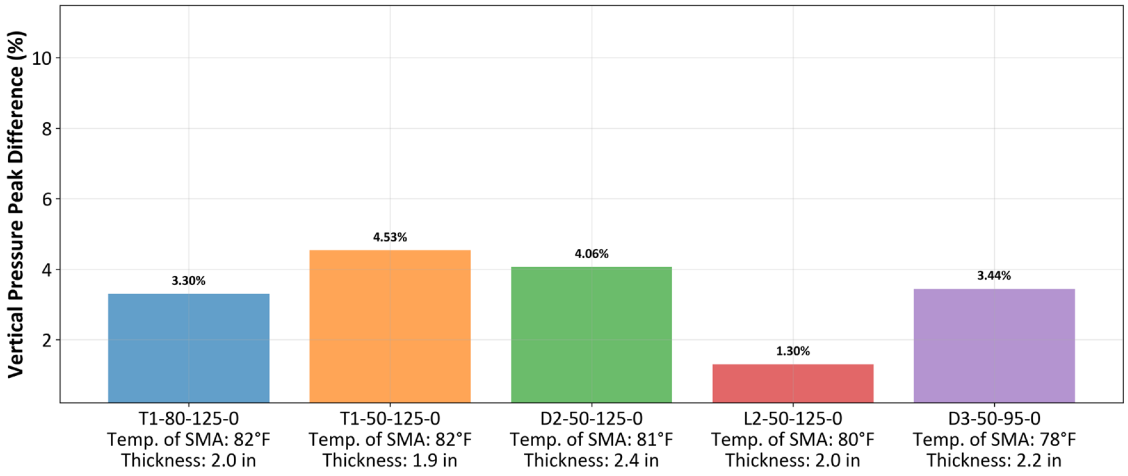

(e) 14 kip

Figure 106. Graph. Vertical stress peak difference for various loads: (a) 8 kip, (b) 9 kip, (c) 10 kip, (d) 12 kip, and (e) 14 kip.

Table 35. Tire-Pavement Contact Length Change with Various Loading (De Beer et al. 2012)

Load (kip)	Tire imprint at 125 psi inflation pressure
6	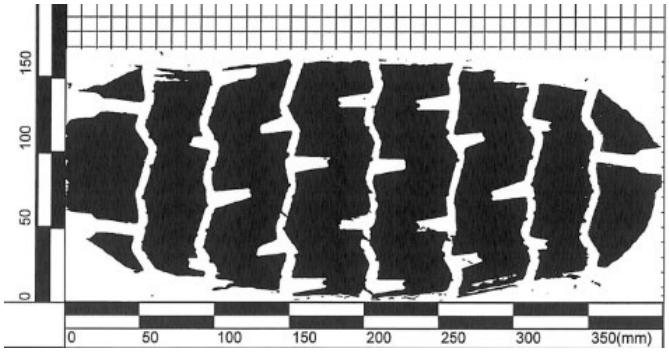
8	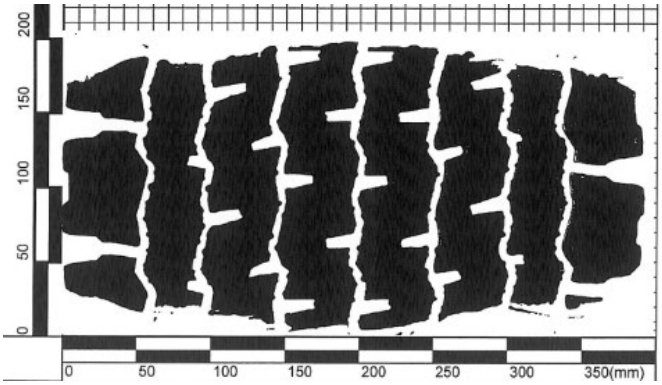
10	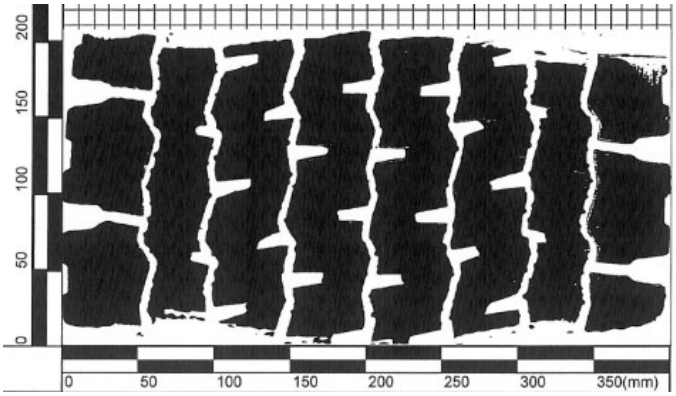

Load (kip)	Tire imprint at 125 psi inflation pressure
14	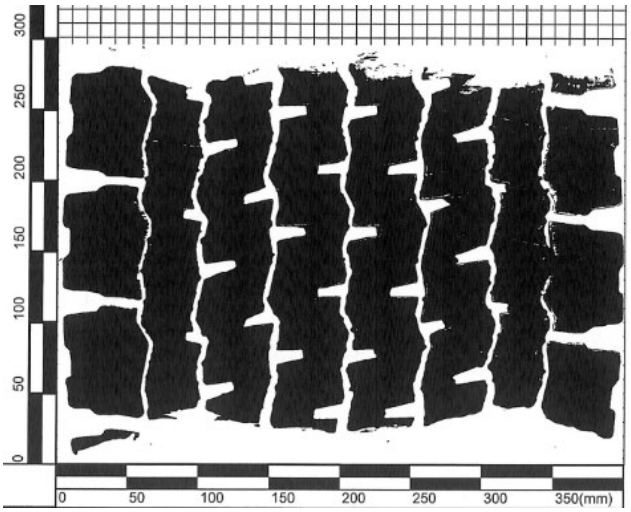
18	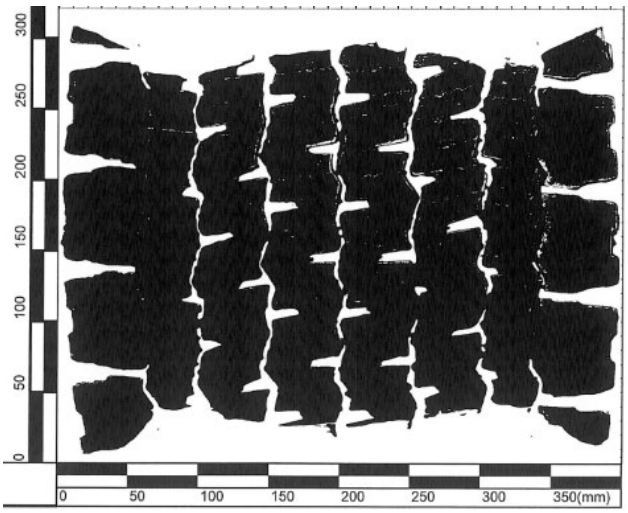

Effect of Tire Pressure on Pavement Recovery

As tire inflation pressure increased from 80 to 120 psi, longitudinal strain peak differences did not display a consistent trend across sections (Figure 107). At 80–100 psi, stiffer or thinner layers (D3, D4) exhibited differences of > 10%, but at 120 psi, values did not converge uniformly. Transverse strain peak differences did not exhibit a clear pressure-dependent trend (Figure 108). At 80 psi, values reached > 40%, and at 120 psi they remained within 20%–35%, demonstrating that tire pressure did not meaningfully alter lateral strain contrast or pavement recovery behavior.

T1-80 and D4-50 exhibited the lowest transverse strain differences across inflation cases, implying faster lateral recovery and reduced strain accumulation in those mixtures. Vertical stress differences varied only slightly with inflation (Figure 109). At 80 psi, values ranged 4.8%–9.0%, while at 120 psi they were approximately 3.3%–8.6%, reinforcing that tire pressure exerted minimal influence on leading–trailing stress differential compared with other loading variables.

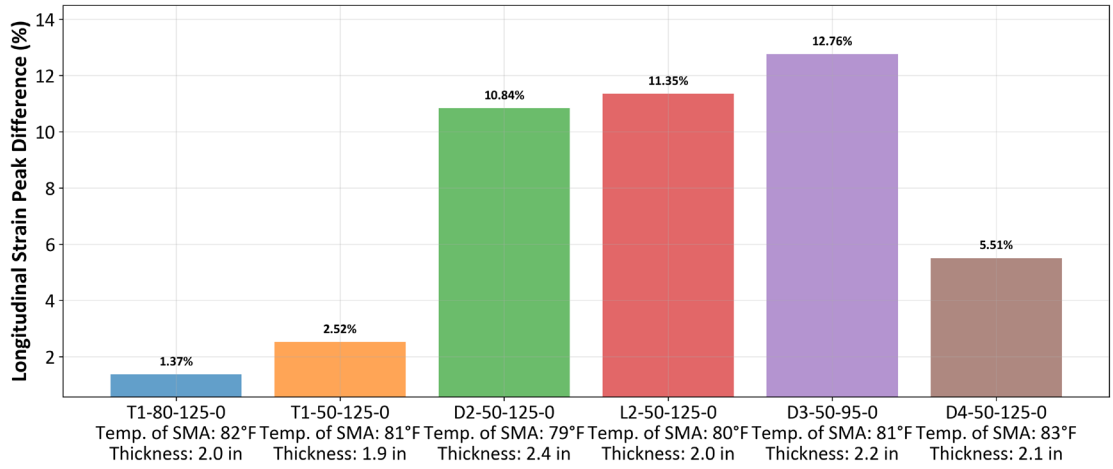

(a) 80 psi

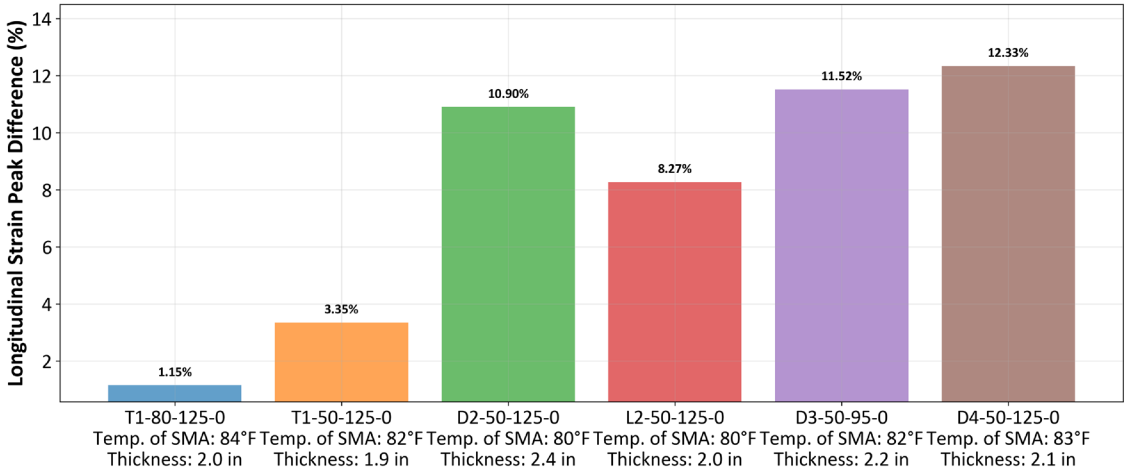

(b) 100 psi

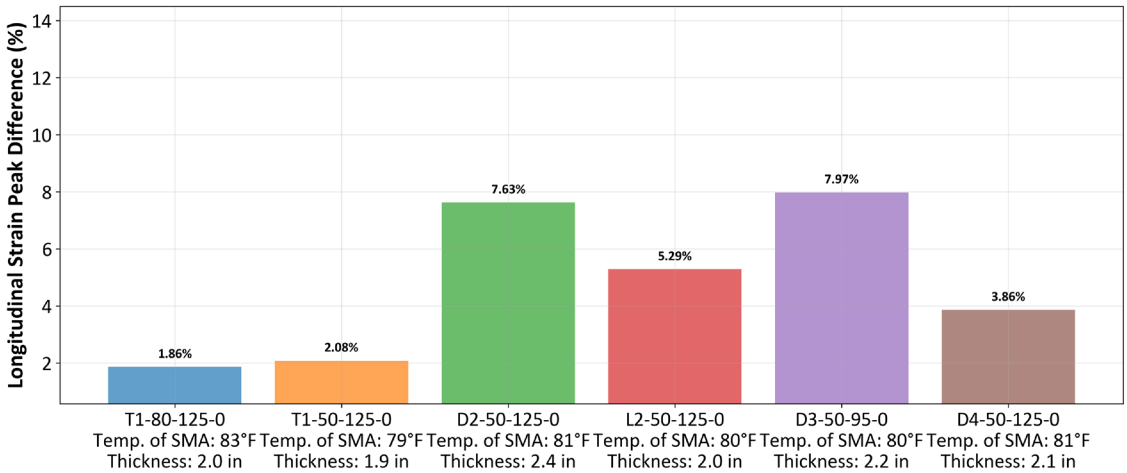

(c) 120 psi

Figure 107. Graph. Longitudinal strain peak difference at various tire pressures: (a) 80 psi, (b) 100 psi, and (c) 120 psi.

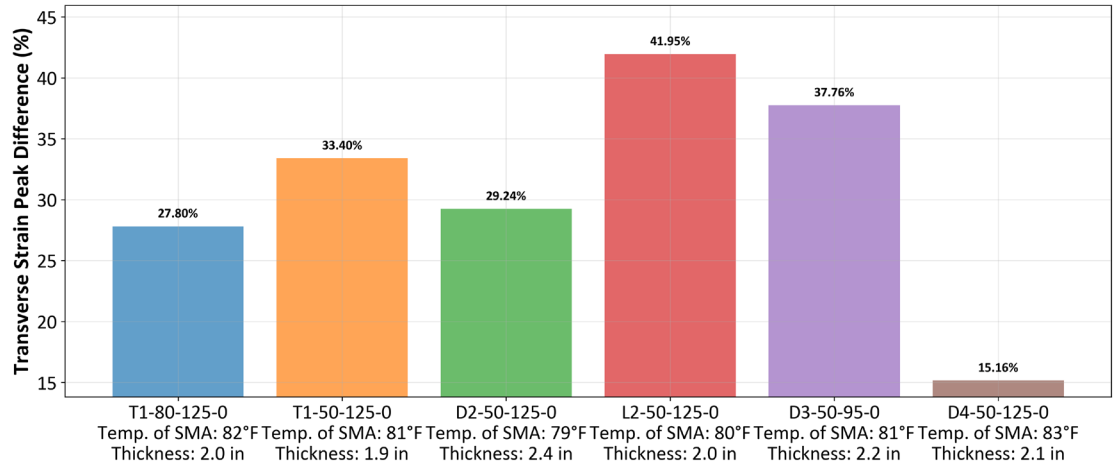

(a) 80 psi

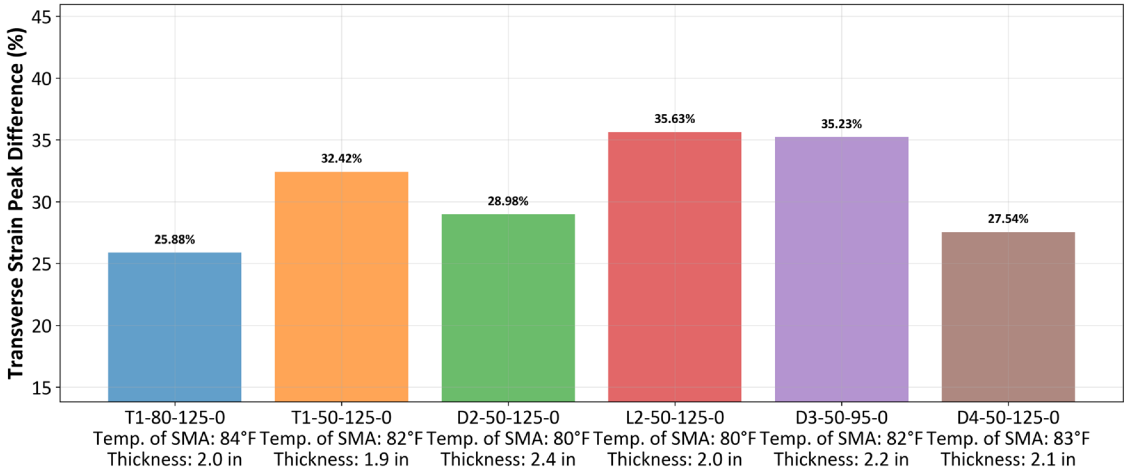

(b) 100 psi

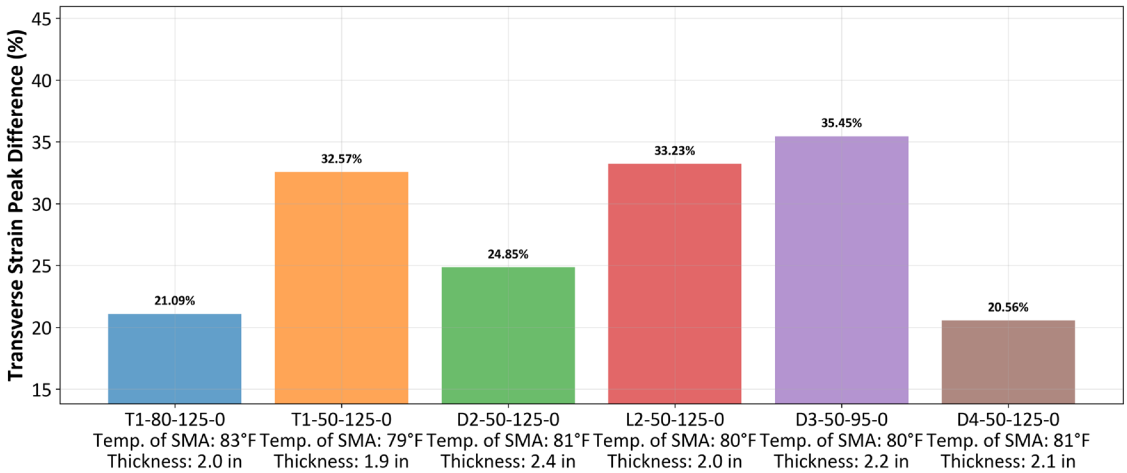

(c) 120 psi

Figure 108. Graph. Transverse strain peak difference at various tire pressures: (a) 80 psi, (b) 100 psi, and (c) 120 psi.

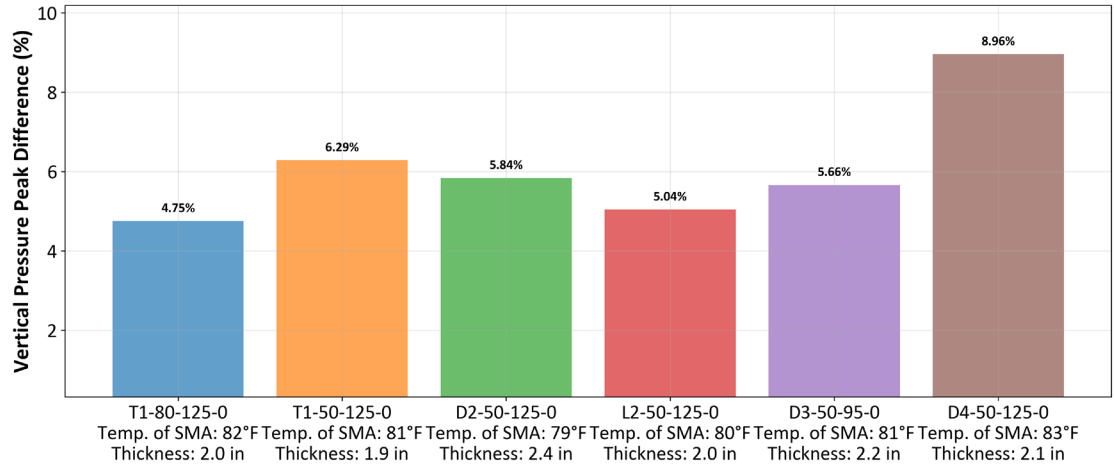

(a) 80 psi

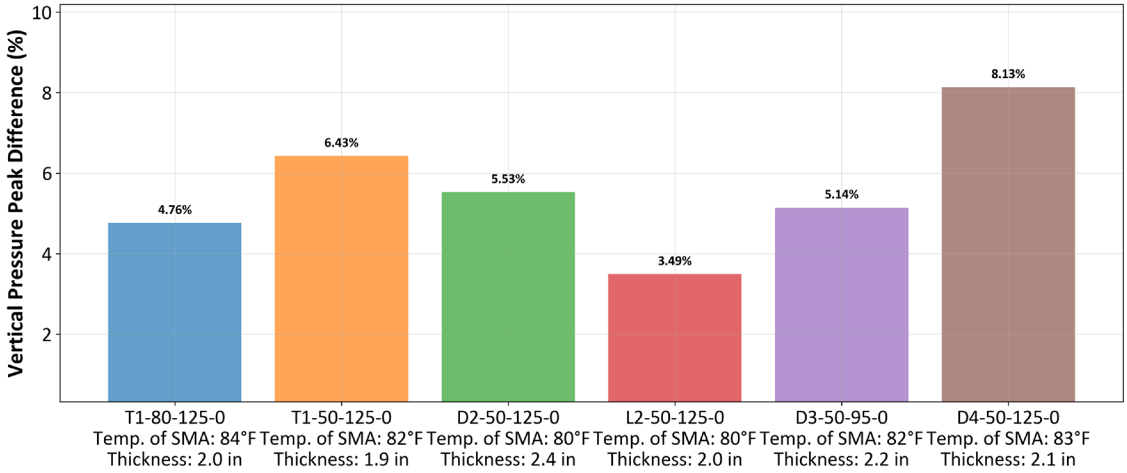

(b) 100 psi

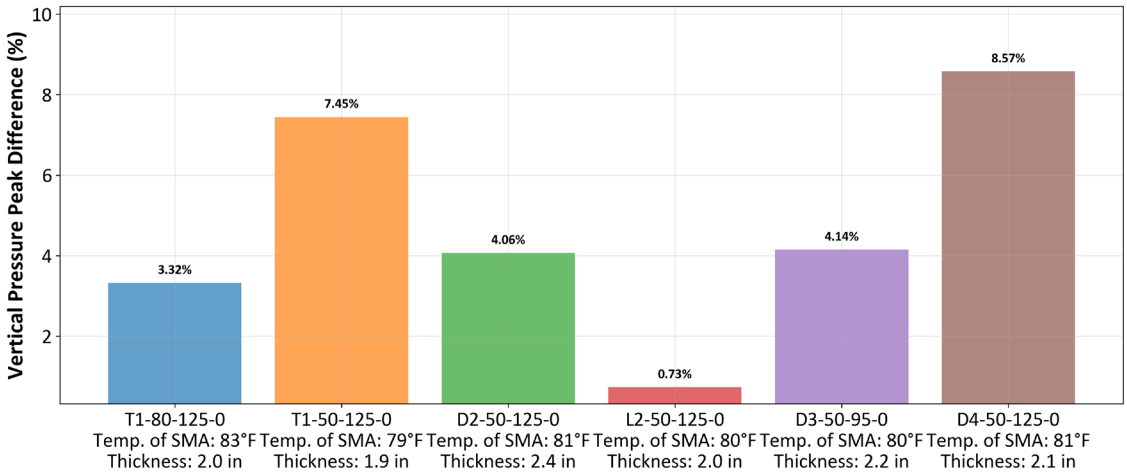

(c) 120 psi

Figure 109. Graph. Vertical stress peak difference at various tire pressures: (a) 80 psi, (b) 100 psi, and (c) 120 psi.

Strain Recovery in Loading Direction

In general, the trailing tire produced greater strain and vertical stress than the leading tire, consistent with delayed viscoelastic recovery. In the direction parallel to traffic, at a given point in the pavement, the point experiences compression before the load passes directly over it. Then the response reaches a maximum and becomes tensile (as expected). Shortly after, the load moves ahead and the point returns toward compression, accelerating recovery (Figure 110). The viscoelastic SMA layer experiences an initial compression–tension–compression cycle as the tire approaches and departs, promoting forced recovery and limiting differential strain accumulation between leading and trailing tires. Hence, relative strain peak values in the longitudinal direction were small and likely insignificant.

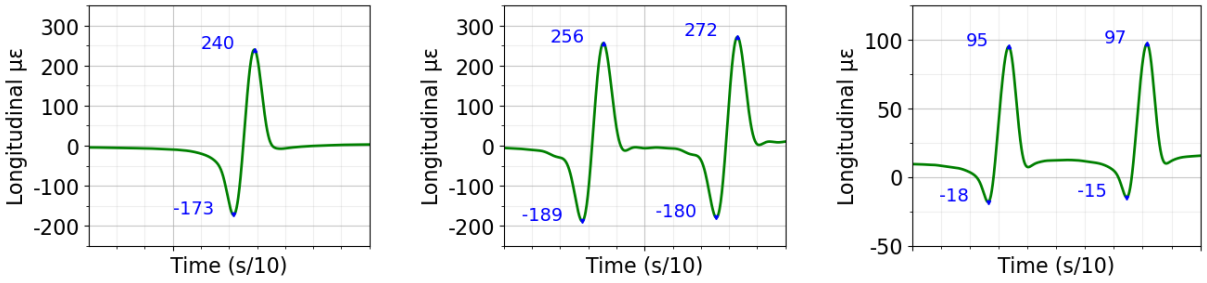

(a) Single axle (D4-50-12.5-0) (b) Tandem axle (D4-50-12.5-0) (c) Tandem axle (L2-50-12.5-0)

Figure 110. Graph. Longitudinal strain response at 10 kip, 120 psi, 5 mph, and 80°F: (a) single axle on D4-50-12.5-0, (b) tandem axle on D4-50-12.5-0, and (c) tandem axle on L2-50-12.5-0.

Effect of SMA on Pavement Recovery

To evaluate the influence of various parameters on pavement recovery, a statistical analysis was performed using the percentage difference transverse strain peaks between the leading and trailing tires. In this analysis, the effect of size was measured using eta-squared (η^2). Eta-squared represents the proportion of variability in the response that may be explained by a specific factor. A larger η^2 value indicates a stronger influence on pavement recovery. For example, $\eta^2 = 0.40$ means 40% of the variation in recovery behavior is due to that factor, while values below 0.10 represent small or negligible effect.

Figure 111 summarizes the transverse strain response peaks across the six SMA sections. The sections exhibited distinctly different recovery behaviors. Sections D4-50-12.5-0 and T1-80-12.5-0 consistently demonstrated the *lowest* peak differences (approximately 19%–23%), indicating rapid transverse strain recovery. In contrast, sections T1-50-12.5-0, L2-50-12.5-0, and D3-50-9.5-0 exhibited relatively high transverse strain peak differences (≈31%–33%), suggesting comparatively slower recovery. The statistical test confirmed a strong SMA-section effect ($\eta^2 = 0.437$, $p < 0.001$), where approximately 44% of the variance in recovery could be attributed to SMA section configurations. Speed also has a strong impact and is discussed below.

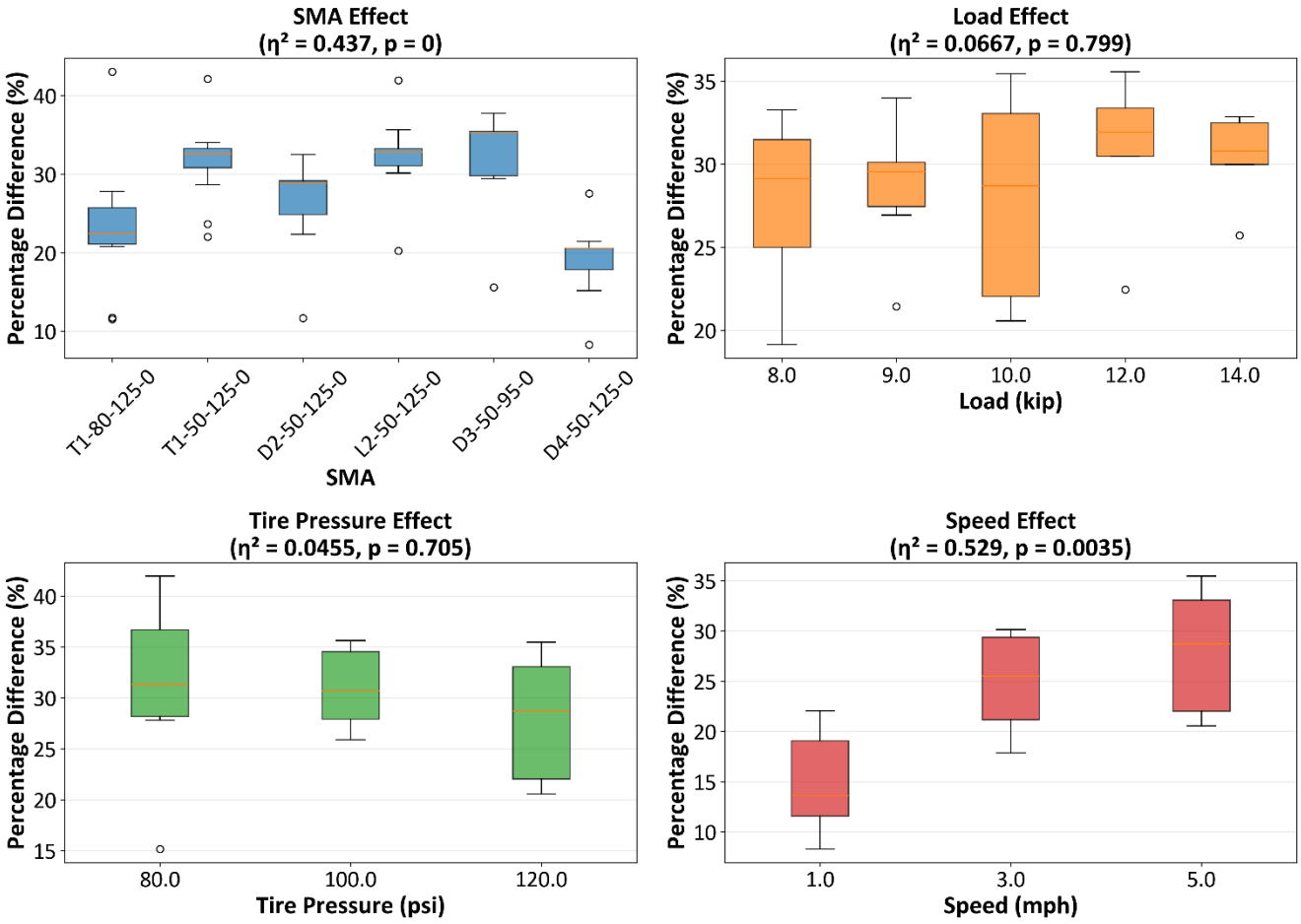

Figure 111. Box plot. Material and loading characteristic effects on transverse strain peak difference.

Figure 112 presents a comparative effect on all evaluated factors. SMA displays a significant effect, but two additional parameters, speed and temperature, also had a substantial influence. Specifically, speed exhibited a large effect ($\eta^2 = 0.529$), demonstrating that higher speeds reduced available recovery time, thereby increasing trailing-tire peak. Temperature, on the other hand, is the most influential parameter overall ($\eta^2 = 0.841$), reflecting that SMA viscoelasticity has a strong impact. In addition, a deflated tire had a significant effect, as expected. This finding suggests that load ($\eta^2 = 0.0667$) and symmetric inflation pressure ($\eta^2 = 0.0455$) are not primary drivers of transverse strain recovery for SMA under these conditions.

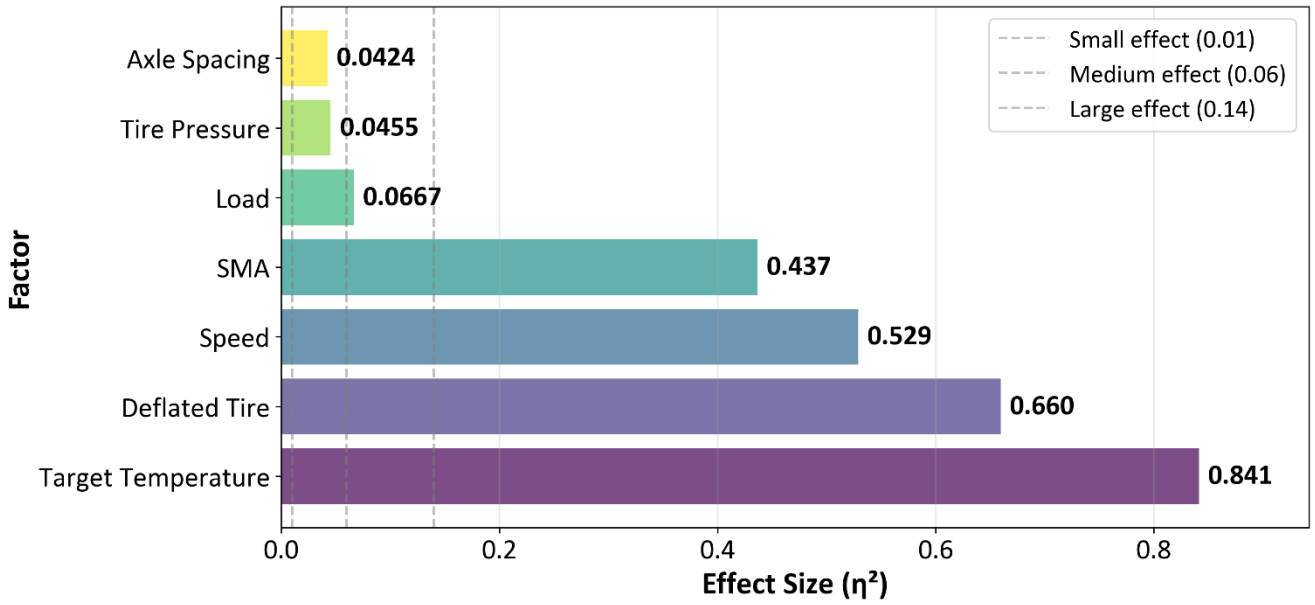

Figure 112. Graph. Effect size (η^2) comparison across all parameters.

Figure 113 further illustrates the relative importance of each factor by displaying the percentage of variance explained. Variance explained was quantified by comparing the average within-group variance of the response to its total variance, following an ANOVA variance decomposition framework. This metric represents the proportion of overall variability attributable to systematic differences between factor levels (e.g., section, load, or tire pressure), rather than random variability within each group.

Temperature and deflated-tire conditions explain more than 60% of total variance, while speed explains approximately 47%. SMA explains about 40%, reinforcing that mixture design and layer composition remain fundamental to recovery performance. Negative values for load and tire pressure simply indicate that these factors do not meaningfully improve the model's ability to explain variability, which is consistent with their small or negligible effect sizes. The axle-spacing comparison was conducted only for T1-80-12.5-0 and T1-50-12.5-0 at 3.5 ft, 4.0 ft, and 4.5 ft.

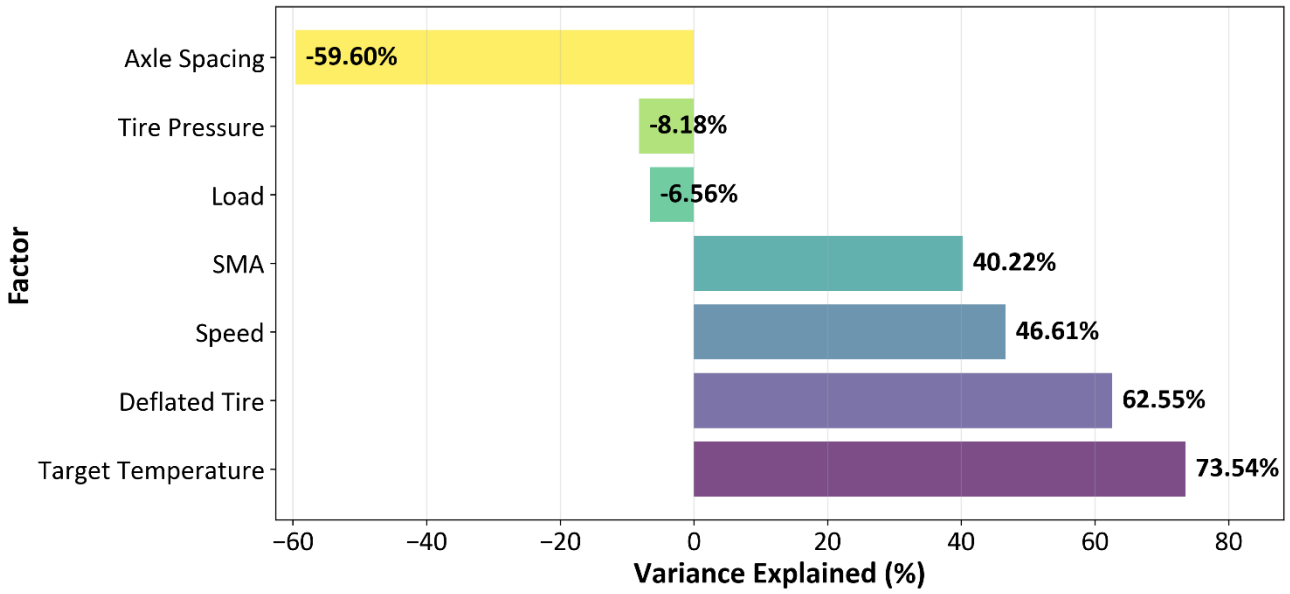

Figure 113. Graph. Variance explained (%) for all parameters affecting transverse strain peak difference.

Differential Tire Inflation Pressure Impact on Pavement Response

Differential tire inflation pressure is an important factor because underinflated tires are common in truck operations on highways. Tire pressure affects tire stiffness, contact area, and load transfer onto pavements. Tire inflation pressure nonlinearly influence near-surface pavement responses (Tielking & Roberts, 1987; Bonaquist et al., 1988; Sebaaly & Tabatabaee, 1989; Pozzzi & Luo 2005).

At 80 psi, pavement responses were lower than those at 100 psi. However, responses at 100 and 120 psi were similar (typical tire inflation of a wide-base tire is 120 psi), suggesting that the tire crown and sidewalls function independently at higher pressures, and that near-surface pavement behavior is not significantly affected by mild underinflation. In contrast with the rest of the responses measured, Figure 114 demonstrates that severe underinflation has a much stronger influence on pavement responses than load magnitude or speed. When the trailing tire was severely underinflated (e.g., 80 psi), the critical responses did not occur under the trailing tire.

Lead tire inflated with 80 psi, trailing tire inflated with 120 psi	Lead tire inflated with 120 psi, trailing tire inflated with 80 psi
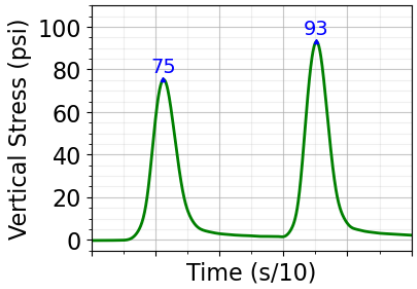	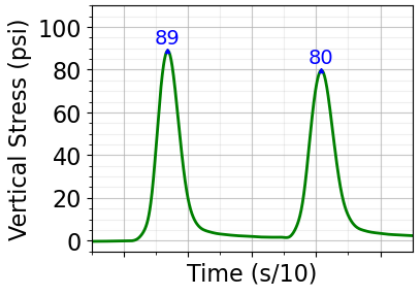
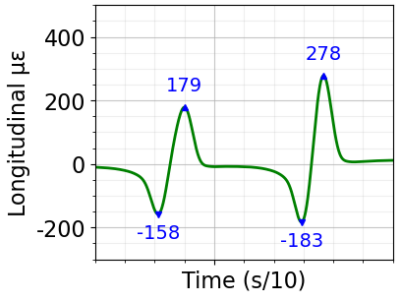	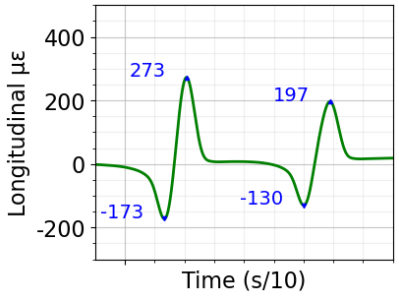
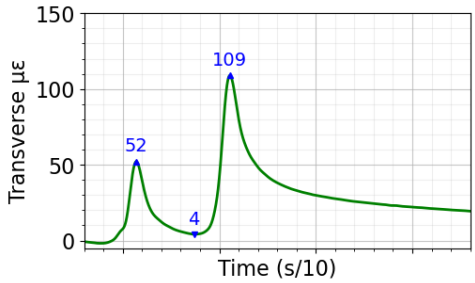	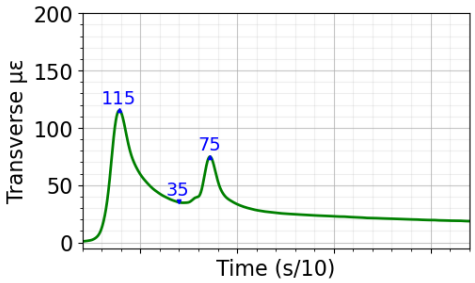

Figure 114. Graph. D4-50-12.5-0 pavement section responses under tandem-axle load with an underinflated tire.

Figure 115 and Figure 116 compare responses across all SMA sections under two asymmetric inflation conditions (80/120 psi and 120/80 psi). Despite differences in mixture type, including NMAS, the overall patterns were consistent across sections. The response under underinflated tire (80 psi) is always lower despite the axle location, leading or training. This suggests that having an underinflated tire has a significant impact.

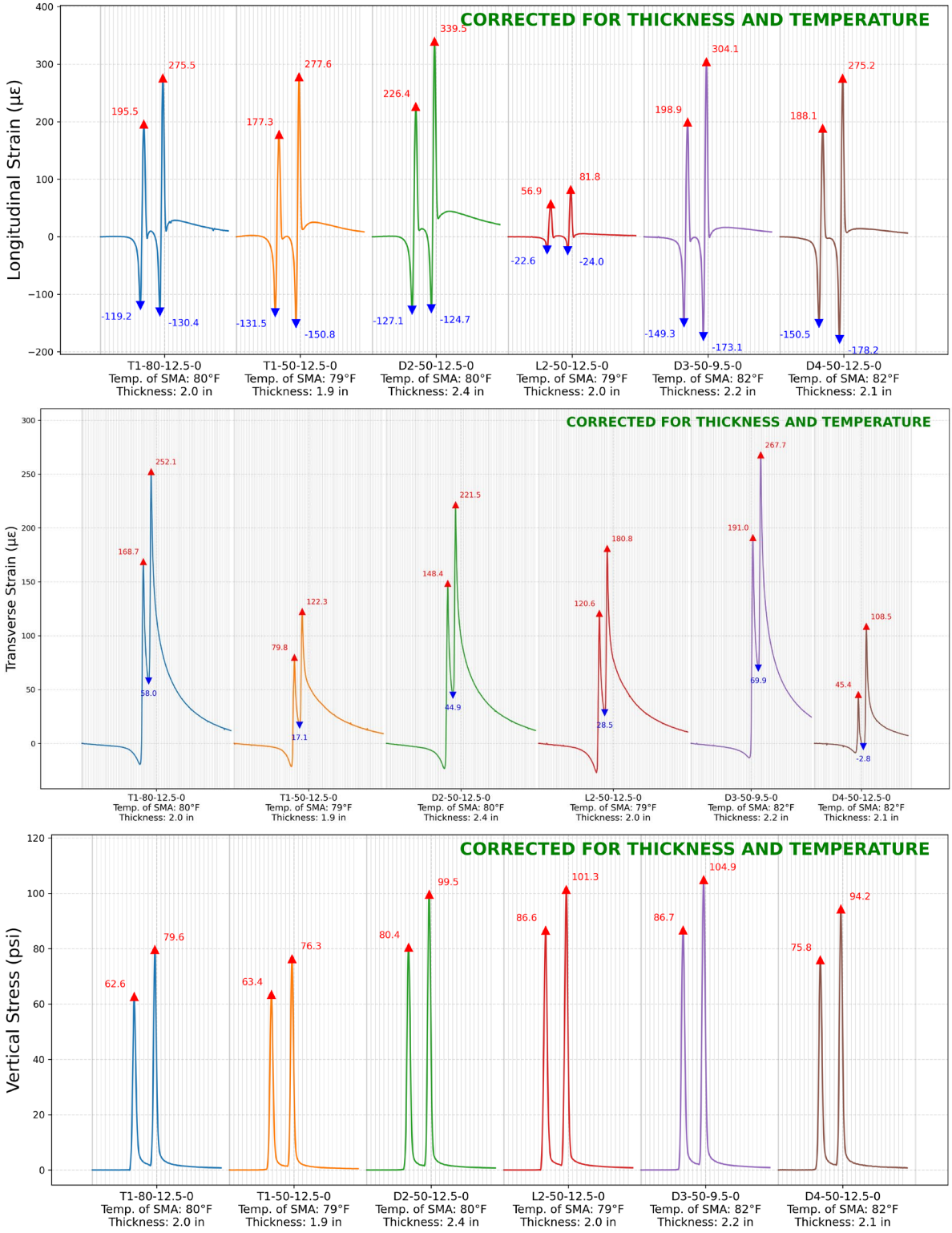

Note: Examination of all L2-50-12.5-0 longitudinal strain data indicates consistently low readings, likely due to gauge misalignment.

Figure 115. Graph. Comparison of pavement responses across sections under tandem-axle loading (80 psi–120 psi tire inflation pressure, 10 kip–10 kip axle loads, 5 mph, and 3.5 ft axle spacing).

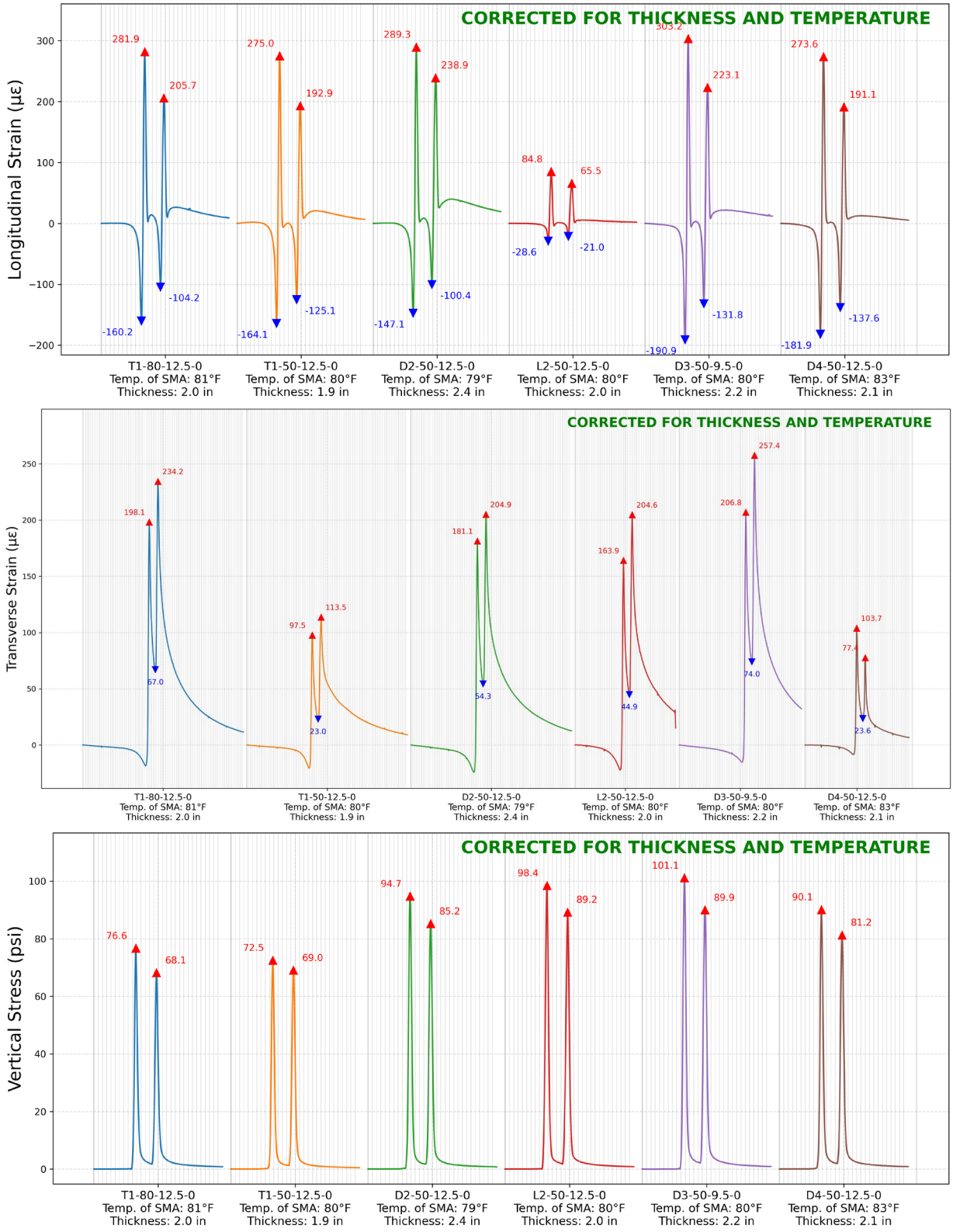

Figure 116. Graph. Comparison of pavement section responses under tandem-axle loading (120 psi–80 psi tire inflation pressure, 10 kip–10 kip axle loads, 5 mph, and 3.5 ft axle spacing).

As presented in Figure 117, the longitudinal strain peak difference depended strongly on the inflation pressure ratio. When inflation increased from 80 to 120 psi, longitudinal peak differences rose sharply to 40%–55%, indicating stronger stress concentration and a stiffer tire-pavement interaction. When pressure decreased from 120 to 80 psi, the peak differences turned negative (−16% to −29%), showing reduced strain magnitude and wider load dispersion.

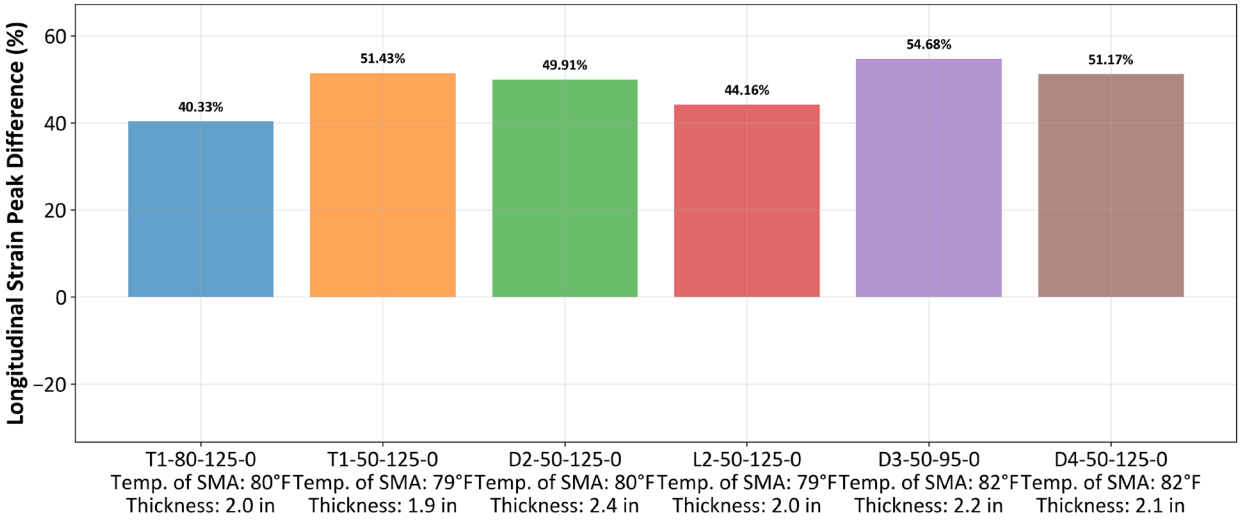

(a) 80/120 psi

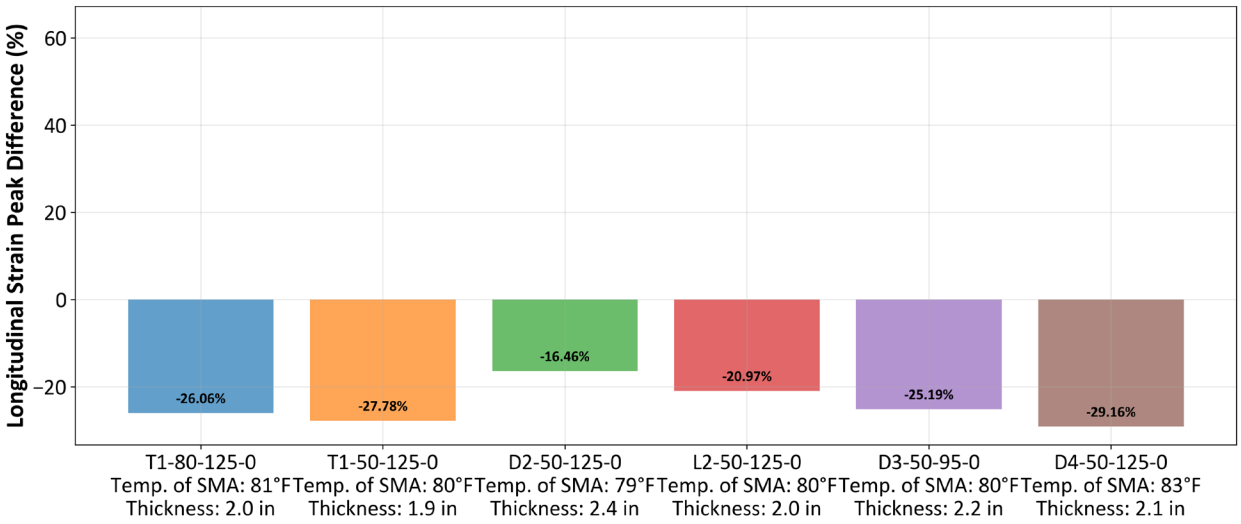

(b) 120/80 psi

Figure 117. Graph. Effect of deflated tire pressure of a tandem axle on longitudinal strain peak difference: (a) 80/120 psi and (b) 120/80 psi.

Transverse strain peak differences demonstrated a similar pattern (Figure 118). Increasing tire pressure produced 45%–72% higher lateral strain differences, while lowering tire pressure reduced or reversed the difference, especially in thinner pavement sections. This finding indicates that higher tire inflation amplifies shear effects and surface strain concentration. Vertical stress peak differences

followed the same trend with smaller magnitudes (Figure 119). Increasing tire inflation raised vertical stress contrast to 16%–29%, while deflating reduced it to −6% to −12%. The higher tire inflation increases localized stress intensity, whereas lower pressure promotes more uniform load sharing.

Because the difference between leading- and trailing-tire responses reflects the extent of pavement recovery within the axle spacing interval, the findings have direct implications on SMA recovery behavior. Across all SMA sections, the results demonstrated that differential tire inflation pressure influenced recovery behavior more than load magnitude or vehicle speed, underscoring the need to account for variable tire pressure when evaluating tandem-axle pavement performance.

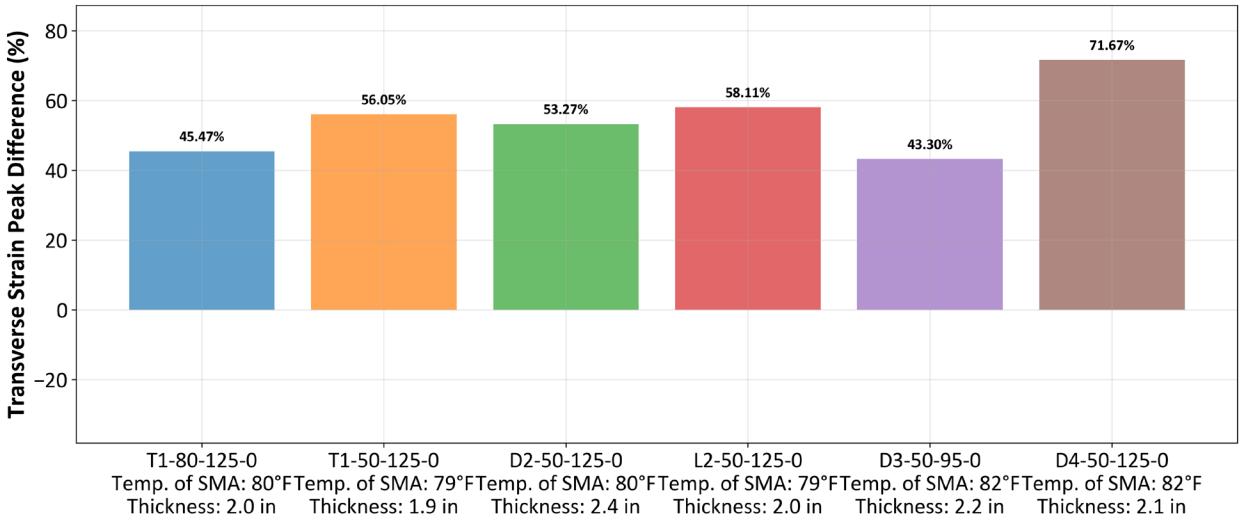

(a) 80/120 psi

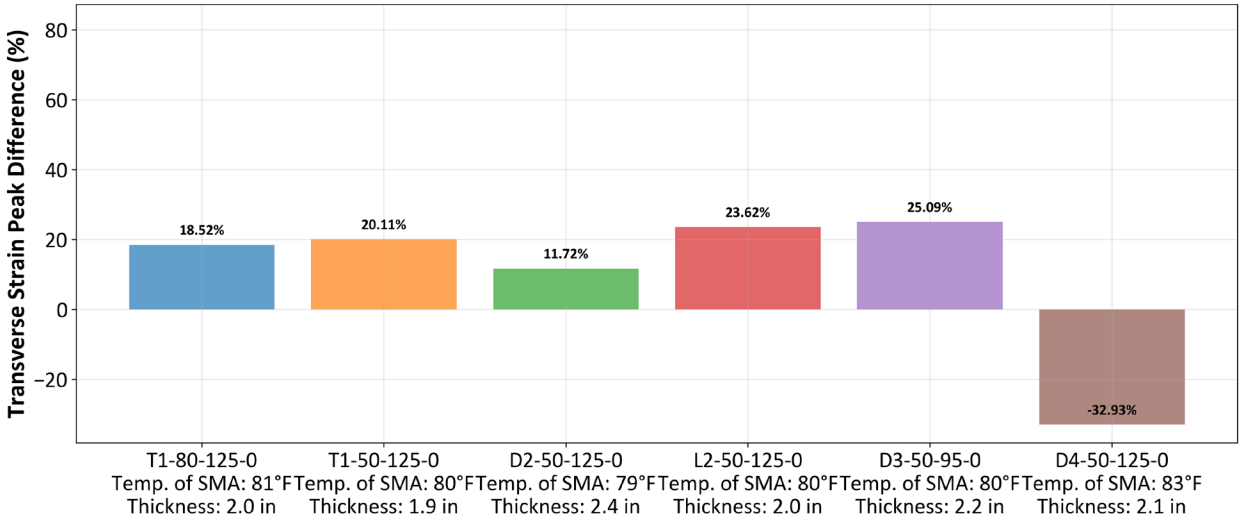

(b) 120/80 psi

Figure 118. Graph. Effect of a deflated tire pressure of a tandem axle on transverse strain peak difference: (a) 80/120 psi and (b) 120/80 psi.

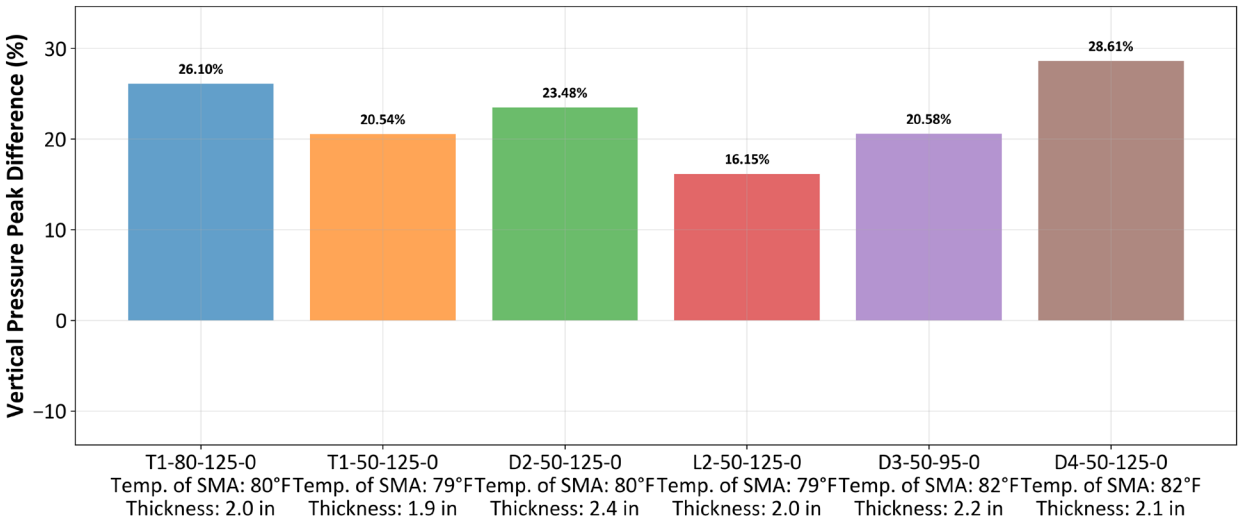

(a) 80/120 psi

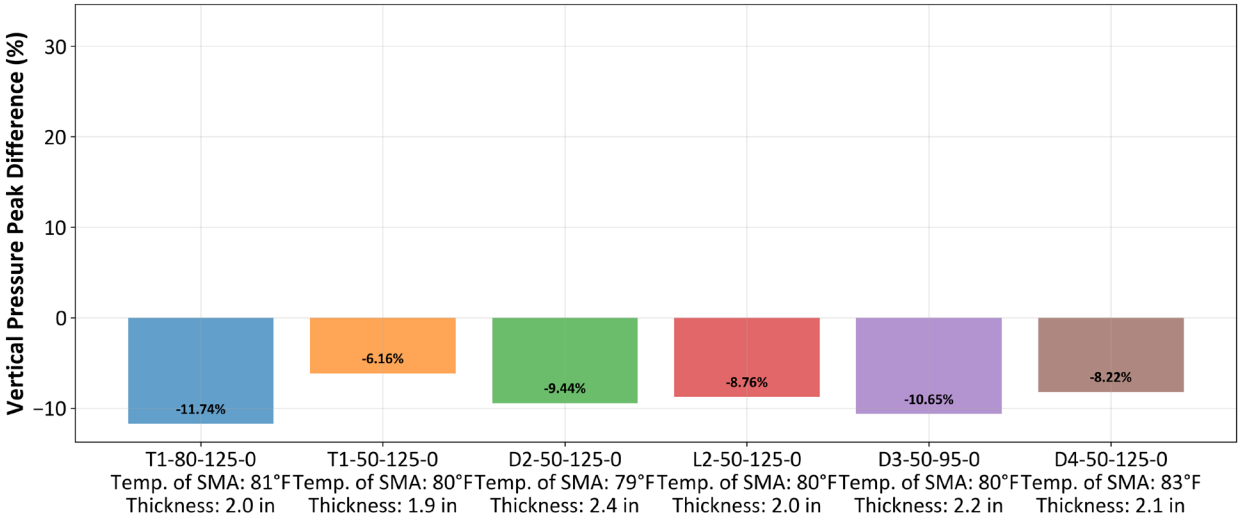

(b) 120/80 psi

Figure 119. Graph. Effect of a deflated tire pressure of a tandem axle on vertical stress peak difference: (a) 80/120 psi and (b) 120/80 psi.

SUMMARY

Full-scale pavement response measurements demonstrated that SMA sections exhibited predominantly viscoelastic behavior. The loading response waveform remained consistent across loading scenarios, while response magnitudes varied with material, temperature, and loading rate. Increased axle loads increased vertical stresses and strains. Also, when axle loading speed increased, strain magnitudes decreased, while vertical stress slightly reduced due to the limited increase in SMA moduli. Trailing tire loading of tandem-axle loading consistently produced greater responses, confirming the delayed viscoelastic recovery between axles. Although vertical stress responses were

relatively uniform across sections, strain responses—particularly transverse strain—demonstrated dependence on SMA characteristics, highlighting the impact of mix design.

SMA recovery is controlled primarily by mixture characteristics and temperature. Comparative analyses of leading–trailing response peak differences validated that pavement recovery is governed primarily by SMA characteristics and temperature at loading. These results were also supported by statistical analysis. Warmer SMA temperatures promoted faster stress relaxation, while higher speeds reduced available recovery time and amplified trailing-tire responses. In contrast, symmetric tire inflation pressure exhibited a negligible effect on pavement recovery within the tested range. On the other hand, significant differential tire inflation fundamentally altered responses.

CHAPTER 5: ACCELERATED LOADING OF FULL-SCALE SMA PAVEMENT SECTIONS

After a series of full-scale tests that measured pavement responses to various loading configurations and a temperature range, the pavement sections were loaded unidirectionally with no wander to assess resiliency. The pavement sections were initially subjected to 60,000 passes of tandem axles at 10 kip each axle. To accelerate pavement loading further, the loading was increased to 12 kip for 30,000 additional passes, followed by 30,000 passes at 14 kip. The traffic was channelized with no wander, and tread-to-tread spacing was minimized to 1.6 in, which is within safe limits to ensure proper operation. This induced an overlap of responses from both tires, making second axle loading more critical. The SMA target temperature of 80°F was based on summer weather data from Illinois. Tire pressure was 120 psi in each tire.

The tests were conducted during different periods of the year, which resulted in varying impacts from sublayer temperatures. During winter, heat radiates upward from the lower layers, while heat transfer occurs primarily from the surface downward during summer. During the Smart Road instrumentation response study, tests were conducted using the same load and similar ambient temperatures in April and October; however, the pavement responses differed due to variations in the temperature profile distribution within the pavement structure (Al-Qadi et al. 2004).

In the present study, to minimize seasonal effects, pavement temperature was controlled based on feedback from thermocouples located 1 in (25 mm) below the surface. In addition, the sections were covered during testing to ensure a constant temperature. Another important factor influencing the results was the duration of testing for each section. Although the original intent was to apply 120,000 load passes continuously, I-APT operations were occasionally interrupted due to parts replacement, routine maintenance, and other operational constraints. These interruptions extended the overall testing duration for some sections, potentially allowing for additional viscoelastic recovery of the SMA. The following is a summary of each section:

- T1-80-12.5-0 was tested between October 15 and November 26, 2025, under relatively cool conditions. Several intermittent loading days occurred, resulting in the longest overall testing duration among all sections.

- T1-50-12.5-0 was loaded between September 18 and October 15, 2025, corresponding to late summer and early fall conditions. This section had the shortest testing duration, with fewer interruptions.

- D2-50-12.5-0 was tested between August 1 and August 28, 2025, during warm and humid summer conditions. Loading was applied in a near-continuous daily pattern, with limited interruptions. Several consecutive days of rainfall and thunderstorms occurred during testing, which may have influenced pavement temperature stability. The combination of high temperatures and limited recovery time contributed to comparatively higher rate of rutting accumulation.

- L2-50-12.5-0 was loaded between June 11 and July 10, 2025, under early summer conditions. The testing campaign was of moderate length and included alternating dry and wet periods. Testing during the summer may have contributed to rutting.

- D3-50-9.5-0 was tested between March 2 and April 17, 2025, during highly variable late winter to spring conditions. This testing period experienced rapid temperature fluctuations and multiple consecutive rainy days. Loading was applied in a segmented manner.

- D4-50-12.5-0 was tested between October 24 and November 25, 2024, during a fall cooling period with intermittent rain events, including several consecutive wet days in early November.

PAVEMENT RESPONSES DURING CONTINOUS LOADING

Pavement temperatures and responses during loading are presented in Figure 120–Figure 131. Vertical stress was monitored to verify load consistency and magnitudes. The results reflect the pressure at the bottom of the SMA and demonstrated a rise as axle load increased. Temperature control was successfully maintained throughout testing, and SMA temperature was held at 80 ± 5°F. Brief deviations occurred during severe rain events, when surface water and wind drew heat away from the chamber. Strain results demonstrated oscillations due to the viscoelastic nature of the SMA and HMA materials. The peak transverse strain increased during loading and relaxed over time during recovery. The strain from the trailing tire caused strain accumulation and delayed recovery, so its peak is always greater than that of the leading tire. Longitudinal strain remained stable (not displayed here), which is consistent with previous observations. There was no significant difference between the leading and trailing tire. The observed cyclic response is due to the change in pavement temperature between the day and night despite the controlled temperature.

The longitudinal strain gauge in section T1-80-12.5-0 was damaged prior to the section loading. On the other hand, data were difficult to collect from the longitudinal strain gauge in section D3-50-9.5-0 due to I-APT operational limitations during testing.

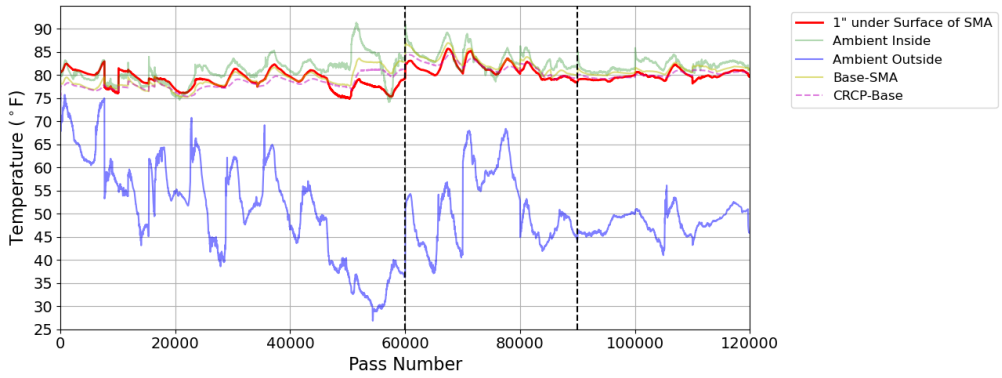

Figure 120. Graph. Pavement temperature recorded for T1-80-12.5-0.

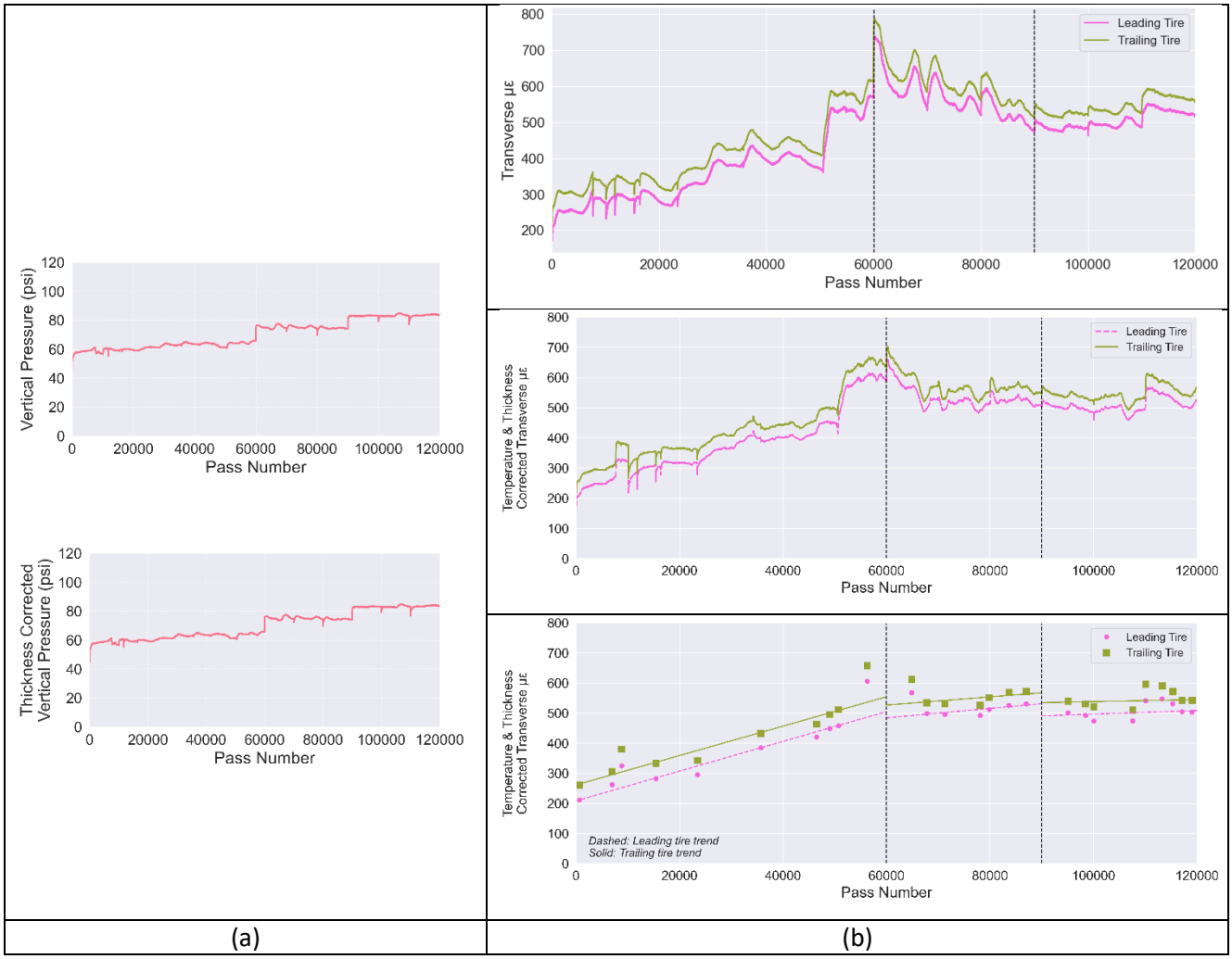

Figure 121.Graph. Pavement responses recorded and corrected for Section T1-80-12.5-0: (a) measured vertical stress and thickness-corrected vertical stress; (b) measured data, temperature- and thickness-corrected data, and response curves at every 2,500 passes.

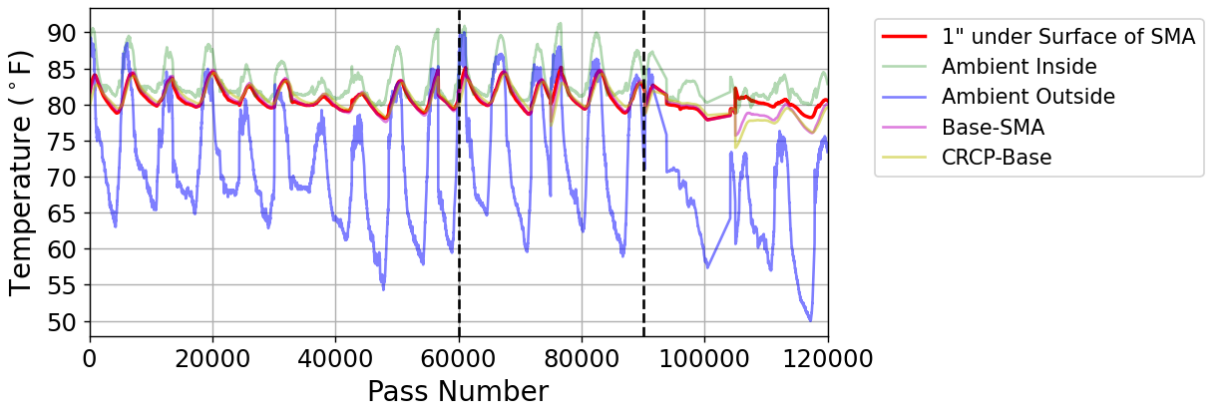

Figure 122. Graph. Pavement temperature recorded for T1-50-12.5-0.

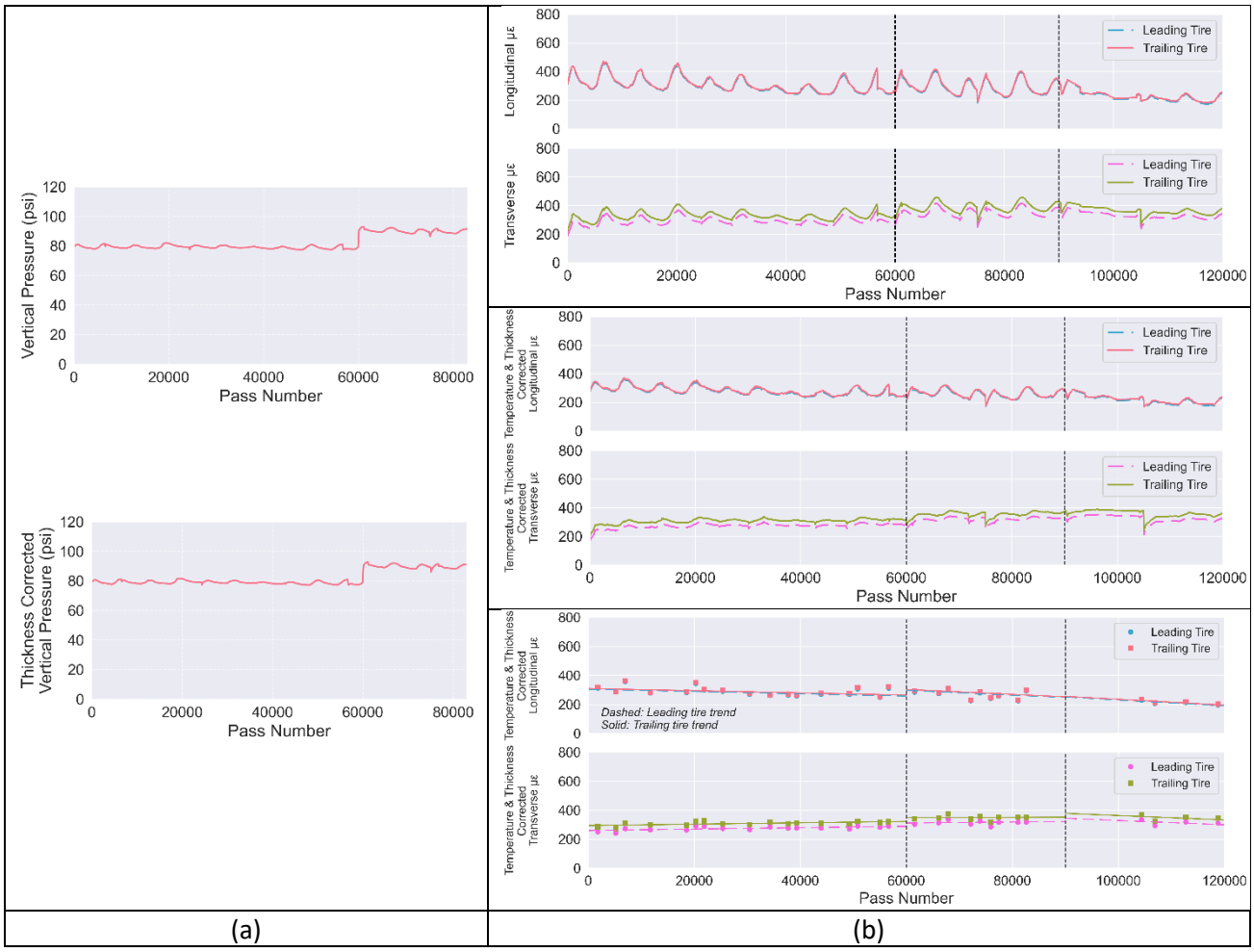

Figure 123.Graph. Pavement responses recorded and corrected for T1-50-12.5-0: (a) measured vertical stress and thickness-corrected vertical stress; (b) measured data, temperature- and thickness-corrected data, and response curves at every 2,500 passes.

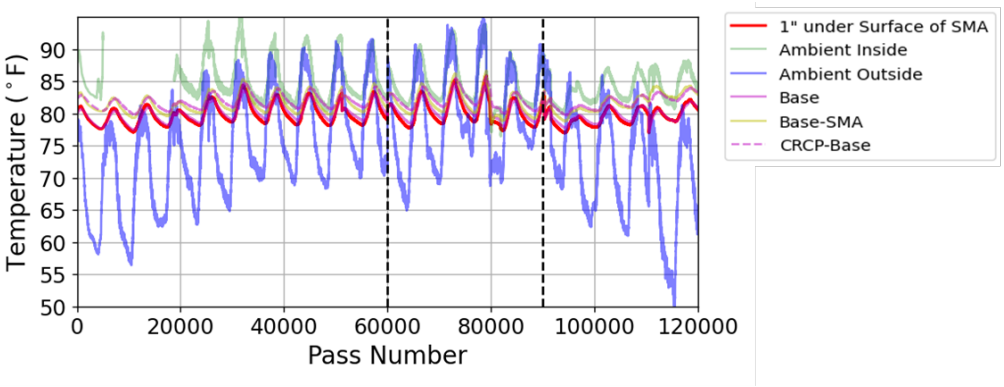

Figure 124. Graph. Pavement temperature recorded for D2-50-12.5-0.

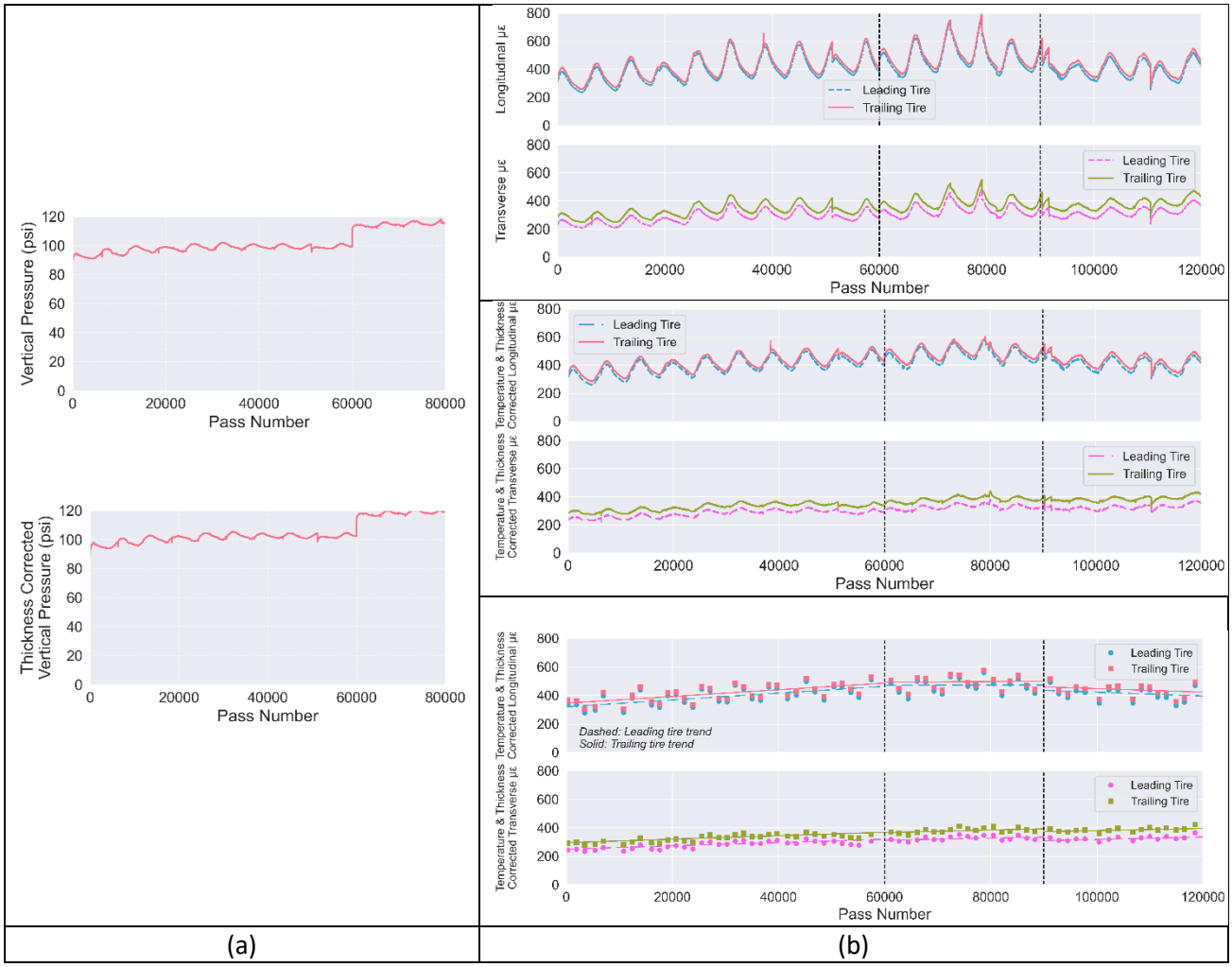

Figure 125. Graph. Pavement responses recorded and corrected for D2-50-12.5-0: (a) measured vertical stress and thickness-corrected vertical stress; (b) measured data, temperature- and thickness-corrected data, and response curves at every 2,500 passes.

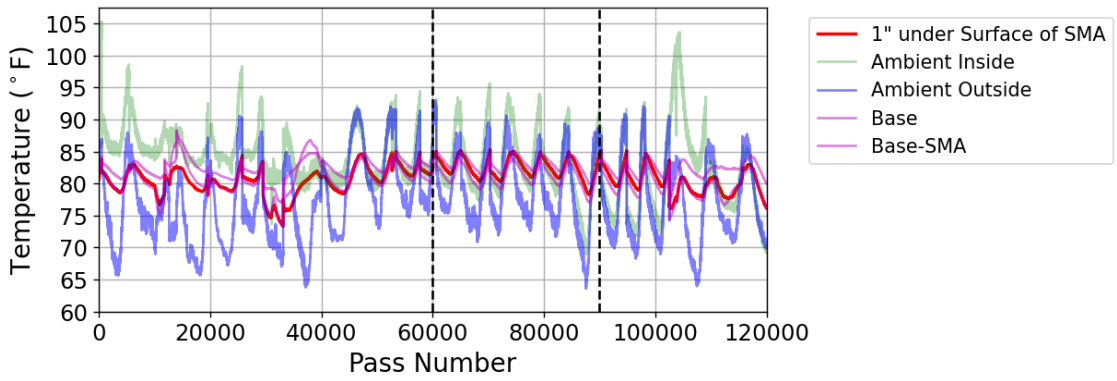

Figure 126. Graph. Pavement temperature recorded for L2-50-12.5-0.

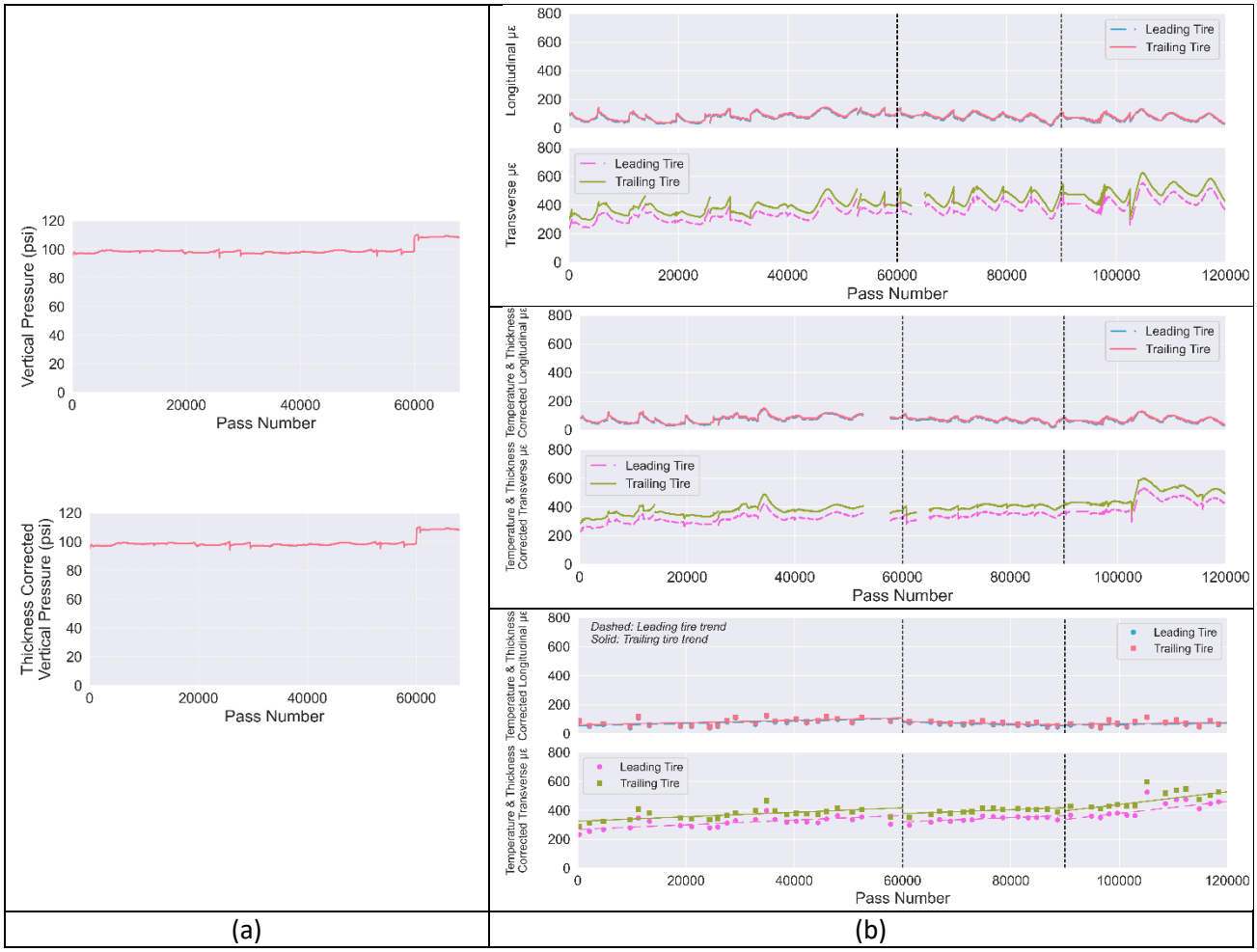

Figure 127. Graph. Pavement responses recorded and corrected for L2-50-12.5-0: (a) measured vertical stress and thickness-corrected vertical stress; (b) measured data, temperature- and thickness-corrected data, and response curves at every 2,500 passes.

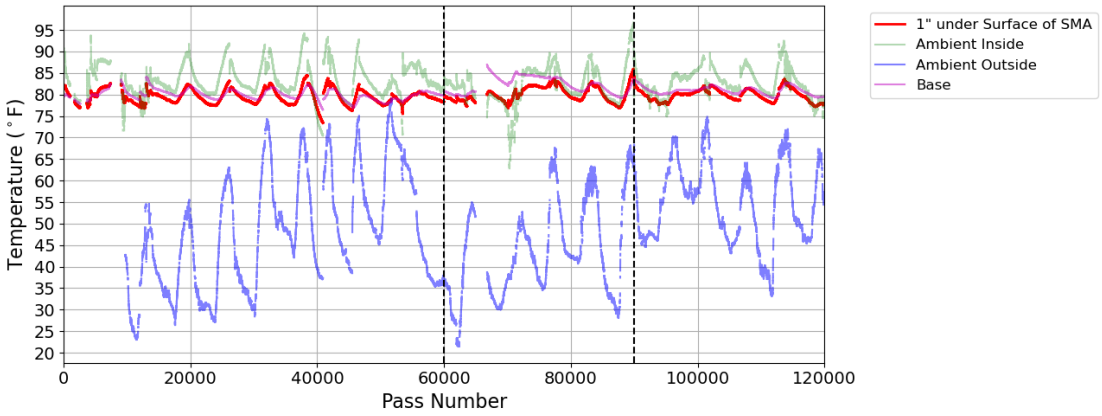

Figure 128. Graph. Pavement temperature recorded for D3-50-9.5-0.

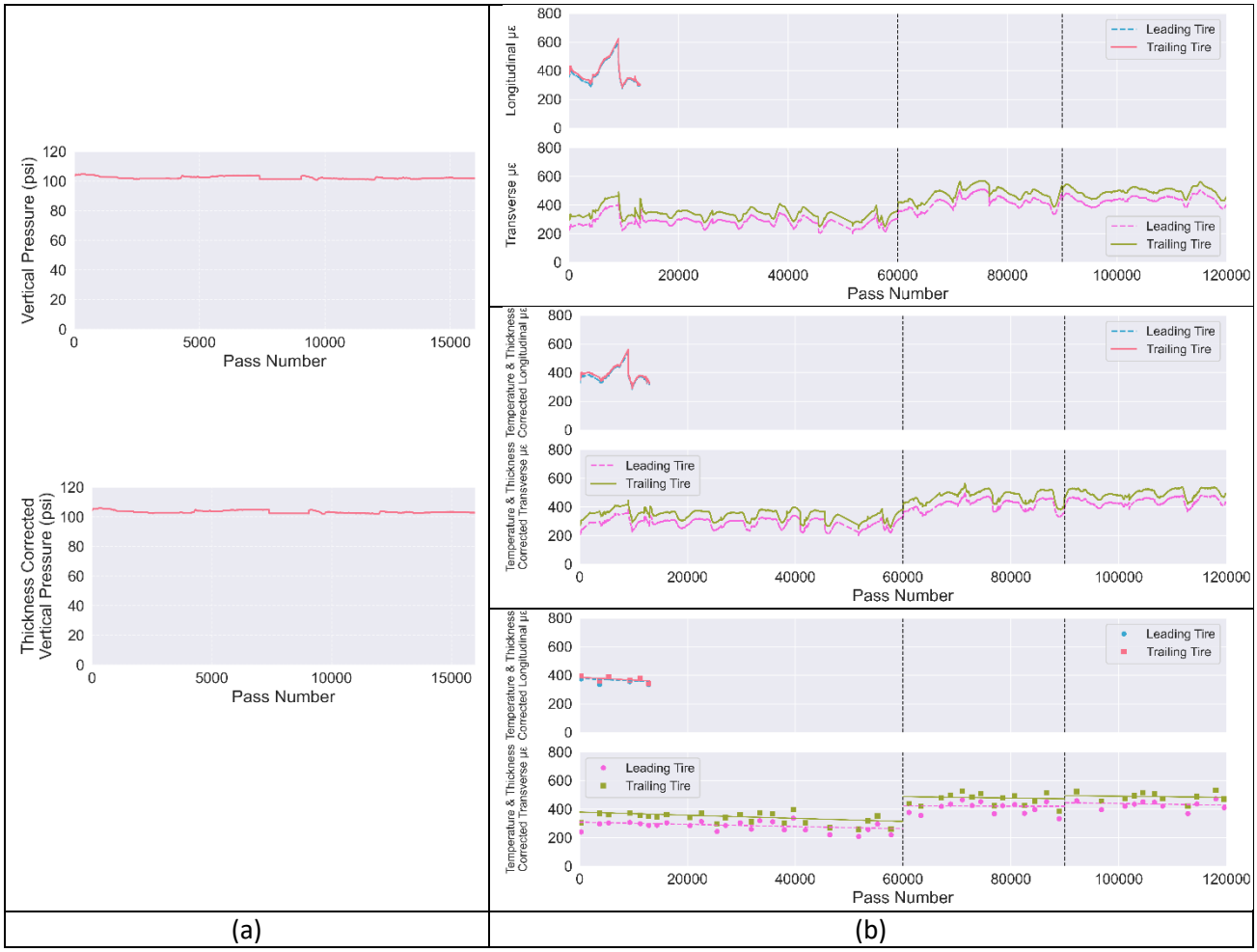

Figure 129. Graph. Pavement responses recorded and corrected for D3-50-9.5-0: (a) measured vertical stress and thickness-corrected vertical stress; (b) measured data, temperature- and thickness-corrected data, and response curves at every 2,500 passes.

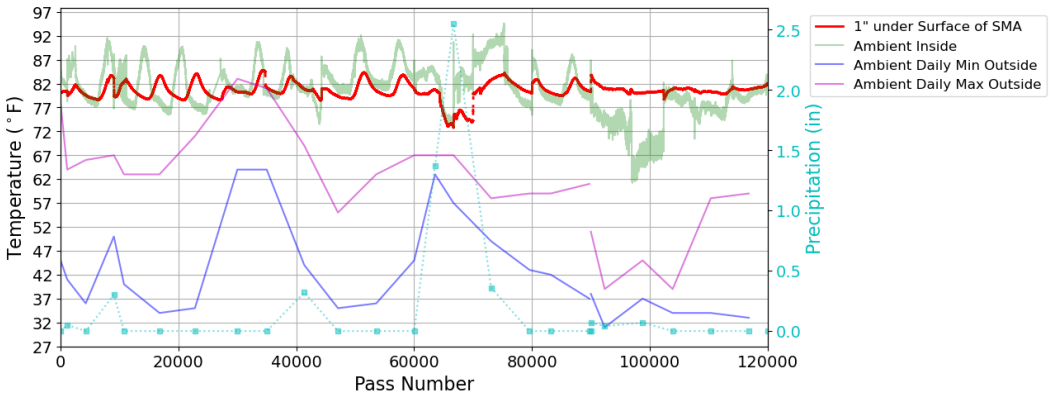

Figure 130. Graph. Pavement temperature recorded for D4-50-12.5-0.

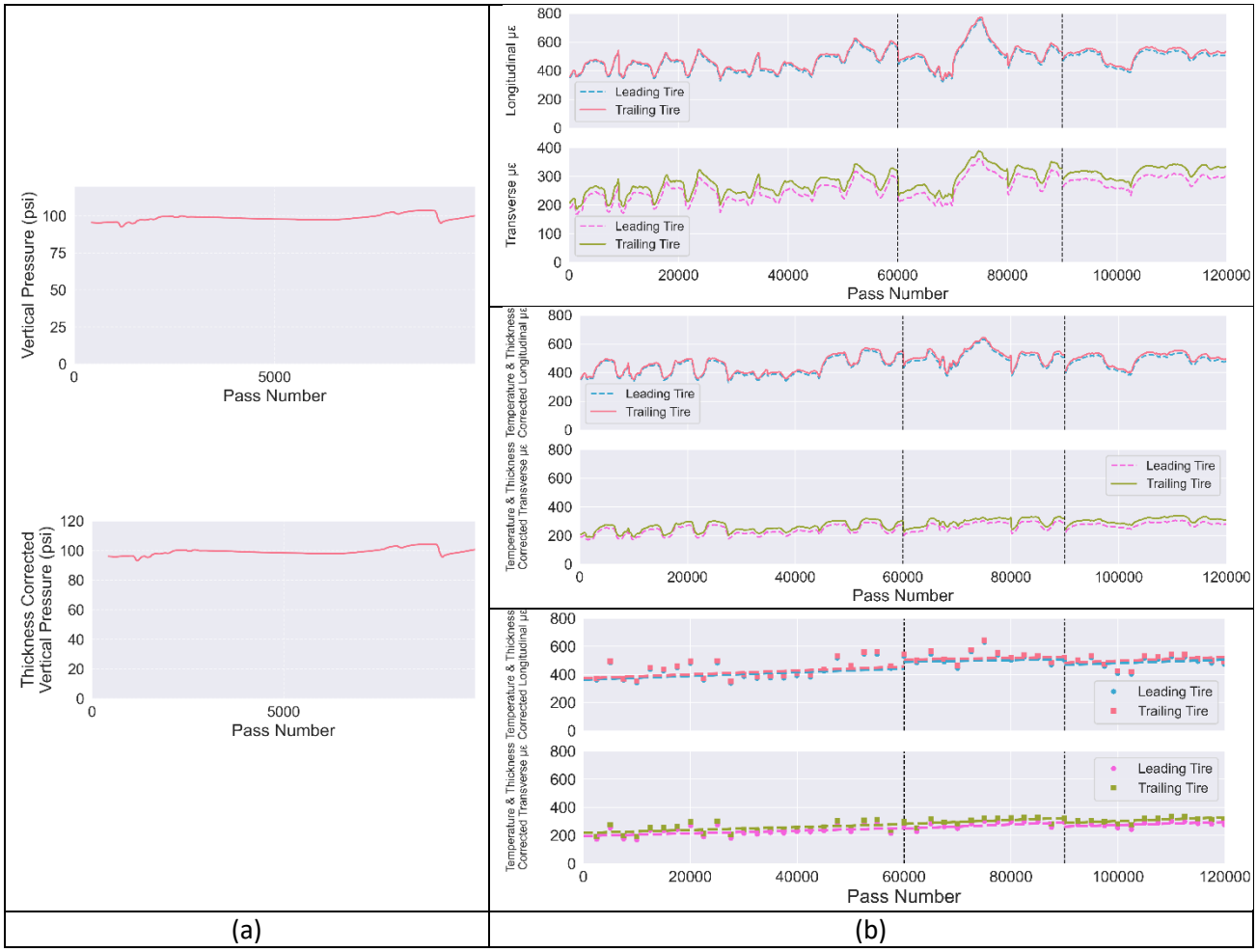

Figure 131.Graph. Pavement responses recorded and corrected for D4-50-12.5-0: (a) measured vertical stress and thickness-corrected vertical stress; (b) measured data, temperature- and thickness-corrected data, and response curves at every 2,500 passes.

RUTTING PROGRESSION

Permanent Deformation Measurements

Transverse pavement profiles were measured at two locations within each section, spaced 4 ft apart and at least 4 ft from the nearest sensor. Manual and automated laser methods were used. The manual approach employed plunge measurements with a caliper moved along a certified straightedge, achieving a precision of ±0.02 mils. The automated method used a laser scanner with a resolution of 1.23 mils/pixel in width, 2.36 mils/pixel in length, and 0.02 mils/pixel in height. The scan was 6 ft long and produced three sequential profiles per section. Both measurement techniques are presented in Figure 132. I-APT loading was paused at designated intervals for precise rut depth assessments.

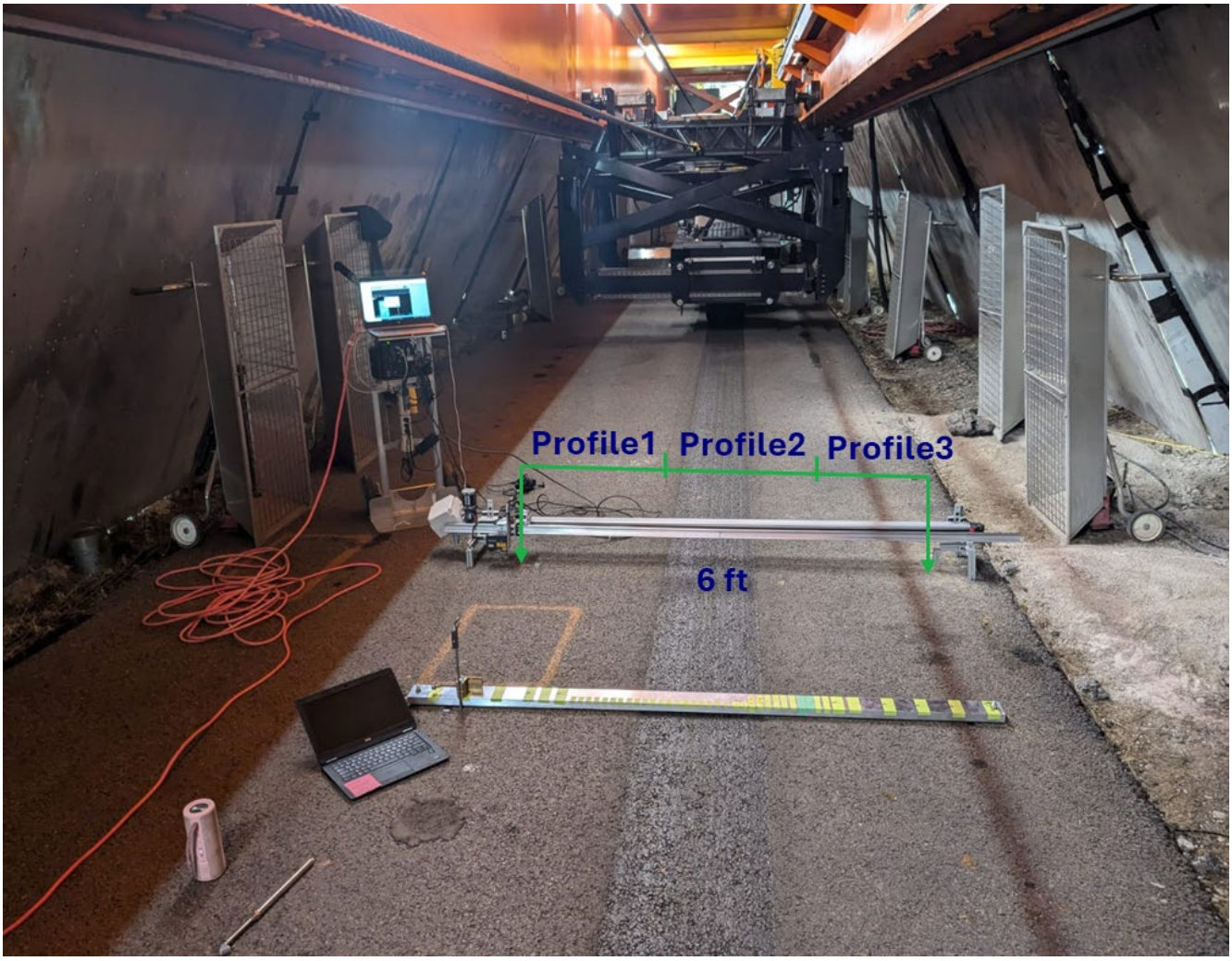

Figure 132. Photo. Manual and laser rutting profile measurements on D4-50-12.5-0.

Pavement Laser Profiler

The automated laser profiler used for rutting measurements incorporated specialized hardware operated through Keyence software. The system operates based on a 3D triangulation principle, enabling high-precision extraction of surface profile data. As illustrated in Figure 133-a, the system consists of a stepping motor and track mechanism that drives the profiler along a predetermined path. An encoder (Figure 133-b) mounted on the opposite end records pulse counts, which are used to trigger the profiler for 3D data capture. Data acquisition is controlled by Keyence's proprietary software (Figure 133-c), which manages the initiation and termination of scanning.

To ensure consistent and accurate data across multiple passes, metal reference blocks were placed at the start and end points of each scan. The markers were used to trim the profiles uniformly, allowing for reliable comparative analysis of rutting depth. Additionally, two downward-pointing lasers mounted near the legs of the profiler were used to accurately align the system with previously scanned pavement locations, ensuring repeatability in data collection.

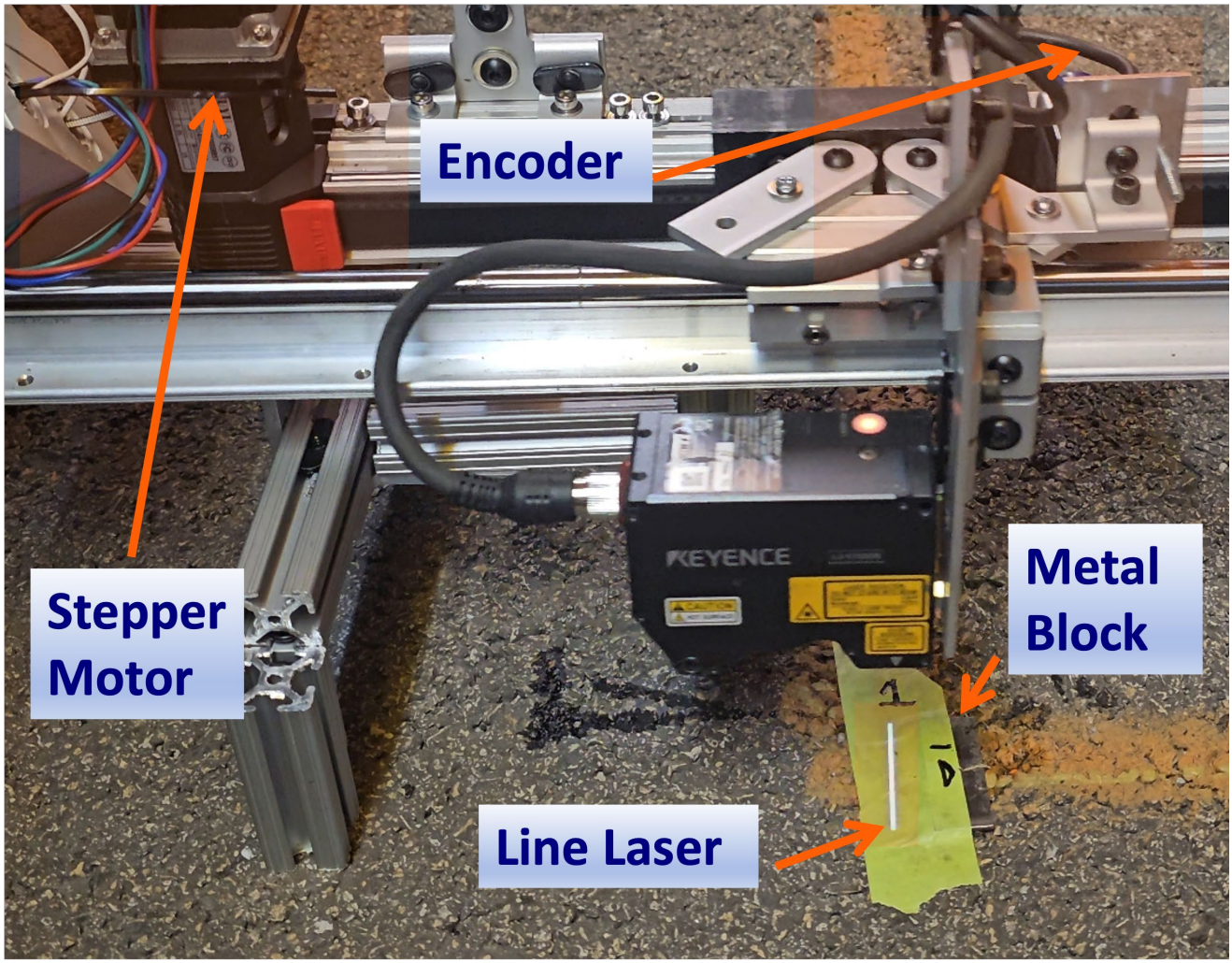

(a) Automated laser profiler

(b) Encoder

(c) Keyence software

Figure 133. Photos. I-APT rutting measurement system: (a) automated laser profiler, (b) encoder, and (c) Keyence data collection software.

Postprocessing of Profiles

To align transverse profiles across multiple passes and analyze deformation trends under cumulative loading, a customized data-processing pipeline was developed. The process involved the following steps:

- **Step 1: Profile Stitching**—Sequentially merge three captured profiles to reconstruct a complete cross-section of the pavement surface (Figure 134-a).
- **Step 2: Reference Metal Block Extraction**—Identify key points on the reference metal blocks, used for alignment through linear regression techniques (Figure 134-b).
- **Step 3: Low-Pass Filtering**—Apply a low-pass filter to smooth the profiles and reduce noise, enhancing the accuracy of rutting parameter extraction (Figure 134-c).
- **Step 4: Reference Profile Subtraction**—To isolate rutting, remove the initial pavement condition from each profile. A direct reference profile was not available for D4-50-12.5-0 (Section F), so a polynomial regression was used to approximate the initial state.
- **Step 5: Linear Regression Correction**—Fit a line between two points at the outer edges of the profile—areas presumed unaffected by traffic loading—and subtract to correct for slight variations in profiler leg height caused by maintenance adjustments or dust accumulation (Figure 134-e).

Finally, a moving average filter was applied to further reduce resolution artifacts while preserving essential deformation features.

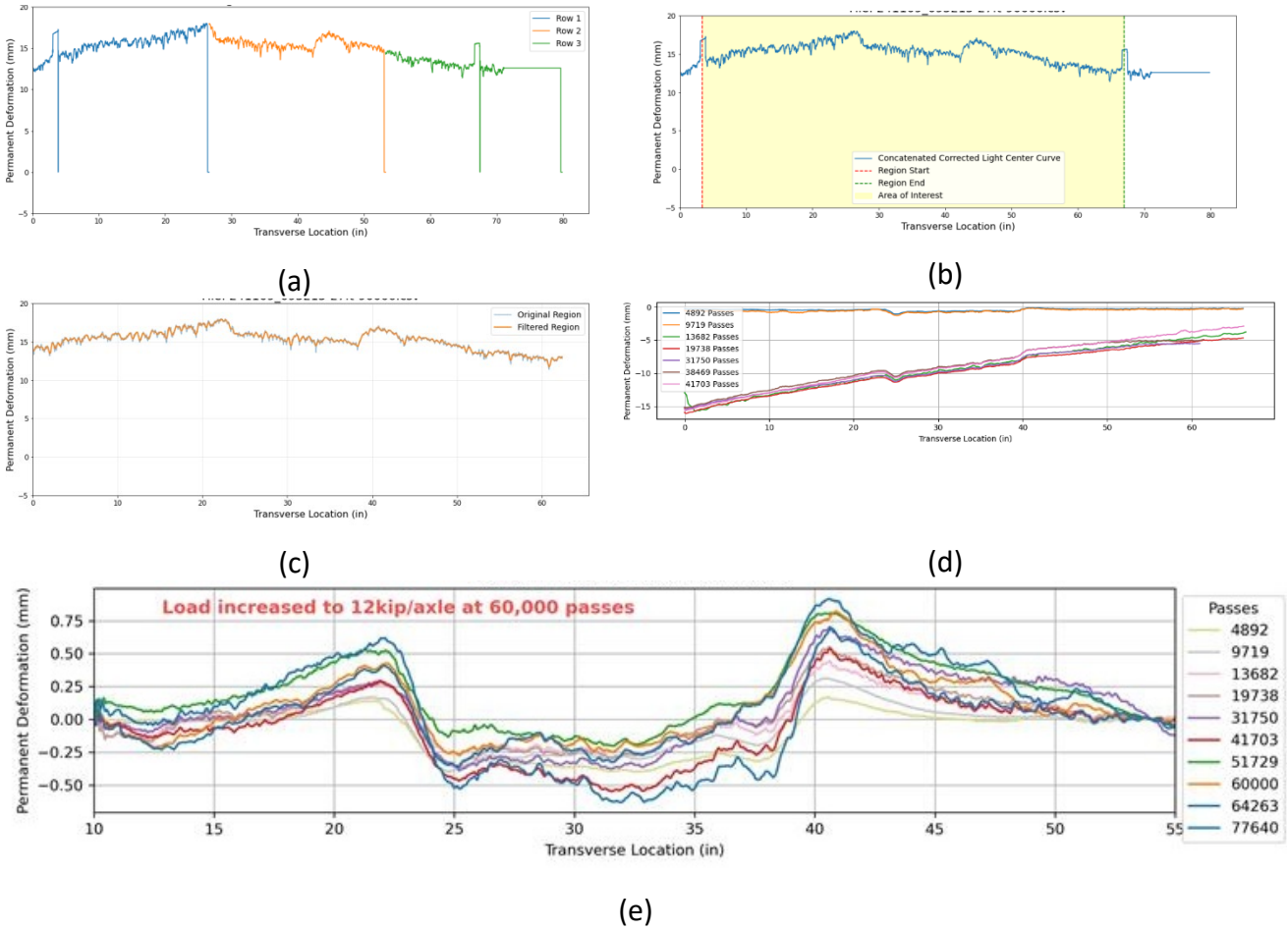

Figure 134. Photos. Workflow of the laser-scanner and rutting profile analysis.

Computation of Shoving and Rutting Parameter

To quantify pavement rutting, the following parameters were computed:

- Shoving: The peak elevations on either side of the central rut were identified.
- Depression: Measured as the average deformation within the central 15 in of the wheel path, representing the rut depth.
- Total Rutting: Computed as the sum of average shoving and depression values, providing the total rutting.

A detailed graphical representation of these parameters is included in Figure 135. The shoulder peak shoving values were measured at 1.43 mm at 22.8 in and 1.32 mm at 41.5 in, so the shoving for this location's passes is 1.38 mm. Additionally, the Middle Average value, calculated as the average deformation within the central rutting zone, was −0.64 mm at 31.8 in, with the central 15 in section used for rutting depth computation. Therefore, the total permanent deformation is 2.02 mm (1 mm = 0.04 in).

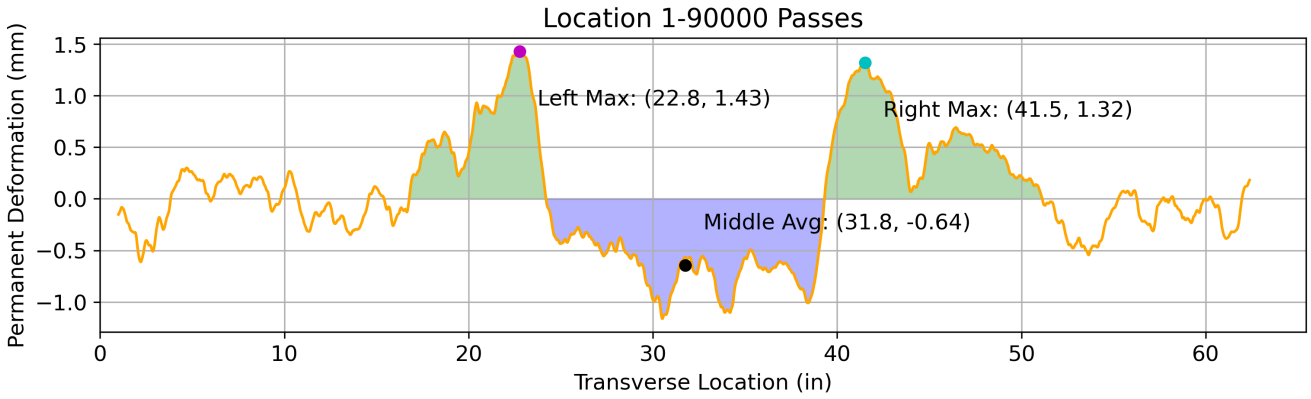

Figure 135. Photo. Shoving and rutting parameter computation.

In general shoving was more pronounced; it occurred at a faster rate than depression within the wheel path, as illustrated in Figure 136, because the underlying CRCP did not deform. Consequently, the SMA and HMA layers experienced measured shoving and depression.

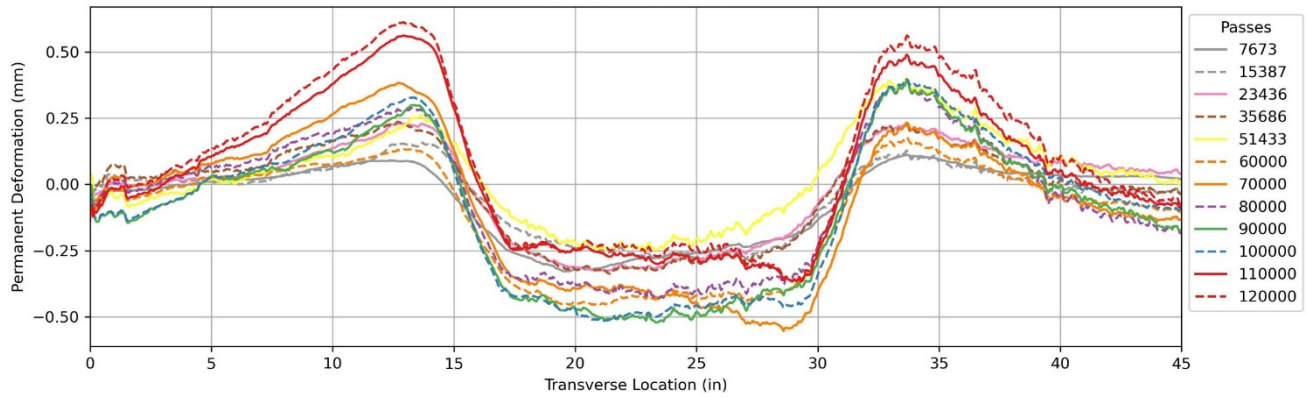

Figure 136. Graph. Laser transverse profiles progression for T1-80-12.5-0.

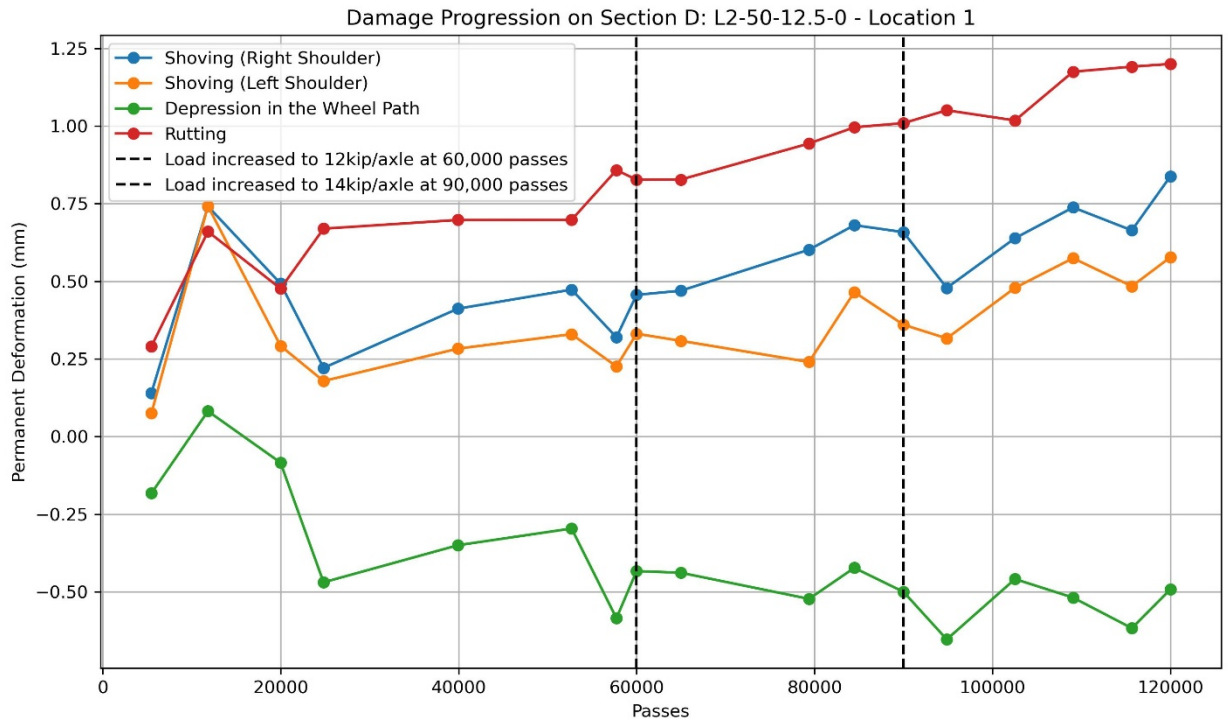

(a) L2-50-12.5-0

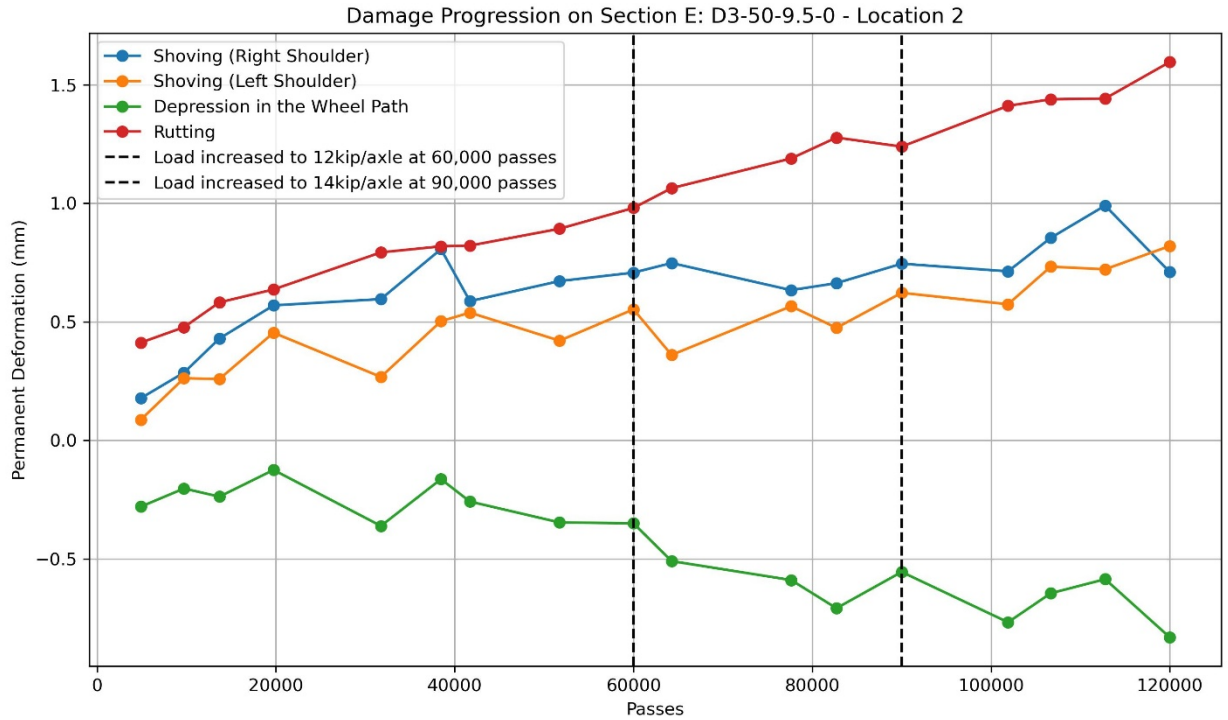

(b) D3-50-9.5-0

Figure 137. Graph. Accumulation of shoving and depression in the wheel path during continuous loading for two sections.

Verification of Measurement Goodness

Pavement section data were revised for any rest periods during testing due to surface measurements or operational logistics. If the rest period resulted in pavement rebound or recovery when the pavement was not loaded, the corresponding data points were excluded from further analysis, as illustrated in Figure 138 through Figure 143. Scheduled stops for load ramping are identified with vertical dot black lines and unexpected stops with red dash vertical lines. The data screening was performed using a two-step iterative procedure:

1. Rutting trend, to define expected rutting progression, was first established for each section:
    - 0–60,000 passes: Power-law model.
    - 60,000–90,000 and 90,000–120,000 passes: Linear models, each starts at the last fitted point of the preceding segment.
2. Identification and removal of inconsistent data points:
    - Data after a loading stop.
    - Extended pavement recovery inconsistent with expected rutting trend.

In Figure 138 through Figure 143, measured rutting data are shown as blue circular markers and excluded data points are identified with an added orange outline. Extrapolation was added to illustrate the expected rutting progression should no load ramps exist.

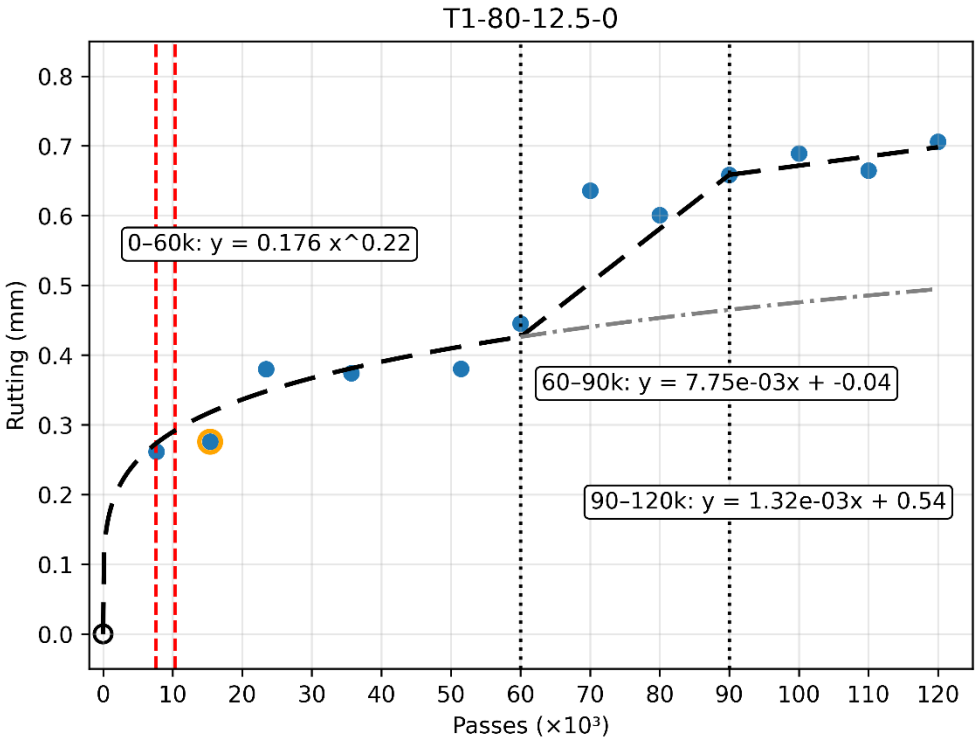

Figure 138. Graph. Rutting progression for SMA section T1-80-12.5-0 with piecewise trend fitting.

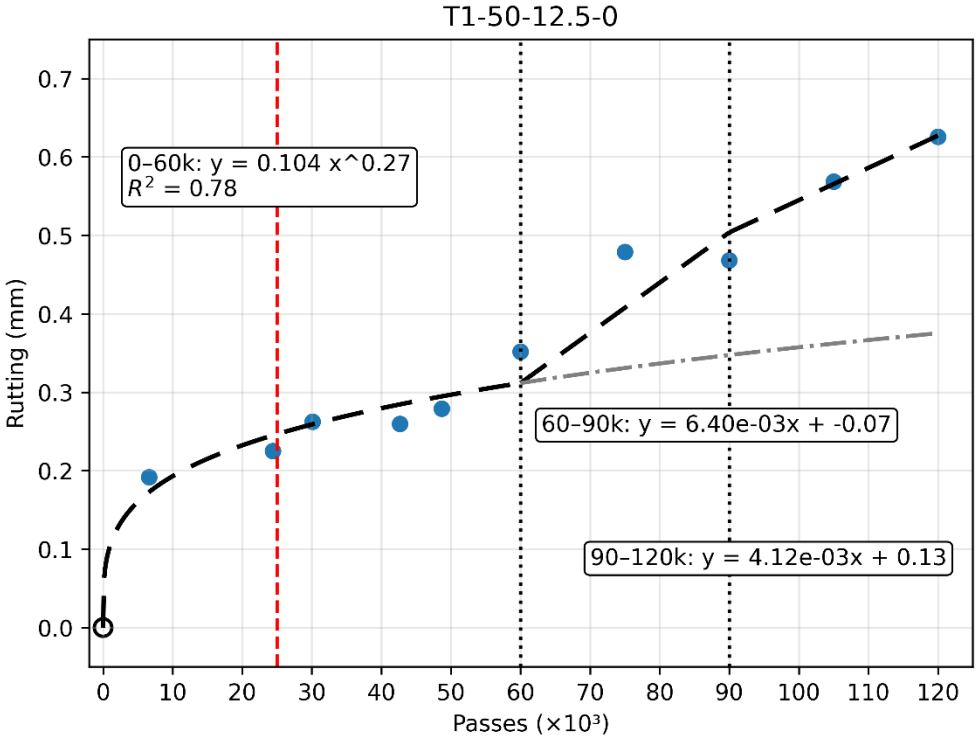

Figure 139. Graph. Rutting progression for SMA section T1-50-12.5-0 with piecewise trend fitting.

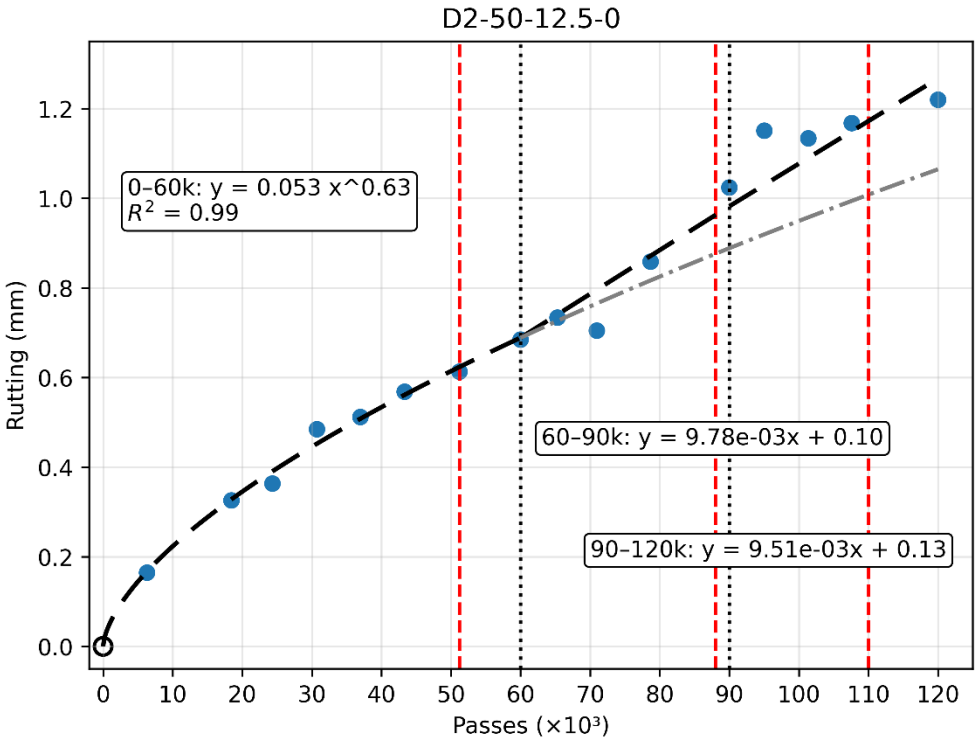

Figure 140. Graph. Rutting progression for SMA section D2-50-12.5-0 with piecewise trend fitting.

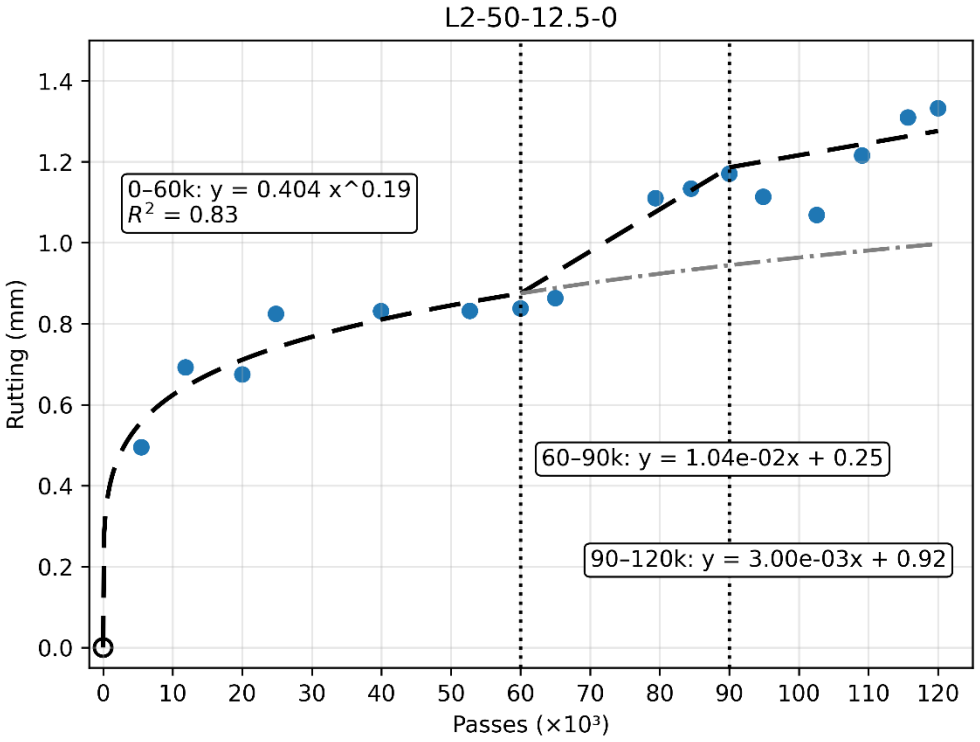

Figure 141. Graph. Rutting progression for SMA section L2-50-12.5-0 with piecewise trend fitting.

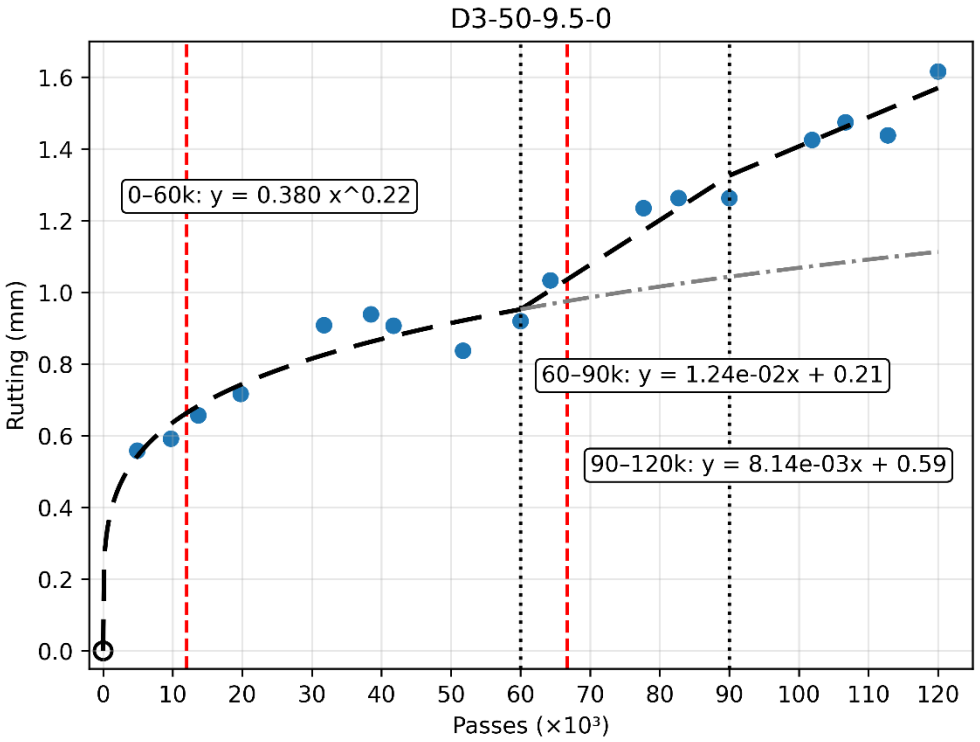

Figure 142. Graph. Rutting progression for SMA section D3-50-9.5-0 with piecewise trend fitting.

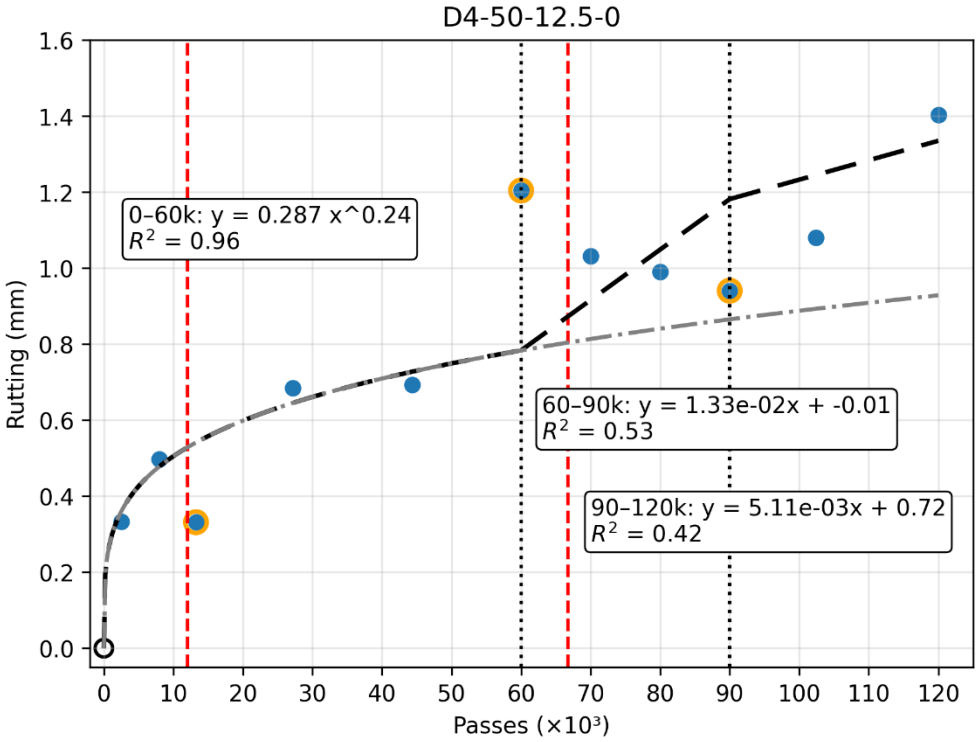

Figure 143. Graph. Rutting progression for SMA section D4-50-12.5-0 with piecewise trend fitting.

Permanent Deformation Results

The results in Figure 144 demonstrate that the pavement sections had excellent performance. D4-50-12.5-0 and D3-50-9.5-0 performed better than expected, particularly considering the HWTT rut depth values exceeded 12.5 mm after 20,000 passes.

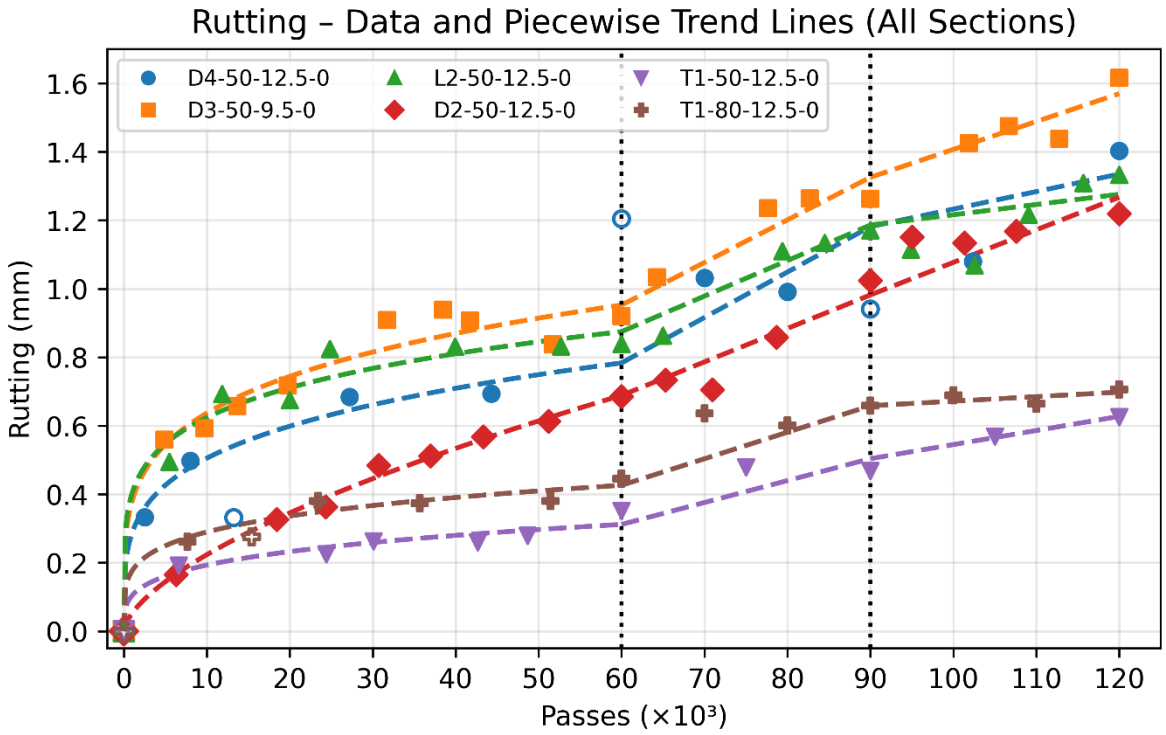

Figure 144. Graph. Damage accumulation during I-APT loading.

The initial phase of the rutting progression is usually characterized by rapid densification. More than 60% of the rutting observed within the first 60,000 passes of a typical 10 kip axle load on SMA with local aggregates occurred within the initial few thousand passes. Following this, the rutting rate stabilized, and all SMA samples exhibited a consistent slope (steady flow). When the load was escalated, the associated rutting slope increased, reflecting a rise in the SMA shear. In the last loading sequence, 14 kip/tire, rutting rates decreased despite the additional ~2 kip/tire. This suggested that load-induced stiffening from prior trafficking outweighed the effect of increased load. Hence, rutting progression became stable, and its increasing rate was reduced. The elevated loading scenario, which is not typically encountered in the field, was implemented to expedite the pavement damage process.

As evidenced by the ABI results during production and compaction, SMA aggregate structure was impacted and that was reflected at the start of trafficking. This explained the relatively high initial rutting in SMAs with local aggregates. No additional breakage occurred during loading (discussed in the following sections). However, the aggregate breakage during mixing and construction increased aggregate rounding which in turn increased mobility, especially during early trafficking. Local aggregates are relatively more susceptible to polishing and degradation than imported aggregates, as

indicated by ΔTexture and soundness, respectively. Final aggregate damage values are presented in Table 36.

Table 36. Total Damage Recorded

SMA Section	Shoving Average (in) [mm]	Depression in Wheel Path (in) [mm]	Total Rutting (in) [mm]
T1-80-12.5-0	0.026 [0.65]	−0.002 [−0.05]	0.028 [0.71]
T1-50-12.5-0	0.015 [0.37]	−0.010 [−0.26]	0.025 [0.63]
D2-50-12.5-0	0.033 [0.84]	−0.015 [−0.37]	0.048 [1.22]
L2-50-12.5-0	0.022 [0.57]	−0.030 [−0.77]	0.052 [1.33]
D3-50-9.5-0	0.034 [0.87]	−0.030 [−0.75]	0.064 [1.62]
D4-50-12.5-0	0.026 [0.66]	−0.029 [−0.74]	0.055 [1.40]

Overall, total rutting remained low across all sections, and all SMA sections demonstrated robust performance. Further comparison between laboratory and full-scale tests are presented next.

AGGREGATE BREAKAGE AFTER I-APT LOADING

Cores were obtained from the middle of the wheel path after I-APT loading was completed as well as from the unloaded mid-lane. The measured thickness and density of the SMA layer of each core is presented in Table 37. Statistical comparisons were performed using a two-tailed t-test, assuming unequal variances (Welch's t-test) with a significance level of 0.05. The results indicated that the wheel-path thickness after testing was statistically lower only in D2-50-12.5-0 and higher in T1-80-12.5-0 and T1-50-12.5-0. The differences are within paving thickness tolerance and may be disregarded. Measured densities were statistically higher in T1-50-12.5-80, D2-50-12.5-0, D3-50-9.5-0, and D4-50-12.5-0, with an average density difference of approximately 1.1%. The difference may be attributed to tack coat migration or debris accumulation.

Table 37. SMA Lift Thickness and Density from Wheel-path Field Cores after I-APT Loading

SMA Section	Core	Average Thickness (in)+	Thickness (in)	Thickness Std Dev	G_{mb}	Density (%)	Average Density (%)	Density Std Dev
T1-80-12.5-0	1	2.1	2.1	0.03	2.276	93.4	93.9	0.7
	2	2.1			2.299	94.4		
T1-50-12.5-0	1	2.0	2.0	0.04	2.368	97.3	97.4	0.1
	2	2.0			2.372	97.5		
D2-50-12.5-0	1	2.2	2.2	0.05	2.389	97.8	97.6	0.2
	2	2.2			2.382	97.5		
L2-50-12.5-0	1	2.1	2.1	0.02	2.361	97.1	97.2	0.1
	2	2.0			2.365	97.3		
D3-50-9.5-0	1	2.2	2.2	0.07	2.364	95.9	96.3	0.5
	2	2.2			2.383	96.7		
D4-50-12.5-0	1	2.3	2.2	0.07	2.405	98.4	98.5	0.2
	2	2.2			2.413	98.7		

*Note: Statistically different values are in bold; + from three measurements.

Aggregate breakage was measured from field cores within the wheel path after I-APT loading was completed. The aggregates on the sawed surface of the cores were removed before the aggregates were recovered. The ABIs measured on field cores are presented in Figure 145, along with the values obtained for field cores taken before I-APT loading. To determine whether I-APT loading caused meaningful aggregate degradation, a paired statistical comparison was performed between ABI values before and after loading across all SMA sections (T1-80-12.5-0, T1-50-12.5-0, D2-50-12.5-0, L2-50-12.5-0, D3-50-9.5-0, and D4-50-12.5-0). The paired t-test resulted in a p-value of 0.180, indicating that the observed differences are statistically insignificant. Section-by-section examination showed ABI changes ranging from 2 to 10 units, which is comparable to the average ABI standard deviation of 6.1 (from field cores before APT). All SMA sections, except D4-50-12.5-0, exhibited changes well within expected measured ABI variability. Even for D4-50-12.5-0, the increase was statistically insignificant considering the overall paired analysis.

The results and analysis suggest that no meaningful aggregate breakage had occurred during I-APT loading and that ABI remained generally stable across loading of all SMA sections. This finding implies that aggregate degradation is associated with plant-production and field-compaction processes rather than in-service loading in the mixtures evaluated in this study.

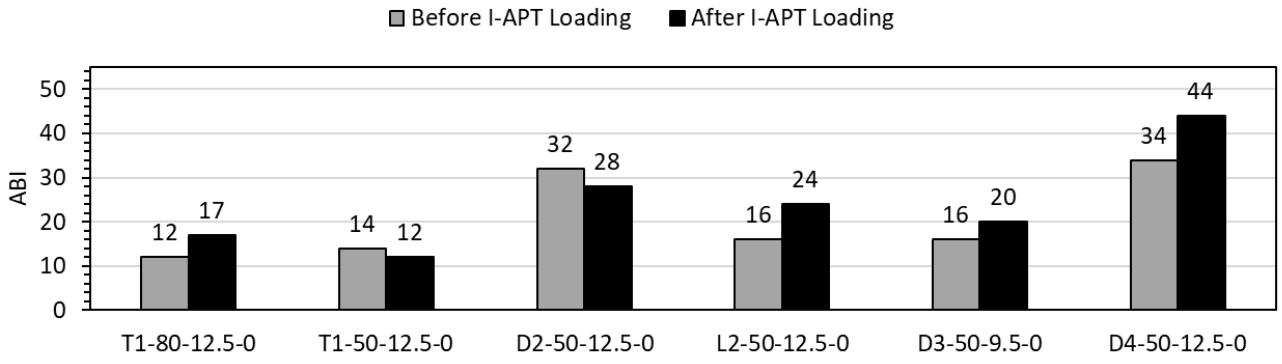

Figure 145. Graph. ABI for field cores taken before and after I-APT loading.

PAVEMENT RECOVERY DURING LOADING

Given that rutting was not associated with aggregate breakage during I-APT loading, plastic flow was further investigated. Transverse strain responses during loading were analyzed, and two metrics were used to characterize pavement recovery behavior (Figure 146): (i) peak transverse strain difference between successive wheel passes and (ii) recovery slope. Recovery slope is defined as the derivative of a logarithmic fit to the post-peak strain tail, evaluated at $t = t_o + 0.2$ s, where t_o corresponds to the second strain peak.

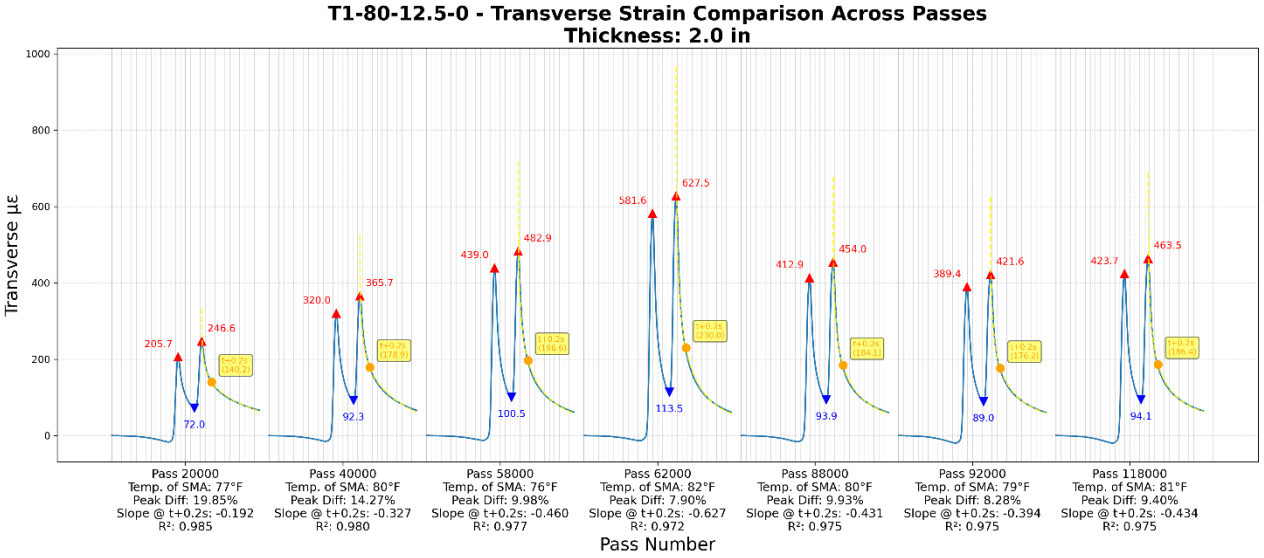
T1-80-12.5-0 - Transverse Strain Comparison Across Passes
Thickness: 2.0 in
Transverse με
Pass Number
Pass 20000
Temp. of SMA: 77°F
Peak Diff: 19.85%
Slope @ t+0.2s: -0.192
R²: 0.985
Pass 40000
Temp. of SMA: 80°F
Peak Diff: 14.27%
Slope @ t+0.2s: -0.327
R²: 0.980
Pass 58000
Temp. of SMA: 76°F
Peak Diff: 9.98%
Slope @ t+0.2s: -0.460
R²: 0.977
Pass 62000
Temp. of SMA: 82°F
Peak Diff: 7.90%
Slope @ t+0.2s: -0.627
R²: 0.972
Pass 88000
Temp. of SMA: 80°F
Peak Diff: 9.93%
Slope @ t+0.2s: -0.431
R²: 0.975
Pass 92000
Temp. of SMA: 79°F
Peak Diff: 8.28%
Slope @ t+0.2s: -0.394
R²: 0.975
Pass 118000
Temp. of SMA: 81°F
Peak Diff: 9.40%
Slope @ t+0.2s: -0.434
R²: 0.975

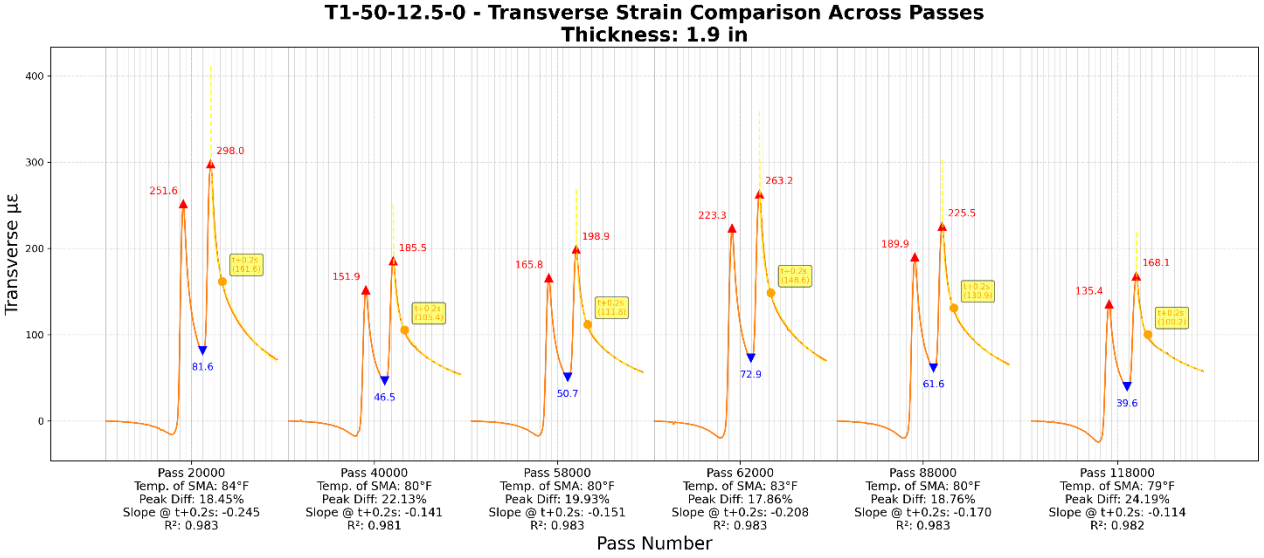
T1-50-12.5-0 - Transverse Strain Comparison Across Passes
Thickness: 1.9 in
Transverse με
Pass Number
Pass 20000
Temp. of SMA: 84°F
Peak Diff: 18.45%
Slope @ t+0.2s: -0.245
R²: 0.983
Pass 40000
Temp. of SMA: 80°F
Peak Diff: 22.13%
Slope @ t+0.2s: -0.141
R²: 0.981
Pass 58000
Temp. of SMA: 80°F
Peak Diff: 19.93%
Slope @ t+0.2s: -0.151
R²: 0.983
Pass 62000
Temp. of SMA: 83°F
Peak Diff: 17.86%
Slope @ t+0.2s: -0.208
R²: 0.983
Pass 88000
Temp. of SMA: 80°F
Peak Diff: 18.76%
Slope @ t+0.2s: -0.170
R²: 0.983
Pass 118000
Temp. of SMA: 79°F
Peak Diff: 24.19%
Slope @ t+0.2s: -0.114
R²: 0.982

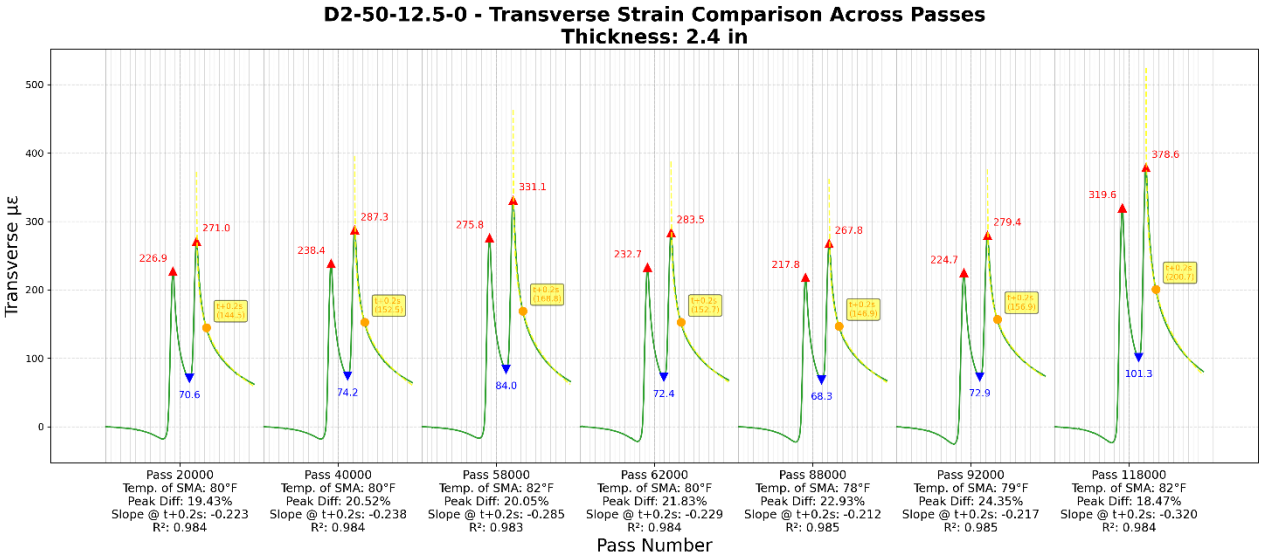
D2-50-12.5-0 - Transverse Strain Comparison Across Passes
Thickness: 2.4 in
Transverse με
Pass Number
Pass 20000
Temp. of SMA: 80°F
Peak Diff: 19.43%
Slope @ t+0.2s: -0.223
R²: 0.984
Pass 40000
Temp. of SMA: 80°F
Peak Diff: 20.52%
Slope @ t+0.2s: -0.238
R²: 0.984
Pass 58000
Temp. of SMA: 82°F
Peak Diff: 20.05%
Slope @ t+0.2s: -0.285
R²: 0.983
Pass 62000
Temp. of SMA: 80°F
Peak Diff: 21.83%
Slope @ t+0.2s: -0.229
R²: 0.984
Pass 88000
Temp. of SMA: 78°F
Peak Diff: 22.93%
Slope @ t+0.2s: -0.212
R²: 0.985
Pass 92000
Temp. of SMA: 79°F
Peak Diff: 24.35%
Slope @ t+0.2s: -0.217
R²: 0.985
Pass 118000
Temp. of SMA: 82°F
Peak Diff: 18.47%
Slope @ t+0.2s: -0.320
R²: 0.984

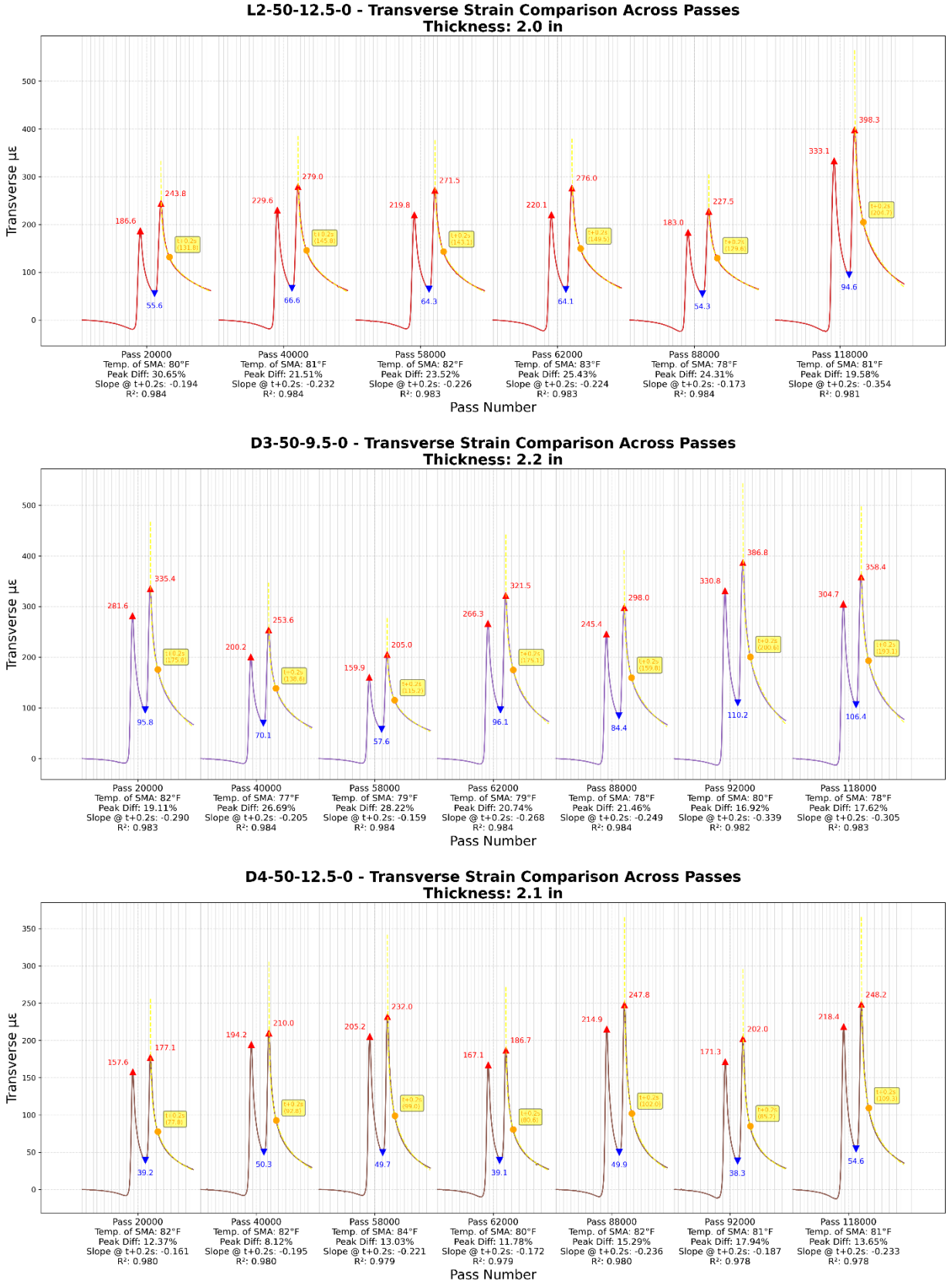

Figure 146. Graph. Pavement recovery progression during APT.

Figure 147 presents the evolution of recovery slope with traffic for all SMA sections. Across all SMA sections, the recovery slope did not exhibit a systematic change with increasing the number of loading passes. Variations in slope were primarily associated with temperature fluctuations rather than traffic accumulation, which suggested stable mixes and good packing of aggregates for all mixes. This effect was most noticeable for T1-80-12.5-0, which exhibited greater slope variability with temperature, while the remaining mixtures showed similar recovery slopes at t+0.2s. The T1 sections were loaded in late fall 2025 into December.

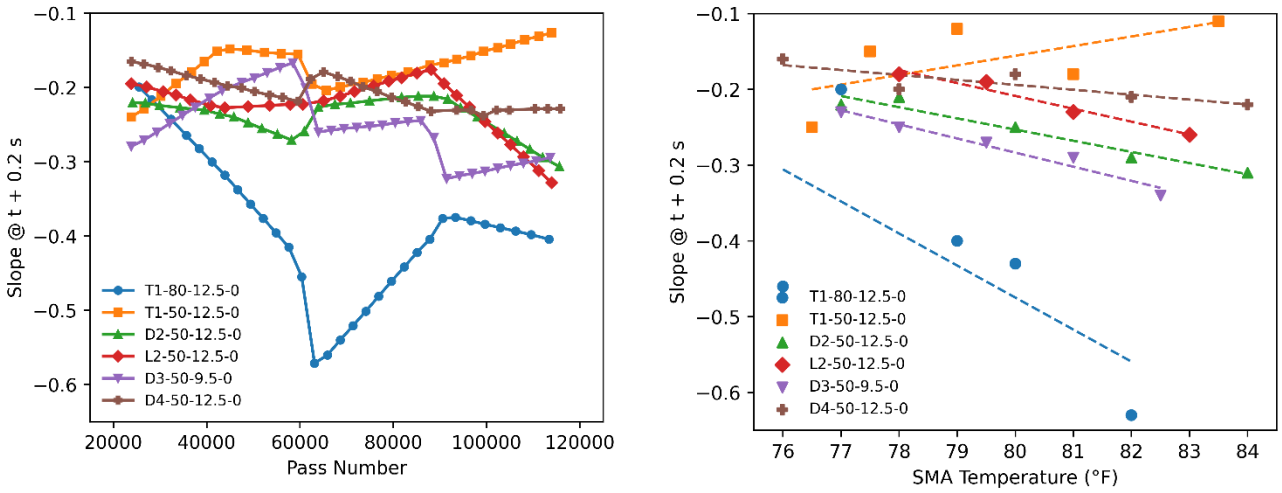

Figure 147. Graph. Recovery slope at t = t_o + 0.2 s as a function of pass number and temperature for all SMA sections.

The average peak transverse strain differences for each SMA section are summarized in Table 38. All SMA sections demonstrated effective strain recovery and provided a resilient pavement surface, exhibiting no evidence of damage even after substantial loading, including extreme axle loads.

Table 38. Section Average Peak Transverse Strain Difference

SMA Section	Average Peak Difference (%)
T1-80-12.5-0	11.4
T1-50-12.5-0	20.2
D2-50-12.5-0	21.9
L2-50-12.5-0	24.2
D3-50-9.5-0	21.5
D4-50-12.5-0	12.4

The relationship between HWTT results and full-scale pavement performance was evaluated. In addition, pavement section rutting progression was modeled using a power-law formulation. The model parameters were linked to SMA characteristics.

RELATIONSHIP BETWEEN I-APT AND HWTT RUTTING MEASUREMENTS

The relationship between rutting progression, obtained from three experiments, was assessed. The three rutting tests are as follows: HWTT using lab-produced, lab-compacted (LPLC) SMA, HWTT using plant-produced, lab-compacted (PPLC) SMA, and full-scale I-APT. The HWTT rut depth (mm) and rate of damage, slope (mm/pass) from 5000–20,000 passes were used to predict full-scale pavement performance. The pavement performance parameters include I-APT rutting (mm) and I-APT rate of damage (mm/pass), which was computed as the slope between 10,000 and 60,000 load passes. Results are presented on Table 39.

Table 39. HWTT Rut Depths and Damage Rates

SMA Section	LPLC Rutting (mm)	LPLC Slope	PPLC Rutting (mm)	PPLC Slope	I-APT Rut Depth (mm)	I-APT Rutting Slope (mm/pass)
T1-80-12.5-0	6.2	1.7E-04	3.5	0.5E-04	0.7	0.0038
T1-50-12.5-0	7.4	2.2E-04	4.2	0.8E-04	0.6	0.0029
D2-50-12.5-0	8.6	2.3E-04	4.8	0.8E-04	1.2	0.0086
L2-50-12.5-0	12.0	3.9E-04	6.5	1.5E-04	1.3	0.0030
D3-50-9.5-0	16.4	6.9E-04	7.4	1.9E-04	1.6	0.0065
D4-50-9.5-0	18.9	7.7E-04	8.3	2.3E-04	1.4	0.0140

Table 40 summarizes the Pearson correlation coefficients between HWTT results and full-scale I-APT performance metrics. The LPLC rut depth showed good correlation with the I-APT damage rate, whereas the PPLC rut depth was a good predictor of final I-APT rutting. These strong correlations indicate that, although HWTT is an empirical test, it provides a reliable indication of full-scale rutting behavior. This finding supports the use of HWTT-derived performance-based parameters as viable criteria for evaluating SMA and ensuring adequate potential field performance. The behavior of T1-50-12.5-0 and D2-50-12.5-0 was similar despite the difference in aggregate.

Table 40. Pearson Correlation between HWTT Metrics and I-APT Performance Indicators

Predictor	R-value (I-APT Slope Prediction)	R-value (I-APT Rutting Prediction)
LPLC Rutting	0.691	0.843
LPLC Slope	0.667	0.809
PPLC Rutting	0.636	0.873
PPLC Slope	0.631	0.817

The rut depths measured using HWTT and I-APT were closely related, despite differences in their damage mechanisms. HWTT subjects SMA specimens to repeated loading from a steel wheel while submerged in water at elevated temperatures, whereas I-APT applies actual tire loading at average service temperatures on a dry pavement structure. Consequently, HWTT provides a conservative assessment of SMA rutting susceptibility compared with full-scale accelerated pavement testing.

RELATIONSHIP BETWEEN I-APT AND HWTT BASED ON SMA AGGREGATE SKELETON AND PROPERTIES

Figure 148 and Figure 149 illustrate the relationships between aggregate properties per the HWTT results and I-APT rutting progression rate. Aggregate soundness and susceptibility to polish appear to be related to I-APT rutting results as well.

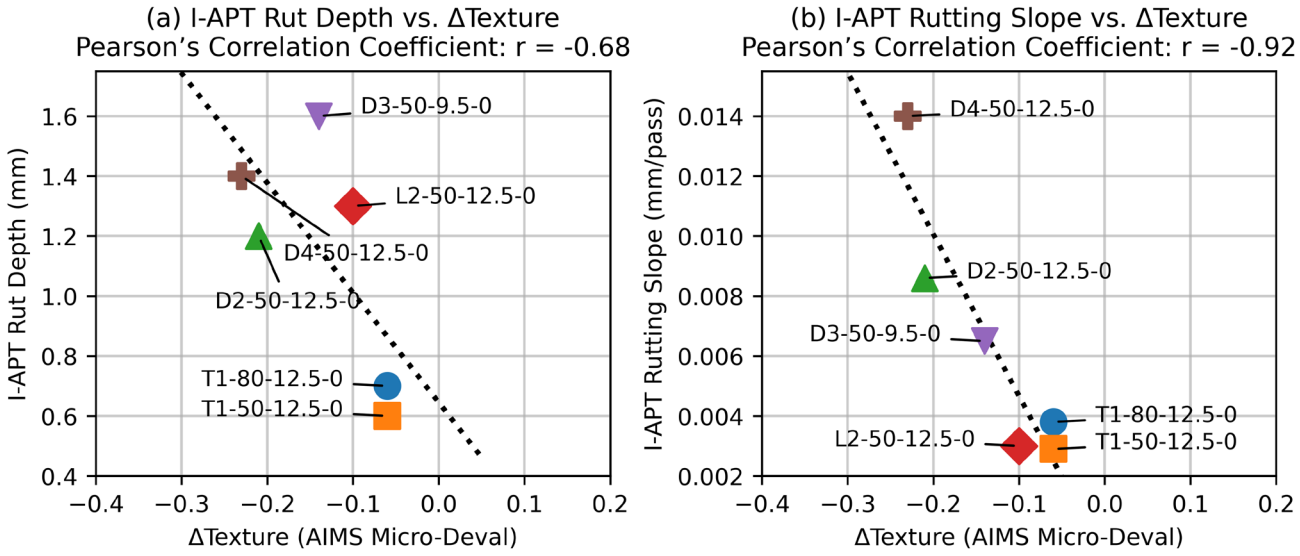

Figure 148. Graph. I-APT (a) rut depth and (b) rutting slope versus aggregate surface texture loss (ΔTexture) measured using AIMS after Micro-Deval testing.

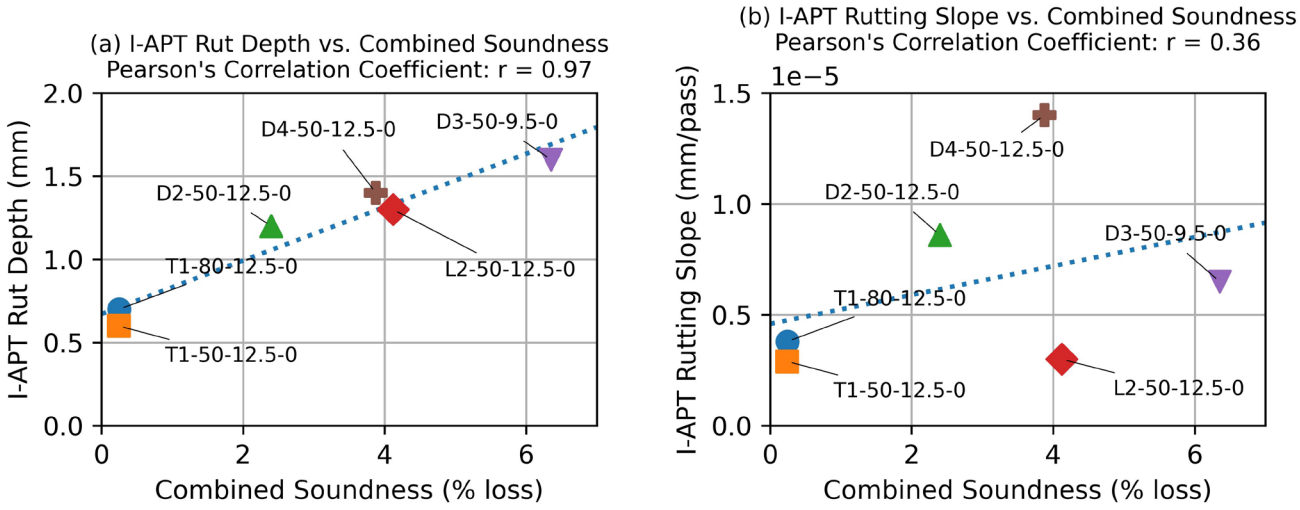

Figure 149. Graph. Relationships between aggregate combined soundness and APT rutting performance for the evaluated SMA sections: (a) total rut depth and (b) rutting slope.

Although the soundness test was originally developed to simulate aggregate degradation under weathering cycles, it has been recognized as an indicator of aggregate mechanical integrity. Crystallization pressure generated during the soundness test induces internal tensile stresses that propagate microcracks and exploit weak mineral bonds and poorly cemented grain boundaries, which are the same features that fracture aggregate under mechanical loading (Lees & Kennedy, 1975). Consequently, weak aggregates would experience mass loss, regardless of stress source (i.e., environmental or mechanical loading). Figure 15 showed that aggregates with relatively higher soundness loss exhibited greater degradation during SMA compaction. Therefore, the soundness test has been used by agencies to screen aggregates prone to breakdown during production, construction, and early service life of unbound layers (Saeed et al., 2001).

The ABIs for all SMA are presented in Figure 150. Aggregate breakage was observed during laboratory compaction, laboratory loading, and field compaction, with the magnitude governed by aggregate quality and compaction effort, as discussed in Chapter 2. In contrast, little to no additional aggregate breakage was measured following I-APT loading. ABI values were higher after plant production than after laboratory production, indicating plant production is more aggressive on aggregates than laboratory mixing. Similarly, field compaction resulted in greater aggregate breakage than laboratory compaction, especially for D2-50-12.5-0 and D4-50-12.5-0. The two mixes exhibited relatively greater aggregate degradation during construction compared with the other SMAs, regardless of I-APT loading.

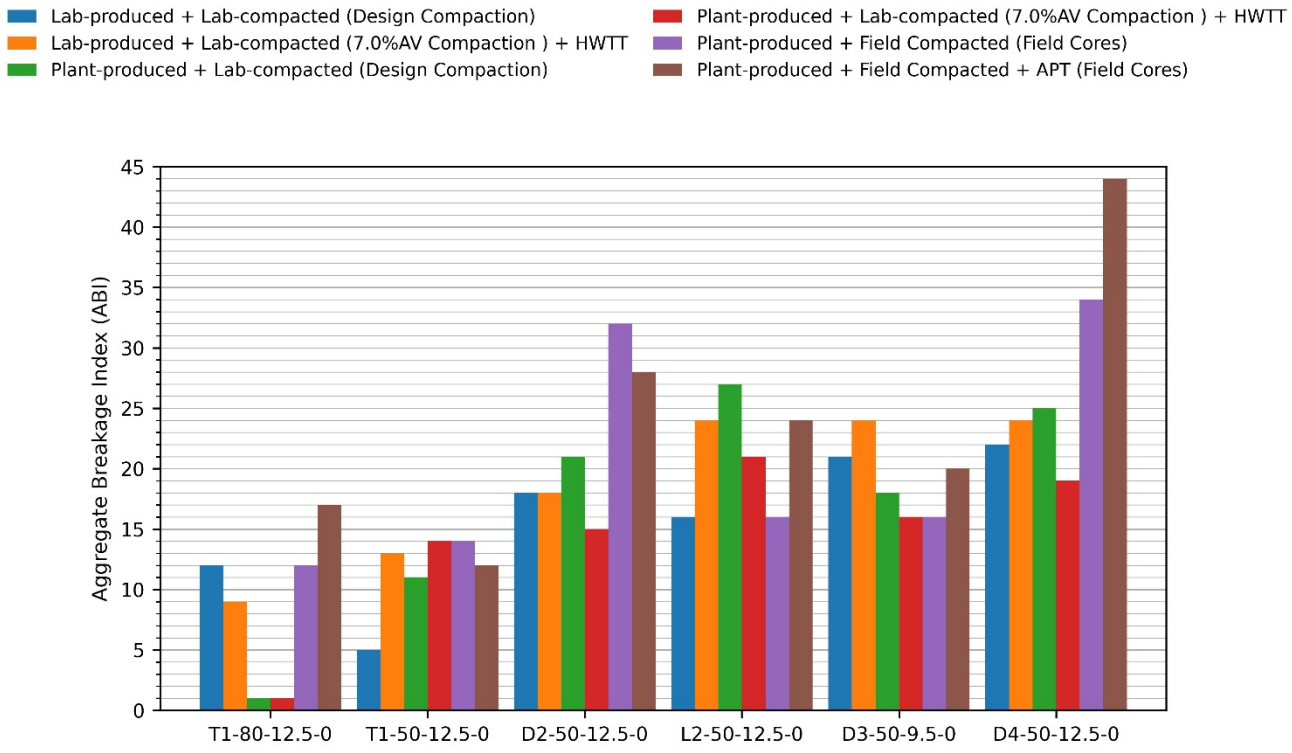

Figure 150. Graph. ABI for all SMAs measured at laboratory, field-compacted, and post I-APT stages, illustrating the evolution of aggregate degradation through production, compaction, and trafficking.

Additionally, SMAs with local aggregates showed slightly more gradation change than imported aggregates across all production and construction stages for SMA designs compacted to the same number of gyrations. Although some degradation was observed, the overall level was acceptable; when properly controlled during mixture design and construction, it should not pose a performance concern. Collectively, these findings indicate that once the SMA aggregate skeleton is established during construction, it remains stable under severe repeated traffic loading. Overall, the results highlight the critical role of mixture design and construction processes—rather than in-service traffic loading—in controlling aggregate degradation in SMA.

To evaluate the effect of aggregate breakage on rutting, early rutting after 10,000 passes was examined in relation to both in-place density and aggregate breakage. Aggregate breakage was quantified using ABI measured on plant-produced and field-compacted cores. Pearson correlation analysis showed that early I-APT rutting was moderately correlated with in-place density (r = 0.59). This confirms that compaction level governs the magnitude of early rutting. In contrast, a direct correlation between early rutting and ABI, measured on field cores, was negligible (r = 0.04). Hence, aggregate breakage alone may not explain early rutting behavior. To isolate the contribution of aggregate breakage from the dominant effect of compaction, a partial correlation analysis was performed, which quantifies the relationship between two variables after removing the linear influence of a third variable. After accounting for density, the correlation between early rutting and ABI became moderate and negative (see Figure 151). Residuals quantify the deviation between observed values and those predicted from density, allowing the influence of aggregate breakage on rutting to be evaluated independently of compaction. These results do not indicate that ABI led to greater rutting, but SMA was stable after construction.

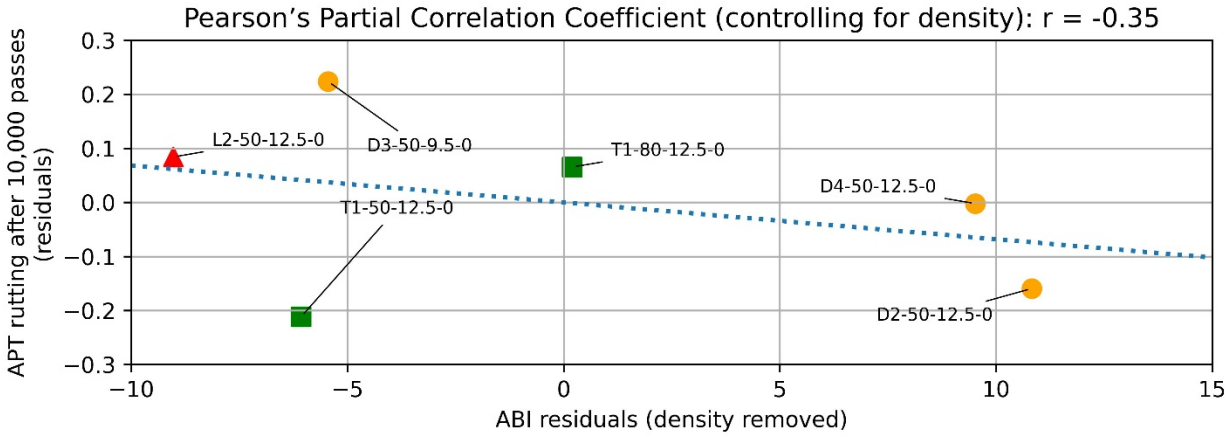

Figure 151. Graph. Partial Pearson correlation between ABI measured on plant-produced, field-compacted cores and I-APT rutting after 10,000 passes.

Rutting Prediction Model for SMA Overlays

This section describes the developed shear-based rutting model for the SMA test sections. The approach links rutting progression to the mechanistic shear responses, using readily available input parameters from SMA design.

Rutting in asphalt mixtures, including SMA, is due to densification and shear distortion. Densification dominates the initial rutting stage and is associated with volumetric reduction under the wheel path. Shear distortion usually occurs at a later stage and is associated with material flow with negligible net volume change. Generally, SMA is known to experience lower densification and distortion than HMA due to the stone-to-stone structure.

For the tested SMA sections, rutting was observed as a wheel-path depression with shoulder heaving (transverse shoving), indicating lateral material movement. This could be caused by two reasons: (i) the relatively strong underlying support by CRCP, and (ii) SMA stone-to-stone strong aggregate skeleton. Hence, shear distortion was dominant in the SMA section.

Studies have attributed rutting to near-surface shear flow at approximately 50–60 mm below the surface (Deacon et al., 2002). This region is associated with relatively higher shear concentrations under a moving wheel load (Wang & Al-Qadi, 2010). To identify critical strain response at this depth, strain components were determined using linear viscoelastic finite element (FE) under the I-APT condition. The FE calculated strains for section T1-50-12.5-0 under two tandem load levels (9 and 14 kip/tire) are presented in Figure 152 for transverse, longitudinal, and shear strains.

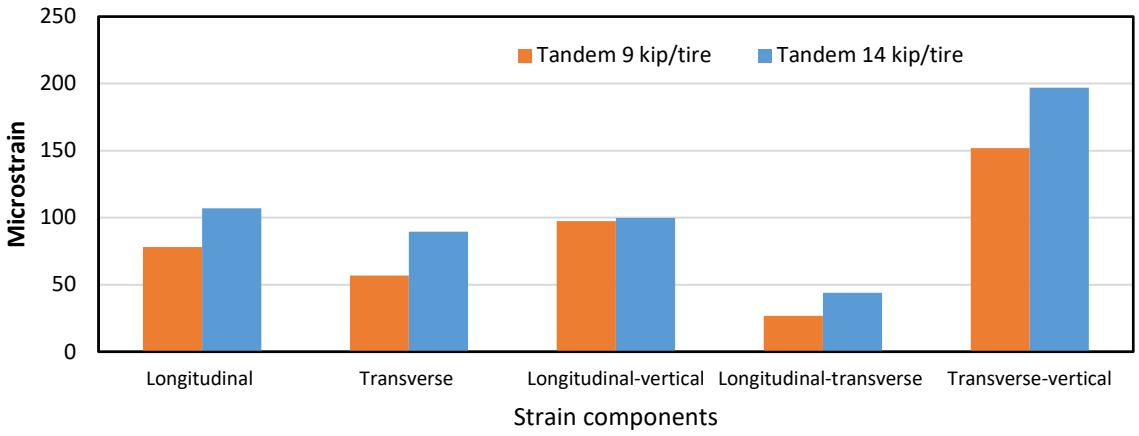

Figure 152. Graph. Calculated strains of section T1-50-12.5-0 at the bottom of the SMA layer.

Due to the relatively stiff support provided by the underlying CRCP and HMA binder layer, longitudinal and transverse normal strains showed limited sensitivity to load level (9 vs 14 kip/tire). The shear strains, on the other hand, were greater than the normal strains, due to shear flow-dominated response. The transverse-vertical shear strain (ϵ_{32}) was the largest and increased with wheel loading relative to other shear strains. The ϵ_{32} strain is consistent with the direction of transverse shear distortion induced by the wheel path. Therefore, ϵ_{32} was selected as the governing mechanistic response associated with rutting in the SMA sections.

The rut depth was referenced to an initial baseline profile from the laser profiler. As with any relative profile measurement, small baseline offsets may occur due to profile initialization and measurement repeatability. In addition, the initial loading period includes aggregate seating and packing, as well as mixture densification. This results in rapid early rutting, which is not representative of the shear-flow-

dominated response targeted by the mechanistic model. Therefore, the early rut depth in each section was excluded, while subsequent measurements were retained for analysis.

A power law function was adopted to relate the incremental rut depth accumulated during each load stage to mechanistic shear response and number of load applications:

$$\Delta RD = C * \epsilon_{32}^{m} * \Delta N^{b}$$

Figure 153. Equation. Incremental rutting transfer function.

where $\Delta RD > 0$ is incremental rut depth (mm) accumulated within a given loading stage, ϵ_{32} is transverse-vertical shear strain (transverse direction "3," vertical direction "2" evaluated for tire edge at bottom of SMA layer, $\Delta N > 0$ is number of passes applied during a stage, and *C*, *m*, and *b* are "calibrated" model parameters.

To compare rutting susceptibility across the SMA sections, a mechanistic shear input was normalized as follows:

$$\hat{\epsilon} = \frac{\epsilon_{32}}{\epsilon_{ref}}$$

Figure 154. Equation. Normalized transverse-vertical shear strain.

where ϵ_{ref} is the average maximum ϵ_{32} at the bottom of the SMA layer under 9 kip/tire tandem loading across all sections. This normalization enabled the calibration coefficient *C* to be interpreted as a mixture-specific rutting-susceptibility parameter rather than a scale factor driven solely by strain magnitude.

Rutting progression within each stage was modeled using a time-hardening power-law form:

$$RD = \left[RD_o^{\frac{1}{b}} + C^{\frac{1}{b}} \hat{\epsilon}^{\frac{m}{b}} \Delta N \right]^{b}$$

Figure 155. Equation. Time hardening rutting progression model.

where RD is the rut depth (mm) at end of a defined stage, RD_o is rut depth at start of the stage, and ΔN is number of passes accumulated within that stage. This approach preserved continuity across the full loading history. In this framework, *C* captures mixture-specific rutting susceptibility, *b* governs the curvature of rut accumulation with load repetitions, and *m* controls sensitivity to the mechanistic shear term.

Surrogate for Mechanistic Input

The mechanistic shear strain required for rutting model calibration is typically obtained from an FE analysis (or linear-elastic layered analysis, but less accurate). Neither of these methods is ready for practical implementation. Therefore, a mechanistic-empirical (ME) surrogate was developed to

replace the shear strain requirement with readily available mixture and structure parameters. The surrogate preserves the expected physical trend: Shear demand increases with applied wheel load magnitude and decreases with mixture stiffness and structural capacity.

A normalized unitless ME term was defined as follows:

$$\hat{\epsilon}_{ME} = \left(\frac{W}{W_{ref}}\right)^{p} * \frac{G^*_{ref}}{G^*_{80}} * \frac{1}{F_{thick}}$$

Figure 156. Equation. Normalized ME term.

where *W* is wheel load (kip/tire), W_{ref} is tandem 9 kip/tire reference load, *p* is load exponent (p = 1), G^*_{80} is shear modulus at 80°F and 1.13 Hz, computed from isotropic linear viscoelastic relationship $G^*_{80} = \frac{E^*_{80}}{2(1+v)}$, E^*_{80} is measured dynamic modulus at 80°F and 1.13 Hz, v = Poisson's ratio of SMA layer (assumed 0.35), G^*_{ref} is computed from a fixed reference modulus E^*_{ref} = 140 ksi using the same relationship and F_{thick} is a thickness correction factor referenced to a 2.0 in SMA lift thickness and was obtained from the thickness sensitivity relationship in Chapter 4.

The rutting transfer function was then written as follows:

$$\Delta RD = C * (\hat{\epsilon}_{ME})^{m} * (\Delta N)^{b}$$

Figure 157. Equation. General rutting transfer function using normalized ME term.

The final equivalent equation, assuming constant v, cancels the conversion factor in the modulus ratios. This formulation produced a normalized, unitless ME term that could be used as a general rutting model:

$$\Delta RD = C * \left(\frac{W}{9} * \frac{140}{E^*_{80}} * \frac{1}{F_{thick}}\right)^{m} * (\Delta N)^{b}$$

Figure 158. Equation. Proposed ME rutting transfer function.

Rutting Model Calibration and Validation

For model calibration, stage-wise rut increments were used after the effective start of each loading stage. Rutting was expressed as an increment (ΔRD), and passes were expressed as ΔN. Only points with $\Delta N > 0$ and $\Delta RD > 0$ were used in the fit. Hence, negative increments caused by measurement noise are removed, resulting in rut growth within each stage.

The calibration procedure was performed on each SMA section using least-squares fitting. Each section included three loading stages. Estimating three parameters (*C*, *m*, and *b*) for each stage produces non-unique solutions and overfits the loading history. Therefore, the exponent *m* was set to

1.0 to impose a linear dependence on the ME normalized term and improve stability across the three load levels.

The shape exponent *b* was constrained to 0.2 ≤ b ≤ 1.0. The upper bound controls accelerating rut growth with load passes, while the lower bound avoids sharp curvature when *b* is relatively small. The bounds are consistent with monotonic, non-accelerating rutting trends observed in the I-APT result curves. Therefore, a single globe shape parameter (*b*) was adopted to stabilize comparisons across the SMA and estimated at = 0.558.

An example of SMA section with fixed *b* and *m* is shown in Figure 159 for section D3-50-9.5-0. Measured and predicted rut depth progressions are illustrated.

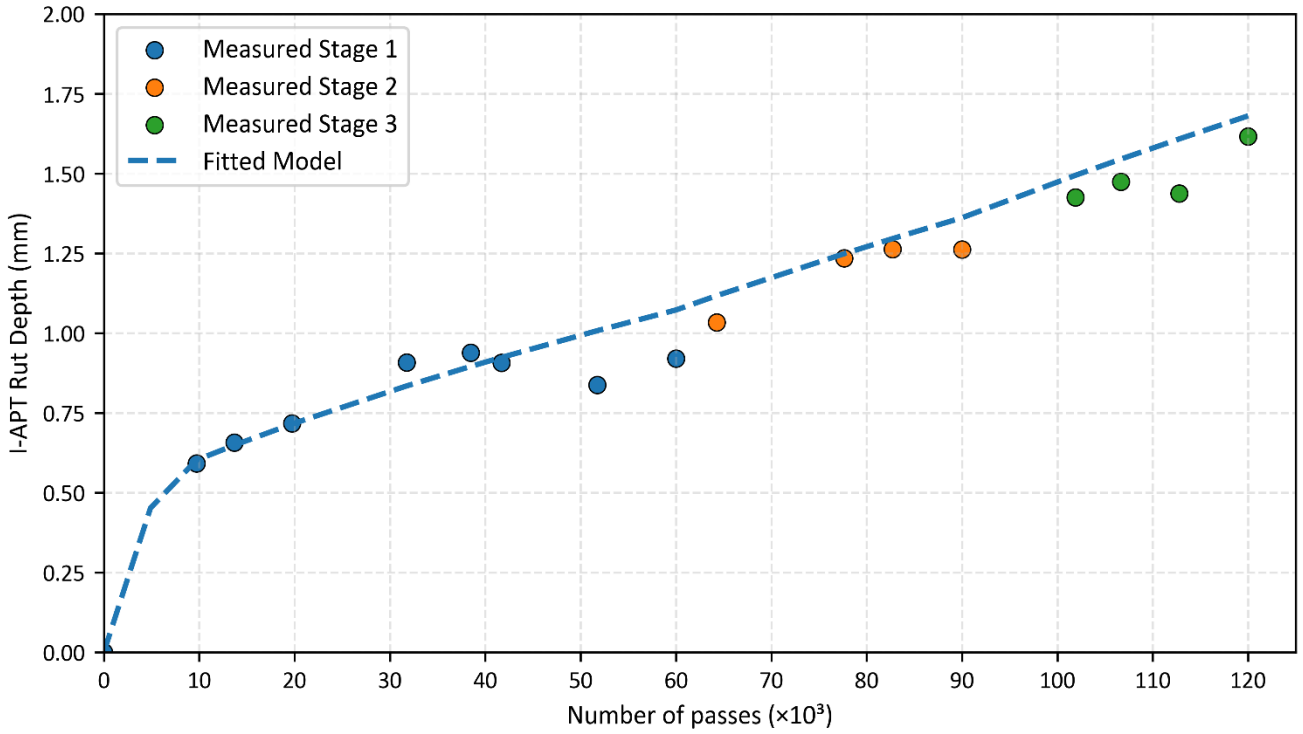

Figure 159. Graph. Measured and predicted rut depth progression for section D3-50-9.5-0.

The rutting progression model performance was evaluated using R^2, summarized in Table 41. The results showed that R^2 values ranged from 0.787 to 0.956, with an average of 0.901. The predicted values explain the rutting depth progression well, and hence, results support the use of a common rutting curve shape across the evaluated sections. The varied fitted *C* values, across the SMA sections, suggest a difference in rutting susceptibility under same loading due to SMA characteristics.

Table 41 Rutting Model Performance

Section	C	R^2	LOSO R^2
T1-80-12.5-0	6.42E-04	0.787	0.785
T1-50-12.5-0	7.18E-04	0.915	0.908
D2-50-12.5-0	1.93E-03	0.956	0.952
L2-50-12.5-0	1.61E-03	0.885	0.883
D3-50-9.5-0	1.74E-03	0.919	0.917
D4-50-12.5-0	1.29E-03	0.946	0.948
Average	–	0.901	0.899

The transferability of the curve was also evaluated using leave-one-section-out (LOSO) cross-validation. In each LOSO run, one section was withheld as the test case. The remaining five sections were used to predict the withheld section by refitting only *C*. The LOSO performance was assessed using R^2 between the measured and predicted rut depth over the modeled region shown in Table 41. LOSO R^2 values ranged from 0.785 to 0.952 with an average of 0.899 and showed minimum reduction in data explanation. The rutting curve shape was generally transferable across the evaluated sections, with section-to-section differences captured primarily through *C*.

Estimating Parameter C from Mixture Characteristics

The calibrated coefficient *C* represents mixture-specific rutting susceptibility, which is not captured by a normalized ME term. For the six SMAs, variability in *C* was attributed to mixture characteristics not explicitly modeled, including aggregate skeleton stability, aggregate durability, and internal friction.

Based on the findings reported in Chapter 2, rutting potential depends on volumetric characteristics and coarse aggregate quality. Among the evaluated aggregate indices, the soundness parameter showed the strongest agreement with HWTT rut depth. Therefore, soundness test results were used as a practical method to estimate C.

A semi-log relationship was used to fit C to soundness:

$$C = 0.0111828 * S^{0.258}$$

Figure 160. Equation. Proposed definition of *C* as a function of combined soundness.

where *S* is combined soundness (% loss).

The fitted relationship showed that *C* increased with increasing soundness for the evaluated SMAs (Figure 161). The Pearson correlation between *C* and soundness is 0.753, indicating that soundness provided a practical way to interpret mixture susceptibility using an agency-available durability indication.

Based on the framework described in this section, an illustrative example is provided for predicting rutting for the six SMA sections. The rutting susceptibility coefficient *C* was computed using the fitted *C*-soundness relationship. Using dynamic modules at 80°F and 1.13 Hz, at their respective SMA thickness, the total rut depth was predicted over 120,000 tandem axle passes of 12 kips/axle as

shown in Figure 162. The star marker shows the transition point separating the early densification stage from the shear-flow dominated stage in the model.

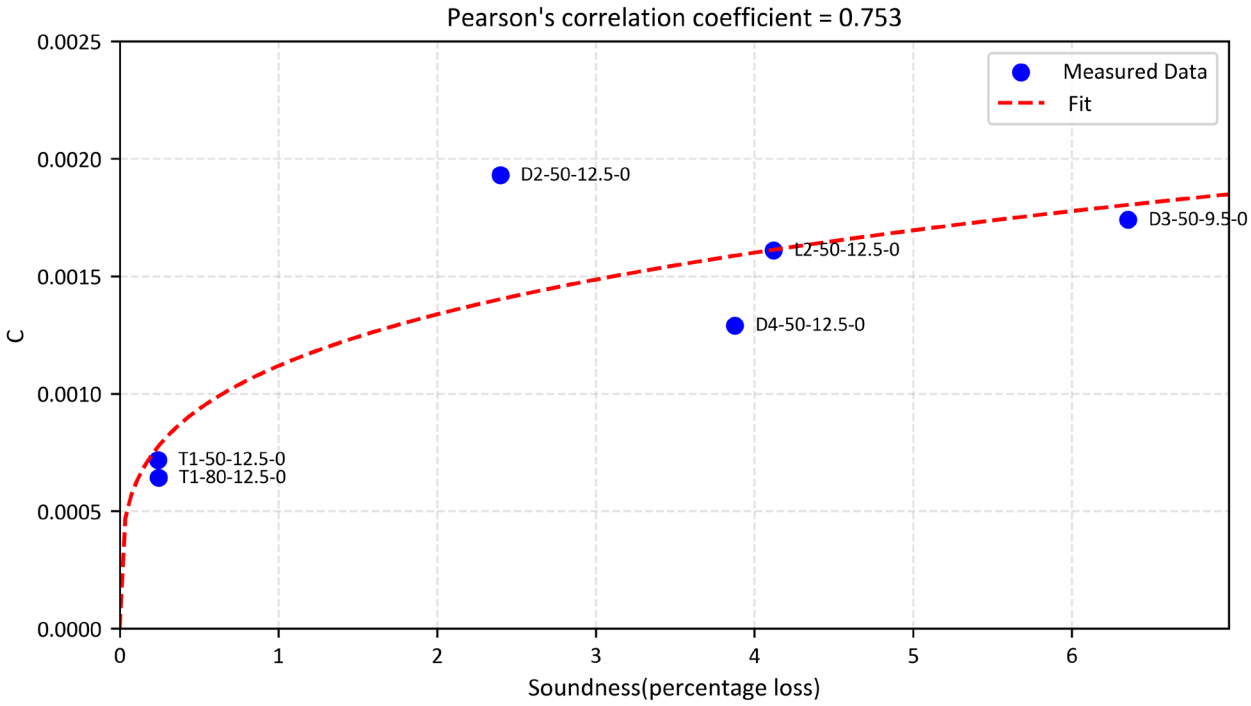

Figure 161. Graph. Relationship between *C* and aggregate soundness (percentage loss).

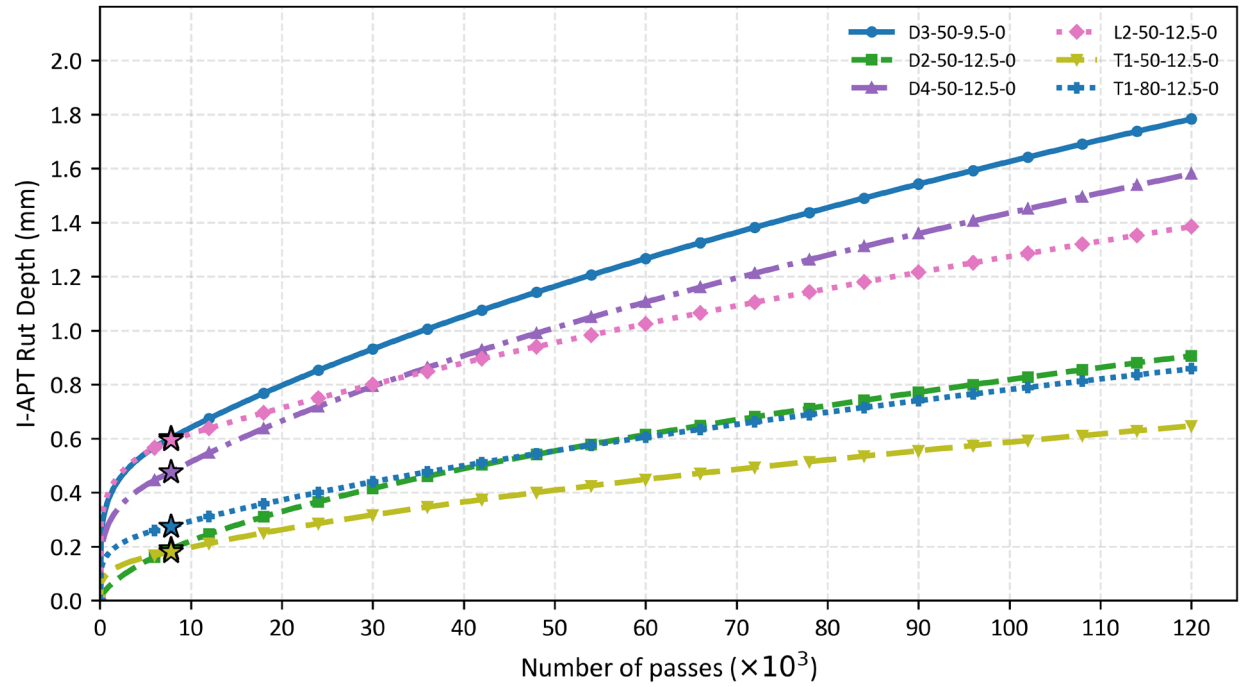

Figure 162. Graph. Predicted rut progression for SMA sections under 12 kip/tire loading.

Similarly, SMA section L2-50-12.5-0 was plotted with experimental rut depth data, followed by shear model predictions at three loading levels (10, 10, 12, and 14 kip/tire). Rutting is reported as total rut depth, capturing both densification and shear flow. Early densification is highlighted with a shaded area, after which shear flow dominates. At 10 kip/tire, the model follows the experimental trend more closely up to 60,000 passes, whereas 12 and 14 kip/tire produce progressively deeper ruts over the loading history.

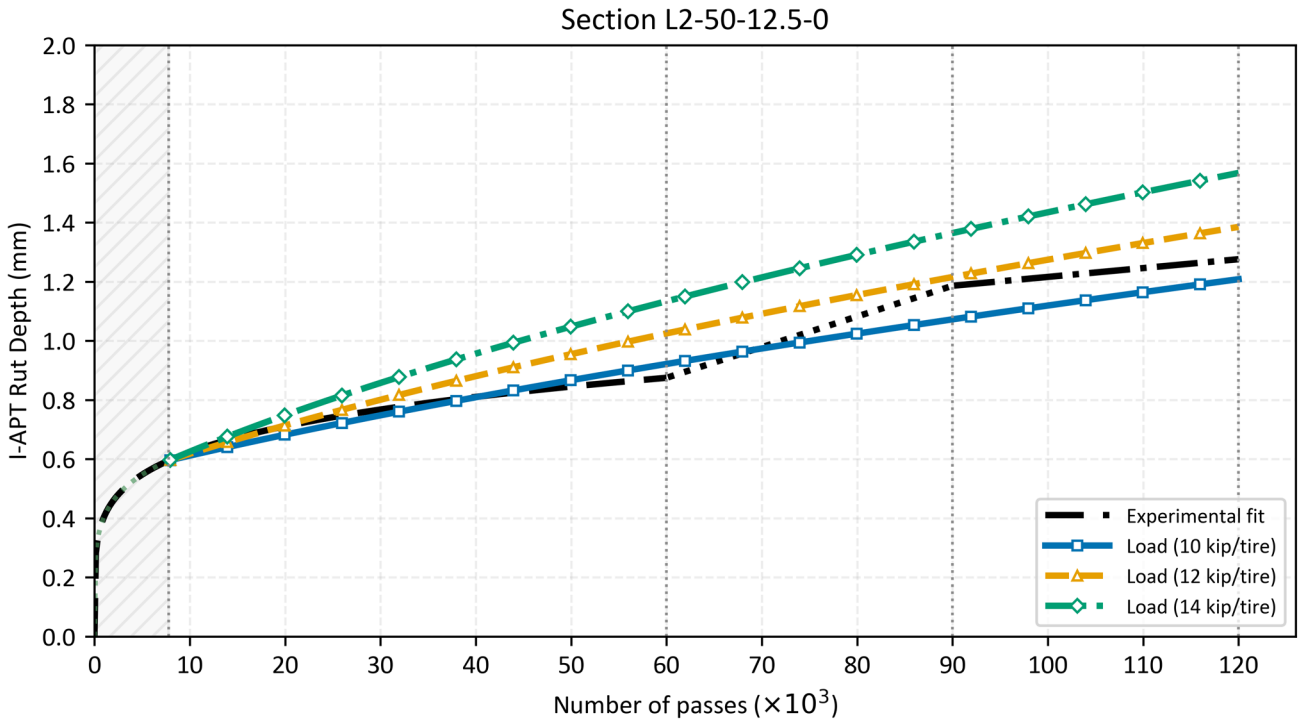

Figure 163. Graph. Rut depth response for SMA section L2-50-12.5-0: experimental piecewise fit and shear-model predictions (10/12/14 kip/tire).

SUMMARY

The responses of the six SMA sections to I-APT loading and the resulting rutting behavior were evaluated. Continuous tandem-axle loading was applied under controlled temperature conditions (80 ± 5°F) with progressively increasing axle loads over a total of 120,000 tandem-axle passes (i.e., 10 kip/axle for 60,000 passes, 12 kip/axle for 30,000 passes, and 14 kip/axle for 30,000 passes). Pavement temperature was recorded continuously, and the pavement sections were monitored systematically to assess structural response, rutting progression, and potential material degradation.

Overall, all SMA sections demonstrated excellent performance, exhibiting minimal rutting even under severe loading conditions. Under channelized loading, wheel path rutting was primarily governed by lateral material flow (shoving) rather than vertical deformation. Total rutting remained low for all mixtures, with values below 1.6 mm after up to 120,000 loading passes. Although SMAs containing local aggregates generally accumulated slightly higher rutting than the control SMAs with imported aggregates, the differences were modest and occurred mainly during the initial few thousand passes

and following the increase in axle loads to 12 and 14 kip. Consequently, these differences do not indicate structural inadequacy.

Notably, sections D3-50-9.5-0 and D4-50-12.5-0 performed better than anticipated based on their laboratory HWTT results. This behavior, combined with the stiff support provided by the underlying CRCP, indicates stable mixtures, effective aggregate packing, and limited aggregate degradation. Paired statistical comparisons of ABI values from field cores collected before and after I-APT testing confirmed insignificant aggregate breakage or degradation. Further analysis suggested that most of the aggregate degradation occurred during the mixing process and field construction with limited degradation occurring during loading of pavement sections. In addition, HWTT results showed a similar trend as that of rutting under I-APT for SMAs.

As expected, transverse strain increased with higher axle loads, whereas longitudinal strain remained stable across all sections. Pavement recovery behavior was evaluated using recovery slope and peak transverse strain difference metrics. For all SMA sections, the strain recovery paths remained consistent with increasing traffic, and observed variability was primarily attributed to temperature fluctuations rather than progressive material damage.

CHAPTER 6: BENEFIT QUANTIFICATION

In this chapter, life cycle assessment (LCA) and life cycle cost analysis (LCCA) tools were used to quantify the respective environmental and economic benefits of utilizing Illinois local aggregates in SMA. I-APT results provided performance inputs that determine maintenance and rehabilitation timing. Mixes produced with Illinois aggregates were compared against control mixes, and the robustness of the outcomes were tested through sensitivity analyses.

BACKGROUND

Life cycle assessment quantifies the environmental impact across a product system's full life cycle, from raw material extraction until its end of life. For pavements, the life cycle encompasses five stages: materials production, construction, use, maintenance, and end of life. Numerous studies demonstrate the value of using LCA in flexible pavement decision-making. In one study, for example, LCA demonstrated that reclaimed asphalt pavement (RAP) can reduce the emissions of binder course manufacturing by up to 28% (Aurangzeb et al., 2014). Similar studies have also been conducted to evaluate the environmental performance of similar recycled materials such as fly ash, steel slag, and plastics. In another, replacing styrene-butadiene-styrene (SBS) polymers with waste plastics in HMA potentially reduced the energy consumption of the materials stage by up to 8% (Diab & Al-Qadi, 2024). In addition, evidence from LCAs indicates that replacing 10% of the asphalt binder with a bio-based alternative can lower CO_2 emissions by a factor of 5 and methane emissions by a factor of 3 (Samieadel et al., 2018). Besides the materials stage, LCA has also been used for decision-making in other life cycle stages such as the construction and maintenance of asphalt pavements. For instance, using cold in-place recycling for rehabilitation can reduce energy consumption and acidification by up to 18%, compared to traditional mill-and-fill approaches (Turk et al., 2016).

Life cycle cost analysis evaluates the economic efficiency of competing pavement alternatives by converting all relevant costs over a defined analysis period to their present net value. Federal Highway Administration (FHWA) guidance outlines standard steps to conduct pavement LCCA. These steps include defining alternatives and performance-based treatment schedules; estimating costs for construction, routine maintenance, rehabilitation, and end-of-life actions; treating uncertainty; and reporting results in consistent terms for comparison (FHWA, 2022). In practice, agencies apply LCCA to decisions such as selecting higher RAP contents versus virgin mixes, choosing in-place recycling over conventional overlays, or comparing warm-mix and hot-mix asphalt (Babashamsi et al., 2016). In pavement decisions, environmental and economic objectives often pull in different directions: Lower-impact options can carry higher upfront costs, while least-cost choices may shift burdens to energy use, emissions, or future maintenance. Hence, it is important that LCA and LCCA are conducted in parallel when choosing between alternatives. Examples include higher use of reclaimed materials such as RAP, which agencies adopt for simultaneous cost savings and embodied-impact reductions (Qiao et al., 2019).

The consideration of all life cycle stages gives LCA the totality that is needed to obtain accurate environmental impacts without overlooking important components. Many pavement LCAs restrict their scope to materials production and construction. Extending the boundary to the use stage and to

maintenance and rehabilitation requires credible forecasts of deterioration, traffic loading, climate exposure, and treatment timing. When field performance data are available, material choices can be linked to observable performance under realistic loads and climates, resulting in more accurate LCA and LCCA results. FHWA (2025) demonstrated that controlled, repeatable loading on full-scale structures supported the verification of performance models that ultimately feed life cycle inventories and maintenance schedules.

Using locally sourced aggregates for SMA can help lower economic and environmental costs, as long as pavement performance is not compromised, by reducing the need to transport materials from neighboring states. In this project, LCA and LCCA were employed to quantify the respective environmental and economic costs of using local aggregates available in Illinois compared to hauling them from other states.

LIFE CYCLE ASSESSMENT METHODOLOGY

This LCA is conducted based on the standards provided by the International Standardization Organization (ISO), more precisely ISO 14040/14044 (2006), which describe the principles, framework, and requirements for conducting an LCA. As recommended by these standards, LCA must be conducted in four main steps: (1) goal and scope definition, (2) life cycle inventory, (3) life cycle impact assessment, and (4) interpretation.

Goal and Scope Definition

The purpose of this study is to quantify and compare the environmental burdens of SMA pavements produced with (i) locally sourced Illinois aggregates and (ii) imported aggregates from neighboring states to inform material-sourcing and specification decisions. The study adopts a comparative, attributional LCA aligned with FHWA current pavement LCA guidance (Harvey et al., 2016).

The functional unit is 1 lane-mile of flexible pavement (12 ft lane width) with a 2 in SMA surface course, designed for an analysis period of 50 years under typical Illinois climatic and traffic conditions. All inventories, impacts, and maintenance plans are normalized to this unit. Two primary scenarios were considered: (i) SMA with local aggregates and (ii) SMA with imported aggregates. For each scenario, four project locations were considered across the state of Illinois, labeled as Case 1, Case 2, Case 3, and Case 4, as illustrated in Figure 164. For each project location, the closest local and non-local quarry was found and used for the impact calculations of the six mix designs used in the I-APT and presented in Table 7.

The comparative LCA system boundary includes four pavement life cycle stages: materials, construction, use, and maintenance. The end-of-life stage is excluded from the system boundary, as it is assumed to be identical across the LCA alternatives (Figure 165). Energy and water were modeled as inputs to each life cycle stage, and emissions and waste were modeled as outputs to air, water, and land. The boundary was applied identically to both sourcing scenarios—namely, SMA with Illinois aggregates and SMA with imported aggregates. The following sections describe the main processes included in each stage for LCA calculations.

Figure 164. Illustration. Project locations used for the LCA scenarios.

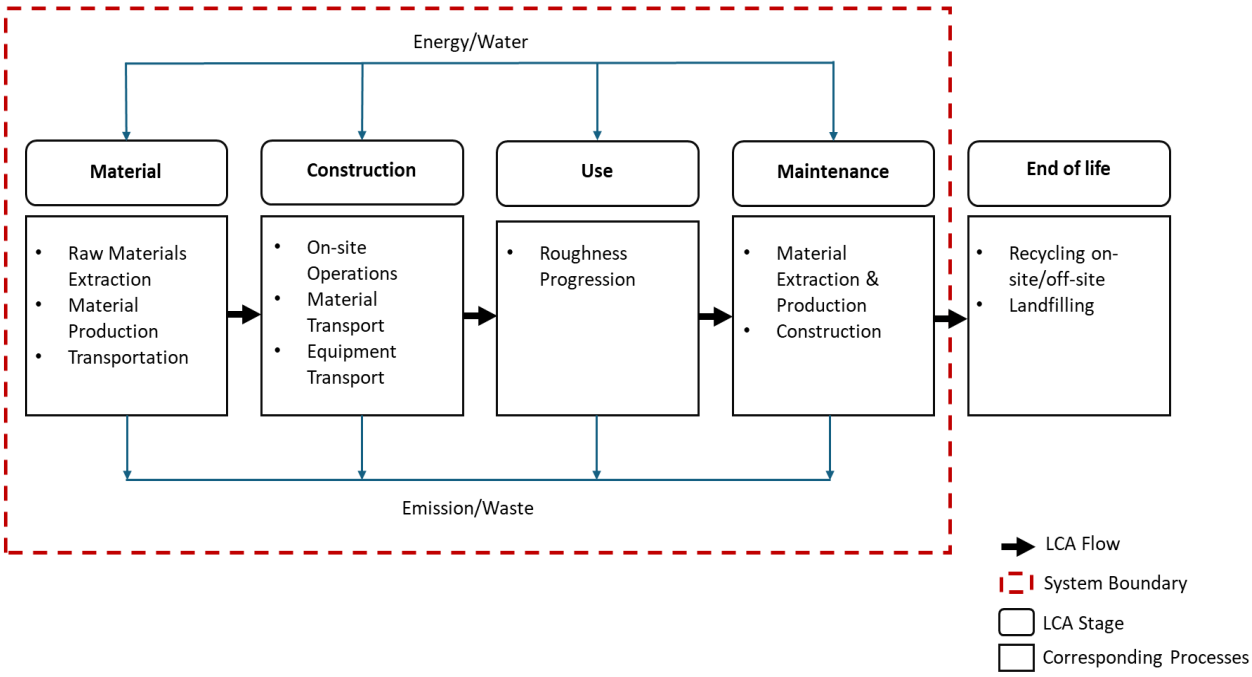

Figure 165. Illustration. Life cycle assessment system boundary.

Materials Stage

Included processes in this stage comprise raw material extraction at quarries (drilling, blasting, overburden handling, on-site hauling, dust suppression), aggregate processing (crushing, screening, washing, stockpiling, moisture management), and production of asphalt binder and additives (polymer modifier, cellulose fiber, mineral filler). Inbound transportation of aggregates, binder, and additives to the asphalt plant is included using scenario-specific distances and modes. Mixing of SMA at the plant, including burner fuel, electricity, evaporation of moisture, and plant yield losses, is within scope.

Construction Stage

This stage covers placement and compaction of the 2 in SMA lift, fuel use for paver and rollers, auxiliary equipment, transport of the mixture from plant to site with queue and idling assumptions, and mobilization and demobilization of equipment.

Use Stage

This stage considers excess fuel consumption due to pavement condition deterioration in terms of roughness. A threshold of 60 in/mi is used for IRI, and the extra fuel consumed by vehicles due to IRI above that is what is attributed to the pavement's use-stage impacts. Historical field rutting measurements were used to extrapolate IRI progression during the analysis period.

Maintenance and Rehabilitation

Routine and periodic surface treatments over the 50-year analysis period were modeled with explicit quantities of materials, plant mixing, transport, and on-site construction energy. The timing of the treatments was dictated by the condition of the pavement, which in turn influenced IRI progression and the resulting use-stage impacts.

End of Life

End of life includes milling of the SMA surface, on-site handling and loading of reclaimed asphalt, transport to processing or disposal facilities, processing of RAP prior to reuse, and landfilling of any residuals not recovered.

Life Cycle Inventory

Life cycle inventory (LCI) includes the data collection and calculation procedures for all processes included in the system boundary. For this LCA, different data sources were used for various processes of the pavement life cycle, as explained in the following sections.

Asphalt Binder Production

The model developed by Yang et al. (2016) is used to quantify the emissions of asphalt binder production. This model focuses on upstream stages of crude oil extraction with associated gas flaring, crude transport, refinery operations, refined-product transport, and storage. The model is regionalized by the Petroleum Administration for Defense Districts (PADDs), so crude source shares, transport distances and modes, and refinery fuels, efficiencies, and electricity mixes are parameterized by US region, causing binder inventories to vary with project location. To complement this, emission factors on binder production from Sphera's Managed LCA Content (MLC) database are used and modeled in Sphera's LCA for Experts Software (Sphera, 2025). Emissions are calculated by multiplying emission factors, weighted by PADD shares by the quantity of asphalt binder used in each mix, as presented in Figure 166.

$$TE_{binder} = EF_{binder} \times Q_{binder}$$

Figure 166. Equation. Total emission of asphalt binder.

TE_{binder} is total emissions of asphalt binder, EF_{binder} is unit process emission factor per kg of asphalt binder, and Q_{binder} is quantity of the asphalt binder used in the mix in kg.

Aggregate Production

Aggregate production is modeled with unit processes from Sphera's MLC database. For the local scenario, inventories are drawn for limestone, at mine, and dolomite, at mine. Whereas, for the non-local scenario, inventories are drawn for basalt, at mine. The "at mine" unit processes include drilling, blasting, loading, crushing, and screening. Emissions are calculated by applying the unit-process emission factors to the quantities of each aggregate type in the mix and summing the contributions across operations, with off-site hauling modeled separately.

Materials Hauling

Transport of aggregates from a quarry to an asphalt plant is modeled using Sphera MLC road-freight unit processes for diesel-powered combination trucks. Two processes were employed to reflect distance-dependent performance: a short-haul combination truck process (used for trips < 250 mi) and a long-haul combination truck process (used for trips > 250 mi). These processes embed differences in fuel intensity, payload utilization, and operating cycles and are applied to limestone/dolomite in the local scenario and basalt in the non-local scenario.

For each aggregate stream i, ton-mile are computed as displayed in Figure 167:

$$TE_{haul,i} = EF_{short/long\ haul} \times m_i \times d_i$$

Figure 167. Equation. Total hauling emission.

where $TE_{haul,i}$ is total hauling emissions for material *i*, $EF_{short/long\ haul}$ is short- or long-haul emission factor per t-mi, m_i is delivered mass (in lb) of material *I*, $d_i$is one-way distance of transporting material *i* from supplying quarry to asphalt plant, or from asphalt plant to construction site (in mi).

To have the option of choosing the closest aggregate quarry for each scenario (local and non-local), a list of local and non-local quarries was prepared. The list consisted of 134 quarries in Illinois and 9 quarries in neighboring states. Illinois quarries were identified using an Illinois State Geological Survey report (Miao et al., 2016). The non-local quarries were identified using Google Maps and verified using quarry websites to confirm available aggregate types. Appendix J includes the complete list of quarries and their locations. For each of the four project locations, the closest quarry was found, and the emissions were calculated.

Asphalt Plant Operations

Plant operations included were based on the framework explained by Al-Qadi et al. (2015). The processes included in this framework were aggregate receiving and cold-feed metering, frying and heating with burner fuel and dust collection, as well as binder storage and blending. In addition, the impact of electricity use at the plant was also included and the electricity mix used was obtained from the US Energy Information Administration for the year 2025. Emissions were determined by applying fuel- and electricity-specific emission factors to calculated consumption for each operation and summing the contributions per ton of mix, then normalizing to the lane-mile functional unit.

Construction Activities

This inventory included all on-site processes required to place and compact the SMA surface using two main equipment types: an asphalt paver and a tandem smooth-drum vibratory roller. Fuel use was calculated from equipment power ratings, load factors, and operating durations; laydown and compaction durations were tied to production rate, lift thickness, lane width, and target density. Table 42 displays the inventory data associated with the equipment used in this LCA.

Table 42. Construction Equipment Properties

Equipment	Paver	Roller Compactor
Weight (tons)	23	17
Horsepower	175	175
Fuel Type	Diesel	Diesel
Fuel Efficiency (gal/hr)	4.15	4.08

To accurately include compaction effort differences between the sections, roller-mounted ground-penetrating radar (GPR) measurements collected on the same sections were used. Abufares et al. (2025) used GPR to generate pass-density curves for each section for pavement performance evaluation. The density curves enabled the identification of the pass count at which the mat approached a specified density target. For the analysis, the pass number corresponding to 94% of the theoretical maximum density (TMD) was adopted. IDOT practice commonly targets at least 93% of TMD for SMA surface lifts (Pfeifer, 2022). Therefore, the 94% modeling target used in this project is conservative. Table 43 displays the number of roller passes obtained for each section.

Table 43. Number of Roller Compactor Passes Obtained from GPR Measurements

SMA Section	Number of Passes for 94% TMD			
	Left Sub-lane	Middle Sub-lane	Right Sub-lane	**Average**
T1-80-12.5-0	12	–	14	**13**
T1-50-12.5-0	4	3	4	**4**
D2-50-12.5-0	3	3	3	**3**
L2-50-12.5-0	10	9	10	**10**
D3-50-9.5-0	3	3	2	**3**
D4-50-12.5-0	3	4	3	**4**

Equipment emissions are directly related to the fuel consumed by equipment to complete a construction job with a specific quantity. For accurate compaction calculations, it is important to calculate the number of coverages of the roller per one pass. That was calculated using the equation in Figure 168.

$$C = v \times w \times (1 - o) \times 63360$$

Figure 168. Equation. Cover per pass calculation.

C is coverage per pass (in^2/hr), v is speed (mph), w is drum width (in), and o is lane overlap fraction.

This is then used to calculate the number of hours the roller is operating and the corresponding fuel consumption using the equation in Figure 169.

$$\frac{Average\ number\ of\ passes\ \times Pavement\ area}{Coverage\ per\ pass}$$

Figure 169. Equation. Number of hours operated by a roller.

For the paver, operation hours are calculated using the quantity of paved material and the productivity of the paver. EPA's Motor Vehicle Emission Simulator (MOVES5) was used for both types of equipment to quantify emissions with the latest version published in December 2024 (US EPA, 2024). MOVES5 uses specific values for equipment fuel consumption. Therefore, the actual fuel consumed by the equipment was used to adjust the MOVES results. MOVES provides emission rates based on engine work (hp-hr), which could be converted to an equivalent amount of fuel using standard fuel-to-work relationships. The calculated fuel consumption for this LCA was then compared to the estimated MOVES fuel use, and the emissions were scaled accordingly. This approach is recommended by EPA to ensure the final emissions reflect real on-site fuel usage (US EPA, 2019).

Pavement Damage

Three in-service SMA pavement sections in Illinois were selected as representative field case studies. The selected sections are located on I-70 near Brownstown, I-57 near Peotone, and I-64 near St. Clair. The sections represent typical Illinois SMA construction, while having varying layer thicknesses and traffic levels. As presented in Figure 170, the I-70 Brownstown section consists of a 2 in SMA surface over a 2.25 in polymer-modified HMA binder course and a 2.25 in HMA binder course, overlaying an 8 in CRCP pavement on a 6 in granular subbase. The I-57 Peotone section includes a 2 in SMA surface over an HMA binder course (2–4 in), overlaying an 8 in CRCP on a 6 in granular subbase. The I-64 St. Clair section includes a 2 in SMA surface over a 2.25 in polymer-modified HMA binder course and a 2.25 in HMA binder course, overlaying an 8 in CRCP base and a 4 in granular subbase. Field rutting measurements for those sections were obtained from IDOT and used to characterize in-service rutting progression. A damage-rate approach was used to transfer the I-APT rutting results to the field sections and to estimate rutting-driven time to major rehabilitation, which was used to establish a comparative LCA to represent maintenance timing.

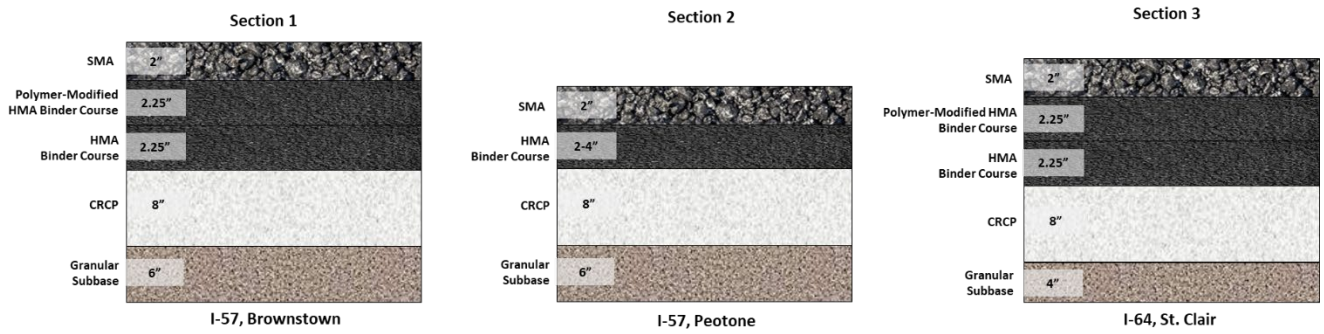

Figure 170. Illustration. Field pavement section.

Field rutting trends of the three SMA sections are presented in Figure 171 using rut-depth data provided by IDOT for the period 2016–2024. The I-APT rutting results were used to translate the observed rutting patterns into section-specific rehabilitation timelines. It was assumed that rutting

was the governing distress for major rehabilitation. The predicted rehabilitation schedules were then used to represent realistic in-service performance in the 50-year LCA analysis.

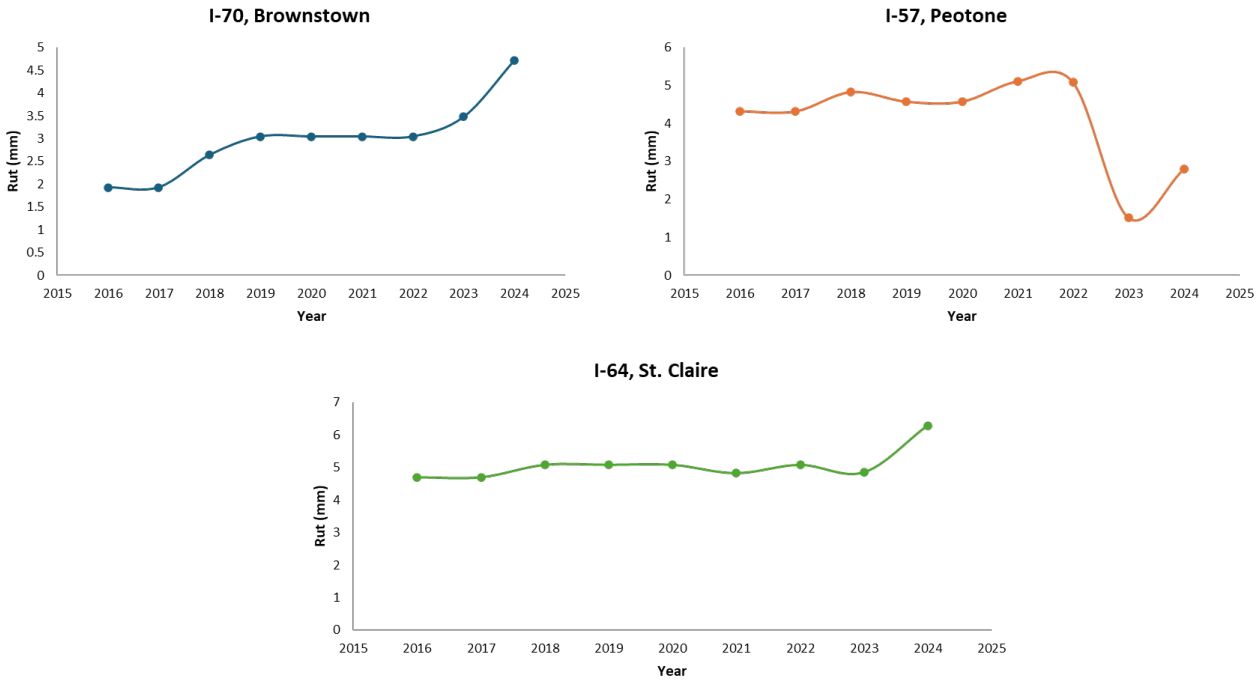

Figure 171. Graph. Rutting progression of the three field sections.

A rate-based calibration approach was adopted to relate I-APT accumulation rutting to field rutting progression. The approach matches I-APT and field sections' long-term rutting damage rates, rather than absolute rut depths.

During the I-APT loading of the SMA sections, rutting damage was accumulated under three sequential tandem-axle loading levels to accelerate pavement distress development. The measured rutting response reflects the combined influence of progressively increasing loading. To account for this loading protocol, separate rutting damage rates were calculated for each loading stage.

For each SMA section, rutting damage rate, corresponding to a given loading stage, was computed as the average increase in rut depth per load repetition (Figure 172).

$$m_{\text{APT},i} = \frac{r_{i,2} - r_{i,1}}{N_{i,2} - N_{i,1}}$$

Figure 172. Equation. Rutting damage rate calculation.

where $m_{\text{APT},i}$ is rutting damage rate for loading stage i, $r_{i,1}$and $r_{i,2}$ are measured rut depths at the beginning and end of each stage, and $N_{i,1}$and $N_{i,2}$ are corresponding numbers of load applications. The three damage rates, therefore, correspond to the 10 kip, 12 kip, and 14 kip axle load stages, respectively.

Initial rutting measured at low numbers of load applications was attributed primarily to densification and seating of the pavement layers rather than load-related rut accumulation. Accordingly, rutting prior to the number of passes where the rutting slope changes (~10,000 passes) was excluded from the calibration of long-term rutting behavior. For extrapolation to field conditions, the damage rate obtained under a 10 kip axle load was selected. This load level closely approximates typical in-service traffic loading for the reference SMA section. The higher axle load stages were retained to characterize the sensitivity of rutting behavior to increased load severity.

Field rutting progression for the reference SMA section was characterized by measured rut depths over multiple years of service. A field rutting damage rate was calculated as the average increase in rut depth per year over a stable accumulation period. Because the goal was to predict the year at which the rutting reached a specific rehabilitation threshold, only positive slopes were considered in computing the average damage rate. The calculation was performed for each of the three field sections separately (Figure 173).

$$m_{\text{field}} = \frac{\Delta r_{\text{field}}}{\Delta t}$$

Figure 173. Equation. Field rut depth calculation.

where Δr_{field} is change in measured rut depth over a selected time interval, Δt. The I-APT-to-field calibration factor, expressed as equivalent I-APT passes per year, was then obtained by long-term I-APT rutting rate to field rutting rate (Figure 174).

$$\lambda = \frac{m_{\text{field}}}{m_{\text{APT}}}$$

Figure 174. Equation. Total emission of asphalt binder.

where m_{APT} is damage rate associated with the 10 kip tire loading stage.

A rut-depth threshold of 12.5 mm was adopted to represent the onset of rutting-driven rehabilitation. This value is consistent with IDOT's pavement distress coding, which classifies rutting greater than 12.5 mm as the highest rutting severity category. Linear extrapolation of the long-term rutting trend was performed to reach the threshold. The number of I-APT passes required to reach the threshold was estimated by assuming constant rutting accumulation beyond the start of the long-term rutting phase (Figure 175).

$$N_{\text{th}} = N_0 + \frac{r_{\text{th}} - r_0}{m_{\text{APT}}}$$

Figure 175. Equation. I-APT number of passes to reach rutting threshold.

where $N_0$and $r_0$are number of load applications and rut depth at the beginning of the long-term rutting phase, respectively, and $r_{\text{th}}$is rutting threshold. Then, corresponding field time to rutting-driven rehabilitation was calculated (Figure 176).

$$t_{\text{rut}} = \frac{N_{\text{th}} - N_0}{\lambda}$$

Figure 176. Equation. Time to rehabilitate due to rutting.

This procedure yielded rutting-controlled rehabilitation times for each I-APT section, which were subsequently used to define maintenance timing in the LCA.

No cracking was observed during accelerated testing; hence, no other pavement distresses were considered in the I-APT-to-field transfer. Therefore, the analysis focuses on rutting-driven rehabilitation, which is consistent with the distress mechanism captured by the I-APT loading and allows a comparative LCA. Table 44 presents the estimated number of passes per year obtained for each I-APT-section using the corresponding field section to reach the rut-depth value of 12.5 mm.

Table 44. Estimated Number of Passes Per Year of I-APT Sections Using Field Sections

	Number of Passes/Year			Average Passes/Yr
I-APT Section	**I-70, Brownstown**	**I-57, Peotone**	**I-60, St. Claire**	
T1-80-12.5-0	183,646	202,567	181,420	189,211
T1-50-12.5-0	241,453	266,330	238,526	248,770
D2-50-12.5-0	80,919	89,256	79,939	83,371
L2-50-12.5-0	231,073	254,881	228,272	238,075
D3-50-9.5-0	106,998	118,022	105,701	110,240
D4-50-12.5-0	51,433	56,732	50,809	52,991

Maintenance and Rehabilitation Activities

Based on the aforementioned calculations, the number of years until the first rehabilitation triggered by rutting was obtained for each section. Given that there are other parallel distresses that are expected to occur during the service life, it was assumed that rutting contributes to 65% of the service life while other distresses contribute to the remaining 35%. Table 45 presents the final service life until first rehabilitation for each section.

Table 45. Projected Rehabilitation Trigger Period

SMA Section	Years until Major Rehab		
	I-70, Brownstown	**I-57, Peotone**	**I-60, St. Claire**
T1-80-12.5-0	11	10	11
T1-50-12.5-0	11	10	11
D2-50-12.5-0	10	9	10
L2-50-12.5-0	10	9	11
D3-50-9.5-0	10	9	10
D4-50-12.5-0	10	9	10

The rehabilitation treatment assumed for all sections consisted of mill-and-overlay of a 2 in SMA. Emissions associated with rehabilitation activities were estimated based on construction equipment fuel consumption, which was calculated using MOVES 5.0. The rehabilitation process included the use

of a milling machine, paver, vibratory roller, and static roller. In addition to equipment operations, the LCI for this stage included the production of the overlay materials and transporting them to/from the plant as well as the production of SMA/HMA.

For the LCA analysis period of 50 years, the overlay service period was assumed to be equal to the service life of the original surface for each section. Based on the predicted rutting-driven service lives (presented in Table 45), sections with 10 or 11 years of service life require four mill-and-overlay cycles within the 50-year period, whereas sections with a 9-year service life require five cycles. Accordingly, while the rehabilitation treatment type and unit processes are the same across various alternatives, the number of rehabilitation events differed, leading to different maintenance and rehabilitation (M&R) stage impacts among the sections.

Excess Fuel Consumption

Use-stage emissions are primarily driven by excess vehicle fuel consumption resulting from increased pavement roughness once the IRI exceeds 60 in/mi. Historical IRI data for the three field sections were obtained from IDOT. An average IRI progression rate was calculated using data from 2016 to 2024 and was assumed to remain constant over the 50-year analysis period. The IRI was assumed to start at 60 in/mi at initial construction and to return to the same value following each overlay rehabilitation, reflecting restoration of surface smoothness. Figure 177 illustrates the resulting IRI progression for each field section based on the rutting-driven service life predicted from the corresponding I-APT sections. For example, for I-70 near Brownstown, T1-80-12.5-0 was predicted to have an 11-year service life, whereas D2-50-12.5-0 was predicted to have a 10-year service life.

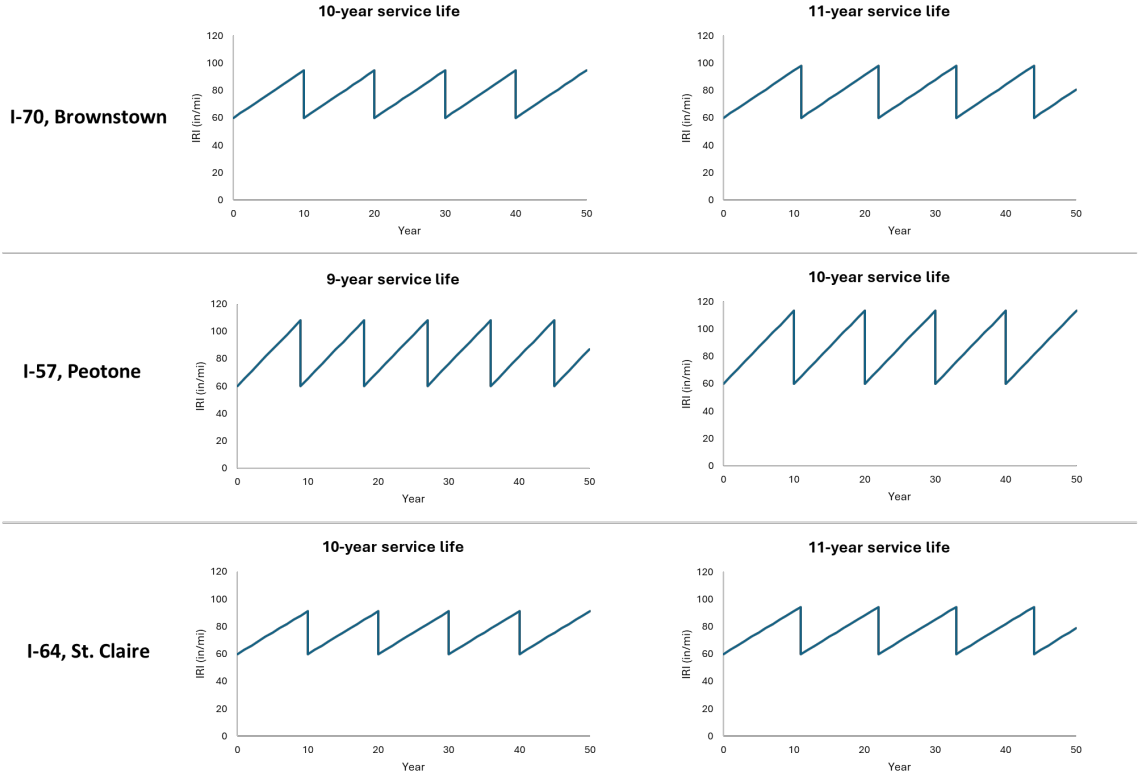

Figure 177. Graph. IRI progression for each field section.

Excess vehicle fuel consumption associated with pavement roughness was estimated using the roughness–speed impact (RSI) model developed by Ziyadi et al. (2018). The RSI model quantifies the incremental increase in fuel consumption and emissions resulting from pavement-vehicle interaction as a function of IRI and vehicle operating speed, based on vehicle-specific power (VSP) theory and calibrated using EPA's MOVES framework. The model was applied in an incremental form to estimate additional fuel consumption beyond a baseline IRI of 60 in/mi, which represents the smoothness condition of a newly constructed or rehabilitated pavement. This approach enables direct integration of pavement roughness effects into the use-stage component of the LCA without double-counting baseline vehicle energy consumption.

One of the main inputs of the RSI model is the average annual daily traffic (AADT), which was obtained for the exact locations of the field sections using traffic counts from IDOT's "Getting Around Illinois" website (IDOT, 2025). In addition, the distribution of passenger cars, small trucks, medium trucks, and large trucks was obtained using FHWA's VM-4 table (FHWA, 2023). Table 46 presents the traffic details.

Table 46. Field Section Traffic Details

	I-70, Brownstown	I-57, Peotone	I-64, St. Claire
AADT	22,600	37,425	41,900
Passenger Car (%)	55.77		
Small Truck (%)	7.71		
Medium Truck (%)	2.5		
Large Truck (%)	32.29		

LIFE CYCLE IMPACT ASSESSMENT

Life cycle impact assessment (LCIA) is where emissions calculated in the previous step are transformed into environmental indicators. In this study, impacts are calculated with EPA's Tool for Reduction and Assessment of Chemicals and Other Environmental Impacts (TRACI) version 2.2. TRACI provides US-specific midpoint characterization for categories including global warming potential, acidification, eutrophication, photochemical smog formation, ozone depletion, respiratory effects, human health (cancer and non-cancer), ecotoxicity, and fossil fuel depletion (US EPA, 2015). These categories capture a broad range of potential environmental and human health consequences associated with energy use and pollutant emissions across the pavement life cycle. By applying TRACI, emissions from construction, maintenance, and use stages were consistently converted into comparable environmental indicators, enabling meaningful comparison of alternative pavement sections.

Results

Materials Production

The LCA results for the production of materials (asphalt binder and aggregates), excluding transportation impacts, are presented in Figure 178 for six TRACI impact categories. The magnitude of impacts varies by category due to differences in material composition and production processes.

Acidification, which represents the potential for emissions such as sulfur dioxide and nitrogen oxides to form acidic compounds that can damage soils, surface waters, and ecosystems, is higher for mixtures produced with local aggregates. This increase is primarily driven by the higher asphalt binder content used in local-aggregate SMA. In contrast, this trend does not hold for ozone depletion and particulate matter ($PM_{2.5}$) impacts. Ozone depletion reflects the potential of certain emissions to degrade stratospheric ozone, which protects human health and ecosystems from harmful ultraviolet radiation, while particulate matter impacts represent the health burden associated with fine airborne particles that can penetrate deep into the respiratory system. For these categories, SMA incorporating non-local aggregates exhibited higher impacts. This outcome is largely attributed to the production of basaltic aggregates, such as trap rock, which generates substantially higher $PM_{2.5}$ emissions compared to limestone and dolomite. The elevated emissions outweigh the effects of increased binder content associated with local aggregate mixtures.

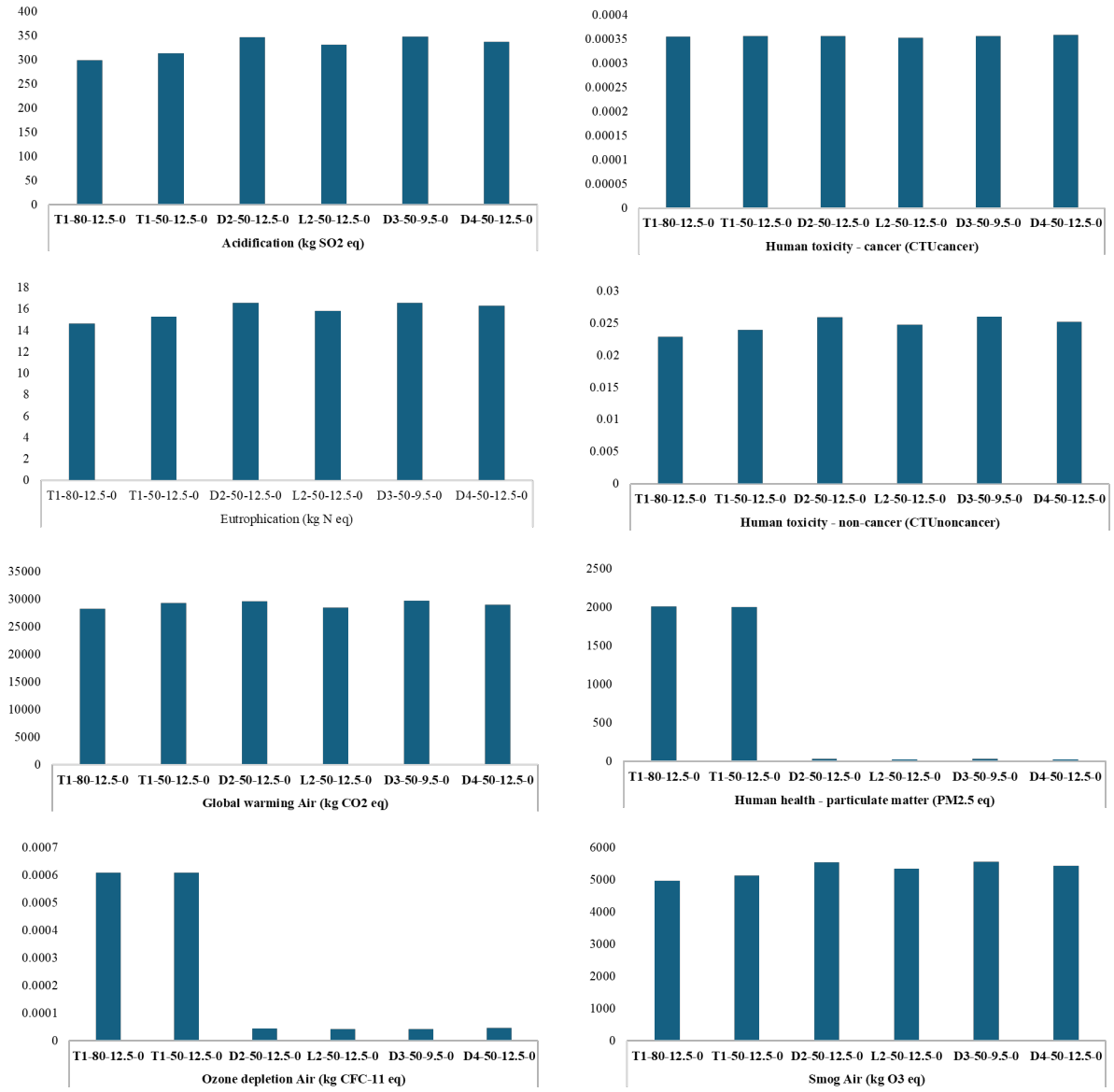

Figure 178. Graph. LCA results for material production processes.

Material Transportation

Figure 179 compares hauling acidification and global warming potential (GWP) burdens for the two sourcing options: (1) local limestone and dolomite aggregates moved by short-haul combination trucks and (2) imported trap rock aggregates moved by long-haul combination trucks. Across GWP, NO_x, $PM_{2.5}$, smog formation, acidification, and eutrophication, the SMA with trap rock was consistently greater due to the high difference in travelled ton-mile.

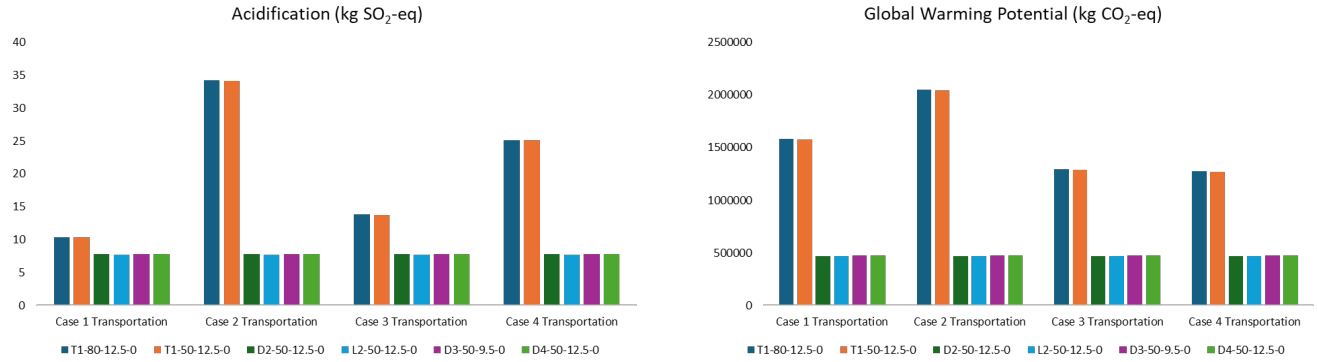

Figure 179. Graph. LCA results for material transportation.

Construction Activities

Figure 180 presents the GWP expressed as kg CO_2-equivalent for different paving and compaction scenarios, with contributions separated between the paver and the roller compactor. Consistent with the roller-pass analysis presented earlier, the paver contribution remains relatively constant across all cases at approximately 250 kg CO_2-eq, while the roller compactor accounts for most of the variation in total GWP. Scenarios that require a higher number of roller passes to achieve target compaction levels (94%), such as T1-80-12.5-0 and L2-50-12.5-0, exhibit substantially higher GWP due to increased compaction effort. In contrast, cases where adequate compaction was achieved with fewer roller passes, including D2-50-12.5-0 and D3-50-9.5-0, display noticeably lower roller-related emissions and reduced total GWP.

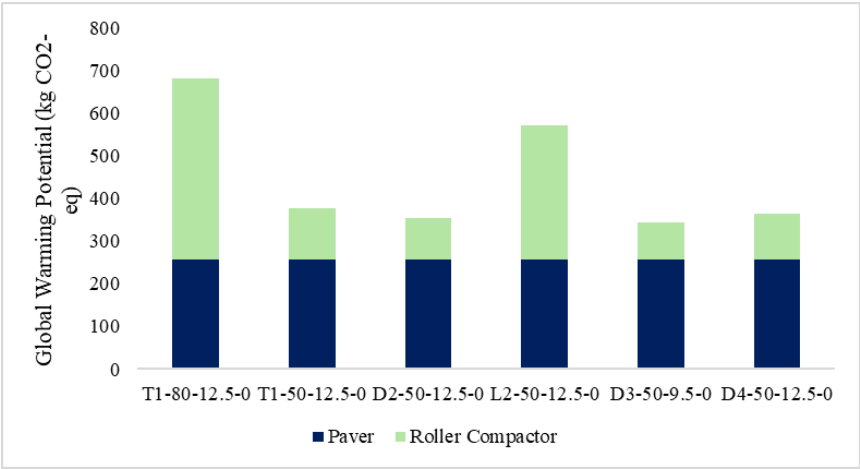

Figure 180. Graph. Construction equipment global warming potential.

Rehabilitation Activities

For each field project location, the total number of rehabilitation events occurring within the 50-year analysis period was determined based on the rutting-driven service life estimates derived earlier and summarized in Table 45.

Figure 181 presents GWP with rehabilitation activities over the analysis period. For the I-70 and I-64 sections, all mix types require four overlay rehabilitations within 50 years. Consequently, the higher GWP values observed for the non-local aggregate mixes in these sections could be attributable primarily to increased emissions from material production and aggregate transportation, rather than differences in rehabilitation frequency.

In contrast, for the I-57 section, local aggregate mixes require one additional rehabilitation event over the analysis period due to their shorter predicted service life. Despite this, the SMA with imported aggregates still exhibited higher cumulative GWP. The environmental benefits gained from shorter transportation distances and reduced upstream material impacts are evident in spite of possible reduced life.

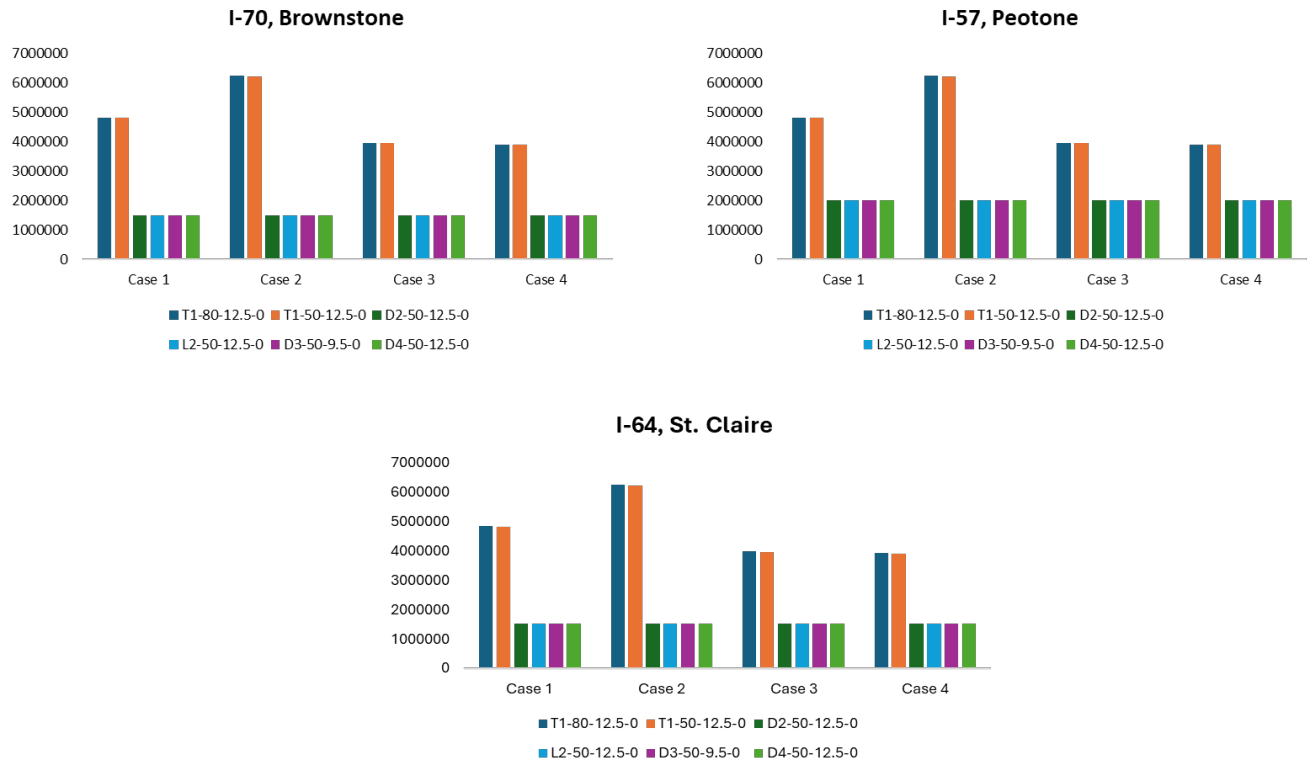

Figure 181. Graph. Global warming potential results for rehabilitation stage.

Excess Fuel Consumption

For the use stage of the pavement life cycle, the traffic loading applied to the SMA surface over time and the timing of rehabilitation activities were the primary factors governing IRI progression. Additional energy consumption attributable to pavement roughness was calculated for each year in

which the IRI exceeded 60 in/mi. The annual excess fuel demands were accumulated over the entire analysis period. The resulting life cycle fuel consumption values were presented in Figure 182. The results indicate that the additional rehabilitation events required for the local-aggregate mixes do not result in a substantial increase in cumulative fuel consumption. Instead, traffic volume (ADT) and the distribution of vehicle classes exerted a stronger influence on use-stage energy consumption, as evidenced by the higher fuel use observed for the I-64 pavement section.

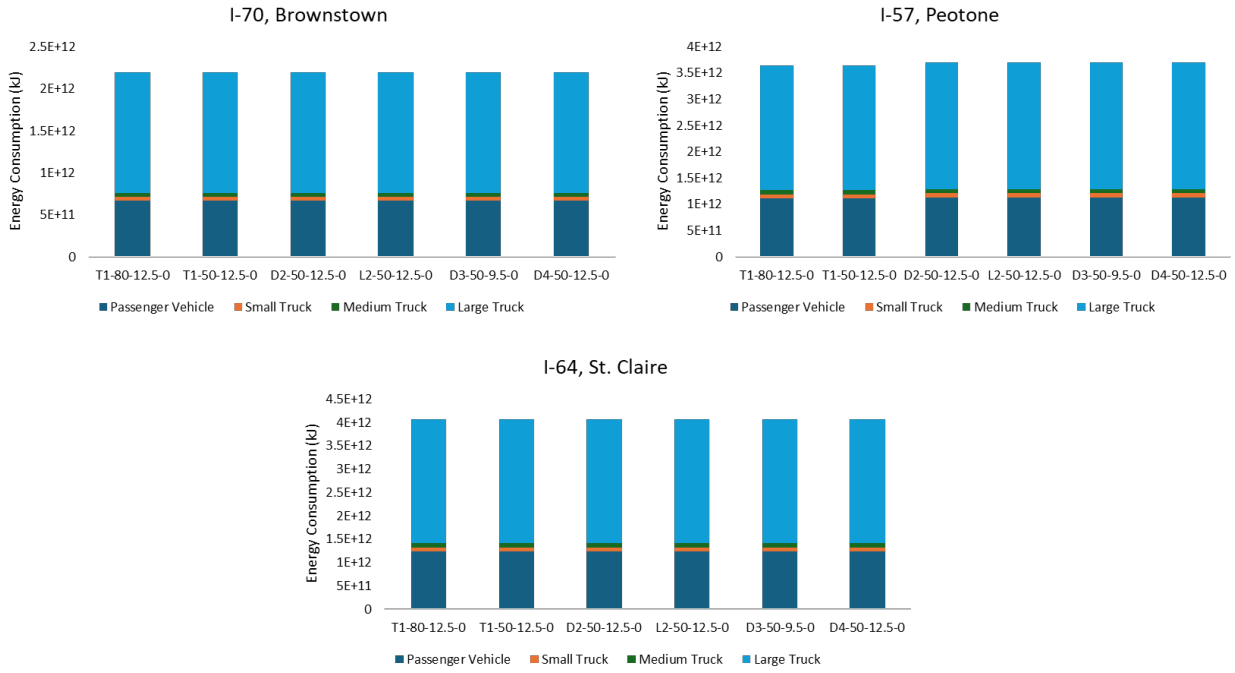

Figure 182. Graph. Excess fuel consumption for each field pavement section.

LIFE CYCLE COST ANALYSIS

Goal and Scope

An LCCA was conducted to quantify and compare the agency costs associated with the SMA alternatives over a 50-year analysis period. The objective of the LCCA was to evaluate the economic impacts associated with using local versus imported aggregates in SMA, while accounting for the impact of material transportation requirements and rutting-driven rehabilitation schedules. The analysis focused on costs incurred by the roadway agency and did not include user costs.

The total life cycle cost for each alternative consists of the following three components:

1. Initial Construction Costs: SMA material production and placement. The costs were estimated using IDOT published pay items and unit costs, ensuring consistency with current agency contracting practices. By separating hauling costs from material production and placement costs, the LCCA directly reflects the economic benefit of reduced transportation distances associated with locally sourced aggregates.

2. Material Transportation Costs: Depends on aggregate source location. Material hauling costs were calculated separately to explicitly capture the economic impact of aggregate source location. Hauling costs were estimated using IDOT-provided truck productivity assumptions, including truck payload capacity and dollar-per-hour operating costs. Transportation distances were defined based on representative haul lengths for local and imported aggregate sources.

3. Rehabilitation Costs: Periodic SMA mill-and-overlay treatments are required to address pavement distresses over the analysis period. The rehabilitation treatments were assumed to consist of a 2 in SMA mill-and-overlay treatment, identical to the original wearing surface, and each rehabilitation event was assumed to restore the pavement surface to its initial condition. The number and timing of rehabilitation events for each section were determined based on the rutting-driven service life estimates reported earlier in this study. Sections with shorter service lives required more frequent rehabilitation within the 50-year analysis period, while sections with longer service lives required fewer interventions.

Net Present Worth Formulation

All future rehabilitation and hauling costs were converted to net present worth (NPW) to account for the time value of money. A real discount rate of 3% was used, consistent with FHWA and IDOT guidance for pavement LCCA. The NPW of each alternative was calculated using the following expression in Figure 183:

$$NPW = \sum_{k=0}^{n} \frac{C_k}{(1+i)^{t_k}}$$

Figure 183. Equation. Calculation of net present worth.

where C_k= cost of activity k,, t_k= year in which activity k occurs, i= real discount rate (3%), and n= total number of cost events over the analysis period.

Initial construction costs occurred at year zero and were therefore not discounted. Rehabilitation and hauling costs occur later in the life cycle and were discounted based on their timing. The LCCA was performed for multiple scenarios reflecting the following combinations: (i) local and imported aggregate sources and (ii) different SMA section designs corresponding to the three field sections: I-70 (Brownstown), I-57 (Peotone), and I-64 (St. Clair). For each field section, four cases were evaluated, representing different combinations of SMA design parameters and aggregate sourcing. The cases are presented in Figure 164.

Results

Figure 184 and Figure 185 present the respective hauling and construction NPW results for each field section and scenario. Across all sections, scenarios using locally sourced aggregates consistently

exhibited lower hauling costs due to shorter transportation distances. In contrast, imported aggregate scenarios incurred substantially higher hauling costs, which persisted across the entire life cycle.

Although local-aggregate SMA alternatives generally required earlier or additional rehabilitation events due to a predicted shorter rutting service life, the increase in discounted rehabilitation cost is relatively modest. In all cases, as presented in Table 47, the percentage reduction in hauling cost exceeded the increase in rehabilitation cost, resulting in comparable or lower total NPW for the SMA with local-aggregate scenarios.

For the I-70 and I-64 sections, the number of rehabilitation events were identical across aggregate sourcing options, and differences in NPW were dominated by the hauling costs. For the I-57 section, local-aggregate alternatives required one additional rehabilitation event within the analysis period. However, even in that case, the additional discounted rehabilitation cost did not offset the economic benefits of reduced hauling costs.

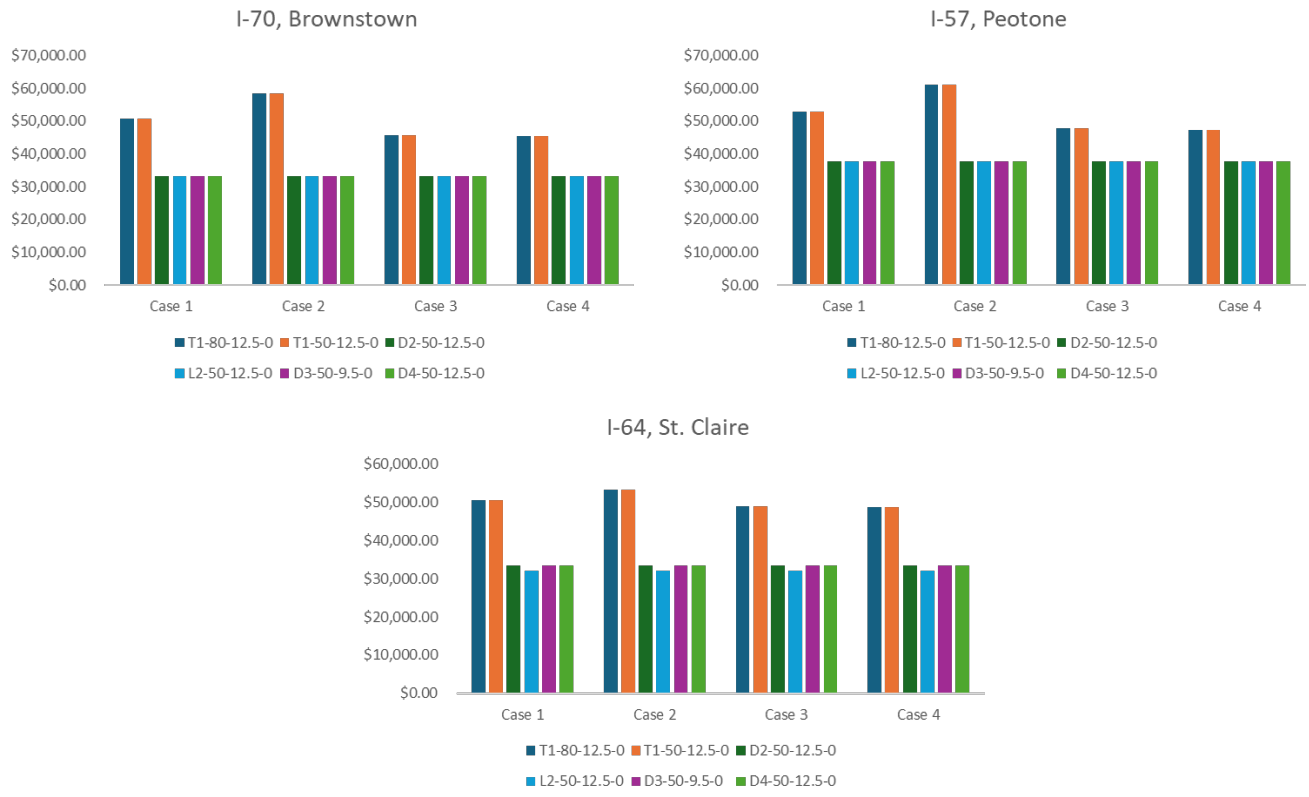

Figure 184. Graph. Material hauling cost results.

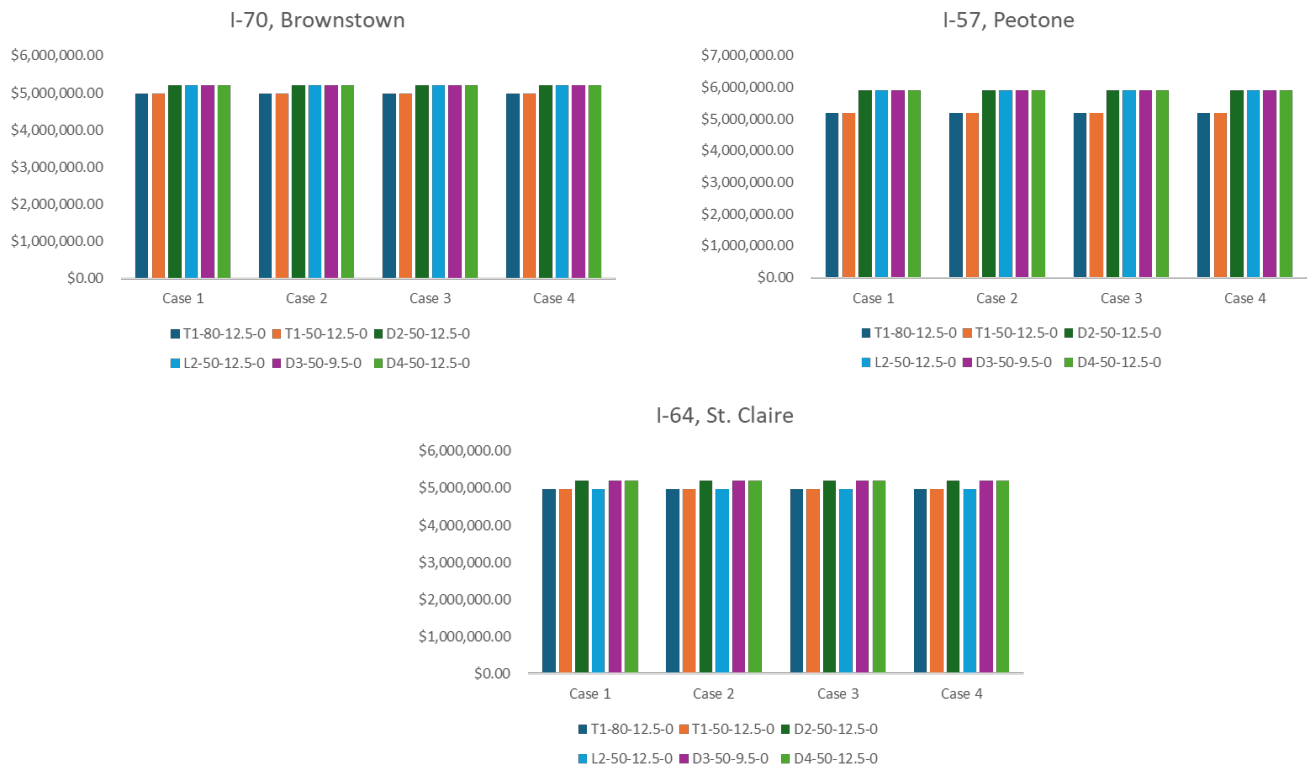

Figure 185. Graph. Initial construction and rehabilitation cost results.

Table 47. Percentage Changes in Cost Across the Scenarios

	I-70 Brownstown	I-57 Peotone	I-64 St. Claire
Decrease in Hauling Costs (%)	34.06	28.41	34.06
Increase in Rehabilitation Costs (%)	4.43	13.73	4.43

SUMMARY

The environmental and economic implications of using locally sourced versus imported aggregates in SMA pavements were assessed using LCA and LCCA. The analysis considered three representative in-service SMA pavement sections in Illinois and assessed the impacts over a 50-year analysis period. Material production, transportation, construction activities, rehabilitation, and use-stage effects were considered in the LCA, while initial construction, rehabilitation, and transportation costs were considered in the LCCA.

The LCA was performed using the TRACI impact assessment method and quantified impacts across multiple environmental categories. Material production results demonstrated that impact trends varied substantially by category. SMAs produced with local aggregates exhibited higher acidification impacts, primarily due to increased asphalt binder content. In contrast, SMAs incorporating imported, basaltic aggregates demonstrated higher ozone depletion and particulate matter ($PM_{2.5}$) impacts, driven by the energy- and emission-intensive production processes associated with trap rock.

Transportation analysis revealed that aggregate haul distance was a dominant contributor to life cycle impacts, with long-haul transport of imported aggregates resulting in consistently higher GWP, acidification, eutrophication, smog formation, and particulate matter emissions despite improved per-ton efficiency of long-haul trucking.

Construction-stage impacts were highly sensitive to compaction effort. While paver-related emissions remained relatively constant across scenarios, roller compaction accounted for most of the variability in construction GWP. Scenarios requiring a greater number of roller passes to achieve target density exhibited significantly higher emissions, highlighting the importance of constructability and compaction efficiency in reducing environmental burdens.

Rehabilitation impacts were evaluated based on rutting-driven service life predictions derived from I-APT results. Although some SMA alternatives with local aggregates required earlier or additional rehabilitation events, particularly for the I-57 section, the cumulative environmental impacts over the analysis period remained lower for local aggregate scenarios. This outcome was primarily driven by reduced material transportation and upstream production impacts, which outweighed the emissions associated with the additional rehabilitation activity.

The LCCA complemented the environmental analysis by evaluating agency costs using NPW calculations with a real discount rate of 3%. Cost differences among alternatives were driven by the tradeoff between reduced hauling costs for local aggregates and increased rehabilitation costs resulting from possible shorter service life. Across most sections, the percentage reduction in hauling costs associated with local aggregates exceeded the increase in discounted rehabilitation costs. Even in cases where an additional overlay was required, total NPW remained comparable or lower for local-aggregate scenarios.

The combined LCA and LCCA results demonstrated that aggregate source location strongly influenced the long-term environmental and economic performance of SMA pavements. Although locally sourced aggregates resulted in higher acidification impacts during material production and, in some cases, shorter rutting-based service life, these effects were offset by substantially lower transportation-related impacts. Long-haul transport of non-local aggregates consistently increased life cycle environmental burdens, particularly GWP and particulate matter. From a cost perspective, earlier or additional rehabilitation required for local-aggregate SMA increased discounted rehabilitation costs, but these increases were generally smaller than the savings from reduced hauling. Overall, the results indicate that the use of local aggregates can provide net environmental and economic benefits when evaluated over a full pavement life cycle.

CHAPTER 7: SUMMARY, FINDINGS, CONCLUSIONS, AND RECOMMENDATIONS

SUMMARY

Stone-mastic asphalt (SMA) is widely recognized for its superior rutting resistance, durability, and structural stability compared with conventional dense-graded hot-mix asphalt. Despite these advantages, the use of SMA in Illinois has been limited, primarily due to higher initial construction costs associated with the reliance on imported, high-quality aggregates. The costs are largely driven by long-haul transportation. Hence, there was a need to design resilient SMA with local aggregates that provides comparable field performance as traditional SMA, while reducing both economic and environmental burdens over the pavement life cycle. Therefore, this study was conducted to assess the feasibility of incorporating locally available aggregates in Illinois in the design and construction of SMA.

An integrated approach was followed encompassing extensive laboratory mixture design and performance testing, full-scale field construction and accelerated pavement testing, and life cycle environmental and cost analyses. The SMAs were designed using both imported control aggregates and a range of locally sourced Illinois aggregates with varying lithologies and material qualities. To accommodate local aggregates, laboratory design compaction effort was reduced, while stone-on-stone aggregate skeleton was preserved to ensure SMA stability and resiliency.

Significant efforts were spent on developing SMA designs. The laboratory evaluation comprised volumetric characterization and performance tests. The tests include rutting and cracking potential, complex modulus, moisture susceptibility, and aggregate degradation. During the laboratory evaluation, aggregate degradation was quantified systematically at multiple stages: after compaction and after rutting potential tests.

To validate the laboratory findings, six SMAs were selected and produced at an asphalt plant and constructed as full-scale pavement sections at the Illinois Center for Transportation testing facility. The SMA layers were placed over a dense-graded HMA leveling course constructed on a continuously reinforced concrete pavement (CRCP). The test sections were instrumented with strain gauges and pressure cells at the bottom of the SMA layers and thermocouples through the SMA thickness. The sections were subjected to various loading configurations and temperatures using the Illinois Accelerated Pavement Tester (I-APT). This includes both single- and tandem-axle loading, various loadings, tire pressure levels, tandem spacings, and differential tire pressures.

The six SMA sections were exposed to I-APT loading for 120,000 passes each. The first 60,000 passes were at 10 kip while the following two 30,000 passes were at 12 and 14 kip, respectively. Pavement responses, including stresses and strains, as well as viscoelastic recovery behavior and surface rutting were continuously monitored. Post-testing aggregate degradation was also performed to estimate aggregate breakage due to axle loading.

Based on SMA pavement sections' characteristics and aggregate soundness, a rutting model was developed to describe the shear-induced flow and consequent permanent deformation of the SMA sections.

Life cycle assessment (LCA) and life cycle cost analysis (LCCA) were conducted in parallel over a 50-year analysis period to quantify the environmental and economic impacts due to aggregate source selection. The analyses considered material production, transportation, construction, rehabilitation activities, and long-term performance. SMA using local aggregates was benchmarked against conventional SMA constructed with imported aggregates.

FINDINGS

The following are the findings of this study:

1. Mixture Design and Laboratory Performance

    - SMAs designed with reduced compaction effort (50 gyrations) met volumetric requirements and maintained stone-on-stone contact while reducing aggregate degradation.

    - Reduced-gyration SMAs often exhibited equal or higher complex moduli than those designed with 80 gyrations.

    - Aggregate breakage occurred primarily during compaction (laboratory or field). The breakage magnitude is governed by aggregate quality and compaction effort. Minimal additional aggregate degradation occurred during Hamburg wheel-tracking test (HWTT) loading.

    - Two SMAs with marginal rutting resistance were successfully stabilized using dry hydrated lime.

2. Full-Scale Construction and Accelerated Pavement Testing

    - All SMA sections demonstrated excellent resiliency, with minimal total rut depths after 120,000 tandem-axle passes, even under increased axle loads. Rutting was governed mainly by lateral flow (shoving) rather than vertical deformation.

    - SMA sections with local aggregates demonstrated slightly higher early-stage rutting due to densification and slightly higher damage rates than imported-aggregate controls. However, the differences were modest.

    - Although HWTT is an empirical approach, a strong relationship was observed between HWTT and I-APT rutting trends. Hence, HWTT may be used to predict field rutting, combined with aggregate soundness test results.

- As expected, all SMA layers' responses increased with increasing load, tire pressure, and temperature. On the other hand, they reduced with increased speed and tandem spacing. Axle load and speed influenced strain magnitude, while symmetric tire inflation pressure had minimal effect.

- SMA behavior, as a viscoelastic material, demonstrated that the trailing axle resulted in greater stress and transverse strain impacts. To account for SMA viscoelasticity, temperature and thickness corrections were implemented for SMA responses.

- Transverse strain revealed the critical impact of trailing loads occurred before full pavement recovery. The relative peak difference serves as a descriptor of pavement recovery and is sensitivity to axle configuration and load spacing. Pavement recovery behavior was controlled by temperature and SMA characteristics. The recovery of SMAs was stable throughout the APT continuous loading.

- Aggregate Breakage Indices (ABI) confirmed that most aggregate breakage occurred before or during construction, not during in-service loading. Minimal additional aggregate degradation occurred during accelerated loading, and the ABI before I-APT loading was related to damage rate. This suggests that once SMA is constructed, the aggregate skeleton remains. Aggregate polish resistance demonstrated potential as a surrogate indicator for field aggregate breakage susceptibility.

3. Rutting Model

    - A rutting model was developed that incorporates SMA viscoelastic properties and aggregate quality. The model uses axle loading and complex modulus as a surrogate for a more mechanistic formulation. This surrogate captures the steady-flow trend associated with vertical shear strain on the plane parallel to loading, which was considered the primary mechanism driving rutting development. A parameter based on aggregate soundness test results was used to represent susceptibility to rutting.

4. Life Cycle Environmental and Economic Performance

    - LCA results indicated aggregate transportation distance was a dominant driver of environmental impacts. Hence, imported aggregates consistently increased environmental burdens due to long-haul transportation.

    - Compared to imported aggregates, locally sourced aggregates reduced global warming potential, particulate matter, smog, and eutrophication impacts, despite higher acidification impacts during material production.

    - Construction-stage impacts were sensitive to compaction effort, with roller passes driving variability in emissions.

- LCCA demonstrated that although SMAs with locally sourced aggregates might sometimes require earlier rehabilitation, savings from reduced hauling costs generally exceeded increased rehabilitation costs, resulting in comparable or lower net present worth.

CONCLUSIONS

SMA incorporating locally sourced Illinois aggregates—when designed using reduced compaction effort and appropriate performance-based validation—can provide comparable performance, improved sustainability, and reduced life cycle costs. The following are the conclusions reached during this study:

- A 50-gyration SMA with local aggregates in Illinois was developed that offers durable, cost-effective, and environmentally responsible pavement layer. This was supported by a combined laboratory design, field construction, and pavement performance under axle loading, along with environmental and cost analyses. Full-scale accelerated testing confirmed that SMA with local aggregates exhibit excellent rutting resistance, viscoelastic recovery, and long-term stability.
- Aggregate degradation of local aggregates in SMA was controlled by SMA design and construction processes. Reducing design compaction to 50 gyrations is effective in limiting aggregate degradation while maintaining SMA structural integrity and rutting resistance.
- SMA modification, such as hydrated lime, may be used to compensate for the limitation of incorporating some Illinois local aggregates to achieve comparable volumetric characteristics and performance potential of conventional SMAs while mitigating aggregate degradation.
- A model was developed to predict SMA overlay rutting using axle loading, modulus, layer thickness, and aggregate soundness.
- The use of Illinois locally sourced aggregates in SMA provides net environmental and economic benefits over the life of the SMA, demonstrating that aggregate proximity can outweigh moderate reductions in rutting-based service life.

RECOMMENDATIONS

The outcome of this study supports the broader adoption of locally sourced aggregates in SMA pavements and offers practical guidance for mixture design, construction, and policy decisions aimed at improving pavement performance while minimizing environmental and economic impacts. This study recommends the following:

- Permit local aggregate use in SMA and design SMA with Illinois aggregates at N_{des} = 50 to control aggregate breakage and rutting potential, while maintaining stone-on-stone contact. SMA with local aggregates must meet the volumetric and performance testing criteria used for conventional SMA.

- Limit excessive laboratory and field compaction and optimize rolling patterns, because aggregate degradation occurs primarily during mixing and compaction, not under traffic loading.

- Use dry hydrated lime modification to stabilize SMA with local aggregate when necessary to meet performance criteria. This would reduce rutting, improve strength, and limit aggregate breakage.

- Incorporate life cycle cost analysis and life cycle assessment into aggregate selection decisions, as local aggregates generally provide net economic and environmental benefits due to reduced transportation impacts.

- Future research must develop strategies to restore pavement friction as needed. Although not examined in this study, SMA with local aggregates may polish more rapidly than conventional SMA, warranting closer attention. Furthermore, the impact of incorporating recycled materials should be rigorously evaluated to ensure long-term performance.

REFERENCES

Abufares, L., Chen, Y., & Al-Qadi, I. L. (2025). Asphalt concrete density monitoring during compaction using roller-mounted GPR. *Automation in Construction*, *174*, 106158. https://doi.org/10.1016/j.autcon.2025.106158

Airey, G. (2003). Rheological properties of styrene butadiene styrene polymer modified road bitumens. *Fuel*, *82*(14), 1709–1719. https://doi.org/10.1016/s0016-2361(03)00146-7

Al-Hadidy, A. I., & Yi-qiu, T. (2010). Comparative performance of the SMAC made with the SBS and ST-modified binders. *Journal of Materials in Civil Engineering*, *22*(6), 580–587. https://doi.org/10.1061/(ASCE)MT.1943-5533.0000057

Al-Qadi, I. L., Dessouky, S. H., Kwon, J., & Tutumluer, E. (2008). Geogrid in flexible pavements: Validation mechanism. *Transportation Research Record: Journal of the Transportation Research Board*, *2045*(1), 102–109. https://doi.org/10.3141%2F2045-12

Al-Qadi, I. L., Elseifi, M., & Leonard, D. (2003). Development of an overlay design model for reflective cracking with and without steel reinforcing nettings. *Asphalt Paving Technology: Association of Asphalt Paving Technologists—Proceedings of the Technical Sessions*, *72*, 388–423.

Al-Qadi, I. L., Hernandez, J. A., Gamez, A., Ziyadi, M., Gungor, O. E., & Kang, S. (2018). Impact of wide-base tires on pavements: A national study. *Transportation Research Record*, *2672*(40), 186–196. https://doi.org/10.1177/0361198118757969

Al-Qadi, I. L., Loulizi, A., Elseifi, M., & Lahouar, S. (2004). The Virginia Smart Road: The impact of pavement instrumentation on understanding pavement performance. *Journal of the Association of Asphalt Paving Technologists*, *73*(3), 427–465.

Al-Qadi, I. L., Portas, S., Coni, M., & Lahouar, S. (2010). Runway instrumentation and response measurements. *Transportation Research Record*, *2153*(1), 162–169. https://doi.org/10.3141/2153-18

Al-Qadi, I. L., Yang, R., Kang, S., Ozer, H., Ferrebee, E., Roesler, J. R., Salinas, A., Meijer, J., Vavrik, W. R., & Gillen, S. L. (2015). Scenarios developed for improved sustainability of Illinois Tollway: Life-cycle assessment approach. *Transportation Research Record*, *2523*(1), 11–18. https://doi.org/10.3141/2523-02

American Association of State Highway and Transportation Officials. (2001). *AASHTO standard PP28. Standard practice for superpave volumetric design for hot mix asphalt (HMA)*. https://global.ihs.com/doc_detail.cfm?document_name=AASHTO%20PP%2028&item_s_key=00512332

American Association of State Highway and Transportation Officials. (2008). *AASHTO standard M 325. Standard specification for stone matrix asphalt (SMA)*. https://standards.globalspec.com/std/10182318/aashto-m-325

American Association of State Highway and Transportation Officials. (2010). *AASHTO standard T 340. Standard method of test for determining rutting susceptibility of hot mix asphalt (HMA) using the Asphalt Pavement Analyzer (APA*). https://standards.globalspec.com/std/13399763/aashto-t-340

American Association of State Highway and Transportation Officials. (2012). *AASHTO standard T 327.*

Standard Method of test for resistance of coarse aggregate to degradation by abrasion in the Micro-Deval apparatus. https://standards.globalspec.com/std/14316815/AASHTO%20T%20327.

American Association of State Highway and Transportation Officials. (2017a). *AASHTO standard M 323. Standard specification for Superpave volumetric mix design*. https://standards.globalspec .com/std/10182225/AASHTO%20M%20323

American Association of State Highway and Transportation Officials. (2017b). *AASHTO standard M 320. Standard specification for performance-graded asphalt binder*. https://standards.globalspec .com/std/10182242/AASHTO%20M%20320

American Association of State Highway and Transportation Officials. (2017c). *AASHTO standard T 378. Standard method of test for determining the dynamic modulus and flow number for asphalt mixtures using the Asphalt Mixture Performance Tester (AMPT).* https://standards.globalspec.com/std/10182831/aashto-t-378

American Association of State Highway and Transportation Officials. (2019). *AASHTO standard T 324. Standard method of test for Hamburg wheel-track testing of compacted asphalt mixtures.* https://standards.globalspec.com/std/13399758/aashto-t-324

American Association of State Highway and Transportation Officials. (2022a). *AASHTO standard T 283. Standard method of test for resistance of compacted asphalt mixtures to moisture-induced damage.* https://standards.globalspec.com/std/13053352/aashto-t-283

American Association of State Highway and Transportation Officials. (2022b). *AASHTO standard T 321. Standard method of test for determining the fatigue life of compacted asphalt mixtures subjected to repeated flexural* bending. https://standards.globalspec.com/std/14554299/t-321

American Society for Testing and Materials. (2017). *ASTM D6928-17. Standard test method for resistance of coarse aggregate to degradation by abrasion in the Micro-Deval apparatus*. ASTM International. https://doi.org/10.1520/D6928-17

Apostolidis, P., Liu, X., Erkens, S., & Scarpas, A. (2020). Use of epoxy asphalt as surfacing and tack coat material for roadway pavements. *Construction and Building Materials*, *250*, 118936. https://doi.org/10.1016/j.conbuildmat.2020.118936

Asi, I. M. (2006). Laboratory comparison study for the use of stone matrix asphalt in hot weather climates. *Construction and Building Materials*, *20*(10), 982–989. https://doi.org/10.1016/j.conbuildmat.2005.06.011

Aurangzeb, Q., Al-Qadi, I. L., Ozer, H., & Yang, R. (2014). Hybrid life cycle assessment for asphalt mixtures with high RAP content. *Resources, Conservation and Recycling*, *83*, 77–86. https://doi.org/10.1016/j.resconrec.2013.12.004

Aurilio, V., Pine, W. J., & Lum, P. (2005). The Bailey method of achieving volumetrics and HMA compactability. In *Proceedings of the Fiftieth Annual Conference of the Canadian Technical Asphalt Association* (pp. 159–183).

Austroads Pavement Research Group. (1993). APRG Technical Note 2 Stone Mastic Asphalt. Australian Road Research Board. Accessed Oct. 2020, http://www.onlinepublications.austroads.com.au/

Awanti, S. S. (2013). Laboratory evaluation of SMA mixes prepared with SBS modified and neat bitumen. *Procedia—Social and Behavioral Sciences*, *104*, 59–68. https://doi.org/10.1016/j.sbspro.2013.11.098

Babashamsi, P., Md Yusoff, N. I., Ceylan, H., Md Nor, N. G., & Salarzadeh Jenatabadi, H. (2016). Evaluation of pavement life cycle cost analysis: Review and analysis. *International Journal of Pavement Research and Technology*, *9*(4), 241–254. https://doi.org/10.1016/j.ijprt.2016.08.004

Baker, H. B., Buth, M. R., & Van Deusen, D. A. (1994). *Minnesota Road Research Project: Load Response Instrumentation Installation and Testing Procedures* (Report No. MN/PR-94/01). Minnesota Department of Transportation.

Barlow, C. A., Grespin, M., & Best, E. A. (2018). Asbestos fiber length and its relation to disease risk. *Inhalation Toxicology*, *29*(12-14), 541–554. https://doi.org/10.1080/08958378.2018.1435756

Becker, Y., Mendez, M. P., & Rodriguez, Y. (1999). Polymer modified asphalt. *Wisconsin Technology*, *9*, 39–50.

Behbahani, H., Nowbakht, S., Fazaeli, H., & Rahmani, J. (2009). Effects of fiber type and content on the rutting performance of stone matrix asphalt. *Journal of Applied Sciences*, *9*, 1980–1984. https://doi.org/10.3923/jas.2009.1980.1984

Beuving, E. (2018). Use of SMA in Europe [PowerPoint]. http://hosou.hscet.com/img/SMA%20presentation%20Japan%202018%20Egbert%20Beuving(2).pdf

Bhagwat, S. B. (2016). *Construction aggregates and silica sand in the economy of Illinois* (Special Report 5). Illinois State Geological Survey.

Bilski, M., & Sowik, M. (2018). Natural asphalt modified binders used for high stiffness modulus asphalt concrete. *IOP Conference Series: Materials Science and Engineering*, *356*(1). https://doi.org/10.1088/1757-899X/356/1/012007

Blazejowski, K. (2011). *Stone matrix asphalt: Theory and practice*. CRC Press.

Bonaquist, R. F., Churilla, C. J., & Freund, D. F. (1988). *Effect of load, tire pressure, and tire type on flexible pavement response. Transportation Research Record*, *1207*, 207–216. https://onlinepubs.trb.org/Onlinepubs/trr/1988/1207/1207-019.pdf

Brandon, T. L., Al-Qadi, I. L., Lacina, B. A., & Bhutta, S. A. (1996). Construction and instrumentation of geosynthetically stabilized secondary road test sections. *Transportation Research Record*, *1534*(1), 50–57.

Bražiūnas, J., Sivilevičius, H., & Virbickas, R. (2013). Dependences of SMA mixture and its bituminous binder properties on bitumen batching system, mixing time and temperature on asphalt mixing plant. *Journal of Civil Engineering and Management*, *19*(6), 862–872. https://doi.org/10.3846/13923730.2013.843587

Brown, E. R., & Cooley, L. A. (1999). *Designing stone matrix asphalt mixtures for rut-resistant pavements* (Report No. 245). National Cooperative Highway Research Program, National Research Council, Transportation Research Board. http://onlinepubs.trb.org/onlinepubs/nchrp/nchrp_rpt_425.pdf

Brown, E. R., Haddock, J. E., Mallick, R. B., & Lynn, T. A. (1997). Development of a mixture design procedure for stone matrix asphalt (SMA). *Journal of the Association of Asphalt Paving Technologists*, *66*, 1–25.

Brown, E. R., & Mallick, R. B. (1994). *Stone matrix asphalt properties related to mixture design* (Report No. 94-2). National Center for Asphalt Technology. http://www.eng.auburn.edu/research/centers/ncat/files/reports/1994/rep94-02.pdf

Brown, E. R., Mallick, R. B., Haddock, J. E., & Bukowski, J. (1997). *Performance of stone matrix asphalt (SMA) mixtures in the United States* (Report No. 97-1). National Center for Asphalt Technology.

Bushing, H., & Antrim, D. (1968). Fiber reinforcement of bituminous mixtures. *Proceeding of the Association of Asphalt Paving Technologist*, *37*, 629–659.

Campbell, C. (1999). The use of stone mastic asphalt on aircraft pavements. Submitted in fulfillment of the requirements for SEN713 Research/Professional Practice Projects, School of Engineering and Technology, Deakin University, Australia.

Cao, W., Liu, S., & Feng, Z. (2013). Comparison of performance of stone matrix asphalt mixtures using basalt and limestone aggregates. *Construction and Building Materials*, *41*, 474–479. https://doi.org/10.1016/j.conbuildmat.2012.12.021

Carpenter, S. (1994). *Stone matrix asphalt (SMA) mixtures (Project IB-H1)*. Illinois Transportation Research Center, Illinois Department of Transportation. https://idot.illinois.gov/content/dam/soi/en/web/idot/documents/transportation-system/research/illinois-transportation-research-center/1994.07.01---stone-matrix-asphalt-(sma)-mixtures---ib-h1-fy92.pdf

Celaya, B. J., & Haddock, J. E. (2006). *Investigation of coarse aggregate strength for use in stone matrix asphalt* (Report No. FHWA/IN/JTRP-2006/4). Purdue University.

Choudhary, J., Kumar, B., & Gupta, A. (2018). Effect of filler on the bitumen-aggregate adhesion in asphalt mix. *International Journal of Pavement Engineering*, *21*(12), 1–9. https://doi.org/doi:10.1080/10298436.2018.1549325

Cooley, L. A., Brown, E. R., & Watson, D. E. (2000). *Evaluation of OGFC mixtures containing cellulose fibers* (NCAT Report 00-05). National Center for Asphalt Technology. https://doi.org/10.3141/1723-03

Cooley, L. A., Hunter, M. S., & James, R. H. (2002). *Micro-deval testing of aggregates in the southeast* (NCAT Report 02-09). National Center for Asphalt Technology, Alabama.

Dahhan, A. Z., & Miller, J. D. (2018). Stone matrix asphalt (SMA) case study, Thornton, Illinois: Analysis of 20-year stone matrix asphalt material on Williams Street. 1st International Conference on Stone Matrix Asphalt (SMA), Atlanta, Georgia, November 6.

De Beer, M., Maina, J. W., Van Rensburg, Y., & Greben, J. M. (2012). Toward using tire-road contact stresses in pavement design and analysis. *Tire Science and Technology*, *40*(4), 246–271.

Deacon, J. A., Harvey, J. T., Guada, I., Popescu, L., & Monismith, C. L. (2002). Analytically based approach to rutting prediction. *Transportation Research Record: Journal of the Transportation Research Board*, *1806*(1), 9–18. https://doi.org/10.3141/1806-02

Descantes, Y., & Hamard, E. (2015). Parameters influencing the polished stone value (PSV) of road surface aggregates. *Construction and Building Materials*, *100*, 246–254. https://doi.org/10.1016/j.conbuildmat.2015.10.002

Diab, L., & Al-Qadi, I. L. (2024). Life cycle assessment for the use of waste plastics in asphalt concrete mixes. *Transportation Research Record*, 03611981241245674. https://doi.org/10.1177/03611981241245674

Eluri, Z. (2018). *Modified micro-Deval procedure for polishing of fine asphalt mix aggregates* (No. FHWA-ICT-18-006). Illinois Center for Transportation, University of Illinois Urbana-Champaign. https://doi.org/10.36501/0197-9191/18-007

Energy Information Administration. (2025). U.S. Energy Information Administration—EIA - Independent Statistics and Analysis. Last modified October 16, 2025. https://www.eia.gov/state/?sid=IL

European Asphalt Pavement Association. (2018). Heavy duty surfaces—the arguments for SMA. European Asphalt Pavement Association.

Federal Highway Administration. (2021). Freight analysis framework. Last modified February 23, 2021. https://ops.fhwa.dot.gov/freight/freight_analysis/faf/index.htm.

Federal Highway Administration. (2022). Life Cycle Cost Analysis. Last modified December 8, 2022. https://www.fhwa.dot.gov/pavement/lcca/

Federal Highway Administration. (2025). Pavement Testing Facility Overview. Last modified August 26, 2025. https://highways.dot.gov/turner-fairbank-highway-research-center/labs/pavement

Fernandes, M. R. S., Forte, M. M. C., & Leite, L. F. M. (2008). Rheological evaluation of polymer-modified asphalt binders. *Materials Research*, *11*(3), 381–386. https://doi.org/10.1590/s1516-14392008000300024

FHWA, 2023. Table VM-4 - Highway Statistics 2023 - Policy | Federal Highway Administration [WWW Document]. Accessed December 23, 2025. https://www.fhwa.dot.gov/policyinformation /statistics/2023/vm4.cfm

Friel, S., Kane, M., & Woodward, D. (2013). Use of Wehner Schulze to predict skid resistance of Irish surfacing materials. In *Proceedings of 2013 Airfield and Highway Pavement Conference*. https://doi.org/10.1061/9780784413005.067

García Mainieri, J. J., & Al-Qadi, I. L. (2024). Optimizing stone-mastic asphalt sustainability through the use of limestone, dolomite, and crushed gravel aggregates. *Journal of Transportation Engineering, Part B: Pavements*, *151*(1). https://doi.org/10.1061/JPEODX.PVENG-1614

Gamez, A., Hernandez, J. A., Ozer, H., & Al-Qadi, I. L. (2018). Development of domain analysis for determining potential pavement damage. Jo*urnal of Transportation Engineering, Part B: Pavements*, *144*(3), 04018030. https://doi.org/10.1061/JPEODX.0000059.

Géber, R., & Gömze, L. A. (2010). Characterization of mineral materials as asphalt fillers. *Materials Science Forum*, *659*, 471–476. https://doi.org/10.4028/www.scientific.net/MSF.659.471

Georgia Department of Transportation. (2013). *Standard specifications construction of transportation*

systems. http://www.dot.ga.gov/PartnerSmart/Business/Source/specs/DOT2013.pdf

Gierhart, D. (2007) Analysis of Oklahoma mix designs for the National Center for Asphalt Technology test track using the Bailey method. Practical approaches to hot-mix asphalt mix design and production quality control testing. *Transportation Research Board Circular E-C124*.

Goh, S. W., Akin, M., You, Z., & Shi, X. (2011). Effect of deicing solutions on the tensile strength of micro-or nano-modified asphalt mixture. *Construction and Building Materials*, *25*(1), 195–200. https://doi.org/10.1016/j.conbuildmat.2010.06.038

Hafeez, I., Kamal, M. A., & Mirza, M. W. (2015). An experimental study to select aggregate gradation for stone mastic asphalt. *Journal of the Chinese Institute of Engineers*, *38*(1), 1–8. https://doi.org/10.1080/02533839.2014.953242

Hainin, M. R., Akhir, N. M., Jaya, R. P., Yusoff, N. I. M., Yaacob, I., Ismail, C. R., & Hassan, N. H. (2013). Aggregate degradation characteristics of stone mastic asphalt mixtures. *Journal of Technology*, *65*(3), 111–114. https://doi.org/10.11113/jt.v65.2155

Hainin, R., Reshi, W. F., & Niroumand, H. (2012). The importance of stone mastic asphalt in construction. *Electronic Journal of Geotechnical Engineering*.

Hajek, J. J., Phang, W. A., & Prakash, A. (1987). Estimating the life of asphalt overlays using long-term pavement performance data. https://onlinepubs.trb.org/Onlinepubs/trr/1987/1117/1117-017.pdf

Hajj, E. Y., Aschenbrener, T. B., & Nener-Plante, D. (2021). *Case studies on the implementation of balanced mix design and performance tests for asphalt mixtures: Illinois Department of Transportation* (Report No. WRSC-TR-21-03). University of Nevada, Reno.

Harvey, J., Meijer, J., Hasan, O., Al-Qadi, I. L., Saboori, A, & Kendall, A. (2016). *Pavement life cycle assessment framework* (Report No. FHWA-HIF-16-014). Applied Pavement Technology, Federal Highway Administration.

Hernandez, J. A., Gamez, A., & Al-Qadi, I. L. (2016). Effect of wide-base tires on nationwide flexible pavement systems: Numerical modeling. *Transportation Research Record*, *2590*(1), 104–112. https://doi.org/10.3141/2590-12.

Huang, B., Shu, X., & Chen, X. (2007). Effects of mineral fillers on hot-mix asphalt laboratory-measured properties. *International Journal of Pavement Engineering*, *8*(1), 1–9. https://doi.org/10.1080/10298430600819170

Hughes, C. S. (2002). *Designing and constructing SMAs: State-of-the-practice*. National Asphalt Pavement Association. https://www.il-asphalt.org/files/5114/4890/3754/NAPA-QIP122-DesigningAndConstructingSMAMixtures.pdf

Hugo, F., & Epps Martin, A. L. (2004). *Significant findings from full-scale accelerated pavement testing* (NCHRP Synthesis 433). The National Academies Press. https://doi.org/10.17226/23380

Illinois Department of Transportation. (2020). Pavement preservation and rehabilitation strategies. Chapter 53 in the Bureau of Design and Environment Manual. https://public.powerdms.com/IDOT/documents/1881647

Illinois Department of Transportation. (2021a). *Specific Gravity (Gsb) List*. IDOT, Bureau of Materials.

Illinois Department of Transportation. (2021b). *Manual for Test Procedures for Materials*. https://public.powerdms.com/IDOT/documents/1851375/Manual%20of%20Test%20Procedures%20for%20Materials%202022

Illinois Department of Transportation. (2022). *Standard specifications for road and bridge construction*.

Indiana Department of Transportation. (2015). Class as Aggregate for Use in SMA Mixture ITM No. 220-15T. https://www.in.gov/indot/div/mt/itm/pubs/220_testing.pdf

Indiana Department of Transportation. (2020). Standard specifications. https://www.in.gov/dot/div/contracts/standards/book/sep19/2020%20INDOT%20Standard%20Specifications.pdf

Iskender, E. (2013). Rutting evaluation of stone mastic asphalt for basalt and basalt–limestone aggregate combinations. *Composites Part B: Engineering*, *54*, 255–264. https://doi.org/10.1016/j.compositesb.2013.05.019

ISO. (2006). ISO 14040:2006. ISO. https://www.iso.org/standard/37456.html

Jarabo, R., Fuente, E., Monte, M. C., Savastano, H., Mutjé, P., & Negro, C. (2012). Use of cellulose fibers from hemp core in fiber-cement production. Effect on flocculation, retention, drainage and product properties. *Industrial Crops and Products*, *39*, 89–96. https://doi.org/10.1016/j.indcrop.2012.02.017

Kandhal, P. S. (2002). *Designing and constructing SMAs: State-of-the-practice*. National Asphalt Pavement Association. https://www.il-asphalt.org/files/5114/4890/3754/NAPA-QIP122-DesigningAndConstructingSMAMixtures.pdf

Kohler, E., & Roesler, J. (2006). *Accelerated pavement testing of extended life continuously reinforced concrete pavement sections.* University of Illinois Institutional Repository. https://hdl.handle.net/2142/46013

Langer, W. H. (2011). *Aggregate resource availability in the conterminous United States, including suggestions for addressing shortages, quality, and environmental concerns* (Report No. Open-File Report 2011–1119). U.S. Geological Survey. https://pubs.usgs.gov/of/2011/1119/pdf/OF11-1119_report_508.pdf

Lasemi, Z., & Butler, S. K. (2015). Overview of high-calcium limestone resources in Illinois for flue-gas desulfurization systems. In *Proceedings of the 47th Forum on the Geology of Industrial Minerals: Illinois State Geological Survey*, Circular 587 (pp. 153–164).

Lees, G., & Kennedy, C. K. (1975). Quality, shape, and degradation of aggregates. *Quarterly Journal of Engineering Geology,* 8, 193–209. https://doi.org/10.1144/GSL.QJEG.1975.008.03.03

Limón-Covarrubias, P., Cueva, D. A., Vidal, G. V., Ortiz, O. J. R., Hernández, R. O. A., & González, J. R. G. (2019). Analysis of the behavior of SMAs with different fillers through the semicircular bend (SCB) fracture test. *Materials*, *12*(2), 288. https://doi.org/10.3390/ma12020288

Liu, H., Hao, P., & Xu, J. (2017). Effects of nominal maximum aggregate size on the performance of stone matrix asphalt. *Applied Sciences*, *7*(2), 126. https://doi.org/10.3390/app7020126

Loulizi, A., Al-Qadi, I. L., Lahouar, S., & Freeman, T. E. (2001). Data collection and management of the instrumented smart road flexible pavement sections. *Transportation Research Record*, *1769*(1), 142–151.

Louw, L., Semmelink, C. J., & Verhaeghe, B. M. J. A. (1997). Development of a stone mastic asphalt design method for South African conditions. In Proceedings of Eighth International Conference on Asphalt Pavements (pp. 535–554).

Manzo, F. (2014). Highway Construction Costs: How Does Illinois Compare? Prepared for Illinois Economic Policy Institute (ILEPI) Economic Commentary #7. Accessed December 2025, https://illinoisepi.org/site/wp-content/themes/hollow/docs/infrastructure-investment/ILEPI-Economic-Commentary-Per-Lane-Mile1.pdf.

Maryland Department of Transportation. (2018). MDOT standard specification for construction and materials. https:// roads.maryland.gov/mdotsha/pages/Index.aspx?PageId=853&utm

McGhee, K. K., & Clark, T. M. (2007). Cost-comparison methodology for selecting appropriate asphalt concrete mixes. *Transportation Research Record: Journal of the Transportation Research Board*, *2057*, 1–6. https://doi.org/10.3141/2057-01

McLaughlin, M. (2018). Thin SMA surfacing. In Proceedings of First International Conference on Stone Matrix Asphalt.

Metcalf, J. B. (1996) NCHRP Synthesis of Highway Practice 235: Application of Full-Scale Accelerated Pavement Testing. TRB, National Research Council, Washington D.C.

Miao, X., Lasemi, Z., Mikulic, D. G., & Falter, M. (2016). Directory of Illinois mineral producers, and maps of extraction sites. Illinois State Geological Survey, Circular 584, p. 52.

Michaut, J. P. (1995). Ruflex or stone mastic asphalt. *Asphalt Review*, *4*(2), 7–10.

Miranda, H. M. B., Batista, F. A., de Lurdes Antunes, M., & Neves, J. (2020). Influence of laboratory aggregate compaction method on the particle packing of stone mastic asphalt. *Construction and Building Materials*, *259*. https://doi.org/10.1016/j.conbuildmat.2020.119699

Moalla Hamed, F. K. (2010). Evaluation of fatigue resistance for modified asphalt concrete mixtures based on dissipated energy concept. PhD diss., Technische Universität Darmstadt. https://tuprints.ulb.tu-darmstadt.de/id/eprint/2108

Moghaddam, A. M., Ziaee, S. A., Mollashahi, H. F., & Qazizadeh, M. J. (2014). Effects of waste fibers stabilizers on the draindown and moisture damage sensitivity properties of SMAs. *International Journal of Transportation Engineering*, *2*(2), 155–165. https://doi.org/10.22119/IJTE.2014.7877

Mokhtari, A., & Moghadas Nejad, F. (2012). Mechanistic approach for fiber and polymer modified SMAs. *Construction and Building Materials*, *36*, 381–390. https://doi.org/10.1016/j.conbuildmat.2012.05.032

Myadaraboina, H., Law, D., & Patnaikuni, I. (2014). Durability of basalt fibers in concrete medium. *Proceedings of International Structural Engineering and Construction*, *1*(1), 445–450. https://doi.org/10.14455/ISEC.res.2014.41

National Asphalt Pavement Association. (1994). Guidelines for materials, production, and placement

of stone matrix asphalt (SMA) (Publication No. IS118). Technical Working Group (TWG).

National Asphalt Pavement Association. (2002). NAPA Quality Improvement Series 122. Designing and Constructing SMAs—State-of-the-Practice. National Asphalt Pavement Association, Maryland.

National Cooperative Highway Research Program. (2015). NCHRP Synthesis 475. Fiber Additives in Asphalt Mixtures. Transportation Research Board. https://www.nap.edu/read/22191/

Neves, J., Freire, A.C., Qamhia, I., Al-Qadi, I.L., & Tutumluer, E. (2023). Full-Scale Accelerated Pavement Testing and Instrumentation. In Chastre, C., Neves, J., Ribeiro, D., Neves, M.G., Faria, P. (eds), *Advances on Testing and Experimentation in Civil Engineering*. Springer Tracts in Civil Engineering. Springer, Cham. https://doi.org/10.1007/978-3-031-05875-2_7

Olard, F. (2012). GB5 mix design: High-performance and cost-effective asphalt concretes by use of gap-graded curves and SBS modified bitumens. *Road Materials and Pavement Design*, *13*(1), 234–259. https://doi.org/10.1080/14680629.2012.657074

Panda, M., Suchismita, A., & Giri, J. (2013). Utilization of ripe coconut fiber in stone matrix asphalt mixes. *International Journal of Transportation Science and Technology*, *2*(4), 289–302. https://doi.org/10.1260/2046-0430.2.4.289

Partl, N., Vinson, T., & Hicks, R. (1994). Mechanical properties of stone mastic asphalt. In *Proceedings of the Third Materials Engineering Conference* (pp. 849–858).

Pasetto, M., & Baldo, N. (2014). Influence of the aggregate skeleton design method on the permanent deformation resistance of stone mastic asphalt. *Materials Research Innovations*, 18, 96–101. https://doi.org/10.1179/1432891714Z.000000000588

Pfeifer, B. (2022). IDOT HMA Technical Briefs. https://il-asphalt.org/files/4017/1112/0216/1-6-2024_IDOT_Technical_Update_for_IAPA_-_Pfeifer_Brian_Pfeifer.pdf

Pourtahmasb, M. S., & Karim, M. R. (2014). Utilization of recycled concrete aggregates in stone mastic asphalt mixtures. *Advances in Materials Science and Engineering*, 1–9. https://doi.org/10.1155/2014/902307

Prowell, B. D., Watson, D. E., Hurley, G. C., & Brown, E. R. (2009). *Evaluation of stone matrix asphalt (SMA) for airfield pavements* (Report No. AAPTP 04-04). NCAT Final Report.

Prozzi, J. A., & Luo, R. (2005). *Quantification of the joint effect of wheel load and tire inflation pressure on pavement response. Transportation Research Record*, *1919*, 134–141. https://doi.org/10.1177/0361198105191900114

Putman, B. J., & Amirkhanian, S. N. (2004). Utilization of waste fibers in stone matrix asphalt mixtures. *Resources, Conservation & Recycling*, *42*, 265–274. https://doi.org/10.1016/j.resconrec.2004.04.005

Qiao, Y., Dave, E., Parry, T., Valle, O., Mi, L., Ni, G., Yuan, Z., & Zhu, Y. (2019). Life cycle costs analysis of reclaimed asphalt pavement (RAP) under future climate. *Sustainability*, *11*(19), 5414. https://doi.org/10.3390/su11195414

Qiu, Y. F., & Lum, K. M. (2006). Design and performance of stone mastic asphalt. *Journal of Transportation Engineering*, *132*, 956–963. https://doi.org/10.1061/(ASCE)0733-

947X(2006)132:12(956)

Ramakrishnan, A., & Al-Qadi, I. L. (2023). Axle weight limits for single and tandem axles. *Journal of Transportation Engineering, Part B: Pavements*, *149*(3), 04023016. https://doi.org/10.1061/JPEODX.PVENG-1211.

Renshaw, G., Al-Qadi, I. L., & Kohler, E. R. (2024). *Enhanced capabilities of the Illinois Accelerated Pavement Tester* (No. FHWA-ICT-24-017). Illinois Center for Transportation.

Rivera-Perez, J., Kang, S., Sayeh, W., García Mainieri, J. J., Al-Qadi, I. L., & Özer, H. (2022). Statistical analysis of hot-mix asphalt pay for performance versus quality control for performance. *Journal of Transportation Engineering, Part B: Pavements*, *148*(2). https://doi.org/10.1061/jpeodx.0000365

Saeed, A., Hall Jr., J. W., & Barker, W. (2001). NCHRP Report 453. Aggregate tests related to durability of aggregates in pavements. Transportation Research Board. https://onlinepubs.trb.org/onlinepubs/nchrp/nchrp_rpt_453.pdf

Saeed, A., & Hall, J. W. Jr. (2003). *Accelerated pavement testing: Data guidelines.* The National Academies Press. https://doi.org/10.17226/21958

Samieadel, A., Schimmel, K., & Fini, E. H. (2018). Comparative life cycle assessment (LCA) of bio-modified binder and conventional asphalt binder. *Clean Technologies and Environmental Policy*, *20*(1), 191–200. https://doi.org/10.1007/s10098-017-1467-1

Sebaaly, P., & Tabatabaee, N. (1989). *Effect of tire pressure and type on response of flexible pavement. Transportation Research Record*, *1227*, 115–127.

Sengoz, B., & Isikyakar, G. (2008). Analysis of styrene-butadiene-styrene polymer modified bitumen using fluorescent microscopy and conventional test methods. *Journal of Hazardous Materials*, *150*(2), 424–432. https://doi.org/10.1016/j.jhazmat.2007.04.122

Sholar, G. A., Page, G. C., & Musselman, J. A. (2002). Precision statements for ignition oven for use with plant-produced mixtures. *Transportation Research Record*, *1813*(1), 142–150. https://doi.org/10.3141/1813-17

Šernas, O., Vorobjovas, V., Šneideraitienė, L., & Vaitkus, A. (2016). Evaluation of asphalt mix with dolomite aggregates for wearing layer. *Transportation Research Procedia*, *14*, 732–737. https://doi.org/10.1016/j.trpro.2016.05.340

Son, S., Al-Qadi, I. L., & Zehr, T. (2015). 4.75 mm SMA performance and cost-effectiveness for asphalt thin overlays. *International Journal of Pavement Engineering*, *17*(9), 799–809. https://doi.org/10.1080/10298436.2015.1019500

Sphera. (2025). Managed LCA Database. Sphera. https://sphera.com/solutions/product-stewardship/life-cycle-assessment-software-and-data/managed-lca-content/

Steyn, W. (2012). Significant findings from full-scale accelerated pavement testing. *The National Academies Press*. https://doi.org/10.17226/22699

Tabatabaee, N., Al-Qadi, I. L., & Sebaaly, P. E. (1992). Field evaluation of pavement instrumentation methods. *Journal of Testing and Evaluation*, *20*(2), 144–151.

Takarli, M., Phelipot-Mardele, A., & Prince, W. (2009). Adaptation of the Micro-Deval test for

assessing the surface weathering degree of granite. *Journal of ASTM International*, *6*(9), 1–11. https://doi.org/10.1520/JAI102251

Tanaka, S., & Maruyama, K. (2018). Development of a high-performance SMA suited to the surface course of national highways in Japan's cold, snowy regions. In *Proceedings of First International Conference on Stone Matrix Asphalt*.

Texas Department of Transportation. (2014). TxDOT standard specifications for construction and maintenance of highways, streets, and bridges. https://ftp.txdot.gov/pub/txdot-info/cmd/cserve/specs/2014/standard/specbook-2014.pdf

Thompson, P. D., Ford, K. M., National Research Council (U.S.), National Cooperative Highway Research Program, American Association of State Highway and Transportation Officials, & United 15 States (Eds.). (2012). *Estimating life expectancies of highway assets*. Transportation Research Board.

Tielking, J. T., & Roberts, F. L. (1987). *Tire contact pressure and its effect on pavement strain. Journal of Transportation Engineering*, *113*, 56–67.

Turk, J., Mauko Pranjić, A., Mladenovič, A., Cotič, Z., & Jurjavčič, P. (2016). Environmental comparison of two alternative road pavement rehabilitation techniques: Cold-in-place-recycling versus traditional reconstruction. *Journal of Cleaner Production*, *121*, 45–55. https://doi.org/10.1016/j.jclepro.2016.02.040

US DOT. (2024). Transportation Services Contributed 6.7% to U.S. GDP in 2022; Rising Above 6.3% in 2019 | Bureau of Transportation Statistics. https://www.bts.gov/newsroom/transportation-services-contributed-67-us-gdp-2022-rising-above-63-2019

US EPA. (2015, December 17). Tool for Reduction and Assessment of Chemicals and Other Environmental Impacts (TRACI) [Data and Tools]. https://www.epa.gov/chemical-research/tool-reduction-and-assessment-chemicals-and-other-environmental-impacts-traci

US EPA. (2024). Latest Version of Motor Vehicle Emission Simulator (MOVES) [Data and Tools]. https://www.epa.gov/moves/latest-version-motor-vehicle-emission-simulator-moves.

US EPA. (2019). Can MOVES Report Output in Terms of Fuel Consumption? [URL https://www.epa.gov/moves/can-moves-report-output-terms-fuel-consumption (accessed 12.24.25).

Van der Poel, C. (1954). A general system describing the visco-elastic properties of bitumen and its relation to routine test data. *Journal of Applied Chemistry*, *4*, 221–236.

Vansteenkiste, S., De Visscher, J., & Vanelstraete, A. (2013). Impact of hydrated lime on the durability of SMAs: Laboratory and field evaluation. *Road Materials and Pavement Design*, *14*, 162–174. https://doi.org/10.1080/14680629.2013.774753

Vavrik, W. R., Pine, W. J., & Carpenter, S. H. (2002). Aggregate blending for asphalt mix design: Bailey method. *Transportation Research Record*, *1789*(1), 146–153. https://doi.org/10.3141/1789-16

Virginia Department of Transportation. (2020). VDOT 2020 road and bridge specifications. http://www.virginiadot.org/business/const/spec-default.asp

Wang, H., & Al-Qadi, I. L. (2010). Near-surface pavement failure under multiaxial stress state in thick asphalt pavement. *Transportation Research Record: Journal of the Transportation Research Board*, *2154*(1), 91–99. https://doi.org/10.3141/2154-08

Wang, H., & Al-Qadi, I. L. (2013). Importance of nonlinear anisotropic modeling of granular base for predicting maximum viscoelastic pavement responses under moving vehicular loading. *Journal of Engineering Mechanics*, *139*(1), 29–38. https://doi.org/10.1061/(ASCE)EM.1943-7889.0000465.

Wang, D., Wang, H., Bu, Y., Schulze, C., & Oeser, M. (2015). Evaluation of aggregate resistance to wear with Micro-Deval test in combination with aggregate imaging techniques. *Wear*, 338–339, 288–296. https://doi.org/10.1016/j.wear.2015.07.002

Wasilewska, M. (2017). Evaluation of skid resistance of wearing course made of stone mastic asphalt mixture in laboratory conditions. *IOP Conference Series: Materials Science and Engineering*, *245*(2), 22–43. https://doi.org/10.1088/1757-899X/245/2/022043

Watson, D., & Jared, D. (1996). Summary of Georgia's experience with stone matrix asphalt mixes. Transportation Research Board.

West, R. C., Moore, J. R., Jared, D. M., & Wu, P. Y. (2007). Evaluating Georgia's compaction requirements for stone matrix asphalt mixtures. *Transportation Research Record*, *2001*(1), 93–101. https://doi.org/10.3141/2001-11

White, G., & Jamieson, S. (2018). Introduction of stone matrix asphalt to Australian runways. In *Proceedings of First International Conference on Stone Matrix Asphalt*.

Wisconsin Department of Transportation. (2018). WisDOT experiences with SMA [Presentation]. NAPA International SMA Conference, Atlanta, Georgia, November 6, 2018. https://www.asphaltpavement.org/uploads/documents/EngineeringPubs/2018SMAConference/30.%20SMA%20-%20A%20Wisconsin%20Experience%20-%20Schwerman.pdf

Wisconsin Department of Transportation. (2021). 2021 standard specifications 460 hot mix asphalt pavement. https://wisconsindot.gov/rdwy/stndspec/ss-04-60.pdf

Wonson, K. (1996). SMA—The European experience. 1996 AAPA Pavements Industry Conference, Asphalt Review, Australian Asphalt Pavement Association, *15*(2).

Woodside, A. R., Woodward, W. D. H., & Akbulut, H. (1998). Stone mastic asphalt: Assessing the effect of cellulose fibre additives. *Proceedings of the Institution of Civil Engineers—Municipal Engineer*, *127*(3), 103–108. https://doi.org/10.1680/imuen.1998.30985

Wu, M. M., Li, R., Zhang, Y., Fan, L., Lv, Y., & Wei, J. (2015). Stabilizing and reinforcing effects of different fibers on asphalt mortar performance. *Petroleum Science*, *12*, 189–196. https://doi.org/10.1007/s12182-014-0011-8

Wu, S., Xue, Y., Ye, Q., & Chen, Y. (2006). Utilization of steel slag as aggregates for stone mastic asphalt (SMA) mixtures, *Building and Environment*, *2*(42), 2580–2585. https://doi.org/10.1016/j.buildenv.2006.06.008

Xie, H., Watson, D. E., & Brown, E. R. (2005). Evaluation of two compaction levels for designing stone matrix asphalt. *Transportation Research Record*, *1929*(1), 149–156.

https://doi.org/10.1177/0361198105192900118

Xu, G., Wang, H., & Zhu, H. (2017). Rheological properties and anti-aging performance of asphalt binder modified with wood lignin. *Construction and Building Materials*, *151*, 801–808. https://doi.org/10.1016/j.conbuildmat.2017.06.151

Yang, R., Ozer, H., & Al-Qadi, I. L. (2016). Regional upstream life-cycle impacts of petroleum products in the United States. *Journal of Cleaner Production*, *139*, 1138–1149. https://doi.org/10.1016/j.jclepro.2016.08.164

Yastremsky, D. A., Abaidullina, T. N., & Chepur, P. V. (2018). Determination of stone-mastic asphalt concrete durability. *Journal of Physics: Conference Series*, 1015. https://doi.org/10.1088/1742-6596/1015/3/032150

Yin, F., & West, R. C. (2018). Performance and life-cycle cost benefits of stone matrix asphalt (Report No. 18-03). National Center for Asphalt Technology. http://eng.auburn.edu/research/centers/ncat/files/technical-reports/rep18-03.pdf

Ziyadi, M., Ozer, H., Kang, S., & Al-Qadi, I. L. (2018). Vehicle energy consumption and an environmental impact calculation model for the transportation infrastructure systems. *Journal of cleaner production*, *174*, 424–436.

APPENDIX A: CURRENT STATE OF KNOWLEDGE OF STONE-MASTIC ASPHALT

Stone-mastic asphalt (SMA), also referred to as stone-matrix asphalt, is a gap-graded hot-mix asphalt (HMA) composed of large-sized crushed aggregates bound with thick asphalt-filler mastic. Stone-mastic asphalt has a higher amount of coarse aggregate than conventional dense-graded HMA to increase stone-on-stone contact and aggregate interlock, lower amounts of fine aggregates (FAs), and higher asphalt content. This results in higher stresses being transferred through the coarse aggregate (CA) skeleton during compaction and traffic loading. Binder modification with polymers and cellulose fibers are typically used to prevent potential drain down of the increased binder content. Stone-mastic asphalt are expected to yield better overall performance and, hence, lower life cycle costs when compared to traditional dense-graded HMA. With its improved performance and resistance to rutting in particular, the use of SMA for wearing surface layers has increased in response to the increase in truck traffic volume, higher allowable axle loads, and prolonged maintenance intervals.

The superior performance of SMA is contingent on optimization of its mix design and enhanced quality and properties of its components. In this Appendix, a literature review is presented that focuses on the advantages of using SMA in flexible pavements, particularly in overlays; the properties, characteristics, and proportioning of the aggregates; and other constituents. The challenges faced in securing aggregates that meet the high-quality standards, necessary for superior performance of SMA mix, along with strategies to overcome these challenges are discussed.

CONSTITUENT MATERIALS OF SMA

Aggregates

Requirements for aggregate suitability for incorporation in an SMA mix are stricter than those for HMA. Coarse aggregates, suitable for SMA, are selected based on their high strength, angularity, and shape. Specific aggregate characteristics required are prescribed in AASHTO M 325 (2008) and other specifications. Critical requirements limit aggregate potential degradation, proportion of flat and elongated particles, presence of deleterious materials, and proportion of aggregates with crushed faces, water absorption, among other properties. The fine aggregates in SMA serve as fillers of the voids between the coarse aggregates, without having to resist mechanical stresses. Hence, requirements on fine aggregates are less critical.

Asphalt Binder

Stone-mastic asphalts are characterized by high voids in mineral aggregates (VMA) and high voids filled with asphalt (VFA). The binder content in SMA commonly ranges from 5% to 7%, which is higher than that of conventional mixes. To ensure stability and prevent drain down during construction, cellulose fibers are typically introduced (Wu et al., 2015; Moghaddam et al., 2014). The inclusion of fibers and use of polymer modifiers in binders also help in reducing the temperature susceptibility of the mix and increase its stiffness at high temperatures, reducing early-stage rutting (Fernandes et al., 2008; Bilski & Sowik, 2018; Al-Hadidy & Yi-qiu, 2010). The use of modified binders in SMA reduces

stripping and lowers oxidation potential, both of which aid in prolonging its fatigue service life (Goh et al., 2011; Xu et al., 2017; Moalla Hamed, 2010; Awanti, 2013).

Polymer-modified HMA has gained popularity because of its ability to reduce rutting at high temperatures. Binder modification may improve one or more of the binder's properties such as fatigue resistance, stiffness modulus, rutting resistance, stripping potential, temperature susceptibility, and oxidation potential (Moalla Hamed, 2010; Bilski & Sowik, 2018; Al-Hadidy & Yi-qiu, 2010; Goh et al., 2011; Fernandes et al., 2008; Xu et al., 2017). Both high elastic modulus and high fatigue life can be achieved with polymer-modified binder (Awanti, 2013). The binder grade used in SMA should be selected following AASHTO specifications M 323 and M 320 or state-specific guidance.

Currently, elastomer styrene-butadiene-styrene (SBS) is the most popular polymer for asphalt modification (Fernandez et al., 2008; Sengoz & Isikyakar, 2008; Airey, 2003), followed by other polymers such as styrene-butadiene rubber, ethylene-vinyl acetate, and polyethylene. SBS block copolymers are classified as elastomers, which increase the elasticity of bitumen, and they are likely the most appropriate polymers for bitumen modification (Sengoz & Isikyakar, 2008). Becker et al. (1999) noted that polymers increased the low temperature flexibility characteristics of asphalt. They also stated that a decrease in strength and resistance to penetration was observed at higher temperatures. Al-Hadidy and Yi-qiu (2010) observed improved mixture performance with better rut resistance and resilient modulus and lesser drain down compared to the control mixture when added asphalt binder with 5% of solid SBS copolymer to SMA without a stabilizing additive.

Mineral Fillers

Filler material, also referred to as mineral filler or dust, is the fraction of aggregates finer than 0.075 mm; that is, the portion of fine aggregates passing the 0.075 mm sieve. When mixed with asphalt binder, they form a high-consistency paste (referred to as mastic) that coats the CAs and the relatively large FAs and binds them together to form a sturdy and stable aggregate skeleton. It is not recommended to use mineral fillers with Rigden voids (the fractional voids in a dry-compacted mineral filler) greater than 50% in SMA (per AASHTO M 325 [2008]).

The adhesion between fillers and asphalt binder is defined by the chemical and mineral content of fillers (Huang et al., 2007). Hydrophobic materials, such as limestone, adhere well to binder. Hydrophilic materials have lower absorption of asphalt binder and produce poor-quality and low-strength HMA (Géber & Gömze, 2010). Choudhary et al. (2018) reported that hydrophobic fillers have a hydrophilic coefficient value lower than 1, indicating a higher attraction to asphalt than water. Coarser filler particles fill voids present in mixes, improve packing, and reduce permeability (Choudhary et al., 2018). Limón-Covarrubias et al. (2019) obtained the best performance of SMA using fillers with the lowest proportion of aluminum and silicon (harmful clay components). Choudhary et al. (2018) concluded that calcium-based fillers such as natural stone dust generally result in significant improvement in adhesion, while silica-based glass powder fillers result in the worst adhesion.

Fibers

Various types of fiber have been incorporated in HMA, including cellulose, mineral rock, wool, glass, siliceous acid (artificial silica), rubber powder and rubber granules, as well as polymer, which is less frequently used. The main function of fiber reinforcement in HMA/SMA is to provide additional tensile strength and to act as stress arrestors (Al-Qadi et al., 2003). In SMA, an additional important role of mineral fibers is to prevent drainage of the binder during transport and placement (Moghaddam et al., 2014; Panda et al., 2013; Michaut, 1995; Austroads Pavement Research Group, 1993). AASHTO specification M 325 (2008) indicates that the quantity of mineral or cellulose fibers to be added to SMA shall be approximately 0.3% or more of the mixture's total mass to prevent potential drain down of the binder. Mineral and cellulose fibers are the most common types of fibers used in SMA (Awanti, 2013; Putman & Amirkhanian, 2004). Mineral fibers are manufactured by melting minerals, and cellulose fibers are plant-based fibers (NCHRP, 2015).

The inclusion of cellulose or mineral fibers as a stabilizing agent in SMA has several advantages: i) Increase film thickness on the aggregate by 30%–40%, ii) increase mix stability, iii) provide better interlock between the binder and aggregates, and iv) reduce the possible binder drain down during transport and paving (Moghaddam et al., 2014; Panda et al., 2013; Campbell, 1999).

Cooley et al. (2000) reported that using cellulose fibers led to mixes with better performance, lower optimum binder content, and less rutting than mineral fibers. Additionally, cellulose fiber improves the moisture susceptibility of SMA more than mineral fiber (Mokhtari & Nejad, 2012). The results of the mechanistic-empirical design that was conducted by Mokhtari and Nejad (2012) indicated that cellulose fiber had a higher layer thickness reduction (9.82%) than mineral fiber (8.52%). In another study on the effect of fiber type and content on the performance of SMA, Behbahani et al. (2009) found that using cellulose fiber led to better results in terms of indirect tensile strength and dynamic creep, while using mineral fiber led to better results for the Marshall stability test.

Mineral fibers are composed of any nonmetallic, inorganic fibers such basalt, glass, graphite, and asbestos. Basalt fibers have not been found to perform well in alkali environments, while asbestos fibers (Myadaraboina et al., 2014) have been found to be degradable (Bushing & Antrim, 1968) and pose health hazards (Barlow et al., 2018). Although there are environmental concerns about moisture absorption of cellulose fibers (Jarabo et al., 2012; Cooley et al., 2000), cellulose fibers are proven to be superior in practice when both technical aspects and costs are considered (Wonson, 1996). Availability, cost considerations, and ease of application greatly affect the choice of fiber.

Researchers have evaluated the addition of differing types of cellulose fiber (loose and pelletized) on the performance of SMA using a range of common laboratory-based test methods. The addition of loose cellulose fiber to an SMA increased particle loss, as shown by Cantabro test results (a test in which an AC gyratory cylinder is abraded in a drum). The addition of excess loose cellulose fiber may produce a "dry" mix that could have future durability problems (Woodside et al., 1998). Poor distribution of fibers may also limit their positive effects (Partl et al., 1994). Brown, Mallick, et al. (1997) conducted a study on mix design and performance data obtained from 86 SMA projects and found that fiber had been added in a loose state rather than in pellets in most SMA projects.

ADVANTAGES AND CHALLENGES OF USING SMA

Research studies have shown that SMA, especially when used in wearing courses, feature several advantages over conventional HMA, such as the following:

- Higher resistance to rutting (Austroads Pavement Research Group, 1993; Michaut, 1995; Watson & Jared, 1996; Brown, Haddock, et al., 1997; Dahhan & Miller, 2018).
- Greater resistance to raveling and surface wear (European Asphalt Pavement Association [EAPA], 2018).
- Increased durability (Hainin et al., 2012; Watson & Jared, 1996; Qiu & Lum, 2006; EAPA, 2018; Dahhan & Miller, 2018).
- Increased resistance to moisture damage and better visibility (Yin & West, 2018).
- Improved frictional resistance and noise reduction (Yin & West, 2018; Son et al., 2015).
- Better resistance to cracking (Hainin et al., 2012; Watson & Jared, 1996; EAPA, 2018).
- Lower life cycle cost (McGhee & Clark, 2007; Campbell, 1999).

The challenges of using SMA include the following:

- Increased binder drain down and segregation susceptibility (Moghaddam et al., 2014; Brown, Mallick, et al., 1997).
- Increased production and construction costs due to using polymer modification, aggregate hauling, and longer open-to-traffic delays (Yin & West, 2018; Hainin et al., 2012).
- Lower initial friction (Campbell, 1999).
- Clay presence might be detrimental to cracking performance (Limón-Covarrubias et al., 2019).
- Increased screening to obtain the required aggregate gradation (Son et al., 2015).
- Greater susceptibility to aggregate breakage and polishing during compaction and service life when using weak aggregates (Wasilewska, 2017; Pourtahmasb & Karim, 2014; Prowell et al., 2009; Asi, 2006).

STONE-MASTIC ASPHALT DESIGN

Gyration Number

In general, for HMA and SMA in particular, strength and the presence of flat, elongated, or weak aggregate particles may cause differences between designed and lab- or plant-compacted mixes

because of particle reorientation and fracturing. Reorientation may also happen if aggregates are not properly interlocked. Additionally, aggregates have friction requirements to avoid excessive wearing and smoothness when they are on a wearing surface.

Stone-mastic asphalt were developed in Europe using the Marshall method. Fifty Marshall hammer blows were used for sample preparation based on the European experience (National Asphalt Pavement Association [NAPA], 2002). With the development of SuperPave, the number of gyrations needed to obtain the same compaction as a 50 Marshall hammer blow was evaluated. Carpenter (1994) reported 50 blows were not enough for SMA and instead recommended 75, although aggregate breakage was observed for limestone aggregates. The first correlation between the Marshall blow and gyratory compaction was determined by Brown and Cooley (1999). The results indicated that 50-blow Marshall compaction was, on average, equivalent to 78 gyrations in an SGC, which was rounded to 75 gyrations as N_{design} and standardized in AASHTO PP28 (2001). However, the mechanism of both compaction methods are completely different.

West et al. (2007) compared Georgia's SMA 50-blow Marshall design with 50, 75, and 100 gyrations using SuperPave. The study evaluated the asphalt content, VFA, and density. Mixes using the gyratory compactor resulted in a lower optimum asphalt content than those designed using the Marshall hammer. The results indicated that 35 gyrations provided the same density as 50 Marshall hammer blows. The 35 gyrations were determined by data extrapolation. However, a compaction effort of 50 gyrations was selected because 35 gyrations are outside the recommended ranges of SuperPave.

Similar studies have compared the Marshall and SuperPave compactors solely based on density. Brown and Cooley (1999) determined that 100 gyrations obtained the same density as 50 Marshall hammer blows. West et al. (2007) determined that 70 gyrations would achieve the same density for 50 Marshall blows in Alabama mixes. The differences between the optimum gyration was due to aggregate breakdown. Xie et al. (2005) reported that 100 gyrations were found to be excessive for weak aggregates. As a result, 65 gyrations for SMA compaction were studied for weak aggregates based on optimum asphalt content, VMA, and rut depth. The study found that mixes designed using 65 gyrations meet the VMA requirements without compromising rut depth. The mixes compacted using 100 gyrations increased aggregate breakdown by 0.62%. In addition, the gyratory compactor tends to cause less aggregate breakdown than the Marshall hammer.

Currently, the number of gyrations used for N_{design} depends on the Los Angeles (LA) abrasion results of the aggregate. The N_{design} of 100, 75, and 45 gyrations are used for aggregates with LA abrasions of 0 to 30, 30 to 45, and > 45, respectively (Kandhal, 2002). In Illinois, the current specification requires an N_{design} of 80 gyrations (IDOT, SSRBC), similar to the guidelines from Kandhal (2002). The selection of gyratory compaction levels lower than the AASHTO-recommended 100 gyrations depends on the aggregate source. The main factor to consider is the capacity of the aggregate to resist compaction and the correlation between the SuperPave density and aggregate field degradation. Deciding SuperPave gyratory levels based on the Marshall number of blows is not necessarily a reliable factor that can represent field conditions.

Nominal Maximum Aggregate Size

Nominal maximum aggregate size (NMAS) is an important parameter in SMA. Rut resistance and dynamic modulus of SMA increase with an increase of NMAS and decrease with an increase in the test temperature. At the same time, increasing NMAS increases the susceptibility of binder drain down and reduces the fatigue life of SMA (Hafeez et al., 2015). Hafeez et al. (2015) recommended a 12.5 mm NMAS for hot climate areas like Pakistan. Liu et al. (2017) reported that VMA and VFA of SMA increased with a decrease of NMAS; a decrease in NMAS enhanced the cracking resistance of SMA at low and medium temperatures and increased raveling resistance.

Aggregate Proportioning

The Federal Highway Administration's SMA Technical Working Group (NAPA, 1994) aggregate gradation guidelines suggest a range of 20% to 28% passing the 4.75 mm sieve to help ensure the formation of a proper coarse aggregate skeleton and stone-on-stone contact in SMA. Previous works by the IDOT and the ICT (Carpenter, 1994; Son et al., 2015) and the National Center for Asphalt Technology (Brown & Mallick, 1994) have shown that the percent passing the 4.75 mm sieve is a critical factor in the formation of stone-on-stone contact in SMA. It should be limited to ensure a greater coarse-to-fine aggregate proportion.

Aggregate proportioning limits for SMA mixes are presented in AASHTO specification M 325. Aggregate availability and mix performance test results define the aggregate proportions of an HMA design. Stone-on-stone contact is fundamental for SMA design, and therefore aggregate proportioning shall be confronted with extra considerations. The Bailey method could be a useful tool to complete this task.

Bailey Method for Designing SMA

The Bailey method was developed to assist in the selection of the combined blend aggregate gradation for HMA design. The initial intent of the method was to promote coarse aggregate interlock for dense-graded HMA to improve rutting resistance. It was later adapted for SMA, gap-graded, and other mixes regardless of the NMAS of the mix (Vavrik et al., 2002).

The Bailey method guides the designer in dictating mix type as a function of CA volume by selecting the Coarse Aggregate chosen unit weight (CA CUW), expressed as a percentage of the CA loose unit weight (dense-graded), or a percentage of the CA rodded unit weight (SMA). This is the first Principle of The Bailey Method. For fine-graded mixes, the recommended CA CUW is 60%-80% of the CA loose unit weight, to ensure the CA is "floating" in a matrix of FA. For coarse-graded mixes, the recommended CA CUW is 95% to 105% of the CA loose unit weight to ensure some degree of particle-to-particle contact of the CA (Figure 186). The recommended range for the CA CUW for SMA is 110% to 125% of the CA rodded unit weight. SMA is designed to have the maximum possible contact between coarse aggregate particles to achieve the best packing (Aurilio et al., 2005). For fine-graded, coarse-graded, and SMA mixes, the voids created by the coarse aggregate are filled with an equal volume of FA.

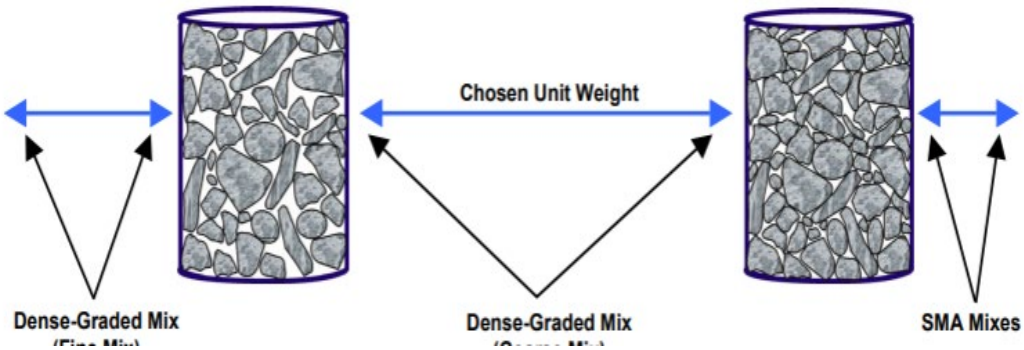

Figure 186. Illustration. The chosen unit weight of SMA coarse aggregate (Vavrik et al. 2002)

The sieve that separates the fine and coarse fractions is denoted as the primary control sieve (PCS), which is defined as 22% of the NMAS (PCS = 0.22*NMAS). The coarse aggregate creates voids in the aggregate skeleton, which are filled by the FA and binder. The second Principle (CA ratio) characterizes particle size distribution in the coarse fraction (plus PCS). The third (FAc ratio) and fourth (FAf ratio) principles characterize the overall fine fraction (minus PCS) and the fine part of the fine fraction (minus SCS), respectively. Table 48 describes the control sieves used for SMA mixes.

Table 48. Control Sieves for SMA

NMAS	19.0	12.5	9.5	4.75
Half Sieve	9.5	6.25	4.75	2.36
Primary Control Sieve	4.75	2.36	2.36	1.18
Secondary Control Sieve	1.18	0.600	0.600	0.300
Tertiary Control Sieve	0.300	0.150	0.150	0.075

Table 49 provides recommended ranges for the aggregate ratios in SMA. Gierhart (2007) conducted field testing at the National Center of Asphalt Technology using SMA that met the recommended Bailey ratios.

Table 49. Recommended Ranges for Aggregate Ratios in SMA

NMAS	19.0 mm	12.5 mm	9.5 mm
CA Ratio	0.35–0.50	0.25–0.40	0.15–0.30
FA_c Ratio	0.60–0.85	0.60–0.85	0.60–0.85
FA_f Ratio	0.65–0.90	0.65–0.90	0.65–0.90

The Bailey method complements SuperPave by providing the analytical framework for aggregate proportioning. Pasetto and Baldo (2014) compared the fatigue and moisture performance of SMA with and without Bailey method guidelines. Mixes designed using the Bailey method showed higher fatigue life and moisture resistance than those designed via experience only. In addition, permanent deformation (rutting) is less for SMA whose aggregate structure meets Bailey parameters (Passeto & Baldo, 2016).

In summary, the use of the Bailey method in SMA helps to achieve improved fatigue life and rutting and moisture performance while providing a systematic approach to select an aggregate gradation that meets mix design control requirements.

CURRENT USE AND SPECIFICATIONS IN ILLINOIS

The SMA paved by the State of Illinois in the intersection of Williams and Margaret Streets in Thornton, Illinois, remained in place and in use for over two decades with minimal to no maintenance. It was resurfaced in 2017. The intersection serves as the main gateway to one of the largest stone quarries in the country. The SMA design remained durable over the 20-year pavement life. This was largely due to an adequate aggregate selection, high asphalt binder content, high film thickness, and a high polymer content that remained effective over the pavement life (Dahhan & Miller, 2018).

The air voids (AV) on the placed SMA were targeted to be higher than dense-graded HMA and expected to remain high throughout the life of the pavement, preserving a coarse and interlocked aggregate skeleton. No densification was expected after construction if stone-on-stone contact was achieved. The SMA in Thornton, Illinois, had a density above 94% during production. Little to no additional compaction was possible, as demonstrated by less than 2% increase in density achieved over the 20-year pavement life cycle (Dahhan & Miller, 2018).

IDOT started constructing SMA in the mid-1990s. In correspondence with the authors on December, 26, 2021, IDOT's Jim Trepanier stated that it was already widely used in Districts 1, 8, and occasionally in Districts 2 and 4. District 6 planned to use it on interstates wherever pavement evaluations indicate that all of the previous overlays need to be removed all the way down to the possibly weak concrete layer. SMA was ideal in such applications because it could be statically rolled and thus does not impose high risk of damage to the weak concrete layer. IDOT also encouraged the use of SMA for bridge deck overlays, where dynamic compaction was not favored. High cost was the main reason for not using much in the southern regions of the state, except for District 8, where suitable aggregates such as trap rock and chert were readily accessible.

Son et al. (2015) used Illinois local aggregates to design a 4.75 mm NMAS SMA for use as a thin overlay. The mixes were tested in the field (on IL-72 in Hoffman Estates and Barrington, Illinois) using actual loading. The mix was shown to allow for a thinner thickness and similar performance to 9.5 mm or 12.5 mm dense-graded HMA. Apart from this example, SMA in Illinois has been constructed using imported coarse aggregates and, with a few exceptions, with a gyration level (N_{des}) of 80.

Wearing surface course SMA typically used in Illinois have typically utilized the following type and source of coarse aggregates: Steel slag from Gary, Indiana; quartzite from Wisconsin; trap rock from Iron Mountain, Missouri or Ontario, Canada; and chert gravel from Missouri. Binder course SMA in District 1 are produced with dolomite coarse aggregates from quarries in Districts 1 and 2 (Jim Trepanier, pers. comm.). Trials of using SMA with local coarse aggregates and lower N_{des} have begun in District 6 in 2021.

Aggregate Sources Available in Illinois

Igneous rocks are usually used as coarse aggregates in SMA. Unfortunately, there are no economically minable igneous rocks or operations in Illinois. The closest operations for granite and trap rock are in northern Wisconsin and Minnesota (Langer, 2011). Illinois' surface geology is of sedimentary origin. Sedimentary aggregates are often weaker than igneous aggregates and exhibit larger variability in their engineering properties.

Limestone and dolomite quarries are abundant throughout Illinois (Lasemi et al., 2015; Miao et al., 2016). Northeastern Illinois has the highest quality of dolomite aggregates, sand, and gravel. The central part of the state has several active quarries producing Pennsylvanian limestones. Western, southwestern, and southern Illinois are other areas of active high-quality limestone mining.

Hauling aggregates for construction activities is common in the US. Based on 2018 data from FHWA's Freight Analysis Framework (2021), gravel was the top freight commodity by tonnage moved by trucks. It is expensive, however, as the cost of truck transportation can double the consumer bill around 20 to 50 miles from the point of extraction, depending on the aggregate and road profile (Bhagwat, 2016). Thus, using local aggregates for SMA production has the potential not only to reduce the long-term costs associated with longer performance life, but also to reduce initial investment costs.

Current Stone-Mastic Asphalt Specifications in Illinois

IDOT's Standard Specifications for Road and Bridge Construction (SSRBC, 2022) indicate that SMA shall be designed according to Illinois-modified AASHTO M 325, T 305, and R 46 (IDOT, 2021b) except as modified in the SSRBC.

SSRBC Art. 1004.03(b) stipulates that coarse aggregates for SMA shall meet the minimum requirements of Grade B. SSRBC Art. 1004.01 sets limits for LA abrasion (maximum 40%), sodium sulfate soundness (Na_2SO_4, maximum 15%), and deleterious materials (maximum varies). As for flat and elongated ratio requirements, limits are defined in the Illinois-modified AASHTO M 325 (20% max for 3 to 1; 5% max for 5 to 1; SSRBC Art. 1004.03[d]). Additionally, there is a 2.5% maximum limit for water absorption (SSBRC Art. 1004.03 [e]), which is intended to minimize binder drain down.

Art. 1004.03 (a) of the SSRBC classifies HMA based on traffic level and friction requirements and state's requirements for the composition of their aggregate blends. Five SMA types are identified:

- Binder
- C (N_{des} 50 surface for high and low ESAL traffic)
- D (N_{des} 50 surface for high ESAL traffic)
- E (N_{des} 80 surface for high ESAL traffic)
- F (N_{des} 80 surface for high ESAL traffic)

Table 50 designates the average daily traffic (ADT) levels allowable for each wearing surface mixture, with a few exceptions that require extra friction such as having a large volume of heavy commercial vehicle traffic or the pavement surface remaining wet for extended periods of time.

Table 50. Frictional Requirements for Surface Mixtures from Chapter 53 of IDOT's Bureau of Design and Environment Manual

Number of Lanes in Both Directions	Frictional Requirements (ADT levels for the expected year of construction)			
	Mixture C	Mixture D	Mixture E	Mixture F
≤ 2	≤ 5,000	> 5,000	N/A	N/A
4	≤ 5,000	5,001 to 25,000	25,001 to 100,000	> 100,000
≥ 6	N/A	5,001 to 60,000	60,001 to 100,000	> 100,000

Friction characteristics are controlled by the lithology of the aggregate blend. For SMA, the blend can include crushed gravel, carbonate crushed stone, crystalline crushed stone (metamorphic or igneous stone, including but not limited to, quartzite, granite, trap rock), crushed sandstone, crushed air-cooled blast furnace slag, and crushed steel slag. Limestone is not allowed for SMA types E and F, because it would not meet the friction requirements of a surface course. To avoid blending soft aggregate with hard aggregate and to avoid the risk of crushing soft aggregate during SMA production Limestone can only be used partially (as a fraction of total aggregate blend) for type D. Carbonate crushed stone cannot be used in SMA N_{des} 80. In SMA N_{des} 50 carbonate crushed stone cannot be blended with any of the other aggregates allowed alone in N_{des} 50 SMA binder or N_{des} 50 SMA surface.

The fine aggregate specifications for SMA are the same as for other AC mixes (SSRBC, Art. 1030.03) except the only FA allowed in SMA are FA/FM 20 or FA/FM 22. Mineral filler for use in SMA is to be free from organic impurities and have a plasticity index ≤ 4, as per SSRBC Art. 1011.01 (c). Mineral filler can't be stored with collected dust as per Art. 1102.01(a)(4)(b). Table 51 presents the requirements for other components of SMA and its mix design in Illinois.

Crushed limestone, crushed dolomite, and crushed chert gravel aggregates are mainly commercialized for other purposes in Illinois. The amount of processed aggregate that could be suitable for SMA during production, gradation, demand, readily available at all locations in the state (for IDOT's Districts to specify them in SMA construction projects) are still unknown. The gradations of aggregate sources, allowed with less restrictions for SMA, such as crushed gravel, may need to be appear on producers' listings. Therefore, a survey to quantify and map SMA-suitable coarse aggregate in Illinois was distributed to quarries in the state. The coarse aggregates collected for this project were selected based on the results of that survey (Appendix C).

Table 51. Illinois Specifications for Components of SMA and Mix Design Requirements

Requirement	Limits		Notes	Reference
Binders	SBS PG 76-28 or SBS PG 76-22			Figure 53-4.M of Chapter 53 of IDOT's *Bureau of Design and Environment Manual*: Pavement Preservation and Rehabilitation Strategies (2025)
Fibers	Enough to have a maximum 0.3% drain down by weight of the mix when held at plant temperature for one hour as per Illinois Modified AASHTO T 305 (IDOT, 2021b)		Cellulose or Mineral	Illinois Modified AASHTO M 325 (IDOT, 2021b) and SSRBC Art. 1030.02 (h) Note 2
Recycled Material Allowed:	Maximum of 25% Asphalt Binder Replacement from FRAP/RAS (IDOT SSRBC 1031.06)			
NMAS	9.5 mm	12.5 mm		
Minimum VMA (%)	17.0	16.0 for N 50, 17.0 for N 80		Art. 1030.05 (b)
Design AV	4.0	4.0		Art. 1030.05 (b)
Sieve	Min (%)- Max (%)	Min (%)- Max (%)	Fine fraction in the aggregate blend shall be FA/FM 20 or FA/FM 22. Coarse aggregate gradation types that shall compose the blend are CA 13, 14, or 16. The maximum percent passing the #635 (20 µm) sieve shall be $\leqslant$ 3%.	SSRBC Art. 1030.05 (a)
1.5 in (37.5 mm)	100	100		
1 in (25.0 mm)	100	100		
3/4 in (19.0 mm)	100	100		
1/2 in (12.5 mm)	100	90–99		
3/8 in (9.5 mm)	70–95	50–85		
No. 4 (4.75 mm)	30–50	20–40		
No. 8 (2.36 mm)	20–30	16–24		
No. 16 (1.18 mm)	Max 21	–		
No. 30 (600 um)	Max 18	–		
No. 50 (300 um)	Max 15	–		
No. 200 (75 um)	8.0-11.0	8.0–11.0		

Current Performance Tests in Illinois for SMA Design Approval

Table 52 presents the current performance test requirements for SMA design approval.

Table 52. Current SMA Design Approval Performance Tests

Test	Standard	Requirement	Notes	Reference
Hamburg wheel-tracking test	Illinois-modified AASHTO T 324	Maximum 0.5 in (12.5 mm) at 20,000 passes	-	SSRBC Art. 1030.05 (d) (3)
Tensile strength ratio	Illinois-modified AASHTO T 283	Minimum 0.85 at 6.0 ± 0.5% air voids	The minimum allowable conditioned tensile strength shall be 80 psi.	Illinois-modified AASHTO M 325 and SSRBC Art. 1030.05 (c)

IDOT has introduced the Illinois Flexibility Index Test (I-FIT) as a mix design approval and quality control test is required for all mixes in the state. The SMA minimum flexibility index is 16.0 after short-term aging and 10.0 after long-term aging, per IDOT SSRBC (d) (4).

Stone-Mastic Asphalt Construction Particularities Specified in Illinois

The SSRBC states the following construction considerations shall apply to SMA.

- SMA shall be placed on a dry surface when the temperature of the roadbed is above 50°F and at a minimum mixture temperature (behind paver screed) of 310°F when using SBS PG 76-28 and 300°F when using SBS PG 76-22, as per Art. 406.06(c)(2).
- Surface and binder layers of 12.5 mm NMAS shall be constructed, at minimum, in 2-in-thick compacted lifts, as per Art. 406.06(e).
- No intermediate rollers shall be used for compaction. Pneumatic and vibratory rollers are not allowed, as per Art. 406.07(a).
- Quality Control individual test density control limits shall be 93.5%–97.4%, as per Art. 1030.09 for Quality Control/Quality Assurance quality management program applications.
- Dust/asphalt binder ratio is unrestricted.

USE AND SPECIFICATION OF SMA IN OTHER STATES

States such as Georgia and Maryland investigated the use of SMA in the 1990s. By the 2010s, the use of SMA has become common. Currently, various state highway agencies have SMA specifications developed based on AASHTO M 325 requirements (2008). However, each state has implemented modifications based on local needs and/or availability and properties of materials. In this section, the SMA design requirements of the following states are compared in Table 53: Indiana, Texas, Wisconsin, Georgia, Maryland, and Virginia.

Table 53. SMA Component and Mix Design Requirements for Selected States

State	Indiana			Texas			Wisconsin		Georgia			Maryland			Virginia		
CA LA abrasion	30 max			30 max			35 max		28 max			30 max			40 max		
CA flat and elongated ratios	AASHTO M 325 (2008): 20% max. for 3 to 1; 5% max. for 5 to 1																
FA angularity (loose uncompacted voids)	45 min			85 min			45 min		–			–			45 min		
Binders	PG 76-22, PG 70-22			PG 76 - (Varies)			PG 58-28 PG 58-34		PG 76-22			PG 76-22			PG 64-22		
Fibers	Cellulose or mineral			Cellulose or mineral			Cellulose		Cellulose or mineral			Cellulose or mineral			Cellulose or mineral		
Recycled Material Allowed	Reclaimed Asphalt Pavement (RAP)			RAP and Recycled Asphalt Shingles (RAS)			RAP and RAS		–			–			RAP		
Gyrations	75			50			65		50			100			75		
NMAS	9.5	12.5	19	Coarse	Medium	Fine	9.5	12.5	9.5	12.5	19	9.5	12.5	19	9.5	12.5	19
VMA	17	16	15	17.5	17.5	17.5	17	16	16	15	14	18	18	18	18	18	17
AV	4	4	4	3.7% and 7.0% (in place)			5	5	3.5			3.5	3.5	3.5	2–4		
Sieve	Gradation: (%) Passing																
1.5 in (37.5 mm)			100														
1 in (25.0 mm)		100	100								100				100	100	100
3/4 in (19.0 mm)	100	100	90–99	100	100			100	100	100	90–100	100	100	100	90–100	83–93	85–95
1/2 in (12.5 mm)	100	90–99	50–88	80–90	85–99	100	100	90–97	98–100	85–100	44–70	100	90–99	82–88	65–75	80 Max	50–60
3/8 in (9.5 mm)	70–95	50–80	25–60	25–60	50–75	70–100	90–100	58–80	70–100	50–75	25–60	75–90	70–85	60 Max	25–32	22–28	30–45
No. 4 (4.75 mm)	30–50	20–35	20–28	20–28	20–32	30–60	35–45	25–35	28–50	20–28	20–28	30–50	28–40	22–30			
No. 8 (2.36 mm)	20–30	16–24	16–24	14–20	16–28	20–40	18–28	15–25	15–30	16–24	15–22	20–30	18–30	14–20	15–25	16–24	16–24
No. 16 (1.18 mm)	Max. 21			8–20	8–28	6–30											
No. 30 (600 um)	Max. 18			8–20	8–28	6–30	18 max.	18 max.								15–20	12–16
No. 50 (300 um)	Max. 15			8–20	8–28	6–30			10–17	10–20	10–20						
No. 200 (75 um)	8–15	8–11	8–11	8–12	8–12	4–12	8–12	8–11	8–13	8–12	8–12	8–13	8–11	9–11	9–11	9–11	8–10
Reference	InDOT, 2015 and 2020			TxDOT, 2014			WisDOT, 2018 and 2021		GDOT, 2013			MDOT, 2018			VDOT, 2020		

The PG 76 binder is the most common selection for SMA independent of the climate requirement. The main difference in the SMA specifications among the states lies in the design number of gyrations, irrespective of abrasion properties. The range of gyrations varies from 35 (Georgia) to 100 (Maryland). Another requirement that varied was the air void content (from 3.5% to 5%). VMA requirements are related to the NMAS in Indiana, Wisconsin, Georgia, and Virginia; while the same VMA is required for all SMA in Texas and Maryland.

The six states studied require aggregates with high resistance to abrasion for SMA. However, Georgia, Texas, and Indiana allow the use of carbonated crushed stone aggregates. Additionally, in Indiana, steel furnace slag, sandstone, and crushed dolomite can be used in SMA, provided the mixtures are designed following the Indiana Test Method 220. As per the method, the Micro-Deval abrasion loss value for an acceptable coarse aggregate or blend of coarse aggregates shall be 18.0% or less. For aggregate degradation—defined as the difference in the percent passing the #8 sieve between the extracted gradation of a gyratory compacted specimen and an uncompacted mix sample—the loss value for an acceptable coarse aggregate or blend of coarse aggregates shall be 3.0% or less (INDOT, 2015).

In Texas, Class B aggregates, which include limestone, may be blended with a Class A aggregate if at least 50% of the material's weight is retained on the No. 4 sieve originating from the Class A aggregate source. In Georgia, carbonated stone is required to have a minimum of 25% insoluble residue retained on the #200 sieve to be used in SMA. Maryland allows the use of high-quality crushed limestone available in the western part of the state. Crushed limestone diabase is used in central Maryland for SMA. Imported aggregate is used in eastern Maryland close to the Chesapeake Bay area, where crushed greenstone from Pennsylvania or western Maryland is often used for SMA. Carbonate stone aggregates are not typically used for SMA in Wisconsin or Virginia because the states have other sources of premium aggregate for SMA, such as quartzite and trap rock.

The use of fibers in SMA is required in all states studied. Fibers contribute to the effectiveness of SMA by reducing binder drain down while increasing mastic stiffness. Fibers must meet the same requirement limits of those adopted in Illinois. Recently, Maryland initiated research into the use of fiberless SMA to avoid the difficulties of cleaning truck beds hauling SMA containing> Fiberless SMA mainly consisting of SMA warm-mix asphalt. The SMA warm-mix asphalt requires a lower mixing temperature, reducing the potential of drain down without the need of fibers. Although this material is not currently in Maryland DOT specifications, it is still undergoing investigation and implementation in several pilot projects.

Table 54 presents performance test requirements for SMA design approval adopted by the six state DOTs. Cracking performance tests are still not included in the six other state's specifications.

Table 54. SMA Design Approval Performance Tests in the Six States

State	Indiana	Texas	Wisconsin	Georgia	Maryland	Virginia
Rutting test						
Test	No Test	Hamburg Wheel-Tracking Test	No Test	Asphalt Pavement Analyzer	No Test	No Test
Specification		AASHTO T 324 (2019)		AASHTO T 340 (2010)		
Requirement		Maximum 0.5 in at 20,000 passes		0.3 in (7 mm) maximum		
Strength test						
Test	TSR	No Test*	TSR	TSR	TSR	TSR
Specification	AASHTO T 283 (2022a)		AASHTO T 283			
Requirement	Minimum 0.70 at 6.0 ± 0.5% air voids		Minimum 0.80 at 4.5% air voids	Minimum 0.60 at 6.0 ± 0.5% air voids	Minimum 0.85 at 6.0 ± 0.5% air voids	Minimum 0.80 at 6.0 ± 0.5% air voids
Other						
Test	No other test reported in the SMA specification	Boil Test	No other test is reported in the SMA specification.	Fatigue Life	No other test is reported in the SMA specification.	No other test is reported in the SMA specification.
Specification		Tex-530-C		AASHTO T 321 (2022b)		
Requirement		Not reported		Not reported		
Test		Cantabro Loss				
Specification		Tex-245-F				
Requirement		Not reported in the Specification				
Test		Overlay Test				
Specification		Tex-248-F				
Requirement		Not reported in the specification				

* Texas has a local tensile strength ratio (TSR) specification, but it has not been applied for SMA. Texas uses other acceptance tests such as the overlay and boil tests to accept SMA designs.

Stone-mastic asphalt on interstates might save the Virginia DOT in excess of $7,500 per lane mile in net present value costs. This value could be as high as $25 million if extrapolated to the entire Virginia interstate system for an SMA-only resurfacing program (EAPA, 2018). The performance and life cycle cost benefits of SMA were compared with those of polymer-modified SuperPave dense-graded mixtures (Yin & West, 2018). The findings showed that while SMA was not as cost-effective as comparable SuperPave mixtures for Michigan, it was more cost-effective for Virginia and Maryland. The estimated savings when using SMA amounted to 16% over a 23-year analysis period. Consequently, every state highway agency needs to conduct independent analysis according to their conditions to estimate whether the increase in life expectancy is worth the cost.

Use and Specification of SMA in Other Countries

Stone-mastic asphalt is used worldwide (Iskender, 2013). Research related to the development and use of SMA was identified for the conditions found in the countries in Table 55.

Table 55. Countries for Which Research Related to the Development and Use of SMA Was Identified

Country	Reference	Country	Reference	Country	Reference
Belgium	Vansteenkiste, 2013	Czech Republic	Blazejowski, 2011	Scotland	McLaughlin, 2018
Germany	Hainin et al., 2012	Ireland	Friel et al., 2013	France	Olard, 2012
Russia	Yastremsky et al., 2018	Turkey	Iskender, 2013	United Kingdom	Iskender, 2013
Poland	Wasilewska, 2017	Netherlands	Apostolidis et al., 2020	Europe in general	Beuving, 2018
Australia	White & Jamieson, 2018	China	Liu et al., 2017	India	Awanti, 2013
Iran	Behbahani et al., 2009	Japan	Tanaka & Maruyama, 2018	Jordan	Asi, 2006
Lithuania	Bražiūnas et al., 2013	Mexico	Limón-Covarrubias et al., 2019	Portugal	Miranda et al., 2020
South Africa	Louw et al., 1997	–	–	–	–

Applications of SMA have been reported in Argentina, Brazil, Israel, Korea, the Philippines, and Taiwan (Iskender, 2013). In contrast to the US, SMA specifications in Europe specify using limestone dust as mineral filler and having a maximum polishing requirement for aggregates (Descantes & Hamard, 2015). The polished stone value of aggregates, often required in SMA specifications outside the US, gives a measure of resistance to the polishing action of vehicle tires.

Some research studies specifically evaluate the use of alternative, local available aggregates:

- Wu et al. (2006) evaluated substituting the coarse fraction of a basalt SMA with steel slag designed using the Marshall method. Volumetric requirements were achieved even

though more asphalt was required. They evaluated indirect tensile tests, rutting tests, and friction measurements in a test section in Japan. They concluded the substitution was successful in utilizing a cost-effective aggregate resource. Aggregate breakage was not mentioned.

- Iskender (2013) evaluated whether limestone aggregates could be used as filler and fine fractions in SMA with basalt in Turkey. The requirements for European specifications were met, and rutting resistance of the SMA relatively decreased (less than 0.5%) with the incorporation of limestone aggregate.

- Šernas et al. (2016) indicated Lithuania has an issue similar to Illinois. Basalt aggregates are typically used for wearing courses but are imported. Lithuania has local access to dolomitic aggregates. The researchers performed a 100% substitution with dolomitic aggregates for two SMAs. However, adequate air voids were not achieved, and rutting resistance decreased with respect to a control granite dense-graded mix.

- Cao et al. (2013) compared the performance of three kinds of SMA using basalt, limestone, and a blend. They concluded that aggregate type has a significant effect on rutting resistance, but no significant difference in low-temperature cracking susceptibility or moisture susceptibility. Aggregate breakage was not reported.

ADDITIONAL PERFORMANCE TESTS FOR STONE-MASTIC ASPHALT DESIGN APPROVAL

The inclusion of weak aggregates as part of the coarse aggregate skeleton may result in aggregate degradation, breakdown, and consequent mix instability during compaction and service-life loading. Several tests have been adopted to address the suitability of aggregates for use in SMA.

Aggregate Breakdown

Prowell et al. (2009) reviewed adopted methods in Europe that target aggregate breakdown. In Germany, practitioners commonly used the Schlagversuch impact test, while practitioners in Sweden used abrasion tests for both the aggregate and mixture, in addition to the impact test, which was used for the aggregate only. Prowell et al. (2009) recovered gradations from 50-blow Marshall, 100 gyrations, and field-compacted samples and compared the mean percent material passing the 4.75 mm sieve using analysis of variance (ANOVA). Both laboratory compaction methods approximated breakdown in the field to an acceptable degree. LA abrasion loss and breakdown during laboratory compaction for both compaction methods were correlated. Based on the analysis, the authors concluded that the 30% maximum loss specification for LA abrasion was a reasonable criterion and the use of aggregate with higher LA abrasion loss values would result in excessive breakdown.

The SGC may be used to simulate the action of the field roller, yielding a similar trend in aggregate degradation (Hainin et al., 2013). The Hamburg wheel-tracking test (HWTT), in contrast, can simulate the rutting action that occurs in the surface layer mix of the pavement in the field. As such, both SGC and HWTT can be used to evaluate whether an SMA surface mix with weak aggregates would be susceptible to aggregate deterioration and breakdown during compaction and early service life.

Therefore, the aggregate breakdown potential of an SMA should be measured after SGC and after HWTT. Both should be compared to the control SMA without breakdown susceptible aggregates to determine if significant differences are found. If possible, the thresholds should be validated with data from field cores after service in the field. A comparison may be made on the half sieve, and the primary, secondary, and tertiary control sieves of the Bailey method to ensure the design placed in the field is similar enough to the conceptual one.

Another popular method of assessing aggregate breakdown is the Micro-Deval test, whose basis was developed in France during the 1960s. It provides a measure of toughness, abrasion resistance of aggregates in the presence of water, and an abrasive charge. In this test, aggregate samples are soaked in water and then placed in a cylinder together with steel balls. The cylinder is then rotated at 100 revolutions per min (rpm) for a specified time. After completion, the sample is screened by a 1.18 mm sieve and the percentage of material loss is calculated and reported as the abrasion value. The Micro-Deval test specifications are found in ASTM D 6928 (2017) and AASHTO T 327 (2012).

The Micro-Deval test could distinguish different kinds of CA efficiently using their mineral composition, even if they had the same performance (Cooley et al., 2002). In his adaptation of the Micro-Deval test for assessing the surface-weathering degree of granite, Takarli (2009) obtained a relationship between the wear coefficient and mineral composition of rock using the modified Deval test. He concluded that the wear testing method was a good indicator of the rock weathering degree and that the imposed weathering process decreases the abrasion resistance of the aggregate and increases its micro-fragmentation ability. Wang et al. (2015) later established a correlation between the Micro-Deval test and morphological properties of 11 roadway aggregates.

Celaya and Haddock (2006) investigated coarse aggregate strength requirements for use in SMA using six aggregates (steel slag, three gravels, and two dolomites). In that study, 9.5 NMAS SMAs were compacted using 100 gyrations targeting 4.0% air voids. The authors suggested that to obtain a 17.0% VMA, the aggregate blend should have certain characteristics: LA abrasion should be under 21%, Micro-Deval degradation under 9%, and the breakdown on the PCS under 3%. They concluded that a maximum LA abrasion of 30% alone is not enough as an indicator of quality aggregate for SMA. The Micro-Deval was a suitable complement for the LA abrasion test. However, it was not enough to predict the compaction degradation of aggregates in the SGC. Indiana DOT requires a 3% limit on aggregate degradation on the PCS after SGC because it has a correlation with VMA and limiting that would help achieving mix design volumetrics.

APPENDIX B: ACCELERATED PAVEMENT TESTING INSTRUMENTATION

Accelerated pavement testing (APT) is defined as “the application of wheel loads to specially constructed or in-service pavements to determine pavement response and performance under a controlled and accelerated accumulation of damage in a short period of time” (Saeed & Hall, 2003). Even though conducting an APT test is more expensive than other laboratory tests, such as the Hamburg wheel-tracking test, HWTT, because of its full-scale nature, it provides enhanced reliability and the option to monitor other important features of performance such as friction and load-related cracking. While APT can be a stand-alone testing activity, it is most useful when complemented with laboratory testing programs (Hugo & Epps Martin, 2004). Together they can provide an extensive understanding of the performance of a pavement.

ILLINOIS ACCELERATED PAVEMENT TESTING

Accelerated pavement testing began as early as 1909 with a test track in Detroit, Michigan (Metcalf, 1996). Historically, the most notable of these in terms of the effect on highway pavement engineering is the road test conducted by the American Association of State Highway Officials (AASHO) in the late 1950s. The Advanced Transportation Research and Engineering Laboratory (ATREL, now ICT) acquired the Accelerated Transportation Loading System (ATLAS) in 2000 from Applied Research Associates (ARA). After significant revamping in 2023, it was renamed as Illinois Accelerated Pavement Testing (I-APT). Like other APT devices, I-APT had the capability to subject full-scale pavement test sections to real-life traffic and environmental conditions (Renshaw et al., 2024). The system can simulate truck, aircraft, or rail-bogey loading on various types of pavement systems. I-APT has three main components: the control trailer, the mechanical trailer, and the test machine, shown in Figure 187.

After 20 years of operation, ATLAS was extensively renovated between 2021-2024. Major changes were made to the loading and drive systems. Loading system changes included a newly designed carriage and replacement of the load applying actuators with new units. The new carriage design provides tandem axle loading capability, with adjustable center-to-center axle spacing. The new actuators have a reduced overall capacity, 35 kip per axle, with higher resolution and increased accuracy and precision, accompanied by in-line load cells. These changes increased the pavement load measurement accuracy by an order of magnitude, which is now on the order of (+/-) 50 lbs, and provide greater control of the load on the pavement along the entire trafficked test section. The drive system changes included replacement of a conventional APT vector drive system to a hydraulic motor drive system. This change eliminated nearly all electro-magnetic field, EMF, noise in proximity to the test machine, which protects the integrity of sensitive measurement signals and provides the opportunity to collect more accurate pavement sensor readings. In addition, I-APT is now capable of applying shear loading to simulate tire breaking and acceleration, and it provides for yaw angle adjustment of the loading wheels up to (+/-) 6 degrees.

Table 56 presents the equipment specifications after the renovations.

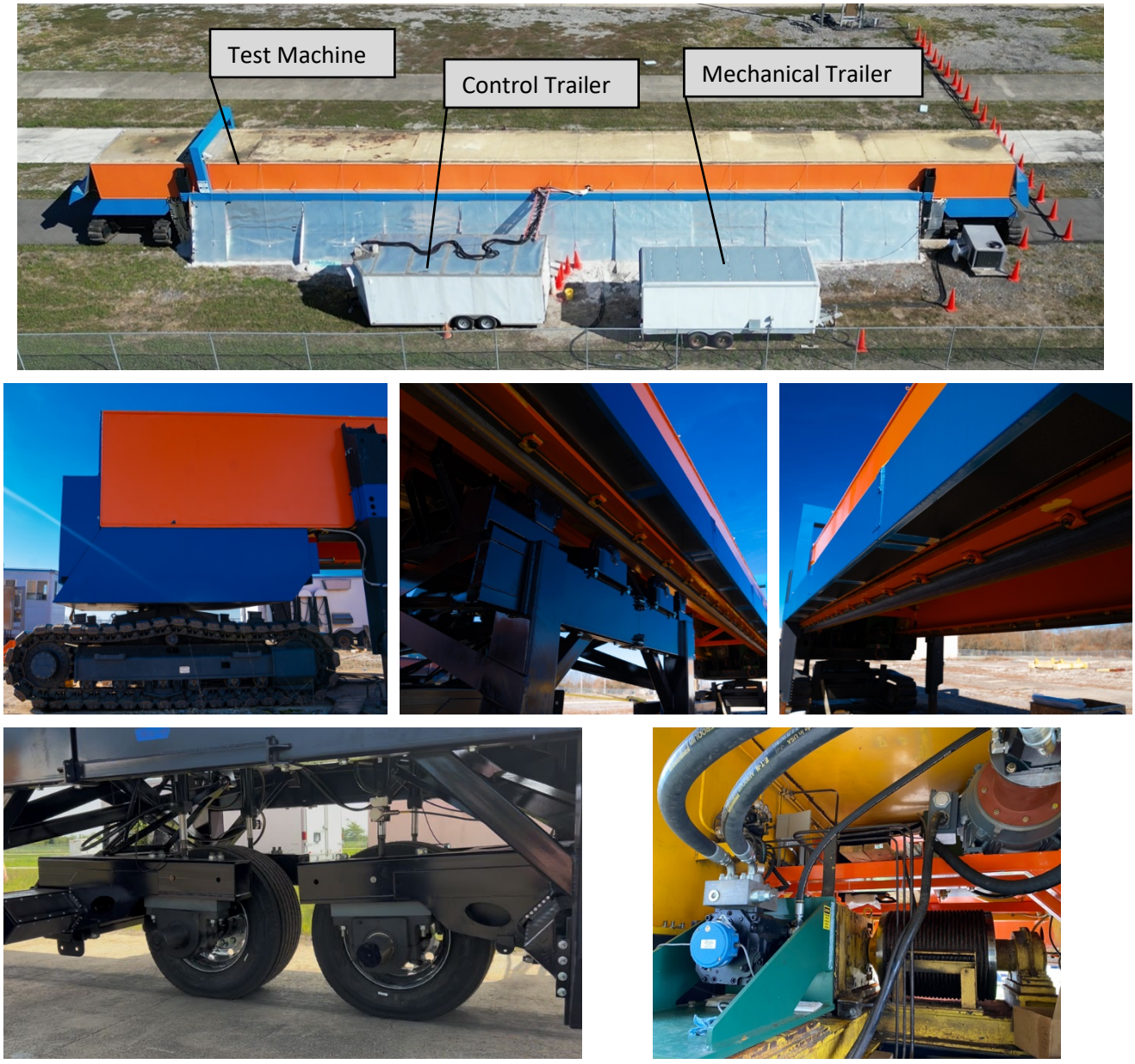

Figure 187. Photo. I-APT facility and major components of the test machine.

Table 56. I-APT Specifications after the 2024 Renovation

Parameter	Unit	I-APT
Gross Weight	kips	156
Length	feet	124
Height	feet	12
Width	feet	12
Machine Displacement Method		Crawler Tracks
Data Acquisition System		Static and Dynamic
Temperature Control		Yes: Heating and Cooling
Simulated Tire Types		Single
		Dual
		Aircraft
		Single axle rail bogey
Maximum Capacity	kips	Pre renovation: 80 Post renovation: 35
Loading Axle		Single or Tandem (Adjustable axle spacing)
Total Tire Displacement Length	feet	85
Total Tire Constant Speed Displacement Length	feet	65
Maximum Speed	mph	10
Lateral Wander	feet	3
Displacement Mode		Uni- and bidirectional
Features		Shear Loading Application (Breaking / Acceleration)
		Wheel Yaw (+/-) 6 degrees

APPENDIX C: QUARRY SURVEY AND RESPONSES

SURVEY SAMPLE

Availability of Illinois' Coarse Aggregates for Stone-Matrix Asphalt (SMA) Survey

The intent of this survey is to quantify and map the availability of aggregates that are suitable for Stone-Matrix Asphalt (SMA) in Illinois. Your responses will be used in IDOT's project *R27-216: Optimizing the Use of Local Aggregates for Stone-Matrix Asphalt*, which is conducted by the Illinois Center for Transportation (ICT).

The main objective of this project is to enable the use of local coarse aggregates for SMA. If local coarse aggregates are approved for SMA, demand for the products described ahead is likely to increase.

All the information gathered will be treated in a **confidential** manner: Producers' identification will be disassociated from the survey responses.

We appreciate your time in responding to this survey! it should require only a few minutes to complete. Responses should be sent **by January 29th, 2021**.

If you have any question, please email Mr. Javier García Mainieri (MS) at jjg5@illinois.edu.

SMA-suitable aggregates are required to have the following characteristics.

What is the quantity (US tons/year) of SMA-suitable aggregate gradations that you currently produce or are able to produce?

	Crushed Limestone	Crushed Dolomite	Crushed Sandstone	Crushed Gravel South of I-80	Crushed Chert Gravel	Crushed Steel Slag	Crushed Crystalline Stone*
Quantity of CM12							
Quantity of CM13							
Quantity of CM14							
Quantity of CM15							

Quantity of CM16							
Quantity of CM20							

* Crushed crystalline stone is either metamorphic or igneous stone, including: quartzite, granite, and trap rock

Do you expect a significant increase (+%) or decrease (-%) in your production in upcoming years? Please indicate in the table.

	Crushed Limestone	Crushed Dolomite	Crushed Sandstone	Crushed Gravel South of I-80	Crushed Chert Gravel	Crushed Steel Slag	Crushed Crystalline Stone*
Quantity of CM12							
Quantity of CM13							
Quantity of CM14							
Quantity of CM15							
Quantity of CM16							
Quantity of CM20							

Do you have any relevant comments about the estimates provided?

How much would your operations have to be modified to produce more SMA-suitable aggregates?

1 2 3 4 5

○ ○ ○ ○ ○

How would producing SMA-suitable aggregates impact your current operations?

Address and contact

*Mandatory field

IDOT Producer Number:

Quarry Name:

Quarry County: *

Quarry Address:

Street Address

City

Zip Code

Name of Contact Person:

First Name Last Name

Phone Number:

Area Code Phone Number

Email:

Provide an email to get a copy for your answers

Submit

RESPONSES

Illinois Center for Transportation
University of Illinois at Urbana-Champaign

ILLINOIS

Survey Results

"Where Excellence and Transportation Meet"

Illinois Center for Transportation
University of Illinois at Urbana-Champaign

What is the quantity (US tons/year) of SMA-suitable aggregate gradations that you currently produce or are able to produce?

What is the quantity (US tons/year) of SMA-suitable aggregate gradations that you currently produce or are able to produce?

	Crushed Limestone	Crushed Dolomite	Crushed Sandstone	Crushed Gravel South of I-80	Crushed Chert Gravel	Crushed Steel Slag	Crushed Crystalline Stone*
Quantity of CM12							
Quantity of CM13							
Quantity of CM14							
Quantity of CM15							
Quantity of CM16							
Quantity of CM20							

1-5000
5000-15000
15000-25000
25000-35000
35000-45000
45000-55000
more than 55000

"Where Excellence and Transportation Meet" 2

- **No Sandstone or Crystalline Sources**
- **Only one quarry: Chert Gravel CM13 and CM14**

Statewide-accumulated Quantity Lower-bound Approximations (US ton/year)							
Gradation/ Source	Crushed Limestone	Crushed Dolomite	Crushed Sandstone	Crushed Gravel South of I-80	Crushed Chert Gravel	Crushed Steel Slag	Crushed Crystalline Stone
CM12	130000	0	0	0	0	55000	0
CM13	210000	435000	0	95000	40000	110000	0
CM14	182500	232500	0	10000	40000	60000	0
CM15	155000	10000	0	0	0	0	0
CM16	545000	670000	0	125000	0	110000	0
CM20	142500	0	0	65000	0	0	0

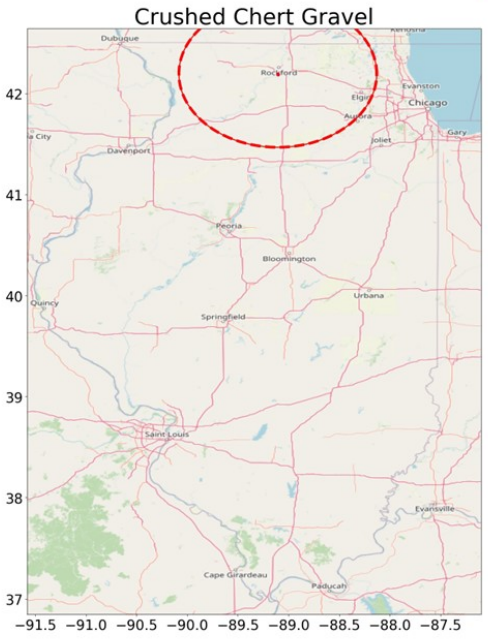

Illinois Center for Transportation
University of Illinois at Urbana-Champaign

Limestone Dolomite Gravel South of I-80 Steel Slag

Color							
Quantity (US ton/year)	1-5000	5000-15000	15000-25000	25000-35000	35000-45000	45000-55000	>55000

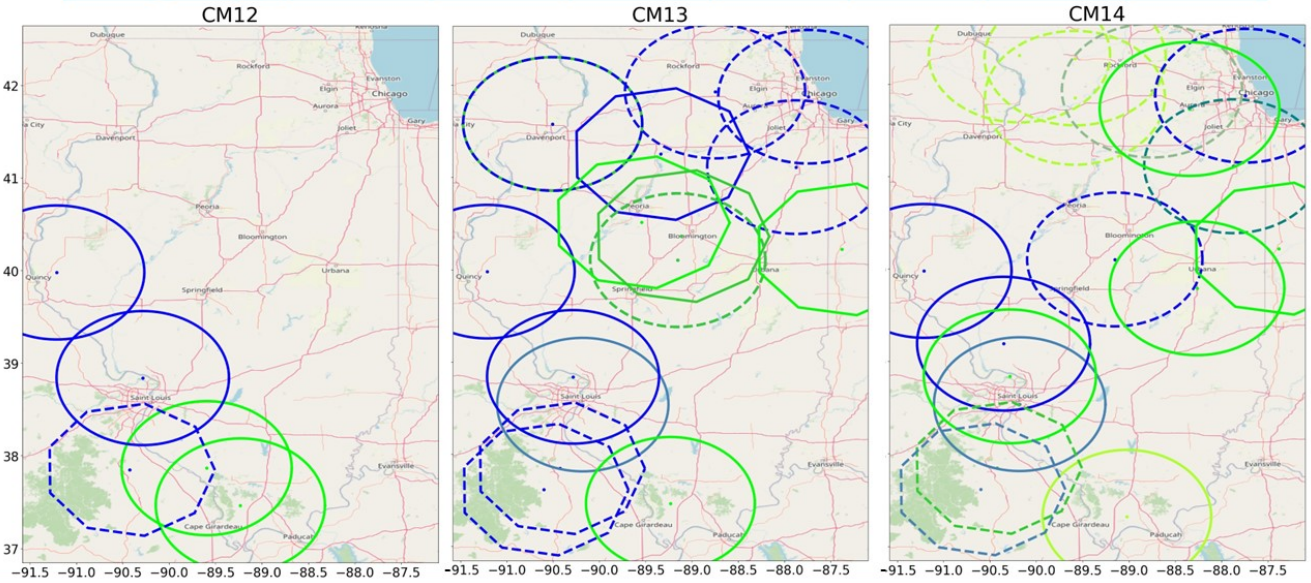

Illinois Center for Transportation
University of Illinois at Urbana-Champaign

Limestone Dolomite Gravel South of I-80 Steel Slag

Color							
Quantity (US ton/year)	1-5000	5000-15000	15000-25000	25000-35000	35000-45000	45000-55000	>55000

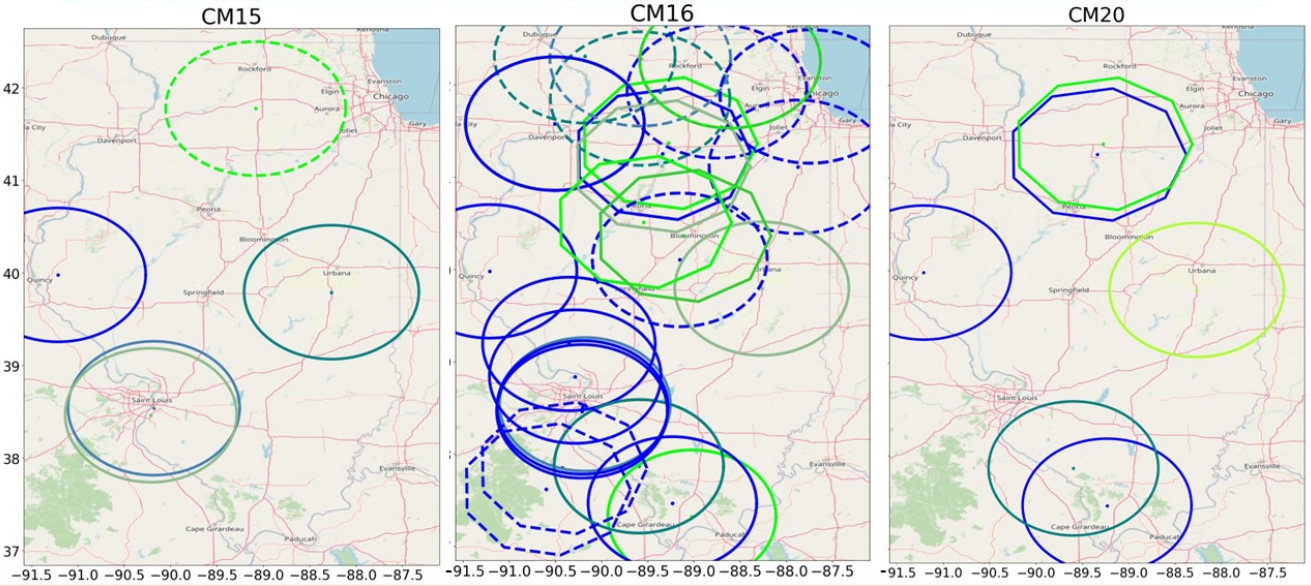

Illinois Center for Transportation
University of Illinois at Urbana-Champaign

Do you expect a significant increase (+%) or decrease (-%) in your production in upcoming years?

- **Expected increase** reported on 35 products
- One Chert Gravel producer: -50% (or more) on CM13 and CM14
- One Limestone quarry: -50% (or more) on CM14
- One Limestone quarry: -20% on CM16
- One Dolomite quarry: -10% on CM16
- One Limestone quarry: -20% on CM20

- **Four submissions included a comment about the producer being able to produce more if there were more demand.**

How much would your operations have to be modified to produce more SMA-suitable aggregates?

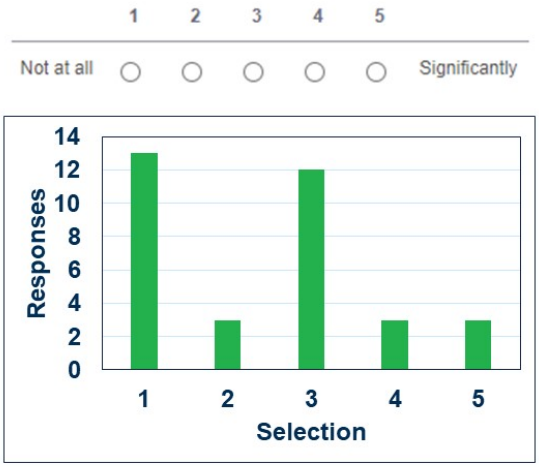

- **Five left blank**

How would producing SMA-suitable aggregates impact your current operations?

- Two quarries would not be able to do it
- Three indicated uncertainty
- Three mentioned a sales/cost impact
- Seven reported no impact
- "An increase in the use of SMA pavements is going to aggravate the existing fines problem as SMA pavements do not utilize a large fraction of fines. If we can't get rid of the fines the price of the course aggregates will go up. The use of SMA surfaces needs to be paired with fine graded binders to balance aggregate needs."

Conclusions

- **Chert Gravel and Gravel South of I-80 are not as frequent**
- **Most frequent source: Limestone**
  - Specially for CM13 and CM16
- **Dolomite sources appear to be in the north of the state close to Wisconsin's aggregates**
  - Where are the quarries in WI?
  - Is there Dolomite in South IL?
- **Increasing SMA-suitable aggregate supply does not seem to negatively impact quarry operations**
  - If extra fines production is compensated
- **SMA-suitable aggregate demand can be covered by local aggregates**

APPENDIX D: DISTRICT QUESTIONNAIRE AND RESPONSES

QUESTIONNAIRE

For the purpose of this research and survey "local aggregate" is defined as mined/produced in Illinois.

1) Is your District currently using, or planning to use SMA?

   Ans: If Not (Respond to a) before skipping to Question #2)

   a) Would your district be interested using SMA if the research determines that local aggregates can be used in SMA successfully resulting in lower cost?

   Ans: If Yes (Respond to b) through f) before responding to Question #2)

   b) How many contractors in your district typically bid on SMA projects? (please also include total number of contractors that typically do work in your district)

      Number of contractors that bid SMA: _____ Total number of contractors: _____

   c) What is the estimated tons of SMA let or planned to be let during the 2021 calendar year? _____ tons

   d) What is the estimated tons of SMA planned to be let during the 2022 calendar year? _____ tons

   e) Please check all of the applications SMA would be used in and list the sizes of SMA that would be considered for each application (i.e. 9.5mm, 12.5mm ***or future use of 19.0mm-if research determines this new size is viable***):

      - Full Depth – Surface lift_____
      - Full Depth – Binder top lift_____
      - Full Depth – Binder lower lift(s)_____
      - Overlay – Surface lift_____
      - Overlay – Binder lift_____

   f) What circumstances would warrant your districts use of SMA. Please check all that apply:

      - More stable mix that increased capability of handling heavy traffic
      - More durable mix that will provide a longer service life
      - Better friction properties due to enhanced macrotexture
      - Applications where vibratory compaction is not allowed (i.e. bridge decks, overlaying distressed PCC concrete, city streets w/ vulnerable infrastructure, etc.)

Other (please describe) __ _-

_____

_____

_____

2) Assuming the ICT research outcome demonstrates that N50 SMA designs with local aggregates are comparable in stability to the current N80 SMAs and can be used in all traffic applications (following friction requirements) would your District consider the following (check one of the following & explain):

   - Increase usage of SMA? (please discuss new applications) _____

   _____

   - Keep SMA usage the same? _____

   _____

3) Are there any impediments in using more SMA in your district? If so, please explain. _____

   _____

   _____

4) What percentage would SMA make up in total HMA planned for calendar year:

   - 2021? _____
   - 2022? _____

Can you provide a list of 2021 and 2022 planned projects that would use SMA?

Are you willing to collaborate with ICT and IDOT Central Bureau of Materials by allowing the use of local aggregates in a pavement section?

Illinois Center for Transportation
University of Illinois at Urbana-Champaign

ILLINOIS

District Questionnaire Responses

Usage and Contractor Availability

District	1	2	3	4	5	6	7	8	9	Total or Average
SMA contractors	20	6	6	2	2	1	2	3	3	45
Total contractors	A lot	9	10	2	3	6	2	4	3	39+
Ratio		0.67	0.6	1	0.67	0.17	1	0.75	1	0.73
SMA usage 2021	240	10	28.5	92	16.4	34.8	35		36	492.7
SMA expected usage 2022	300	33	55.5	65	60	27.3	78			618.8
Expected Increase	20%	70%	49%	-42%	73%	-27%	55%			28%

Sizes of SMA that will be used

1. 12.5mm,
2. 9.5mm,
3. and 19.0mm.

What circumstances would warrant your districts use of SMA. Please check all that apply:

- 9/9 More stable mix that increased capability of handling heavy traffic
- 9/9 More durable mix that will provide a longer service life
- 6/9 Better friction properties due to enhanced macrotexture
- 6/9 Applications where vibratory compaction is not allowed (i.e. bridge decks, overlaying distressed PCC concrete, city streets w/ vulnerable infrastructure, etc.)

Assuming the ICT research outcome demonstrates that N50 SMA designs with local aggregates are comparable in stability to the current N80 SMA mixtures and can be used in all traffic applications (following friction requirements) would your District consider the following (check one of the following & explain):

- **Same: Interstate and high-volume road overlays**
- **Add:**
  - Overlaying CIR or Rubblized
  - Shoulders often used for parking
  - Highways with seasonal truck traffic
  - Heavily trafficked intersections (with turning points)
  - Sub out N70E

Are there any impediments in using more SMA in your district? If so, please explain.

- **Scarce sources of aggregate supply.**
- **Limited experience with SMA (Contractors: few bids/Districts: selection of quality control strategy)**
- **Cost of SMA**
- **SMA resists cracking on CRPCC, but D7 is hesitant to use on jointed pavement. (R27-204)**
- **Plant capabilities generate complains about baghouse fines restriction.**

What percentage would SMA make up in total HMA planned for calendar year?

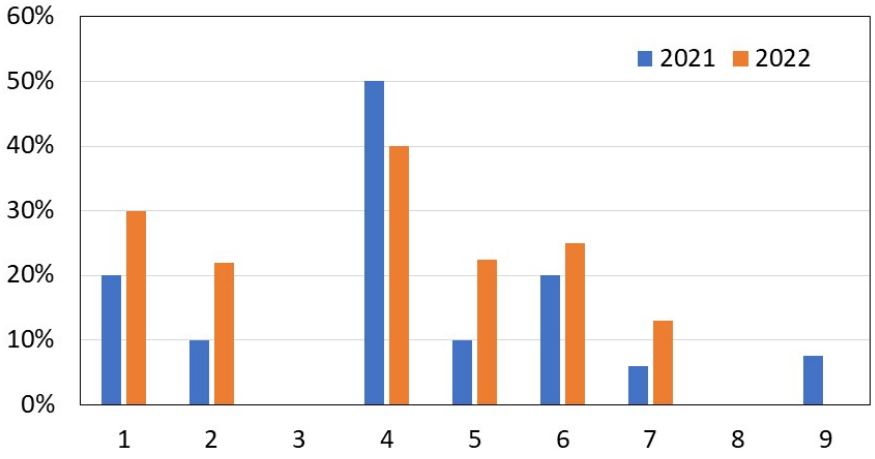

D3, D8 , and D9(2022) did not provide rough estimate

Illinois Center for Transportation
University of Illinois at Urbana-Champaign

Are you willing to collaborate with ICT and IDOT Central Bureau of Materials by allowing the use of local aggregates in a pavement section?

- **Yes**
  - D1-5, 7, and 8
  - D6: Already done on contracts 72L26 (US67), 72G46 (I-55), and 72823 (I-72).
  - D9: Potentially

Takeaways

- The survey outcome supports the direction of projects 216 and 204.
- SMA use is expected to increase by ~10-30%.
- Potential use of SMA as overlay for various rehabilitation approaches.
- Considering Missouri Trap Rock for the control SMAs was supported. appears to be used frequently and should be selected for LCA/LCCA.
- D6 is lacking bidders.

APPENDIX E: I-APT SMA DESIGNS

Producer Number & Name -->		T1-80-12.5-0	<--- Plant Location
Material Code Number ---->			

Plant Bin #	#7	#6	#5	#4	#3	#2	#1	MF	RCY	RCY	RCY	RCY	ASPHALT
Size	022CM14	022CM16	038FM20					004MF01					SBS
Source (PROD #)	CONFIDENTIAL	CONFIDENTIAL	CONFIDENTIAL					CONFIDENTIAL					CONFIDENTIAL
(NAME)	CONFIDENTIAL	CONFIDENTIAL	CONFIDENTIAL					CONFIDENTIAL					CONFIDENTIAL
(LOC)	CONFIDENTIAL	CONFIDENTIAL	CONFIDENTIAL					CONFIDENTIAL					CONFIDENTIAL
(ADD. INFO)													#N/A
									0.0	0.0	0.0	0.0	< AB in RCY
	Aggregate Blend:											Plan PG Grade >	PG 76-28
	59.5	11.2	21.3	0.0	0.0	0.0	0.0	8.0	0.0	0.0	0.0	0.0	100.0
	Mixture Blend:												Totals: ↕
	0.0	0.0	0.0	0.0	0.0	0.0	0.0	0.0	0.0	0.0	0.0	0.0	6.0

Agg No. / Sieve Size	#7	#6	#5	#4	#3	#2	#1	MF	RCY	RCY	RCY	RCY	Aggregate Blend	Mixture Comp Spec
1" (25.0mm)	100.0	100.0	100.0	100.0	100.0	100.0	100.0	100.0	100.0	100.0	100.0	100.0	100	
3/4"(19.0mm)	100.0	100.0	100.0	100.0	100.0	100.0	100.0	100.0	100.0	100.0	100.0	100.0	100	100
1/2" (12.5mm)	89.2	100.0	100.0	100.0	100.0	100.0	100.0	100.0	100.0	100.0	100.0	100.0	94	90-99
3/8" (9.5mm)	46.3	98.8	100.0	100.0	100.0	100.0	100.0	100.0	100.0	100.0	100.0	100.0	68	50-85
No.4 (4.75mm)	2.2	29.6	97.4	100.0	100.0	100.0	100.0	100.0	100.0	100.0	100.0	100.0	33	20-40
No.8 (2.36mm)	0.9	4.2	67.1	100.0	100.0	100.0	100.0	100.0	100.0	100.0	100.0	100.0	23	16-24
No.16 (1.18mm)	0.6	1.4	38.1	100.0	100.0	100.0	100.0	100.0	100.0	100.0	100.0	100.0	17	
No.30 (600µm)	0.4	0.7	21.4	100.0	100.0	100.0	100.0	100.0	100.0	100.0	100.0	100.0	13	
No.50 (300µm)	0.3	0.5	12.7	100.0	100.0	100.0	100.0	100.0	100.0	100.0	100.0	100.0	11	
No.100 (150µm)	0.2	0.3	9.2	100.0	100.0	100.0	100.0	99.7	100.0	100.0	100.0	100.0	10	
No.200(75µm)	0.2	0.2	7.2	100.0	100.0	100.0	100.0	96.8	100.0	100.0	100.0	100.0	9.4	8.0-11.0
2021 Gsb	2.663	2.628	2.608	1.000	1.000	1.000	1.000	2.800	1.000	1.000	1.000	1.000	2.658	
Design Gsb	2.663	2.628	2.608	1.000	1.000	1.000	1.000	2.800	1.000	1.000	1.000	1.000	2.658	Dust/AB
Absorption, %	0.30	0.80	3.40	1.00	1.00	1.00	1.00	1.00	1.00	1.00	1.00	1.00	0.44	Ratio
												SP GR AB	1.000	1.57
											Change in Combined Gsb		0.000	

SUMMARY OF SUPERPAVE GYRATORY DESIGN DATA

DATA for N-int.	7								
	AB, %MIX	Gmb	Gmm	Voids (Pa)	VMA	VFA	Vbe	Pbe	Pba
MIX 1	5.5	2.088	2.480	15.8	25.8	38.7	9.94	4.76	0.78
MIX 2	6.0	2.106	2.460	14.4	25.5	43.6	11.14	5.29	0.76
MIX 3	6.5	2.126	2.449	13.2	25.2	47.7	12.03	5.66	0.90
MIX 4	6.5	2.126	2.449	13.2	25.2	47.7	12.03	5.66	0.90

DATA for N-des.	80								
		Gmb	Gmm	Voids (Pa)	VMA	VFA	Vbe	Pbe	Gse	Pba
MIX 1	5.5	2.352	2.480	5.2	16.4	68.5	11.20	4.76	2.714	0.78
MIX 2	6.0	2.367	2.460	3.8	16.3	76.8	12.52	5.29	2.713	0.76
MIX 3	6.5	2.381	2.449	2.8	16.2	82.9	13.48	5.66	2.723	0.90
MIX 4	6.5	2.381	2.449	2.8	16.2	82.9	13.48	5.66	2.723	0.90

Performance Test Data	
Hamburg No. Passes	
Hamburg Wheel Depth	
Unaged Flexibility Index (FI)	
LTA FI (SURFACE ONLY)	
TSR Information	
Conditioned	
Unconditioned	
TSR	
CA Strip Rating	
FA Strip Rating	
Additive Prod #	
Additive Product Name	
Additive %	

OPTIMUM DESIGN DATA @ Ndes											
GYRATIONS	AB	Gmb	Gmm	%VOIDS (Pa) Target	VMA Out	VFA	Gse	Gsb	TSR	RCY AB	Virgin AB	ABR
80	6.0	2.362	2.460	4.0	16.5	75.7	2.713	2.658	0.00	0.00	6.00	#VALUE!

REMARKS LINE 1: 0.3% Cellulose Fiber
REMARKS LINE 2:

HMA AGED: HOURS @

Producer Number & Name -->		T1-50-12.5-0	<--- Plant Location
Material Code Number ---->			

Plant Bin #	#7	#6	#5	#4	#3	#2	#1	MF	RCY	RCY	RCY	RCY	ASPHALT
Size	022CM14	022CM16	038FM20					004FM01					SBS
Source (PROD #)	CONFIDENTIAL	CONFIDENTIAL	CONFIDENTIAL					CONFIDENTIAL					CONFIDENTIAL
(NAME)	CONFIDENTIAL	CONFIDENTIAL	CONFIDENTIAL					CONFIDENTIAL					CONFIDENTIAL
(LOC)	CONFIDENTIAL	CONFIDENTIAL	CONFIDENTIAL					CONFIDENTIAL					CONFIDENTIAL
(ADD. INFO)													#N/A
									0.0	0.0	0.0	0.0	< AB in RCY
	Aggregate Blend:											Plan PG Grade >	PG 76-28
	58.3	11.0	22.6	0.0	0.0	0.0	0.0	8.1	0.0	0.0	0.0	0.0	100.0
	Mixture Blend:												Totals: ↕
	0.0	0.0	0.0	0.0	0.0	0.0	0.0	0.0	0.0	0.0	0.0	0.0	6.3

Agg No. / Sieve Size	#7	#6	#5	#4	#3	#2	#1	MF	RCY	RCY	RCY	RCY	Aggregate Blend	Mixture Comp Spec
1" (25.0mm)	100.0	100.0	100.0	100.0	100.0	100.0	100.0	100.0	100.0	100.0	100.0	100.0	100	100
3/4"(19.0mm)	100.0	100.0	100.0	100.0	100.0	100.0	100.0	100.0	100.0	100.0	100.0	100.0	100	90-100
1/2" (12.5mm)	89.2	100.0	100.0	100.0	100.0	100.0	100.0	100.0	100.0	100.0	100.0	100.0	94	75-89
3/8" (9.5mm)	46.3	98.8	100.0	100.0	100.0	100.0	100.0	100.0	100.0	100.0	100.0	100.0	69	
No.4 (4.75mm)	2.2	29.6	97.4	100.0	100.0	100.0	100.0	100.0	100.0	100.0	100.0	100.0	35	40-60
No.8 (2.36mm)	0.9	4.2	67.1	100.0	100.0	100.0	100.0	100.0	100.0	100.0	100.0	100.0	24	26-42
No.16 (1.18mm)	0.6	1.4	38.1	100.0	100.0	100.0	100.0	100.0	100.0	100.0	100.0	100.0	17	15-30
No.30 (600µm)	0.4	0.7	21.4	100.0	100.0	100.0	100.0	100.0	100.0	100.0	100.0	100.0	13	
No.50 (300µm)	0.3	0.5	12.7	100.0	100.0	100.0	100.0	100.0	100.0	100.0	100.0	100.0	11	6-15
No.100 (150µm)	0.2	0.3	9.2	100.0	100.0	100.0	100.0	99.7	100.0	100.0	100.0	100.0	10	4-9
No.200(75µm)	0.2	0.2	7.2	100.0	100.0	100.0	100.0	96.8	100.0	100.0	100.0	100.0	9.6	3-6
2021 Gsb	2.663	2.628	2.608	1.000	1.000	1.000	1.000	2.800	1.000	1.000	1.000	1.000	2.657	
Design Gsb	2.663	2.628	2.608	1.000	1.000	1.000	1.000	2.800	1.000	1.000	1.000	1.000	2.657	Dust/AB
Absorption, %	0.30	0.80	3.40	1.00	1.00	1.00	1.00	1.00	1.00	1.00	1.00	1.00	0.45	Ratio
												SP GR AB	1.000	1.53
											Change in Combined Gsb		0.000	

SUMMARY OF SUPERPAVE GYRATORY DESIGN DATA

DATA for N-int.	6								
	AB, %MIX	Gmb	Gmm	Voids (Pa)	VMA	VFA	Vbe	Pbe	Pba
MIX 1	6.0	2.114	2.467	14.3	25.2	43.2	10.89	5.15	0.90
MIX 2	6.2	2.120	2.459	13.8	25.2	45.2	11.38	5.37	0.89
MIX 3	6.5	2.126	2.446	13.1	25.2	48.1	12.12	5.70	0.86
MIX 4	7.0	2.141	2.432	12.0	25.1	52.2	13.10	6.12	0.95

DATA for N-des.	50									
		Gmb	Gmm	Voids (Pa)	VMA	VFA	Vbe	Pbe	Gse	Pba
MIX 1	6.0	2.352	2.467	4.7	16.8	72.3	12.11	5.15	2.722	0.90
MIX 2	6.2	2.348	2.459	4.5	17.1	73.6	12.61	5.37	2.721	0.89
MIX 3	6.5	2.373	2.446	3.0	16.5	81.9	13.53	5.70	2.719	0.86
MIX 4	7.0	2.372	2.432	2.5	17.0	85.5	14.52	6.12	2.726	0.95

Performance Test Data	
Hamburg No. Passes	
Hamburg Wheel Depth	
Unaged Flexibility Index (FI)	
LTA FI (SURFACE ONLY)	
TSR Information	
Conditioned	
Unconditioned	
TSR	
CA Strip Rating	
FA Strip Rating	
Additive Prod #	
Additive Product Name	
Additive %	

OPTIMUM DESIGN DATA @ Ndes

GYRATIONS	AB	Gmb	Gmm	%VOIDS (Pa) Target	VMA	VFA	Gse	Gsb	TSR	RCY AB	Virgin AB	ABR
50	6.3	2.358	2.456	4.0	16.8	76.3	2.723	2.657	0.00	0.00	6.30	#VALUE!

REMARKS LINE 1: 0.3% Cellulose Fiber
REMARKS LINE 2:

HMA AGED: HOURS @

Producer Number & Name -->		D2-50-12.5-0		<--- Plant Location	
Material Code Number ---->					

Plant Bin #	#7	#6	#5	#4	#3	#2	#1	MF	RCY	RCY	RCY	RCY	ASPHALT
Size	022CA14	022CA16	038FM20					004FM01					SBS
Source (PROD #)	CONFIDENTIAL	CONFIDENTIAL	CONFIDENTIAL					CONFIDENTIAL					CONFIDENTIAL
(NAME)	CONFIDENTIAL	CONFIDENTIAL	CONFIDENTIAL					CONFIDENTIAL					CONFIDENTIAL
(LOC)	CONFIDENTIAL	CONFIDENTIAL	CONFIDENTIAL					CONFIDENTIAL					CONFIDENTIAL
(ADD. INFO)													#N/A
									0.0	0.0	0.0	0.0	< AB in RCY
	Aggregate Blend:											Plan PG Grade >	PG 76-28
	63.6	11.4	17.6	0.0	0.0	0.0	0.0	7.4	0.0	0.0	0.0	0.0	100.0
	Mixture Blend:												Totals: ↕
	0.0	0.0	0.0	0.0	0.0	0.0	0.0	0.0	0.0	0.0	0.0	0.0	7.0

Agg No. / Sieve Size	#7	#6	#5	#4	#3	#2	#1	MF	RCY	RCY	RCY	RCY	Aggregate Blend	Mixture Comp Spec
1" (25.0mm)	100.0	100.0	100.0	100.0	100.0	100.0	100.0	100.0	100.0	100.0	100.0	100.0	100	
3/4"(19.0mm)	100.0	100.0	100.0	100.0	100.0	100.0	100.0	100.0	100.0	100.0	100.0	100.0	100	100
1/2" (12.5mm)	91.0	100.0	100.0	100.0	100.0	100.0	100.0	100.0	100.0	100.0	100.0	100.0	94	90-99
3/8" (9.5mm)	57.0	92.0	100.0	100.0	100.0	100.0	100.0	100.0	100.0	100.0	100.0	100.0	72	50-85
No.4 (4.75mm)	4.5	20.8	97.4	100.0	100.0	100.0	100.0	100.0	100.0	100.0	100.0	100.0	30	20-40
No.8 (2.36mm)	2.2	2.6	67.1	100.0	100.0	100.0	100.0	100.0	100.0	100.0	100.0	100.0	21	16-24
No.16 (1.18mm)	2.0	2.3	38.1	100.0	100.0	100.0	100.0	100.0	100.0	100.0	100.0	100.0	16	
No.30 (600µm)	1.9	2.3	21.4	100.0	100.0	100.0	100.0	100.0	100.0	100.0	100.0	100.0	13	
No.50 (300µm)	1.9	2.2	12.7	100.0	100.0	100.0	100.0	100.0	100.0	100.0	100.0	100.0	11	
No.100 (150µm)	1.8	2.1	9.2	100.0	100.0	100.0	100.0	99.7	100.0	100.0	100.0	100.0	10	
No.200(75µm)	1.6	2.0	7.2	100.0	100.0	100.0	100.0	96.8	100.0	100.0	100.0	100.0	9.7	8.0-11.0
2021 Gsb	2.593	2.623	2.608	1.000	1.000	1.000	1.000	2.800	1.000	1.000	1.000	1.000	2.613	
Design Gsb	2.593	2.623	2.608	1.000	1.000	1.000	1.000	2.800	1.000	1.000	1.000	1.000	2.613	Dust/AB
Absorption, %	2.80	2.40	3.40	1.00	1.00	1.00	1.00	1.00	1.00	1.00	1.00	1.00	2.50	Ratio
												SP GR AB	1.000	1.38
											Change in Combined Gsb		0.000	

SUMMARY OF SUPERPAVE GYRATORY DESIGN DATA

DATA for N-int.	6								
	AB, %MIX	Gmb	Gmm	Voids (Pa)	VMA	VFA	Vbe	Pbe	Pba
MIX 1	6.5	2.074	2.474	16.2	25.8	37.3	9.62	4.64	1.99
MIX 2	7.0	2.093	2.444	14.4	25.5	43.7	11.16	5.33	1.80
MIX 3	7.2	2.094	2.448	14.5	25.6	43.6	11.16	5.33	2.01
MIX 4	7.5	2.098	2.429	13.6	25.7	47.0	12.11	5.77	1.87

DATA for N-des.	50									
		Gmb	Gmm	Voids (Pa)	VMA	VFA	Vbe	Pbe	Gse	Pba
MIX 1	6.5	2.343	2.474	5.3	16.2	67.2	10.87	4.64	2.756	1.99
MIX 2	7.0	2.353	2.444	3.7	16.3	77.1	12.54	5.33	2.742	1.80
MIX 3	7.2	2.350	2.448	4.0	16.5	75.8	12.53	5.33	2.758	2.01
MIX 4	7.5	2.357	2.429	3.0	16.6	82.1	13.60	5.77	2.747	1.87

Performance Test Data	
Hamburg No. Passes	20000
Hamburg Wheel Depth	8.64
Unaged Flexibility Index (FI)	53.9
LTA FI (SURFACE ONLY)	19.2
TSR Information	
Conditioned	98.0
Unconditioned	85.0
TSR	1.15
CA Strip Rating	1
FA Strip Rating	1
Additive Prod #	
Additive Product Name	
Additive %	

OPTIMUM DESIGN DATA @ Ndes											
GYRATIONS	AB	Gmb	Gmm	%VOIDS (Pa) Target	VMA	VFA	Gse	Gsb	TSR	RCY AB	Virgin AB	ABR
50	7.0	2.346	2.444	4.0	16.5	75.8	2.742	2.613	1.15	0.00	7.00	0.0

REMARKS LINE 1: 0.3% Cellulose Fibers DD=0.09%&0.10% @170&185ºC

REMARKS LINE 2: VCAMIX=33.5<VCADRC=41.0

HMA AGED: 2 HOURS @: 152ºC

Producer Number & Name -->		L2-50-12.5-0		<--- Plant Location	
Material Code Number ---->					

Plant Bin #	#7	#6	#5	#4	#3	#2	#1	MF	RCY	RCY	RCY	RCY	ASPHALT
Size	022CM14	022CM16	038FM20					004FM01					SBS
Source (PROD #)	CONFIDENTIAL	CONFIDENTIAL	CONFIDENTIAL					CONFIDENTIAL					CONFIDENTIAL
(NAME)	CONFIDENTIAL	CONFIDENTIAL	CONFIDENTIAL					CONFIDENTIAL					CONFIDENTIAL
(LOC)	CONFIDENTIAL	CONFIDENTIAL	CONFIDENTIAL					CONFIDENTIAL					CONFIDENTIAL
(ADD. INFO)													#N/A
									0.0	0.0	0.0	0.0	< AB in RCY
	Aggregate Blend:											Plan PG Grade >	PG 76-28
	66.2	11.7	15.0	0.0	0.0	0.0	0.0	7.1	0.0	0.0	0.0	0.0	100.0
	Mixture Blend:												Totals: ↕
	0.0	0.0	0.0	0.0	0.0	0.0	0.0	0.0	0.0	0.0	0.0	0.0	6.4

Agg No. / Sieve Size	#7	#6	#5	#4	#3	#2	#1	MF	RCY	RCY	RCY	RCY	Aggregate Blend	Mixture Comp Spec
1" (25.0mm)	100.0	100.0	100.0	100.0	100.0	100.0	100.0	100.0	100.0	100.0	100.0	100.0	100	100
3/4"(19.0mm)	100.0	100.0	100.0	100.0	100.0	100.0	100.0	100.0	100.0	100.0	100.0	100.0	100	90-100
1/2" (12.5mm)	89.2	99.7	100.0	100.0	100.0	100.0	100.0	100.0	100.0	100.0	100.0	100.0	93	75-89
3/8" (9.5mm)	50.8	92.7	100.0	100.0	100.0	100.0	100.0	100.0	100.0	100.0	100.0	100.0	67	
No.4 (4.75mm)	8.2	32.1	97.4	100.0	100.0	100.0	100.0	100.0	100.0	100.0	100.0	100.0	31	40-60
No.8 (2.36mm)	2.7	4.6	67.1	100.0	100.0	100.0	100.0	100.0	100.0	100.0	100.0	100.0	20	26-42
No.16 (1.18mm)	2.4	3.8	38.1	100.0	100.0	100.0	100.0	100.0	100.0	100.0	100.0	100.0	15	15-30
No.30 (600µm)	2.2	3.4	21.4	100.0	100.0	100.0	100.0	100.0	100.0	100.0	100.0	100.0	12	
No.50 (300µm)	2.1	3.2	12.7	100.0	100.0	100.0	100.0	100.0	100.0	100.0	100.0	100.0	11	6-15
No.100 (150µm)	2.0	3.0	9.2	100.0	100.0	100.0	100.0	99.7	100.0	100.0	100.0	100.0	10	4-9
No.200(75µm)	1.9	2.8	7.2	100.0	100.0	100.0	100.0	96.8	100.0	100.0	100.0	100.0	9.5	3-6
2021 Gsb	2.623	2.602	2.608	1.000	1.000	1.000	1.000	2.800	1.000	1.000	1.000	1.000	2.630	
Design Gsb	2.623	2.602	2.608	1.000	1.000	1.000	1.000	2.800	1.000	1.000	1.000	1.000	2.630	Dust/AB
Absorption, %	1.40	1.70	3.40	1.00	1.00	1.00	1.00	1.00	1.00	1.00	1.00	1.00	1.52	Ratio
												SP GR AB	1.000	1.49
											Change in Combined Gsb		0.000	

SUMMARY OF SUPERPAVE GYRATORY DESIGN DATA

DATA for N-int.	6								
	AB, %MIX	Gmb	Gmm	Voids (Pa)	VMA	VFA	Vbe	Pbe	Pba
MIX 1	6.0	2.073	2.454	15.5	25.9	40.1	10.39	5.01	1.05
MIX 2	6.4	2.090	2.435	14.2	25.6	44.7	11.43	5.47	0.99
MIX 3	6.5	2.081	2.437	14.6	26.0	43.9	11.42	5.49	1.08
MIX 4	7.0	2.093	2.430	13.9	26.0	46.6	12.12	5.79	1.30

DATA for N-des.	50								
		Gmb	Gmm	Voids (Pa)	VMA	VFA	Vbe	Pbe	Gse	Pba
MIX 1	6.0	2.337	2.454	4.8	16.5	71.0	11.71	5.01	2.705	1.05
MIX 2	6.4	2.354	2.435	3.3	16.2	79.5	12.88	5.47	2.700	0.99
MIX 3	6.5	2.346	2.437	3.7	16.6	77.5	12.88	5.49	2.707	1.08
MIX 4	7.0	2.362	2.430	2.8	16.5	83.0	13.68	5.79	2.723	1.30

Performance Test Data	
Hamburg No. Passes	
Hamburg Wheel Depth	
Unaged Flexibility Index (FI)	
LTA FI (SURFACE ONLY)	
TSR Information	
Conditioned	
Unconditioned	
TSR	
CA Strip Rating	
FA Strip Rating	
Additive Prod #	
Additive Product Name	
Additive %	

OPTIMUM DESIGN DATA @ Ndes											
GYRATIONS	AB	Gmb	Gmm	%VOIDS (Pa) Target	VMA	VFA	Gse	Gsb	TSR	RCY AB	Virgin AB	ABR
50	6.4	2.341	2.439	4.0	16.7	76.0	2.705	2.630	0.00	0.00	6.40	#VALUE!

REMARKS LINE 1: 0.3% Cellulose Fiber
REMARKS LINE 2:

HMA AGED: HOURS @:

Producer Number & Name -->		D3-50-9.5-0	<--- Plant Location
Material Code Number ---->			

Plant Bin #	#7	#6	#5	#4	#3	#2	#1	MF	RCY	RCY	RCY	RCY	ASPHALT
Size	022CM1301	022CM1601	038FM20					004MF01					SBS
Source (PROD #)	CONFIDENTIAL	CONFIDENTIAL	CONFIDENTIAL					CONFIDENTIAL					CONFIDENTIAL
(NAME)	CONFIDENTIAL	CONFIDENTIAL	CONFIDENTIAL					CONFIDENTIAL					CONFIDENTIAL
(LOC)	CONFIDENTIAL	CONFIDENTIAL	CONFIDENTIAL					CONFIDENTIAL					CONFIDENTIAL
(ADD. INFO)													#N/A
									0.0	0.0	0.0	0.0	< AB in RCY
	Aggregate Blend:											Plan PG Grade >	PG 76-28
	65.7	16.6	10.7	0.0	0.0	0.0	0.0	7.0	0.0	0.0	0.0	0.0	100.0
	Mixture Blend:												Totals: ↕
	0.0	0.0	0.0	0.0	0.0	0.0	0.0	0.0	0.0	0.0	0.0	0.0	7.0

Agg No. / Sieve Size	#7	#6	#5	#4	#3	#2	#1	MF	RCY	RCY	RCY	RCY	Aggregate Blend	Mixture Comp Spec
1" (25.0mm)	100.0	100.0	100.0	100.0	100.0	100.0	100.0	100.0	100.0	100.0	100.0	100.0	100	
3/4"(19.0mm)	100.0	100.0	100.0	100.0	100.0	100.0	100.0	100.0	100.0	100.0	100.0	100.0	100	100
1/2" (12.5mm)	97.6	100.0	100.0	100.0	100.0	100.0	100.0	100.0	100.0	100.0	100.0	100.0	98	95-100
3/8" (9.5mm)	83.0	92.4	100.0	100.0	100.0	100.0	100.0	100.0	100.0	100.0	100.0	100.0	88	70-95
No.4 (4.75mm)	29.6	35.5	97.4	100.0	100.0	100.0	100.0	100.0	100.0	100.0	100.0	100.0	43	30-50
No.8 (2.36mm)	9.1	8.5	67.1	100.0	100.0	100.0	100.0	100.0	100.0	100.0	100.0	100.0	22	20-30
No.16 (1.18mm)	4.5	2.2	38.1	100.0	100.0	100.0	100.0	100.0	100.0	100.0	100.0	100.0	14	< 21
No.30 (600µm)	4.0	1.5	21.4	100.0	100.0	100.0	100.0	100.0	100.0	100.0	100.0	100.0	12	< 18
No.50 (300µm)	3.7	1.4	12.7	100.0	100.0	100.0	100.0	100.0	100.0	100.0	100.0	100.0	11	< 15
No.100 (150µm)	3.4	1.4	9.2	100.0	100.0	100.0	100.0	99.7	100.0	100.0	100.0	100.0	10	
No.200(75µm)	2.1	1.2	7.2	100.0	100.0	100.0	100.0	96.8	100.0	100.0	100.0	100.0	9.1	8.0-11.0
2021 Gsb	2.647	2.632	2.608	1.000	1.000	1.000	1.000	2.800	1.000	1.000	1.000	1.000	2.650	
Design Gsb	2.647	2.632	2.608	1.000	1.000	1.000	1.000	2.800	1.000	1.000	1.000	1.000	2.650	Dust/AB
Absorption, %	2.20	2.30	3.40	1.00	1.00	1.00	1.00	1.00	1.00	1.00	1.00	1.00	2.12	Ratio
												SP GR AB	1.000	1.30
											Change in Combined Gsb		0.000	

SUMMARY OF SUPERPAVE GYRATORY DESIGN DATA

DATA for N-int.	6								
	AB, %MIX	Gmb	Gmm	Voids (Pa)	VMA	VFA	Vbe	Pbe	Pba
MIX 1	6.7	2.082	2.461	15.4	26.7	42.3	11.31	5.43	1.36
MIX 2	7.0	2.095	2.452	14.6	26.5	45.0	11.92	5.69	1.41
MIX 3	7.3	2.099	2.445	14.2	26.6	46.7	12.43	5.92	1.49
MIX 4	7.3	2.099	2.445	14.2	26.6	46.7	12.43	5.92	1.49

DATA for N-des.	50									
		Gmb	Gmm	Voids (Pa)	VMA	VFA	Vbe	Pbe	Gse	Pba
MIX 1	6.7	2.344	2.461	4.8	17.5	72.8	12.73	5.43	2.749	1.36
MIX 2	7.0	2.357	2.452	3.9	17.3	77.6	13.41	5.69	2.753	1.41
MIX 3	7.3	2.364	2.445	3.3	17.3	80.9	13.99	5.92	2.759	1.49
MIX 4	7.3	2.364	2.445	3.3	17.3	80.9	13.99	5.92	2.759	1.49

Performance Test Data	
Hamburg No. Passes	
Hamburg Wheel Depth	
Unaged Flexibility Index (FI)	
LTA FI (SURFACE ONLY)	
TSR Information	
Conditioned	0.0
Unconditioned	0.0
TSR	0.00
CA Strip Rating	
FA Strip Rating	
Additive Prod #	
Additive Product Name	
Additive %	

OPTIMUM DESIGN DATA @ Ndes

GYRATIONS	AB	Gmb	Gmm	%VOIDS (Pa) Target	VMA	VFA	Gse	Gsb	TSR	RCY AB	Virgin AB	ABR
50	7.0	2.358	2.456	4.0	17.3	76.8	2.758	2.650	0.00	0.00	7.00	#VALUE!

REMARKS LINE 1: 0.3% Cellulose Fiber
REMARKS LINE 2:

HMA AGED: HOURS @

Producer Number & Name -->		D4-50-12.5-0		<--- Plant Location	
Material Code Number ---->					

Plant Bin #	#7	#6	#5	#4	#3	#2	#1	MF	RCY	RCY	RCY	RCY	ASPHALT
Size	022CM14	022CM16	038FM20					004FM01					SBS
Source (PROD #)	CONFIDENTIAL	CONFIDENTIAL	CONFIDENTIAL					CONFIDENTIAL					CONFIDENTIAL
(NAME)	CONFIDENTIAL	CONFIDENTIAL	CONFIDENTIAL					CONFIDENTIAL					CONFIDENTIAL
(LOC)	CONFIDENTIAL	CONFIDENTIAL	CONFIDENTIAL					CONFIDENTIAL					CONFIDENTIAL
(ADD. INFO)													#N/A
									0.0	0.0	0.0	0.0	< AB in RCY
	Aggregate Blend:											Plan PG Grade >	PG 76-28
	67.6	10.8	13.6	0.0	0.0	0.0	0.0	8.0	0.0	0.0	0.0	0.0	100.0
	Mixture Blend:												Totals: ↕
	0.0	0.0	0.0	0.0	0.0	0.0	0.0	0.0	0.0	0.0	0.0	0.0	6.8

Agg No. / Sieve Size	#7	#6	#5	#4	#3	#2	#1	MF	RCY	RCY	RCY	RCY	Aggregate Blend	Mixture Comp Spec
1" (25.0mm)	100.0	100.0	100.0	100.0	100.0	100.0	100.0	100.0	100.0	100.0	100.0	100.0	100	100
3/4"(19.0mm)	100.0	100.0	100.0	100.0	100.0	100.0	100.0	100.0	100.0	100.0	100.0	100.0	100	90-100
1/2" (12.5mm)	85.1	100.0	100.0	100.0	100.0	100.0	100.0	100.0	100.0	100.0	100.0	100.0	90	75-89
3/8" (9.5mm)	45.8	98.7	100.0	100.0	100.0	100.0	100.0	100.0	100.0	100.0	100.0	100.0	63	
No.4 (4.75mm)	6.8	35.6	97.4	100.0	100.0	100.0	100.0	100.0	100.0	100.0	100.0	100.0	30	40-60
No.8 (2.36mm)	2.5	4.2	67.1	100.0	100.0	100.0	100.0	100.0	100.0	100.0	100.0	100.0	19	26-42
No.16 (1.18mm)	1.7	1.8	38.1	100.0	100.0	100.0	100.0	100.0	100.0	100.0	100.0	100.0	15	15-30
No.30 (600µm)	1.4	1.4	21.4	100.0	100.0	100.0	100.0	100.0	100.0	100.0	100.0	100.0	12	
No.50 (300µm)	1.4	1.2	12.7	100.0	100.0	100.0	100.0	100.0	100.0	100.0	100.0	100.0	11	6-15
No.100 (150µm)	1.3	1.2	9.2	100.0	100.0	100.0	100.0	99.7	100.0	100.0	100.0	100.0	10	4-9
No.200(75µm)	1.2	1.1	7.2	100.0	100.0	100.0	100.0	96.8	100.0	100.0	100.0	100.0	9.7	3-6
2021 Gsb	2.618	2.069	2.608	1.000	1.000	1.000	1.000	2.800	1.000	1.000	1.000	1.000	2.557	
Design Gsb	2.618	2.609	2.608	1.000	1.000	1.000	1.000	2.800	1.000	1.000	1.000	1.000	2.629	Dust/AB
Absorption, %	2.10	2.60	3.40	1.00	1.00	1.00	1.00	1.00	1.00	1.00	1.00	1.00	2.07	Ratio
												SP GR AB	1.000	1.42
												Change in Combined Gsb	0.072	

REDESIGN REQUIRED

SUMMARY OF SUPERPAVE GYRATORY DESIGN DATA

DATA for N-int.	6								
	AB, %MIX	Gmb	Gmm	Voids (Pa)	VMA	VFA	Vbe	Pbe	Pba
MIX 1	6.5	2.069	2.456	15.8	26.4	40.4	10.63	5.14	1.45
MIX 2	7.0	2.072	2.447	15.3	26.7	42.6	11.38	5.49	1.62
MIX 3	7.5	2.078	2.423	14.2	26.9	47.0	12.63	6.08	1.53
MIX 4	6.8	2.076	2.450	15.3	26.4	42.2	11.13	5.36	1.54

DATA for N-des.	50								
	Gmb	Gmm	Voids (Pa)	VMA	VFA	Vbe	Pbe	Gse	Pba
MIX 1	6.5	2.339	2.456	4.8	16.8	71.7	12.02	5.14	2.733	1.45
MIX 2	7.0	2.352	2.447	3.9	16.8	76.9	12.91	5.49	2.746	1.62
MIX 3	7.5	2.352	2.423	2.9	17.3	83.0	14.30	6.08	2.739	1.53
MIX 4	6.8	2.349	2.450	4.1	16.7	75.4	12.59	5.36	2.740	1.54

Performance Test Data	
Hamburg No. Passes	
Hamburg Wheel Depth	
Unaged Flexibility Index (FI)	
LTA FI (SURFACE ONLY)	
TSR Information	
Conditioned	
Unconditioned	
TSR	
CA Strip Rating	
FA Strip Rating	
Additive Prod #	
Additive Product Name	
Additive %	

OPTIMUM DESIGN DATA @ Ndes											
GYRATIONS	AB	Gmb	Gmm	%VOIDS (Pa) Target	VMA	VFA	Gse	Gsb	TSR	RCY AB	Virgin AB	ABR
50	6.8	2.353	2.451	4.0	16.6	75.9	2.741	2.629	0.00	0.00	6.80	#VALUE!

REMARKS LINE 1: 0.3% Cellulose Fiber
REMARKS LINE 2:

HMA AGED: HOURS @:

Illinois Department of Transportation

Illinois Department of Transportation

Material Code: 10132 - AC PG 76-28 MOD

Test ID: 2367093

Completed Date: 12/15/2023

Producer: 2260-03 EMULSICOAT, INCORPORATED, URBANA, IL
Supplier: 2260-03 EMULSICOAT, INCORPORATED, URBANA, IL
Description 1:
Description 2:
Description 3: BC-2106
Sample Status: APPROVED

Contract #:
Sample Date: 5/18/2023
Special ID:
Inspected Qty: 0 TONS
Approved By: William Snyder

Test Name: BC - Bending Beam Rheometer - 1
Version 1

Test Date: 12/12/2023
Tested By: CD

	Result	Unit of Measure
Average m-value	0.341	
m-value Pass/Fail	1	
Average Creep Stiff. (MPa)	158	
Creep Stiffness Pass/Fail	1	
BBR Pass/Fail	1	

Comments:
Test Validated By: William Snyder

Validated Date: 12/15/2023

Test Name: BC - Flash Point Cleveland Open Cup - 1
Version 1

Test Date: 12/12/2023
Tested By: CD

	Result	Unit of Measure
Corrected Flash Temp. °C	310	
Pass/Fail	1	

Comments:
Test Validated By: William Snyder

Validated Date: 12/15/2023

Test Name: BC - Separation of Polymer - 1
Version 1

Test Date: 12/12/2023
Tested By: CD

	Result	Unit of Measure
Difference (C)	0.0	

Comments:
Test Validated By: William Snyder

Validated Date: 12/15/2023

Test Name: BC - PAV DSR - 1
Version 2

Test Date: 12/12/2023
Tested By: CD

	Result	Unit of Measure
G* sin(delta)	1,195	
Pass/Fail	1	

Comments:
Test Validated By: William Snyder

Validated Date: 12/15/2023

Test Name: BC - Rotational Viscosity - 1
Version 2

Test Date: 12/12/2023
Tested By: CD

	Result	Unit of Measure
Average Viscosity (Pa s)	1.397	
Average Viscosity Pass/Fail	1	

Comments:
Test Validated By: William Snyder

Validated Date: 12/15/2023

Test Name: BC - Elastic Recovery - 1
Version 3

Test Date: 12/12/2023
Tested By: CD

	Result	Unit of Measure
Average ER (%)	93.0	
Pass/Fail	1	

Comments:
Test Validated By: William Snyder

Validated Date: 12/15/2023

Test Name: BC - PAV Aging Temperature - 1
Version 2

Test Date: 12/12/2023
Tested By: CD

	Result	Unit of Measure
PAV Chamber Temperature (deg. C)	100	

Comments:
Test Validated By: William Snyder

Validated Date: 12/15/2023

Test Name: BC - RTFO DSR - 1
Version 2

Test Date: 12/12/2023
Tested By: CD

	Result	Unit of Measure
G*/sin(delta)	2.21	

Comments:
Test Validated By: William Snyder

Validated Date: 12/15/2023

Test Name: BC - Separation of Polymer - 1 **Test Date:** 12/12/2023
Version 1 **Tested By:** CD

	Result	Unit of Measure
Pass/Fail	1	

Comments:
Test Validated By: William Snyder **Validated Date:** 12/15/2023

Test Name: IN - Vegetable Oil in Asphalt - 1 **Test Date:** 12/13/2023
Version 1 **Tested By:** JG

	Result	Unit of Measure
	0%	

Comments:
Test Validated By: William Snyder **Validated Date:** 12/15/2023

Test Name: IN - SBS Polymer in Asphalt - 1 **Test Date:** 12/13/2023
Version 1 **Tested By:** JG

	Result	Unit of Measure
% SBS Polymer	5.18	
Pass/Fail	1	

Comments:
Test Validated By: William Snyder **Validated Date:** 12/15/2023

Test Name: BC - Original DSR - 1 **Test Date:** 12/12/2023
Version 1 **Tested By:** CD

	Result	Unit of Measure
G*/sin(delta)	1.11	
Pass/Fail	1	

Comments:
Test Validated By: William Snyder **Validated Date:** 12/15/2023

Test Name: BC - Specific Gravity - Pycnometer - 1 **Test Date:** 12/12/2023
Version 2 **Tested By:** CD

	Result	Unit of Measure
SpG at 15.6 C	1.029	

Comments:
Test Validated By: William Snyder **Validated Date:** 12/15/2023

Test Name: BC - RTFO DSR - 1
Version 2

Test Date: 12/12/2023
Tested By: CD

	Result	Unit of Measure
Pass/Fail	1	

Comments:

Test Validated By: William Snyder

Validated Date: 12/15/2023

Test Name: BC - Change in Mass RTFO - 1
Version 2

Test Date: 12/12/2023
Tested By: CD

	Result	Unit of Measure
Average Mass Change %	-0.257	
Pass/Fail	1	

Comments:

Test Validated By: William Snyder

Validated Date: 12/15/2023

Test Name: BC - 40 hr Delta Tc - 1
Version 1

Test Date: 12/12/2023
Tested By: CD

	Result	Unit of Measure
Critical Temp. (deg. C) [m-value]:	-26.9	
Critical Temp. (deg. C) [Stiffness]:	-32.1	
Pass/Fail	0	

DTc -5.1

Comments:

Test Validated By: William Snyder

Validated Date: 12/15/2023

Illinois Department of Transportation

Illinois Department of Transportation

Material Code: 10132 - AC PG 76-28 MOD

Test ID: 2367094

Completed Date: 12/15/2023

Producer: 2260-03 EMULSICOAT, INCORPORATED, URBANA, IL
Supplier: 2260-03 EMULSICOAT, INCORPORATED, URBANA, IL
Description 1:
Description 2:
Description 3: BC-2107
Sample Status: APPROVED

Contract #:
Sample Date: 5/18/2023
Special ID:
Inspected Qty: 0 TONS
Approved By: William Snyder

Test Name: BC - Bending Beam Rheometer - 1
Version 1

Test Date: 12/12/2023
Tested By: CR

	Result	Unit of Measure
Average m-value	0.323	
m-value Pass/Fail	1	
Average Creep Stiff. (MPa)	163	
Creep Stiffness Pass/Fail	1	
BBR Pass/Fail	1	

Comments:
Test Validated By: William Snyder

Validated Date: 12/15/2023

Test Name: BC - Flash Point Cleveland Open Cup - 1
Version 1

Test Date: 12/12/2023
Tested By: CR

	Result	Unit of Measure
Corrected Flash Temp. °C	250+	
Pass/Fail	1	

Comments:
Test Validated By: William Snyder

Validated Date: 12/15/2023

Test Name: BC - Separation of Polymer - 1
Version 1

Test Date: 12/12/2023
Tested By: CR

	Result	Unit of Measure
Difference (C)	0.5	

Comments:
Test Validated By: William Snyder

Validated Date: 12/15/2023

Test Name: BC - Separation of Polymer - 1 **Test Date:** 12/12/2023
Version 1 **Tested By:** CR

	Result	Unit of Measure
Pass/Fail	1	

Comments:
Test Validated By: William Snyder **Validated Date:** 12/15/2023

Test Name: IN - Vegetable Oil in Asphalt - 1 **Test Date:** 12/13/2023
Version 1 **Tested By:** JG

	Result	Unit of Measure
	0%	

Comments:
Test Validated By: William Snyder **Validated Date:** 12/15/2023

Test Name: IN - SBS Polymer in Asphalt - 1 **Test Date:** 12/13/2023
Version 1 **Tested By:** JG

	Result	Unit of Measure
% SBS Polymer	5.27	
Pass/Fail	1	

Comments:
Test Validated By: William Snyder **Validated Date:** 12/15/2023

Test Name: BC - Original DSR - 1 **Test Date:** 12/12/2023
Version 1 **Tested By:** CR

	Result	Unit of Measure
G*/sin(delta)	1.09	
Pass/Fail	1	

Comments:
Test Validated By: William Snyder **Validated Date:** 12/15/2023

Test Name: BC - Specific Gravity - Pycnometer - 1 **Test Date:** 12/12/2023
Version 2 **Tested By:** CR

	Result	Unit of Measure
SpG at 15.6 C	1.026	

Comments:
Test Validated By: William Snyder **Validated Date:** 12/15/2023

Test Name: BC - PAV DSR - 1
Version 2

Test Date: 12/12/2023
Tested By: CR

	Result	Unit of Measure
G* sin(delta)	1,262	
Pass/Fail	1	

Comments:
Test Validated By: William Snyder

Validated Date: 12/15/2023

Test Name: BC - Rotational Viscosity - 1
Version 2

Test Date: 12/12/2023
Tested By: CR

	Result	Unit of Measure
Average Viscosity (Pa s)	1.420	
Average Viscosity Pass/Fail	1	

Comments:
Test Validated By: William Snyder

Validated Date: 12/15/2023

Test Name: BC - Elastic Recovery - 1
Version 3

Test Date: 12/12/2023
Tested By: CR

	Result	Unit of Measure
Average ER (%)	93.0	
Pass/Fail	1	

Comments:
Test Validated By: William Snyder

Validated Date: 12/15/2023

Test Name: BC - PAV Aging Temperature - 1
Version 2

Test Date: 12/12/2023
Tested By: CR

	Result	Unit of Measure
PAV Chamber Temperature (deg. C)	100	

Comments:
Test Validated By: William Snyder

Validated Date: 12/15/2023

Test Name: BC - RTFO DSR - 1
Version 2

Test Date: 12/12/2023
Tested By: CR

	Result	Unit of Measure
G*/sin(delta)	2.34	

Comments:
Test Validated By: William Snyder

Validated Date: 12/15/2023

Test Name: BC - RTFO DSR - 1
Version 2

Test Date: 12/12/2023
Tested By: CR

	Result	Unit of Measure
Pass/Fail	1	

Comments:

Test Validated By: William Snyder

Validated Date: 12/15/2023

Test Name: BC - Change in Mass RTFO - 1
Version 2

Test Date: 12/12/2023
Tested By: CR

	Result	Unit of Measure
Average Mass Change %	-0.261	
Pass/Fail	1	

Comments:

Test Validated By: William Snyder

Validated Date: 12/15/2023

Test Name: BC - 40 hr Delta Tc - 1
Version 1

Test Date: 12/12/2023
Tested By: CR

	Result	Unit of Measure	
Critical Temp. (deg. C) [m-value]:	-25.6		DTc -6.5
Critical Temp. (deg. C) [Stiffness]:	-32.1		
Pass/Fail	0		

Comments:

Test Validated By: William Snyder

Validated Date: 12/15/2023

Illinois Department of Transportation

Illinois Department of Transportation

Material Code: 10132 - AC PG 76-28 MOD

Test ID: 2367095

Completed Date: 12/15/2023

Producer: 2260-03 EMULSICOAT, INCORPORATED, URBANA, IL
Supplier: 2260-03 EMULSICOAT, INCORPORATED, URBANA, IL
Description 1:
Description 2:
Description 3: BC-2108
Sample Status: APPROVED

Contract #:
Sample Date: 5/19/2023
Special ID:
Inspected Qty: 0 TONS
Approved By: William Snyder

Test Name: BC - Bending Beam Rheometer - 1
Version 1

Test Date: 12/12/2023
Tested By: CD

	Result	Unit of Measure
Average m-value	0.323	
m-value Pass/Fail	1	
Average Creep Stiff. (MPa)	153	
Creep Stiffness Pass/Fail	1	
BBR Pass/Fail	1	

Comments:
Test Validated By: William Snyder

Validated Date: 12/15/2023

Test Name: BC - Flash Point Cleveland Open Cup - 1
Version 1

Test Date: 12/12/2023
Tested By: CD

	Result	Unit of Measure
Corrected Flash Temp. °C	310	
Pass/Fail	1	

Comments:
Test Validated By: William Snyder

Validated Date: 12/15/2023

Test Name: BC - Separation of Polymer - 1
Version 1

Test Date: 12/12/2023
Tested By: CD

	Result	Unit of Measure
Difference (C)	0.5	

Comments:
Test Validated By: William Snyder

Validated Date: 12/15/2023

Test Name: BC - Separation of Polymer - 1 **Test Date:** 12/12/2023
Version 1 **Tested By:** CD

	Result	Unit of Measure
Pass/Fail	1	

Comments:
Test Validated By: William Snyder **Validated Date:** 12/15/2023

Test Name: IN - Vegetable Oil in Asphalt - 1 **Test Date:** 12/13/2023
Version 1 **Tested By:** JG

	Result	Unit of Measure
	0%	

Comments:
Test Validated By: William Snyder **Validated Date:** 12/15/2023

Test Name: IN - SBS Polymer in Asphalt - 1 **Test Date:** 12/13/2023
Version 1 **Tested By:** JG

	Result	Unit of Measure
% SBS Polymer	5.26	
Pass/Fail	1	

Comments:
Test Validated By: William Snyder **Validated Date:** 12/15/2023

Test Name: BC - Original DSR - 1 **Test Date:** 12/12/2023
Version 1 **Tested By:** CD

	Result	Unit of Measure
G*/sin(delta)	1.15	
Pass/Fail	1	

Comments:
Test Validated By: William Snyder **Validated Date:** 12/15/2023

Test Name: BC - Specific Gravity - Pycnometer - 1 **Test Date:** 12/12/2023
Version 2 **Tested By:** CD

	Result	Unit of Measure
SpG at 15.6 C	1.026	

Comments:
Test Validated By: William Snyder **Validated Date:** 12/15/2023

Test Name: BC - PAV DSR - 1
Version 2

Test Date: 12/12/2023
Tested By: CD

	Result	Unit of Measure
G* sin(delta)	1,283	
Pass/Fail	1	

Comments:
Test Validated By: William Snyder

Validated Date: 12/15/2023

Test Name: BC - Rotational Viscosity - 1
Version 2

Test Date: 12/12/2023
Tested By: CD

	Result	Unit of Measure
Average Viscosity (Pa s)	1.437	
Average Viscosity Pass/Fail	1	

Comments:
Test Validated By: William Snyder

Validated Date: 12/15/2023

Test Name: BC - Elastic Recovery - 1
Version 3

Test Date: 12/12/2023
Tested By: CD

	Result	Unit of Measure
Average ER (%)	93.0	
Pass/Fail	1	

Comments:
Test Validated By: William Snyder

Validated Date: 12/15/2023

Test Name: BC - PAV Aging Temperature - 1
Version 2

Test Date: 12/12/2023
Tested By: CD

	Result	Unit of Measure
PAV Chamber Temperature (deg. C)	100	

Comments:
Test Validated By: William Snyder

Validated Date: 12/15/2023

Test Name: BC - RTFO DSR - 1
Version 2

Test Date: 12/12/2023
Tested By: CD

	Result	Unit of Measure
G*/sin(delta)	2.28	

Comments:
Test Validated By: William Snyder

Validated Date: 12/15/2023

Test Name: BC - RTFO DSR - 1
Version 2

Test Date: 12/12/2023
Tested By: CD

	Result	Unit of Measure
Pass/Fail	1	

Comments:

Test Validated By: William Snyder

Validated Date: 12/15/2023

Test Name: BC - Change in Mass RTFO - 1
Version 2

Test Date: 12/12/2023
Tested By: CD

	Result	Unit of Measure
Average Mass Change %	-0.272	
Pass/Fail	1	

Comments:

Test Validated By: William Snyder

Validated Date: 12/15/2023

Test Name: BC - 40 hr Delta Tc - 1
Version 1

Test Date: 12/12/2023
Tested By: CD

	Result	Unit of Measure
Critical Temp. (deg. C) [m-value]:	-26.3	
Critical Temp. (deg. C) [Stiffness]:	-32.1	
Pass/Fail	0	

DTc -5.9

Comments:

Test Validated By: William Snyder

Validated Date: 12/15/2023

Illinois Department of Transportation

Illinois Department of Transportation

Material Code: 10132 - AC PG 76-28 MOD

Test ID: 2367096

Completed Date: 12/15/2023

Producer: 2260-03 EMULSICOAT, INCORPORATED, URBANA, IL
Supplier: 2260-03 EMULSICOAT, INCORPORATED, URBANA, IL
Description 1:
Description 2:
Description 3: BC-2109
Sample Status: APPROVED

Contract #:
Sample Date: 5/19/2023
Special ID:
Inspected Qty: 0 TONS
Approved By: William Snyder

Test Name: BC - Bending Beam Rheometer - 1
Version 1

Test Date: 12/12/2023
Tested By: CD

	Result	Unit of Measure
Average m-value	0.324	
m-value Pass/Fail	1	
Average Creep Stiff. (MPa)	170	
Creep Stiffness Pass/Fail	1	
BBR Pass/Fail	1	

Comments:
Test Validated By: William Snyder

Validated Date: 12/15/2023

Test Name: BC - Flash Point Cleveland Open Cup - 1
Version 1

Test Date: 12/12/2023
Tested By: CD

	Result	Unit of Measure
Corrected Flash Temp. °C	310	
Pass/Fail	1	

Comments:
Test Validated By: William Snyder

Validated Date: 12/15/2023

Test Name: BC - Separation of Polymer - 1
Version 1

Test Date: 12/12/2023
Tested By: CD

	Result	Unit of Measure
Difference (C)	0.5	

Comments:
Test Validated By: William Snyder

Validated Date: 12/15/2023

Test Name: BC - Separation of Polymer - 1 **Test Date:** 12/12/2023
Version 1 **Tested By:** CD

	Result	Unit of Measure
Pass/Fail	1	

Comments:
Test Validated By: William Snyder **Validated Date:** 12/15/2023

Test Name: IN - Vegetable Oil in Asphalt - 1 **Test Date:** 12/13/2023
Version 1 **Tested By:** JG

	Result	Unit of Measure
	0%	

Comments:
Test Validated By: William Snyder **Validated Date:** 12/15/2023

Test Name: IN - SBS Polymer in Asphalt - 1 **Test Date:** 12/13/2023
Version 1 **Tested By:** JG

	Result	Unit of Measure
% SBS Polymer	5.28	
Pass/Fail	1	

Comments:
Test Validated By: William Snyder **Validated Date:** 12/15/2023

Test Name: BC - Original DSR - 1 **Test Date:** 12/12/2023
Version 1 **Tested By:** CD

	Result	Unit of Measure
G*/sin(delta)	1.18	
Pass/Fail	1	

Comments:
Test Validated By: William Snyder **Validated Date:** 12/15/2023

Test Name: BC - Specific Gravity - Pycnometer - 1 **Test Date:** 12/12/2023
Version 2 **Tested By:** CD

	Result	Unit of Measure
SpG at 15.6 C	1.026	

Comments:
Test Validated By: William Snyder **Validated Date:** 12/15/2023

Test Name: BC - PAV DSR - 1
Version 2

Test Date: 12/12/2023
Tested By: CD

	Result	Unit of Measure
G* sin(delta)	1,250	
Pass/Fail	1	

Comments:
Test Validated By: William Snyder

Validated Date: 12/15/2023

Test Name: BC - Rotational Viscosity - 1
Version 2

Test Date: 12/12/2023
Tested By: CD

	Result	Unit of Measure
Average Viscosity (Pa s)	1.447	
Average Viscosity Pass/Fail	1	

Comments:
Test Validated By: William Snyder

Validated Date: 12/15/2023

Test Name: BC - Elastic Recovery - 1
Version 3

Test Date: 12/12/2023
Tested By: CD

	Result	Unit of Measure
Average ER (%)	93.0	
Pass/Fail	1	

Comments:
Test Validated By: William Snyder

Validated Date: 12/15/2023

Test Name: BC - PAV Aging Temperature - 1
Version 2

Test Date: 12/12/2023
Tested By: CD

	Result	Unit of Measure
PAV Chamber Temperature (deg. C)	100	

Comments:
Test Validated By: William Snyder

Validated Date: 12/15/2023

Test Name: BC - RTFO DSR - 1
Version 2

Test Date: 12/12/2023
Tested By: CD

	Result	Unit of Measure
G*/sin(delta)	2.28	

Comments:
Test Validated By: William Snyder

Validated Date: 12/15/2023

Test Name: BC - RTFO DSR - 1
Version 2

Test Date: 12/12/2023
Tested By: CD

	Result	Unit of Measure
Pass/Fail	1	

Comments:

Test Validated By: William Snyder

Validated Date: 12/15/2023

Test Name: BC - Change in Mass RTFO - 1
Version 2

Test Date: 12/12/2023
Tested By: CD

	Result	Unit of Measure
Average Mass Change %	-0.317	
Pass/Fail	1	

Comments:

Test Validated By: William Snyder

Validated Date: 12/15/2023

Test Name: BC - 40 hr Delta Tc - 1
Version 1

Test Date: 12/12/2023
Tested By: CD

	Result	Unit of Measure
Critical Temp. (deg. C) [m-value]:	-26.8	
Critical Temp. (deg. C) [Stiffness]:	-32.5	
Pass/Fail	0	

DTc -5.7

Comments:

Test Validated By: William Snyder

Validated Date: 12/15/2023

APPENDIX F: I-APT HMA LAYER MIX DESIGN

Illinois Department of Transportation

Region 3 / District 5
HMA Mix Record

Bit Mix No:	85BIT5362	Material Code:	19535R	Name:	HMA SC N90 E REC

Matl Code	Material Name	Source	Source Name	% Blend
021CM16	GRAVEL CR CLAQ		*Crushed Gravel*	27.6
022CM16	STONE CR CLAQ		Crushed Dolomite	26.4
039FM20	SPEC AGG CLBQ		Manufactured Sand	22.2
027FM01	SAND NATURAL CLAQ		Natural Sand	8.8
004MF01	MINERAL FILLER		Mineral Filler	3.0
017CM13	AGG REC BIT MIX		FRAP	12.0
10129	AC PG 70-22 MODIFIED			

Note: Original Document Modified to show only material, not source

Mix Formula						Optimum Design Data		
							Original	Current
25 mm / 1":			1.18 mm / # 16:	25		Gmm:	2.437	
19 mm / 3/4":			.600 mm / #30:	17	(+/-4)	Gmb:	2.340	
12.5 mm / 1/2":	100	(+/-6)	.300 mm / #50:	10		% Voids:	4.0	
9.5 mm / 3/8":	99		.150 mm / #100:	7		VMA:	15.5	
4.75 mm / # 4:	63	(+/-5)	.075 mm / #200:	5.3	(+/-1.5)	VFA:	74.2	
2.36 mm / # 8:	38	(+/-5)	AC	6.1	(+/-0.3)	TSR:	0.92	
						Gsb:	2.600	
						I-FIT:	10.20	
						Aged I-FIT:	5.2	

Central Mix Design: 35BIT1276 Effective Date: 2/8/18

Remarks: CONTACT DISTRICT OFFICE FOR RAP INFORMATION
IDOT HWT:-3.97 mm @ 15K PASSES / TNSL STRG: COND= 104 / UNCOND= 111 / TSR= 0.94

Aggregate Quality Reports are on file in the District Materials Office

Producer No.:	6437-04	Name:	OPEN ROAD ASPHALT @ Urbana, IL	County:
				Section:
Type of Plant:	DILLMAN 400 DRUM MIXER			Route:
Batch Size or Ton / Hr:	505 TPH			District:
Plant Approved:		Responsible Loc:	95	Cont. No.:
Copies to:				Job No.:
Res. Engr.:				Project:
Matls Tech:				
Contractor:				
Producer:	OPEN ROAD ASPHALT @ Urbana, IL			
QC Mngr:	JEFF KERN			
File:				

APPENDIX G: FIELD CORE AGGREGATE GRADATIONS

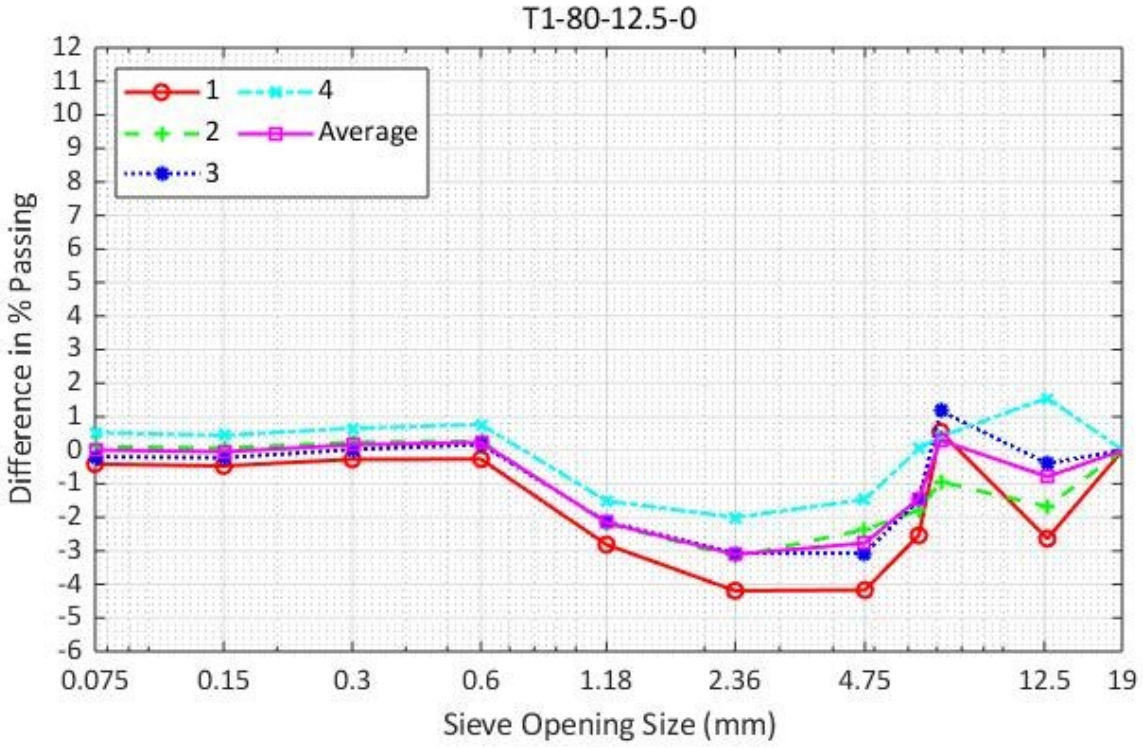

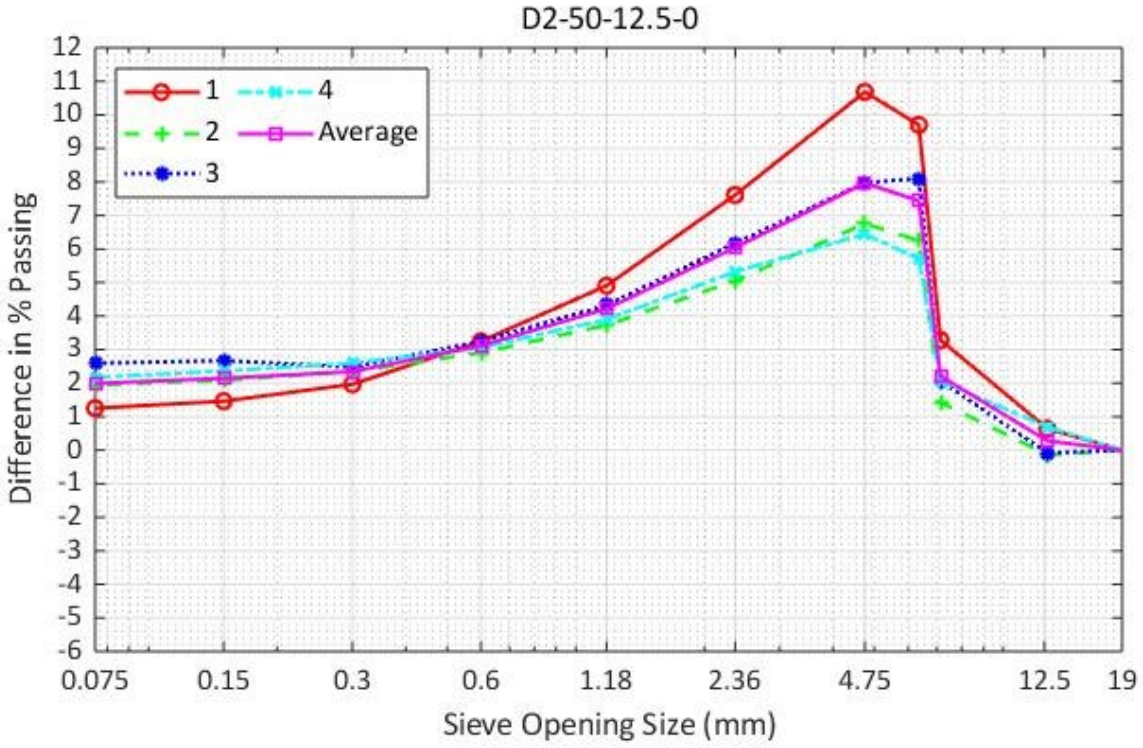

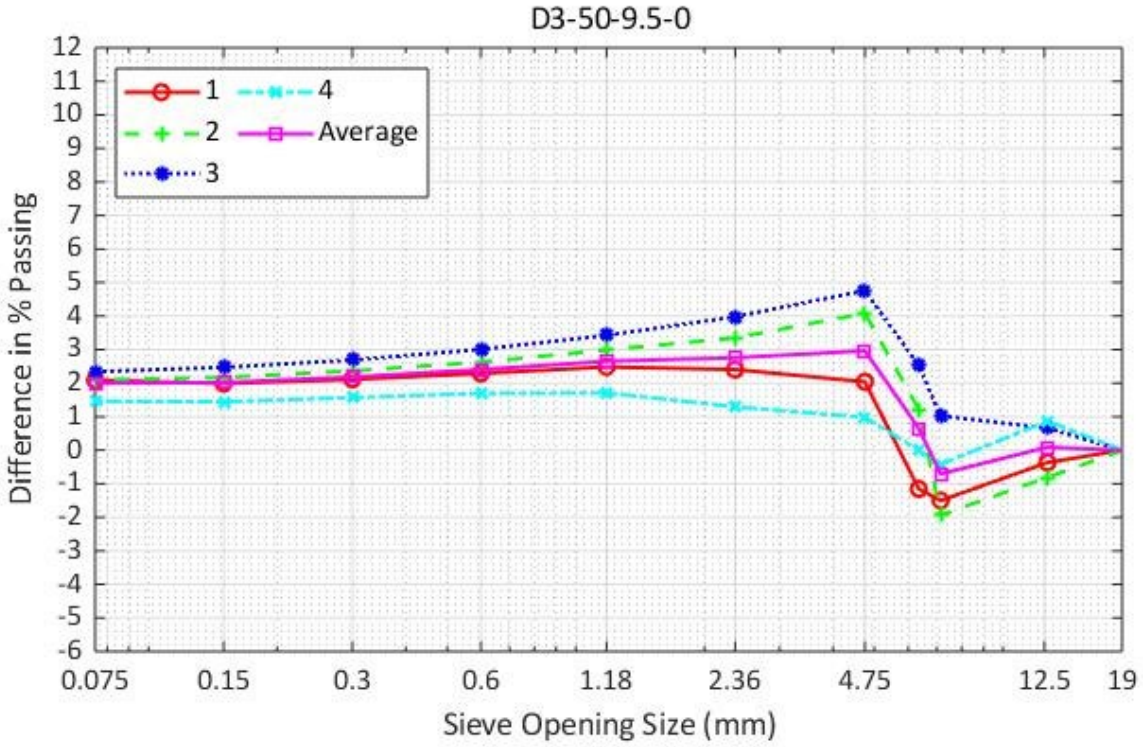
D3-50-9.5-0
1
2
3
4
Average
Difference in % Passing
Sieve Opening Size (mm)
0.075
0.15
0.3
0.6
1.18
2.36
4.75
12.5
19

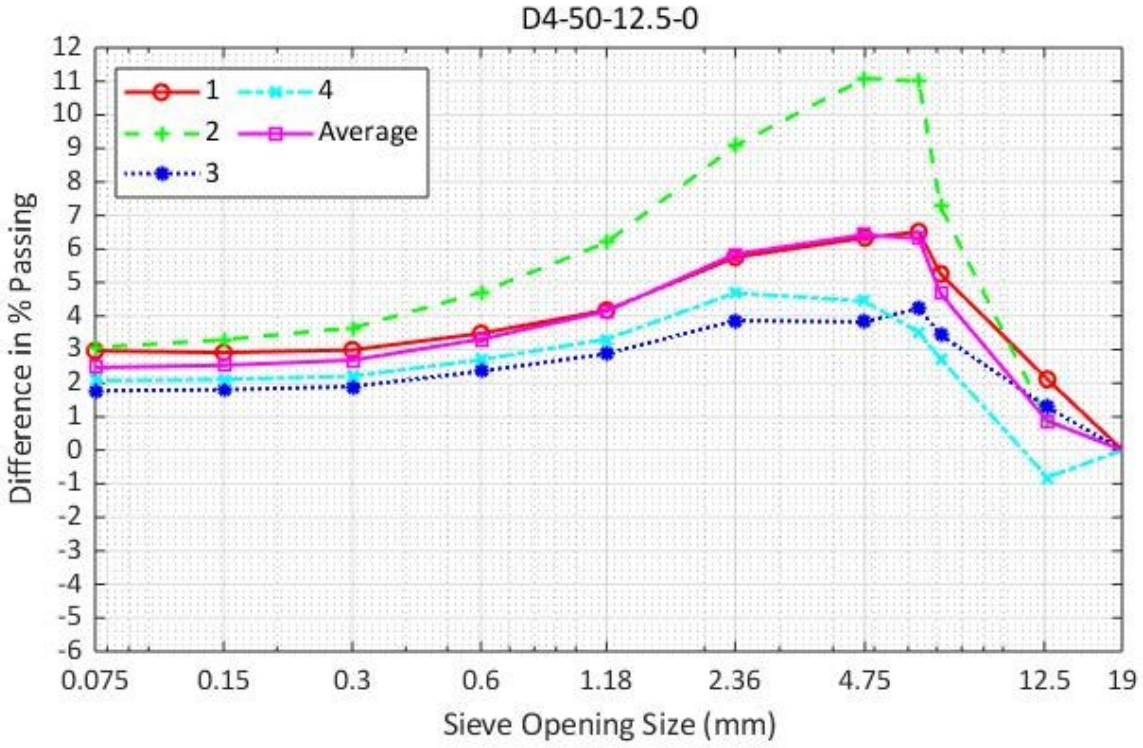
D4-50-12.5-0
1
2
3
4
Average
Difference in % Passing
Sieve Opening Size (mm)
0.075
0.15
0.3
0.6
1.18
2.36
4.75
12.5
19

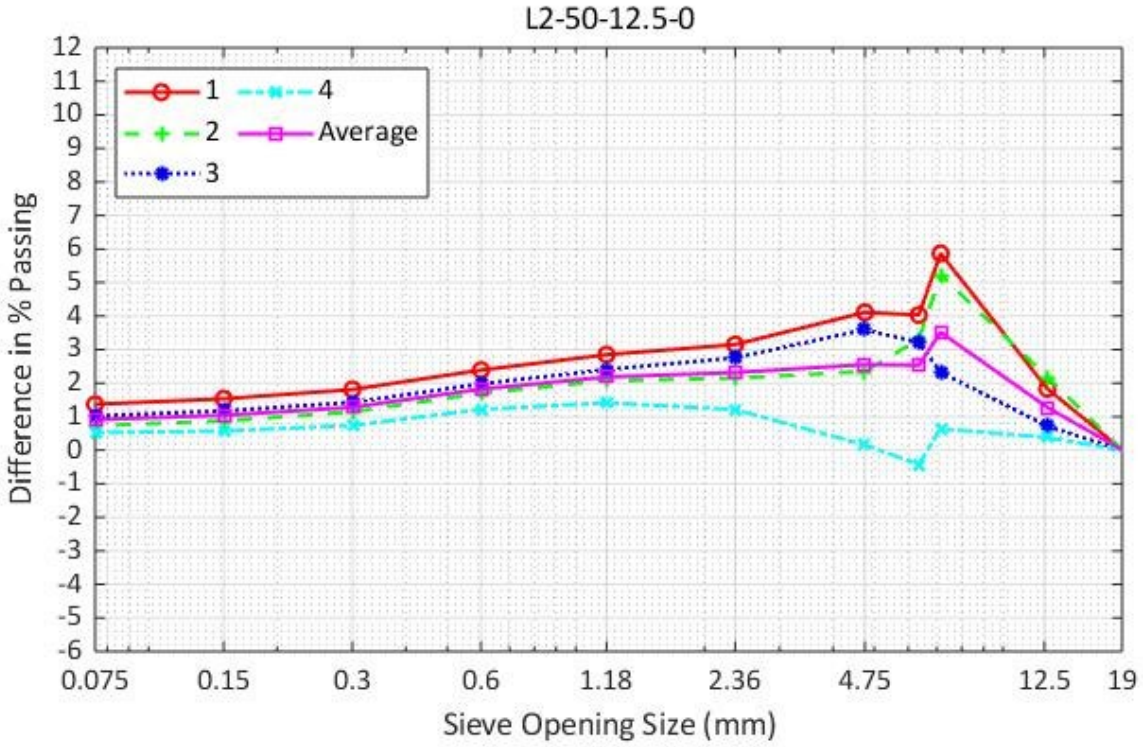
L2-50-12.5-0
1
2
3
4
Average
Difference in % Passing
Sieve Opening Size (mm)
0.075
0.15
0.3
0.6
1.18
2.36
4.75
12.5
19

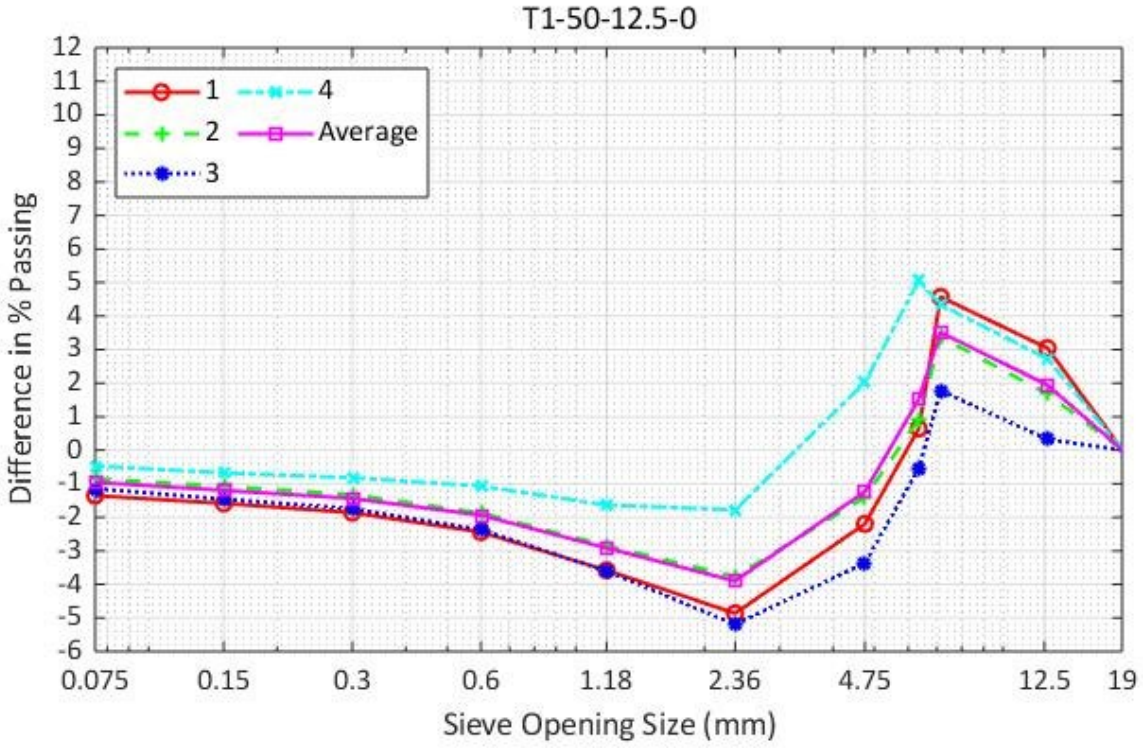
T1-50-12.5-0
1
2
3
4
Average
Difference in % Passing
Sieve Opening Size (mm)
0.075
0.15
0.3
0.6
1.18
2.36
4.75
12.5
19

APPENDIX H: CRITICAL RESPONSES FOR VARIOUS LOADING SCENARIOS

Table 57. Pressure and Strain Measurements for Section T1-80-12.5-0

Scenarios							Average of Ten Measurements at Stability												
Tire 1 Inflation Pressure (psi)	Tire 2 Inflation Pressure (psi)	Tire 1 Load (kip)	Tire 2 Load (kip)	Speed (mph)	Target Temperature (°F)	Axle Spacing (ft)	Pressure 1 Peak 2 (psi)	Pressure 1 Peak 1 (psi)	Pressure 2 Peak 2 (psi)	Pressure 2 Peak 1 (psi)	Longitudinal microstrain Peak 2	Longitudinal microstrain Peak 1	Longitudinal microstrain Dip 2	Longitudinal microstrain Dip 1	Longitudinal microstrain Amplitude 2	Longitudinal microstrain Amplitude 1	Transverse microstrain Peak 2	Transverse microstrain Peak 1	Transverse microstrain valley
0	120	0	8	5	80	NA	0	41	0	66	0	295	0	-164	0	459	0	283	0
0	120	0	9	5	80	NA	0	44	0	71	0	318	0	-152	0	470	0	249	0
0	120	0	10	5	80	NA	0	47	0	76	0	325	0	-182	0	508	0	251	0
0	120	0	12	5	80	NA	0	57	0	87	0	341	0	-194	0	535	0	283	0
0	120	0	14	5	80	NA	0	59	0	89	0	245	0	-158	0	403	0	216	0
0	120	0	10	1	80	NA	0	57	0	84	0	643	0	-303	0	946	0	517	0
0	120	0	10	3	80	NA	0	54	0	81	0	424	0	-241	0	664	0	351	0
0	100	0	10	5	80	NA	0	48	0	73	0	307	0	-189	0	496	0	265	0
0	80	0	10	5	80	NA	0	41	0	63	0	223	0	-149	0	372	0	210	0
120	120	8	8	5	80	3.5	42	41	68	66	288	281	-160	-128	448	409	352	285	96
120	120	9	9	5	80	3.5	45	43	74	70	304	300	-145	-115	449	415	310	244	85
120	120	12	12	5	80	3.5	61	57	90	87	334	331	-194	-151	528	482	393	321	112
120	120	14	14	5	80	3.5	68	65	98	95	274	266	-254	-235	528	501	363	289	105
120	120	10	10	1	80	3.5	59	57	86	84	579	542	-277	-251	856	793	530	475	113
120	120	10	10	3	80	3.5	58	55	84	81	413	409	-231	-226	644	634	406	336	102
100	100	10	10	5	80	3.5	53	48	78	74	305	302	-187	-177	493	479	325	258	86
80	80	10	10	5	80	3.5	46	43	68	65	240	237	-150	-149	390	386	287	225	77
120	80	10	10	5	80	3.5	49	45	77	68	287	213	-168	-110	455	322	244	206	69
80	120	10	10	5	80	3.5	51	39	79	63	274	195	-131	-120	405	315	251	173	60
120	120	8	8	5	low	3.5	25	22	46	42	108	105	-75	-63	183	168	74	52	10
120	120	8	8	5	high	3.5	48	48	75	73	654	634	-318	-269	973	903	588	526	129
120	120	10	10	5	80	4.0	52	49	80	77	339	325	-192	-151	531	476	332	265	82
120	120	10	10	5	80	4.5	50	48	79	76	383	364	-145	-106	528	470	326	267	76
120	120	10	10	5	80	3.5	47	45	77	75	268	263	-158	-125	426	388	367	303	104

Table 58. Temperature Measurements for Section T1-80-12.5-0

Scenarios							Average of Ten Measurements at Stability					
Tire 1 Inflation Pressure (psi)	Tire 2 Inflation Pressure (psi)	Tire 1 Load (kip)	Tire 2 Load (kip)	Speed (mph)	Target Temperature (°F)	Axle Spacing (ft)	Measured Test Temperature (˚F) Air Outside	Measured Test Temperature (˚F) Air Under I-APT	Measured Test Temperature (˚F) at the Bottom of Base	Measured Test Temperature (˚F) Base	Measured Test Temperature (˚F) at the Bottom of SMA	Measured Test Temperature (˚F) 1" into SMA
0	120	0	8	5	80	NA	82	85	81	85	82	82
0	120	0	9	5	80	NA	88	87	80	83	82	82
0	120	0	10	5	80	NA	87	87	73	83	82	82
0	120	0	12	5	80	NA	87	88	74	83	83	83
0	120	0	14	5	80	NA	68	81	72	81	78	79
0	120	0	10	1	80	NA	85	85	73	81	80	81
0	120	0	10	3	80	NA	86	90	74	83	82	83
0	100	0	10	5	80	NA	88	90	74	83	83	84
0	80	0	10	5	80	NA	71	82	73	83	81	81
120	120	8	8	5	80	3.5	74	85	81	85	83	82
120	120	9	9	5	80	3.5	85	84	80	82	81	81
120	120	12	12	5	80	3.5	81	85	81	84	83	83
120	120	14	14	5	80	3.5	78	83	74	83	82	82
120	120	10	10	1	80	3.5	78	83	74	81	79	79
120	120	10	10	3	80	3.5	87	89	74	82	82	83
100	100	10	10	5	80	3.5	87	90	74	83	83	84
80	80	10	10	5	80	3.5	73	83	74	83	82	82
120	80	10	10	5	80	3.5	85	85	73	81	80	81
80	120	10	10	5	80	3.5	83	84	73	81	79	80
120	120	8	8	5	low	3.5	58	62	69	70	66	67
120	120	8	8	5	high	3.5	76	106	86	92	94	96
120	120	10	10	5	80	4.0	86	85	80	83	81	83
120	120	10	10	5	80	4.5	77	82	79	83	80	81
120	120	10	10	5	80	3.5	73	86	82	85	83	83

Table 59. CoV of Measurements for Section T1-80-12.5-0

Scenarios							CoV										
Tire 1 Inflation Pressure (psi)	Tire 2 Inflation Pressure (psi)	Tire 1 Load (kip)	Tire 2 Load (kip)	Speed (mph)	Target Temperature (°F)	Axle Spacing (ft)	Pressure 1 Peak 2 (psi)	Pressure 1 Peak 1 (psi)	Pressure 2 Peak 2 (psi)	Pressure 2 Peak 1 (psi)	Longitudinal microstrain Peak 2	Longitudinal microstrain Peak 1	Longitudinal microstrain Dip 2	Longitudinal microstrain Dip 1	Transverse microstrain Peak 2	Transverse microstrain Peak 1	Transverse microstrain valley
0	120	0	8	5	80	NA		0.77		0.62		1.46		-1.47		1.22	
0	120	0	9	5	80	NA		0.57		0.89		16.83		-35.30		0.97	
0	120	0	10	5	80	NA		1.04		0.55		2.01		-3.44		1.28	
0	120	0	12	5	80	NA		0.88		0.58		1.59		-1.05		1.35	
0	120	0	14	5	80	NA		0.94		0.56		1.04		-0.77		1.01	
0	120	0	10	1	80	NA		0.46		0.43		0.79		-0.39		0.84	
0	120	0	10	3	80	NA		0.59		0.61		1.09		-0.81		1.43	
0	100	0	10	5	80	NA		0.65		0.98		1.19		-0.97		1.36	
0	80	0	10	5	80	NA		0.70		0.90		1.14		-0.92		1.50	
120	120	8	8	5	80	3.5	0.55	0.79	0.32	1.19	1.13	1.44	-0.61	-1.49	1.17	1.82	1.99
120	120	9	9	5	80	3.5	0.77	0.61	0.65	0.70	16.69	16.75	-35.07	-44.57	0.80	1.39	1.63
120	120	12	12	5	80	3.5	0.80	0.87	0.77	0.94	0.92	1.26	-0.53	-1.30	0.68	1.26	1.41
120	120	14	14	5	80	3.5	0.49	0.99	0.73	0.54	52.68	54.08	-56.37	-65.34	0.27	0.81	1.14
120	120	10	10	1	80	3.5	0.35	0.61	0.49	0.54	0.86	0.89	-0.55	-0.93	0.47	1.31	1.37
120	120	10	10	3	80	3.5	0.55	0.85	0.52	0.68	0.97	0.90	-0.84	-0.89	0.77	1.72	1.95
100	100	10	10	5	80	3.5	0.44	1.12	0.31	0.75	0.75	0.99	-0.88	-0.92	0.93	1.64	1.61
80	80	10	10	5	80	3.5	0.99	0.61	0.42	0.75	2.41	1.15	-1.74	-1.75	0.70	0.54	0.61
120	80	10	10	5	80	3.5	1.02	0.58	0.72	0.38	1.10	0.67	-0.52	-1.19	0.62	1.48	2.04
80	120	10	10	5	80	3.5	0.78	0.99	0.61	0.36	1.33	1.47	-1.04	-0.79	0.96	1.57	1.94
120	120	8	8	5	low	3.5	1.07	0.81	0.63	1.53	1.68	1.57	-1.19	-1.46	1.30	3.03	8.52
120	120	8	8	5	high	3.5	0.56	0.49	0.67	0.82	1.30	0.88	-0.79	-0.81	1.10	1.26	1.48
120	120	10	10	5	80	4.0	1.62	1.68	0.45	0.66	1.45	1.15	-0.68	-1.09	0.79	1.72	1.88
120	120	10	10	5	80	4.5	0.77	0.66	0.71	0.66	20.35	21.56	-54.03	-65.86	0.68	1.98	2.62
120	120	10	10	5	80	3.5	0.59	0.72	0.61	0.77	1.21	1.17	-0.80	-1.00	0.71	1.29	1.16

Table 60. CoV of Measurements for Section T1-80-12.5-0 (Continued)

Scenarios							CoV					
Tire 1 Inflation Pressure (psi)	Tire 2 Inflation Pressure (psi)	Tire 1 Load (kip)	Tire 2 Load (kip)	Speed (mph)	Target Temperature (°F)	Axle Spacing (ft)	Measured Test Temperature (˚F) Air Outside	Measured Test Temperature (˚F) Air Under I-APT	Measured Test Temperature (˚F) at the Bottom of Base	Measured Test Temperature (˚F) Base	Measured Test Temperature (˚F) at the Bottom of SMA	Measured Test Temperature (˚F) 1" into SMA
0	120	0	8	5	80	NA	0.33	0.04	0.00	0.00	0.01	0.02
0	120	0	9	5	80	NA	0.19	0.07	0.01	0.01	0.02	0.03
0	120	0	10	5	80	NA	0.14	0.04	0.02	0.00	0.01	0.01
0	120	0	12	5	80	NA	0.17	0.02	0.04	0.01	0.02	0.02
0	120	0	14	5	80	NA	0.15	0.05	0.02	0.00	0.01	0.01
0	120	0	10	1	80	NA	0.20	0.10	0.04	0.02	0.03	0.05
0	120	0	10	3	80	NA	0.29	0.03	0.02	0.02	0.02	0.01
0	100	0	10	5	80	NA	0.15	0.01	0.02	0.01	0.01	0.02
0	80	0	10	5	80	NA	0.05	0.05	0.04	0.01	0.02	0.10
120	120	8	8	5	80	3.5	0.13	0.09	0.01	0.01	0.01	0.03
120	120	9	9	5	80	3.5	0.26	0.08	0.00	0.00	0.01	0.02
120	120	12	12	5	80	3.5	0.77	0.03	0.01	0.00	0.01	0.03
120	120	14	14	5	80	3.5	0.14	0.02	0.05	0.00	0.01	0.02
120	120	10	10	1	80	3.5	0.35	0.02	0.18	0.01	0.01	0.02
120	120	10	10	3	80	3.5	0.18	0.04	0.03	0.01	0.02	0.03
100	100	10	10	5	80	3.5	0.34	0.03	0.02	0.01	0.02	0.02
80	80	10	10	5	80	3.5	0.29	0.02	0.02	0.01	0.01	0.01
120	80	10	10	5	80	3.5	0.13	0.09	0.03	0.01	0.02	0.01
80	120	10	10	5	80	3.5	0.24	0.03	0.06	0.00	0.01	0.31
120	120	8	8	5	low	3.5	0.24	0.08	0.01	0.00	0.01	0.28
120	120	8	8	5	high	3.5	0.06	0.27	0.02	0.02	0.03	0.07
120	120	10	10	5	80	4.0	0.27	0.11	0.00	0.00	0.02	0.05
120	120	10	10	5	80	4.5	0.69	0.13	0.01	0.00	0.01	0.03
120	120	10	10	5	80	3.5	0.23	0.05	0.01	0.00	0.00	0.02

Table 61. Pressure and Strain Measurements for Section T1-50-12.5-0

Scenarios							Average of Ten Measurements at Stability												
Tire 1 Inflation Pressure (psi)	Tire 2 Inflation Pressure (psi)	Tire 1 Load (kip)	Tire 2 Load (kip)	Speed (mph)	Target Temperature (°F)	Axle Spacing (ft)	Pressure 1 Peak 2 (psi)	Pressure 1 Peak 1 (psi)	Pressure 2 Peak 2 (psi)	Pressure 2 Peak 1 (psi)	Longitudinal microstrain Peak 2	Longitudinal microstrain Peak 1	Longitudinal microstrain Dip 2	Longitudinal microstrain Dip 1	Longitudinal microstrain Amplitude 2	Longitudinal microstrain Amplitude 1	Transverse microstrain Peak 2	Transverse microstrain Peak 1	Transverse microstrain valley
0	120	0	8	5	80	NA	0	66	0	58	0	423	0	-234	657	0	0	106	0
0	120	0	9	5	80	NA	0	72	0	64	0	361	0	-205	566	0	0	101	0
0	120	0	10	5	80	NA	0	80	0	72	0	377	0	-220	597	0	0	115	0
0	120	0	12	5	80	NA	0	88	0	83	0	348	0	-216	564	0	0	114	0
0	120	0	14	5	80	NA	0	89	0	89	0	262	0	-184	446	0	0	90	0
0	120	0	10	1	80	NA	0	89	0	79	0	704	0	-370	1074	0	0	262	0
0	120	0	10	3	80	NA	0	85	0	76	0	466	0	-262	728	0	0	169	0
0	100	0	10	5	80	NA	0	75	0	70	0	316	0	-196	511	0	0	130	0
0	80	0	10	5	80	NA	0	62	0	63	0	220	0	-154	374	0	0	110	0
120	120	8	8	5	80	3.5	70	67	61	57	452	441	-244	-227	668	696	132	99	23
120	120	9	9	5	80	3.5	74	70	70	64	351	347	-196	-182	529	547	113	84	16
120	120	12	12	5	80	3.5	93	91	89	85	434	428	-258	-235	663	693	155	116	27
120	120	14	14	5	80	3.5	101	98	100	96	355	350	-223	-202	552	578	157	120	27
120	120	10	10	1	80	3.5	88	87	82	79	653	630	-337	-306	936	989	242	199	32
120	120	10	10	3	80	3.5	87	84	81	77	444	439	-248	-234	673	692	193	150	36
100	100	10	10	5	80	3.5	78	75	76	71	323	312	-188	-178	491	511	157	118	31
80	80	10	10	5	80	3.5	68	64	69	65	241	235	-157	-146	382	398	143	107	28
120	80	10	10	5	80	3.5	78	67	73	68	292	211	-171	-127	338	462	116	96	21
80	120	10	10	5	80	3.5	79	60	76	63	279	184	-152	-130	314	431	118	76	14
120	120	8	8	5	low	3.5	32	29	42	38	99	95	-66	-61	157	164	25	18	-10
120	120	8	8	5	high	3.5	78	77	66	63	776	737	-389	-375	1112	1165	265	214	62
120	120	10	10	5	80	4.0	81	78	77	73	366	360	-209	-196	556	574	130	99	18
120	120	10	10	5	80	4.5	79	76	75	70	375	368	-214	-201	569	589	119	92	14
120	120	10	10	5	80	3.5	77	73	72	67	448	439	-252	-233	672	700	104	78	12

Table 62. Temperature Measurements for Section T1-50-12.5-0

Scenarios							Average of Ten Measurements at Stability					
Tire 1 Inflation Pressure (psi)	Tire 2 Inflation Pressure (psi)	Tire 1 Load (kip)	Tire 2 Load (kip)	Speed (mph)	Target Temperature (°F)	Axle Spacing (ft)	Measured Test Temperature (˚F) Air Outside	Measured Test Temperature (˚F) Air Under I-APT	Measured Test Temperature (˚F) at the Bottom of Base	Measured Test Temperature (˚F) at the Bottom of SMA	Measured Test Temperature (˚F) 1" into SMA	Verification of Test Temperature (˚F) drilled 1" into SMA
0	120	0	8	5	80	NA	81	85	80	81	82	85
0	120	0	9	5	80	NA	88	88	79	79	80	86
0	120	0	10	5	80	NA	89	89	79	80	81	87
0	120	0	12	5	80	NA	87	87	79	80	81	86
0	120	0	14	5	80	NA	70	83	77	77	79	82
0	120	0	10	1	80	NA	86	86	78	79	80	85
0	120	0	10	3	80	NA	87	89	79	81	81	87
0	100	0	10	5	80	NA	88	90	80	82	82	89
0	80	0	10	5	80	NA	73	83	80	81	81	84
120	120	8	8	5	80	3.5	79	85	80	80	82	85
120	120	9	9	5	80	3.5	87	86	78	79	79	85
120	120	12	12	5	80	3.5	84	86	80	81	82	85
120	120	14	14	5	80	3.5	85	86	80	81	82	86
120	120	10	10	1	80	3.5	81	83	77	78	79	83
120	120	10	10	3	80	3.5	86	88	79	80	81	86
100	100	10	10	5	80	3.5	87	89	80	81	82	88
80	80	10	10	5	80	3.5	74	84	81	81	81	85
120	80	10	10	5	80	3.5	86	86	78	79	80	85
80	120	10	10	5	80	3.5	83	84	78	78	79	84
120	120	8	8	5	low	3.5	59	64	68	66	65	66
120	120	8	8	5	high	3.5	76	102	84	89	95	94
120	120	10	10	5	80	4.0	85	85	79	80	81	84
120	120	10	10	5	80	4.5	77	83	78	79	80	83
120	120	10	10	5	80	3.5	73	87	78	78	79	83

Table 63. CoV of Measurements for Section T1-50-12.5-0

Scenarios							CoV					
Tire 1 Inflation Pressure (psi)	Tire 2 Inflation Pressure (psi)	Tire 1 Load (kip)	Tire 2 Load (kip)	Speed (mph)	Target Temperature (°F)	Axle Spacing (ft)	Measured Test Temperature (˚F) Air Outside	Measured Test Temperature (˚F) Air Under I-APT	Measured Test Temperature (˚F) at the Bottom of Base	Measured Test Temperature (˚F) Base	Measured Test Temperature (˚F) 1" into SMA	Verification of Test Temperature (˚F) drilled 1" into SMA
0	120	0	8	5	80	NA	0.43	0.01	0.01	0.01	0.00	0.04
0	120	0	9	5	80	NA	0.19	0.05	0.01	0.02	0.02	0.03
0	120	0	10	5	80	NA	0.25	0.06	0.01	0.02	0.02	0.06
0	120	0	12	5	80	NA	0.17	0.03	0.01	0.01	0.01	0.04
0	120	0	14	5	80	NA	0.20	0.03	0.00	0.01	0.01	0.03
0	120	0	10	1	80	NA	0.38	0.06	0.02	0.03	0.01	0.04
0	120	0	10	3	80	NA	0.27	0.07	0.01	0.02	0.02	0.06
0	100	0	10	5	80	NA	0.12	0.02	0.01	0.02	0.01	0.11
0	80	0	10	5	80	NA	0.12	0.02	0.00	0.00	0.01	0.06
120	120	8	8	5	80	3.5	0.30	0.01	0.00	0.00	0.00	0.04
120	120	9	9	5	80	3.5	0.21	0.10	0.01	0.02	0.01	0.06
120	120	12	12	5	80	3.5	0.55	0.03	0.00	0.01	0.01	0.03
120	120	14	14	5	80	3.5	0.16	0.01	0.00	0.01	0.01	0.03
120	120	10	10	1	80	3.5	0.41	0.05	0.02	0.02	0.04	0.09
120	120	10	10	3	80	3.5	0.54	0.02	0.02	0.03	0.02	0.05
100	100	10	10	5	80	3.5	0.20	0.04	0.01	0.02	0.02	0.03
80	80	10	10	5	80	3.5	0.16	0.03	0.01	0.01	0.01	0.03
120	80	10	10	5	80	3.5	0.37	0.06	0.01	0.02	0.01	0.06
80	120	10	10	5	80	3.5	0.46	0.07	0.01	0.02	0.02	0.04
120	120	8	8	5	low	3.5	0.18	0.11	0.00	0.01	0.02	0.04
120	120	8	8	5	high	3.5	0.12	0.19	0.01	0.02	0.05	0.12
120	120	10	10	5	80	4.0	0.44	0.01	0.01	0.01	0.01	0.04
120	120	10	10	5	80	4.5	0.20	0.02	0.01	0.01	0.01	0.03
120	120	10	10	5	80	3.5	0.28	0.03	0.01	0.01	0.00	0.03

Table 64. CoV of Measurements for Section T1-50-12.5-0 (Continued)

Scenarios							CoV					
Tire 1 Inflation Pressure (psi)	Tire 2 Inflation Pressure (psi)	Tire 1 Load (kip)	Tire 2 Load (kip)	Speed (mph)	Target Temperature (°F)	Axle Spacing (ft)	Measured Test Temperature (˚F) Air Outside	Measured Test Temperature (˚F) Air Under I-APT	Measured Test Temperature (˚F) at the Bottom of Base	Measured Test Temperature (˚F) Base	Measured Test Temperature (˚F) 1" into SMA	Verification of Test Temperature (˚F) drilled 1" into SMA
0	120	0	8	5	80	NA	0.43	0.01	0.01	0.01	0.00	0.04
0	120	0	9	5	80	NA	0.19	0.05	0.01	0.02	0.02	0.03
0	120	0	10	5	80	NA	0.25	0.06	0.01	0.02	0.02	0.06
0	120	0	12	5	80	NA	0.17	0.03	0.01	0.01	0.01	0.04
0	120	0	14	5	80	NA	0.20	0.03	0.00	0.01	0.01	0.03
0	120	0	10	1	80	NA	0.38	0.06	0.02	0.03	0.01	0.04
0	120	0	10	3	80	NA	0.27	0.07	0.01	0.02	0.02	0.06
0	100	0	10	5	80	NA	0.12	0.02	0.01	0.02	0.01	0.11
0	80	0	10	5	80	NA	0.12	0.02	0.00	0.00	0.01	0.06
120	120	8	8	5	80	3.5	0.30	0.01	0.00	0.00	0.00	0.04
120	120	9	9	5	80	3.5	0.21	0.10	0.01	0.02	0.01	0.06
120	120	12	12	5	80	3.5	0.55	0.03	0.00	0.01	0.01	0.03
120	120	14	14	5	80	3.5	0.16	0.01	0.00	0.01	0.01	0.03
120	120	10	10	1	80	3.5	0.41	0.05	0.02	0.02	0.04	0.09
120	120	10	10	3	80	3.5	0.54	0.02	0.02	0.03	0.02	0.05
100	100	10	10	5	80	3.5	0.20	0.04	0.01	0.02	0.02	0.03
80	80	10	10	5	80	3.5	0.16	0.03	0.01	0.01	0.01	0.03
120	80	10	10	5	80	3.5	0.37	0.06	0.01	0.02	0.01	0.06
80	120	10	10	5	80	3.5	0.46	0.07	0.01	0.02	0.02	0.04
120	120	8	8	5	low	3.5	0.18	0.11	0.00	0.01	0.02	0.04
120	120	8	8	5	high	3.5	0.12	0.19	0.01	0.02	0.05	0.12
120	120	10	10	5	80	4.0	0.44	0.01	0.01	0.01	0.01	0.04
120	120	10	10	5	80	4.5	0.20	0.02	0.01	0.01	0.01	0.03
120	120	10	10	5	80	3.5	0.28	0.03	0.01	0.01	0.00	0.03

Table 65. Pressure and Strain Measurements for Section D2-50-12.5-0

Scenarios						Average of Ten Measurements at Stability												
Tire 1 Inflation Pressure (psi)	Tire 2 Inflation Pressure (psi)	Tire 1 Load (kip)	Tire 2 Load (kip)	Speed (mph)	Axle Spacing (ft)	Pressure 1 Peak 2 (psi)	Pressure 1 Peak 1 (psi)	Pressure 2 Peak 2 (psi)	Pressure 2 Peak 1 (psi)	Longitudinal microstrain Peak 2	Longitudinal microstrain Peak 1	Longitudinal microstrain Dip 2	Longitudinal microstrain Dip 1	Longitudinal microstrain Amplitude 2	Longitudinal microstrain Amplitude 1	Transverse microstrain Peak 2	Transverse microstrain Peak 1	Transverse microstrain valley
0	120	0	8	5	NA	0	69	0	77	0	300	0	-137	0	436	0	163	0
0	120	0	9	5	NA	0	74	0	82	0	281	0	-135	0	416	0	155	0
0	120	0	10	5	NA	0	87	0	91	0	297	0	-140	0	436	0	170	0
0	120	0	12	5	NA	0	100	0	103	0	333	0	-162	0	495	0	197	0
0	120	0	14	5	NA	0	111	0	113	0	346	0	-172	0	518	0	208	0
0	120	0	10	1	NA	0	102	0	100	0	778	0	-291	0	1069	0	430	0
0	120	0	10	3	NA	0	93	0	95	0	416	0	-183	0	599	0	246	0
0	100	0	10	5	NA	0	76	0	83	0	217	0	-113	0	330	0	173	0
0	80	0	10	5	NA	0	68	0	74	0	179	0	-100	0	279	0	147	0
120	120	8	8	5	3.5	78	70	83	78	329	306	-141	-118	470	424	206	160	49
120	120	9	9	5	3.5	86	78	90	85	330	304	-144	-122	474	425	207	160	49
120	120	12	12	5	3.5	109	102	109	104	347	317	-159	-130	505	447	234	179	55
120	120	14	14	5	3.5	119	112	119	114	368	336	-173	-137	541	473	253	191	58
120	120	10	10	1	3.5	106	102	104	101	799	789	-290	-261	1089	1051	493	441	105
120	120	10	10	3	3.5	100	95	100	96	441	412	-176	-157	617	569	300	245	75
100	100	10	10	5	3.5	88	81	90	85	250	225	-118	-96	368	322	208	162	50
80	80	10	10	5	3.5	81	73	82	78	206	186	-106	-84	313	271	189	146	45
120	80	10	10	5	3.5	86	81	91	83	247	206	-123	-83	370	289	199	178	54
80	120	10	10	5	3.5	95	75	96	78	292	195	-111	-110	403	305	224	146	44
120	120	10	10	5	3.5	95	89	97	93	314	292	-138	-114	452	405	240	192	60

Table 66. Temperature Measurements for Section D2-50-12.5-0

Scenarios						Average of Ten Measurements at Stability						
Tire 1 Inflation Pressure (psi)	Tire 2 Inflation Pressure (psi)	Tire 1 Load (kip)	Tire 2 Load (kip)	Speed (mph)	Axle Spacing (ft)	Measured Test Temperature (˚F) Air Outside	Measured Test Temperature (˚F) Air Under I-APT	Measured Test Temperature (˚F) at the Bottom of Base	Measured Test Temperature (˚F) Base	Measured Test Temperature (˚F) at the Bottom of SMA	Measured Test Temperature (˚F) 1" into SMA	Measured Test Temperature (˚F) Verification
0	120	0	8	5	NA	79	87	81	80	82	80	85
0	120	0	9	5	NA	73	86	81	79	81	79	84
0	120	0	10	5	NA	67	91	81	79	83	80	87
0	120	0	12	5	NA	72	92	82	80	84	81	88
0	120	0	14	5	NA	74	93	83	80	84	81	88
0	120	0	10	1	NA	71	83	82	80	82	80	85
0	120	0	10	3	NA	77	87	83	80	83	80	86
0	100	0	10	5	NA	74	86	82	79	83	79	86
0	80	0	10	5	NA	75	86	82	79	82	79	86
120	120	8	8	5	3.5	79	90	81	79	83	80	86
120	120	9	9	5	3.5	78	87	81	80	82	80	85
120	120	12	12	5	3.5	67	93	82	79	84	80	88
120	120	14	14	5	3.5	73	93	82	80	84	81	88
120	120	10	10	1	3.5	74	84	82	80	82	80	86
120	120	10	10	3	3.5	77	88	83	80	83	81	86
100	100	10	10	5	3.5	79	87	82	79	82	80	86
80	80	10	10	5	3.5	78	87	82	79	82	79	86
120	80	10	10	5	3.5	76	86	82	79	82	79	86
80	120	10	10	5	3.5	79	88	82	80	83	80	86
120	120	10	10	5	3.5	78	88	82	80	83	81	87

Table 67. CoV of Measurements for Section D2-50-12.5-0

Scenarios						CoV										
Tire 1 Inflation Pressure (psi)	Tire 2 Inflation Pressure (psi)	Tire 1 Load (kip)	Tire 2 Load (kip)	Speed (mph)	Axle Spacing (ft)	Pressure 1 Peak 2 (psi)	Pressure 1 Peak 1 (psi)	Pressure 2 Peak 2 (psi)	Pressure 2 Peak 1 (psi)	Longitudinal microstrain Peak 2	Longitudinal microstrain Peak 1	Longitudinal microstrain Dip 2	Longitudinal microstrain Dip 1	Transverse microstrain Peak 2	Transverse microstrain Peak 1	Transverse microstrain valley
0	120	0	8	5	NA	0.00	0.67	0.00	0.69	0.00	1.15	0.00	-0.46	0.00	1.66	0.00
0	120	0	9	5	NA		0.68		0.74		1.00		-0.76		2.02	
0	120	0	10	5	NA		0.57		0.35		0.77		-0.56		2.12	
0	120	0	12	5	NA		0.66		0.55		1.23		-1.02		1.27	
0	120	0	14	5	NA		0.55		0.29		0.96		-0.53		1.43	
0	120	0	10	1	NA		0.33		0.34		1.10		-0.35		1.72	
0	120	0	10	3	NA		0.68		0.46		1.19		-0.71		1.95	
0	100	0	10	5	NA		0.69		0.65		1.33		-1.15		1.27	
0	80	0	10	5	NA		0.50		0.22		0.85		-0.61		0.72	
120	120	8	8	5	3.5	0.40	0.58	0.43	0.57	1.16	1.95	-0.96	-1.97	1.60	1.05	1.91
120	120	9	9	5	3.5	0.33	0.64	0.39	0.44	0.71	1.40	-0.87	-1.29	1.12	0.96	1.56
120	120	12	12	5	3.5	0.65	0.45	0.27	0.42	1.06	1.29	-0.83	-1.37	1.35	1.22	1.92
120	120	14	14	5	3.5	0.52	0.51	0.25	0.36	1.60	1.09	-0.63	-1.24	1.33	1.10	1.87
120	120	10	10	1	3.5	0.30	0.43	0.42	0.48	1.14	1.22	-1.03	-1.48	0.56	1.16	2.40
120	120	10	10	3	3.5	0.51	0.50	0.48	0.47	0.71	0.69	-0.88	-1.05	0.73	0.90	1.53
100	100	10	10	5	3.5	0.70	0.49	0.36	0.52	1.52	1.61	-0.95	-1.62	1.00	1.20	2.07
80	80	10	10	5	3.5	0.55	0.60	0.67	0.49	1.23	1.02	-0.82	-1.85	0.96	1.17	1.96
120	80	10	10	5	3.5	0.36	0.78	0.45	0.64	0.76	1.16	-0.99	-1.13	1.39	0.87	1.42
80	120	10	10	5	3.5	0.60	0.40	0.62	0.27	1.11	2.65	-1.04	-1.56	1.51	1.35	2.57
120	120	10	10	5	3.5	0.73	0.53	0.46	0.50	2.00	2.91	-3.82	-5.02	0.89	0.85	0.93

Table 68. CoV of Measurements for Section D2-50-12.5-0 (Continued)

Scenarios						CoV						
Tire 1 Inflation Pressure (psi)	Tire 2 Inflation Pressure (psi)	Tire 1 Load (kip)	Tire 2 Load (kip)	Speed (mph)	Axle Spacing (ft)	Measured Test Temperature (˚F) Air Outside	Measured Test Temperature (˚F) Air Under I-APT	Measured Test Temperature (˚F) at the Bottom of Base	Measured Test Temperature (˚F) Base	Measured Test Temperature (˚F) at the Bottom of SMA	Measured Test Temperature (˚F) 1" into SMA	Measured Test Temperature (˚F) Verification
0	120	0	8	5	NA	0.14	0.10	0.01	0.01	0.01	0.00	0.01
0	120	0	9	5	NA	0.18	0.23	0.00	0.00	0.00	0.01	0.01
0	120	0	10	5	NA	0.31	0.69	0.01	0.01	0.01	0.02	0.06
0	120	0	12	5	NA	0.26	0.13	0.01	0.01	0.00	0.02	0.01
0	120	0	14	5	NA	0.52	0.15	0.01	0.01	0.01	0.02	0.02
0	120	0	10	1	NA	0.23	0.29	0.00	0.00	0.01	0.00	0.01
0	120	0	10	3	NA	0.28	0.67	0.02	0.02	0.02	0.01	0.06
0	100	0	10	5	NA	0.50	0.08	0.00	0.01	0.00	0.01	0.01
0	80	0	10	5	NA	0.54	0.08	0.00	0.00	0.00	0.01	0.01
120	120	8	8	5	3.5	0.14	0.24	0.01	0.01	0.00	0.01	0.02
120	120	9	9	5	3.5	0.10	0.23	0.01	0.01	0.00	0.01	0.02
120	120	12	12	5	3.5	0.27	0.46	0.01	0.01	0.01	0.02	0.05
120	120	14	14	5	3.5	0.36	0.26	0.00	0.01	0.01	0.02	0.02
120	120	10	10	1	3.5	0.15	0.35	0.02	0.02	0.03	0.02	0.06
120	120	10	10	3	3.5	0.21	0.42	0.00	0.00	0.00	0.01	0.03
100	100	10	10	5	3.5	0.46	0.24	0.01	0.00	0.01	0.00	0.03
80	80	10	10	5	3.5	0.63	0.33	0.01	0.01	0.01	0.01	0.01
120	80	10	10	5	3.5	0.74	0.07	0.00	0.01	0.01	0.01	0.00
80	120	10	10	5	3.5	0.40	0.18	0.00	0.00	0.00	0.01	0.01
120	120	10	10	5	3.5	0.19	0.09	0.00	0.01	0.01	0.01	0.01

Table 69. Pressure and Strain Measurements for Section L2-50-12.5-0

Scenarios						Average of Ten Measurements at Stability												
Tire 1 Inflation Pressure (psi)	Tire 2 Inflation Pressure (psi)	Tire 1 Load (kip)	Tire 2 Load (kip)	Speed (mph)	Axle Spacing (ft)	Pressure 1 Peak 2 (psi)	Pressure 1 Peak 1 (psi)	Pressure 2 Peak 2 (psi)	Pressure 2 Peak 1 (psi)	Longitudinal microstrain Peak 2	Longitudinal microstrain Peak 1	Longitudinal microstrain Dip 2	Longitudinal microstrain Dip 1	Longitudinal microstrain Amplitude 2	Longitudinal microstrain Amplitude 1	Transverse microstrain Peak 2	Transverse microstrain Peak 1	Transverse microstrain valley
0	120	0	8	5	NA	0	85	0	86	0	90	0	-28	0	118	0	204	0
0	120	0	9	5	NA	0	90	0	91	0	85	0	-27	0	112	0	191	0
0	120	0	10	5	NA	0	95	0	98	0	88	0	-28	0	116	0	193	0
0	120	0	12	5	NA	0	105	0	109	0	90	0	-30	0	119	0	199	0
0	120	0	14	5	NA	0	113	0	119	0	90	0	-31	0	121	0	202	0
0	120	0	10	1	NA	0	98	0	104	0	133	0	-41	0	174	0	358	0
0	120	0	10	3	NA	0	86	0	90	0	93	0	-29	0	122	0	220	0
0	100	0	10	5	NA	0	87	0	93	0	71	0	-25	0	97	0	161	0
0	80	0	10	5	NA	0	81	0	86	0	60	0	-23	0	82	0	146	0
120	120	8	8	5	3.5	85	85	87	87	85	81	-26	-24	111	105	201	152	42
120	120	9	9	5	3.5	91	90	95	94	90	86	-28	-25	118	111	211	162	45
120	120	12	12	5	3.5	107	106	113	112	98	92	-31	-27	128	119	230	174	47
120	120	14	14	5	3.5	116	114	124	123	100	95	-32	-28	132	122	240	181	49
120	120	10	10	1	3.5	101	101	106	105	146	141	-44	-39	190	181	461	384	60
120	120	10	10	3	3.5	98	97	103	101	108	101	-32	-29	140	131	292	225	57
100	100	10	10	5	3.5	89	88	96	92	79	73	-25	-22	104	95	202	149	39
80	80	10	10	5	3.5	83	81	91	86	64	58	-22	-19	86	77	179	126	31
120	80	10	10	5	3.5	96	82	99	90	85	67	-29	-21	114	88	201	163	44
80	120	10	10	5	3.5	95	82	100	86	78	54	-22	-21	101	75	172	109	23
120	120	10	10	5	3.5	96	96	100	99	89	84	-28	-25	117	109	212	159	45

Table 70. Temperature Measurements for Section L2-50-12.5-0

Scenarios						Average of Ten Measurements at Stability					
Tire 1 Inflation Pressure (psi)	Tire 2 Inflation Pressure (psi)	Tire 1 Load (kip)	Tire 2 Load (kip)	Speed (mph)	Axle Spacing (ft)	Measured Test Temperature (˚F) Air Outside	Measured Test Temperature (˚F) Air Under I-APT	Measured Test Temperature (˚F) Base	Measured Test Temperature (˚F) at the Bottom of SMA	Measured Test Temperature (˚F) 1" into SMA	Measured Test Temperature (˚F) Verification
0	120	0	8	5	NA	80	102	84	84	81	87
0	120	0	9	5	NA	77	86	86	86	81	85
0	120	0	10	5	NA	79	89	85	85	81	85
0	120	0	12	5	NA	80	87	85	84	81	85
0	120	0	14	5	NA	78	85	84	84	81	84
0	120	0	10	1	NA	77	93	81	81	79	84
0	120	0	10	3	NA	76	89	84	82	80	84
0	100	0	10	5	NA	79	96	81	81	80	85
0	80	0	10	5	NA	79	97	81	81	80	86
120	120	8	8	5	3.5	76	99	82	83	80	85
120	120	9	9	5	3.5	76	99	82	83	80	85
120	120	12	12	5	3.5	75	99	82	82	80	85
120	120	14	14	5	3.5	75	98	82	82	80	85
120	120	10	10	1	3.5	77	93	82	81	80	86
120	120	10	10	3	3.5	78	84	84	83	80	84
100	100	10	10	5	3.5	78	96	82	81	80	85
80	80	10	10	5	3.5	77	96	81	81	80	85
120	80	10	10	5	3.5	78	30	82	81	80	86
80	120	10	10	5	3.5	75	94	80	82	79	84
120	120	10	10	5	3.5	75	99	82	83	80	85

Table 71. CoV of Measurements for Section L2-50-12.5-0

Scenarios						CoV										
Tire 1 Inflation Pressure (psi)	Tire 2 Inflation Pressure (psi)	Tire 1 Load (kip)	Tire 2 Load (kip)	Speed (mph)	Axle Spacing (ft)	Pressure 1 Peak 2 (psi)	Pressure 1 Peak 1 (psi)	Pressure 2 Peak 2 (psi)	Pressure 2 Peak 1 (psi)	Longitudinal microstrain Peak 2	Longitudinal microstrain Peak 1	Longitudinal microstrain Dip 2	Longitudinal microstrain Dip 1	Transverse microstrain Peak 2	Transverse microstrain Peak 1	Transverse microstrain valley
0	120	0	8	5	NA		0.71		0.89		1.22		-1.56		2.53	
0	120	0	9	5	NA		0.29		1.18		0.84		-1.13		1.90	
0	120	0	10	5	NA		0.49		0.84		1.04		-1.95		1.92	
0	120	0	12	5	NA		0.55		0.80		1.48		-1.63		2.00	
0	120	0	14	5	NA		0.59		0.43		1.32		-1.23		1.70	
0	120	0	10	1	NA		0.35		0.49		0.98		-0.87		1.77	
0	120	0	10	3	NA		35.31		35.12		27.41		-31.05		30.81	
0	100	0	10	5	NA		0.46		0.76		1.09		-1.19		1.98	
0	80	0	10	5	NA		0.33		0.32		1.61		-1.37		0.97	
120	120	8	8	5	3.5	0.66	0.67	0.55	0.29	1.05	1.02	-1.80	-2.31	1.66	1.58	3.51
120	120	9	9	5	3.5	0.46	0.39	0.83	0.54	1.30	1.50	-1.01	-1.56	1.80	1.52	2.68
120	120	12	12	5	3.5	0.54	0.53	0.65	0.38	1.46	1.60	-1.36	-1.26	1.35	1.61	3.26
120	120	14	14	5	3.5	0.31	0.40	0.63	0.58	1.36	0.83	-1.35	-1.73	1.10	1.43	2.35
120	120	10	10	1	3.5	0.24	0.34	0.55	0.44	1.17	0.86	-1.35	-1.09	1.43	1.02	3.36
120	120	10	10	3	3.5	0.24	0.25	0.65	0.37	1.15	1.91	-2.13	-1.62	1.47	1.06	2.02
100	100	10	10	5	3.5	0.41	0.42	0.36	0.32	1.21	1.97	-1.03	-1.33	1.14	0.81	1.28
80	80	10	10	5	3.5	0.43	0.31	0.58	0.44	1.05	1.66	-0.96	-1.85	1.64	0.95	2.40
120	80	10	10	5	3.5	0.52	0.44	0.37	0.57	1.36	1.76	-1.80	-2.68	2.43	1.52	2.51
80	120	10	10	5	3.5	0.43	0.45	0.65	0.43	1.39	2.30	-1.45	-1.88	1.60	2.15	4.52
120	120	10	10	5	3.5	0.62	0.80	0.55	0.42	0.90	1.62	-1.38	-1.78	1.35	1.75	2.42

Table 72. CoV of Measurements for Section L2-50-12.5-0 (Continued)

Scenarios						CoV					
Tire 1 Inflation Pressure (psi)	Tire 2 Inflation Pressure (psi)	Tire 1 Load (kip)	Tire 2 Load (kip)	Speed (mph)	Axle Spacing (ft)	Measured Test Temperature (˚F) Air Outside	Measured Test Temperature (˚F) Air Under I-APT	Measured Test Temperature (˚F) Base	Measured Test Temperature (˚F) at the Bottom of SMA	Measured Test Temperature (˚F) 1" into SMA	Measured Test Temperature (˚F) Verification
0	120	0	8	5	NA	0.06	0.32	0.00	0.01	0.01	0.03
0	120	0	9	5	NA	0.16	1.12	0.01	0.02	0.00	0.06
0	120	0	10	5	NA	0.54	0.53	0.01	0.02	0.01	0.02
0	120	0	12	5	NA	0.40	0.44	0.01	0.01	0.01	0.03
0	120	0	14	5	NA	0.48	0.74	0.01	0.02	0.01	0.03
0	120	0	10	1	NA	0.32	0.62	0.01	0.01	0.03	0.04
0	120	0	10	3	NA	0.44	1.12	0.01	0.02	0.01	0.04
0	100	0	10	5	NA	0.20	0.26	0.01	0.02	0.03	0.03
0	80	0	10	5	NA	0.35	0.48	0.01	0.01	0.02	0.05
120	120	8	8	5	3.5	0.14	0.33	0.00	0.01	0.02	0.07
120	120	9	9	5	3.5	0.15	0.40	0.00	0.01	0.01	0.05
120	120	12	12	5	3.5	0.05	0.48	0.00	0.01	0.01	0.03
120	120	14	14	5	3.5	0.06	0.28	0.01	0.00	0.01	0.03
120	120	10	10	1	3.5	0.16	0.54	0.00	0.00	0.00	0.07
120	120	10	10	3	3.5	0.32	0.52	0.01	0.02	0.01	0.02
100	100	10	10	5	3.5	0.27	0.78	0.01	0.02	0.06	0.29
80	80	10	10	5	3.5	0.31	0.53	0.00	0.02	0.03	0.03
120	80	10	10	5	3.5	0.15	0.00	0.01	0.01	0.02	0.03
80	120	10	10	5	3.5	0.17	0.45	0.02	0.01	0.02	0.02
120	120	10	10	5	3.5	0.18	0.26	0.00	0.00	0.02	0.04

Table 73. Pressure and Strain Measurements for Section D3-50-9.5-0

Scenarios						Average of Ten Measurements at Stability												
Tire 1 Inflation Pressure (psi)	Tire 2 Inflation Pressure (psi)	Tire 1 Load (kip)	Tire 2 Load (kip)	Speed (mph)	Axle Spacing (ft)	Pressure 1 Peak 2 (psi)	Pressure 1 Peak 1 (psi)	Pressure 2 Peak 2 (psi)	Pressure 2 Peak 1 (psi)	Longitudinal microstrain Peak 2	Longitudinal microstrain Peak 1	Longitudinal microstrain Dip 2	Longitudinal microstrain Dip 1	Longitudinal microstrain Amplitude 2	Longitudinal microstrain Amplitude 1	Transverse microstrain Peak 2	Transverse microstrain Peak 1	Transverse microstrain valley
0	120	0	8	5	NA	0	84	0	85	0	240	0	-130	0	370	0	200	0
0	120	0	9	5	NA	0	91	0	92	0	251	0	-146	0	398	0	208	0
0	120	0	10	5	NA	0	98	0	101	0	312	0	-177	0	489	0	275	0
0	120	0	12	5	NA	0	109	0	111	0	270	0	-164	0	434	0	242	0
0	120	0	14	5	NA	0	120	0	121	0	265	0	-157	0	423	0	260	0
0	120	0	10	1	NA	0	107	0	108	0	686	0	-387	0	1072	0	512	0
0	120	0	10	3	NA	0	102	0	104	0	377	0	-225	0	601	0	293	0
0	100	0	10	5	NA	0	94	0	94	0	270	0	-171	0	441	0	211	0
0	80	0	10	5	NA	0	84	0	84	0	192	0	-131	0	323	0	178	0
120	120	8	8	5	3.5	88	86	87	83	243	228	-138	-122	381	350	248	192	68
120	120	9	9	5	3.5	95	94	98	93	262	244	-148	-133	409	377	266	205	73
120	120	12	12	5	3.5	115	113	116	111	282	255	-182	-165	464	420	267	197	55
120	120	14	14	5	3.5	127	124	126	122	263	239	-187	-168	449	407	320	246	104
120	120	10	10	1	3.5	110	109	110	108	719	702	-404	-391	1123	1094	594	514	109
120	120	10	10	3	3.5	106	104	105	102	365	342	-212	-210	577	552	314	243	66
100	100	10	10	5	3.5	98	95	99	94	276	247	-176	-164	452	411	260	192	53
80	80	10	10	5	3.5	89	86	90	85	206	182	-142	-130	348	312	223	162	40
120	80	10	10	5	3.5	101	89	100	90	261	195	-175	-123	436	319	221	176	46
80	120	10	10	5	3.5	103	87	104	86	301	195	-173	-151	474	345	262	183	54
120	120	10	10	5	3.5	103	101	104	100	281	261	-176	-160	457	421	255	188	50

Table 74. Temperature Measurements for Section D3-50-9.5-0

Scenarios						Measured Test Temperature (˚F) Air Inside	Measured Test Temperature (˚F) Base	Measured Test Temperature (˚F) 1" into SMA
Tire 1 Inflation Pressure (psi)	Tire 2 Inflation Pressure (psi)	Tire 1 Load (kip)	Tire 2 Load (kip)	Speed (mph)	Axle Spacing (ft)			
0	120	0	8	5	NA	90	79	84
0	120	0	9	5	NA	89	79	84
0	120	0	10	5	NA	82	81	83
0	120	0	12	5	NA	83	80	82
0	120	0	14	5	NA	84	80	82
0	120	0	10	1	NA	78	79	80
0	120	0	10	3	NA	83	80	82
0	100	0	10	5	NA	89	79	82
0	80	0	10	5	NA	87	78	80
120	120	8	8	5	3.5	89	79	83
120	120	9	9	5	3.5	90	79	84
120	120	12	12	5	3.5	81	79	80
120	120	14	14	5	3.5	82	78	78
120	120	10	10	1	3.5	79	80	81
120	120	10	10	3	3.5	82	78	79
100	100	10	10	5	3.5	90	79	82
80	80	10	10	5	3.5	90	79	81
120	80	10	10	5	3.5	86	78	80
80	120	10	10	5	3.5	91	79	82
120	120	10	10	5	3.5	81	79	80

Table 75. CoV of Measurements for Section D3-50-9.5-0

Scenarios						CoV of Ten Measurements Averaged													
Tire 1 Inflation Pressure (psi)	Tire 2 Inflation Pressure (psi)	Tire 1 Load (kip)	Tire 2 Load (kip)	Speed (mph)	Axle Spacing (ft)	Pressure 1 Peak 2 (psi)	Pressure 1 Peak 1 (psi)	Pressure 2 Peak 2 (psi)	Pressure 2 Peak 1 (psi)	Longitudinal microstrain Peak 2	Longitudinal microstrain Peak 1	Longitudinal microstrain Dip 2	Longitudinal microstrain Dip 1	Transverse microstrain Peak 2	Transverse microstrain Peak 1	Transverse microstrain valley	Measured Test Temperature (˚F) Air Inside	Measured Test Temperature (˚F) Base	Measured Test Temperature (˚F) 1" into SMA
0	120	0	8	5	NA		0.01		0.00		0.03		-0.04		0.01		0.00	0.00	0.00
0	120	0	9	5	NA		0.43		1.32		2.44		-0.92		0.87		0.22	0.01	0.10
0	120	0	10	5	NA		0.00		0.00		0.04		-0.06		0.01		0.00	0.00	0.00
0	120	0	12	5	NA		0.00		0.00		0.02		-0.04		0.01		0.00	0.00	0.00
0	120	0	14	5	NA		0.00		0.01		0.11		-0.31		0.01		0.00	0.00	0.00
0	120	0	10	1	NA		0.25		0.26		1.65		-1.31		1.03		0.43	0.02	0.03
0	120	0	10	3	NA		0.59		0.52		1.32		-1.07		0.96		0.34	0.00	0.04
0	100	0	10	5	NA		0.25		0.35		2.06		-1.29		1.70		0.13	0.01	0.01
0	80	0	10	5	NA		0.51		0.42		2.76		-1.03		0.72		0.32	0.01	0.03
120	120	8	8	5	3.5	0.59	0.60	1.90	1.54	0.69	2.12	-1.22	-1.29	0.84	1.49	1.60	0.13	0.01	0.09
120	120	9	9	5	3.5	0.32	0.22	0.56	0.58	1.52	2.72	-1.33	-3.24	0.68	1.87	2.19	0.23	0.00	0.08
120	120	12	12	5	3.5	0.26	0.45	0.49	0.67	1.35	2.63	-1.01	-1.57	1.54	1.11	4.80	0.15	0.01	0.03
120	120	14	14	5	3.5	0.46	0.37	0.29	0.75	2.88	2.71	-0.87	-2.17	0.62	1.20	1.16	0.13	0.00	0.01
120	120	10	10	1	3.5	0.45	0.20	0.35	0.50	1.37	2.01	-0.91	-1.40	0.74	1.07	1.24	0.51	0.01	0.07
120	120	10	10	3	3.5	0.40	0.44	0.43	0.64	1.86	1.67	-1.10	-1.50	1.04	2.10	3.25	0.30	0.00	0.01
100	100	10	10	5	3.5	0.24	0.25	0.43	0.56	2.14	1.79	-0.75	-1.50	1.25	2.18	5.68	0.27	0.01	0.01
80	80	10	10	5	3.5	0.47	0.29	0.37	0.52	2.05	2.92	-0.95	-2.05	1.59	2.25	8.34	0.42	0.01	0.01
120	80	10	10	5	3.5	0.50	0.39	0.58	0.37	1.48	1.42	-0.75	-1.73	1.65	2.83	7.47	1.18	0.01	0.05
80	120	10	10	5	3.5	0.42	0.42	0.26	0.68	2.20	2.75	-1.70	-0.94	1.68	3.18	7.88	0.14	0.01	0.01
120	120	10	10	5	3.5	0.90	0.33	0.41	0.48	1.38	1.66	-1.14	-1.34	2.18	3.33	8.54	0.19	0.01	0.02

Table 76. Pressure, Temperature, and Strain Measurements for Section D4-50-12.5-0

Scenarios						Measured SMA Temperature (°F)	Average of Ten Measurements at Stability										
Tire 1 Inflation Pressure (psi)	Tire 2 Inflation Pressure (psi)	Tire 1 Load (kip)	Tire 2 Load (kip)	Speed (mph)	Axle Spacing (ft)		Pressure 2 Peak 1 (psi)	Pressure 2 Peak 2 (psi)	Longitudinal microstrain Dip 1	Longitudinal microstrain Peak 1	Longitudinal Amplitude 1	Longitudinal microstrain Dip 2	Longitudinal microstrain Peak 2	Longitudinal Amplitude 2	Transverse microstrain Peak 1	Transverse microstrain valley	Transverse microstrain Peak 2
120	0	8	0	5		79	65		-141	212	352				80		
120	0	9	0	5		80	75		-151	227	378				83		
120	0	10	0	5		81	83		-162	250	412				88		
120	0	10	0	1		82	106		-464	698	1162				216		
120	0	10	0	3		81	94		-235	348	583				119		
100	0	10	0	5		83	85		-199	278	477				95		
80	0	10	0	5		83	69		-148	191	340				48		
120	120	8	8	5	3.5	81	70	78	-157	229	386	-152	237	389	83	18	99
120	120	9	9	5	3.5	81	79	86	-171	244	416	-166	254	420	88	18	106
120	120	10	10	1	3.5	83	108	111	-507	782	1289	-514	796	1310	241	35	261
120	120	10	10	3	3.5	82	97	103	-259	374	633	-250	387	636	125	26	148
100	100	10	10	5	3.5	83	85	92	-196	253	449	-175	285	460	85	17	108
80	80	10	10	5	3.5	83	77	84	-165	219	384	-158	231	388	52	0	60
120	80	10	10	5	3.5	83	83	90	-194	204	398	-147	288	435	75	25	112
80	120	10	10	5	3.5	82	75	97	-188	190	378	-156	288	444	63	64	108
120	120	10	10	5	3.5	81	86	93	-186	258	444	-179	268	448	91	17	110

Table 77. CoV of Measurements for Section D4-50-13.5-0

Scenarios						COV of Ten Measurements Averaged									
Tire 1 Inflation Pressure (psi)	Tire 2 Inflation Pressure (psi)	Tire 1 Load (kip)	Tire 2 Load (kip)	Speed (mph)	Axle Spacing (ft)	Measured Test Temperature (˚F)	Pressure Peak 1 (psi)	Pressure Peak 2 (psi)	Longitudinal microstrain Dip 1	Longitudinal microstrain Peak 1	Longitudinal microstrain Dip 2	Longitudinal microstrain Peak 2	Transverse microstrain Peak 1	Transverse microstrain valley	Transverse microstrain Peak 2
120	0	8	0	5		0.00	0.01		-0.01	0.01			0.05	-0.27	
120	0	9	0	5		0.00	0.01		-0.02	0.02			0.03	-0.31	
120	0	10	0	5		0.00	0.01		-0.05	0.04			0.03	-0.29	
120	0	10	0	1		0.00	0.00		-0.01	0.02			0.05	-0.06	
120	0	10	0	3		0.00	0.01		-0.01	0.02			0.04	-0.04	
100	0	10	0	5		0.00	0.01		-0.01	0.03			0.04	-0.71	
80	0	10	0	5		0.00	0.01		-0.01	0.02			0.05	-0.02	
120	120	8	8	5	3.5	0.00	0.01	0.01	-0.02	0.03	-0.02	0.02	0.04	0.08	0.04
120	120	9	9	5	3.5	0.00	0.01	0.01	-0.01	0.02	-0.02	0.03	0.04	0.08	0.05
120	120	10	10	1	3.5	0.00	0.01	0.01	-0.01	0.02	-0.02	0.02	0.04	0.07	0.04
120	120	10	10	3	3.5	0.00	0.01	0.01	-0.01	0.03	-0.02	0.02	0.03	0.07	0.04
100	100	10	10	5	3.5	0.00	0.01	0.02	-0.01	0.02	-0.12	0.14	0.03	0.30	0.09
80	80	10	10	5	3.5	0.00	0.00	0.01	-0.02	0.03	-0.03	0.04	0.05	-0.29	0.04
120	80	10	10	5	3.5	0.00	0.01	0.00	-0.01	0.02	-0.02	0.02	0.03	0.07	0.07
80	120	10	10	5	3.5	0.00	0.01	0.01	-0.01	0.02	-0.01	0.02	0.04	0.05	0.05
120	120	10	10	5	3.5	0.00	0.02	0.02	0.00	0.01	-0.01	0.02	0.04	0.08	0.03

APPENDIX I: PAVEMENT SECTION RESPONSES

Testing scenarios are defined in Table 24. For figures labeled as "CORRECTED FOR THICKNESS AND TEMPERATURE," measured responses are adjusted to the reference conditions of 80°F SMA temperature and 2.0 in. thickness.

Each testing scenario represents a specific combination of axle configuration, tire inflation pressure, wheel load, speed, axle spacing, and target temperature, as summarized in Table 24. In the figure filenames, these parameters are encoded in sequence to distinguish different loading and environmental conditions (e.g., single- versus tandem-axle loading, load level, speed, and temperature). The scenario labels (A, B, A-T, etc.) are used throughout the figures and captions for clarity and consistency.

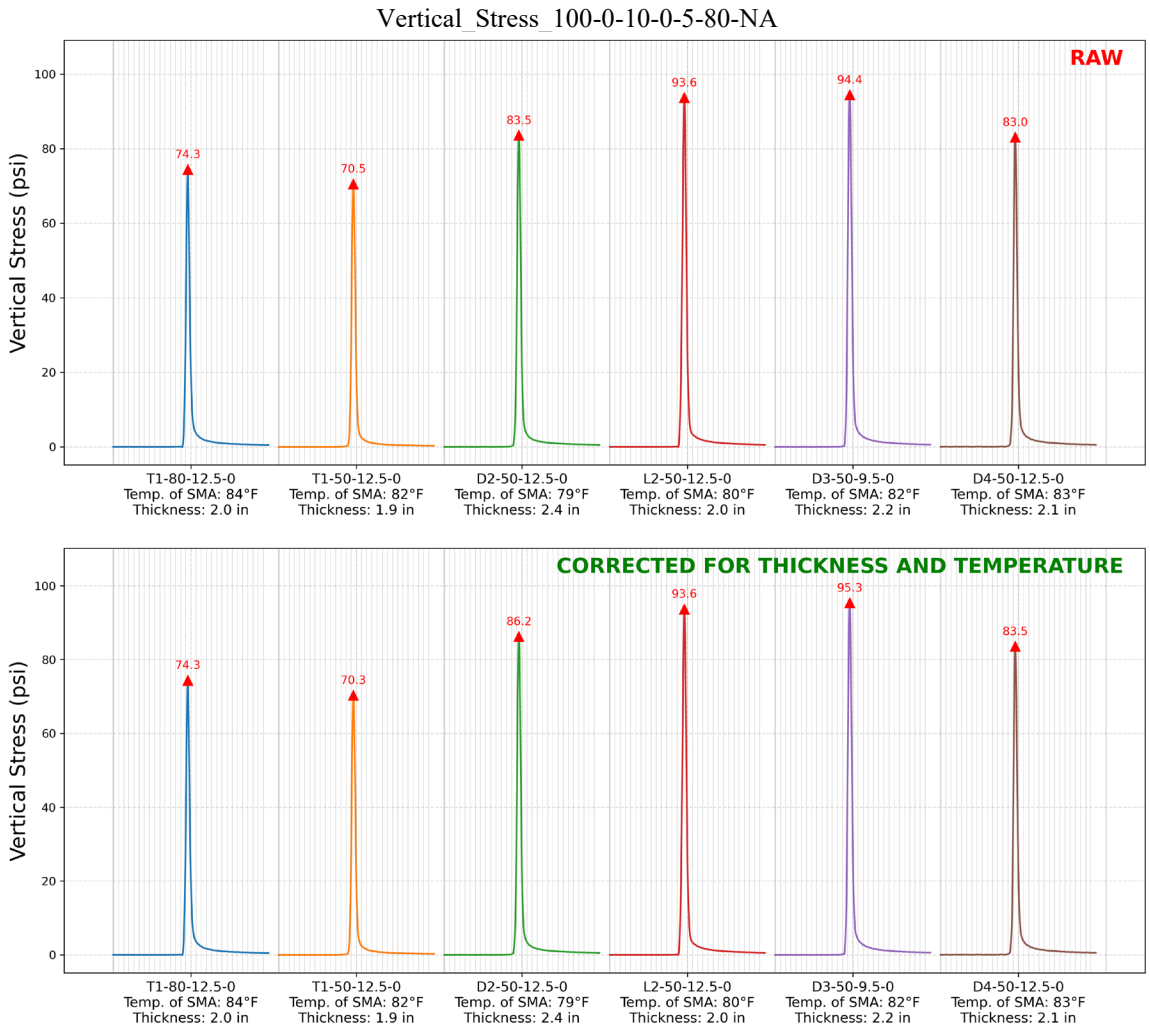

Figure 188. Graph. Comparison of measured and corrected vertical stress under single-axle loading (P_1 = 100 psi; L_1 = 10 kip; speed = 5 mph)

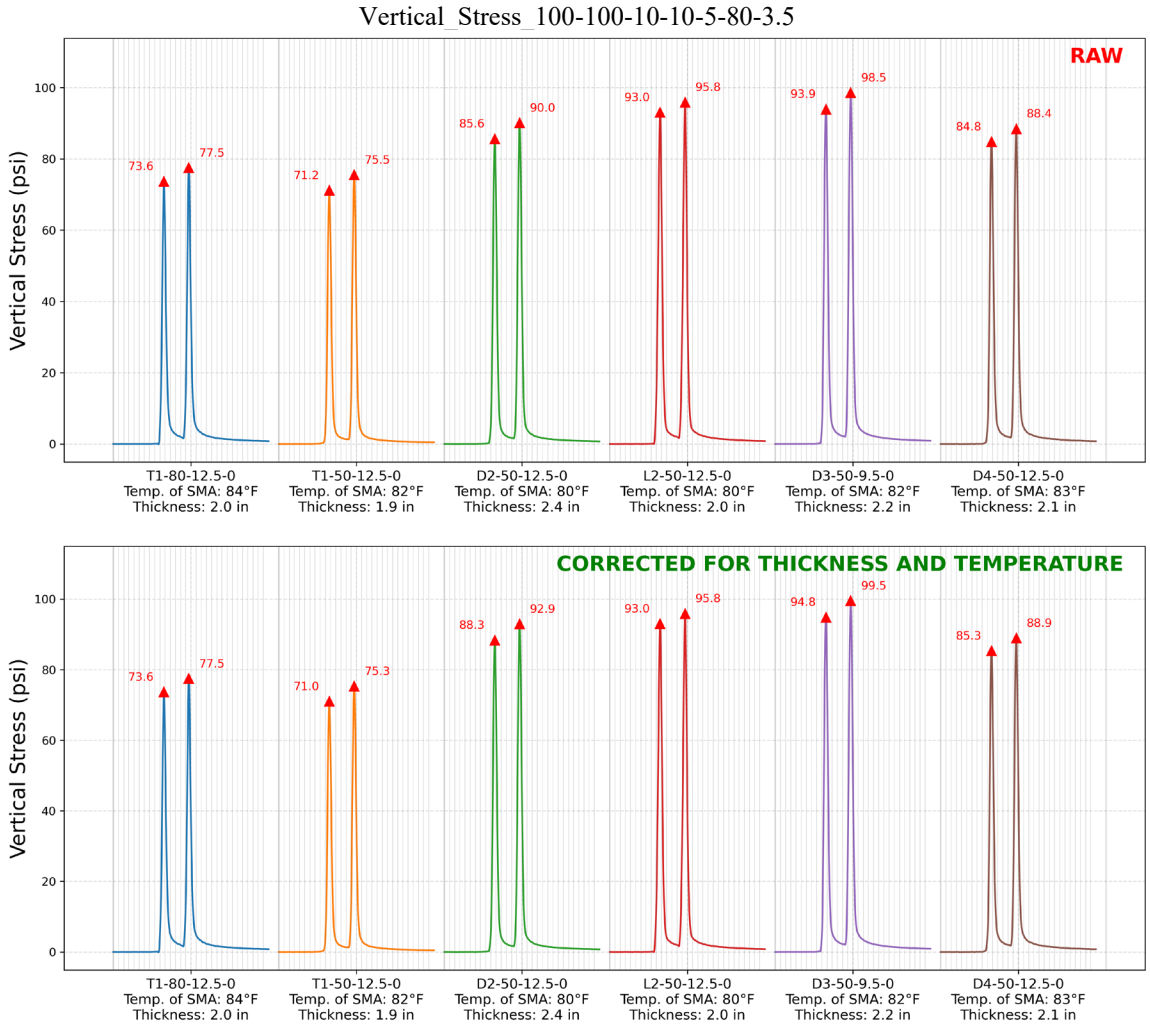

Figure 189. Graph. Comparison of measured and corrected vertical stress under tandem-axle loading (P_1 = 100 psi, P_2 = 100 psi; L_1 = 10 kip, L_2 = 10 kip; speed = 5 mph; axle spacing = 3.5 ft)

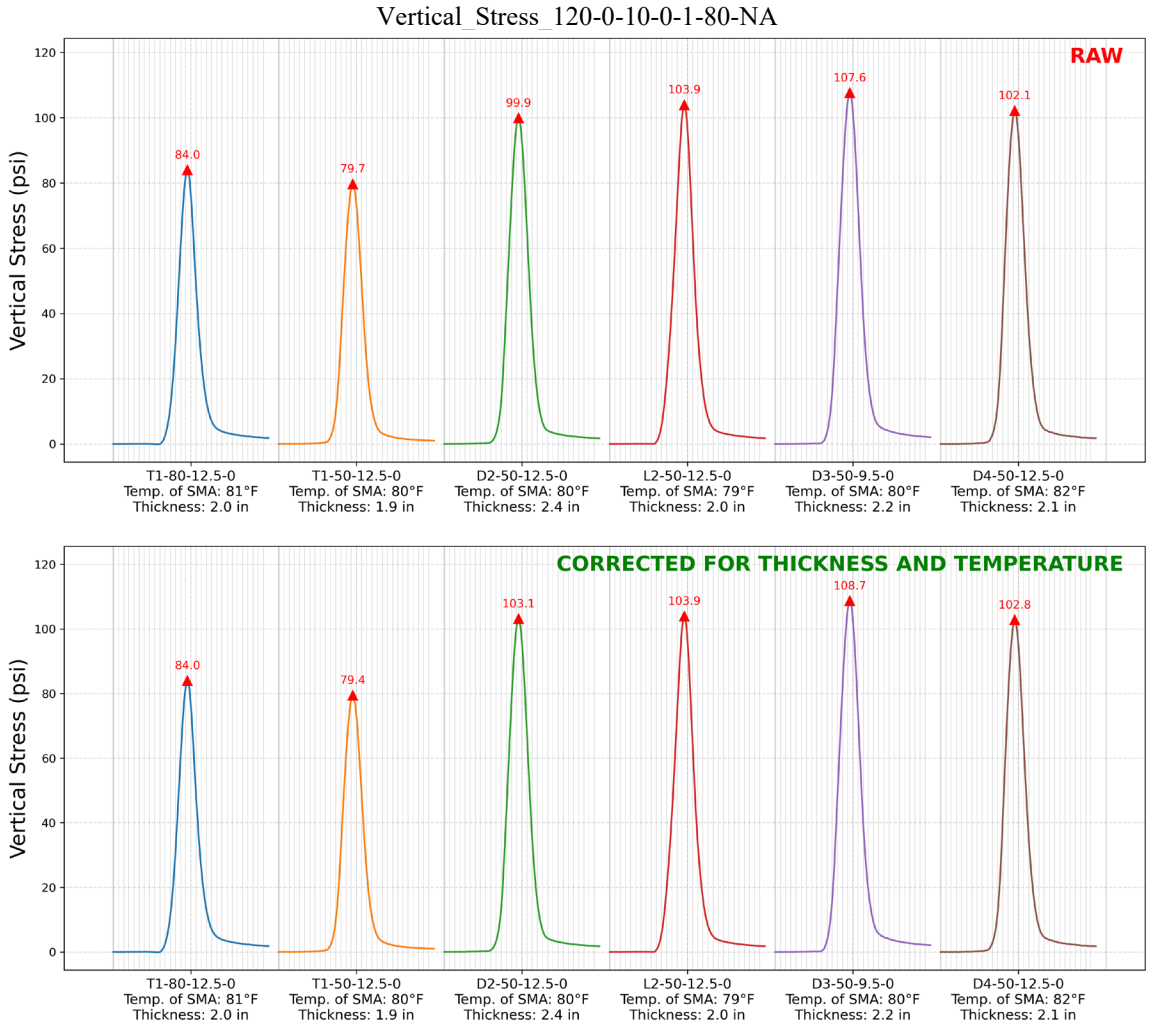

Figure 190. Graph. Comparison of measured and corrected vertical stress under single-axle loading (P_1 = 120 psi; L_1 = 10 kip; speed = 1 mph)

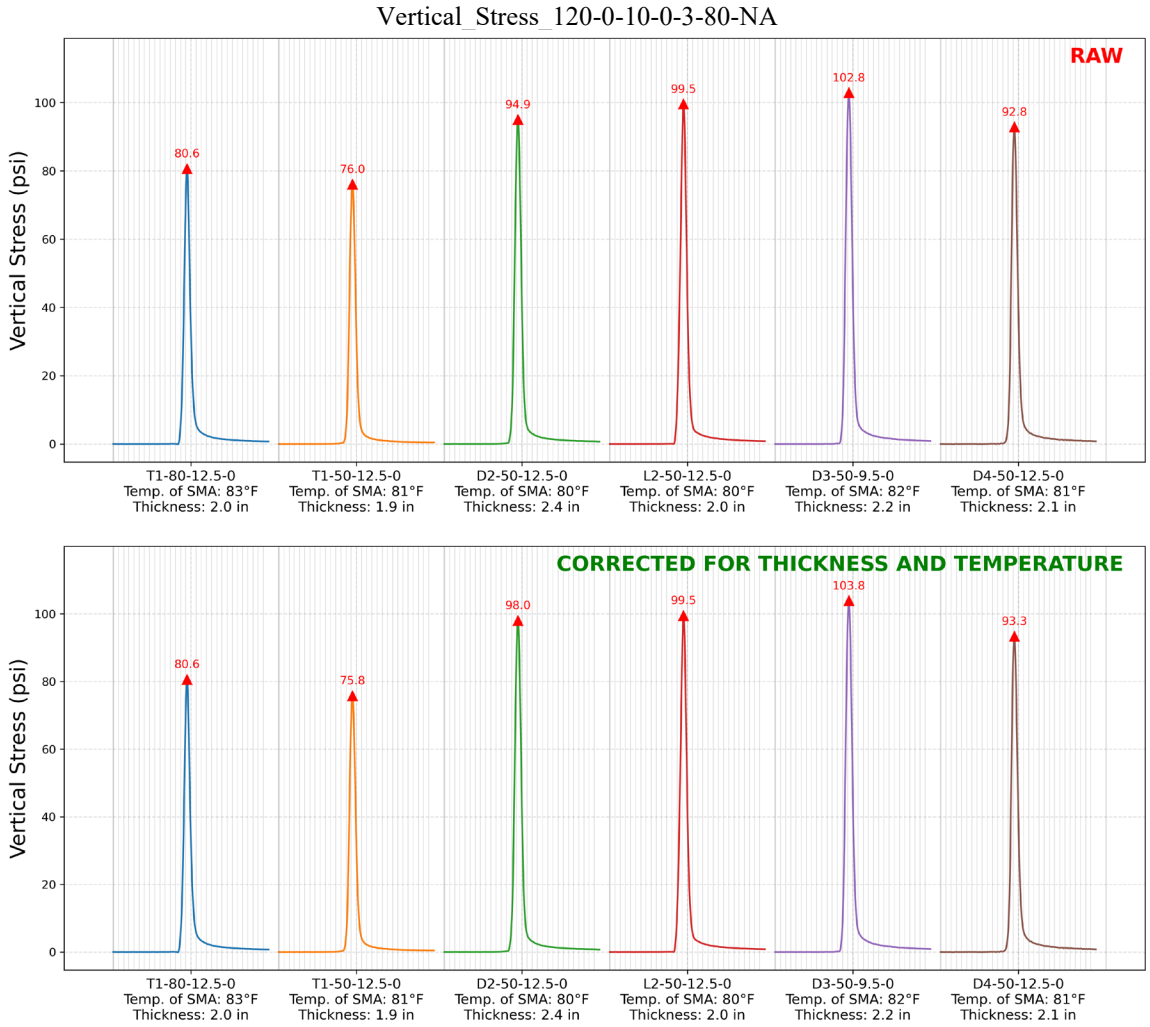

Figure 191. Graph. Comparison of measured and corrected vertical stress under single-axle loading (P_1 = 120 psi; L_1 = 10 kip; speed = 3 mph)

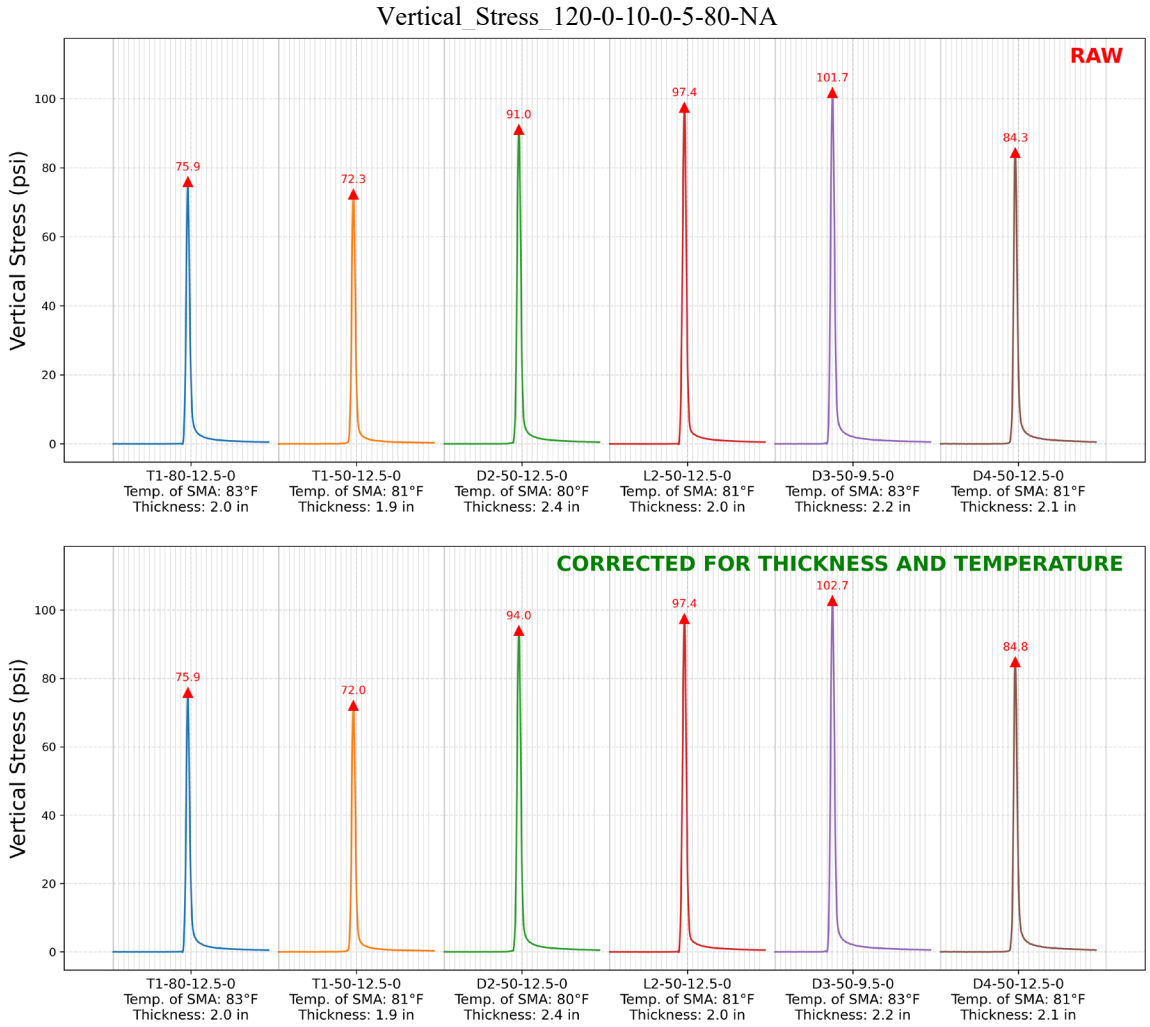

Figure 192. Graph. Comparison of measured and corrected vertical stress under single-axle loading (P_1 = 120 psi; L_1 = 10 kip; speed = 5 mph)

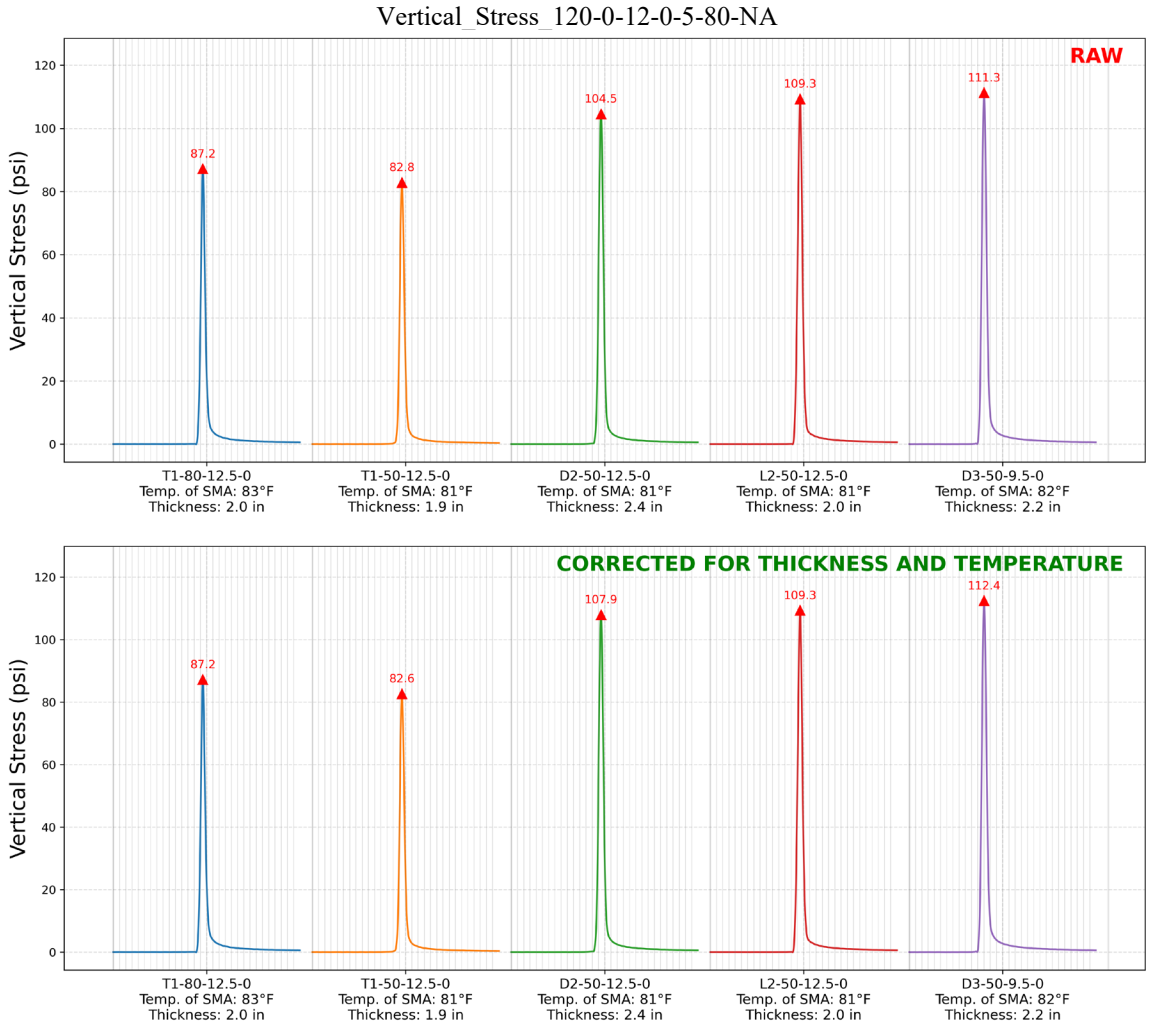

Figure 193. Graph. Comparison of measured and corrected vertical stress under single-axle loading (P_1 = 120 psi; L_1 = 12 kip; speed = 5 mph)

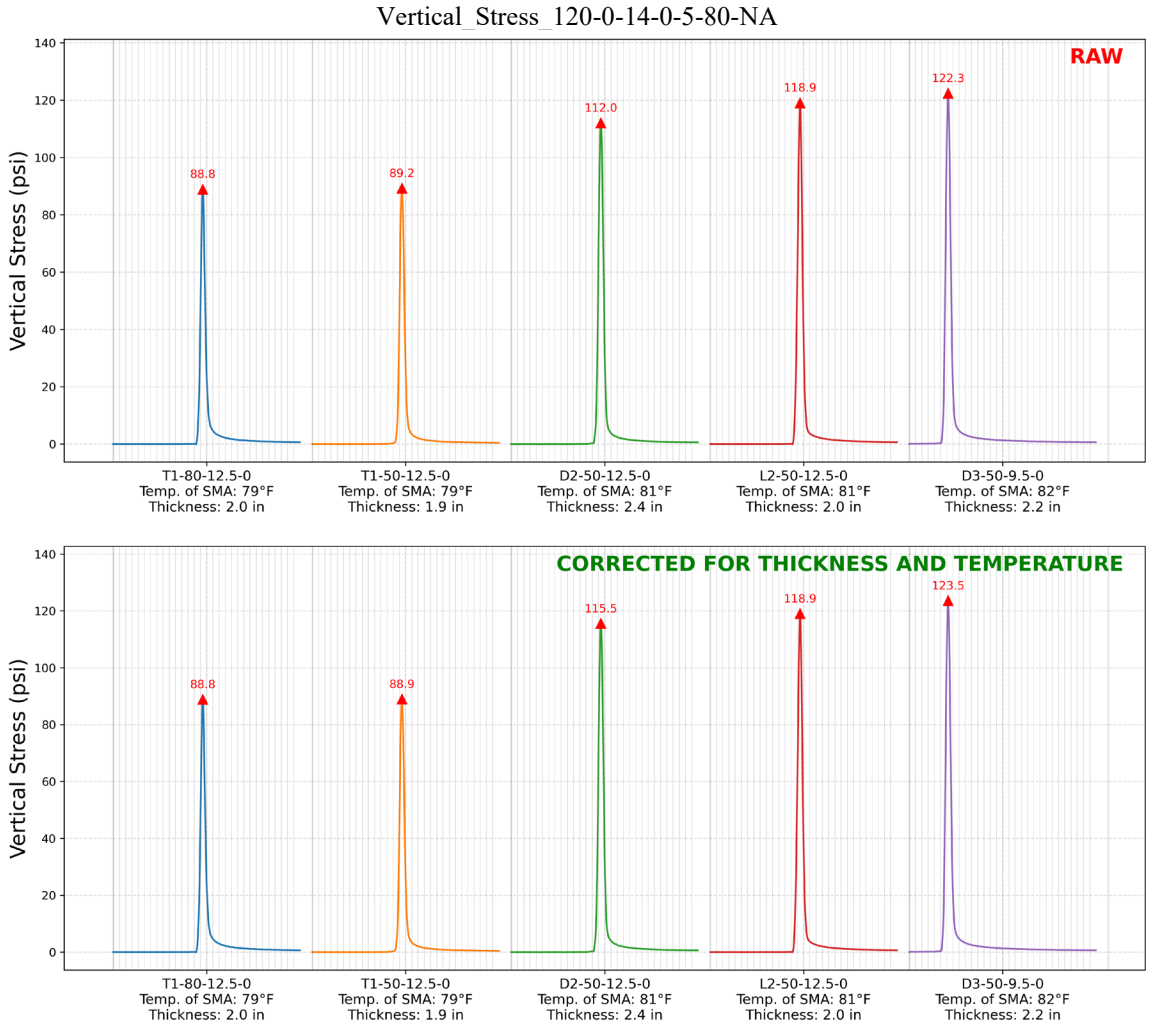

Figure 194. Graph. Comparison of measured and corrected vertical stress under single-axle loading (P_1 = 120 psi; L_1 = 14 kip; speed = 5 mph)

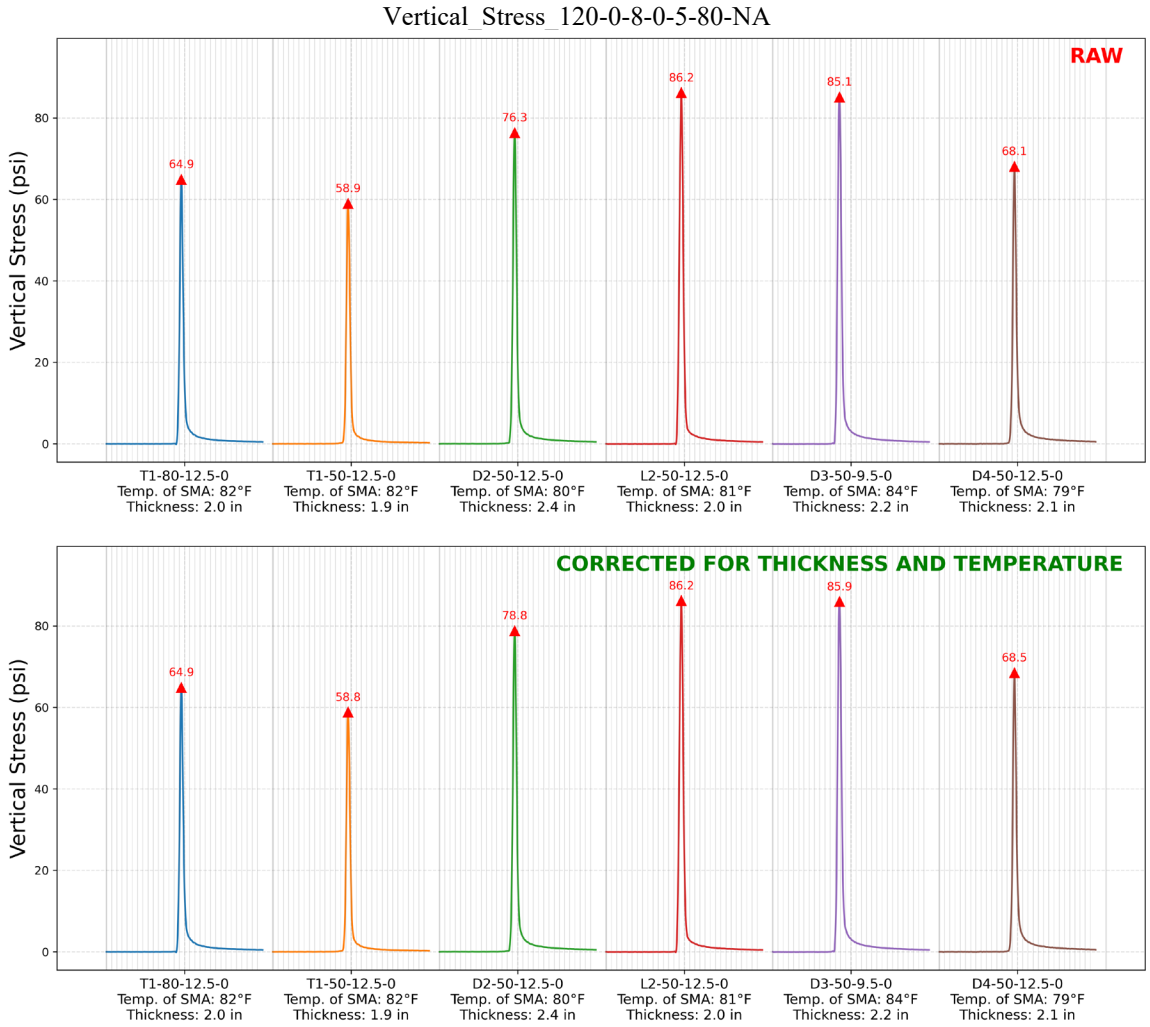

Figure 195. Graph. Comparison of measured and corrected vertical stress under single-axle loading (P_1 = 120 psi; L_1 = 8 kip; speed = 5 mph)

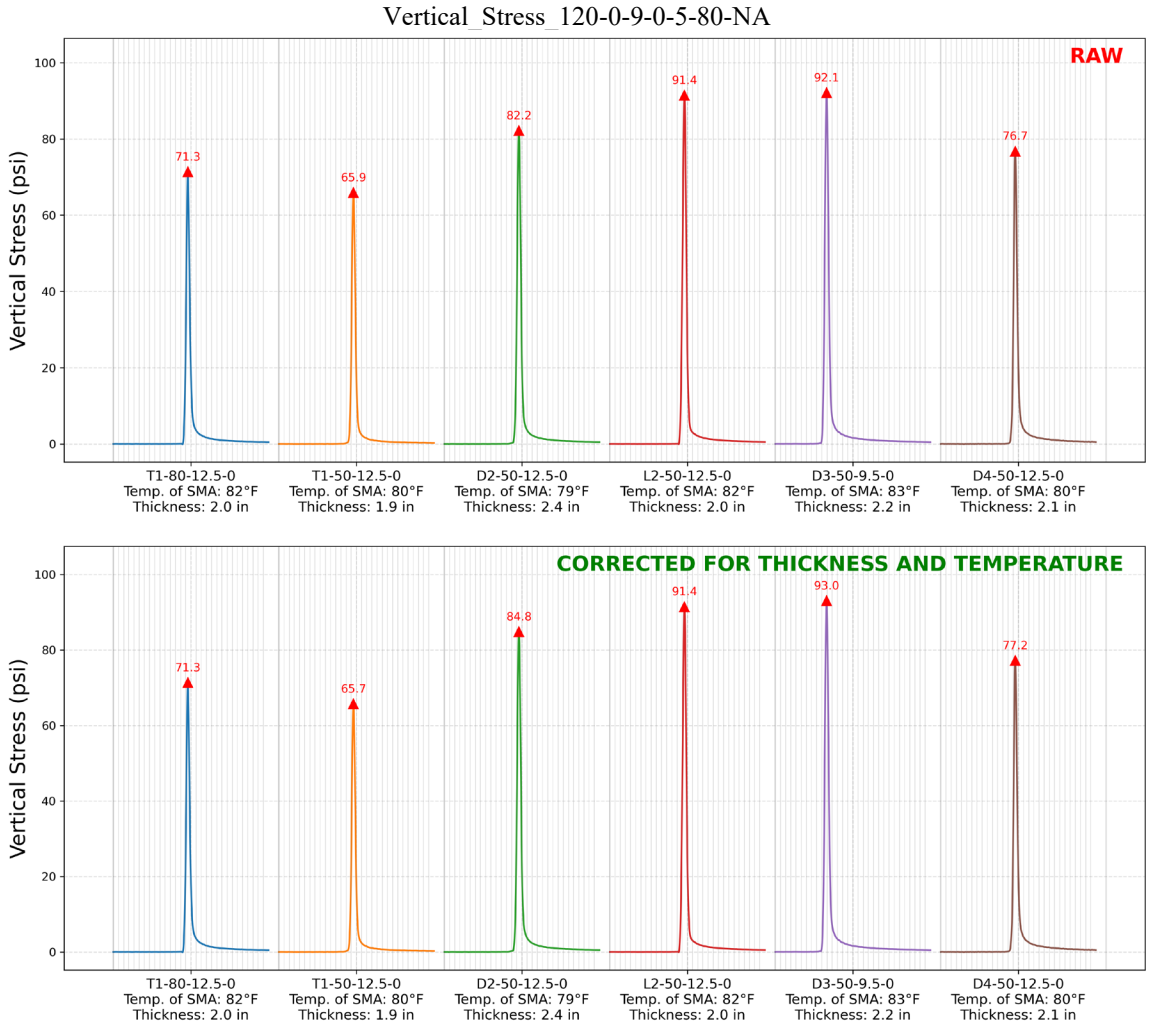

Figure 196. Comparison of measured and corrected vertical stress under single-axle loading (P_1 = 120 psi; L_1 = 9 kip; speed = 5 mph)

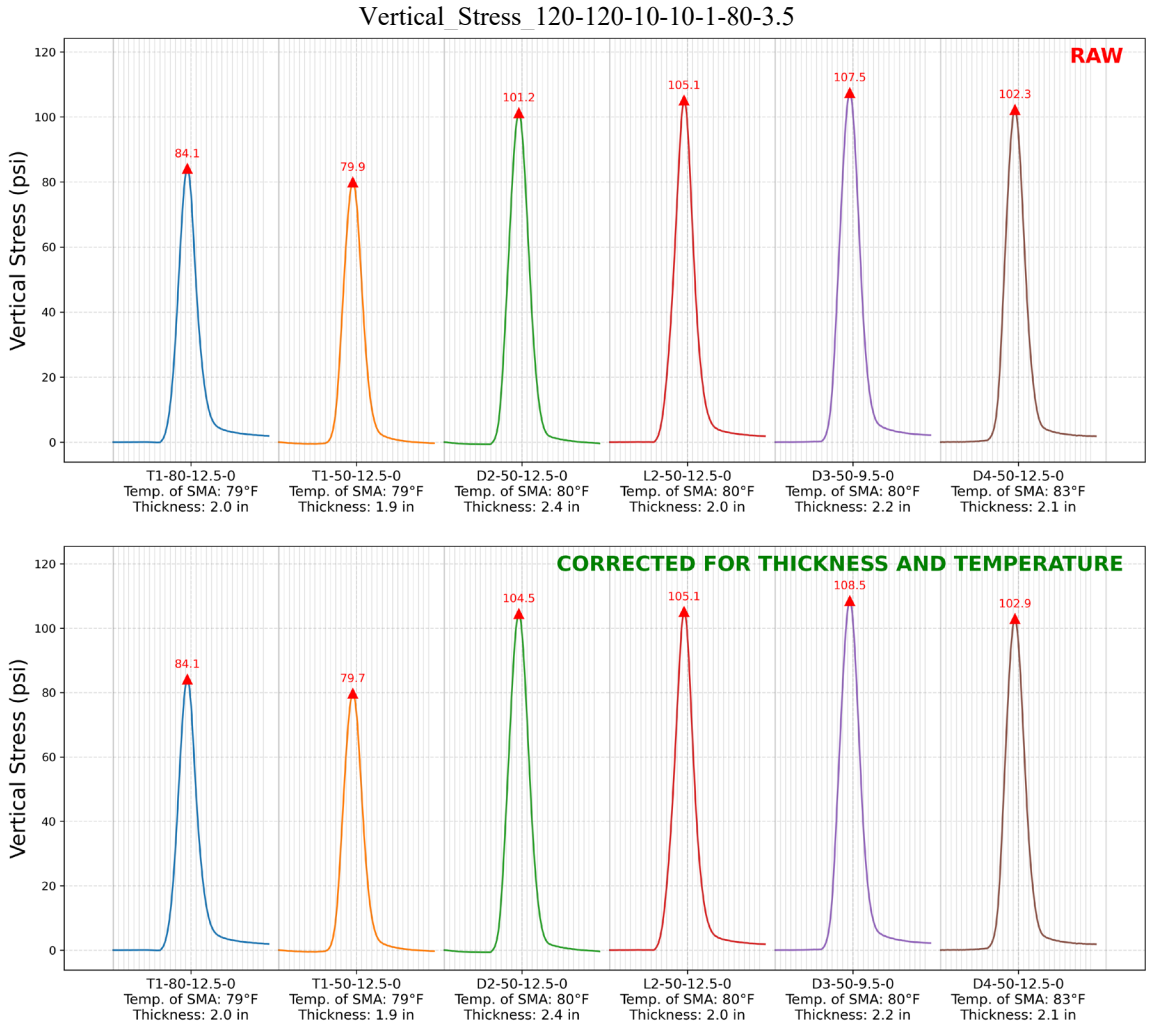

Figure 197. Graph. Comparison of measured and corrected vertical stress under tandem-axle loading (P_1 = 120 psi, P_2 = 120 psi; L_1 = 10 kip, L_2 = 10 kip; speed = 1 mph; axle spacing = 3.5 ft)

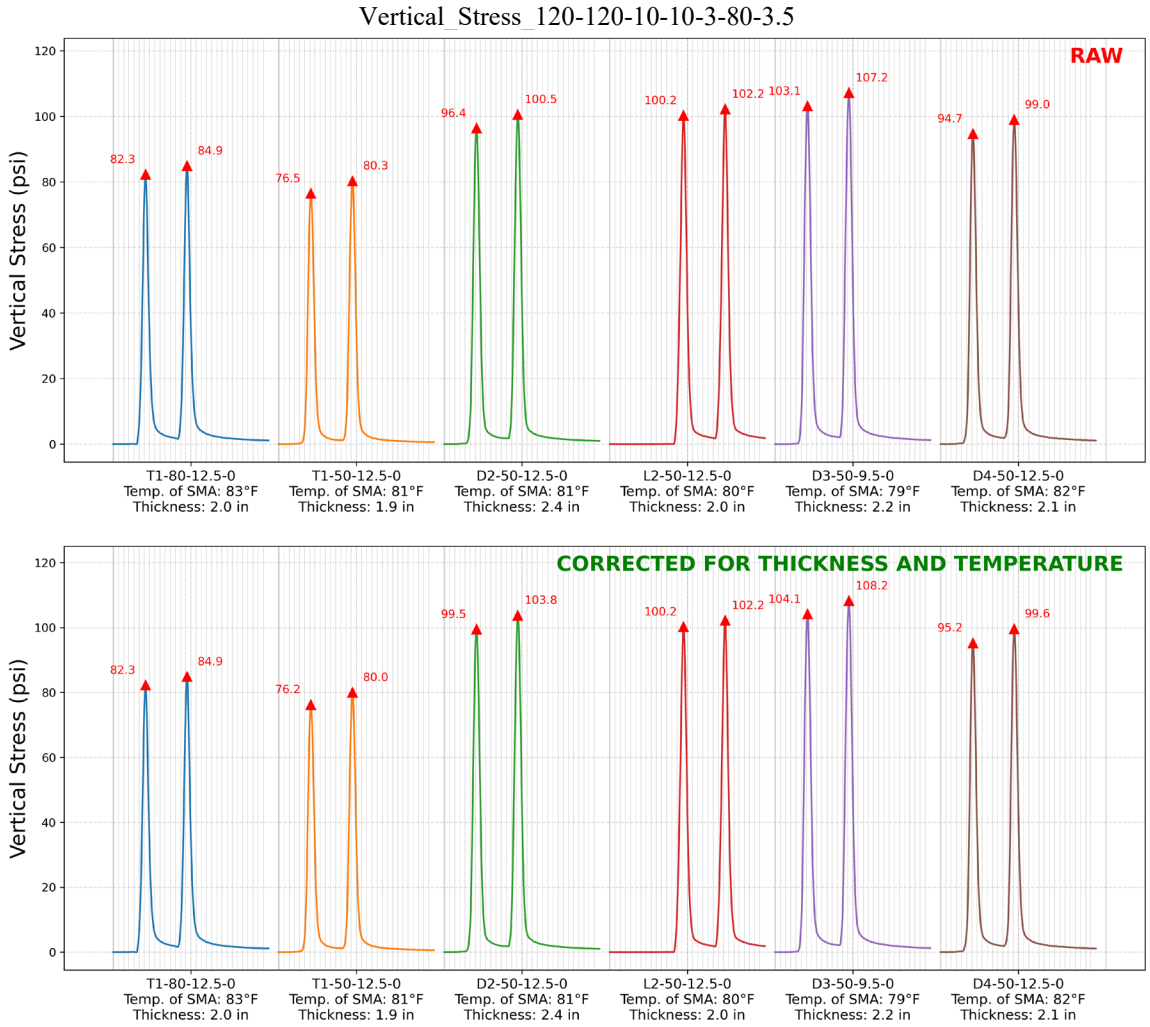

Figure 198. Graph. Comparison of measured and corrected vertical stress under tandem-axle loading (P_1 = 120 psi, P_2 = 120 psi; L_1 = 10 kip, L_2 = 10 kip; speed = 3 mph; axle spacing = 3.5 ft)

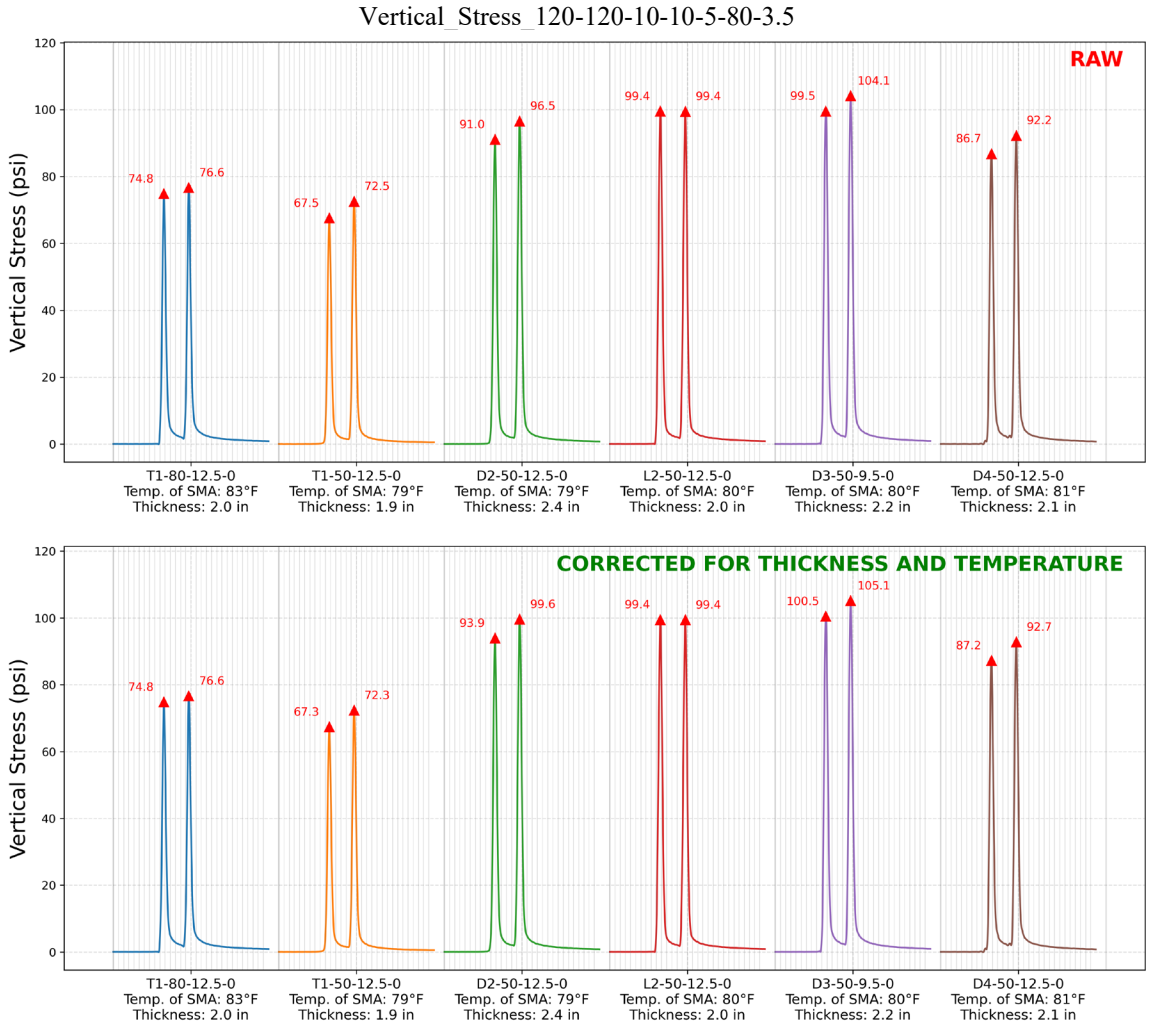

Figure 199. Graph. Comparison of measured and corrected vertical stress under tandem-axle loading (P_1 = 120 psi, P_2 = 120 psi; L_1 = 10 kip, L_2 = 10 kip; speed = 5 mph; axle spacing = 3.5 ft)

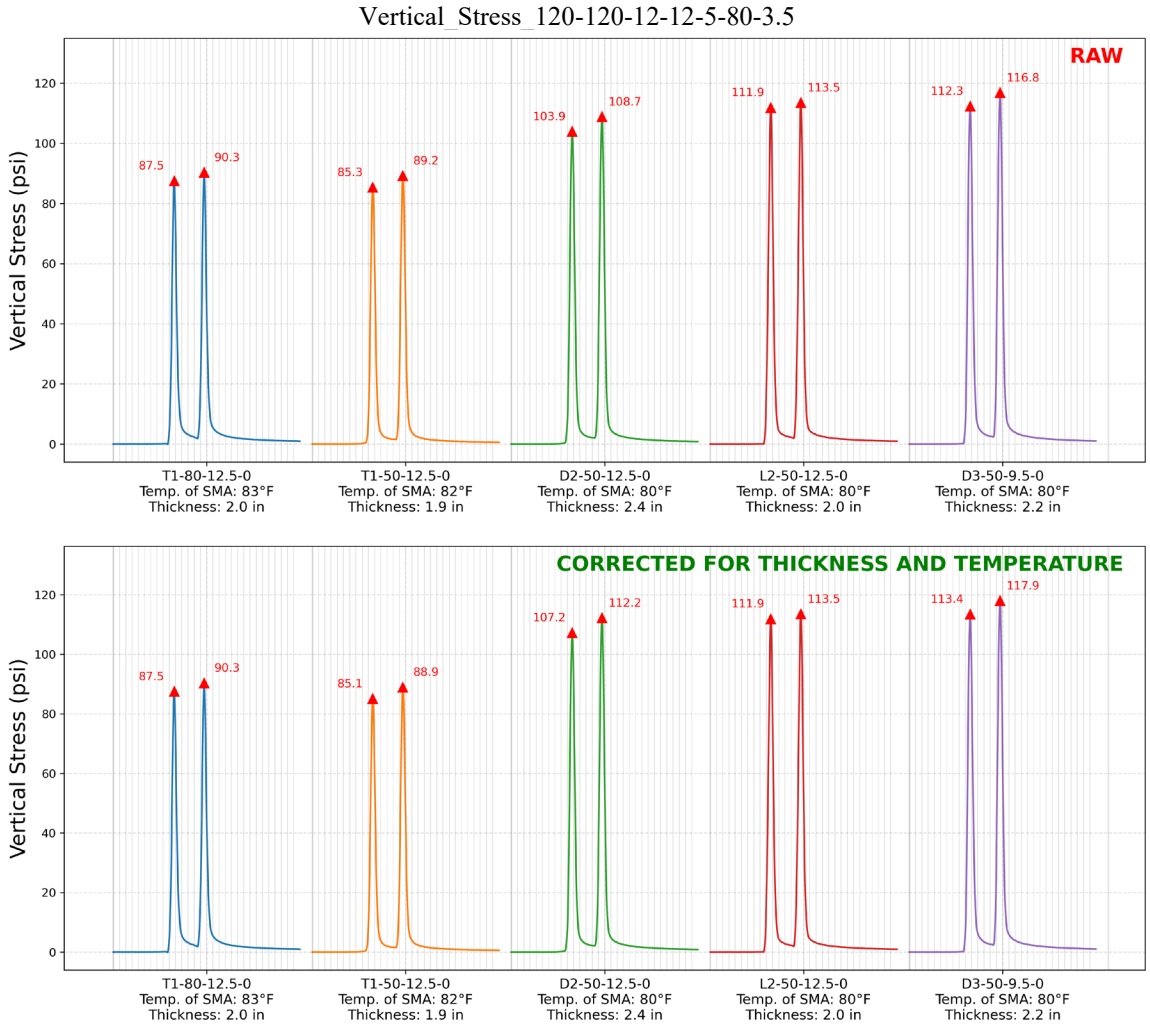

Figure 200. Graph. Comparison of measured and corrected vertical stress under tandem-axle loading (P_1 = 120 psi, P_2 = 120 psi; L_1 = 12 kip, L_2 = 12 kip; speed = 5 mph; axle spacing = 3.5 ft)

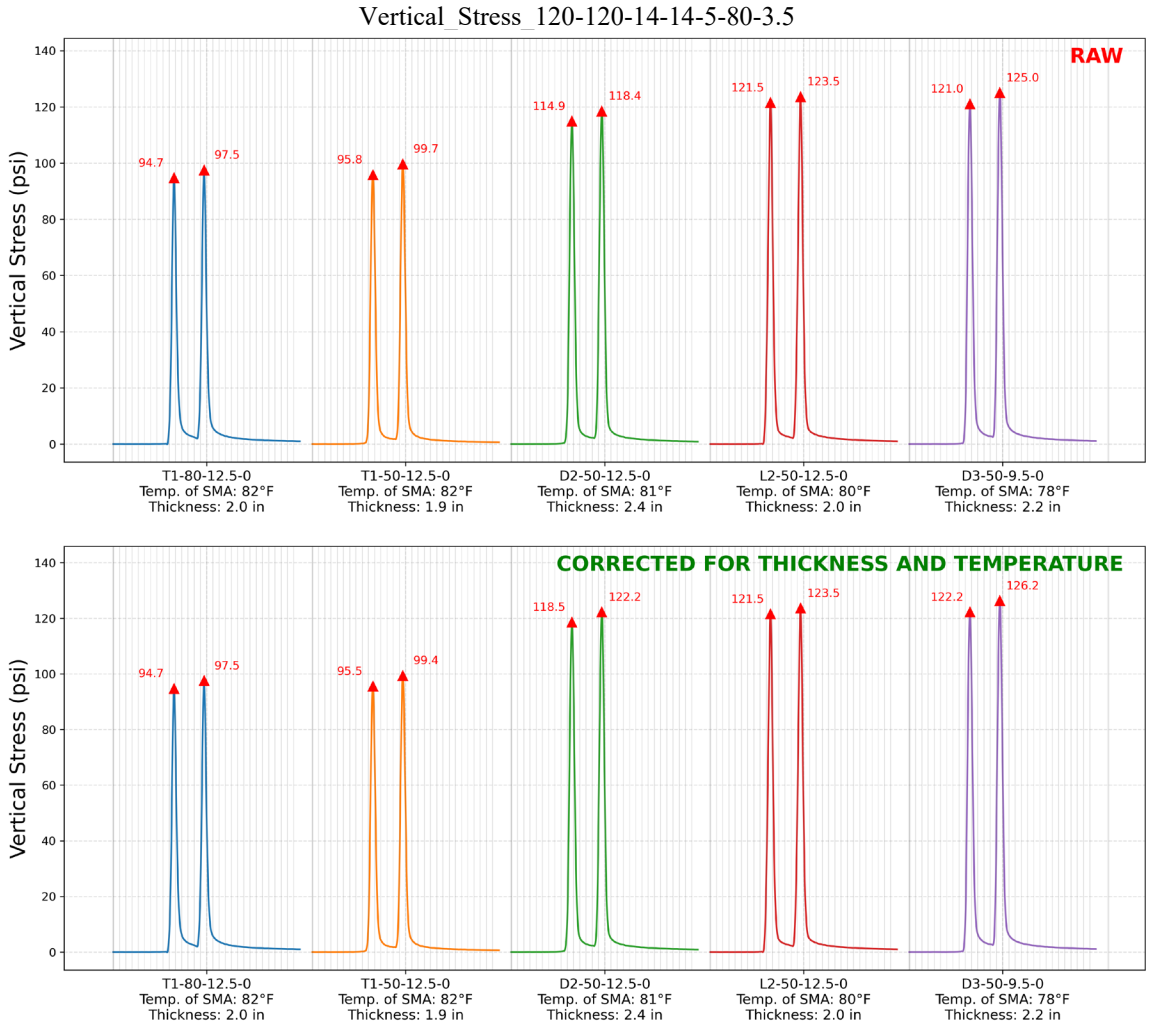

Figure 201. Graph. Comparison of measured and corrected vertical stress under tandem-axle loading (P_1 = 120 psi, P_2 = 120 psi; L_1 = 14 kip, L_2 = 14 kip; speed = 5 mph; axle spacing = 3.5 ft)

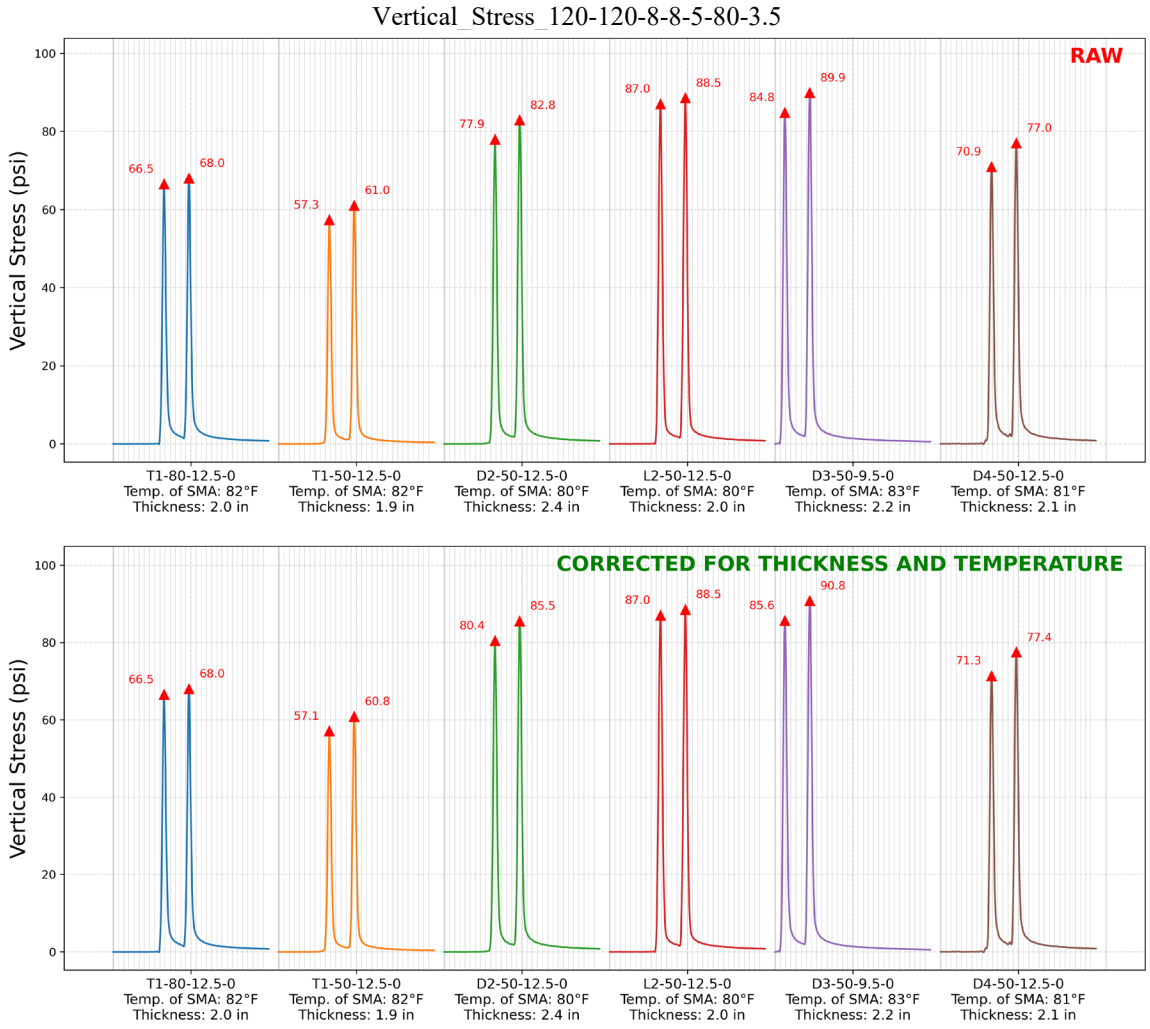

Figure 202. Graph. Comparison of measured and corrected vertical stress under tandem-axle loading (P_1 = 120 psi, P_2 = 120 psi; L_1 = 8 kip, L_2 = 8 kip; speed = 5 mph; axle spacing = 3.5 ft)

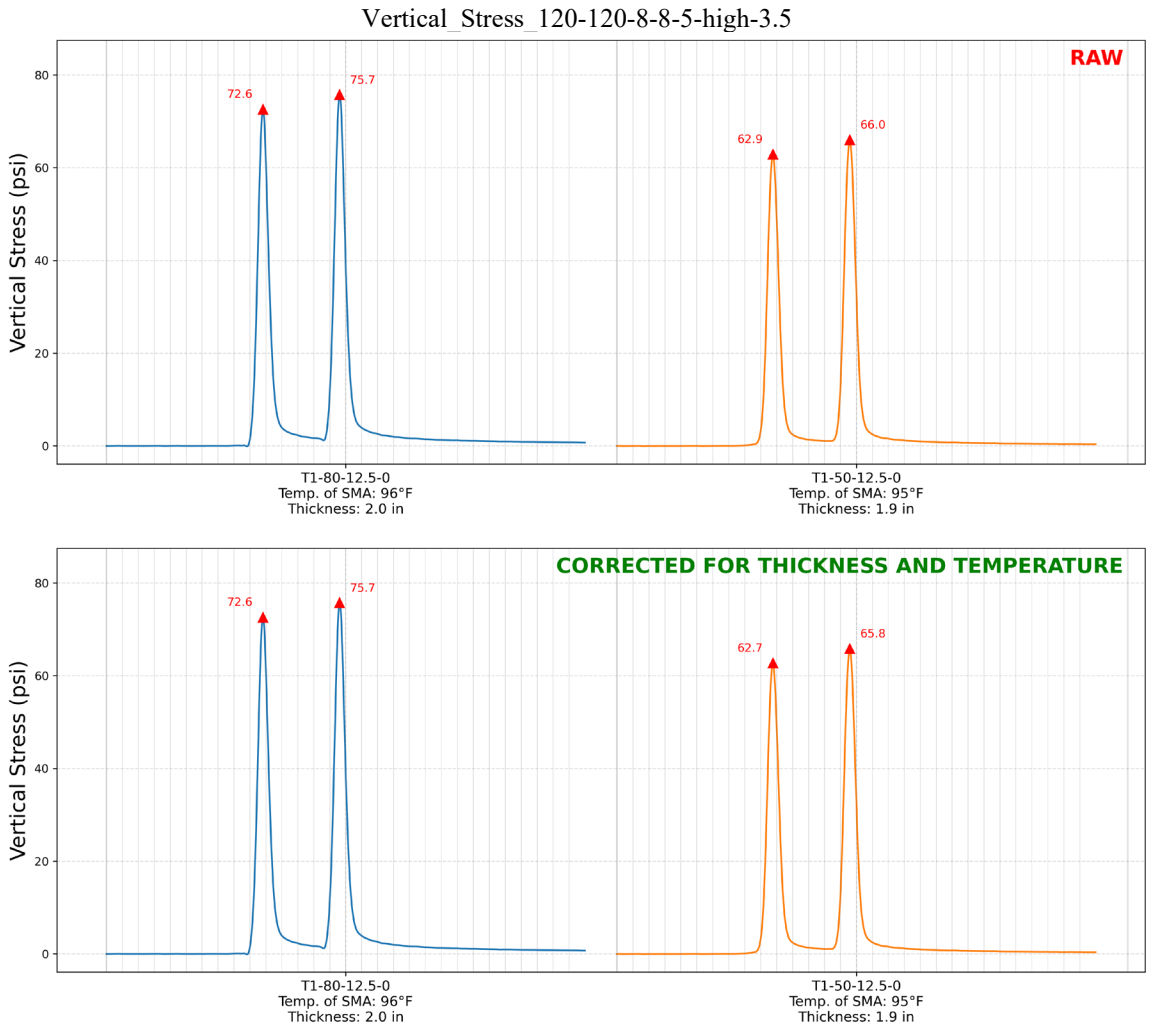

Figure 203. Graph. Comparison of measured and corrected vertical stress under tandem-axle loading at high temperature (P_1 = 120 psi, P_2 = 120 psi; L_1 = 8 kip, L_2 = 8 kip; speed = 5 mph; axle spacing = 3.5 ft)

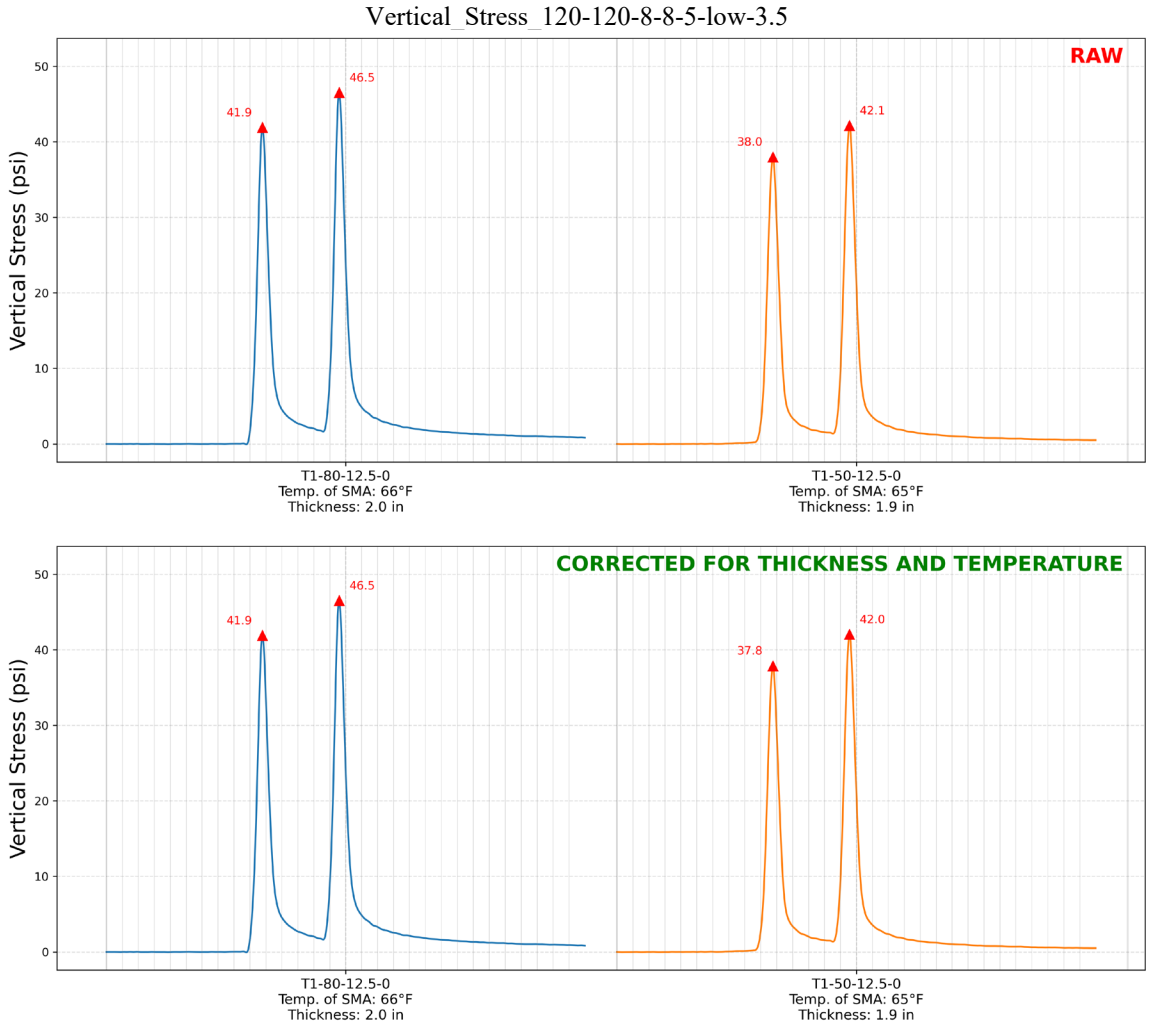

Figure 204. Graph. Comparison of measured and corrected vertical stress under tandem-axle loading at low temperature (P_1 = 120 psi, P_2 = 120 psi; L_1 = 8 kip, L_2 = 8 kip; speed = 5 mph; axle spacing = 3.5 ft)

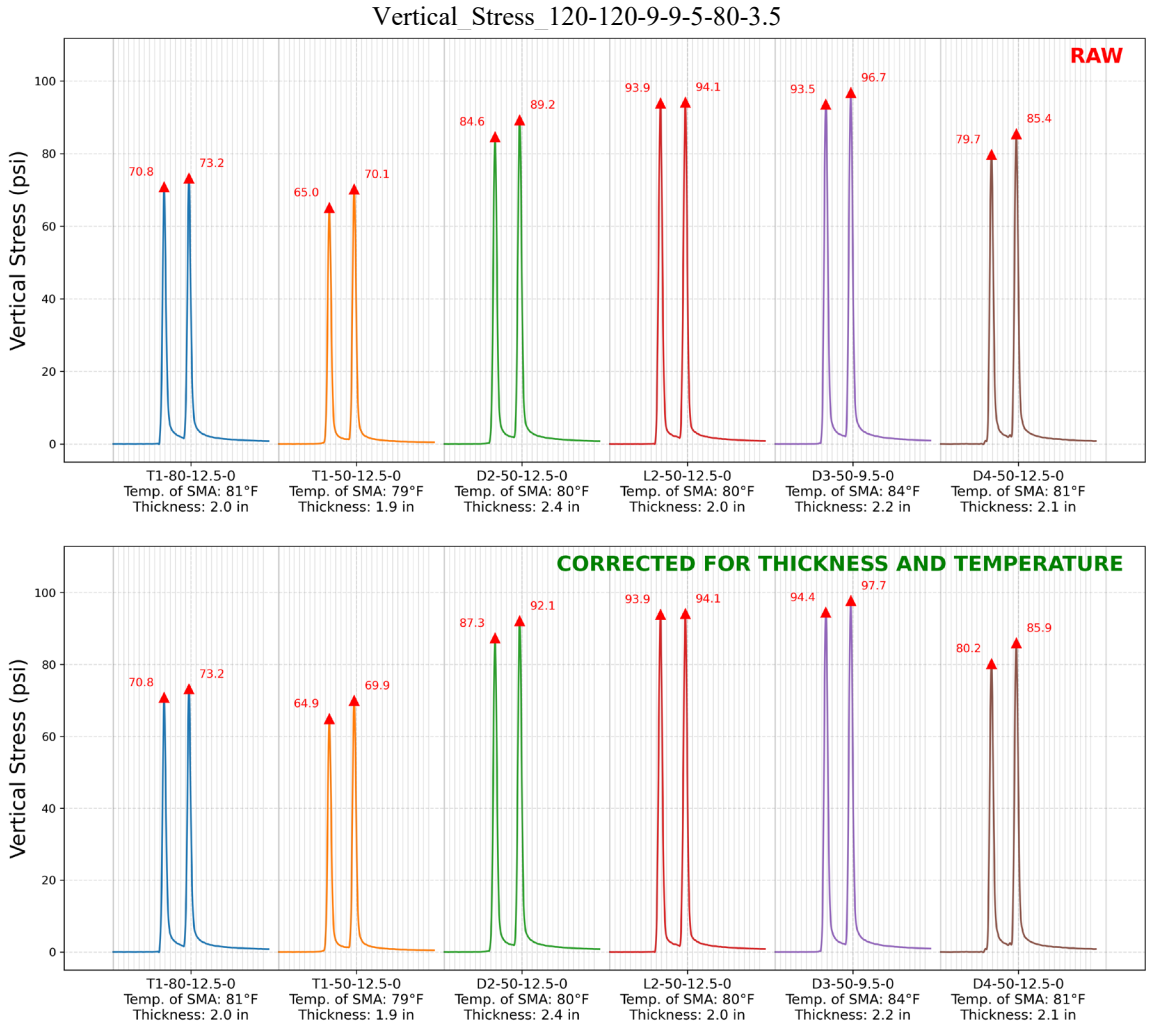

Figure 205. Graph. Comparison of measured and corrected vertical stress under tandem-axle loading (P_1 = 120 psi, P_2 = 120 psi; L_1 = 9 kip, L_2 = 9 kip; speed = 5 mph; axle spacing = 3.5 ft)

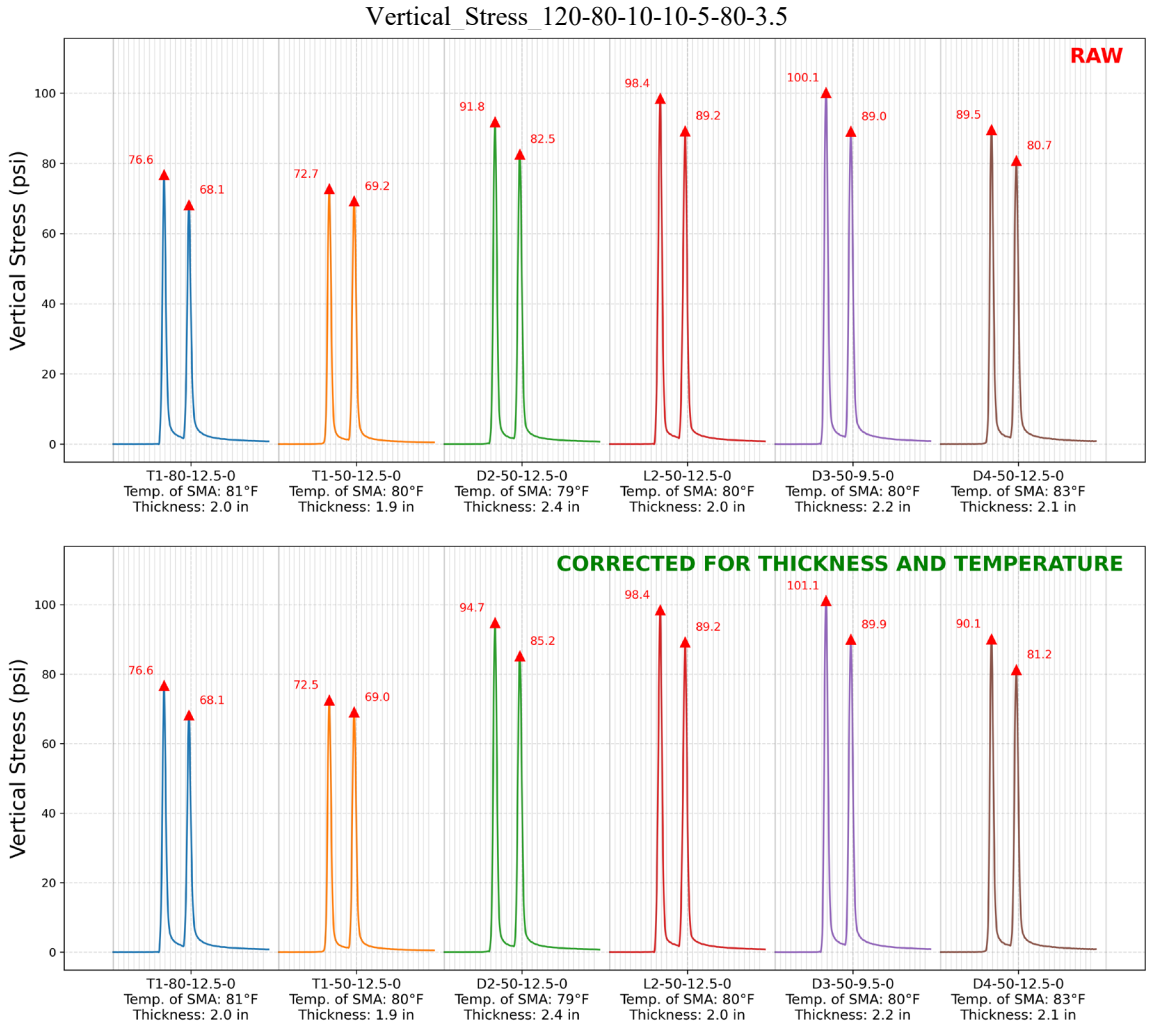

Figure 206. Graph. Comparison of measured and corrected vertical stress under tandem-axle loading with asymmetric tire pressures (P_1 = 120 psi, P_2 = 80 psi; L_1 = 10 kip, L_2 = 10 kip; speed = 5 mph; axle spacing = 3.5 ft)

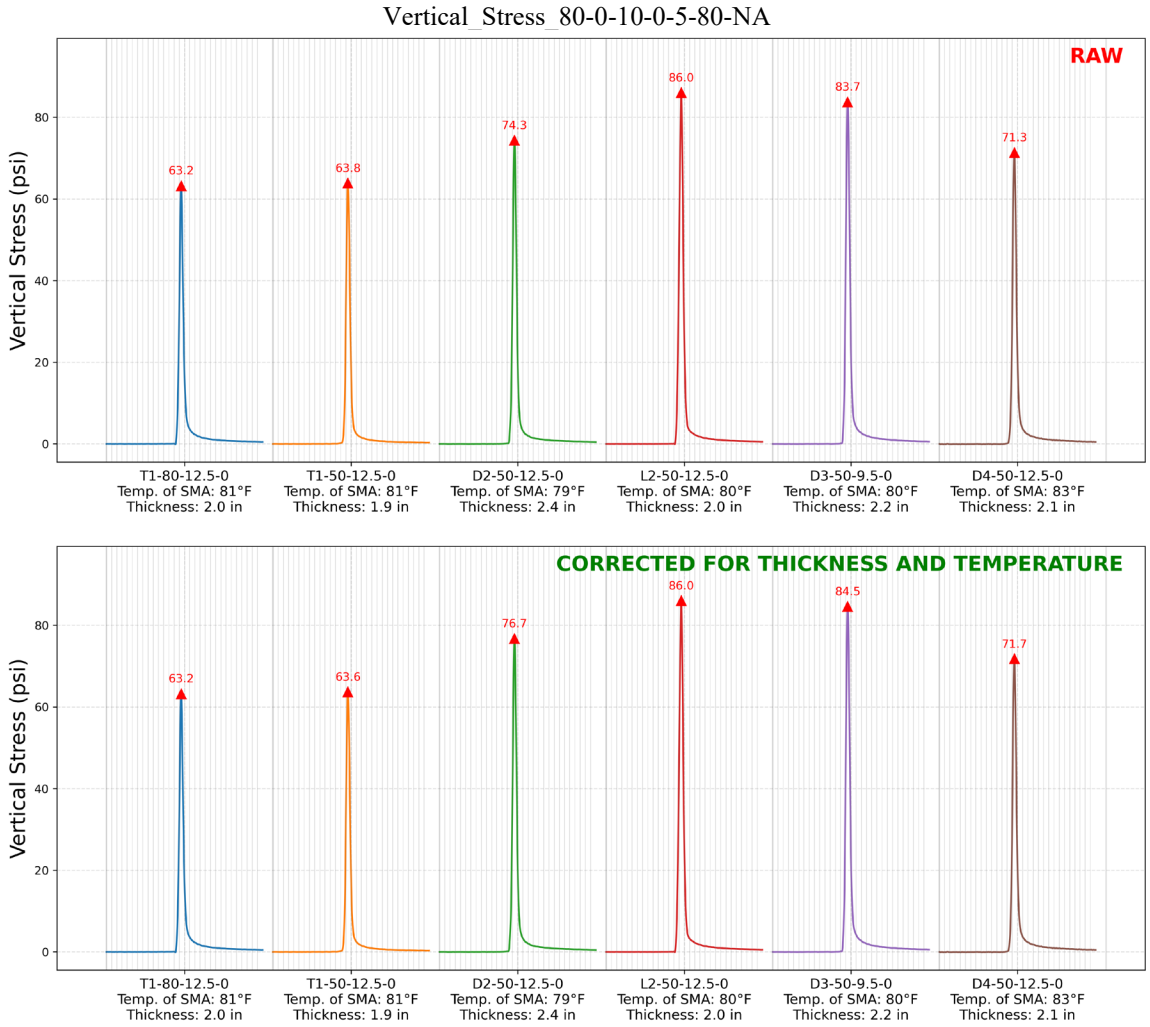

Figure 207. Graph. Comparison of measured and corrected vertical stress under single-axle loading (P_1 = 80 psi; L_1 = 10 kip; speed = 5 mph)

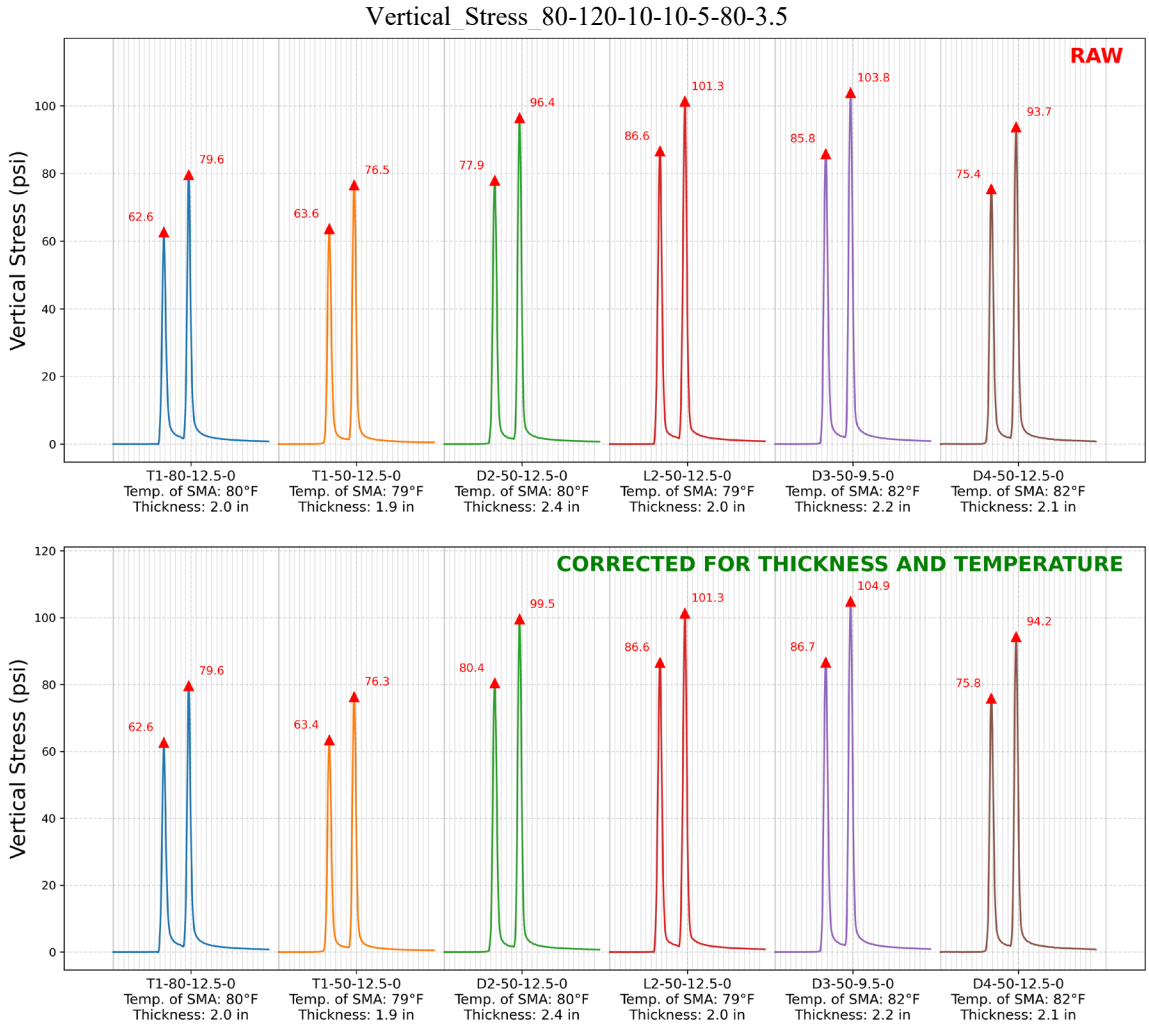

Figure 208. Graph. Comparison of measured and corrected vertical stress under tandem-axle loading with asymmetric tire pressures (P_1 = 80 psi, P_2 = 120 psi; L_1 = 10 kip, L_2 = 10 kip; speed = 5 mph; axle spacing = 3.5 ft)

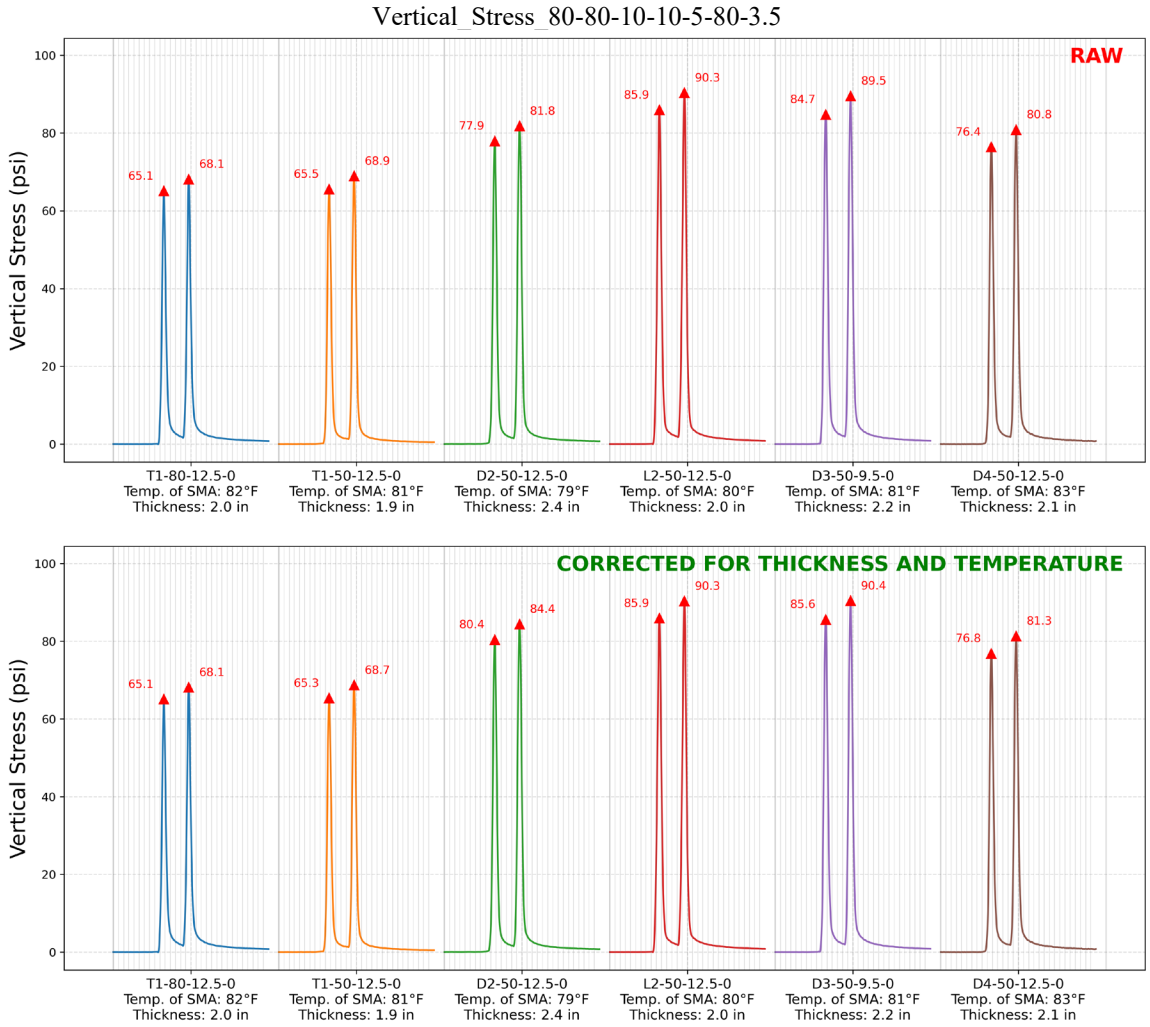

Figure 209. Graph. Comparison of measured and corrected vertical stress under tandem-axle loading (P_1 = 80 psi, P_2 = 80 psi; L_1 = 10 kip, L_2 = 10 kip; speed = 5 mph; axle spacing = 3.5 ft)

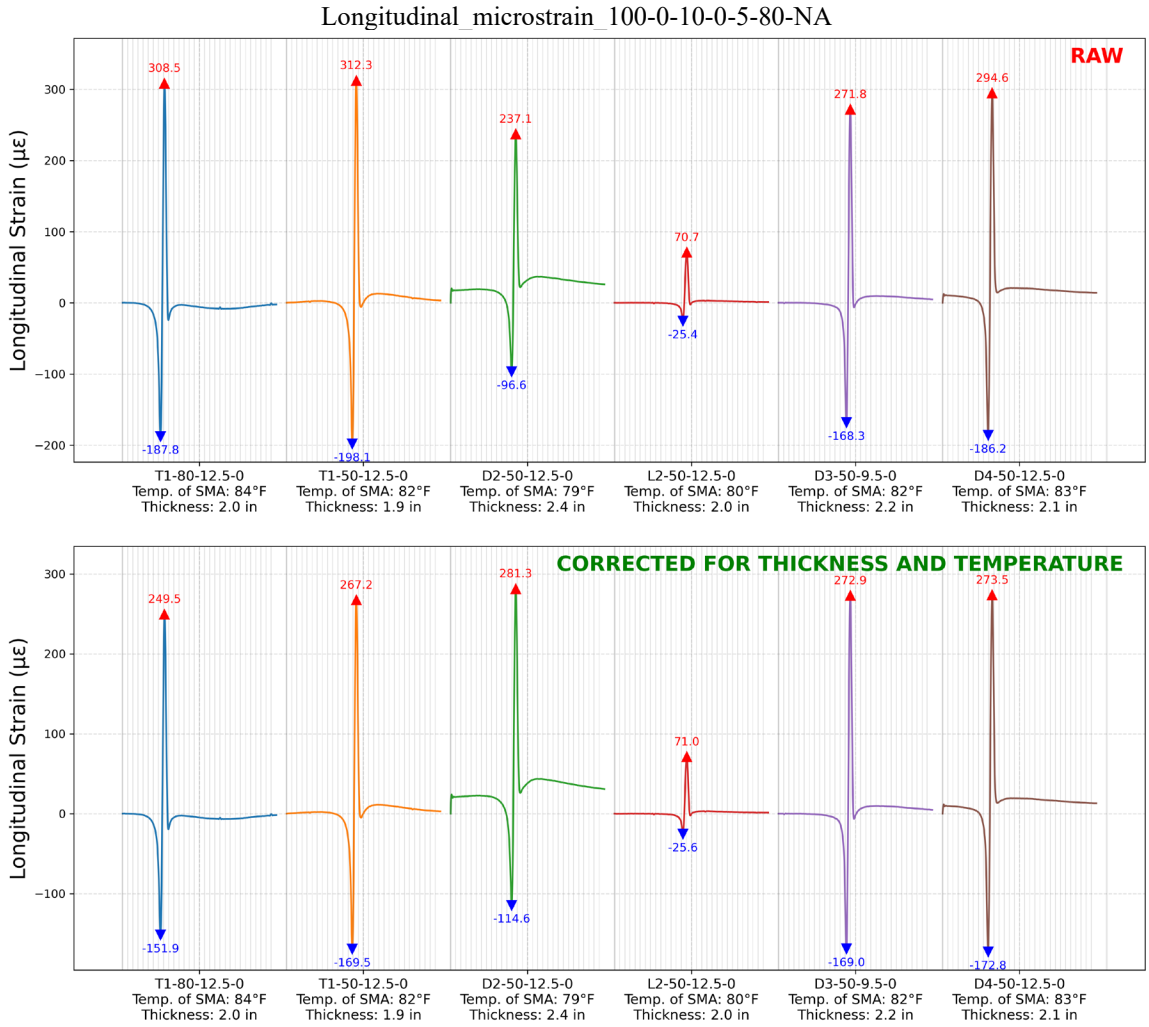

Figure 210. Graph. Comparison of measured and corrected longitudinal microstrain under single-axle loading (P_1 = 100 psi; L_1 = 10 kip; speed = 5 mph)

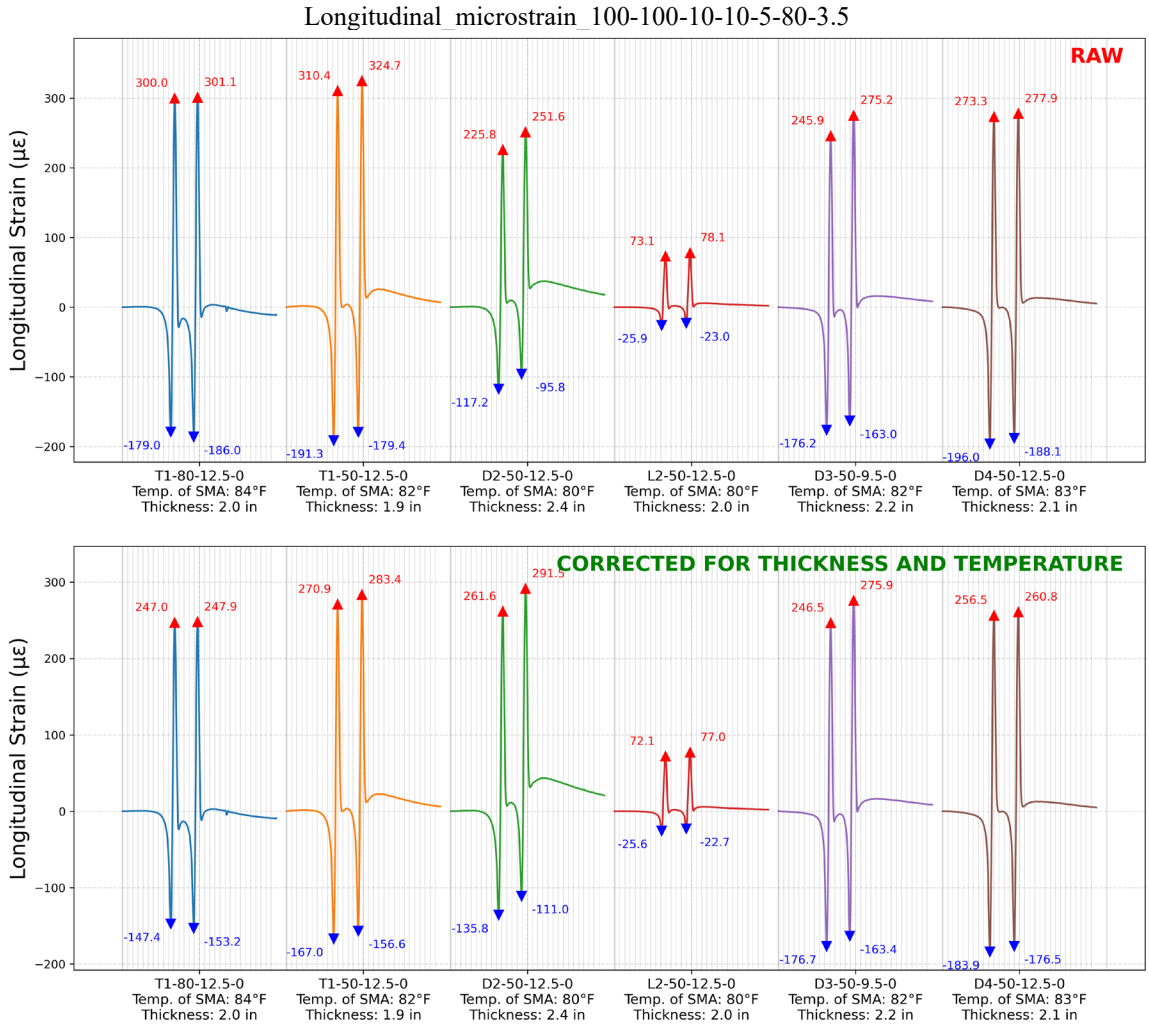

Figure 211. Graph. Comparison of measured and corrected longitudinal microstrain under tandem-axle loading (P_1 = 100 psi, P_2 = 100 psi; L_1 = 10 kip, L_2 = 10 kip; speed = 5 mph; axle spacing = 3.5 ft)

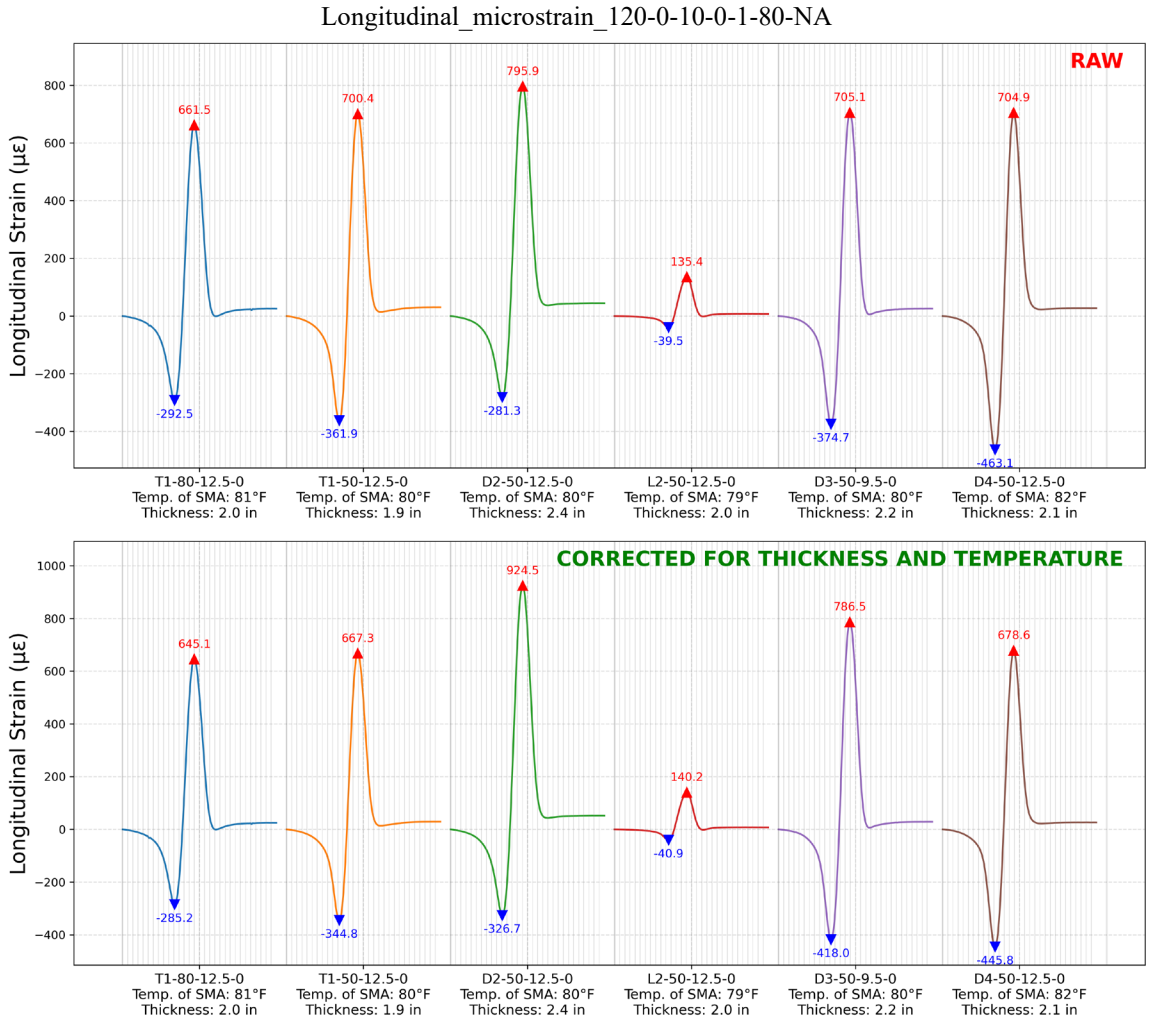

Figure 212. Graph. Comparison of measured and corrected longitudinal microstrain under single-axle loading (P_1 = 120 psi; L_1 = 10 kip; speed = 1 mph)

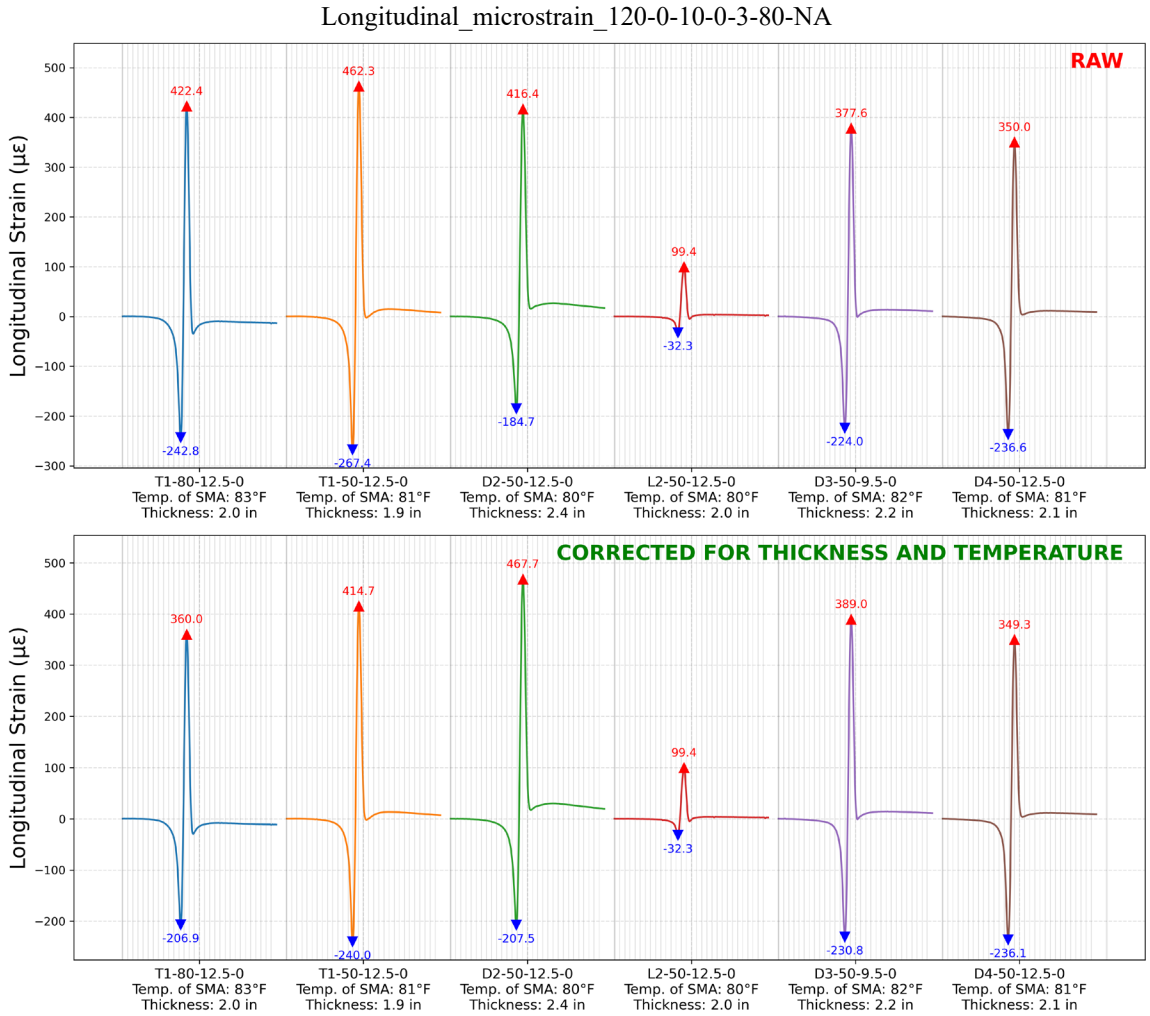

Figure 213. Graph. Comparison of measured and corrected longitudinal microstrain under single-axle loading (P_1 = 120 psi; L_1 = 10 kip; speed = 3 mph)

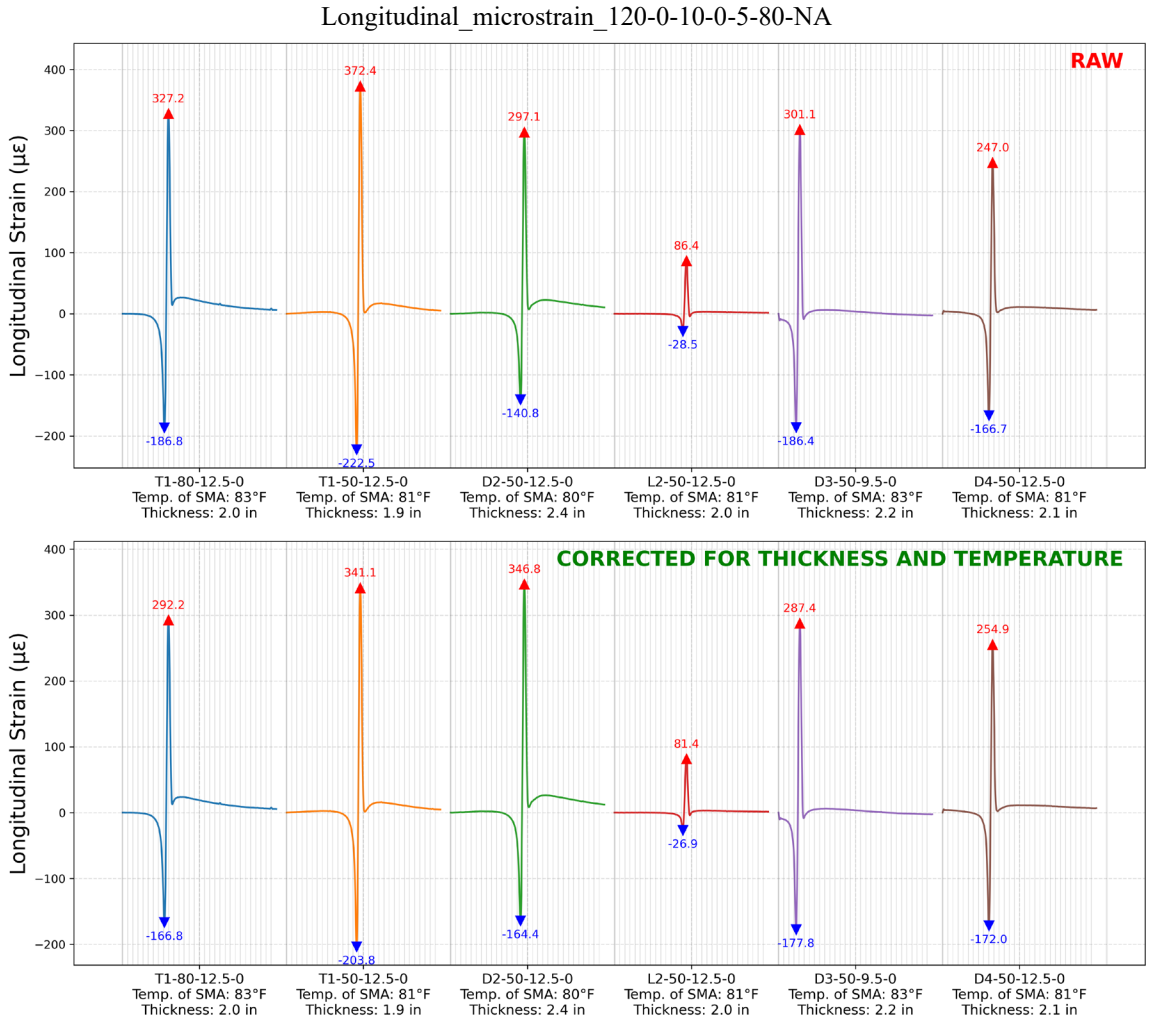

Figure 214. Graph. Comparison of measured and corrected longitudinal microstrain under single-axle loading (P_1 = 120 psi; L_1 = 10 kip; speed = 5 mph)

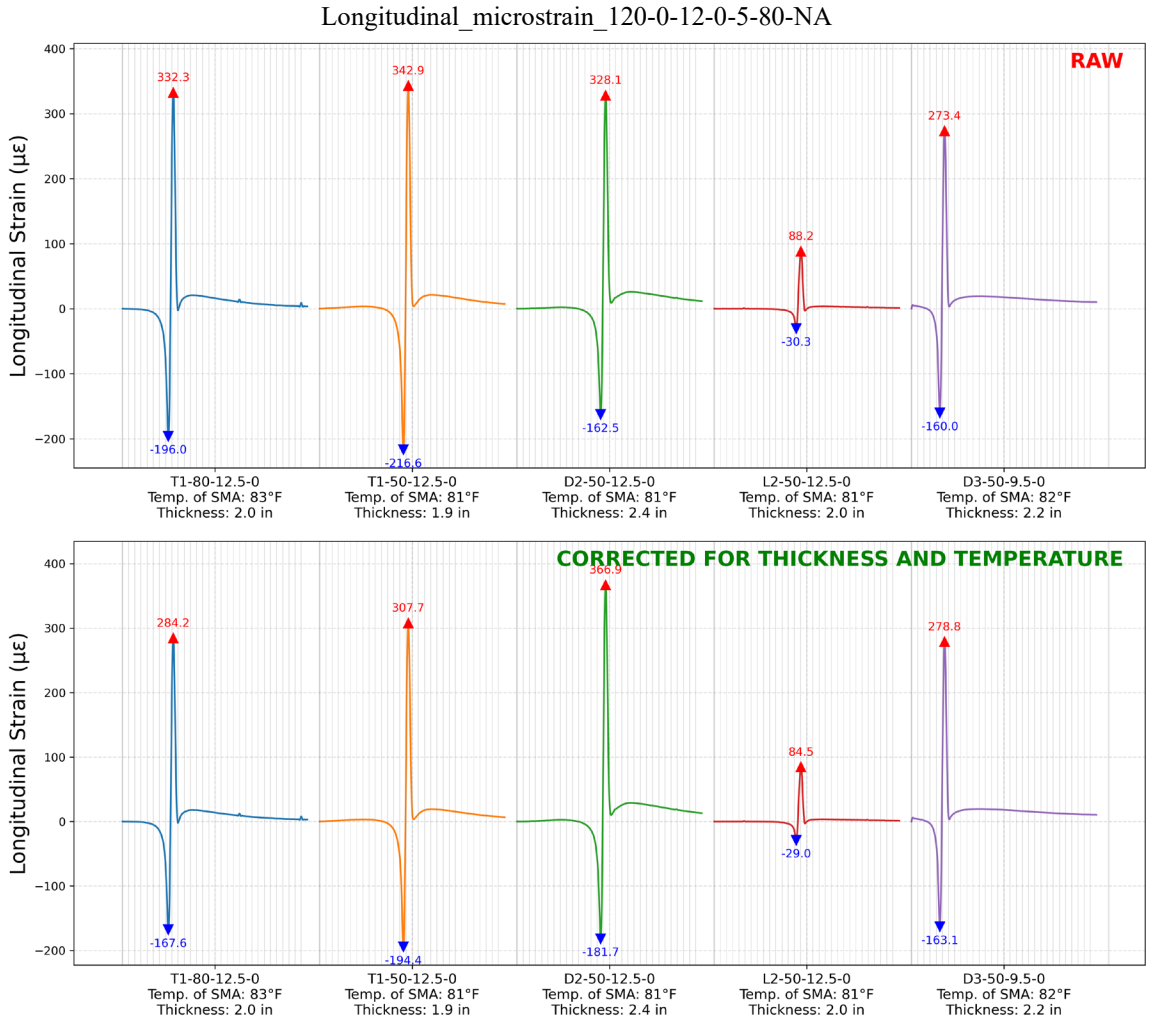

Figure 215. Graph. Comparison of measured and corrected longitudinal microstrain under single-axle loading (P_1 = 120 psi; L_1 = 12 kip; speed = 5 mph)

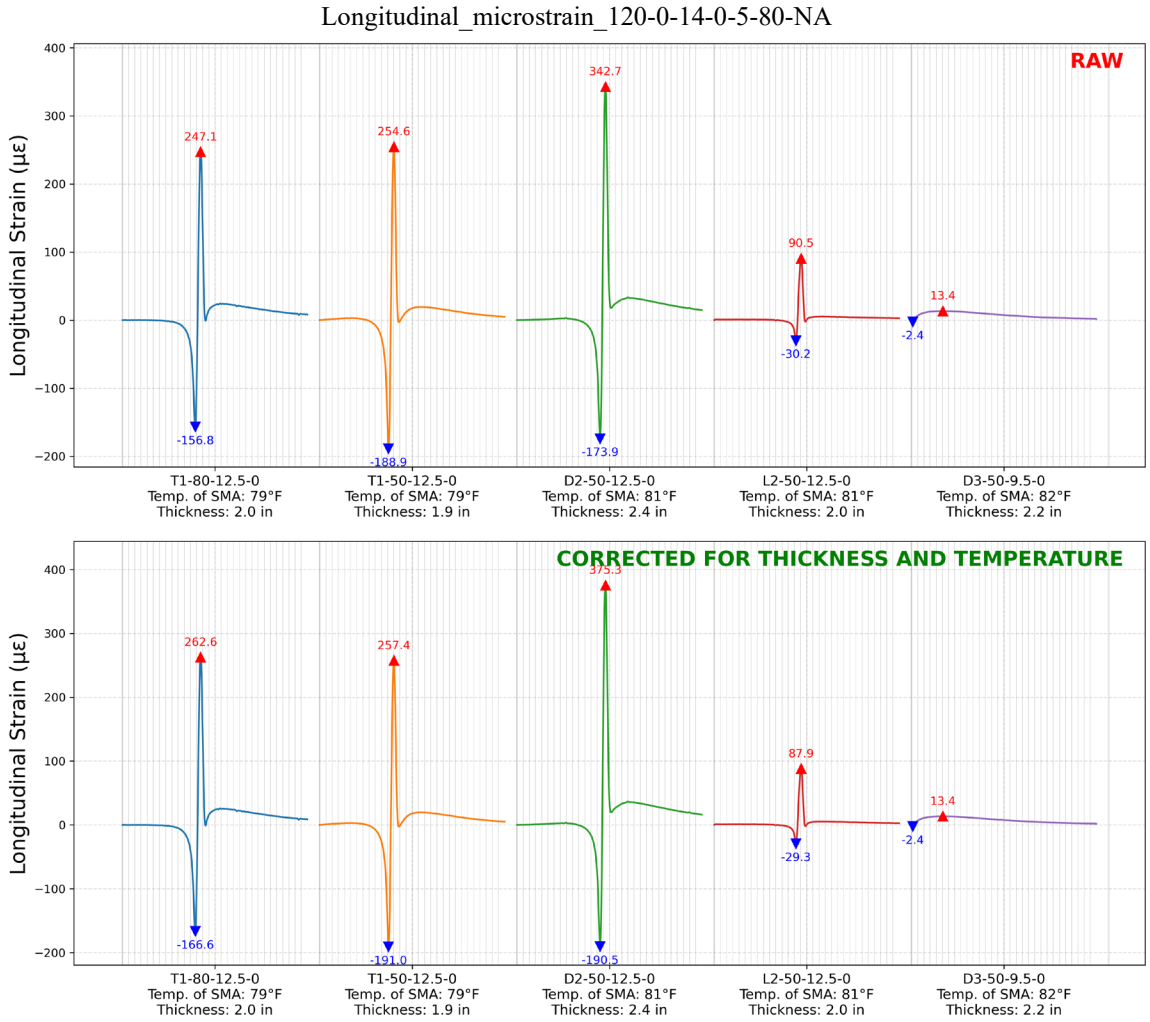

Figure 216. Graph. Comparison of measured and corrected longitudinal microstrain under single-axle loading (P_1 = 120 psi; L_1 = 14 kip; speed = 5 mph)

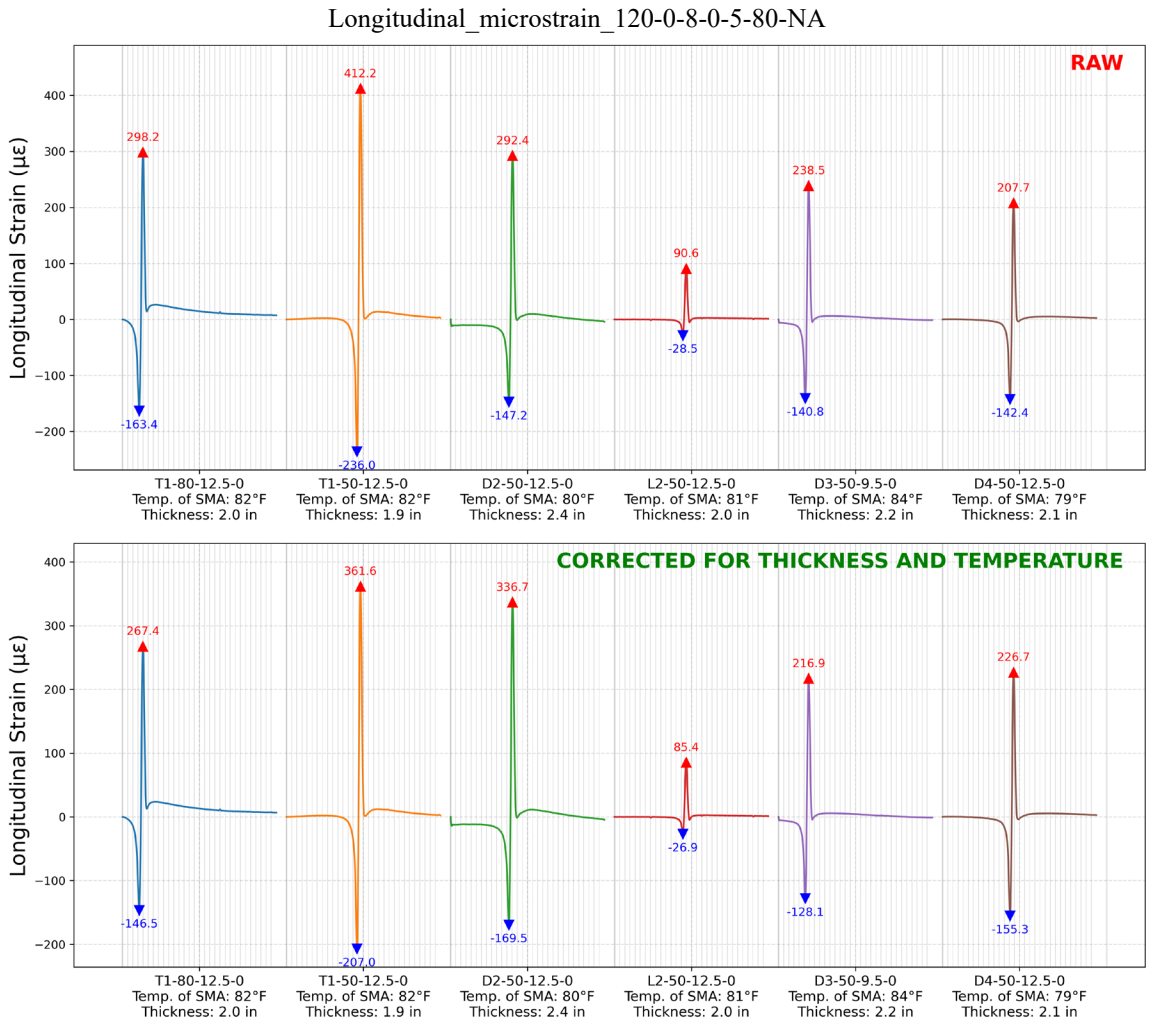

Figure 217. Graph. Comparison of measured and corrected longitudinal microstrain under single-axle loading (P_1 = 120 psi; L_1 = 8 kip; speed = 5 mph)

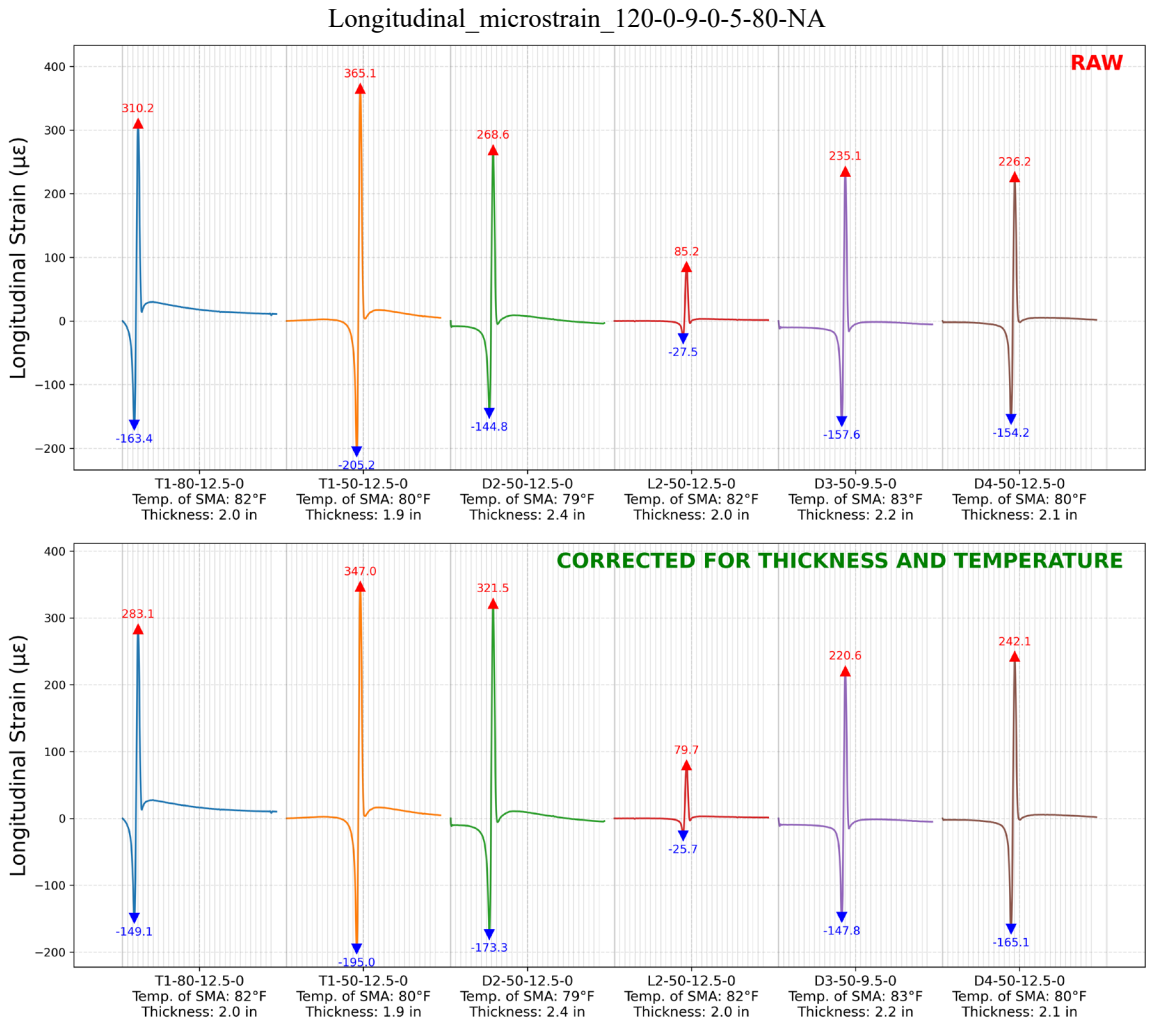

Figure 218. Graph. Comparison of measured and corrected longitudinal microstrain under single-axle loading (P_1 = 120 psi; L_1 = 9 kip; speed = 5 mph)

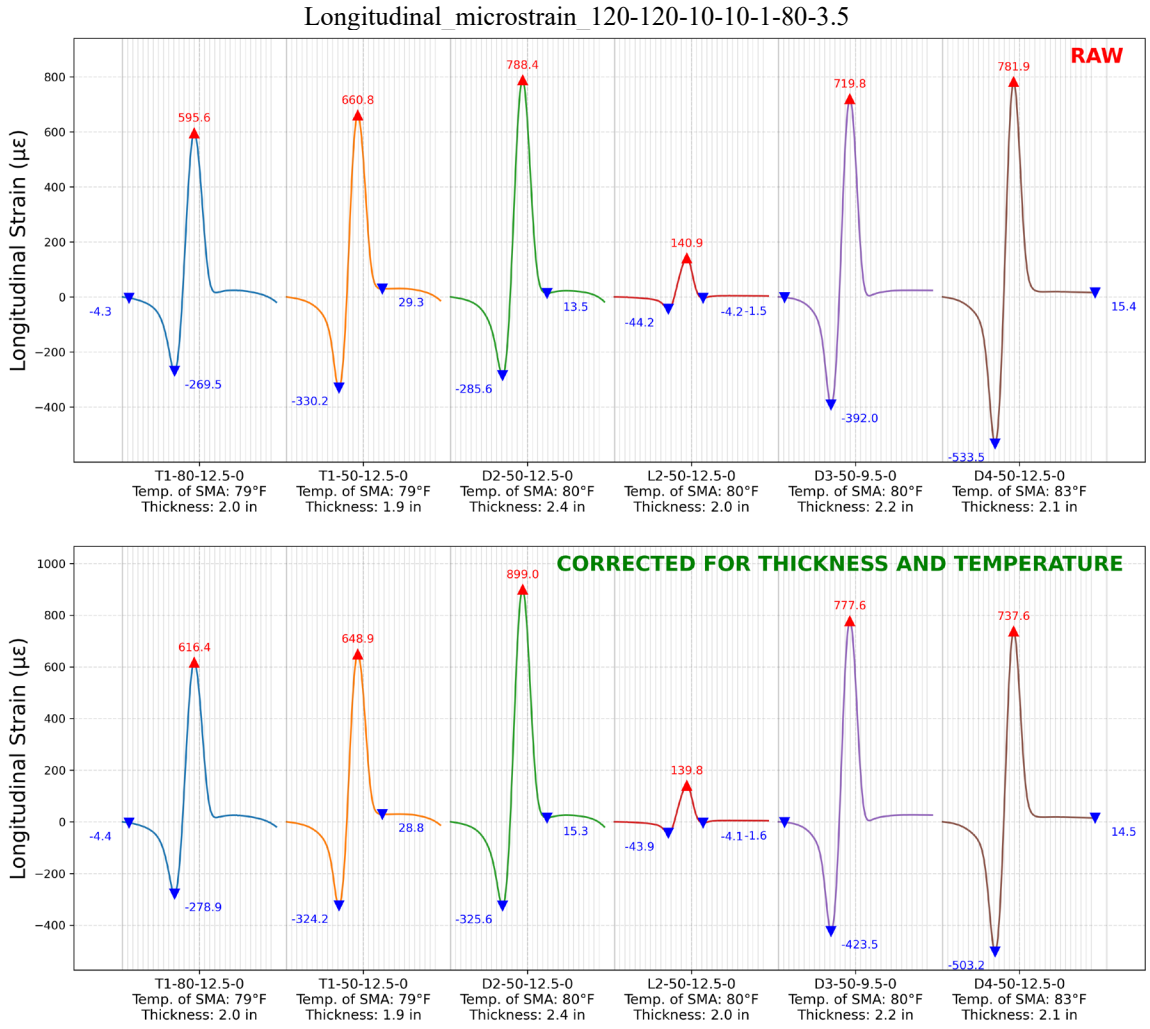

Figure 219. Graph. Comparison of measured and corrected longitudinal microstrain under tandem-axle loading (P_1 = 120 psi, P_2 = 120 psi; L_1 = 10 kip, L_2 = 10 kip; speed = 1 mph; axle spacing = 3.5 ft)

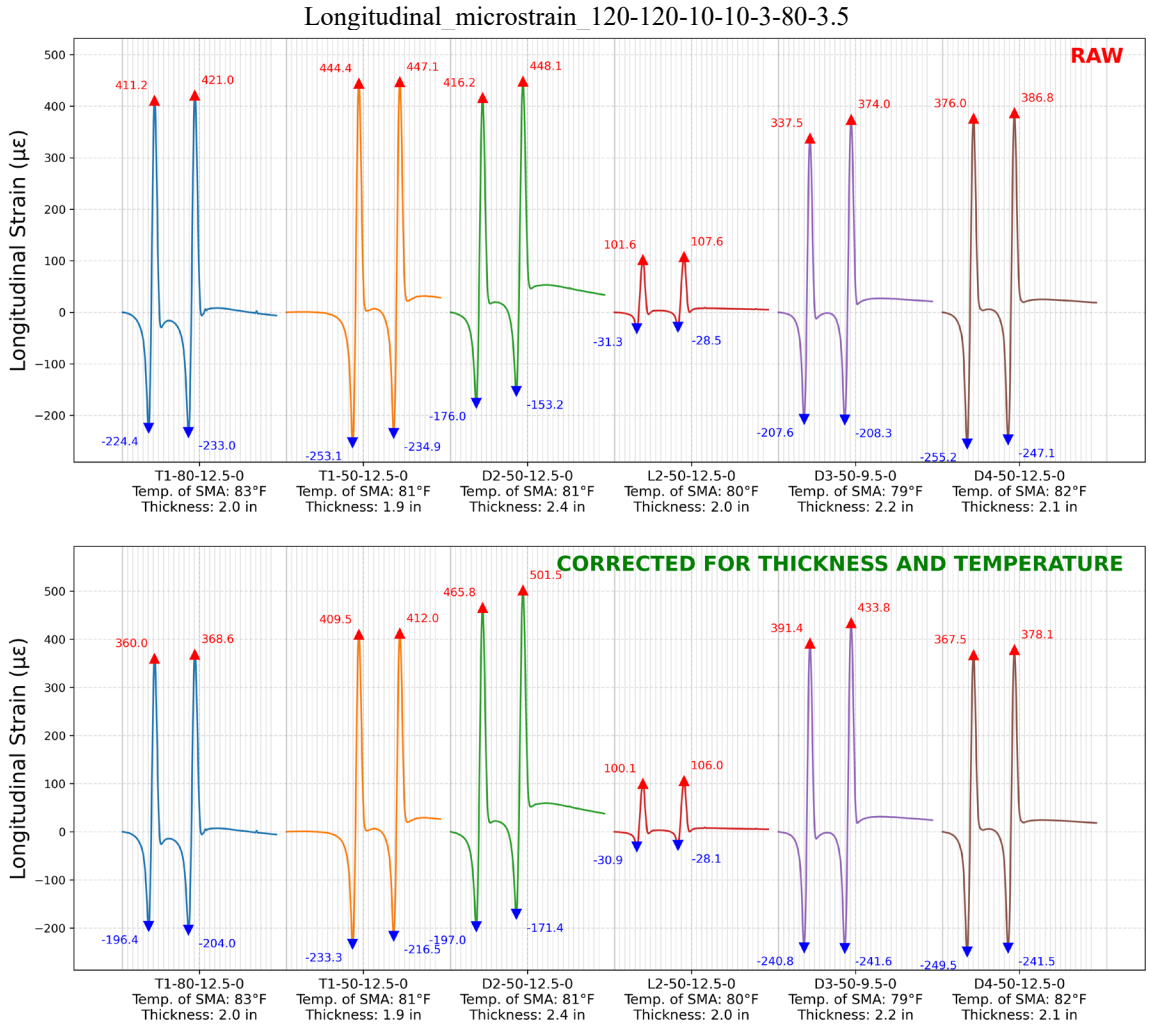

Figure 220. Graph. Comparison of measured and corrected longitudinal microstrain under tandem-axle loading (P_1 = 120 psi, P_2 = 120 psi; L_1 = 10 kip, L_2 = 10 kip; speed = 3 mph; axle spacing = 3.5 ft)

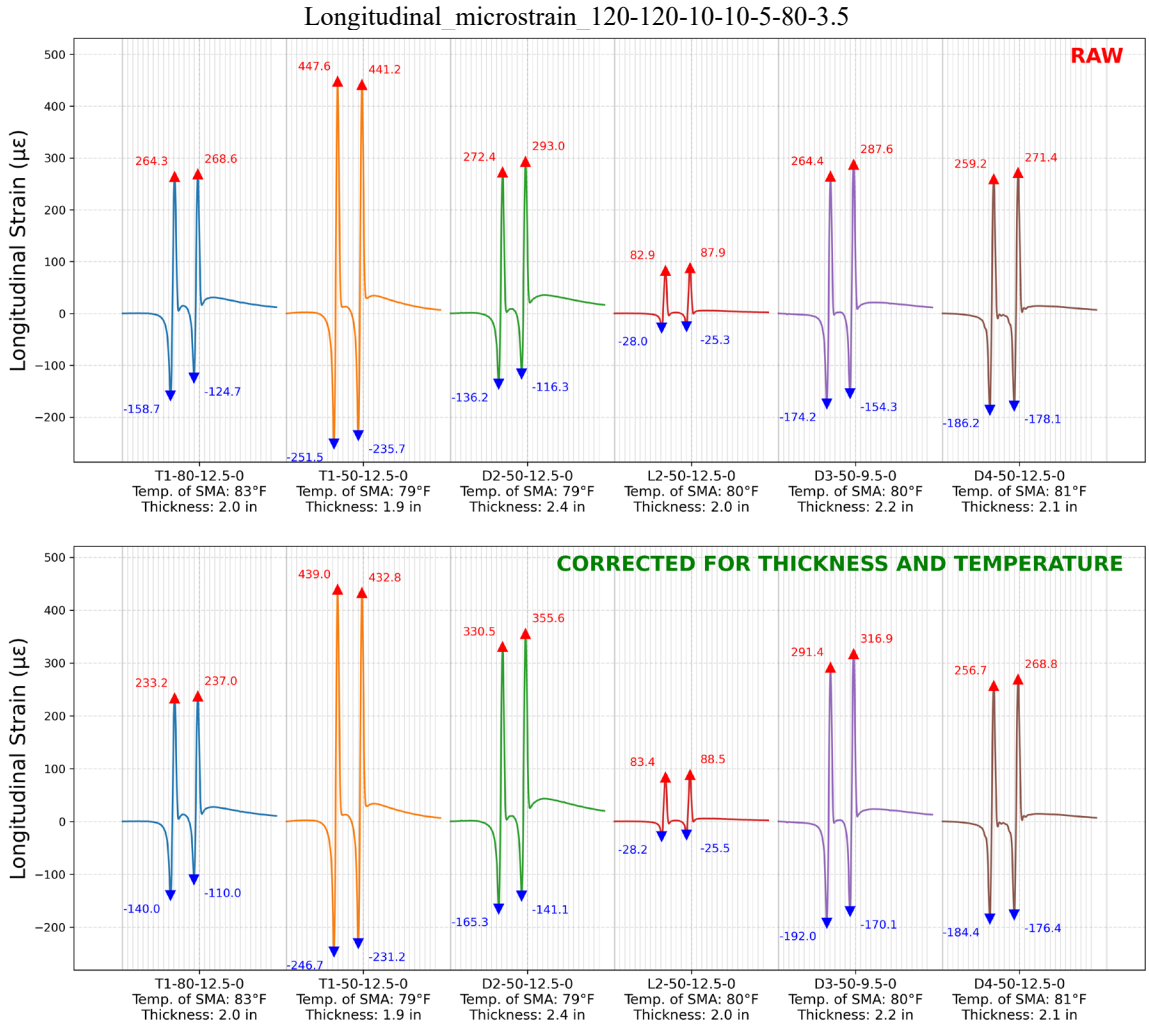

Figure 221. Graph. Comparison of measured and corrected longitudinal microstrain under tandem-axle loading (P_1 = 120 psi, P_2 = 120 psi; L_1 = 10 kip, L_2 = 10 kip; speed = 5 mph; axle spacing = 3.5 ft)

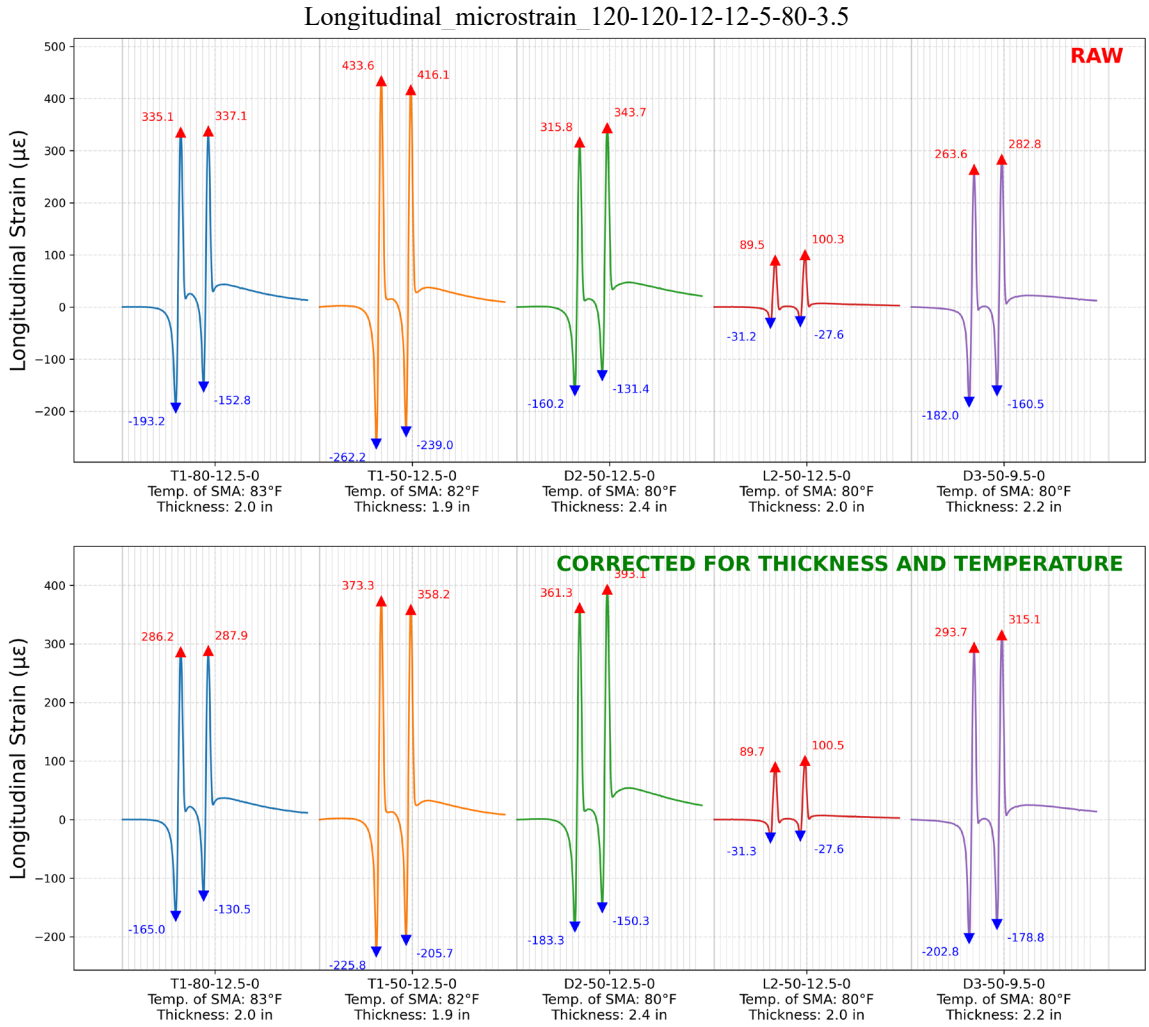

Figure 222. Graph. Comparison of measured and corrected longitudinal microstrain under tandem-axle loading (P_1 = 120 psi, P_2 = 120 psi; L_1 = 12 kip, L_2 = 12 kip; speed = 5 mph; axle spacing = 3.5 ft)

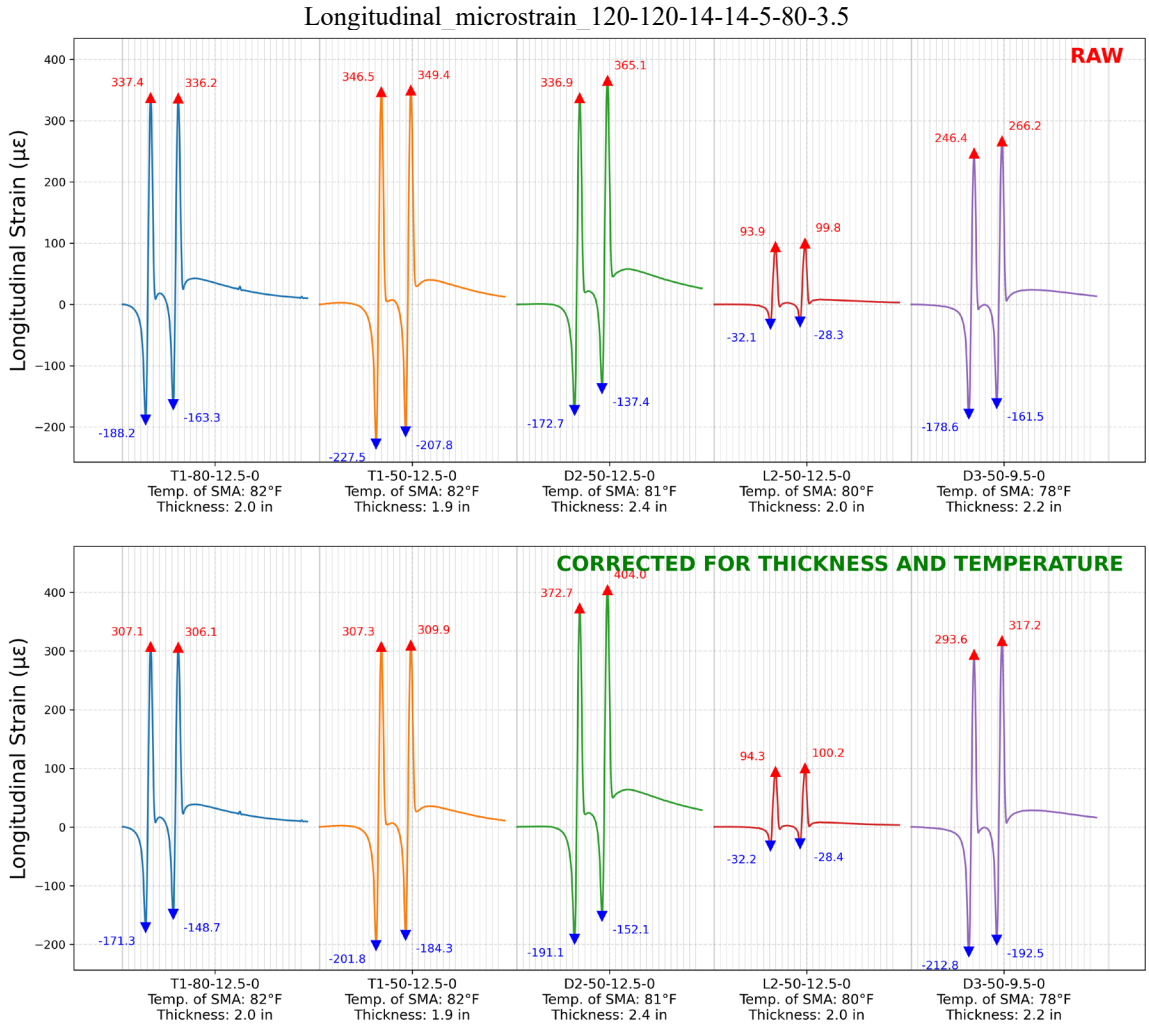

Figure 223. Graph. Comparison of measured and corrected longitudinal microstrain under tandem-axle loading (P_1 = 120 psi, P_2 = 120 psi; L_1 = 14 kip, L_2 = 14 kip; speed = 5 mph; axle spacing = 3.5 ft)

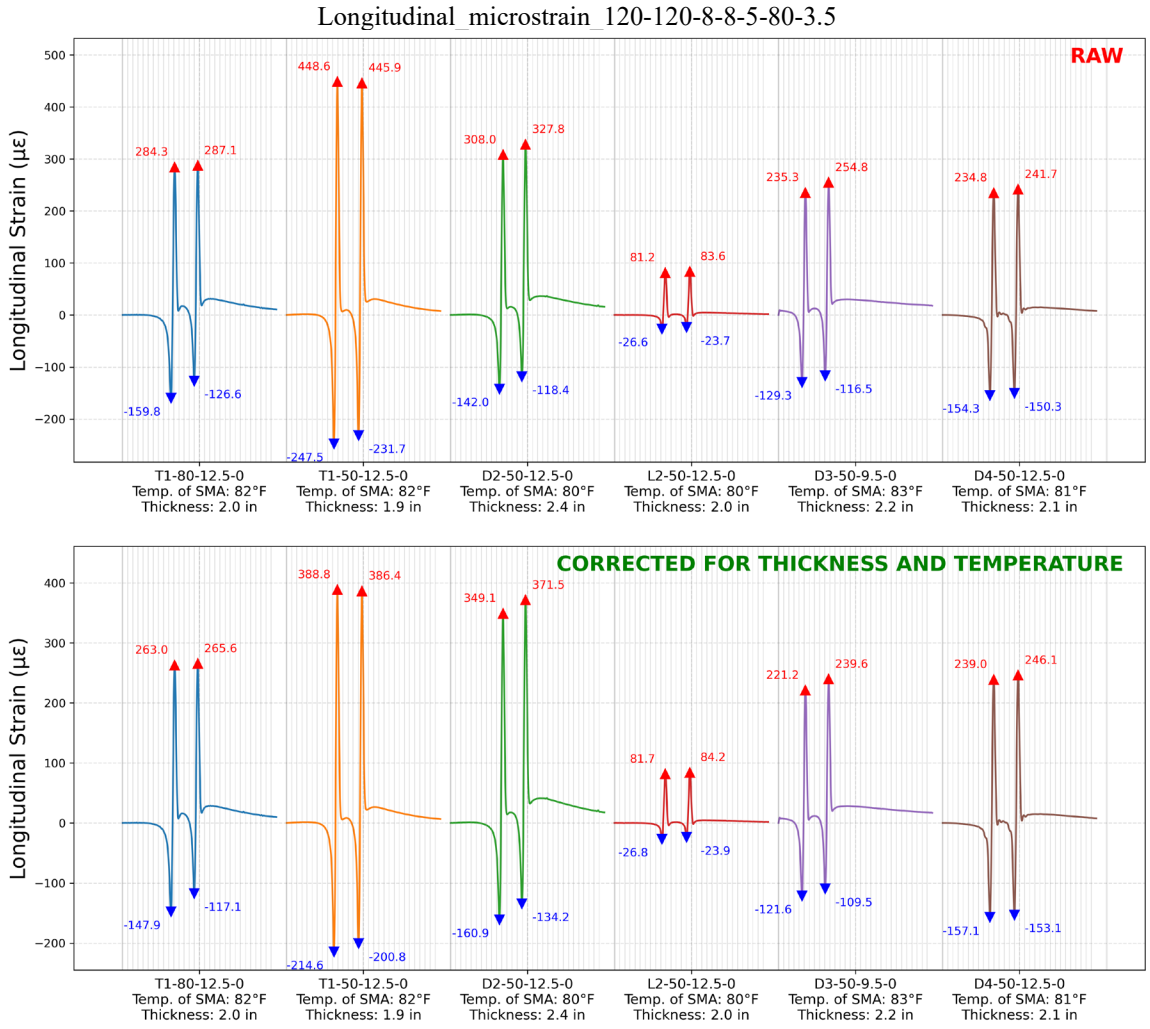

Figure 224. Graph. Comparison of measured and corrected longitudinal microstrain under tandem-axle loading (P_1 = 120 psi, P_2 = 120 psi; L_1 = 8 kip, L_2 = 8 kip; speed = 5 mph; axle spacing = 3.5 ft)

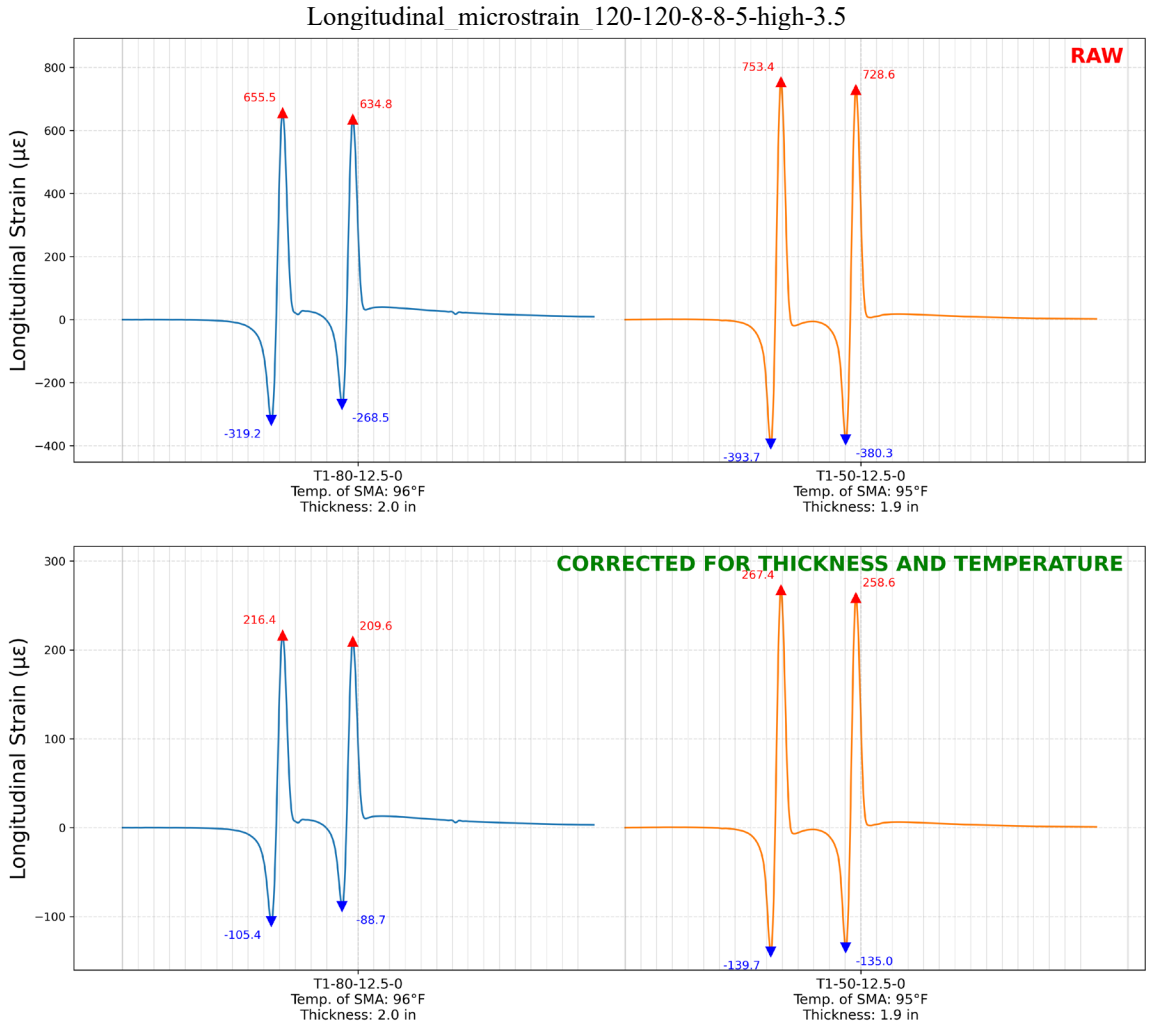

Figure 225. Graph. Comparison of measured and corrected longitudinal microstrain under tandem-axle loading at high temperature (P_1 = 120 psi, P_2 = 120 psi; L_1 = 8 kip, L_2 = 8 kip; speed = 5 mph; axle spacing = 3.5 ft)

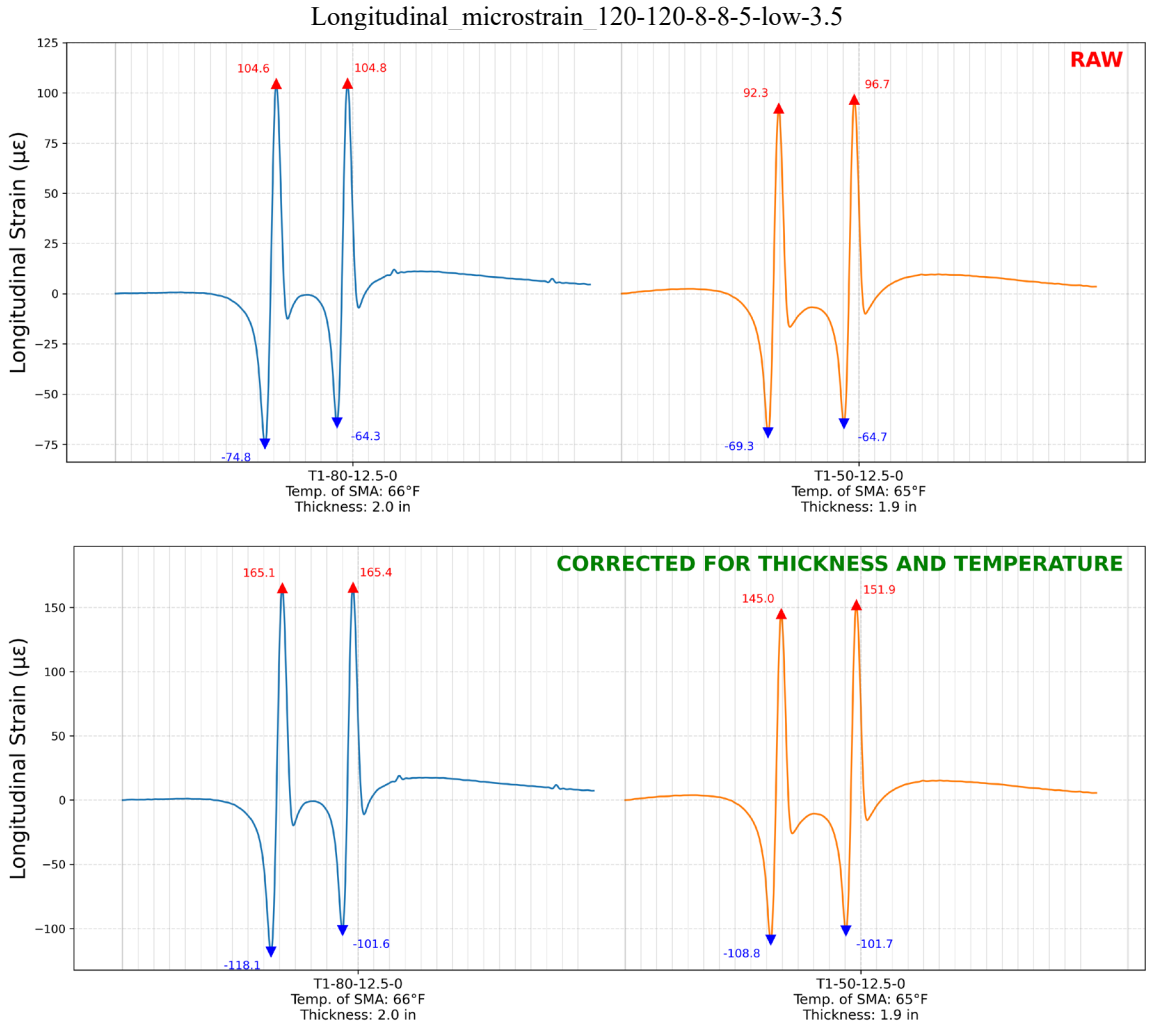

Figure 226. Graph. Comparison of measured and corrected longitudinal microstrain under tandem-axle loading at low temperature (P_1 = 120 psi, P_2 = 120 psi; L_1 = 8 kip, L_2 = 8 kip; speed = 5 mph; axle spacing = 3.5 ft)

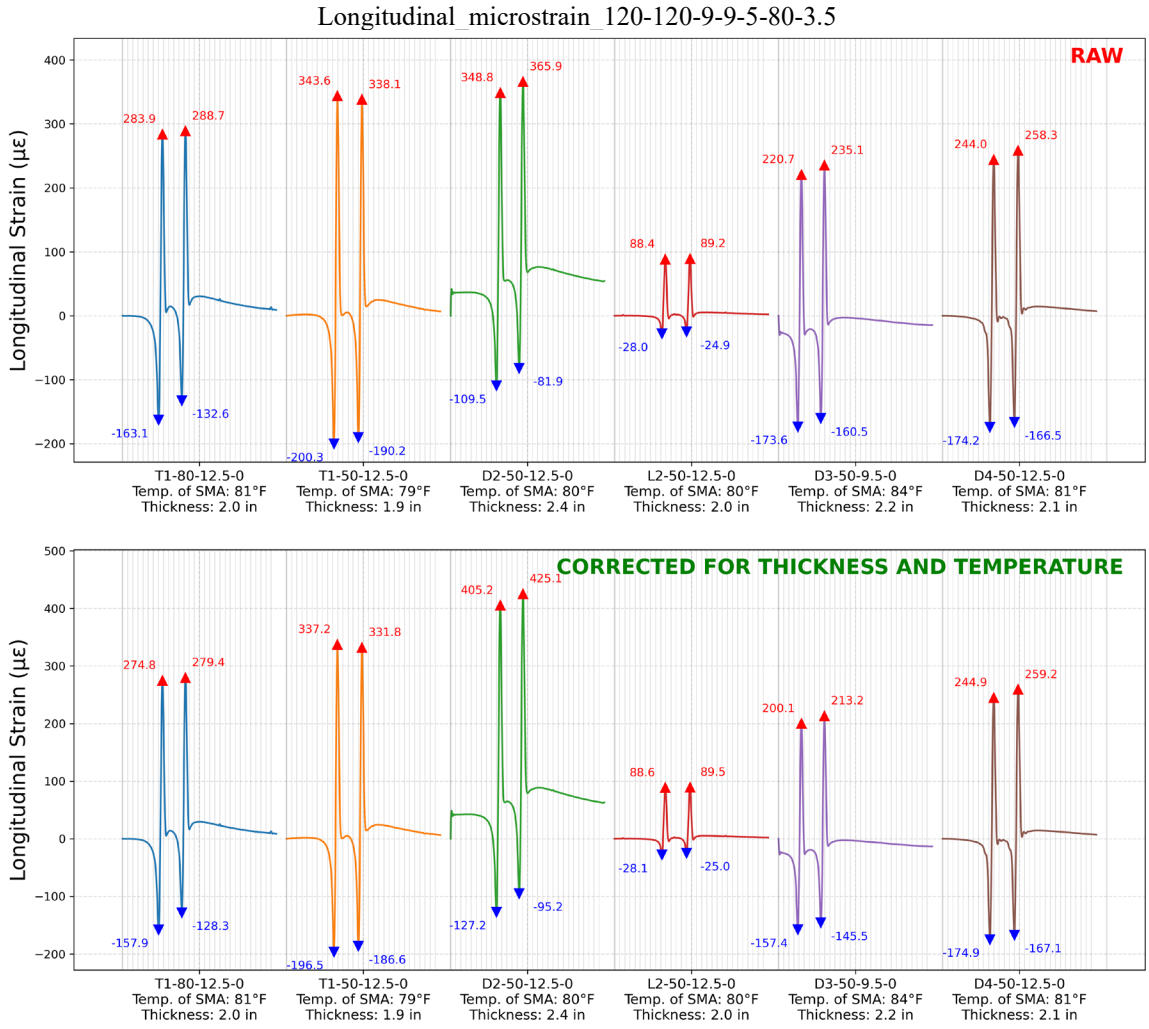

Figure 227. Graph. Comparison of measured and corrected longitudinal microstrain under tandem-axle loading (P_1 = 120 psi, P_2 = 120 psi; L_1 = 9 kip, L_2 = 9 kip; speed = 5 mph; axle spacing = 3.5 ft)

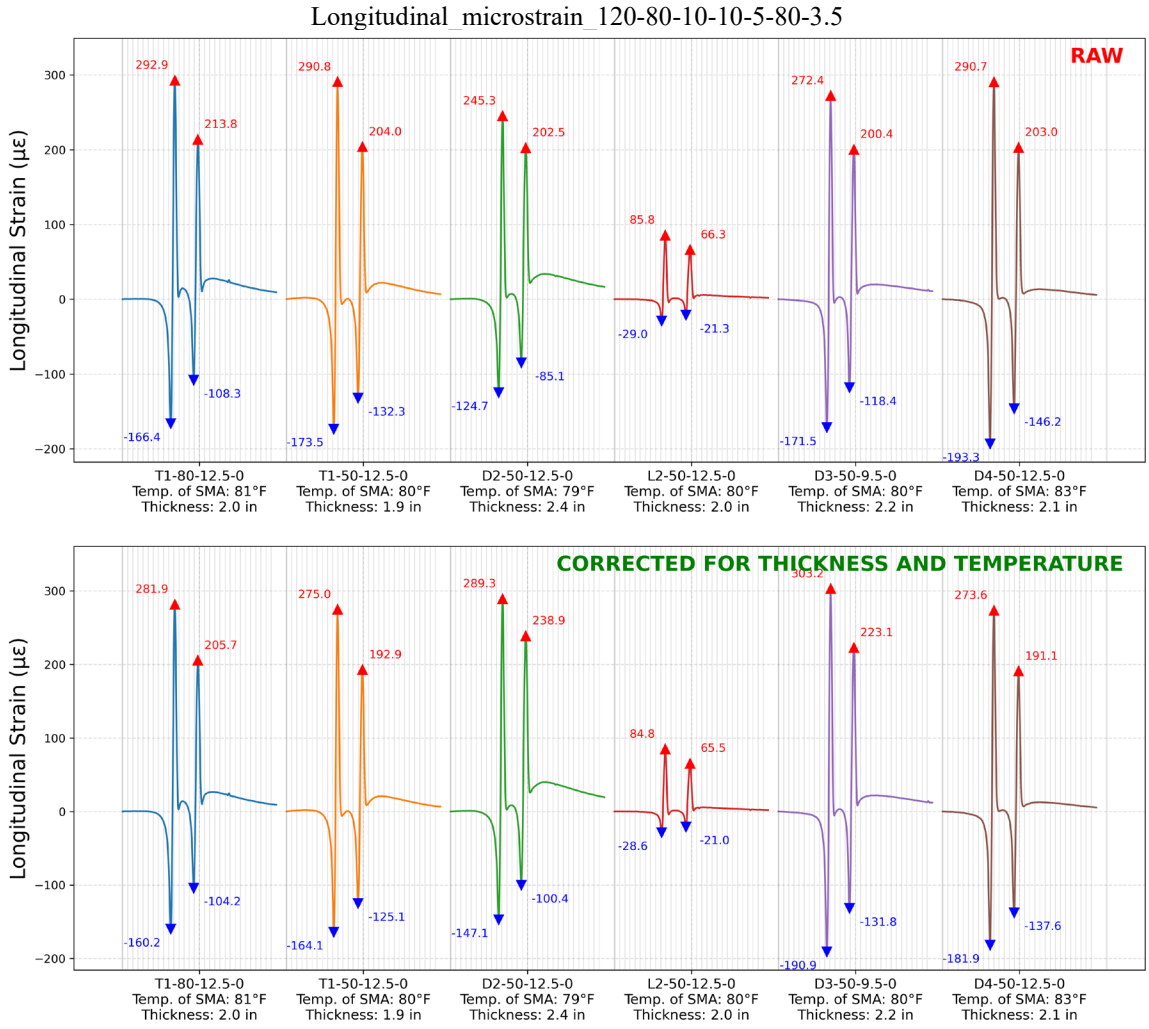

Figure 228. Graph. Comparison of measured and corrected longitudinal microstrain under tandem-axle loading with asymmetric tire pressures (P_1 = 120 psi, P_2 = 80 psi; L_1 = 10 kip, L_2 = 10 kip; speed = 5 mph; axle spacing = 3.5 ft)

Image 20: Longitudinal_microstrain_80-0-10-0-5-80-NA

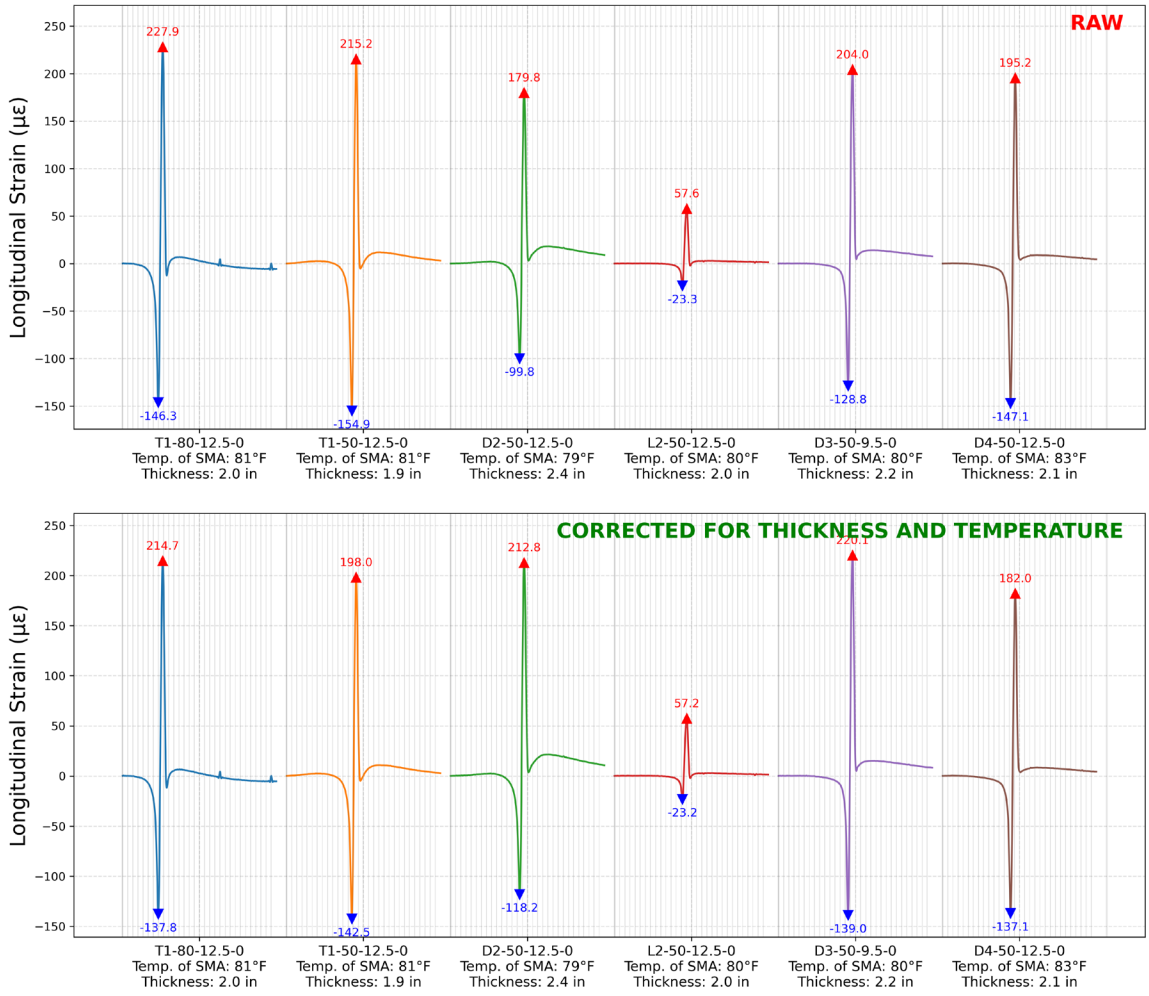

Figure 229. Graph. Comparison of measured and corrected longitudinal microstrain under single-axle loading (P_1 = 80 psi; L_1 = 10 kip; speed = 5 mph)

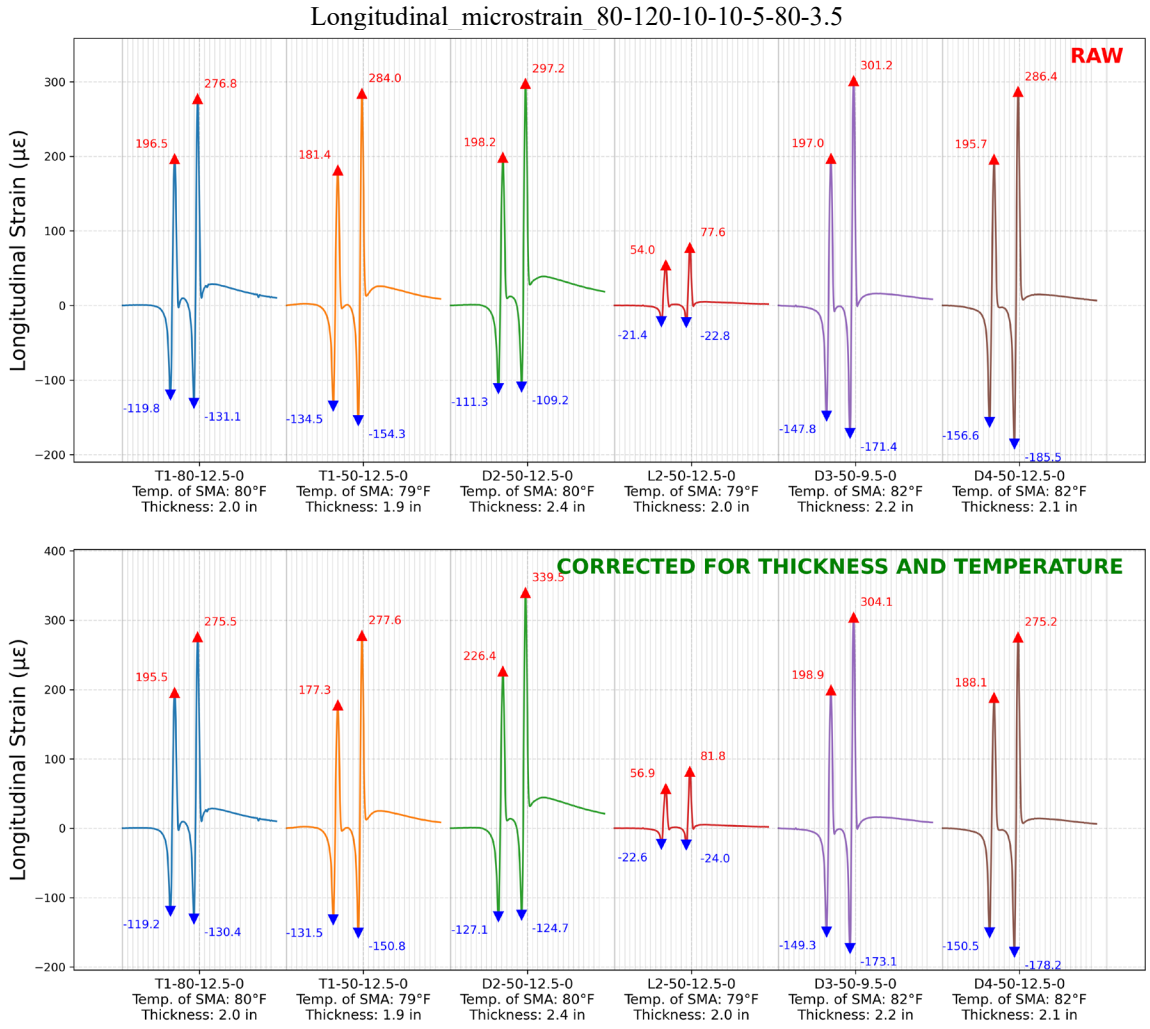

Figure 230. Graph. Comparison of measured and corrected longitudinal microstrain under tandem-axle loading with asymmetric tire pressures (P_1 = 80 psi, P_2 = 120 psi; L_1 = 10 kip, L_2 = 10 kip; speed = 5 mph; axle spacing = 3.5 ft)

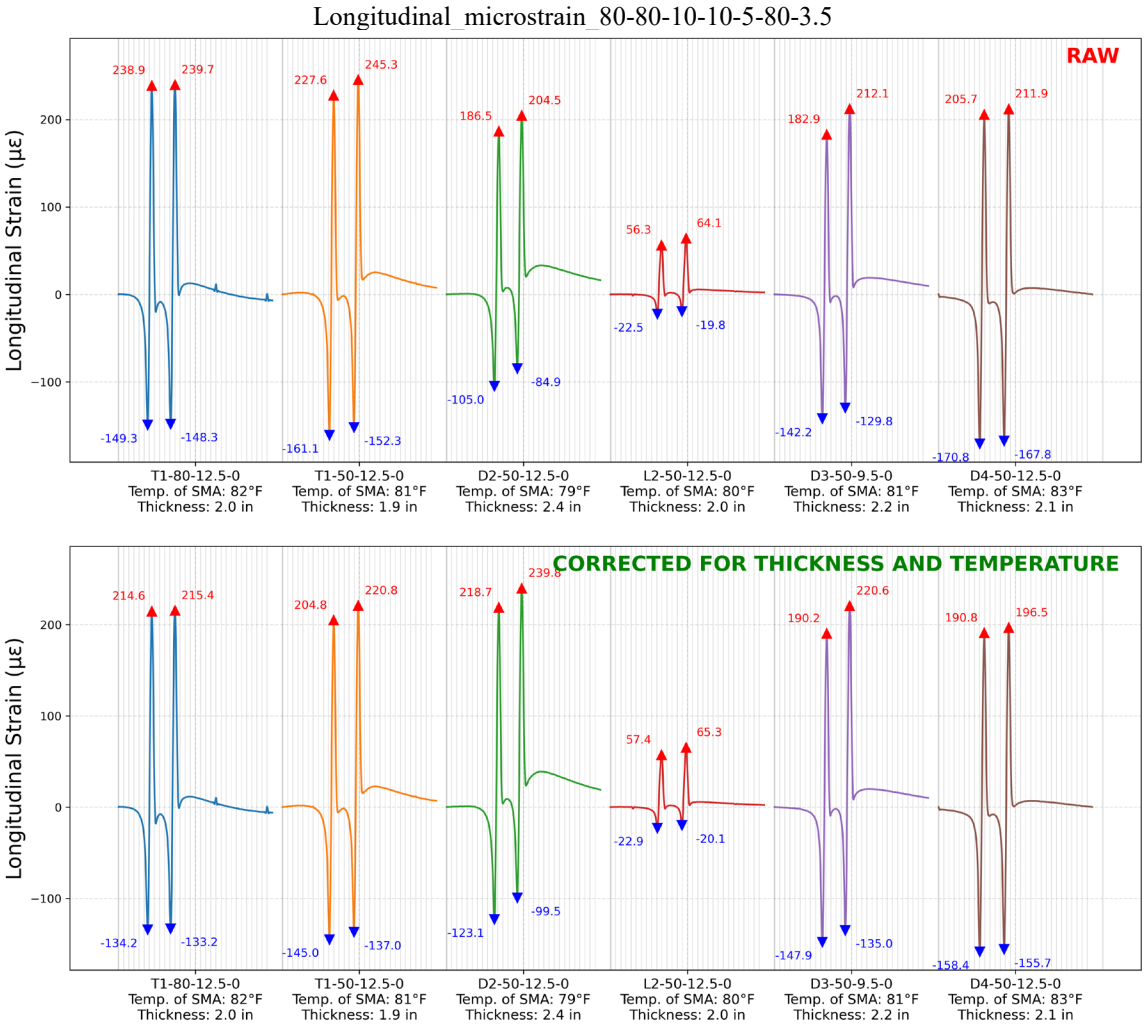

Figure 231. Graph. Comparison of measured and corrected longitudinal microstrain under tandem-axle loading (P_1 = 80 psi, P_2 = 80 psi; L_1 = 10 kip, L_2 = 10 kip; speed = 5 mph; axle spacing = 3.5 ft)

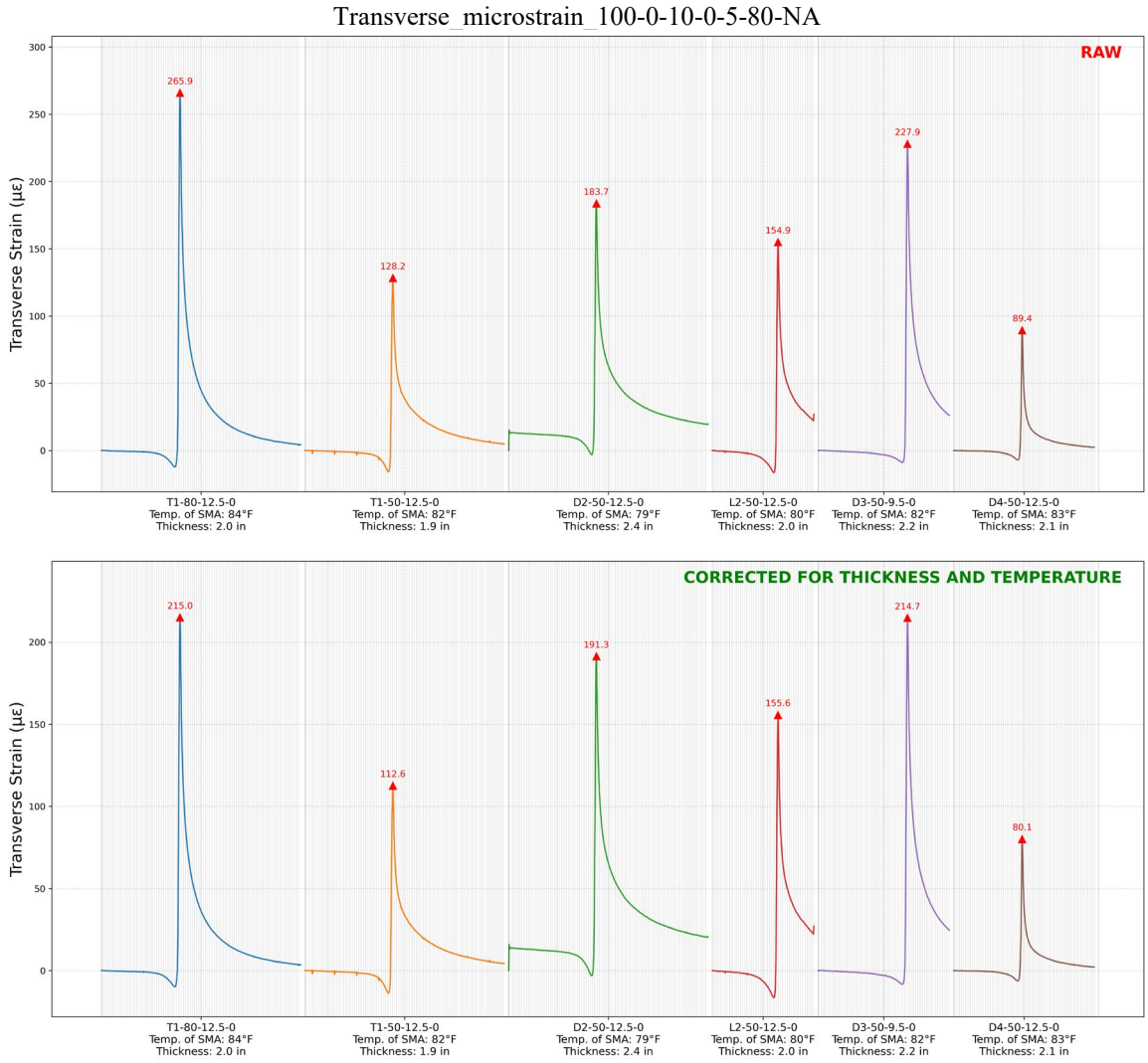

Figure 232. Graph. Comparison of measured and corrected transverse microstrain under single-axle loading (P_1 = 100 psi; L_1 = 10 kip; speed = 5 mph)

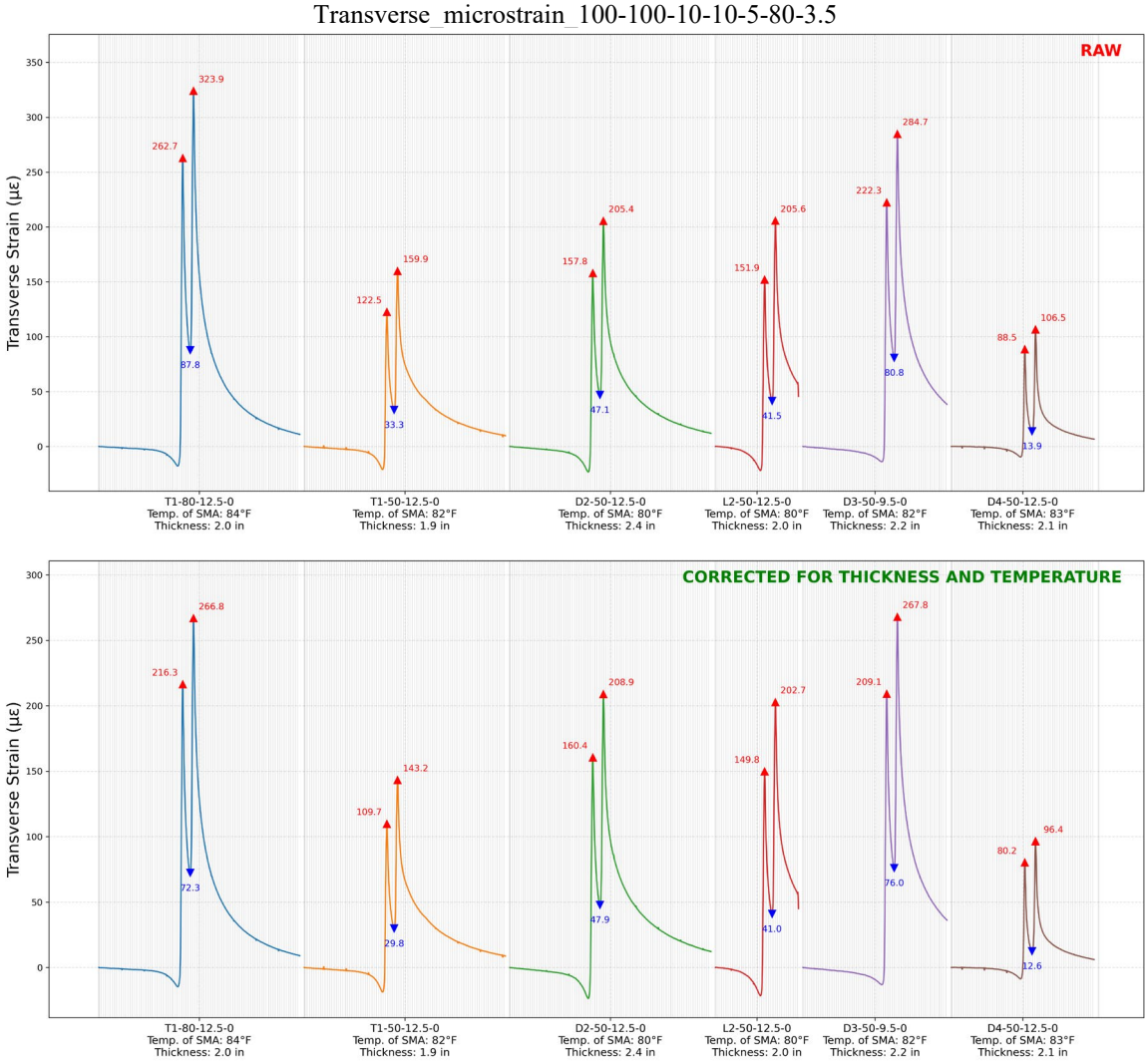

Figure 233. Graph. Comparison of measured and corrected transverse microstrain under tandem-axle loading (P_1 = 100 psi, P_2 = 100 psi; L_1 = 10 kip, L_2 = 10 kip; speed = 5 mph; axle spacing = 3.5 ft)

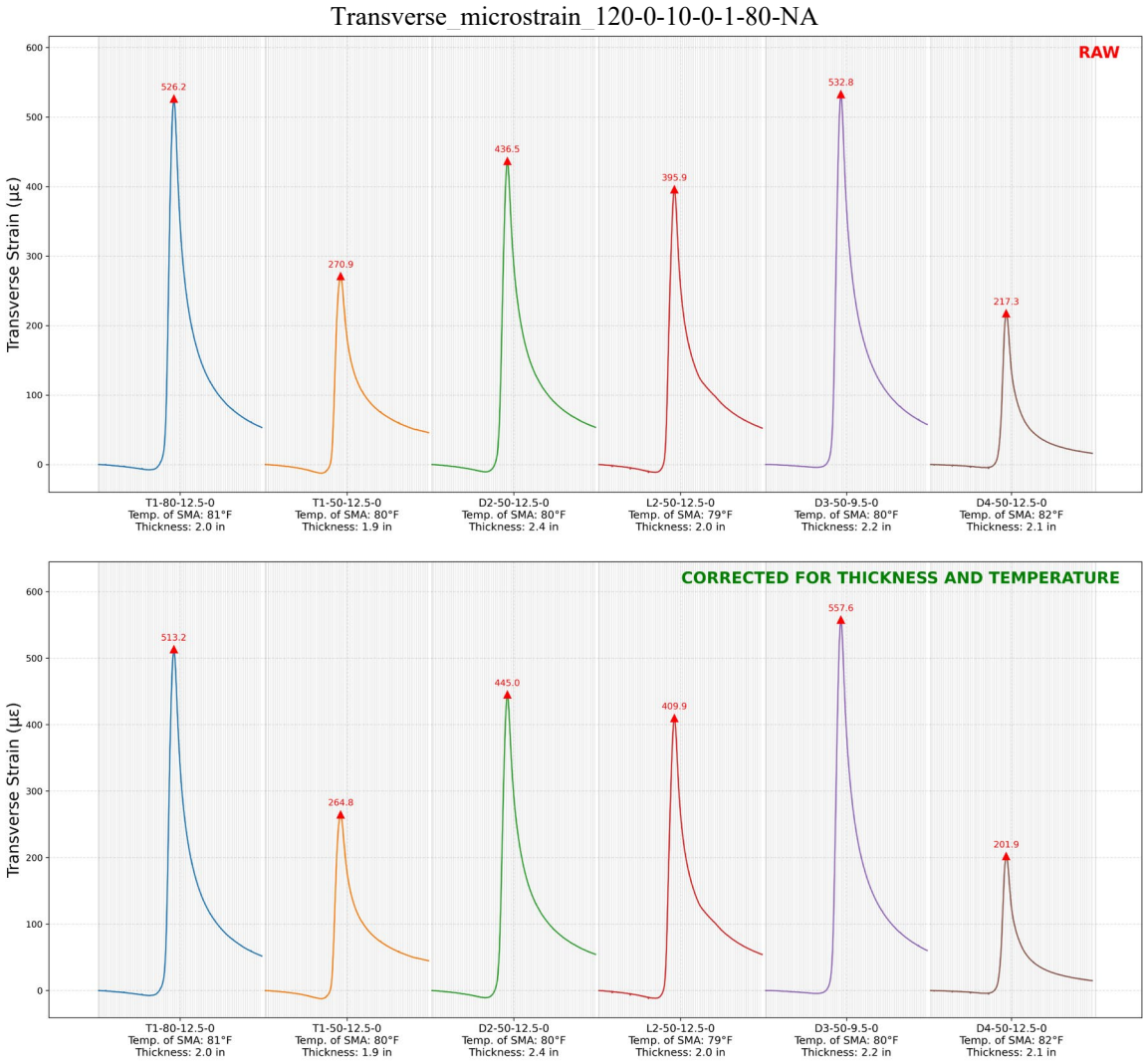

Figure 234. Graph. Comparison of measured and corrected transverse microstrain under single-axle loading (P_1 = 120 psi; L_1 = 10 kip; speed = 1 mph)

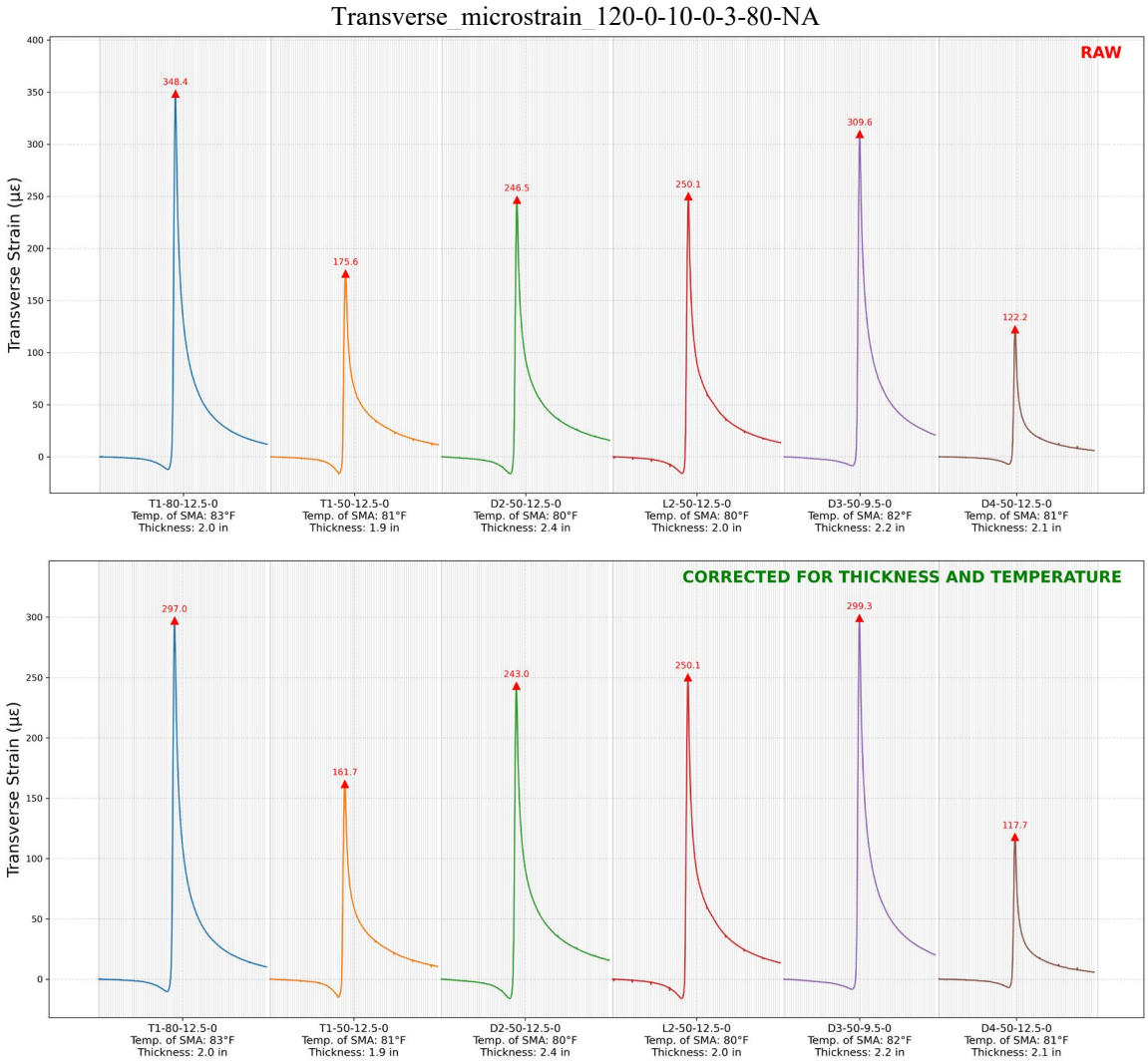

Figure 235. Graph. Comparison of measured and corrected transverse microstrain under single-axle loading (P_1 = 120 psi; L_1 = 10 kip; speed = 3 mph)

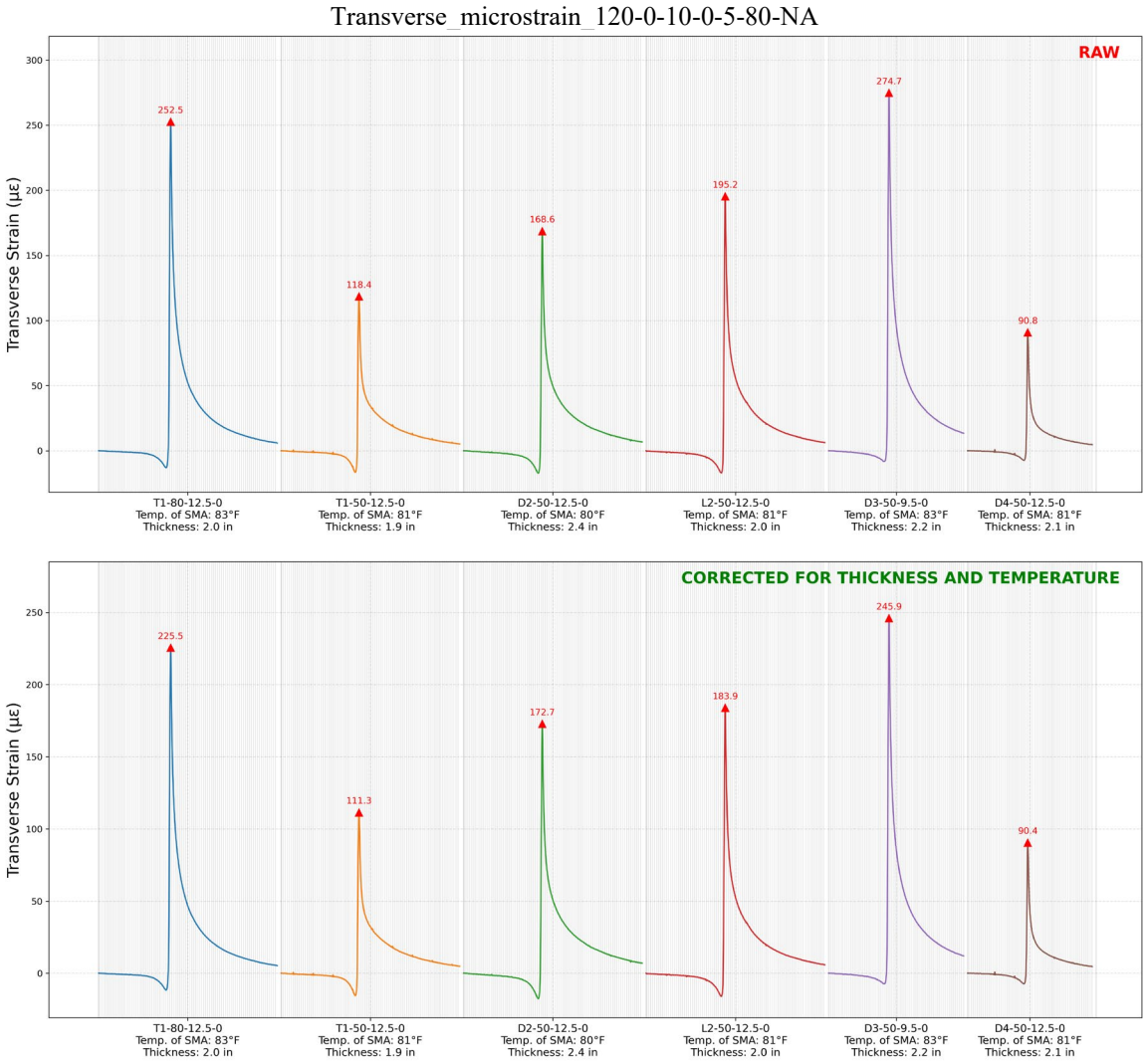

Figure 236. Graph. Comparison of measured and corrected transverse microstrain under single-axle loading (P_1 = 120 psi; L_1 = 10 kip; speed = 5 mph)

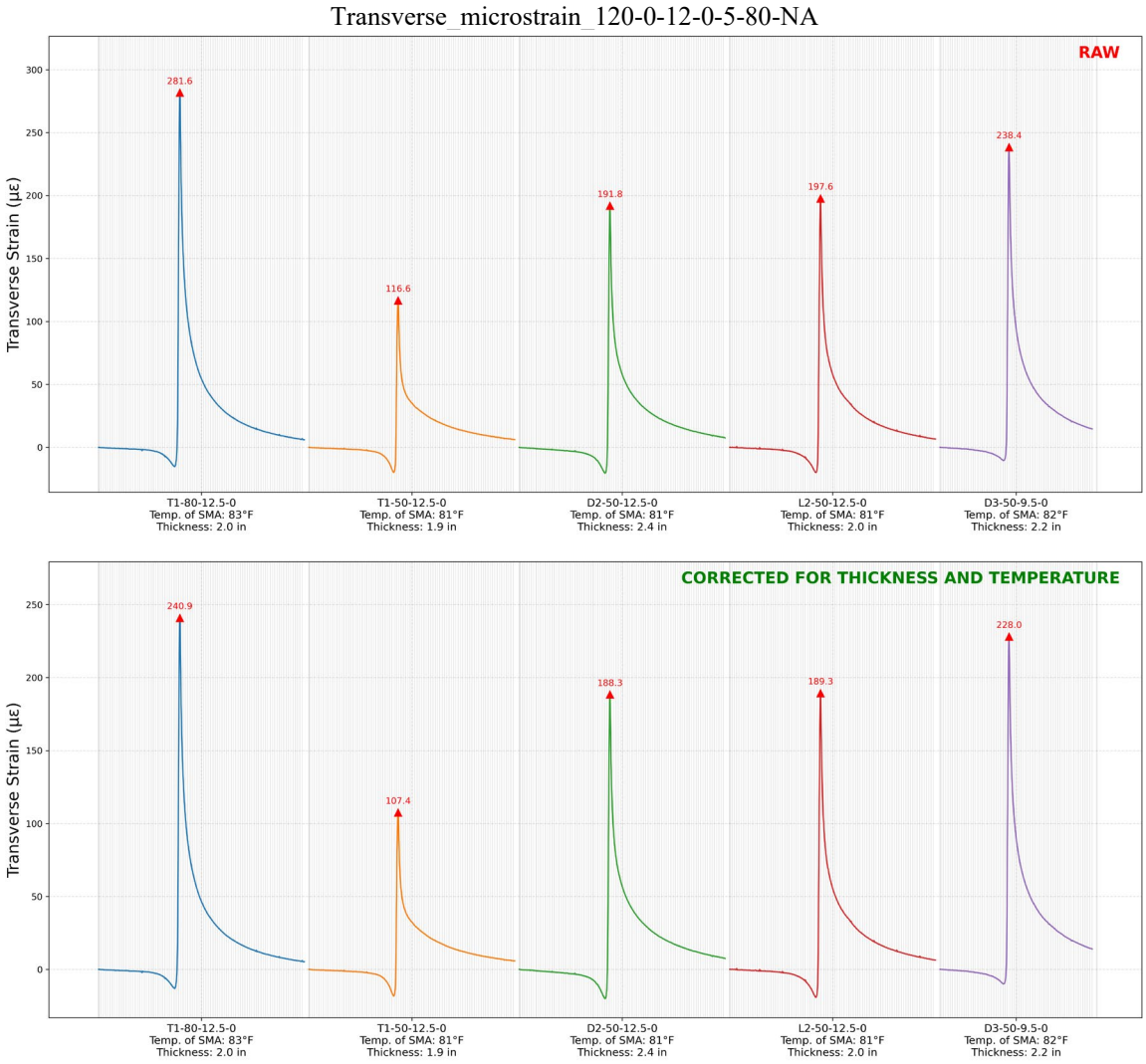

Figure 237. Graph. Comparison of measured and corrected transverse microstrain under single-axle loading (P_1 = 120 psi; L_1 = 12 kip; speed = 5 mph)

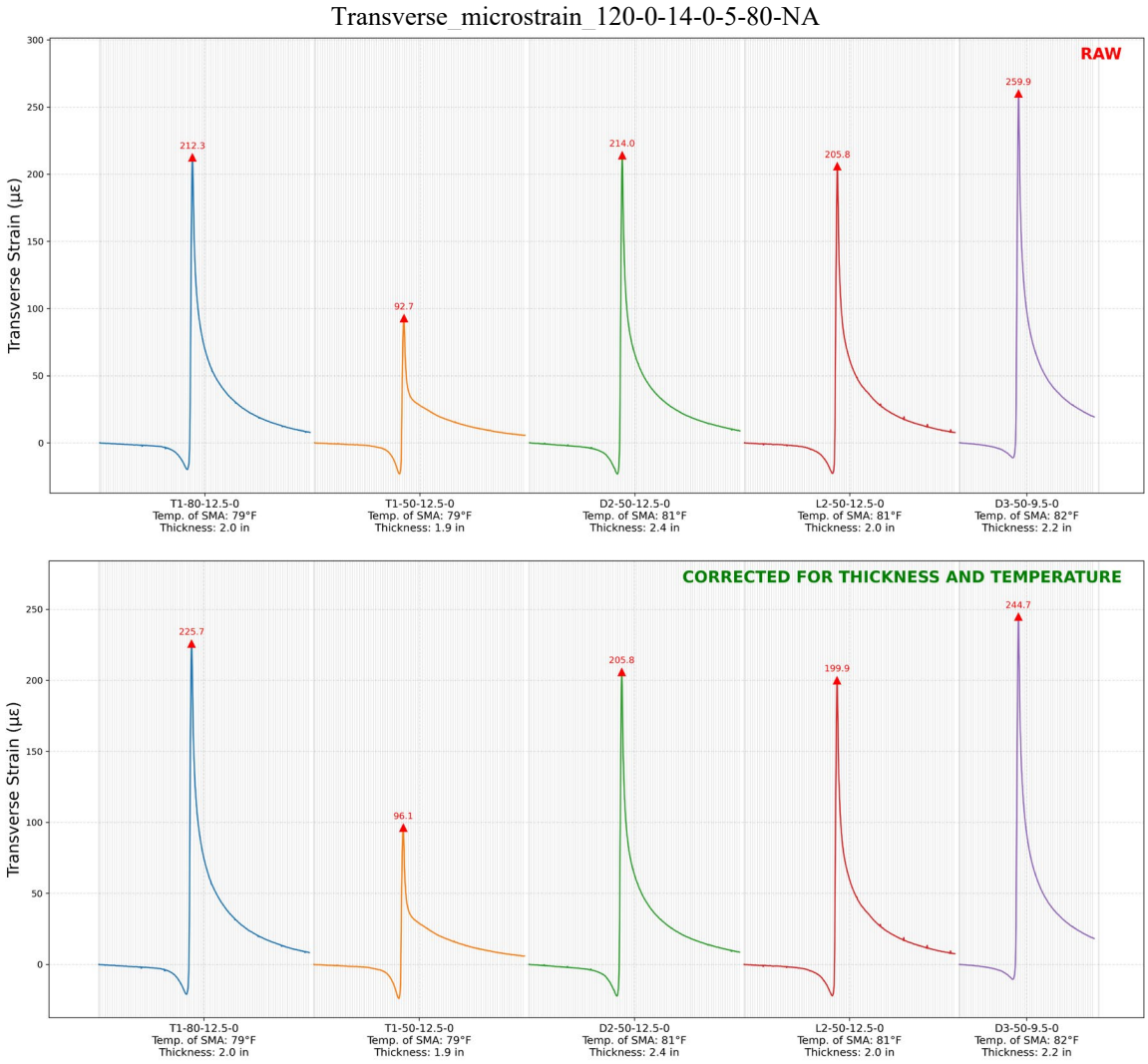

Figure 238. Graph. Comparison of measured and corrected transverse microstrain under single-axle loading (P_1 = 120 psi; L_1 = 14 kip; speed = 5 mph)

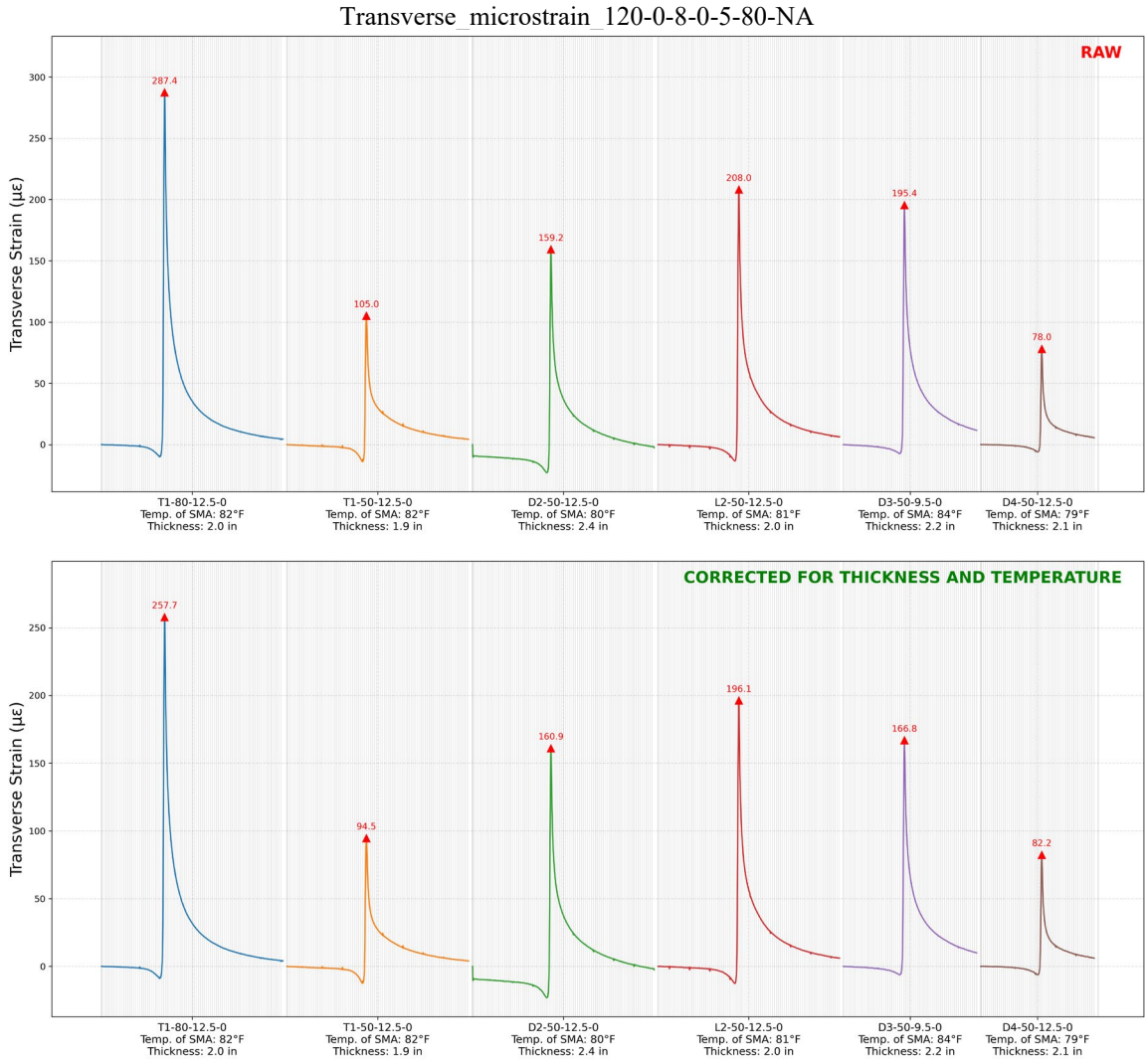

Figure 239. Graph. Comparison of measured and corrected transverse microstrain under single-axle loading (P_1 = 120 psi; L_1 = 8 kip; speed = 5 mph)

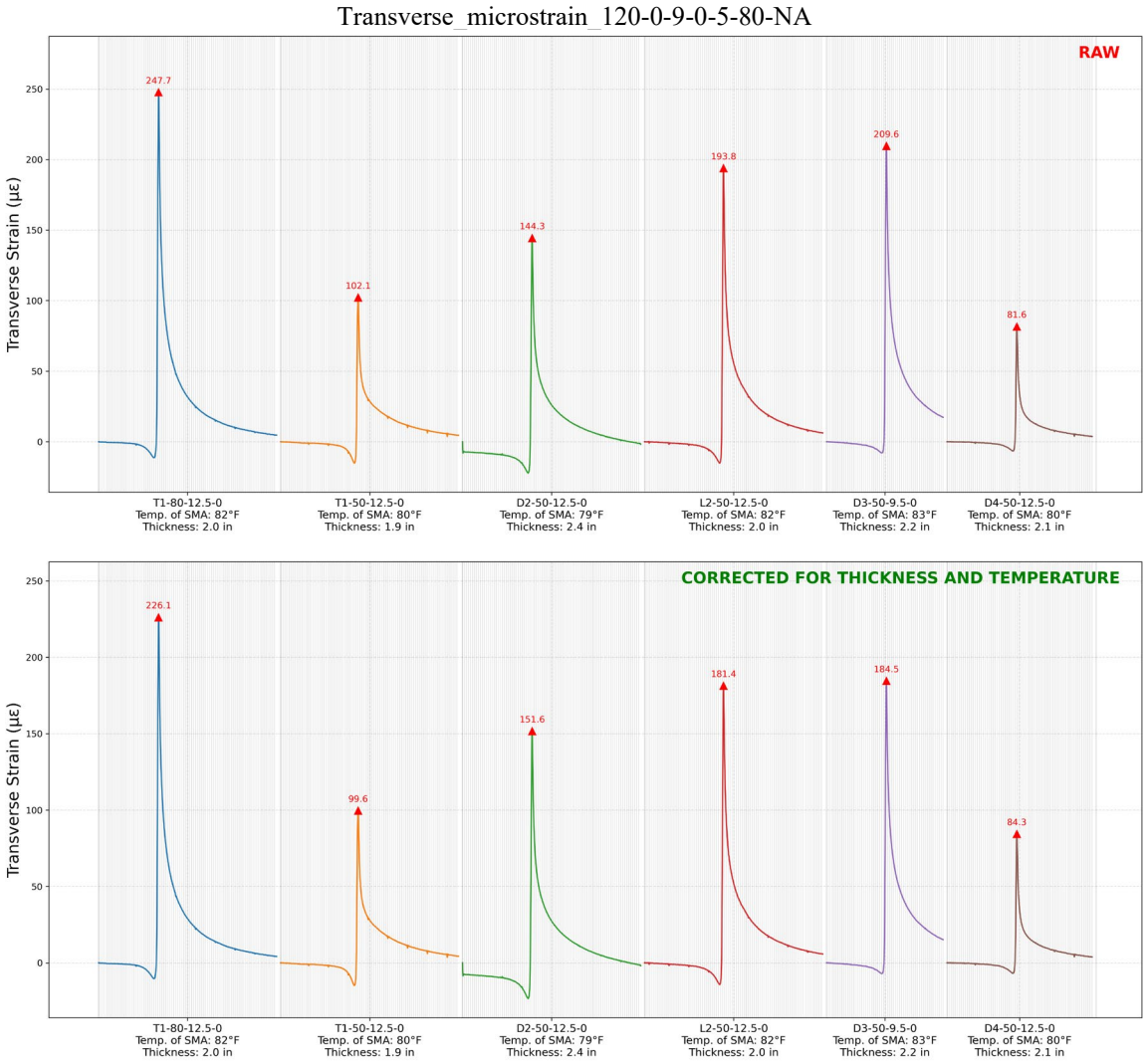

Figure 240. Graph. Comparison of measured and corrected transverse microstrain under single-axle loading (P_1 = 120 psi; L_1 = 9 kip; speed = 5 mph)

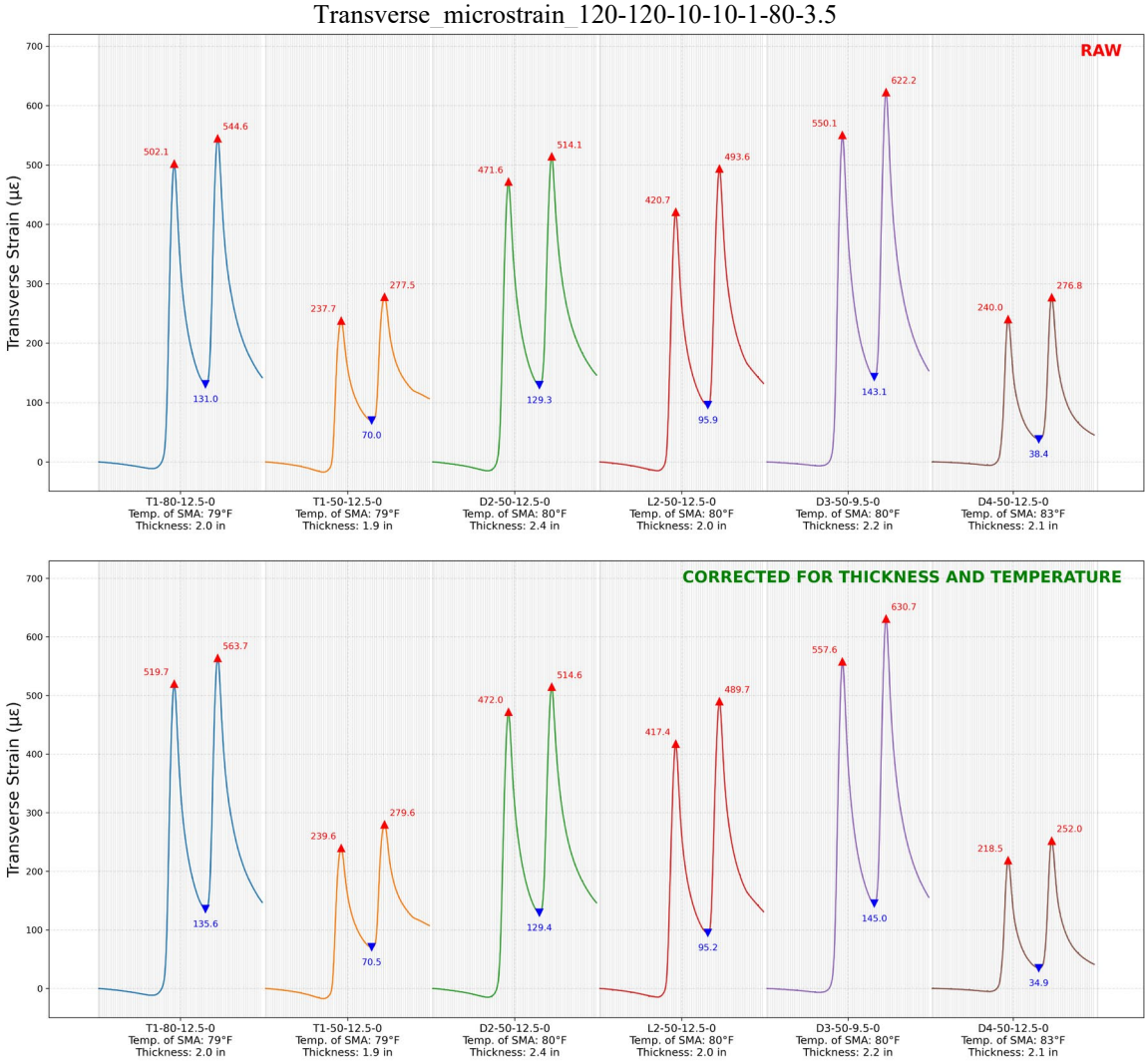

Figure 241. Graph. Comparison of measured and corrected transverse microstrain under tandem-axle loading (P_1 = 120 psi, P_2 = 120 psi; L_1 = 10 kip, L_2 = 10 kip; speed = 1 mph; axle spacing = 3.5 ft)

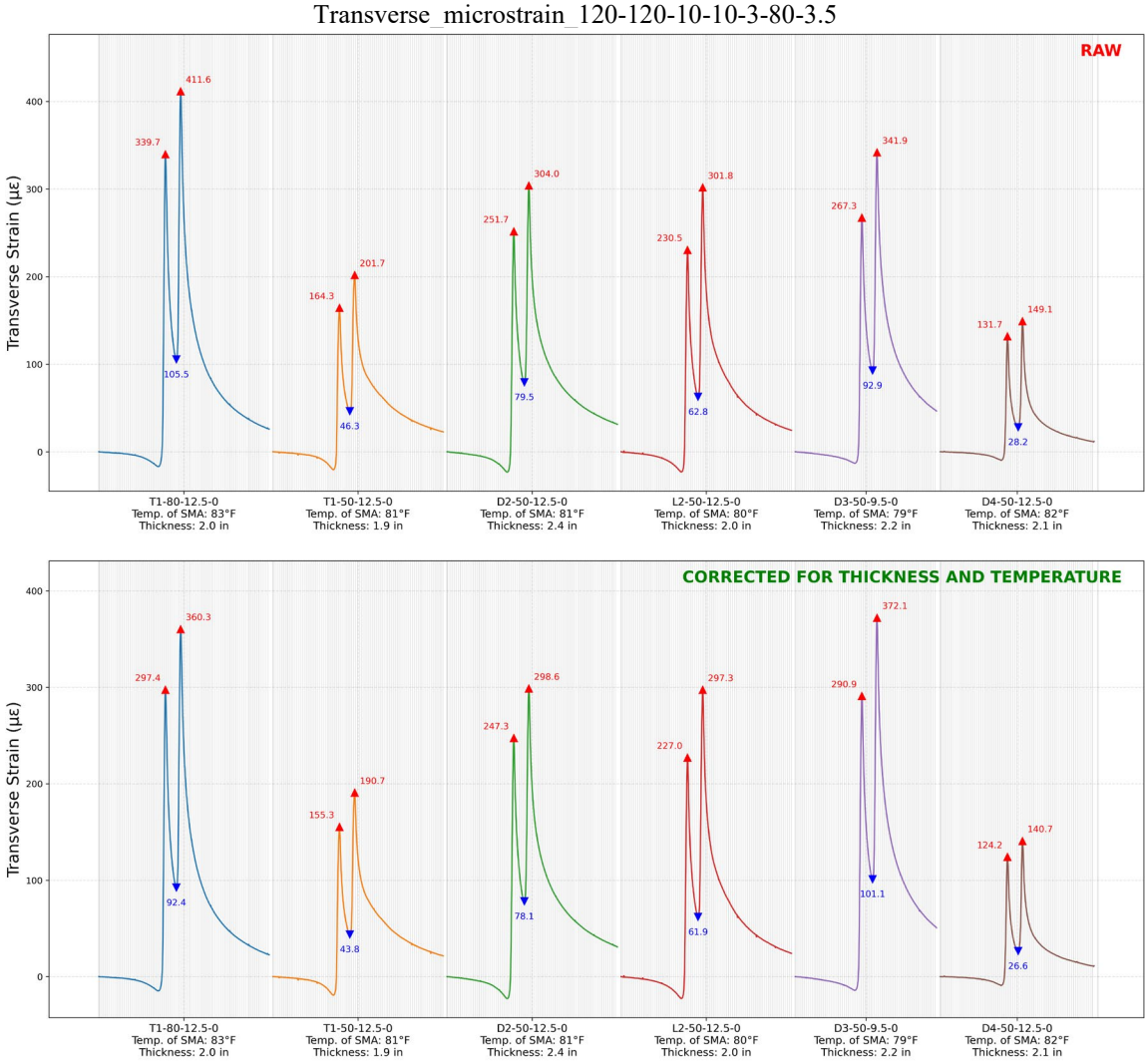

Figure 242. Graph. Comparison of measured and corrected transverse microstrain under tandem-axle loading (P_1 = 120 psi, P_2 = 120 psi; L_1 = 10 kip, L_2 = 10 kip; speed = 3 mph; axle spacing = 3.5 ft)

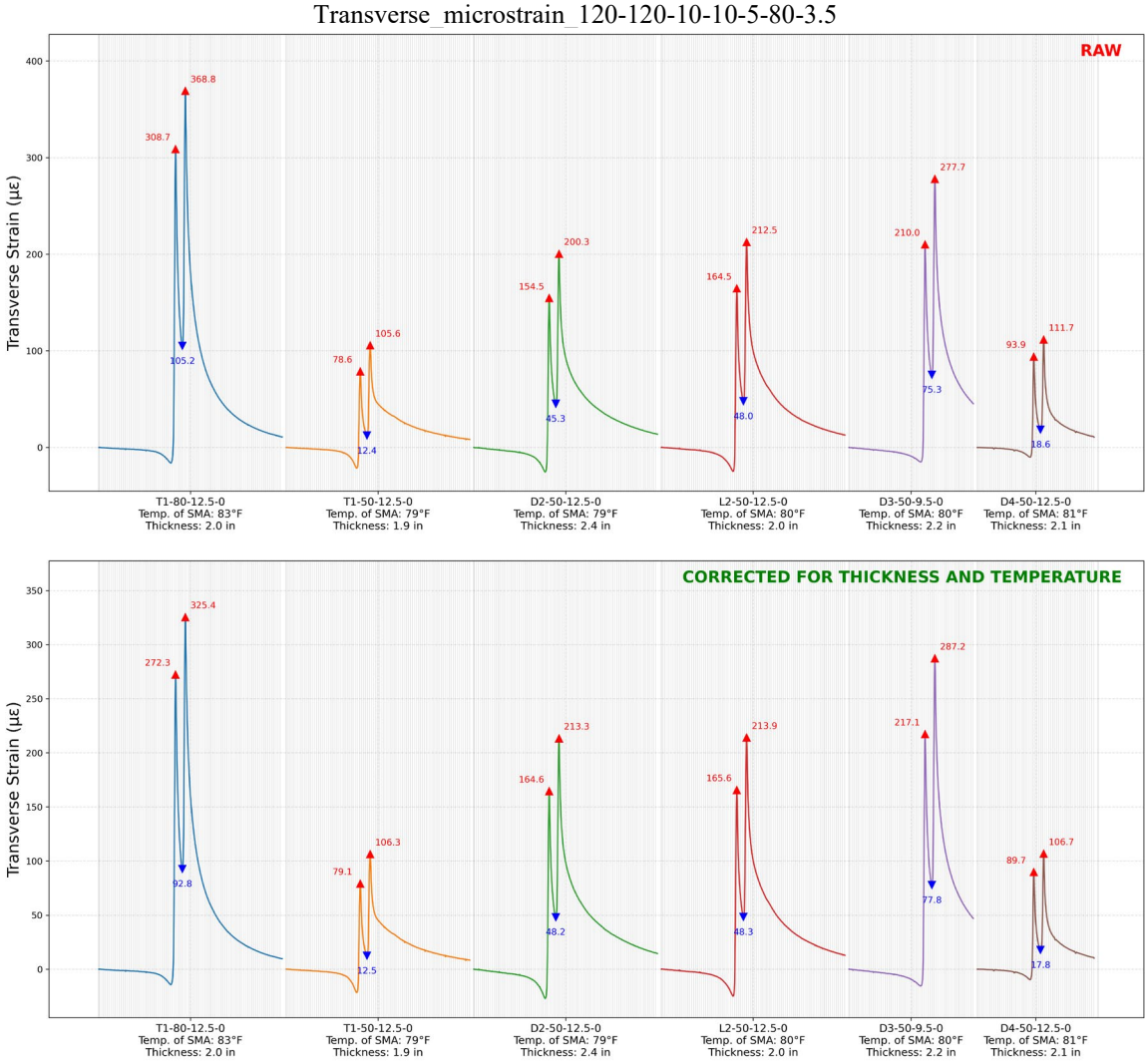

Figure 243. Graph. Comparison of measured and corrected transverse microstrain under tandem-axle loading (P_1 = 120 psi, P_2 = 120 psi; L_1 = 10 kip, L_2 = 10 kip; speed = 5 mph; axle spacing = 3.5 ft)

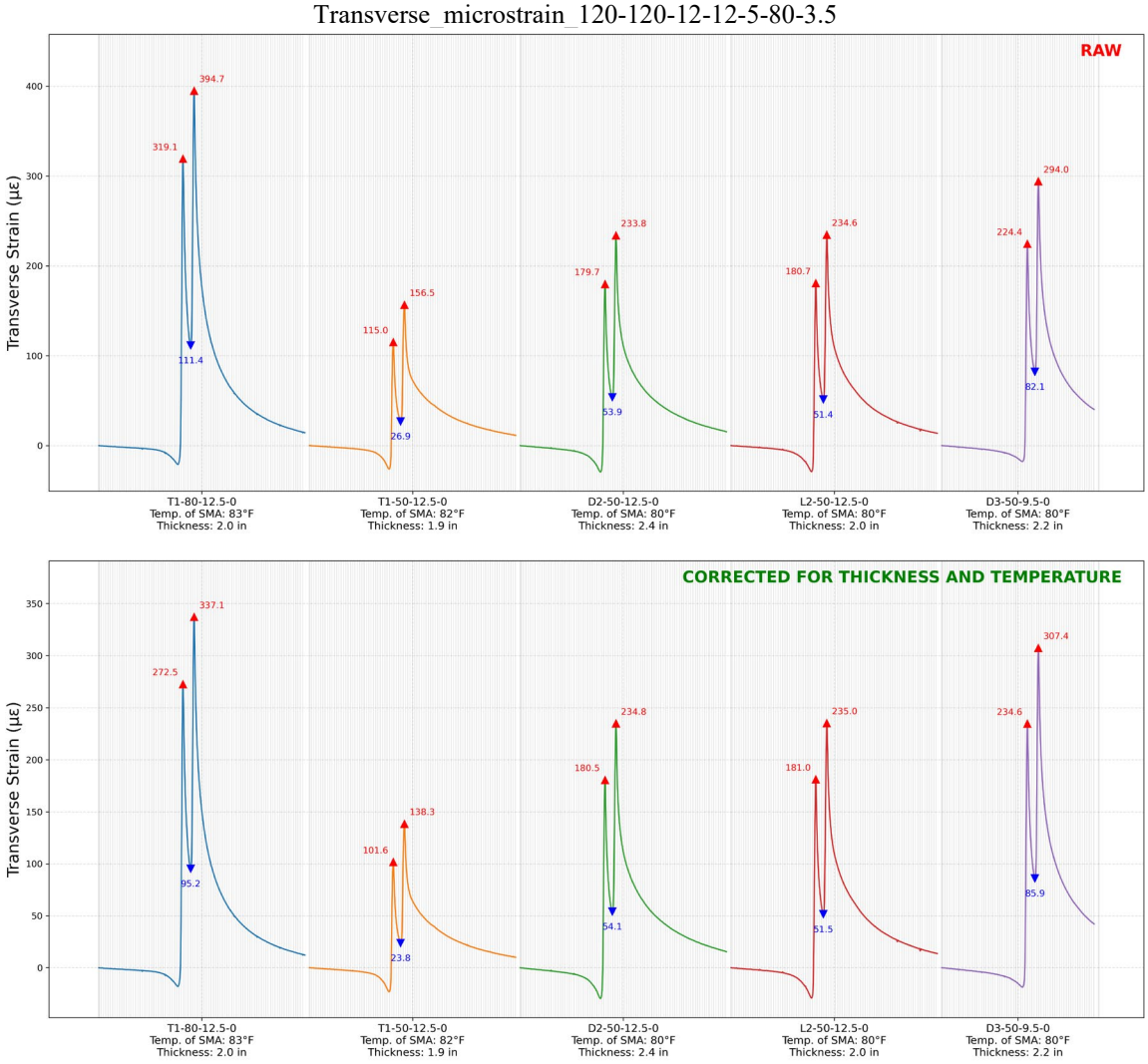

Figure 244. Graph. Comparison of measured and corrected transverse microstrain under tandem-axle loading (P_1 = 120 psi, P_2 = 120 psi; L_1 = 12 kip, L_2 = 12 kip; speed = 5 mph; axle spacing = 3.5 ft)

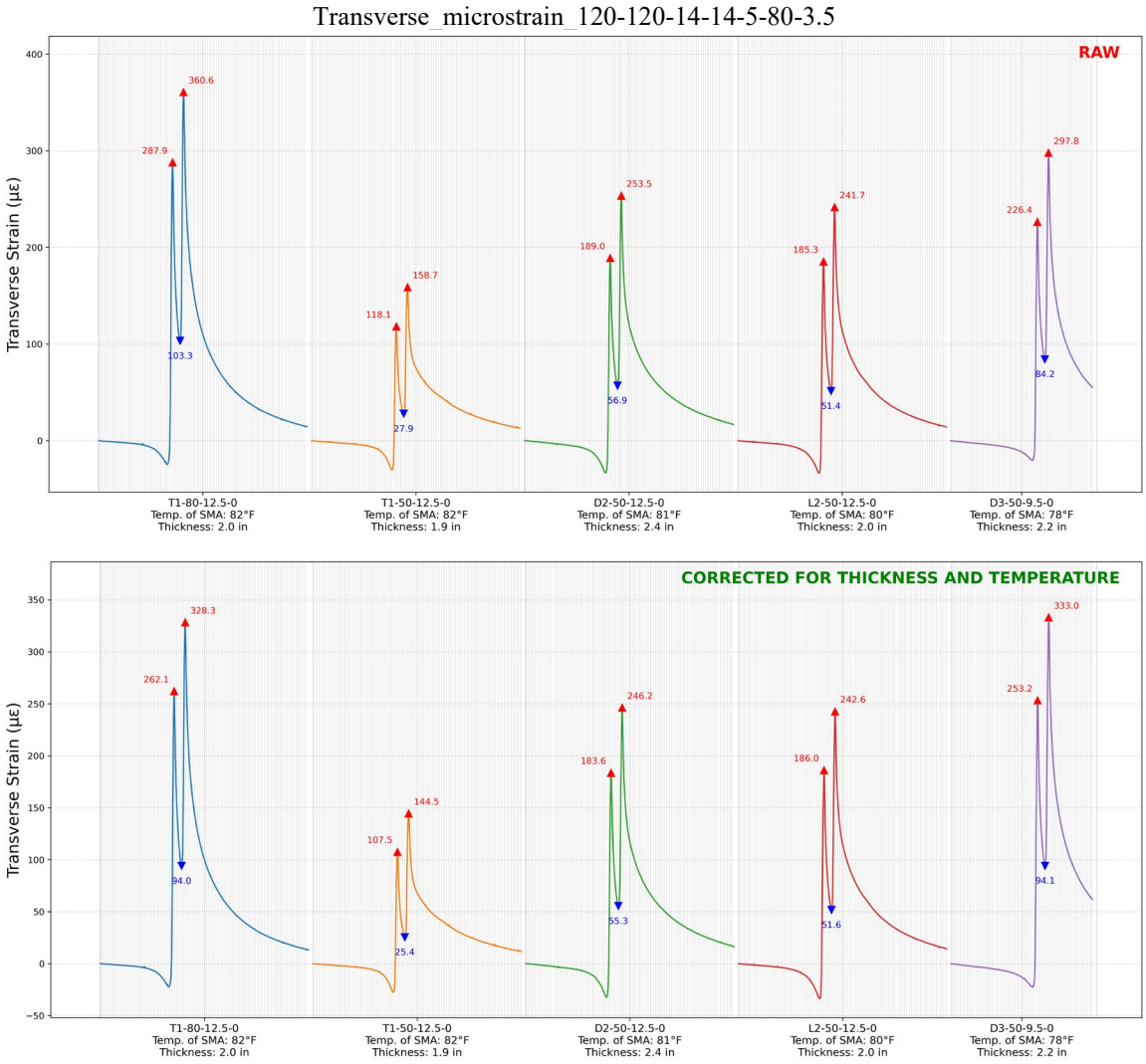

Figure 245. Graph. Comparison of measured and corrected transverse microstrain under tandem-axle loading (P_1 = 120 psi, P_2 = 120 psi; L_1 = 14 kip, L_2 = 14 kip; speed = 5 mph; axle spacing = 3.5 ft)

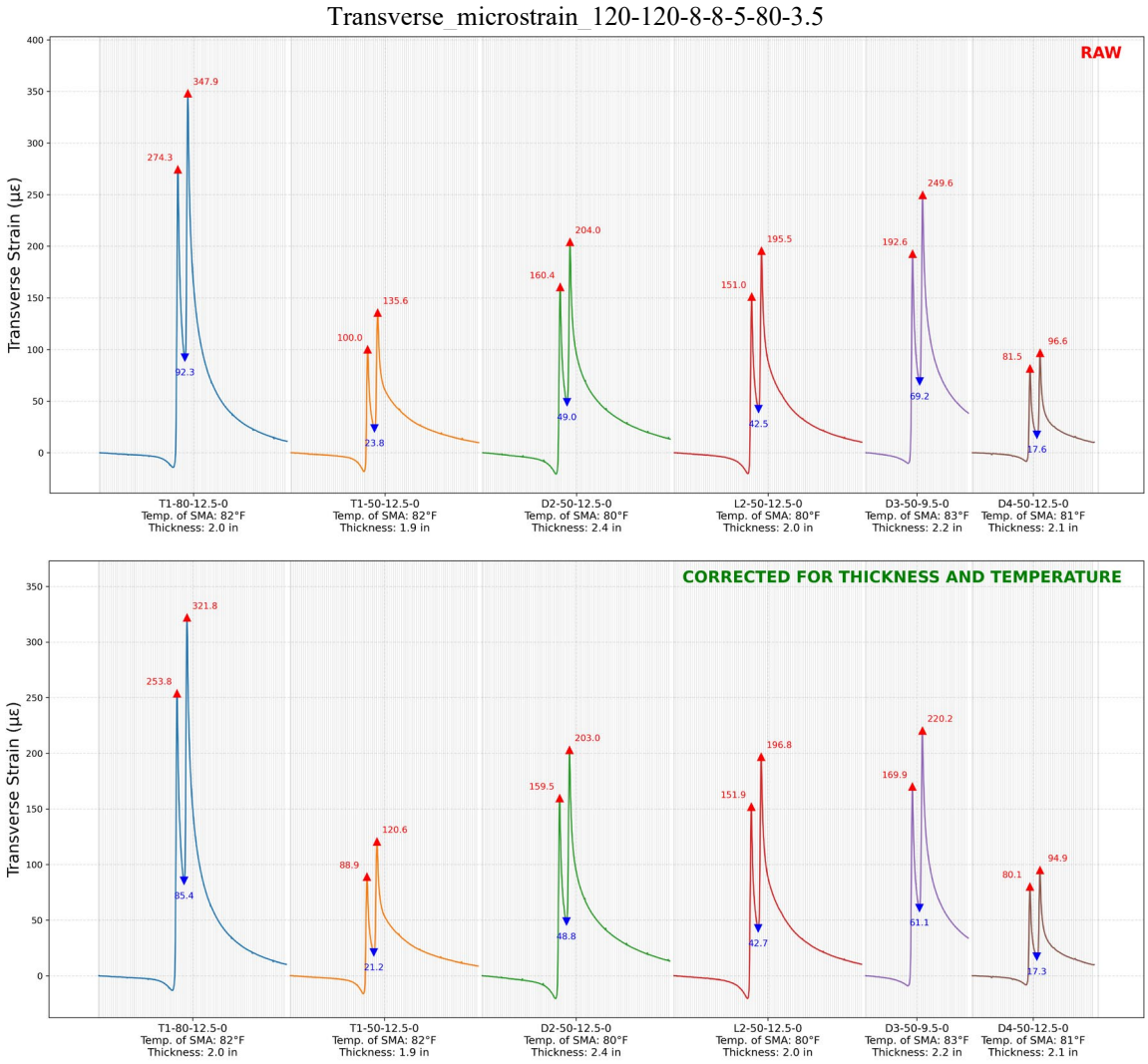

Figure 246. Graph. Comparison of measured and corrected transverse microstrain under tandem-axle loading (P_1 = 120 psi, P_2 = 120 psi; L_1 = 8 kip, L_2 = 8 kip; speed = 5 mph; axle spacing = 3.5 ft)

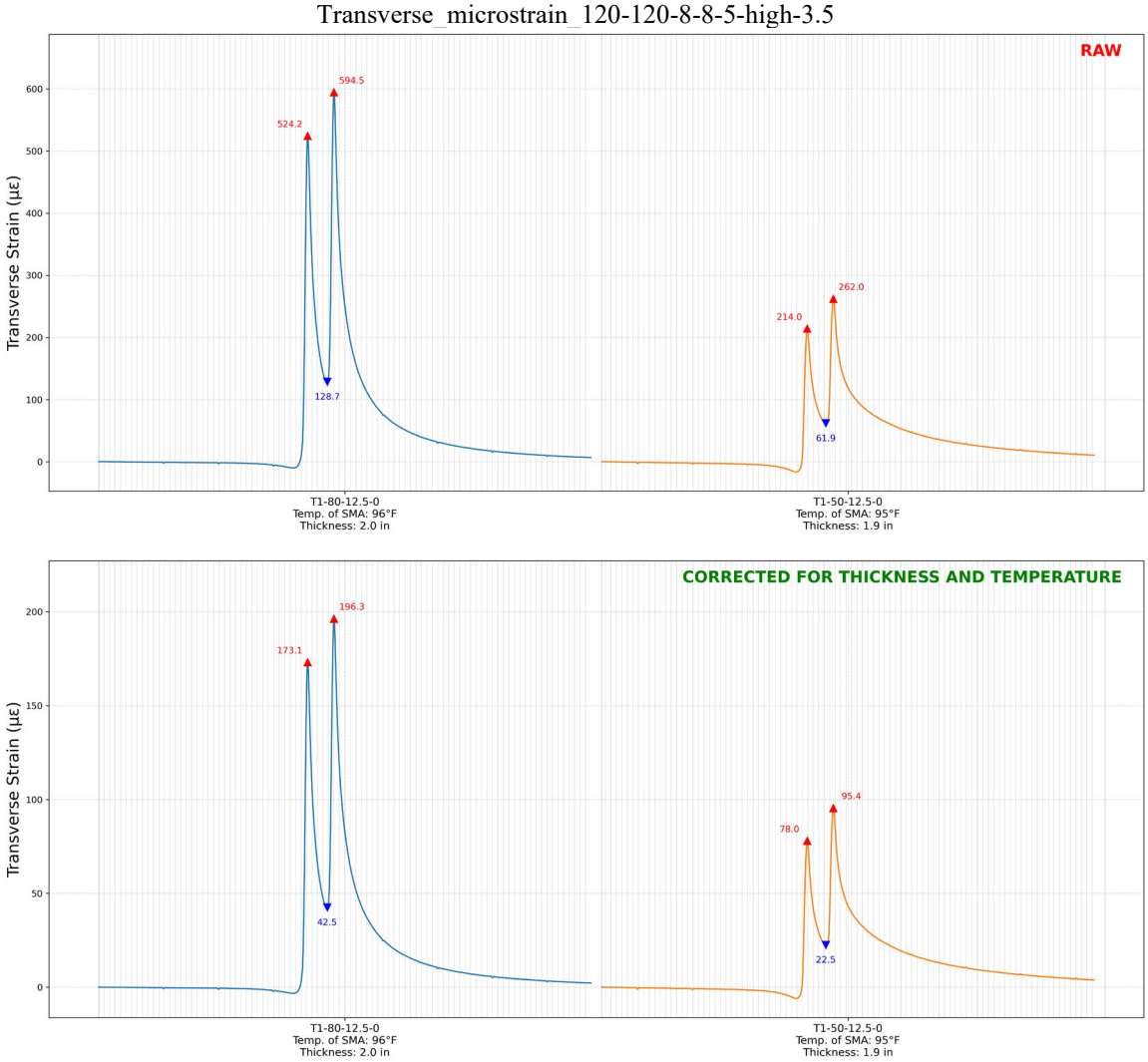

Figure 247. Graph. Comparison of measured and corrected transverse microstrain under tandem-axle loading at high temperature (P_1 = 120 psi, P_2 = 120 psi; L_1 = 8 kip, L_2 = 8 kip; speed = 5 mph; axle spacing = 3.5 ft)

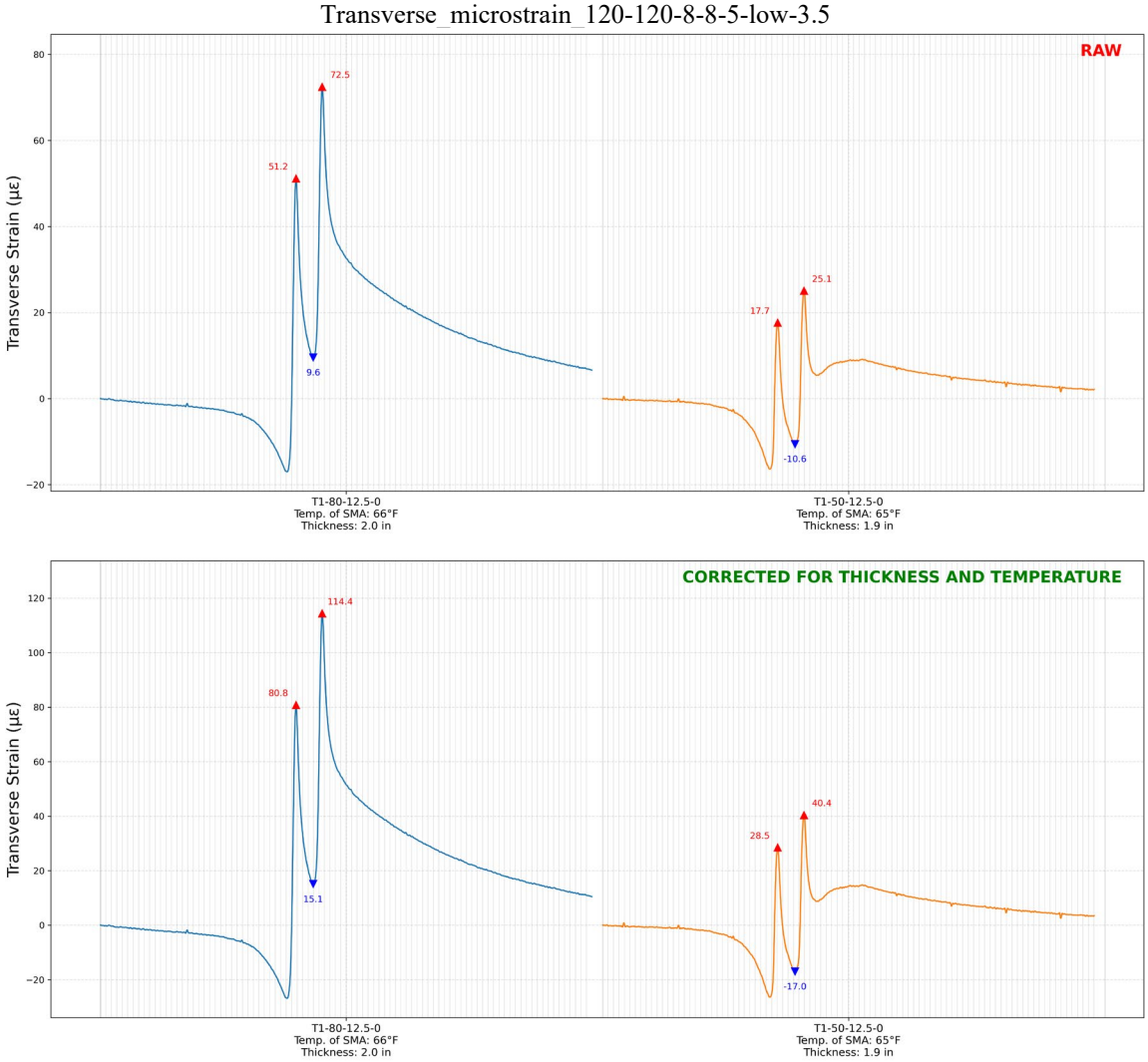

Figure 248. Graph. Comparison of measured and corrected transverse microstrain under tandem-axle loading at low temperature (P_1 = 120 psi, P_2 = 120 psi; L_1 = 8 kip, L_2 = 8 kip; speed = 5 mph; axle spacing = 3.5 ft)

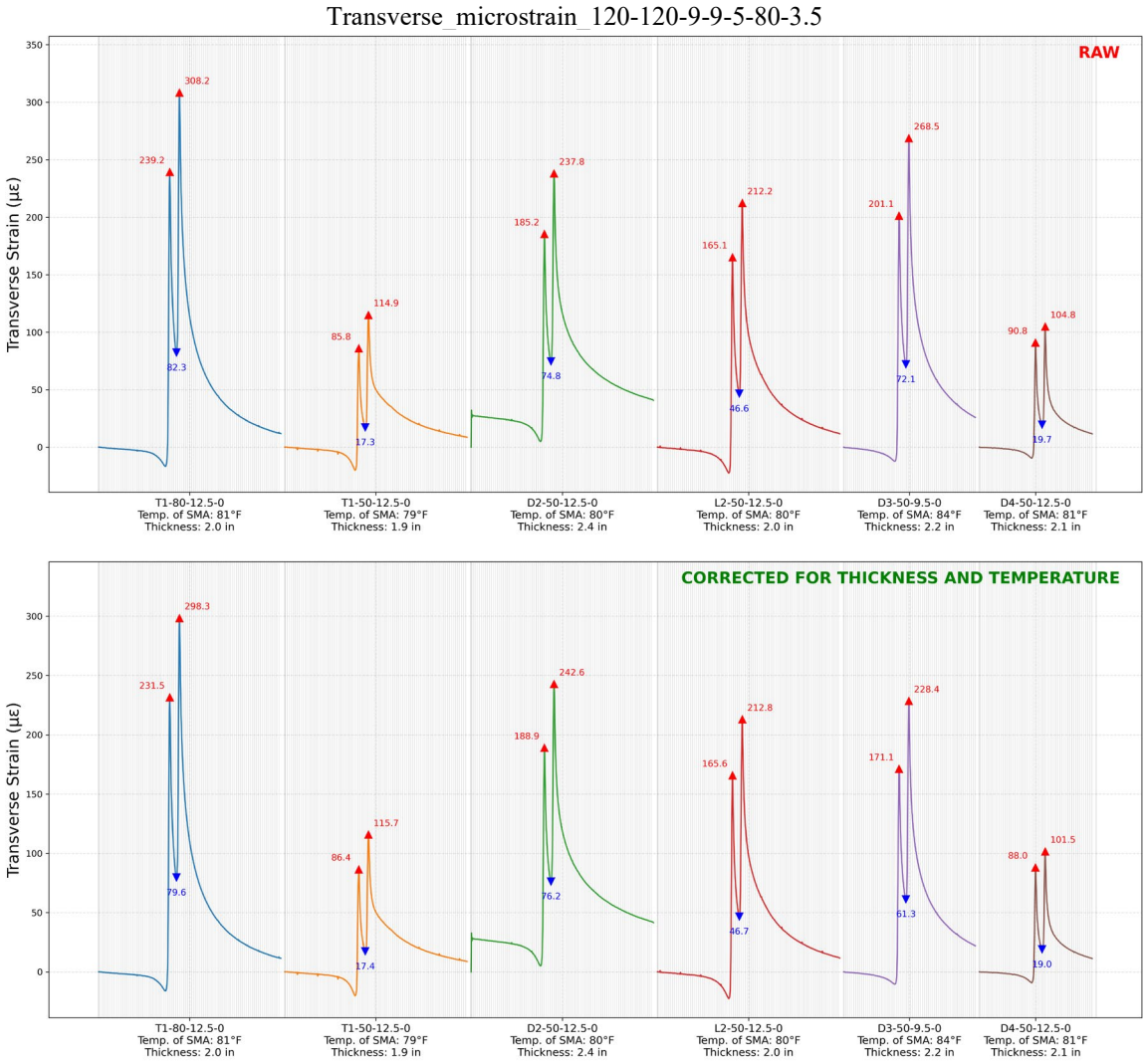

Figure 249. Graph. Comparison of measured and corrected transverse microstrain under tandem-axle loading (P_1 = 120 psi, P_2 = 120 psi; L_1 = 9 kip, L_2 = 9 kip; speed = 5 mph; axle spacing = 3.5 ft)

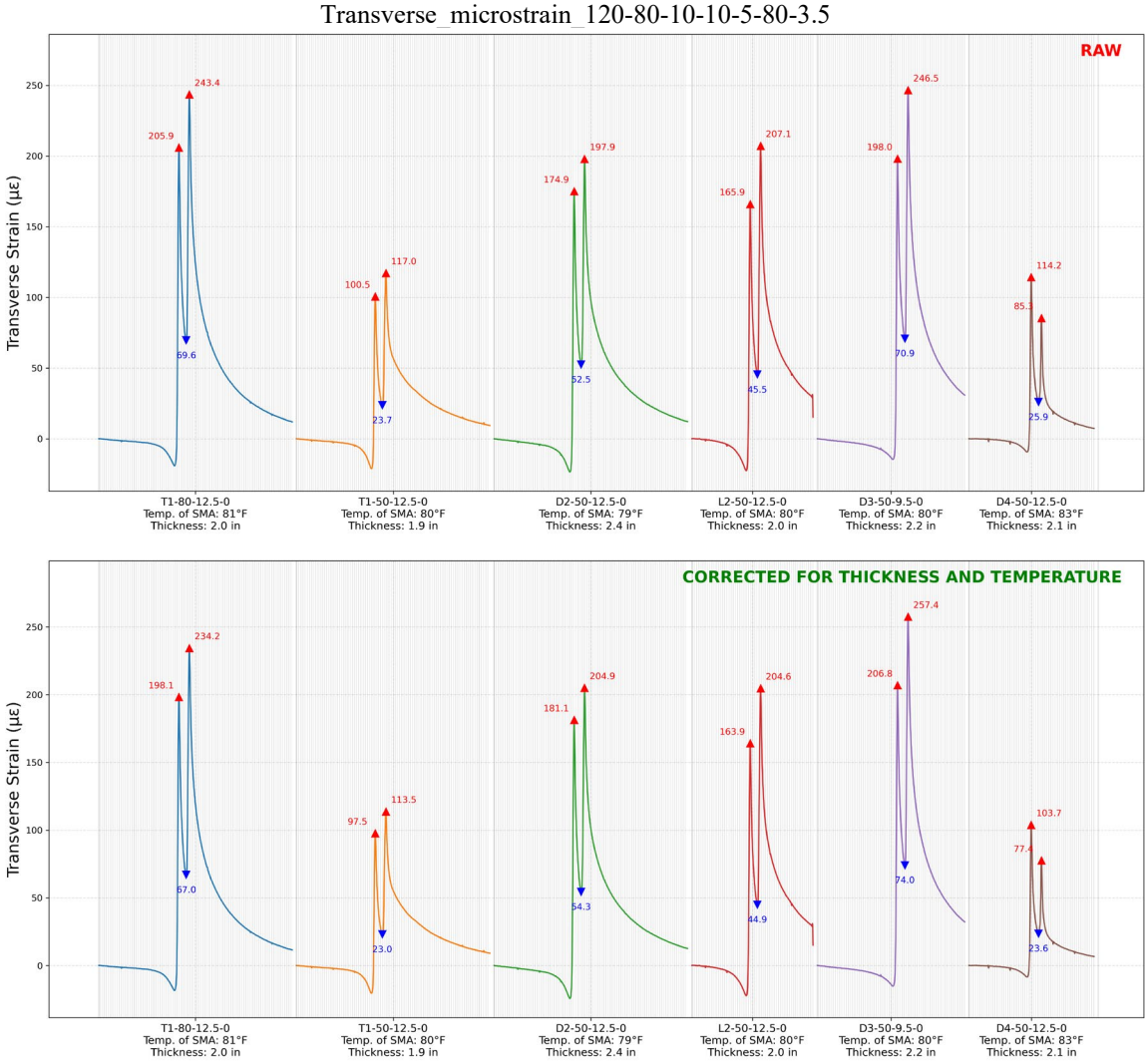

Figure 250. Graph. Comparison of measured and corrected transverse microstrain under tandem-axle loading with asymmetric tire pressures (P_1 = 120 psi, P_2 = 80 psi; L_1 = 10 kip, L_2 = 10 kip; speed = 5 mph; axle spacing = 3.5 ft)

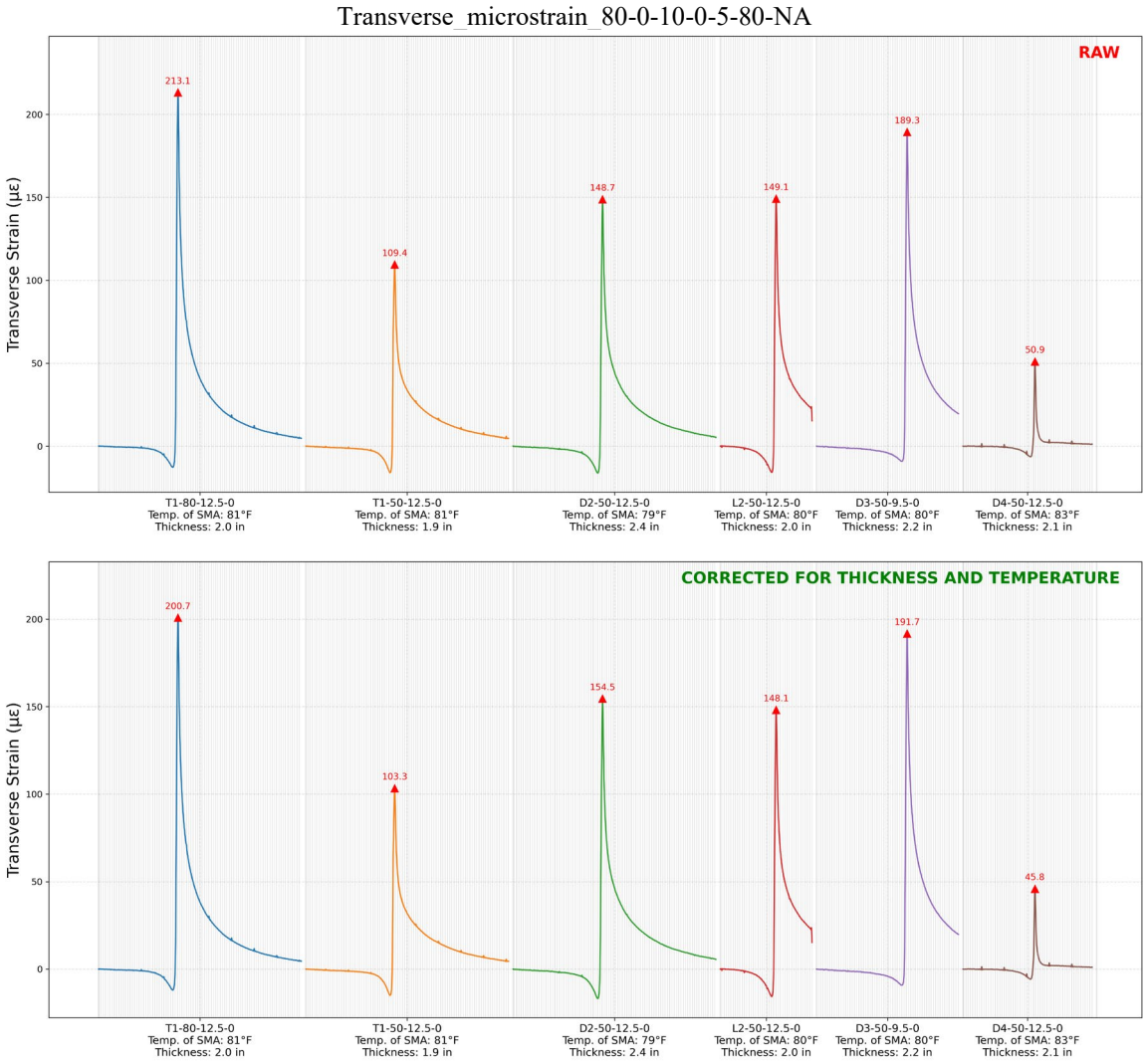

Figure 251. Graph. Comparison of measured and corrected transverse microstrain under single-axle loading (P_1 = 80 psi; L_1 = 10 kip; speed = 5 mph)

Transverse_microstrain_80-120-10-10-5-80-3.5

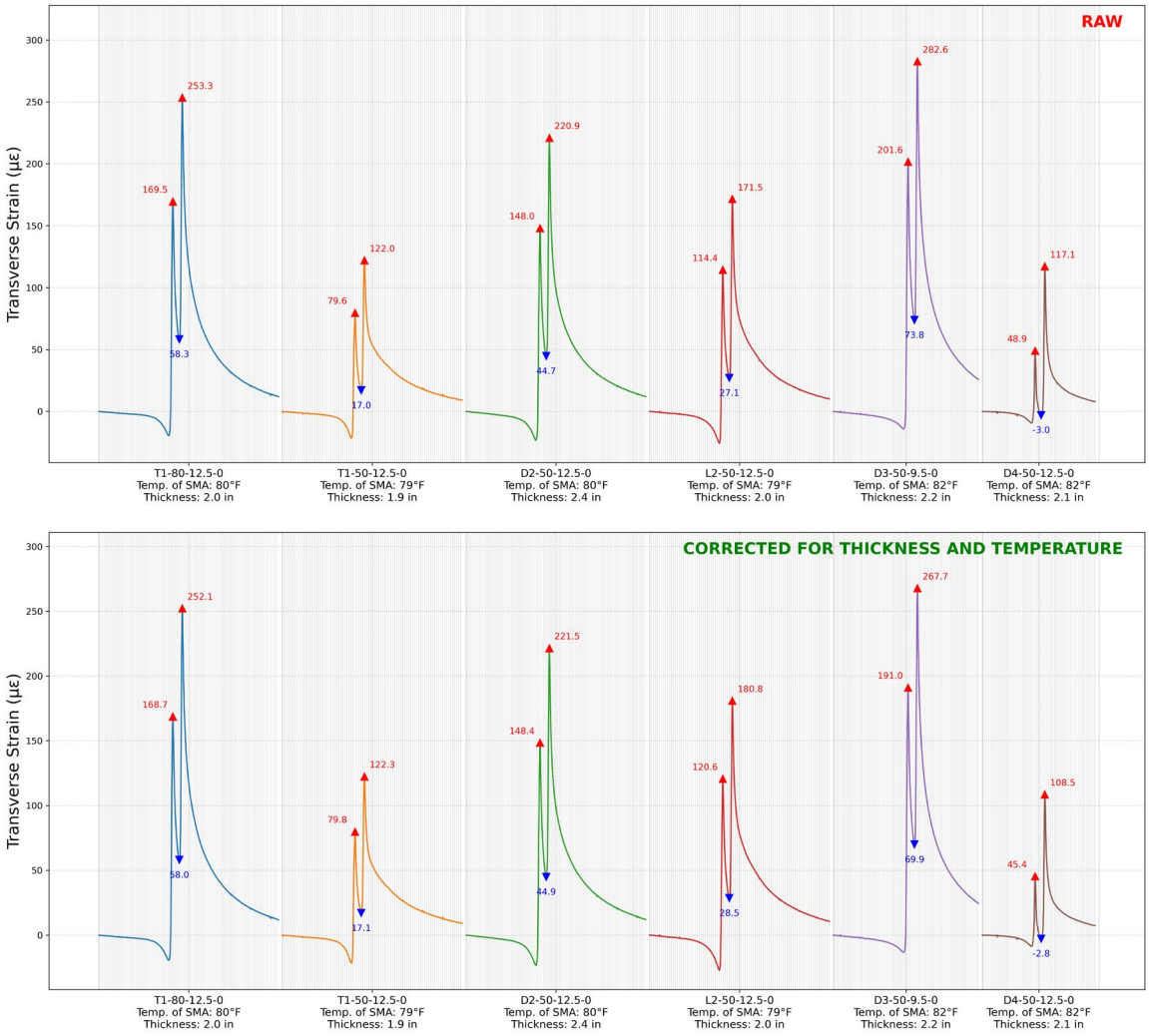

Figure 252. Graph. Comparison of measured and corrected transverse microstrain under tandem-axle loading with asymmetric tire pressures (P_1 = 80 psi, P_2 = 120 psi; L_1 = 10 kip, L_2 = 10 kip; speed = 5 mph; axle spacing = 3.5 ft)

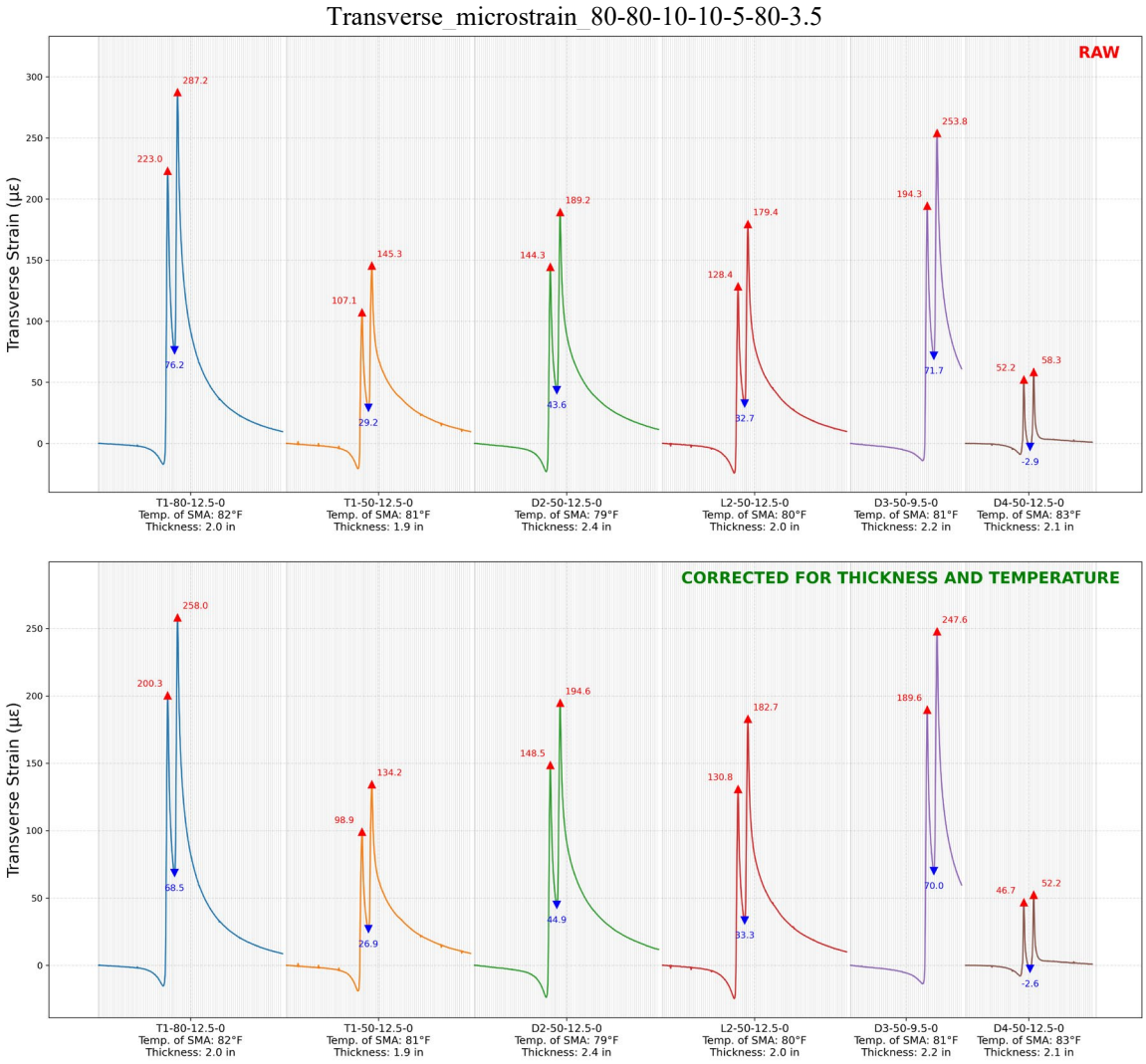

Figure 253. Graph. Comparison of measured and corrected transverse microstrain under tandem-axle loading (P_1 = 80 psi, P_2 = 80 psi; L_1 = 10 kip, L_2 = 10 kip; speed = 5 mph; axle spacing = 3.5 ft)

APPENDIX J: LISTS OF QUARRIES

Table 78. List of Local Quarries

Site Name	County	PLSS Location
Mill Creek CS42	Adams	SW 01 02S 08W
Belvidere Quarry	Boone	09 43N 03E
Lee Quarry	Boone	SE 32 43N 03E
Wheeler Road Quarry	Boone	NE 19 43N 03E
Irene Quarry #116	Boone	NW 09 43N 02E
State Street Quarry	Boone	NW 19 44N 03E
Bedrock Quarry	Carroll	SW 23 25N 03E
Lanark Quarry	Carroll	17 25N 06E
Sword Quarry	Carroll	SE 18 23N 07E
Mt. Carroll Quarry	Carroll	NE 06 24N 05E
Sturtz Quarry	Carroll	SE 17 25N 06E
Heldt Bros. Quarry	Carroll	SW 31 25N 06E
Savanna Quarry	Carroll	SW 18 24N 04E
Mount Carroll Quarry	Carroll	SW 10 24N 04E
Pana Quarry	Christian	SE 18 11N 01W
Casey Stone Quarry	Clark	05 09N 14W
North Quarry #305-Casey	Clark	S2 28 20N 14W
North Quarry	Clark	NW 29 11N 11W
Ashmore and Sand Pits	Coles	NW 32 13N 10E
Federal Quarry	Cook	NW 10 38N 12E
Thornton Quarry	Cook	NE 33 36N 14E
McCook Quarry	Cook	S2 15 38N 12E
DeKalb Quarry	DeKalb	NE 15 40N 05E
Sycamore Quarry	DeKalb	NE 12 41N 04E
Tuscola Quarry	Douglas	NW 06 15N 09E
Kane Quarry #2	Greene	SW 27 09N 12W
Aux Sable Stone	Grundy	30 34N 08E
Carthage Quarry	Hancock	SE 13 05N 06W
Gray Quarry	Hancock	NW 31 05N 08W
O'Neal Quarry	Hancock	NE 24 04N 05W
Hardin County Quarry	Hardin	NW 03 12S 09E
Cave-In-Rock Quarry	Hardin	08 12S 10E
Rosiclare Quarry	Hardin	SE 35 12S 07E
Biggsville Quarry	Henderson	SW 17 10N 04W
Dallas City Quarry	Henderson	SW 36 08N 07W
Cleveland Quarry	Henry	SW 31 18N 02E
Ashkum Quarry	Iroquois	16 28N 10E

Site Name	County	PLSS Location
Kinkaid #1 Quarry	Jackson	NW 06 08S 04W
Sievers Quarry	Jersey	NE 08 08N 13W
A. Distler	Jo Daviess	NE 02 28N 02E
Trannel	Jo Daviess	NE 04 28N 01W
Yungbluth Quarry	Jo Daviess	SW 23 28N 04E
Roth	Jo Daviess	NE 35 29N 02W
Millershone Quarry	Jo Daviess	NW 20 27N 04E
Goodmiller Quarry	Jo Daviess	SE 21 26N 04E
Hahn Quarry	Jo Daviess	21 27N 02E
P. Mark Quarry	Jo Daviess	18 28N 05E
M.J. Stone	Jo Daviess	SW 33 28N 04E
Spillane Quarry	Jo Daviess	12 39N 03E
Cypress Plant #15	Johnson	E2 05 05N 10W
Ramona Quarry	Johnson	NW 11 12S 02E
Fox Flagstone Pit	Kane	22 39N 08E
Manteno Quarry	Kankakee	SW 20 32N 12E
Kankakee Quarry	Kankakee	NW 20 30N 14W
Manteno Quarry (east)	Kankakee	E2 33 32N 12E
Central Quarry	Kendall	SW 28 35N 07E
Kendall County Quarry	Kendall	29 35N 07E
Lisbon Quarry	Kendall	NE 29 35N 07E
Dimmick Quarry	LaSalle	34 34N 01E
Utica Quarry	LaSalle	SE 17 33N 02E
Troy Grove	LaSalle	SW 25 35N 01E
Vermillion Quarry	LaSalle	NW 20 32N 02E
Kehoe Quarry	Lee	NW 33 22N 08E
Stoneridge Quarry	Lee	NE 26 39N 01E
Wastone Quarry	Lee	NW 07 21N 09E
Amboy Quarry (Robbins)	Lee	SW 16 20N 10E
Dixon Quarry (Russel)	Lee	NE 28 21N 09E
Dome Quarry	Lee	27 22N 09E
McDowell Quarry	Livingston	NW 23 27N 05E
Weston Quarry	Livingston	NW 22 27N 05E
Fairbury Quarry	Livingston	06 26N 06E
IFFT Quarry	Livingston	SW 19 27N 05E
McDowell II	Livingston	30 27N 06E
Rowe Quarry	Livingston	31 29N 05E
Lohr Quarry	Madison	E2 05 05N 10W
Tennessee Quarry	McDonough	02 04N 04W
Athens Quarry	Menard	SW 18 19N 05W

Site Name	County	PLSS Location
Waterloo Plant #7	Monroe	NE 08 03S 09W
Nokomis Quarry	Montgomery	NE 10 10N 02W
Nokomis Quarry (duplicate)	Montgomery	NE 10 10N 02W
Kemper Quarry	Ogle	NE 11 22N 08E
Galena Trail Quarry	Ogle	17 23N 08E
Limekiln Quarry	Ogle	NE 32 24N 10E
Oregon Quarry	Ogle	NE 20 23N 10E
Rochelle Quarry	Ogle	NW 40 20N 02E
Boreman Quarry	Ogle	NW 33 25N 09E
Byron Quarry	Ogle	SE 20 25N 11E
Oregon Quarry (Sheely Aggregates)	Ogle	SW 16 23N 09E
Steve Bensh & Sons	Ogle	NE 23 24N 10E
Fairdale Quarry	Ogle	25 42N 02E
Buckeye (Independence 2)	Pike	SE 29 06S 03W
Junction	Pike	NW 16 03S 03W
New Hartford	Pike	02 08S 03W
Valley City Quarry	Pike	NW 20 04S 02W
Chambersburg Quarry	Pike	SE 08 03S 02W
Florence Quarry	Pike	NW 10 05S 02W
Milan Quarry	Rock Island	NW 25 17N 02W
Allied Quarry	Rock Island	SE 14 16N 02E
Midway Stone	Rock Island	SW 16 18N 02E
Thomas Quarry	Scott	SW 35 13N 13W
Brush Creek Quarry	Shelby	25 10N 04E
Casper Stolle	St. Clair	NW 13 01N 10W
Dupo Plant #9	St. Clair	NE 28 01N 10W
East St. Louis Quarry	St. Clair	SE 14 01N 10W
Dwyer Quarry	Stephenson	SE 04 26N 08E
Offenheiser, R. Quarry	Stephenson	NE 02 26N 05E
Brush Creek	Stephenson	SW 01 28N 07E
Tessendorf Quarry	Stephenson	NE 27 28N 06E
Ivey Quarry	Stephenson	16 28N 06E
Mauer (Winneshiek) Quarry	Stephenson	SW 09 27N 08E
Bolen Road Quarry	Stephenson	NW 36 27N 09E
Midwest-Hartline	Union	SE 17 12S 01W
Jonesboro Quarry #4	Union	SW 20 13S 01W
Fairmount Quarry	Vermilion	SE 18 18N 13W
Monmouth Quarry	Warren	01 11N 03W
Valley Quarry MC07	Warren	NW 25 09N 01W
Emerson Quarry (L. Deets)	Whiteside	SE 13 21N 06E

Site Name	County	PLSS Location
Siers Quarry	Whiteside	NW 16 22N 07E
Garden Plain Quarry	Whiteside	NW 21 21N 03E
111th St. Quarry	Will	SE 14 37N 09E
119th St. Quarry	Will	NW 23 37N 09E
Joliet (Bromberek's Flagstone Co.)	Will	22 34N 10E
Barbers Corner Quarry	Will	SW 03 37N 10E
Plainfield Quarry	Will	NW 36 37N 08E
Romeoville Quarry	Will	NW 10 36N 10E
Joliet Quarry	Will	E2 28 35N 10E
Bedrock Quarry	Winnebago	SW 11 45N 02E
Blacks Quarry #127	Winnebago	SE 35 46N 01E
Johnson Quarry	Winnebago	SE 09 43N 02E
Truman, Richard Quarry	Winnebago	SE 27 46N 02E
Daisy Field Quarry	Winnebago	29 44N 01E
Rockton Rock, LLC	Winnebago	35 46N 01E
Warren Oleson	Winnebago	26 26N 10E
Roscoe (Genestra) #133	Winnebago	22 45N 01E

Table 79. List of Non-Local Quarries

Quarry Name	Address	State
New Frontier Trap Rock (Iron Mountain Trap Rock)	1325 Highway N, Ironton, MO 63650	MO
Trap Rock & Granite Quarries, LLC	11313 Hwy N, Ironton, MO 63650	MO
Central Stone Company (Butler Hill Granite Quarry)	5601 Highway DD, Farmington, MO 63640	MO
Shoreline Aggregate Solutions	Regional supplier – Northwest Indiana / Michigan City, IN	IN
Beemsterboer Slag Corporation	3411 Sheffield Ave, Hammond, IN 46327	IN
Dresser Trap Rock, Inc.	W7127 County Road S, Dresser, WI 54009	WI
Milestone Materials (Baraboo Quartzite Quarry)	E11614A Quarry Rd, Baraboo, WI 53913	WI
Mathy Construction / Milestone Materials (Rib Mountain Quarry)	Rib Mountain area, Marathon County, WI	WI
NEI Aggregates / Wisconsin Red Granite Quarries	Marathon and Waupaca Counties, WI	WI


Illinois Department
of Transportation


ILLINOIS